The Effect of Inclusions in Brittle Material

by

Raymond Pinho Janeiro

B.S., Civil Engineering (2003)
University of New Haven

Submitted to the Department of Civil and Environmental Engineering
in Partial Fulfillment of the Requirements for the Degree of
Master of Science in Civil and Environmental Engineering

at the

Massachusetts Institute of Technology

June 2009

Signature of Author.....
Department of Civil and Environmental Engineering
May 8, 2009

Certified by.....
Herbert H. Einstein
Professor of Civil and Environmental Engineering
Thesis Supervisor

Accepted by.....
Daniele Veneziano
Professor of Civil and Environmental Engineering
Chairman, Departmental Committee for Graduate Students

The Effect of Inclusions in Brittle Material

by

Raymond Pinho Janeiro

Submitted to the Department of Civil and Environmental Engineering

on May 8, 2009 in Partial Fulfillment of the

Requirements for the Degree of Master of Science

in Civil and Environmental Engineering

ABSTRACT

This thesis experimentally investigates the cracking behavior of brittle heterogeneous materials. Unconfined, uniaxial compression tests are conducted on prismatic gypsum specimens containing either one, or two, inclusions. These inclusions are of different strengths, stiffnesses, shapes, and sizes. Real-time video and high speed video (HSV) systems are used to capture the sequence of cracking events, such as initiation and propagation. The coalescence processes associated with the specimens containing an inclusion pair was also studied. In addition to examining the effects of shape, strength, and stiffness for an inclusion pair, the effect of the inclusion inclination angle on coalescence is also investigated.

Some observations reported in this study compare well with those of other researchers, while other observations are quite different. In general, the overall cracking sequences are similar to those reported previously; on the other hand, the amount of debonding observed at the inclusion interface is significantly less. Moreover, the extent of shear crack growth at an inclusion boundary increased substantially in specimens containing two inclusions, compared to those with single inclusions. The coalescence patterns associated with specimens containing an inclusion pair is also compared to past work done by the MIT rock mechanics group on specimens containing double flaws. These results are found to be remarkably similar. In addition to studying cracking behavior, the goal of this study is to provide a database for future work in formulating predictive models on the behavior of materials with inclusions.

Thesis Supervisor: Herbert Einstein
Title: Professor of Civil and Environmental Engineering

ACKNOWLEDGEMENTS

If you are reading this, it could only mean one of two things: either you are interested in my research, or you want to collect some dirt on my life. In whichever case…enjoy!

I must begin by thanking Professor Einstein, as I would never have stepped foot at MIT if it wasn't for him. Over the past two years he has been more than just an advisor. To say that he cares deeply for every one of his students is an understatement, and he would always know if there was anything wrong by just looking at someone's face. He never ceases to amaze me in everything from his compassion to his vast knowledge and even his filing system.

I must also thank my cousin (and best-man) Mark, if it wasn't for him I would never have considered graduate school. For that I can't thank you enough. Go Boilermakers!

I would also like to thank all my peers, especially those in the 3rd floor of building one. I have thoroughly enjoyed sharing all the soccer matches and beer with you. Past members of the MIT rock mechanics group, specifically Louis Wong and Jay Miller, have coached me in many aspects of my research, and the current members of the group (Bruno Silva, Zenzi Brooks, and Mike Berry) have worked diligently making this specific research topic better rounded. I would also like to thank Doctor Germaine and Stephen Rudolph for their experimental expertise and for busting my stones at every opportunity. Other notable mentions include Sandi Lipnoski and Jim Bales of the MIT Edgerton Center.

I must thank Megan for *everything* past, present, and future. Whether it was cleaning my apartment, or running unconfined compression tests with me, you always did it with a loving smile. It is now my turn to return the favor.

I also have to thank my parents for working harder than anyone else I know. They made sure, from the very first day they came into this country, that I had every opportunity and ensured that I made the most of it. I also thank my sisters Melissa for always making me laugh and Emily for always making me smile.

TABLE OF CONTENTS

CHAPTER 1 – Introduction

1.1 Motivation

Inclusions are found in many natural, as well as, man-made structural materials. In many natural rocks, grains of one type of mineral composition and size are embedded in a matrix of different mineral compositions and grain sizes. Regarding man-made material, inclusions in the form of aggregate are common in concrete. It is essential, therefore, to understand how these inclusions impact the performance of the material as a whole. More specifically, there is a need to study how the cracking process (initiation, propagation, and coalescence) of the composite material is affected by inclusions.

Understanding how inclusions within a matrix behave is important for a variety of reasons. Inclusions have the potential for weakening, or strengthening, a composite material. Understanding more precisely how inclusions behave within a given material is, therefore, extremely important. A more thorough understanding of inclusion effects on the performance of naturally occurring material is also essential.

1.2 Approach

There are many inclusion characteristics that can impact how the overall material performs. These include the strength, stiffness, shape, and size of the inclusion. Various research groups have studied the effects of a single inclusion placed within a matrix (Grübl, 1979; Maji and Shah, 1989 and others). Little experimental work has been done in understanding how inclusions interact with one another within a confining matrix (e.g., Zaitsev and Wittmann, 1981; Maji and Shah, 1989; 1990), which, nevertheless, forms a basis of this study (a complete literature review will be presented in Section 2.4).

This research involves experimental studies (uniaxial compression tests) on prismatic specimens of gypsum material containing inclusions of various properties (i.e., strength, stiffness, shape,

and size). This study aims to broaden the work done by past researchers, specifically in better understanding the cracking and coalescence processes associated with a composite material. An underlying goal of this study is to also be able to compare the results of this research to that done by past MIT rock mechanics group members. The following points will be addressed in this experimental study to achieve all of the stated goals:

- Perform experiments on molded prismatic specimens of gypsum containing single inclusions of varying shapes, sizes, strengths, and stiffnesses.
- Perform experiments on molded prismatic specimens of gypsum containing two inclusions of varying shapes and stiffnesses, set at various inclination angles.
- Use a high speed video camera during the testing of specimens containing single and double inclusions in order to observe the cracking processes associated with each specimen type; more specifically, to observe the complete sequence of cracking and to differentiate each crack type, whether it is tensile, shear, or a combination of the two.
- Regarding the specimens containing double inclusions, additional observations will be made in order to understand and differentiate the mode of crack coalescence relative to the inclusion pair.
- Integrate the results of this study with previous work done by the MIT rock mechanics group.

1.3 Organization of Thesis

This thesis will be organized in the following manner:

- Chapter 2 presents a background review on general fracture mechanics and previous studies done in this area of research, specifically fracture mechanics associated with a material containing inclusions.

- Chapter 3 explains the preparation of specimens containing inclusions in detail. It also explains the systematic manner in which unconfined, uniaxial tests on prismatic specimens of gypsum were performed and how the experimental data were interpreted.

- Chapter 4 & 5 summarizes the qualitative and quantitative results for the specimens containing single and double inclusions, respectively. Specifically, the cracking sequences for different specimen types and the stresses associated with these events (i.e., maximum stress, crack initiation stress, and coalescence) are studied.

- Chapter 6 presents a summary of the work done in this study and offers recommendations on how this area of research can progress in the future.

CHAPTER 2 – Background

2.1 Introduction

This chapter presents a review of past work done in the area of fracture mechanics. A theoretical approach to the study of fracture mechanics will first be presented, followed by an assessment of the experimental work done in this field. Lastly, the fracture processes of inclusions within a confining matrix will be examined in detail. The research done by Zaitsev and Wittmann (1981), Maji & Shah (1989; 1990), and the MIT rock mechanics group is quite pertinent to this study and will, therefore, be examined in detail.

2.2 Theoretical Fracture Mechanics

Before analyzing the fracture mechanics associated with an inclusion and its surrounding matrix, a brief review of crack propagation theory is presented. Griffith (1920) hypothesized that the theoretical cohesive strength of a brittle material is much greater than what is observed experimentally. Griffith obtained glass fibers and loaded these specimens in tension. According to his calculations, the theoretical atomic bond strength of the material was 100 to 1000 times greater than what his experimental tests measured.

Prior to this observation, Inglis (1913) had already developed an equation that defined the stress distribution around an elliptical void within an infinite plate (Figure 2.1). Inglis calculated the stress at a sharp flaw tip, when the flaw length (2a) is much larger than its width (2b), to be

$$\sigma_A = 2\sigma\sqrt{\frac{a}{r}} \tag{2.1}$$

where σ is the applied far field stress, a is the half-length of the flaw, and r is the radius of curvature of the flaw tip which is equal to b^2/a. Based on this theory, an increase in flaw length will increase the stress concentration at the flaw tip. The stress concentration at the tip will also decrease if the radius of curvature decreases. Crack initiation will occur when this local stress exceeds the tensile strength of the material.

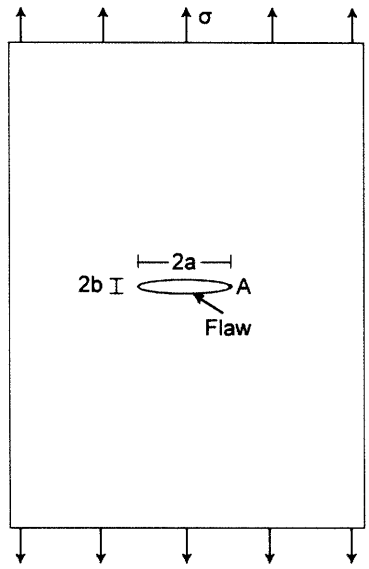

Figure 2.1 – An elliptical void within an infinite plate experiencing a far field tensile stress. Point "A" represents the location where σ_A is calculated from.

Griffith (1920) used the conservation of energy principle to develop a fracture theory prior to the development of his stress based theory. Consider the scenario depicted in Figure 2.1, but now with a plate thickness of B. With an increase in the applied stress, the flaw will increase in length. Therefore, the surface energy of the material surrounding the flaw will also increase in order to equal the increase in potential energy. The incremental increase in flaw surface area, dA, can be expressed as

$$\frac{d\Pi}{d\mathrm{A}} + \frac{dW_s}{d\mathrm{A}} = \frac{d\mathrm{E}}{d\mathrm{A}} = 0 \tag{2.2}$$

where Π is the supplied potential energy and internal strain energy of the system, W_s is the work required to create new crack surfaces, and E is the total energy of the system. Π and W_s can also be written as

$$\Pi = \Pi_o - \frac{\pi\sigma^2 a^2 B}{E} \tag{2.3}$$

$$W_s = 4\gamma aB \tag{2.4}$$

where Π_o is the potential energy of the flawless plate, and γ is the specific surface energy of the material. Griffith used equations (2.2 through 2.4) to calculate the stress (σ_f) needed to propagate a crack, which is written as

$$\sigma_f = \sqrt{\frac{2E\gamma}{\pi a}} \tag{2.5}$$

Inglis (1913) and Griffith (1920) provided the framework for crack propagation in a tensile stress condition. Griffith (1920) also experimented with crack growth in a compressive stress state and witnessed a phenomenon now characterized as wing cracks. This phenomenon was later explained with a sliding wing crack model (see Section 2.4 for derivation), which describes the propagating curvilinear nature of tensile cracks after initiating from an inclined flaw subjected to a compressive stress (Brace and Bombolakis, 1963; Gramberg, 1965; Hoek and Bieniawski, 1965; Moss and Gupta, 1982; Horii and Nemat-Nasser, 1986; Ashby and Sammis, 1990; Kemeny and Cook, 1991; Germanovich and Dyskin, 2000).

There are three main types, or modes, of deformation at a crack tip (Figure 2.2). These are Mode I (tensile opening), Mode II (in-plane shearing), and Mode III (out-of-plane shearing). It should be noted that a crack may also undergo more than one mode of deformation, thereby resulting in a *mixed mode* type of fracture as the crack is subjected to combined stresses.

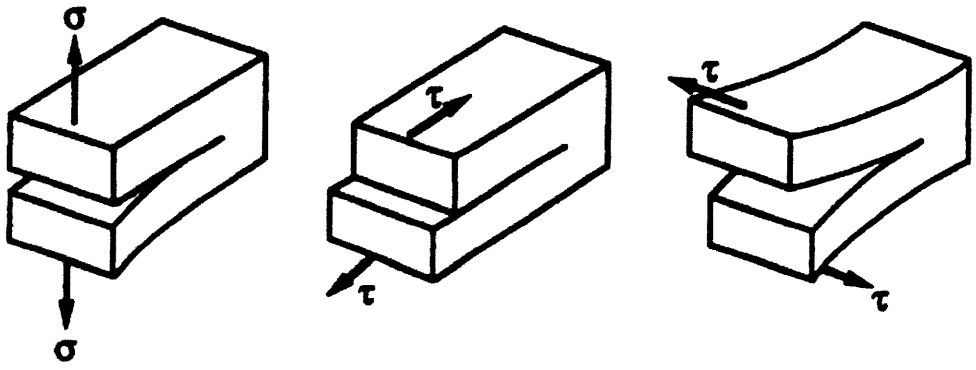

Figure 2.2 – The three modes of crack deformation and fracture. From left to right: Mode I (tensile), Mode II (shear), and Mode III (shear) (Shah, 1995).

Irwin (1957) applied his energy release rate concept to Griffith's energy balance principle. This resulted in the conception of a stress intensity factor, K, which correlates the stresses and displacements around a flaw tip with the energy that is released when a crack is propagating.

Since then, several other criteria have been developed to model fracture in a mixed-mode loading scenario (Erdogan and Sih, 1963; Hussain et al., 1974; and Sih, 1973; 1974).

In the past linear elastic fracture mechanics (LEFM) was used extensively to study rock, since it was believed that brittle material behaved purely elastically. Recently, it was discovered that the area ahead of a crack tip is actually plastic. This inelastic region is the result of microcracking and is commonly referred to as the process zone (Anderson, 2005). The process zone of a crack tip has been studied extensively over the past decades (Friedman et al., 1972; Segall and Pollard, 1983, etc.). More recently, the effects of this process zone have been modeled for brittle materials, such as, concrete (Hillerborg et al., 1976; Hillerborg, 1991) and rock (Reyes, 1987; Bobet, 1997). This was done by using the cohesive zone model (Dugdale, 1960; Barenblatt, 1962).

The interaction of multiple cracks has also been studied extensively. In 1985, two methods for calculating how cracks increase the stress at the tips of adjacent cracks were developed (Costin, 1985; Kachanov, 1985). Costin (1985) formed a model to find the effects of several cracks within a homogenous solid being subjected to a far field stress. In order to calculate the net effect of the crack group, each crack's relative stress intensity had to be individually calculated within the homogenous body. Kachanov (1985), on the other hand, created a method that analyzed crack interaction before propagation. Ashby and Hallam (1986) used the sliding wing crack model and applied it to solids containing several flaws. After tensile crack initiation, tensile wing cracks will propagate adjacent to one another, thereby, creating beams within the solid. As loading continues, these beams will lengthen and eventually deflect. This results in an increase in the stress intensity at the pre-existing crack tips. This model was later modified in order to account for the curved nature of tensile wing cracks (Kemeny and Cook, 1987).

2.3 Experimental Fracture Mechanics

Brace and Bombolakis (1963) were the first documented people to observe the propagation of tensile wing cracks from a pre-existing flaw within a brittle material loaded in compression. Since then, many other experimentalists have studied the various crack processes associated with

pre-existing flaws within various brittle materials. A list of these individuals is presented below, which is also presented in Wong (2008).

Rock-like brittle/semi-brittle materials

- Columbia Resin 39 - (Bombolakis, 1963; Brace & Bombolakis, 1963; Nemat-Nasser & Horii, 1982; Horii & Nemat-Nasser, 1985)
- Glass - (Hoek & Bieniawski, 1965; Bieniawski, 1967)
- Plaster of Paris - (Lajtai, 1970; Nesetova & Lajtai, 1973)
- Polymethylmethacrilate, or PMMA - (Petit & Barquins, 1988; Chaker & Barquins, 1996)
- Molded Gypsum - (Reyes, 1991; Reyes & Einstein, 1991; Shen et al., 1995; Bobet, 1997; Bobet & Einstein, 1998; Sagong, 2001; Sagong & Bobet, 2002)
- Sandstone-like Molded Barite - (Wong, 1997; Wong & Chau, 1997, 1998; Wong et al., 2001)
- Sandstone-like Concrete Mix - (Mughieda & Alzo'ubi, 2004)

Natural rocks

- Sandstone - (Petit & Barquins, 1988)
- Granodiorite - (Ingraffea & Heuze, 1980)
- Limestone - (Ingraffea & Heuze, 1980)
- Granite - (Martinez, 1999; Miller, 2008)
- Marble - (Huang et al., 1990; Chen et al., 1995; Martinez, 1999; Li et al., 2005; Wong 2008)
- Ice - (Wang & Shrive, 1995)

It should be noted that not only did the brittle material vary, but also the specimen size and flaw dimensions. The specimen sizes ranged widely from 50mm x 32mm x 5mm (Petit and Barquins, 1988) to 635mm x 279mm x 203mm (Mughieda and Alzo'ubi, 2004). The flaw lengths varied from 10 mm to 50 mm, while the flaw apertures varied from closed to 3 mm.

The observations reported regarding the fracture processes associated with a single flaw in a brittle material are similar. Tensile cracks were always the first cracks to initiate and propagate.

In rock specimens, shear cracks were typically observed afterwards. Chen et al. (1995) observed an alleged x-shaped band of microcracks that occurred just before specimen failure, but did not provide data to confirm their observation (e.g., SEM analysis). Li et al. (2005) later observed the formation of white patches in locations where tensile cracks would later form. Wong (2008) provides a good summary of other experiments with specimens containing single flaws.

Wong (2008) performed his own study on gypsum and marble specimens containing single flaws. He reported seven major cracks types (Figure 2.3).

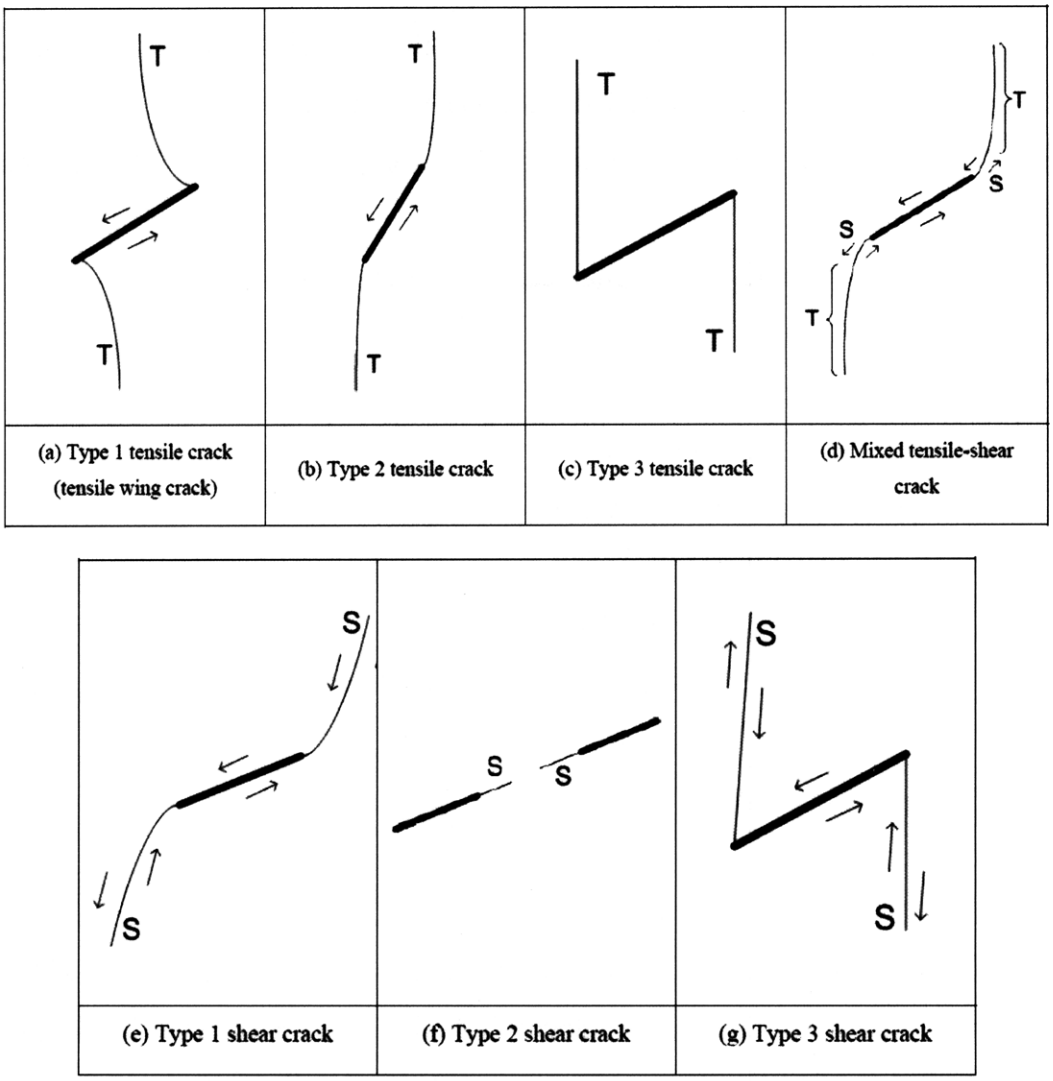

Figure 2.3 – The seven crack types associated with a single flaw in gypsum and marble (Wong, 2008).

Experiments on specimens with single flaws helped define fracture processes, such as, crack initiation and propagation. Typically, however, a material contains several flaw-type defects. Therefore, it is essential to study the fracture processes associated with the interaction of these flaws. Experiments on specimens with double, and sometimes multiple, flaws were performed in order to study interaction and coalescence (e.g., Horii and Nemat-Nasser, 1985). A way of defining various flaw geometries had to be established in order to systemically study the fracture behavior of a flaw pair. A sketch of the description used in this study, which was adopted from Wong (2008), is shown in Figure 2.4. Wong (2008) conducted an extensive review on previous experimental work done by other researchers, but this study will place emphasis on the work done by the MIT rock mechanics group.

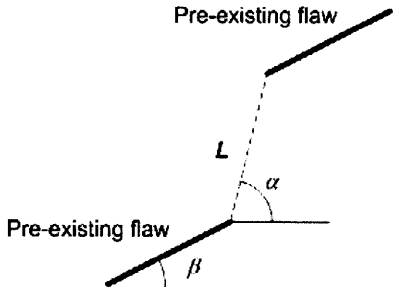

Figure 2.4 – Double flaw geometry used by Wong (2008) defined by an inclination angle (β), a bridging angle (α), and a ligament length (L).

Reyes (1991) performed tests on specimens containing double flaws. These flaws were cast in molded gypsum and loaded in uniaxial compression. Reyes (1991) observed that coalescence occurred by means of secondary cracks when the two flaws did not overlap; whereas, with an overlapping geometry coalescence was caused by primary tensile wing cracks. Surface spalling and material crushing occurred during the propagation of secondary cracks, which suggest these secondary cracks may be shear cracks.

Shen et al. (1995) also conducted tests on specimens containing double flaws, but tested both opened and closed flaw specimens in shear. The coalescence patterns observed are shown in Figures 2.5 and 2.6.

Number	Specimen	Critical Load at Coalescence, MPa	Schematic Path of Coalescence (a) frictional (b) nonfrictional	Description of Coalescence	Mode of Coalescence
1	30°/15° (2 specimens with friction fractures + 1 specimen with nonfrictional fractures)	No coalescence (frictional fractures) 17.2 MPa (nonfrictional fractures)	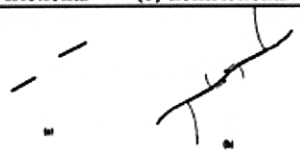	Type of coalescing fracture: secondary fracture. Initiation position: preexisting fracture tips. Surface characterization: rough, with many small kink steps; containing crushed gypsum.	Shearing
2	45°/0° (2 + 2)	21.9, 22.2 MPa (frictional fractures) 19.4, 17.9 MPa (nonfrictional fractures)	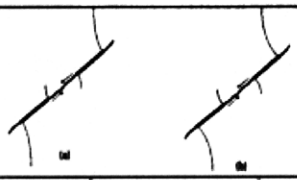	Type of coalescing fracture: secondary fracture. Initiation position: preexisting fracture tips. Surface characterization: rough, with many small kink steps; containing crushed gypsum.	Shearing
3	45°/15° (1 + 1)[§]	17.8 MPa (frictional fractures) 14.1 MPa (nonfrictional fractures)	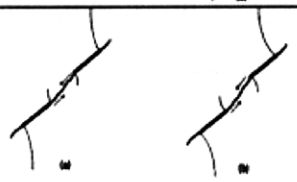	Type of coalescing fracture: secondary fracture. Initiation position: preexisting fracture tips. Surface characterization: rough, with several large kink steps. Noticeable crushed gypsum presented.	Shearing
4	45°/30° (1 + 1)[§]	19.2 MPa (frictional fractures) 14.1 MPa (nonfrictional fractures)		Type of coalescing fracture: secondary fracture. Initiation position: unclear. Surface characterization: rough, with two big kink steps. No noticeable crushed gypsum.	Shearing +tension
5	45°/45° (2 + 1)	(a) 17.8, MPa (a') 16.8* MPa (frictional fractures) (b) 16.4 MPa (nonfrictional fractures)	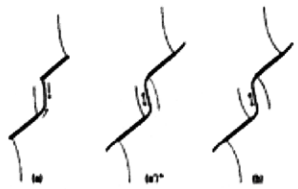	Type of coalescing fracture: (a) wing fracture + secondary fracture; (a') and (b) secondary fracture. Initiation position: (a) preexisting fracture tips; (a') and (b) intact material. Surface characterization: some parts are clean and smooth while other parts are rough with crushed gypsum.	Shearing +tension
6	45°/60° (2 + 1)	17.8, 16.8 MPa (frictional fractures) 16.4 MPa (nonfrictional fractures)	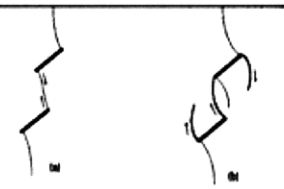	Type of coalescing fracture: wing fracture. Initiation position: preexisting fracture tips. Surface characterization: smooth and clean. Note: additional secondary fractures occur from the outer tips in case (b).	Tension
7	45°/75° (2 + 1)	(a) 21.0 MPa (a') 23.1 MPa (frictional fractures) (b) 17.6 MPa (nonfrictional fractures)	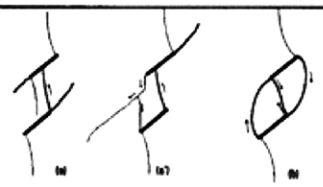	Type of coalescing fracture: wing fracture. Initiation position: preexisting fracture tips. Surface characterization: smooth and clean. Note additional coalescence by secondary fractures occurs in case (b).	Tension

Figure 2.5 – Coalescence patterns reported by Shen et al. (1995), which is continued in Figure 2.6.

Number	Specimen	Critical Load at Coalescence MPa	Schematic Path of Coalescence (a) frictional (b) nonfrictional	Description of Coalescence	Mode of Coalescence
8	60°/-15° (2 + 1)	22.4, 21.4 MPa (frictional fractures) 17.8 MPa (nonfrictional fractures)	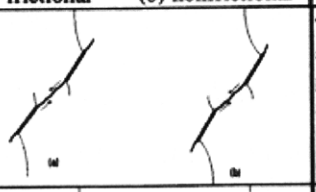	Type of coalescing fracture: secondary fracture. Initiation position: preexisting fracture tips. Surface characterization: rough, with many small kink steps; containing crushed gypsum.	Shearing
9	60°/0° (4+ 1)	20.5, 17.8, 20.3, 20.9 MPa (frictional fractures) 15.2 MPa (nonfrictional fractures)	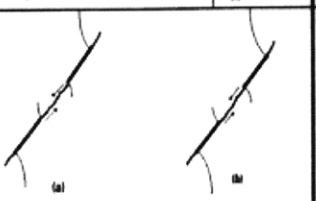	Type of coalescing fracture: secondary fracture. Initiation position: preexisting fracture tips. Surface characterization: rough, with several large kink steps. Noticeable crushed gypsum presented.	Shearing
10	60°/15° (1 + 1)§	18.5 MPa (frictional fractures) 13.7 MPa (nonfrictional fractures)	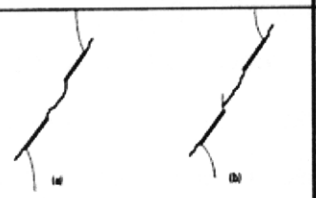	Type of coalescing fracture: (a) secondary fracture ; (b) secondary fracture + wing fracture. Initiation position: pre-existing fracture tips. Surface characterization: rough, with a few kink steps. No noticeable crushed gypsum.	Shearing +tension
11	60°/30° (1 + 1)§	19.2 MPa (frictional fractures) 14.2 MPa (nonfrictional fractures)	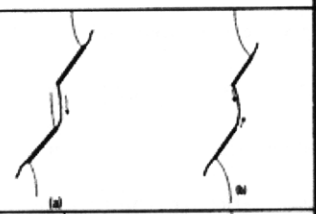	Type of coalescing fracture: (a) wing fracture ; (b) wing fracture + secondary fracture. Initiation position: preexisting fracture tips; Surface characterization: most parts are clean and smooth.	Tension +shearing
12	60°/45° (2 + 1)	19.9, 22.2 MPa (frictional fractures) 18.0 MPa (nonfrictional fractures)	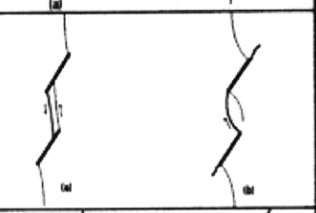	Type of coalescing fracture: wing fracture. Initiation position: preexisting fracture tips. Surface characterization: smooth and clean.	Tension
13	60°/60° (1 + 1)§	23.5 MPa (frictional fractures) 21.0 MPa (nonfrictional fractures)		Type of coalescing fracture: secondary fracture. Initiation position: preexisting fracture tips. Surface characterization: very rough, coated with a lot of crushed gypsum.	Shearing

§ Only two of the three specimens produced useful results, the other specimen failed due to mismanipulation of the loading machine.

* The frictional fractures in this specimen have weaker contact than other frictional fractures. The polyethylene sheets were left longer (45 min) by mistake before they were pulled out. As a result, the created fractures did not close firmly.

Figure 2.6 – Coalescence patterns reported by Shen et al. (1995) (continued).

Shen et al. (1995) also observed that the bridging angle of a flaw pair geometry impacted coalescence. A trend was noticed that can be categorized into three groups.

Small & Negative Bridging Angle – coalescence resulting from shear crack propagation.

Intermediate Bridging Angle – coalescence caused by the combination of shear and tensile cracks.

Large Bridging Angle – coalescence caused primarily by tensile cracks.

Bobet (1997) also tested specimens with open and closed flaws. These specimens were loaded in uniaxial or biaxial compression. Bobet (1997) observed that tensile cracks were the first cracks to initiate at the flaw tips. Secondary cracks also formed, which were identified as shear cracks. This determination was made based on post-mortem fractography analysis. If the surface of the crack had a plumose structure, it was recognized as a tensile crack; conversely, it was recorded as a shear crack if it had a rough, powdery appearance. The downside of this method is that investigation can only be done after failure. It is possible, therefore, to misinterpret the nature and sequence of crack initiation and propagation. Figure 2.7 depicts the five different coalescence types documented by Bobet (1997).

In order to resolve the issues with post-mortem fractography, Martinez (1999) utilized a high-speed video camera when he continued Bobet's (1997) work. Martinez (1999) used geometries tested by Bobet (1997) in two natural rock materials: marble and granite. Martinez (1999) also used a new loading profile, different from the incremental one used by Reyes (1987) and Bobet (1997). An incremental load cycle was needed in order to observe the different coalescence mechanisms. Martinez (1999), on the other hand, was able to continuously load specimens until failure, because of the advantages in using the high-speed camera, which captures fracture processes. Martinez (1999) observed five different types of coalescence, which are shown in Figure 2.8.

Type	Schematic path of Coalescence	Description of Coalescence	Coalescence cracks (Coalescence categories)
I	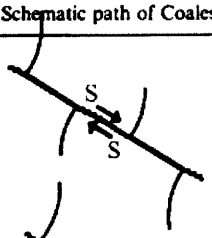	Type of coalescing fracture: secondary shear crack. Initiation position: preexisting flaw tips. Crack surface characterization: rough, with many small kink steps; contains crushed gypsum	Type 2 S + Type 2 S (Category 3)
II		Type of coalescing fracture: secondary shear and tensile cracks. Initiation position: preexisting flaw tips. Crack surface characterization: some parts are clean and smooth while other parts are rough with crushed gypsum	Type 2 S + T + Type 2 S (Category 5)
III	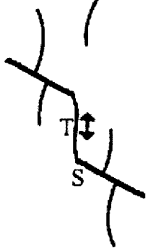	Type of coalescing fracture: secondary shear crack and wing crack. Initiation position: preexisting flaw tips. Crack surface characterization: some parts are clean and smooth while other parts are rough with crushed gypsum	Type 2 T + Type 2 S (Category 5)
IV	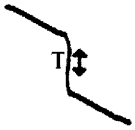	Type of coalescing fracture: wing crack. Initiation position: preexisting flaw tips. Crack surface characterization: smooth and clean.	Type 2 T (Category 6)
V	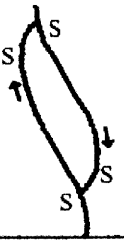	Type of coalescing fracture: secondary crack. Initiation position: preexisting flaw tips. Crack surface characterization: very rough, coated with a lot of crushed gypsum	Type 2 S + Type 1 S (similar coalescence pattern not observed in the present study)

Figure 2.7 – Coalescence patterns reported by Bobet and Einstein (1998).

Wong (2008) continued the flaw pair work done by Bobet (1997) and Martinez (1999). He used double flaws in specimens of gypsum and Carrara marble. Four test series were performed in each material, which are summarized in Table 2.1. The double flaw geometries were divided into two groups described as being either coplanar, or stepped. A coplanar geometry had a bridging angle equal to zero, while a stepped geometry had a bridging angle not equal to zero (refer to Figure 2.4).

TYPE I	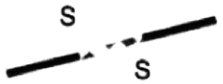	Produced by the linkage of two internal shear cracks
TYPE II	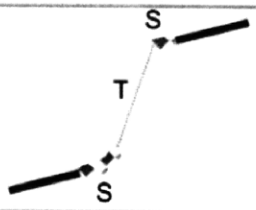	Produced by the linkage of two internal shear cracks by a vertical tensile crack (not a wing crack)
TYPE III	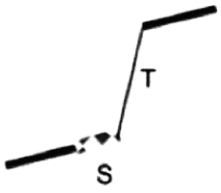	Produced by the propagation of the internal shear crack from one of the flaws until it reaches the internal wing crack of the other flaw
TYPE IV	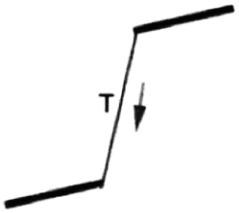	Produced by the propagation of an internal wing crack from one flaw until it reaches the other flaw. Observed only for granite, but not for marble.
TYPE IVB	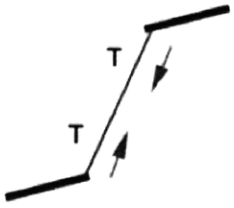	Produced by the linkage of two internal wing cracks that propagate until they join each other half-way. Observed only for granite, but not for marble.

Figure 2.8 – Coalescence patterns reported by Martinez (1999).

Test Series	Description	Ligament Length, L	Bridging Angle α (°)	Inclination Angle B (°)
1	coplanar	2a	0	0, 30, 45, 60, 75
2	stepped	2a	-60, -30, 0, 30, 60, 90, 120	30
3	coplanar	4a	0	0, 30, 45, 60, 75
4	stepped	4a	-60, -30, 0, 30, 60, 90, 120	30

Table 2.1 – Specimen geometries tested by Wong (2008). Refer to Figure 2.4 for details.

Wong (2008) distinguished nine different coalescence patterns, which he described with his seven crack types (Figure 2.3). A summary of these coalescence types is shown in Figure 2.9. Wong (2008) drew various conclusions regarding the flaw geometric parameters and the material type. These results are summarized below.

Ligament Length – A larger ligament length reduces the effects resulting from the interaction of two flaws. This observation was seen more often in coplanar geometries than in stepped geometries.

Flaw Inclination Angle (β) – For coplanar geometries, a zero inclination angle typically resulted in no coalescence. As the inclination angle increased, shear crack coalescence dominated. Tensile crack coalescence was mostly observed at large inclination angles.

Bridging Angle (α) – For stepped geometries, no trend could be determined between the specimens that experienced no coalescence, indirect coalescence, or direct coalescence. Regarding the geometries that coalesced directly, a small bridging angle typically resulted in shear coalescence. As the bridging angle increased, shear-tensile coalescence dominated, followed by pure tensile coalescence at very large bridging angles.

Material – Regardless of the flaw geometry (i.e., coplanar or stepped), tensile cracks occurred more often in marble specimens compared to gypsum specimens.

Category	Coalescence patterns	Crack types involved
1	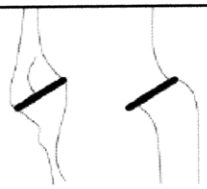	No coalescence
2	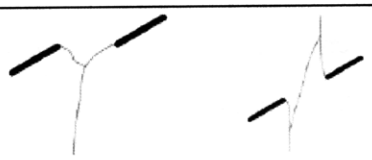	Indirect coalescence by two or multiple cracks (crack types vary)
3	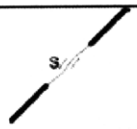	Type 2 S crack(s)
4	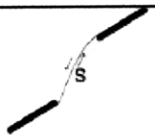	Type 1 S crack(s)
5	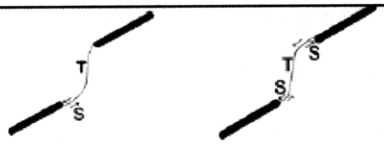	One or more type 2 S crack(s) and type 2 T crack segments between inner flaw tips
6		Type 2 T crack(s). There may be occasional short S segments present along the coalescence crack.
7	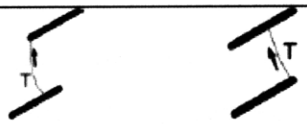	Type 1 T crack(s)
8		Flaw tips of the same side linked up by T crack(s) not displaying wing appearance (crack type not classified). There may be occasional short S segments present along the coalescence crack.
9	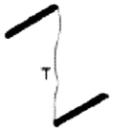	Type 3 T crack(s) linking right tip of the top flaw and left tip of the bottom flaw. There may be occasional short S segments present along the coalescence crack.

Figure 2.9 – The nine coalescence patterns reported by Wong (2008), where T = tensile and S = shear.

2.4 Fracture Mechanics of Materials with Inclusions

The fracture mechanics associated with a brittle heterogeneous material, specifically concrete, will be investigated in this section. Inclusions, which are referred to as aggregate, play a vital role in the composition of concrete. Concrete is a two phase material consisting of inclusions and a surrounding matrix; these two components are bonded together at the interface, which is sometimes referred to as a third phase (Figure 2.10).

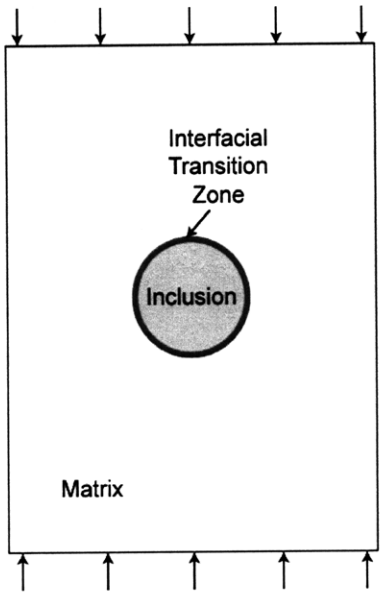

Figure 2.10 – The three components (inclusion, interfacial transition zone, and matrix) of a typical concrete material being subjected to a far field stress.

The interface, or interfacial transition zone, is considered the weakest part of the concrete material (Taylor and Broms, 1964). For a concrete material, the explanation lies within the microstructure of this zone, which is impacted by how the heterogeneous material is compacted and set. The grains of the cement paste are unable to become tightly packed with the moderately larger aggregate particles. This is commonly referred to as the "wall effect" as voids between the paste and aggregate form. The result is a very porous interface, which reduces the strength of this zone and, therefore, the material as a whole. An example of a porous interface observed in this study is depicted in Figure 2.11a. Note that while this applies to concrete it may not apply to other materials.

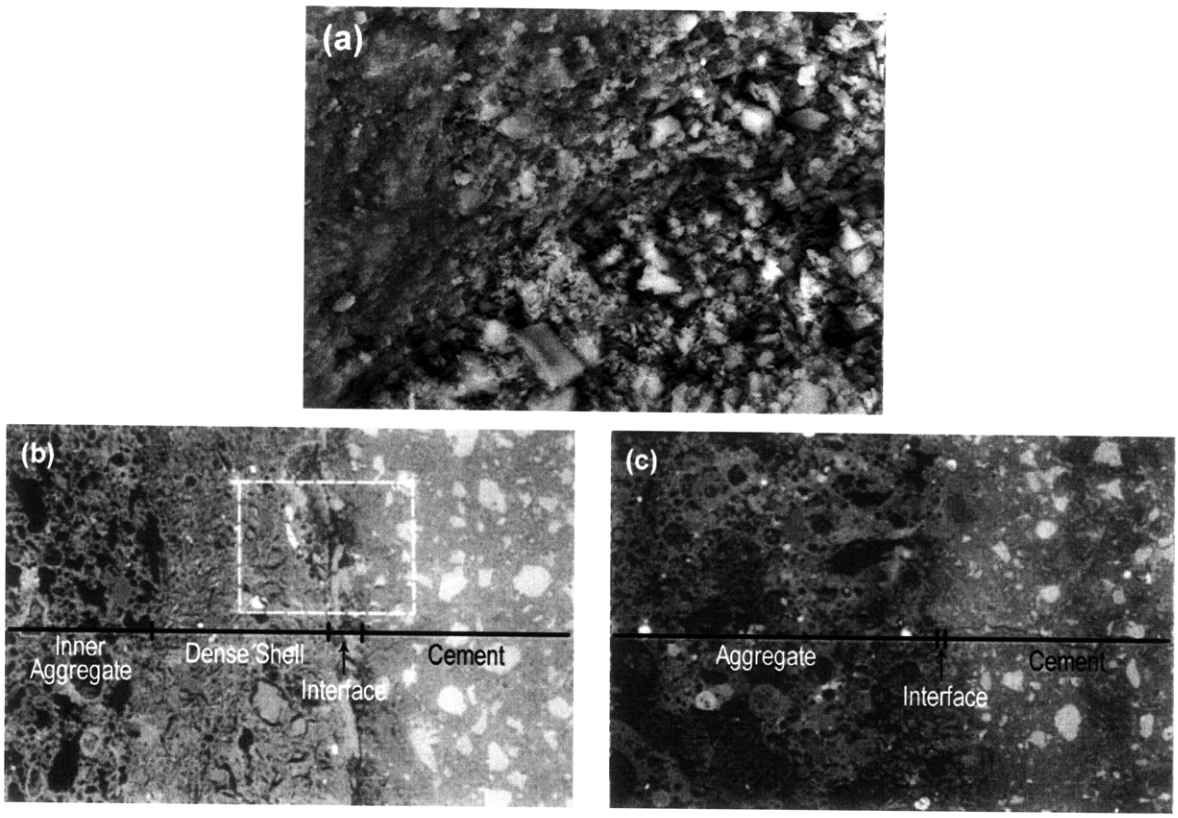

Figure 2.11 – (a) An ESEM image showing the porous interfacial transition zone of a stiff inclusion (top left) and its surrounding gypsum matrix (bottom right) at a 2500x magnification, (b) A SEM image detailing a piece of aggregate with a dense outer shell at a 200x magnification (Zhang and Gjørv, 1990), (c) A SEM image detailing a porous aggregate piece with no outer shell at a 200x magnification (Zhang and Gjørv, 1990).

The type of aggregate will impact the strength and thickness of the interface. Lightweight aggregate typically has a stronger interfacial transition zone than normal, or high-strength, aggregate. Since lightweight aggregate is typically quite porous, it can absorb a portion of the cement paste. This draws the paste closer to the aggregate, thereby reducing the porosity of the aggregate boundary and creating a mechanical interlock. Zhang and Gjørv (1990) and Lo and Cui (2004) showed that this assumption was correct using scanning electron microscopy (SEM). Zhang and Gjørv (1990) cast concrete specimens containing five different types of lightweight aggregate; qualitative observations were only made once the specimens cured (i.e., the specimens were not subjected to loading). They observed that the aggregate with a very dense outer layer (shell) had a very porous interface; whereas, aggregate with a porous shell had a very dense and homogenous interface (Figure 2.11b&c). Lo and Cui (2004) did the same type of

experiments on specimens with normal-weight and lightweight aggregate. They concluded that lightweight aggregate has a smaller interface thickness compared to normal-weight aggregate, which can also be seen in Figures 2.11b&c. This is likely a result of the adsorption of the cement paste into the inclusion.

The inclusion and matrix typically have different mechanical properties, specifically the modulus of elasticity, thermal coefficient, and hardening rate (Mitsui et al., 1994). It is, therefore, important to understand if any stress concentrations develop at the interface because of these mechanical differences. If linear elastic behavior is assumed, the property that has the greatest influence on the internal stress distribution in a composite material is the difference between the elastic constants of the inclusion and the surrounding matrix (Hansen, 1958; Neville, 1997; Aulia, 2000).

When a specimen is loaded, microcracking occurs at the location of largest tensile stress concentration when the tensile strength of the material at that point is exceeded. In other words, microcracks will not initiate unless the tensile stress at a certain location is greater than the tensile strength at that same location. If stress concentrations and the differences between the modulus of elasticity of the matrix (E_m) and aggregate (E_a) are taken into consideration, then the location of tensile crack initiation can be predicted (Grübl, 1979). Figure 2.12 shows the stress concentration factors associated with a hole ($E = 0$) and a rigid inclusion ($E = \infty$) set in an infinite plate subject to a far field uniaxial compressive stress. It should be noted that these solutions match those predicted by Goodier (1933).

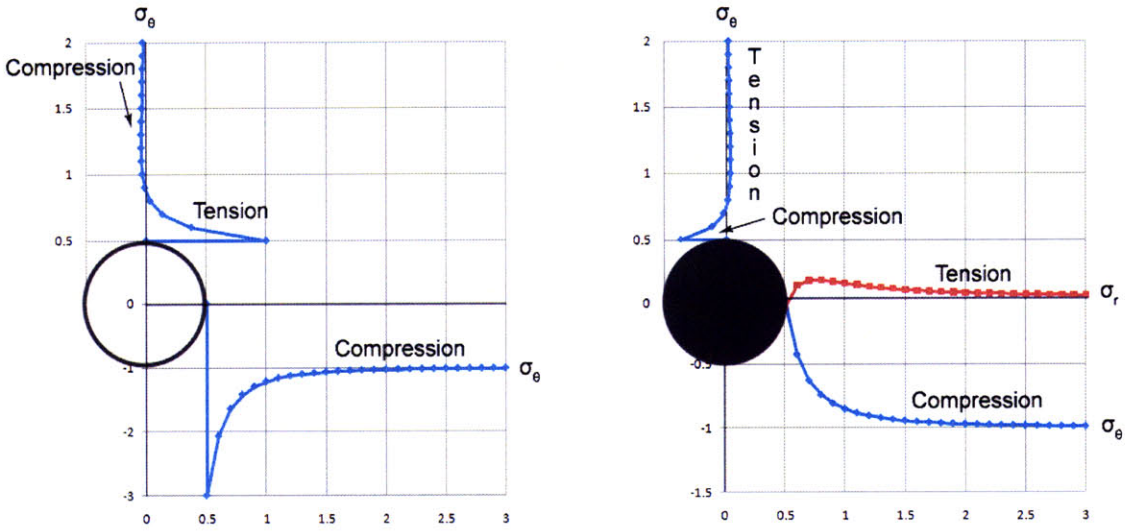

Figure 2.12 – Plots showing the stress concentration factors of a hole (left) and a rigid inclusion (right) cast within an infinite plate (for $\nu = 0.25$) subject to a far field uniaxial compressive stress in the vertical direction.

According to Figure 2.12, the plate model containing a hole experiences high tangential compressive stresses ($\sigma_c = 3\sigma_o$) at the right and left interface boundary and tensile stresses ($\sigma_t = -\sigma_o$) at the top and bottom boundary. Considering, however, that the compressive strength of typical concrete is about ten-times greater than its tensile strength, the assumption that tensile cracks will initiate at the top, or bottom, of the interface can be made. The model containing the rigid inclusion experiences moderate tangential compressive stresses along the top and bottom inclusion interface. On the other hand, radial tensile stresses exist adjacent to the left and right inclusion interface. Therefore, debonding might initiate at the right, or left, boundary before the occurrence of crack initiation at the top or bottom. Notice a small portion of the matrix just above and below the inclusion interface is loaded in compression, and then a transition to tensile stresses occurs.

Aulia (2000) drew somewhat similar conclusions as to where cracks should initiate at inclusions and matrices of different elastic constants, but provided different reasoning using the figures of Grübl (1979). Figure 2.13 shows a circular inclusion cast within a surrounding matrix subject to a far field compressive stress. Aulia (2000) stated that when large differences between E_m and E_a

exist, such for the case of a high-strength concrete ($E_m << E_a$), there are high internal tensile stresses at locations 1 and 1'. Again, since the tensile strength of concrete is quite low microcracking will occur at 1, or 1', as shown in Figure 2.13. Once the tensile crack begins to propagate, the stresses are redistributed onto the inclusion in order to maintain internal stress equilibrium (Figure 2.13). Stable crack growth is thereby achieved. This theory disagrees with the rigid inclusion ($E_a = \infty$) stress concentration values shown in Figure 2.12. As stated earlier, debonding at the sides of a rigid inclusion should theoretically occur prior to tensile crack initiation at the top, or bottom. Also, the rigid inclusion in Figure 2.12 experiences a compressive stress concentration near 1 and 1'.

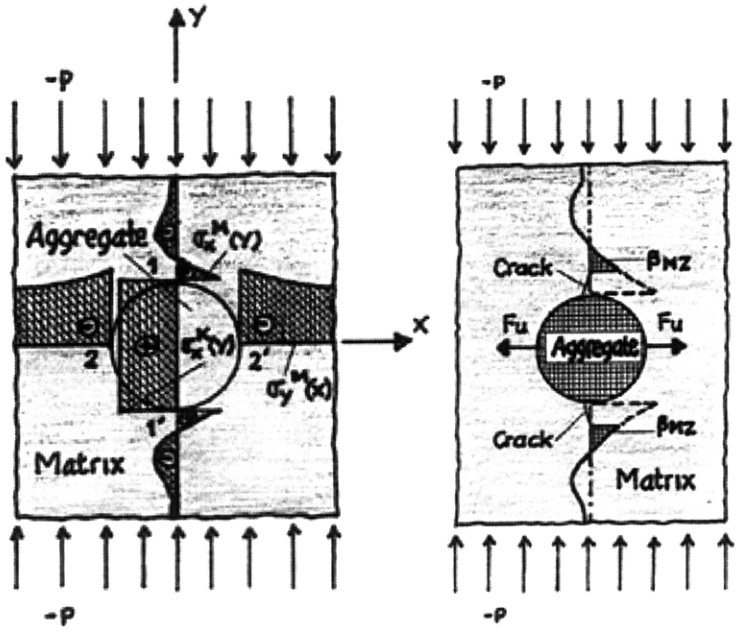

Figure 2.13 – Stress distribution of a circular inclusion within a matrix subjected to a far field stress (left) and the stress redistribution after tensile crack initiation (right), where M represents the matrix, K represents the inclusion, and β_{MZ} is the tensile strength of the matrix (Grübl, 1979).

Aulia (2000) also states that when the differences between E_m and E_a are small, the compressive strength of the boundary at 2, or 2', is exceeded before the stress at 1, or 1', reaches the tensile strength of the matrix. Therefore, crack initiation occurs at 2 or 2'. This disagrees with the closed form solutions shown in Figure 2.14. When ($E_m \approx E_a$) the radial tensile stresses at the left and right interface will increase and the tensile strength of the interface will be exceeded (i.e.,

debonding will occur). Therefore, it is correct to assume that cracks should initiate at 2 or 2', but not as a result of the compressive stresses exceeding the compressive strength of the matrix at that location.

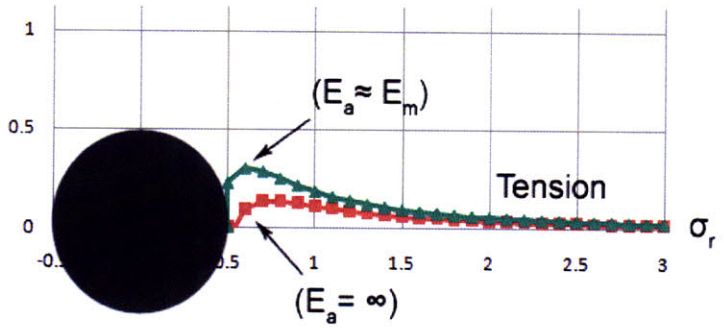

Figure 2.14 – Plot showing the radial stress concentration factors of a soft and rigid inclusion cast within an infinite plate (for $\nu = 0.25$) subject to a far field uniaxial compressive stress in the vertical direction.

Aulia (2000) performed experiments on cylindrical concrete specimens with various aggregate stiffnesses and obtained results that are consistent with his theory. The concrete specimens containing aggregate of basalt (E_a = 89.9 GPa), steatite (E_a = 80 GPa), and diabase (E_a = 71.7 GPa), where the difference between the elastic moduli and the matrix (E_m = 37.9) was high, experienced microcracking at the locations of 1, or 1', shown in Figure 2.13. This disagrees with the closed form solutions shown in Figure 2.12. The reason may be that the closed form solutions do not account for movement along the interface during loading, which would alter the stress concentrations shown in Figure 2.12 and especially reduce the compressive stress concentrations along the top and bottom interface. Aulia (2000) also observed that the concrete specimens containing granulite (E_a = 39.4 GPa) and limestone (E_a = 39.1 GPa), where the difference between the elastic moduli and the matrix was low, experienced microcracking at the locations of 2, or 2', which is also predicted by the closed form solutions.

Zaitsev and Wittmann (1981) began modeling the fracture processes of a heterogeneous material by first considering a randomly inclined flaw in a homogenous plate (Figure 2.15). As the compressive load increases, two tensile cracks develop at both ends of the flaw. The critical stress intensity factor, K_c, for stable crack growth is then

$$K_{Ic} = \frac{T_s \sin(\alpha)}{\sqrt{\pi l_2}} \tag{2.6}$$

where T_s is the resulting force of shear stress τ_s, which results in the shearing of the two flaw sides. If the coefficient of friction, f, is taken into consideration then the resulting shear force can be written as

$$T_s = 2l_1\tau_s = -2l_1 q(\sin\theta_k \cos\theta_k - f\sin^2\theta_k) \tag{2.7}$$

By incorporating equation (2.7) into equation (2.6), the following is obtained:

$$q = -\frac{\sqrt{\pi l_2}}{2l_1}\frac{K_{Ic}}{A(\theta_k, f)} \tag{2.8}$$

where q is the applied far field compressive load, l_1 is half the flaw length, l_2 is length of the propagating tensile crack, and $A(\theta_k,f) = (\sin\theta_k \cos\theta_k - f\sin^2\theta_k)\sin\theta_k$. Stable crack propagation will, therefore, be attained as the applied load, q, increases. This is known as the sliding crack model, which was discussed earlier and was first introduced by Brace and Bombolakis (1963).

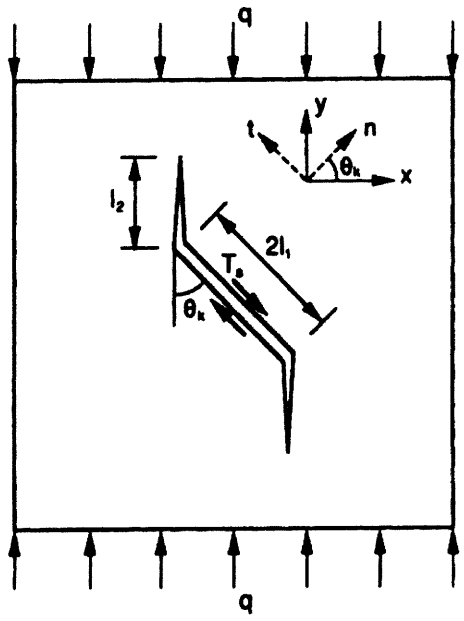

Figure 2.15 – Depiction of two tensile cracks that developed from an inclined flaw (Zaitsev and Wittmann, 1981).

Zaitsev and Wittmann (1981) then applied the sliding crack model to the analysis of a polygon inclusion within an infinite homogenous matrix (Figure 2.16). The sliding crack model does not consider the effects of normal or shear stresses on the flaw surface, since they are not present if

the flaw is open. In the case of an inclusion, however, normal and shear stresses are applied to the inclusion interface. Therefore incorporating a normal stress concentration coefficient, k_n, and a shear stress concentration coefficient, k_s, into the shear force component (T_s) of the sliding crack model will account for the differences, since they have an effect on tensile crack propagation. One of the assumptions made is that the original crack, of length $2l_1$, is shorter than the adjacent side of the inclusion. The inclined crack then begins to propagate in shear (mode II). The propagation of the shear crack starts when

$$q_{II}^{IF} = -\frac{K_{IIc}}{\sqrt{\pi l_1} D^{IF}(\theta_k, f)} \tag{2.9}$$

where the superscript, IF, represents the inclusion interface, and

$$D^{IF}(\theta_k, f) = k_s \sin\theta_k \cos\theta_k - f k_n \sin^2\theta_k \tag{2.10}$$

$D^{IF}(\theta_k, f)$ defines the orientation of the resulting shear force on the interface (modified from the sliding crack model) with the incorporation of the stress concentration coefficients, k_s and k_n.

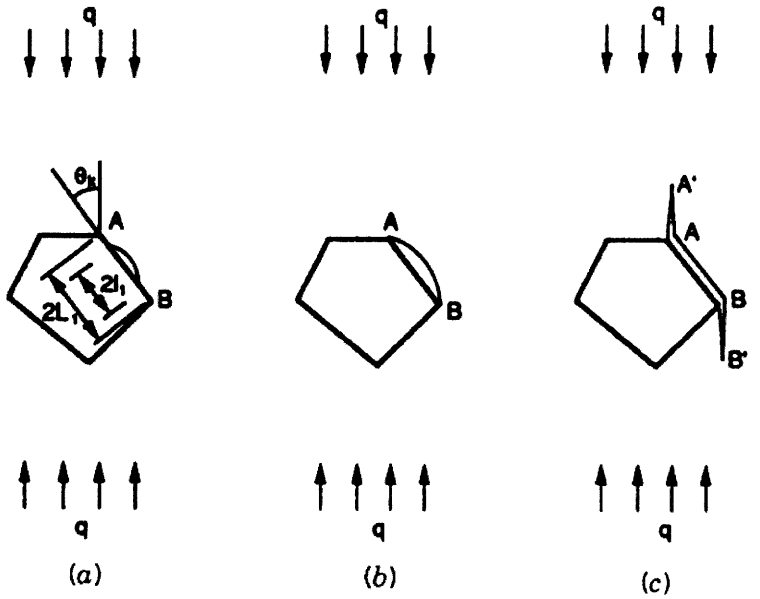

Figure 2.16 – A tensile crack of length, $2l_1$, located adjacent to an inclusion face, AB: (a) the initial crack, (b) propagation of the crack along the inclusion face, (c) propagation of the crack into the surrounding matrix (Zaitsev and Wittmann, 1981).

The shear crack stops once it reaches the same length as the inclusion side (Figure 2.16b). This can be said if the value of K_{IIc} for the surrounding matrix is significantly higher than that of the

interface. The compressive strength of the matrix is also much higher than its tensile strength. Therefore, if the external load continues to increase, a higher critical stress value will be reached that will result in the propagation of tensile cracks into the matrix. Using the modified sliding crack model, the relation between the tensile critical stress intensity factor of the matrix and the applied compressive load is

$$q = -\frac{\sqrt{\pi l_2}}{2L_1}\frac{K_{Ic}^{M}}{A^{IF}(\theta_k, f)} \tag{2.11}$$

where $A^{IF}(\theta_k,f) = D^{IF}(\theta_k,f)\sin\theta_k = (k_s \sin\theta_k \cos\theta_k - fk_n \sin^2\theta_k)\sin\theta_k$, and l_2 is the distance AA' depicted in Figure 2.16c. $A^{IF}(\theta_k,f)$ is simply the $A(\theta_k,f)$ term taken from the sliding crack model with the modification through stress coefficients, k_s and k_n. Equation (2.11) can also be used to find the relation between the tensile critical stress intensity factor of the inclusion, K^{IN}_{Ic}, and the applied compressive load by substituting K^{M}_{Ic}. According to equation (2.11), stable crack propagation will continue as the applied load increases.

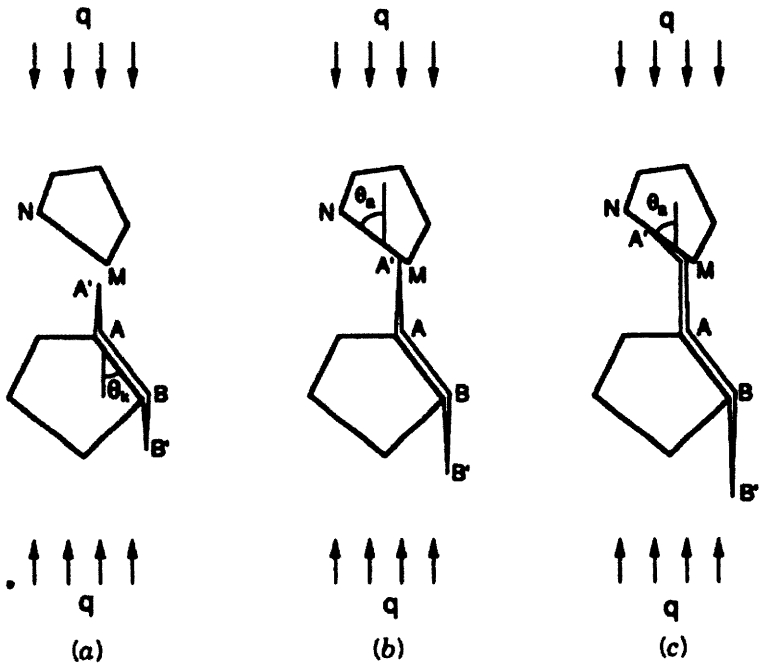

Figure 2.17 – An extension of Figure 2.16, but with more than one inclusion: (a) the initial crack presented in Figure 2.16c, (b) propagation of the crack until its coalescence with the second inclusion, (c) propagation of the crack along the boundary of the second inclusion (Zaitsev and Wittmann, 1981).

For a case with two or more inclusions, the same procedure shown in Figure 2.16 can be applied. In this case, however, the assumption that tensile crack, AA', will coalesce with another inclusion is made (Figure 2.17). It is also assumed that the fracture resistance of the inclusion is much higher than the interface. Crack, AA', will therefore eventually propagate along the inclusion boundary. The crack can either propagate in mode I, or mode II. When the crack on the interface of the second inclusion propagates in tension (mode I), the relationship between the compressive load, q^{IF}_{I}, and the interfacial fracture toughness, K^{IF}_{Ic}, is

$$q_I^{IF} = -\frac{2K_{Ic}^{IF}\sqrt{\pi l^2}/L_1}{A^{IF}(\theta_k, f)[3\cos(\theta_a/2)+\cos(3\theta_a/2)] - 3B^{IF}(\theta_k, f)[\sin(\theta_a/2)+\sin(3\theta_a/2)]} \quad (2.12)$$

On the other hand, if the crack propagates in shear (mode II), the relationship between the compressive load, q^{IF}_{II}, and the interfacial fracture toughness, K^{IF}_{IIc}, is

$$q_{II}^{IF} = -\frac{2K_{IIc}^{IF}\sqrt{\pi l^2}/L_1}{A^{IF}(\theta_k, f)[\sin(\theta_a/2)+\sin(3\theta_a/2)] - B^{IF}(\theta_k, f)[\cos(\theta_a/2)+3\cos(3\theta_a/2)]} \quad (2.13)$$

where $B^{IF}(\theta_k,f) = D^{IF}(\theta_k,f)\cos\theta_k$, and where q^{IF}_{I} and q^{IF}_{II} represent the critical loads required to propagate a crack along the MN interface in mode I and mode II, respectively. Equations (2.11), (2.12), and (2.13) show that the fracture resistance of the inclusion and interface (through K^{IN}_{Ic}, K^{IF}_{Ic}, and K^{IF}_{IIc}), the geometry of the crack path A'ABB' (through θ_a and θ_k), and the inclination of the inclusion interface all have a significant impact on the mode of crack propagation.

Zaitsev and Wittmann (1981) commented that tensile cracks have a greater tendency to propagate through a lightweight aggregate, rather than along the interface. They showed that this is only true if the fracture toughness, K^{IF}_{Ic}, of the interface is greater than that of the inclusion (light weight aggregate), K^{IN}_{Ic}. Aulia (2000) also reported that in concrete specimens containing low strength aggregate, microcrack bands typically propagated through the aggregate.

Zaitsev and Wittmann (1981) performed experiments in order to supplement their theoretical calculations. Concrete prismatic specimens (40mm x 40mm x 160 mm) were prepared containing two steel inclusions (Figure 2.18). Each steel inclusion had a flat side that served as an "a priori" crack. Half of the specimens were cast where α and β had opposite directions, while the other half were cast where α and β had the same direction. The compressive strength

of these specimens was determined, and it was concluded that the specimens with opposite directions of α and β had higher failure stresses, even though no further reasoning was given. The reason may be that the specimens with the same α and β directions have "a priori" cracks that slide in the same direction, thereby allowing the specimen to shear at lower stresses.

Zaitsev (1983) stated that according to equations (2.12) and (2.13), the interface inclination angle, θ_a, has a significant impact on whether the propagation of a crack along the interface is in tension or shear. In the case of $\theta_a < 0$ (measured clockwise from vertical) tension cracks are to be expected; whereas, for $\theta_a > 0$ (measured counterclockwise from vertical) a shear crack is more likely (refer to Figure 2.17). Zaitsev (1983) concluded, however, that the occurrence of normal confining components of an applied stress may prevent tensile cracks from opening at horizontal inclusion boundaries. Shear cracks, which are caused by shear components of the applied stress, will therefore typically form at the boundaries where θ_a is not zero (i.e., if $\theta_a < 0$ a mode II crack can still initiate).

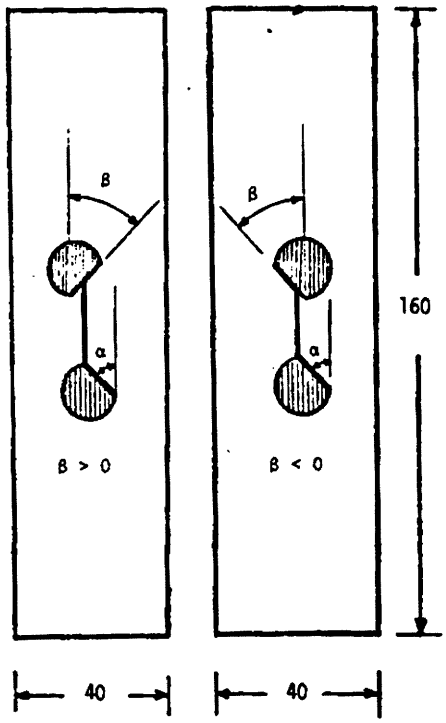

Figure 2.18 – The geometries of the concrete specimens with steel inclusions tested by Zaitsev and Wittmann (1981). The specimens either had opposite inclination directions (left) or had equal inclination directions (right).

Maji and Shah (1989) created prismatic concrete specimens containing circular limestone inclusions and holes, as shown in Figure 2.19. The specimens were loaded incrementally in compression, while holographic interferometry was used to capture the crack processes throughout the test increments. Notice, however, that the specimens containing inclusions of different sizes also have different spacing distances, which introduces another variable.

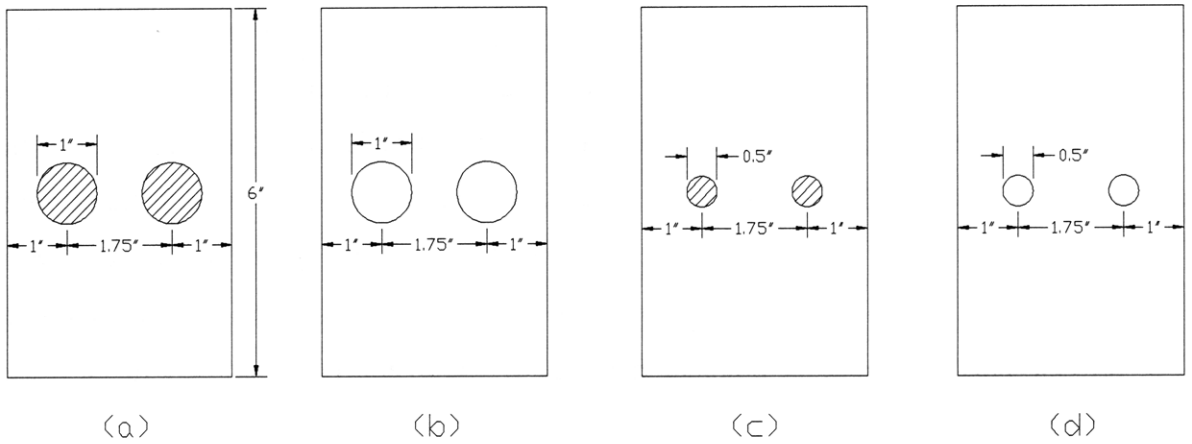

Figure 2.19 – The specimen geometries tested by Maji and Shah (1989): (a) 1" diameter limestone inclusion, (b) 1" diameter hole, (c) ½" diameter limestone inclusion, (d) ½" diameter hole.

Maji and Shah (1989) reported that interface cracks typically propagated along the entire 1" limestone inclusions before propagating into the concrete matrix. These bond cracks initiated at about thirty percent of the peak load (Figure 2.20b). Nonlinearity in the stress-strain curve commenced at this point. Maji and Shah (1989) noted that interface cracking initiated at various points around the inclusions, not just at the right and left inclusion boundary. This suggests that the interface cracks may not be purely tensile in nature. Matrix cracks then initiated at the interface cracks located at the top and bottom of the inclusion, and propagated in the direction of the applied load. It was noted that all matrix cracks propagated vertically regardless of their initiation point on the inclusion boundary. Cracks then initiated within the matrix as the load increased. Just prior to failure, diagonal cracking was observed and commonly coalesced with previously initiated vertical matrix cracks (Figure 2.20c). Post-mortem investigations showed that many of these diagonal cracks did not extend entirely through the specimen. Displacements at the inclusion boundary were measured throughout each test (Figure 2.21a). Total interface

displacements were about five microns. The ratios of the horizontal displacement (dH) to the vertical displacement (dV) were then calculated across the interface at the middle of the inclusion (Figure 2.21b). At the beginning of the test this ratio was about one, which suggests mixed-mode crack growth. Towards the end of the test this ratio gets much larger, which indicates tensile crack opening (Figure 2.21c&d). Similar measurements were done at the matrix cracks and pure tensile opening was observed.

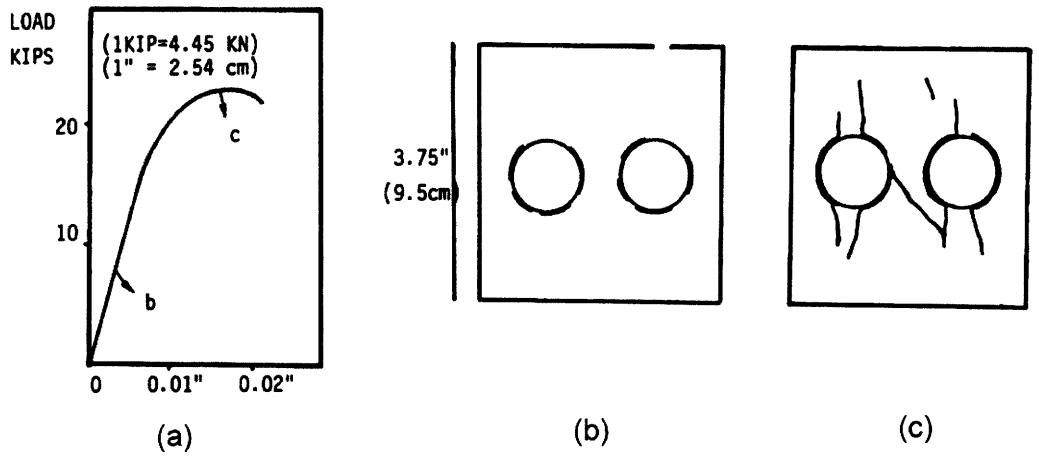

Figure 2.20 – (a) Load-displacement diagram from a 1" diameter limestone specimen (b) sketch of bond crack initiation, (c) sketch of specimen just prior to failure (Maji and Shah, 1989).

Regarding the ½" diameter limestone inclusions, Maji and Shah (1989) reported that no interface and negligible matrix cracking occurred. This may be a result of the increase in spacing distance described above, as Wong (2008) also showed that an increase in ligament length will decrease flaw interaction effects. Post-mortem investigations showed that specimens failed in the same plane as the direction of the applied compressive stress, unlike what was seen with the 1" limestone specimens. These specimens also failed at a lower stress compared to the 1" specimens and showed a more linear stress-strain curve. Maji and Shah (1989) said that a possible reason may be that the 1" inclusions apply greater constraint against crack propagation in the plane of the applied stress direction, and therefore carry a greater load even with the extensive interface cracking. This reasoning seems flawed since the plane in which crack growth occurs within the matrix should not be affected (especially not resisted) by the inclusion size, but on other factors (e.g., uneven loading, etc.).

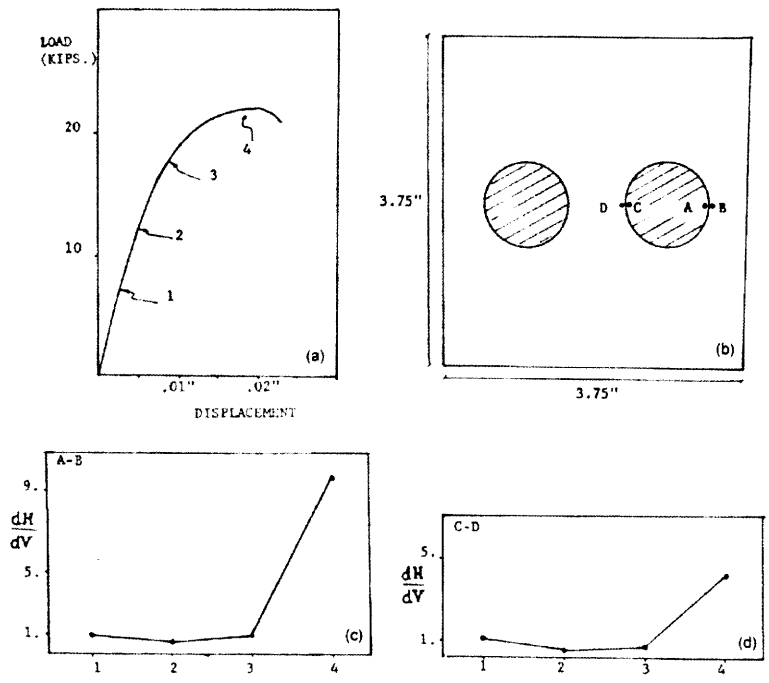

Figure 2.21 – (a) Load-displacement diagram roughly showing the four points when readings were taken, (b) location of the displacement gages on the specimen, (c&d) plots of the dH/dV ratio across points A-B and C-D, respectively (Maji and Shah, 1989).

The 1" and ½" hole specimens behaved differently than the specimens containing inclusions. Matrix cracking always initiated at the top and bottom of the holes, and propagated in the same fashion as the specimens containing inclusions. After matrix crack initiation, stress-strain linearity was still observed, unlike what was seen with the specimens containing inclusions. These specimens also experienced minor diagonal cracking, and failed when the spalling of specimen pieces occurred at one of the boundaries. The 1" hole specimens behaved the most linearly and experienced earlier matrix cracking, compared to the ½" holes. The ½" specimens failed at a higher stress, which again may be a result of the different spacing distances between the two inclusion sizes. Maji and Shah (1989) concluded that the initiation of cracks at a void seems to depend on its size, although this contradicts the elasticity based stress predictions for which the stresses are independent of the void size (Goodier 1933).

Tasdemir et al. (1989) then incorporated the principles of mixed-mode fracture to describe the failure of concrete. The plate depicted in Figure 2.15 is presented again in Figure 2.22, but now with the introduction of a normal stress, σ_B, and a shear stress, τ_B. The plate with the inclined

crack, which can represent a crack at an inclusion interface, is subjected to the same compressive load, q, as before. By taking the geometry of the crack inclination into account, the normal and shear stress values are defined as

$$\sigma_\beta = -q\sin^2\theta_k \tag{2.14}$$

$$\tau_\beta = -q\sin\theta_k\cos\theta_k \tag{2.15}$$

The specimen is subjected to compressive loading; therefore, the flaw cannot open since the normal stress, σ_B, is compressive. Moreover, the flaw cannot close since the crack surfaces are in contact. Therefore, it can be assumed that the tensile (opening) stress intensity factor, K_I, at the flaw tip is zero. Tasdemir et al. (1989) verified this assumption using FEM. The crack surfaces, which are already in contact, can only slide against each other. Therefore, the shear (mode II) stress intensity factor defined by Melville (1977) is applicable to the tip of the flaw and is expressed as

$$K_{II} = -q\sqrt{\pi a}(\sin\theta_k\cos\theta_k - \mu\sin^2\theta_k) \tag{2.16}$$

where, μ, is the interface friction coefficient and, a, is the flaw half-length. This is basically the same equation as (2.9), but without the incorporation of the stress concentration coefficients. The reason is that the stress intensity factor of the flaw tip (not the interface) is being defined in equation (2.16). Note that for sliding to occur the absolute value of the shear stress, $|\tau_B|$, must be greater than $\mu|\sigma_B|$. Therefore, a critical value of θ_k exists, defined as θ_{ko}, where $\theta_{ko} = \cot^{-1}\mu$. The shear stress intensity factor, K_{II}, will conform to equation (2.16) when $\theta_{ko} \geq \theta_k$ (i.e., sliding will occur), and be zero when $\theta_k > \theta_{ko}$.

A crack will initiate at the tip of the flaw in Figure 2.22 when the applied load increases. The stress intensity factors at the flaw tip can be expressed in terms of the angle of propagation, κ (Figure 2.22). It should be noted that there is typically no correlation between θ_k and κ. Several criteria exist that calculate the angle of initiation at the flaw tips (Erdogan and Sih, 1963; Sih, 1974; and Hussein et al., 1974). One common assumption is that the crack will initiate in the direction of the maximum tensile stress intensity factor. Cottrell and Rice (1980) defined the stress intensity factors at the tip of the infinitesimal crack that initiates from a flaw tip to be

$$K_I^{crack} = -\tfrac{3}{4}K_{II}\left(\sin\tfrac{\kappa}{2} + \sin\tfrac{3\kappa}{2}\right) \tag{2.17}$$

$$K_{II}^{crack} = \frac{1}{4} K_{II} \left(\cos \frac{\kappa}{2} + 3 \cos \frac{3\kappa}{2} \right) \tag{2.18}$$

where K^{crack}_{I} and K^{crack}_{II} represent the tensile and shear stress intensity factors at the crack tip, respectively. After the crack initiates at the flaw tip, the K^{crack}_{I} value is no longer zero. Assuming that the crack will initiate in the direction of the maximum tensile stress intensity factor, the maximum value of K^{crack}_{I} occurs when κ is about 71°, which is the root of the derivative of equation (2.17) for all values of θ_k.

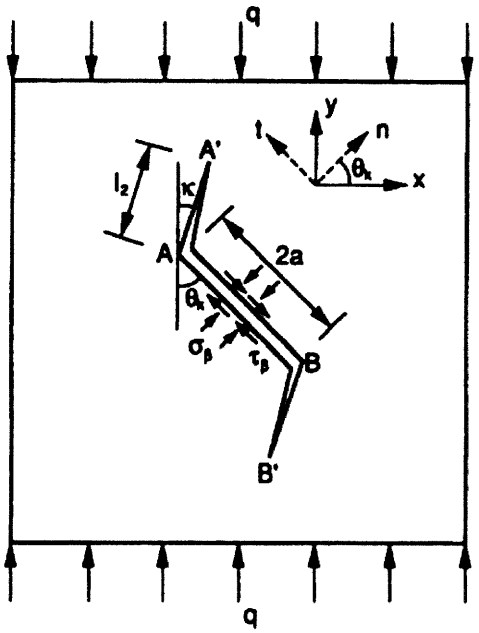

Figure 2.22 – The same inclined flaw presented in Figure 2.15, but now being subjected to a normal and shear stress at the interface (Tasdemir et al., 1989).

The analytical results presented by Tasdemir et al. (1989) were confirmed in a different experimental series performed by Maji and Shah (1989). A test series for prismatic concrete specimens containing a rectangular limestone inclusion were cast. The inclusions were cast at various inclination angles in order to obtain different normal and shear stress ratios at the inclusion boundary (Figure 2.23). As with the circlular inclusions, bond cracks initiated before matrix crack initiation at the interface. The results from the experiments are presented in Table 2.2. The crack initiation, crack propagation, and specimen failure stresses increased as β increased, which was to be expected.

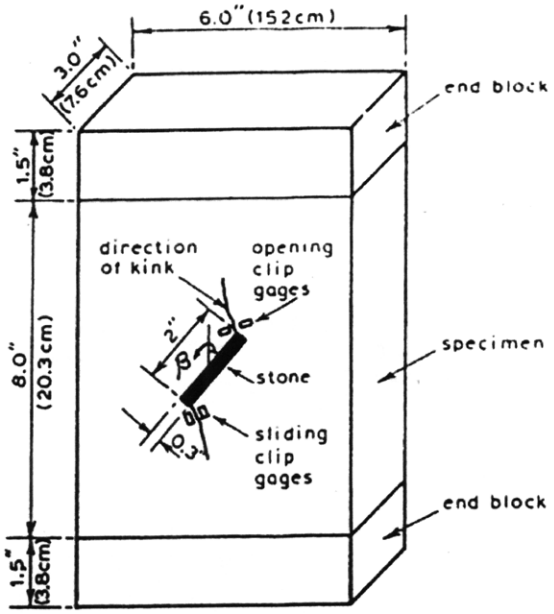

Figure 2.23 – The geometry of a specimen containing a rectangular limestone inclusion (labeled as "stone") cast at an inclination angle β (Maji and Shah, 1989). Also notice the locations of the clip gages that were used to measure displacements.

β	Stresses (psi)				
	Debonding	Initiation $l = 0$"	$l = 0.5$"	$l = 1.0$"	Compressive Strength
18°	293	573	1057	1478	4657
36°	327	550	983	1200	5380
54°	366	851	1187	1524	-
76°	1450	2986	3560	-	-

Table 2.2 – Average stress values from the experimental series performed by Maji and Shah (1989), where l represents the primary crack length.

A finite element (FEM) analysis was performed by Tasdemir et al. (1990) to model the experimental results obtained by Maji and Shah (1989). The primary goal was to obtain the stress intensity factors for progressive matrix crack propagation. There was much scatter in the stress intensity factors when the assumption that the propagating crack was traction free was

made. Normal and shear displacements measured across the crack also widely varied from those calculated by the FEM analysis of the traction-free crack (Figure 2.24).

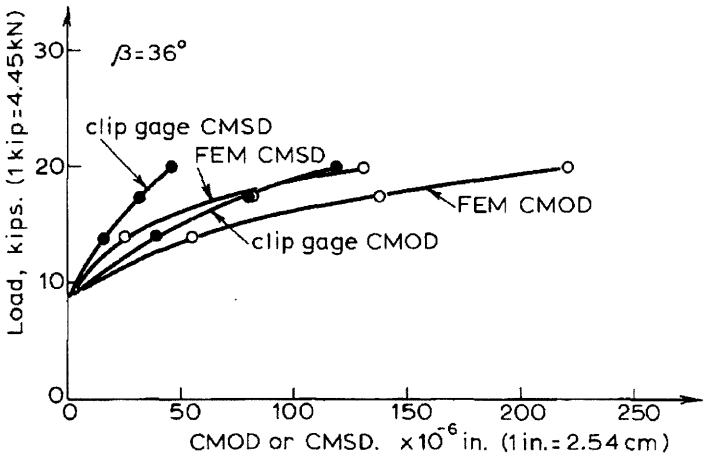

Figure 2.24 – The measured and calculated crack mouth opening and sliding displacements shown in Figure 2.23 (CMOD and CMSD, respectively) (Tasdemir et al., 1990).

To solve this issue, similar specimens were cast with the same procedure, except a void was cast instead of the limestone aggregate (Maji et al., 1991). It was experimentally determined that the initiation of a crack was in mixed-mode, but it was concluded that the mode I stress intensity factor dominated for the propagating crack. This was done by calculating the same displacement ratios discussed earlier with the circular limestone aggregates. The FEM analysis was calibrated with the experimental crack opening and sliding profiles in order to calculate the traction forces on the faces of cracks. The stress intensity factors were then found to lie within a reasonable range (Figure 2.24).

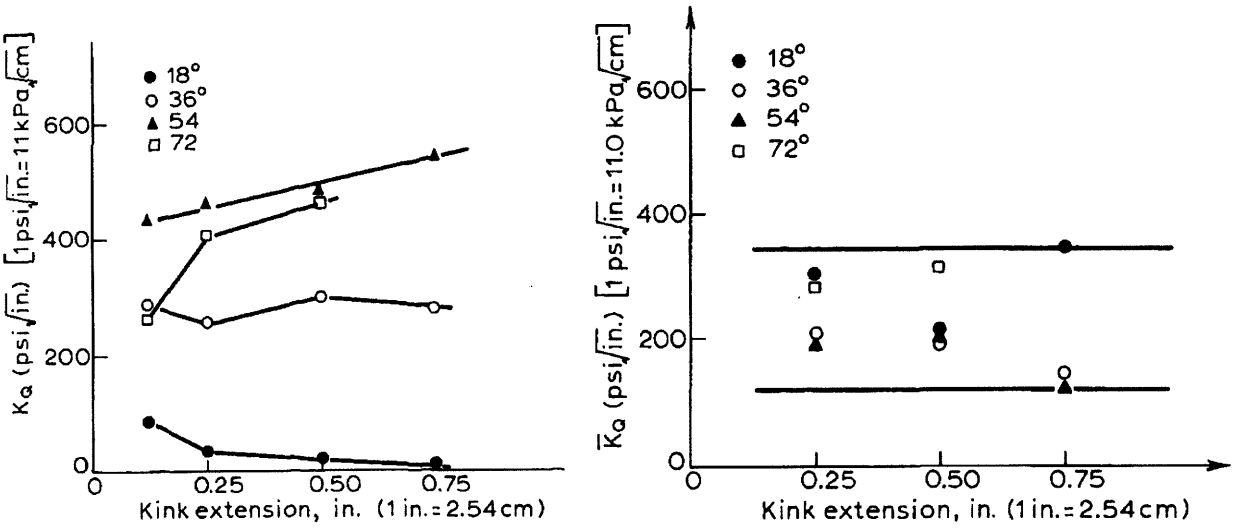

Figure 2.24 –The calculated stress intensity factors prior to calibration (no traction) versus crack length (left), along with the calculated stress intensity factors after calibration (with traction) versus crack length (right) (Tasdemir et al., 1990).

CHAPTER 3 – Uniaxial Compression Tests

3.1 Introduction

In order to understand the various fracture mechanisms associated with an inclusion and its surrounding matrix, unconfined uniaxial compression tests were conducted on cast prismatic gypsum specimens containing either one, or two, inclusions. High speed and real-time video were captured during each experimental test. These recordings were used to visually analyze the processes of crack initiation and propagation. Load-displacement data were acquired for each of the experiments, which were then correlated to the sequence of events from the video recordings. This chapter will cover the experimental details and procedures associated with the performed uniaxial compression tests. It will include the process of specimen preparation, as well as, the analysis of experimental data.

3.2 Material Properties

Molded prismatic specimens of gypsum have been used extensively by the MIT rock mechanics group (Nelson, 1968; Einstein et al., 1969; Motoyama and Hirschfeld, 1971; Einstein and Hirschfeld, 1973; Reyes and Einstein, 1991; Shen et al., 1995; Bobet and Einstein, 1998; Ko et al., 2006; Wong and Einstein, 2009). Three gypsum based materials were used in this study; they are HYDROCAL B-11®, ULTRACAL® 30, and white molding plaster. The Hydrocal and Ultracal material are both comprised of calcium sulfate hemihydrate ($CaSO_4 \cdot 1/2H_2O$) and Portland cement, while the molding plaster only consists of the hemihydrate. In the laboratory, the hemihydrate powder is combined with water in order to create hydrated gypsum specimens ($CaSO_4 \cdot 2H_2O$). Table 3.1 presents the composition and mechanical properties of the three gypsum materials.

Material Properties	Material		
	Hydrocal®	Plaster	Ultracal®
$CaSO_4 \cdot ½H_2O$ (WT%)	>85	100	>85
Portland Cement (WT%)	<10	0	<10
Crystalline Silica (WT%)	<5	<1	<5
Density, ρ [g/cm^3]	1.54**	1.12	1.69
Young's Modulus, E [MPa]	5960*	3300	7500
Compressive Strength, σ_C [Mpa]	33.85**	14.7	43.8
Tensile Strength, σ_T [Mpa]	3.2*	-	-

*From Bobet (1997)
**From Wong (2008)

Table 3.1 – Composition and mechanical properties of the three gypsum materials. The chemical compositions of the Hydrocal, plaster, and Ultracal materials were taken from MSDS #52-140-047, #52-100-016, and #52-140-018, respectively.

3.3 Specimen Preparation

3.3.1 Introduction

This section describes the preparation procedures for the prismatic gypsum specimens used in this study. The dimensions of these specimens were roughly 6 inches (height) x 3 inches (width) x 1.25 inches (thickness) (~152mm x ~76mm x ~32mm). Voids were first cast within a Hydrocal paste perpendicular to the face of the specimen by using a special mold (Figure 3.1). Another paste was later created and poured into the voids in order to create inclusions. An Ultracal paste was used to create stiff inclusions, relative to the surrounding Hydrocal matrix, while the plaster was used to make less stiff inclusions.

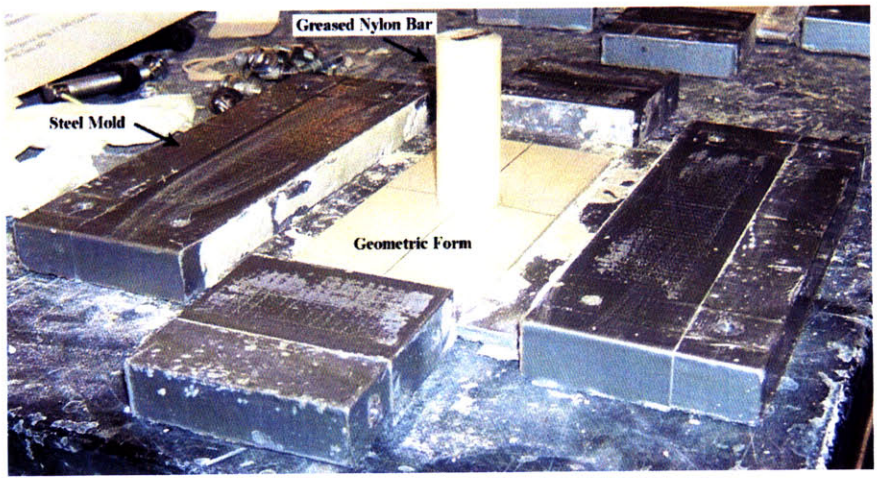

Figure 3.1 – The steel mold used to cast specimens containing a greased nylon bar set within a geometric form (refer to Section 3.3.2).

3.3.2 Procedure

The Hydrocal matrices were created using the methods developed by the MIT rock mechanics group (Reyes & Einstein, 1991; Shen et al., 1995; Bobet & Einstein, 1998; Ko et al., 2006; Wong and Einstein, 2008). In order to create the Hydrocal paste, HYDROCAL B-11® powder, celite powder, and water were combined at a mass ratio of 175:2:70, respectively. After the paste was mixed thoroughly, it was poured into a steel mold. The steel molds used in this study were modified versions of those used by Wong (2008). The mold contained greased nylon bars oriented in specific geometries in order to create the inclusion voids (Figure 3.2). An acrylic holder was installed at the base of the mold to provide stability for the nylon bar. Cardboard forms were created in order to ensure the voids were cast at the correct locations within the specimen. One was secured to the base of the mold and another to the top of the mold (see Figure 3.3). The top geometric form also ensured that the bars remained perpendicular to the base of the steel mold throughout the casting process. The specifics of the void geometries are presented in Chapters 4 and 5.

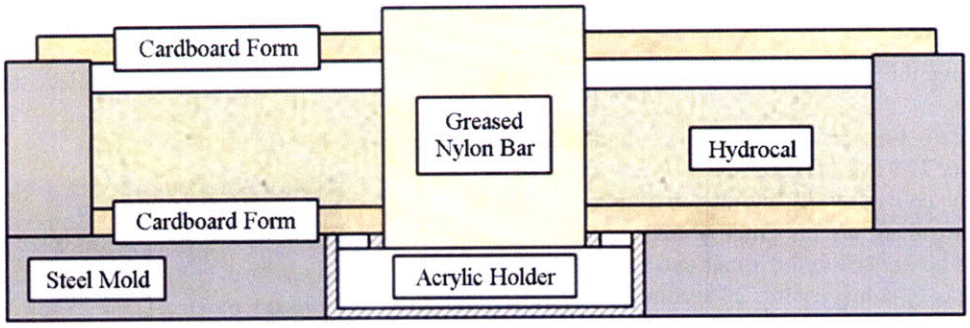

Figure 3.2 – A cross-section of the modified steel molds (containing two greased nylon bars) prior to pouring the Hydrocal paste (left) and a hardened specimen being removed from the mold (right).

The hardened specimens were placed in a 40°C oven after their removal from the mold. These specimens were weighed regularly until a constant mass was reached. The specimens were then submerged in a bucket of water prior to pouring the inclusion paste into the voids (this technique is described in Section 3.3.3). To create the paste for a stiff inclusion, ULTRACAL® 30 powder and water were combined at a mass ratio of 56:19, respectively. For the less stiff inclusion, plaster and water were combined at a mass ratio of 120:81, respectively. The paste was poured into the voids after it was mixed thoroughly. The specimen was then returned to the drying oven until a constant mass was reached. Each specimen was then sanded and measured prior to testing. The complete specimen procedure is presented in Figure 3.4.

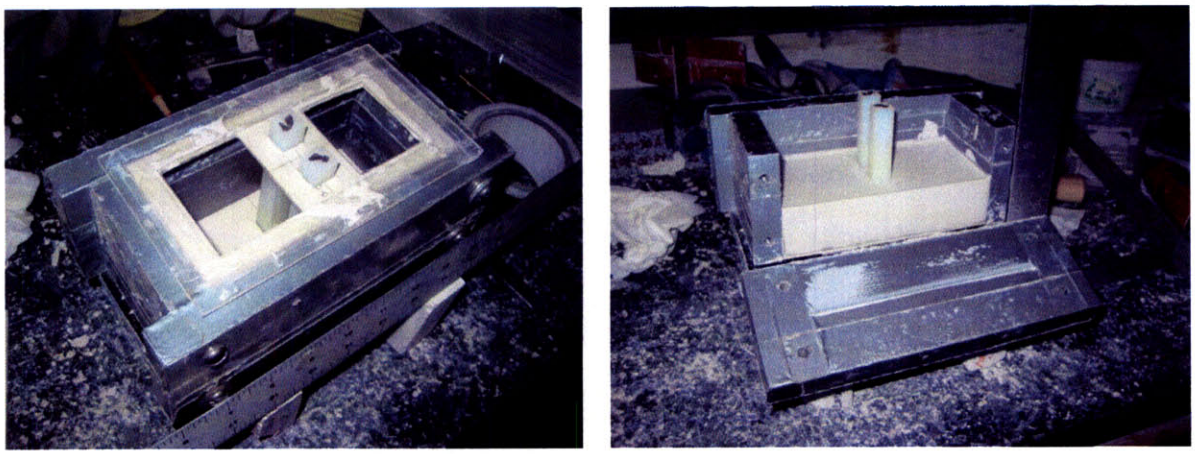

Figure 3.3 – A prepared mold (containing two greased nylon bars) prior to pouring the Hydrocal paste (left) and a hardened specimen being removed from the mold (right).

Procedure for Specimen Fabrication

1. Assemble the steel mold with the geometric forms. Lightly grease the nylon bar(s) and place them into the forms.
2. Measure **6.4 grams** of celite powder and **560 grams** Hydrocal B-11® (gypsum) powder.
3. Measure **224 mL** of water.
4. Pour the celite powder into the mixing bowl.
5. Pour the water into the mixing bowl.
6. Put the bowl back in the mixer and switch on the mixer.
7. Switch off the mixer after **20 seconds**.
8. Remove the bowl from the mixer.
9. **Gently** pour the gypsum powder into the bowl.
10. Put the bowl back into the mixer and switch on the mixer.
11. Switch off the mixer after **four minutes**.
12. Remove the bowl from the mixer.
13. Pour the paste into the steel mold (see Figure 1).
14. Vibrate the mold for **two minutes**.
15. Record the time when the vibration is completed.
16. Put the mold on top of a horizontal bench.
17. After **one hour**, remove the specimen from the mold and also remove the nylon bars from the specimen.
18. Measure the mass of the specimen and label it on its edge.
19. Clean off the excess grease left behind from the inclusion form by passing a fine grit strip of sandpaper over the perimeter of the inclusion void (see Figure 2).
20. Take a damp cloth and clean out the inside of the inclusion voids.
21. Place the specimen into the oven set at 40°C.
22. Measure the mass of the specimen periodically until the mass reaches a constant value.

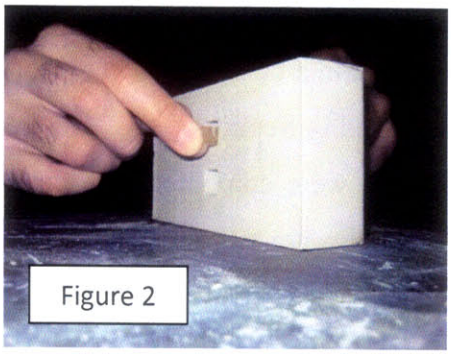

Note: The mixing bowl and tools should be cleaned quickly to prevent the gypsum mixture from hardening onto the utensils.

23. Remove the specimen from the oven and submerge it in water at room temperature for **10 minutes**.

Procedure for Plaster Inclusion Fabrication

24. Measure **60 grams** of plaster powder, and **40.5 mL** of water.
25. Pour the powder into a mixing bowl, and add water.
26. Mix for **2 minutes**.
27. Pour the paste into the inclusion void and vibrate for **1 ½ minutes**.

Procedure for Ultracal Inclusion Fabrication

24. Measure **56 grams** of Ultracal® 30 powder, and **19.0 mL** of water.
25. Pour the powder into a mixing bowl, and add water.
26. Mix for **2 minutes**.
27. Pour the paste into the inclusion void and vibrate for **1 ½ minutes**.

28. Place the specimen into the oven set at 40°C.
29. Measure the mass of the specimen periodically until the mass reaches a constant value.
30. Polish all the faces of each specimen first with coarse (grit #60) and then fine (grit #200) sandpaper.
31. Measure the dimensions and record the mass of the sanded specimen prior to testing.

Figure 3.4 – Procedure for specimen fabrication (several parts taken from Wong (2008)).

3.3.3 Submerged Technique

Prior to testing, three specimens containing a Hydrocal square inclusion were prepared in different ways in order to understand the effects of various casting methods. The first specimen's inclusion was cast without rewetting the matrix, the matrix of the second specimen was rewet only at the inclusion boundary using a damp rag, and the matrix of the third specimen was completely submerged in water for 5 minutes. These three specimens were then loaded until failure. After reviewing the results of the three specimens, two conclusions can be drawn.

After analyzing the post-mortem pictures of the three specimens, it can be seen that the extent of debonding at each inclusion boundary differs. The specimen that was not rewet prior to the pouring of the inclusion paste was almost completely debonded *prior* to testing; whereas, the specimen that was completely submerged debonded about twenty-five to fifty percent from the matrix. The specimen that was rewet using a damp rag debonded between fifty to seventy-five percent (i.e. somewhere between the other two specimens). This observation may explain why Maji & Shah (1989; 1990) experience extensive interface cracking prior to tensile crack initiation, as they cast their inclusions dry.

The tensile crack initiation stresses at the inclusion boundaries were normalized with their respective failure stresses in order to determine if the different inclusion casting methods also affected crack initiation. The results are as follows:

$$\text{No Rewet} \rightarrow \frac{\sigma_{TCI}}{\sigma_f} = 0.263$$

$$\text{Damp Rag} \rightarrow \frac{\sigma_{TCI}}{\sigma_f} = 0.440$$

$$\text{Submerged} \rightarrow \frac{\sigma_{TCI}}{\sigma_f} = 0.729$$

It appears that tensile crack initiation at the inclusion boundary is a function of the bond strength, and insufficient rewetting of the specimen matrix prior to inclusion pouring resulted in "premature" tensile crack initiation. It was also found that, regardless of the inclusion pouring method, shear crack initiation was not impacted by the bond strength of the inclusion boundary. In all three cases shear crack initiation occurred just before failure (see also Section 4.5.3).

3.4 Uniaxial Compression Testing

3.4.1 Introduction

This section will describe the various components of experimental testing performed in this study. A typical experimental setup is depicted in Figure 3.5. A schematic of this setup is shown in Figure 3.6. The three main components of the setup are the loading machine, camcorder, and high speed video camera, which will now be described in detail.

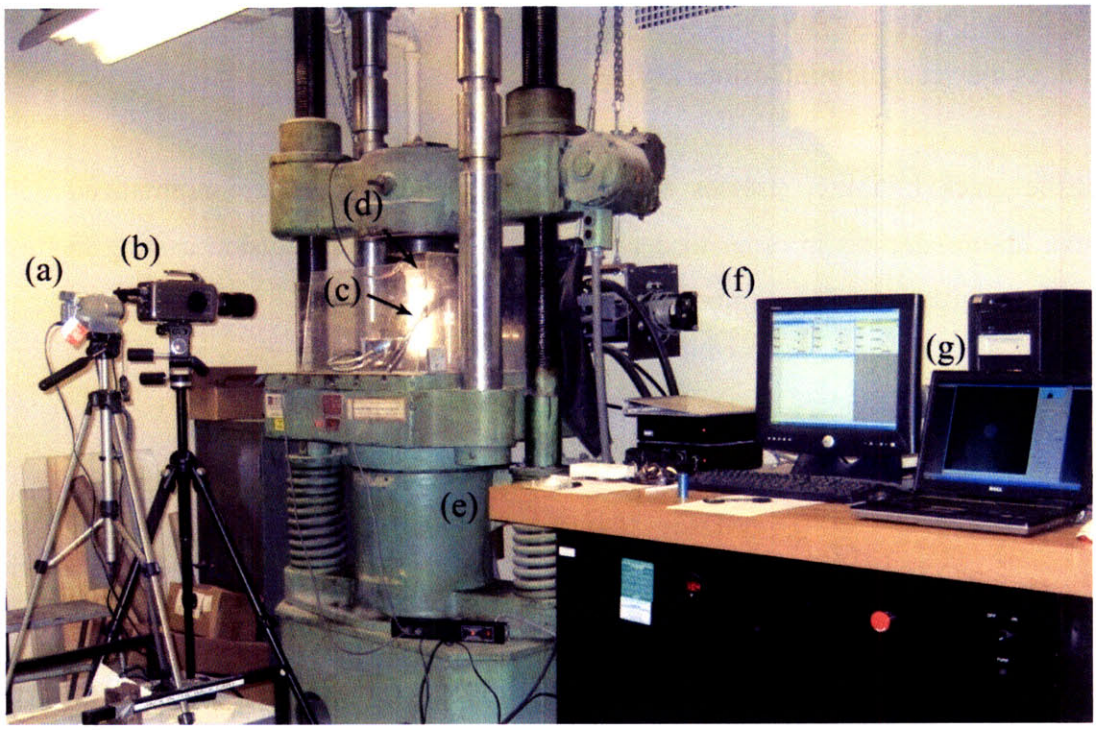

Figure 3.5 – Typical experimental setup consisting of: a) Sony camcorder, b) Phantom high speed video camera, c) specimen, d) end platens, e) Baldwin loading frame, f) MTestW control and data logger, g) high speed camera control.

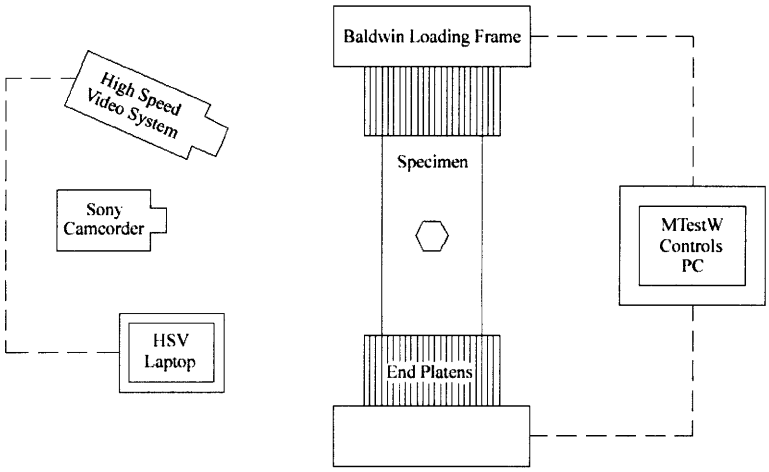

Figure 3.6 – A schematic of a typical experimental setup.

3.4.2 End Platens

In order to perform unconfined compression tests, frictional resistance (confinement) at the loaded boundaries needed to be minimized. Many researchers have incorporated various types of media at the boundaries to achieve this goal. The MIT rock mechanics group has been using brush platens. These platens were first developed by Bobet (1997) and then redesigned for this study. Figure 3.7 shows the details of the platens used in this study.

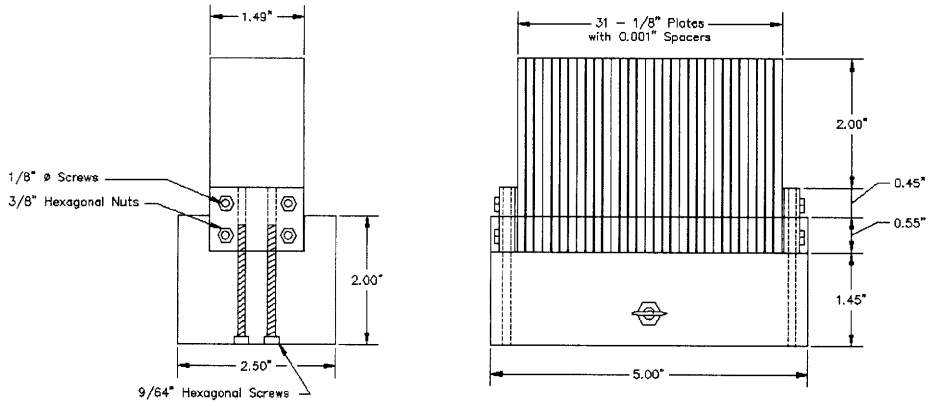

Figure 3.7 – End platens used for the current study.

3.4.3 Uniaxial Compression Tests

All specimens were loaded with a Baldwin 200 kip Loading Frame that was controlled by a computer software program called MTestW (Version M 9.0.7i) created by ADMET. Load, displacement, and time data were recorded at a rate of 1800 samples per minute. Refer to Bobet (1997), Ko (2005), and Appendix A for more information about the loading frame.

Two loading schemes were used by the MIT rock mechanics group in the past. The first one, which was used by Reyes (1988) and Bobet (1997), loaded the specimen incrementally so visual inspections could be performed throughout the test. The later scheme, which was started by Martinez (1999), continuously loaded the specimen while photographic (video) recordings of the specimen were made. This became feasible when the Phantom high speed video camera was utilized. The loading profile used in this study is shown in Table 3.2. For more information regarding the loading profile refer to Appendix A.

	Loading Rate	Range
Stage 1	0.0017 in/sec	0 – 1000 lbs
Stage 2	0.0003 in/sec	1000 – 2500 lbs
Stage 3	38.3333 lb/sec	2500 lbs – Failure

Table 3.2 – Loading profile used in the present study.

3.4.4 Camcorder and High Speed Camera Observation

A camcorder (Sony DCR-HC65) was used to capture video footage of the specimen surface during each experiment. The camcorder was set to start recording after the MTestW software had already began recording data and was set to "standby" mode shortly after specimen failure. The camcorder recorded at a rate of thirty frames per second. After testing, the video footage was converted to a digital format so it could be synchronized with the high speed video footage and stress-strain data. Though the camcorder images only had a one-megapixel resolution, it was very useful to have a continuous visual record of the entire test.

A high speed video (HSV) system (Phantom v7.1) was also used to capture footage of the specimen surface during testing. The primary purpose of the HSV camera was to capture the various cracking processes until failure, and also the crack coalescence sequence (when specimens contained double inclusions). The camera had the capacity of recording up to 30,000 frames per second, but also had a finite amount of memory. Therefore, a lower frame rate had to be used in order to increase the length of high speed footage. A frame rate of 5,000 frames per second was chosen as the camera could then capture 1.081 seconds of video. One issue with the high speed video system was that it had to be triggered manually using a connected laptop. This made capturing high speed footage of failure very difficult since the user's reaction time became a factor. After the experimental work of this study was completed, the MIT rock mechanics developed an automatic trigger switch that resolved the problem.

The HSV system could also be used to capture individual images throughout the experimental trials. These images were taken when a crack event occurred on the specimen face. This was very useful when an analysis of the fracture processes was performed afterwards. These images were later uploaded into Adobe Photoshop where they could be overlaid with each other. This allowed the user to recognize the most subtle of differences between the images taken at different stress levels.

3.5 Data Analysis

3.5.1 Introduction

A thorough analysis of each specimen was conducted in an attempt at understanding the various cracking processes. Three sources of data were obtained during each test: load-displacement, camcorder video, and HSV. Since these sources come from different locations, synchronization between the three sources of data was required. A cracking sequence coupled with a stress-strain curve was, thereby, gathered and reported. The following describes this process in detail.

3.5.2 Synchronization

All three sources of data were taken independently of each other. It was therefore necessary to make a best attempt at synchronizing the qualitative and quantitative data. Unfortunately, a small source of error is introduced since the data were not automatically synchronized. A common point in all three sources of data had to be established. This could either be the initiation of a specific crack, or the occurrence of failure. When a common point between the two videos was established, it was then correlated to a drop in the stress-strain curve that was calculated from the load-displacement data. This proved to be sometimes difficult since all three sources of data were logged at different rates.

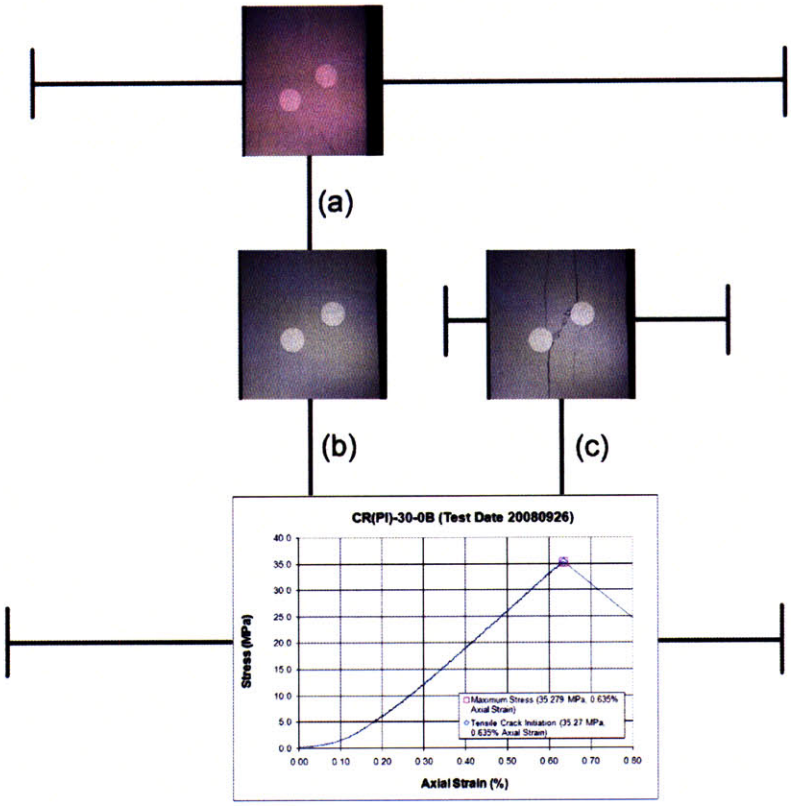

Figure 3.8 – Schematic of the synchronization process. The camcorder timeline is at the top, followed by the HSV timeline, and then by the stress-strain timeline (bottom). In this case, the stress-strain curve was first synchronized to the camcorder and a separate HSV image via tensile crack initiation (a-b). The HSV stream was then synchronized to the stress-strain curve using the incidence of failure (c).

Figure 3.8 illustrates a typical synchronization scheme (data taken from specimen CR(Pl)-30-0B). Three timelines are presented, which represent the stress-strain, HSV, and camcorder timeline. The camcorder timeline is at the top, the HSV timeline is in the middle, and the stress-strain timeline is at the bottom. Notice that the camcorder timeline starts after the stress-strain timeline. In this case, the camcorder was synchronized to the stress-strain curve using the moment of tensile crack initiation, which was also captured in a separate image taken by the HSV camera. The HSV, which was triggered at about the time of failure, then had to be synchronized with the large drop in the stress-strain curve as best as possible. The three sources were thus indirectly synchronized. As a result, the stress-strain data can be correlated to any image from either of the videos. This process is very time consuming and not entirely accurate, which led to the creation of the trigger switch.

3.5.3 Video Analysis

At this point every image can be associated with a unique stress-strain value. It is now essential to create a video analysis that will recognize the sequence and modes of cracking. All of the relevant images are imported into Adobe Photoshop and placed in separate layers. These layers can be superimposed in order to observe even the most minor cracking events. Each crack in the test series is assigned a letter designation until ultimate failure is reached. The type of crack also gets identified. If a crack initiates in tension, it is noted with the letter "T"; while, it is labeled with an "S" if the crack initiates in shear. Arrows are also placed adjacent to a shear crack in order to show the direction of movement. A subscripted number gets added to the label, which represents crack initiation sequence, if several cracks appear on the same image. This labeling system was adopted by Wong (2008). A sketch is then drawn to accompany each image, and is also supplemented with the time and stress level when each image was captured (see Figure 3.9).

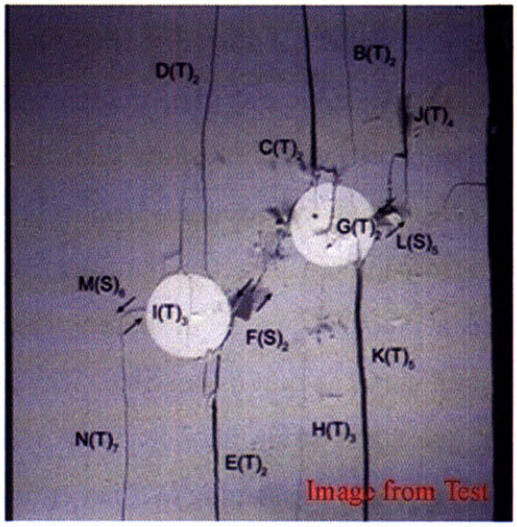

(Recorded by High Speed Video System)

Tensile cracks B&D initiated simultaneously (i.e., in the same HSV image), and therefore get the same subcripted number.

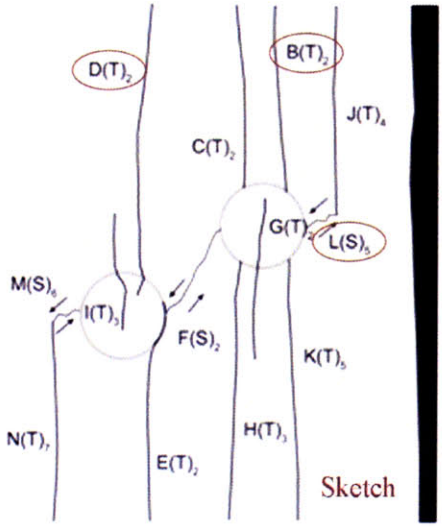

"L" is a shear crack (hence, the S label); it was also the 5th crack to initiate.

(26.46 MPa) Stress

Time: 7 minutes & 33.696 seconds Time

HS Image # - 2269 HSV Image No.

Shear crack (M) initiates at the boundary of the left-hand inclusion and propagates downwards.

Tensile crack (N) then initiates at the lower specimen boundary and propagates upwards until its coalescence with shear crack (M).

Description

Figure 3.9 – A page taken from the analysis of CR(Pl)-30-0B depicting the various fracture processes and their respective orders.

Figure 3.9 contains a page taken from the analysis performed on specimen CR(Pl)-30-0B. The image being interpreted appears in the top left-hand corner, along with the various crack labels. A sketch is placed just below the image for clarity. The stress level, time, and image number is posted in the upper right column, followed by a description of the crack processes occurring in the image.

3.5.4 Stress-Strain Analysis

After the video analysis was completed, the stress-strain data were presented in a plot that isolated critical stress-strain values, such as tensile crack initiation, maximum uniaxial compressive stress, and coalescence (when analyzing double inclusions). The stress-strain plot reported for specimen SQ(Ul)-30-0B is shown in Figure 3.10.

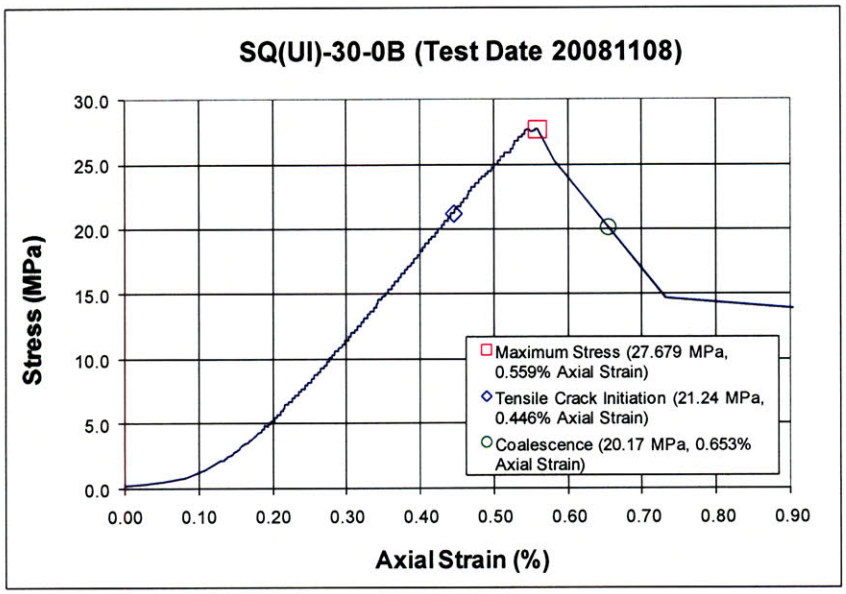

Figure 3.10 – The stress-strain plot of specimen SQ(Ul)-30-0B showing the various significant fracture events.

CHAPTER 4 – Uniaxial Compression Tests of Specimens Containing Single Inclusions

4.1 Introduction

In an attempt to study the impact of inclusions on the performance of brittle material, single inclusions were cast within gypsum prismatic specimens. Unconfined uniaxial compression tests were performed on these specimens until the occurrence of failure. The results of these experiments are described in this chapter. Detailed analyses of the fracturing behavior for specimens containing one-inch and half-inch inclusions are given in Appendix B and Appendix C, respectively.

4.2 Experimental Details

4.2.1 Inclusion Geometry

Initially, four different inclusion geometries were considered in order to understand the effect of inclusion shape on crack processes. The four geometries consisted of a square, hexagon, diamond, and circle. The exact dimensions of these inclusions are depicted in Figure 4.1.

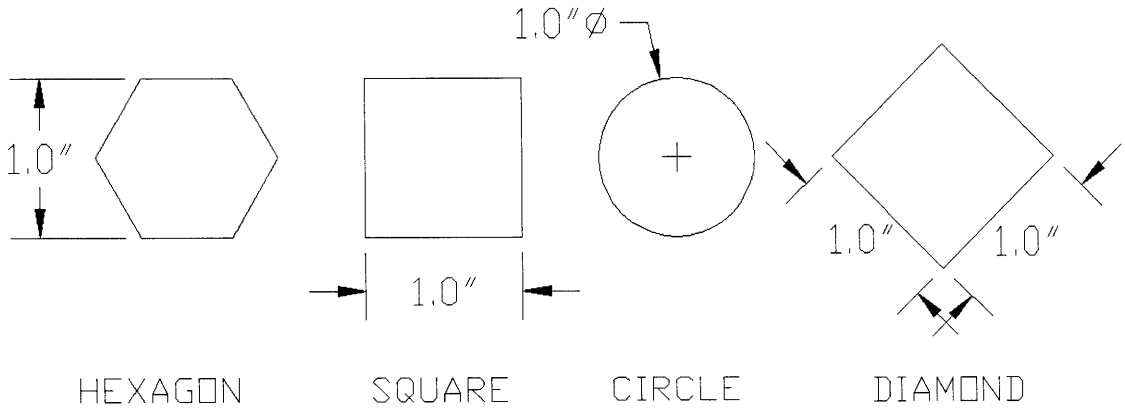

Figure 4.1 – Measurements detailing the four different inclusion geometries used in the specimens containing one-inch single inclusions.

After the single one-inch inclusion series was tested, half-inch circular and square inclusions were then incorporated into specimens. This was done in order to study the effect of inclusion size, as well as, to establish a basis for the double inclusion test series, which will be discussed in Chapter 5.

4.2.2 Pre-test Surface Cracks

As described in Chapter 3, each specimen was placed into the drying oven after the inclusion paste was poured into the Hydrocal matrix. The inclusion paste lost moisture as it hardened, which resulted in shrinkage. The surface area and the intact area of the inclusion lost moisture at different rates, which may have produced non-uniform shrinkage strains. In addition, the constrained boundary condition that the paste was poured into may have increased the tensile stress non-uniformity within the inclusion. Figure 4.2 shows how the inclusion paste was able to shrink without constraint while drying at the surface areas; whereas the intact area served as a confined boundary that restricted contraction. This resulted in pre-test surface cracks (refer to Figure 4.3). These pre-test surface cracks were common in square, diamond, and hexagon shaped inclusions, but not in circular inclusions. This may suggest that the non-uniformity of inclusion geometries affects the shrinkage stresses further. Pre-test surface cracks appear to have an impact on the tensile crack initiation stress of the specimen, which will be discussed in Section 4.5.3.

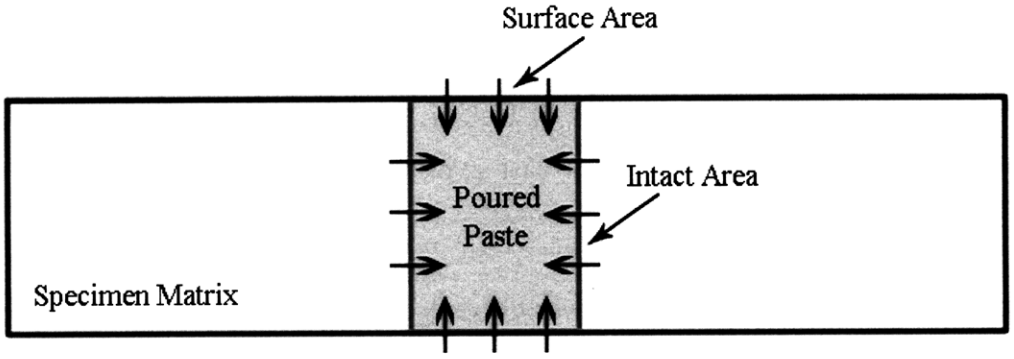

Figure 4.2 – Cross-section showing the differences between the "surface area" and "intact area" of the inclusion paste.

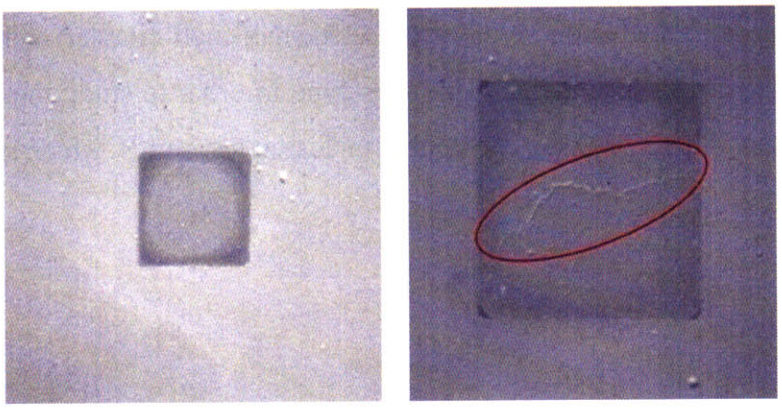

Figure 4.3 – A half-inch square inclusion showing no visible pre-test surface cracks (left) and a one-inch square inclusion containing a distinct pre-test surface crack (right).

4.3 Crack Initiation and Propagation of One-inch Inclusions

4.3.1 Circular Inclusions

A summary of the crack sequences and relative stress levels for one-inch circular inclusions is shown in Table 4.3. Prior to tensile crack initiation, debonding at the boundary of a plaster inclusion occurred sporadically; however, debonding was typical at an Ultracal inclusion. The extent of debonding was limited to the left and right inclusion interface (see Figure 4.4). This disagrees with the findings reported by Maji and Shah (1988). During their experiments on specimens containing a stiffer inclusion relative to the surrounding matrix, "bond cracks" typically initiated and propagated around the entire inclusion prior to tensile crack initiation. The reason may be the differences between specimen preparation, and/or the material properties of the inclusion and matrix. Maji & Shah (1988) used cored limestone as inclusions in a concrete matrix; whereas, this study uses cast gypsum material for both the matrix and the inclusions.

After a portion of the inclusion interface was debonded, tensile cracks then initiated at the ends of the debonded section and propagated towards the respective specimen boundary (Figure 4.4). This phenomenon typically did not occur in specimens containing plaster inclusions. Tensile cracks commonly initiated at the bonded boundaries of plaster inclusions and then propagated

away from the inclusion. Tensile cracks then extended into the inclusion, or initiated other tensile cracks within the inclusion (Figure 4.5).

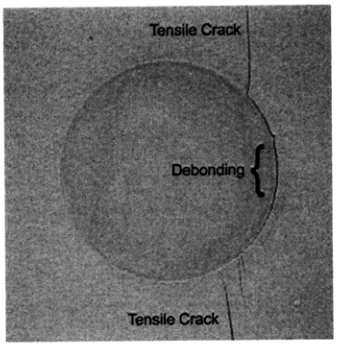

Figure 4.4 – A one-inch inclusion of Ultracal material showing debonding at the right-hand boundary, which occurred prior to tensile crack initiation.

Shear cracks typically initiated after tensile crack initiation. This always occurred at the central outermost portions of the inclusion boundary (see Figure 4.5). Shear cracks frequently initiated at both sides of plaster inclusions, but only initiated on one side of the Ultracal inclusions. When shear cracks initiated on both sides of the inclusion, the two shear cracks typically sheared in the same direction as shown in Figure 4.5. Shear crack initiation at an Ultracal inclusion typically occurred after the specimen's maximum stress. Regarding a plaster inclusion, however, shear crack initiation occurred at about the maximum stress.

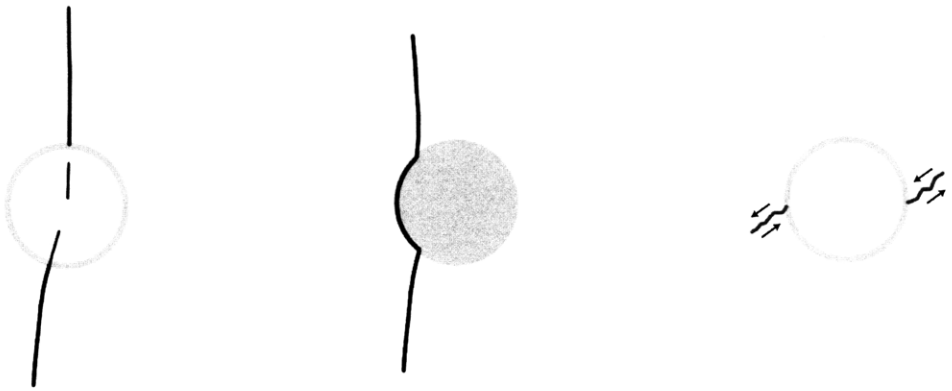

Figure 4.5 – Tensile crack initiation and propagation at a one-inch circular inclusion of plaster material (left), and Ultracal material (center), along with a sketch of shear crack initiation and propagation at a plaster inclusion (right). A summary of all crack sequences and relative stress levels is shown in Table 4.3.

4.3.2 Hexagon Inclusions

A summary of the crack sequences and relative stress levels for one-inch hexagon inclusions is shown in Table 4.3. Debonding prior to tensile crack initiation was not extensive in either case, though it did occur more often at the boundary of an Ultracal inclusion. Extensive debonding occurred at the boundaries of both inclusion types just before failure, however. Tensile crack initiation frequently occurred at the upper and lower boundary corners of an Ultracal inclusion; whereas, the locations of tensile crack initiation were arbitrary along the upper and lower inclusion boundary of a plaster inclusion. Tensile cracks also initiated at pre-test surface cracks located within an inclusion, and were more common with the Ultracal inclusions. After propagating into the matrix, tensile cracks then propagated along the boundary of an Ultracal inclusion. Tensile cracks often propagated into a plaster inclusion, however (see Figure 4.6).

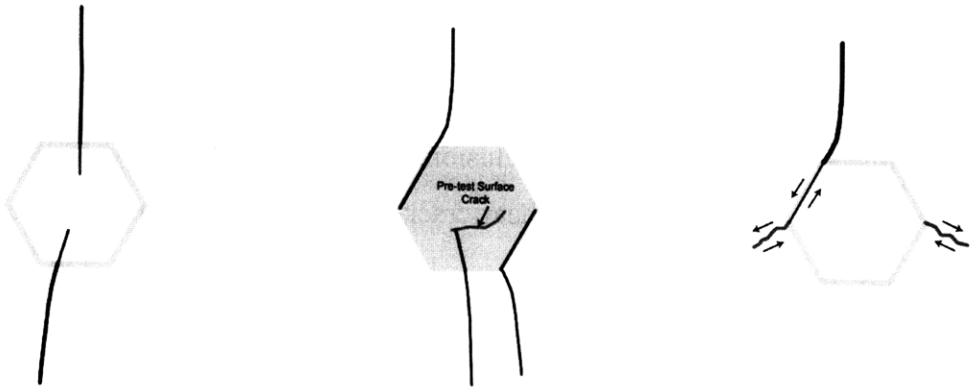

Figure 4.6 – Tensile crack initiation and propagation at a one-inch hexagon inclusion of plaster material (left), and Ultracal material (center), along with debonding and shear crack initiation at a typical inclusion (right). A summary of all crack sequences and relative stress levels is shown in Table 4.3.

Shear cracks usually initiated at both sides of the inclusion, regardless of the material, and the two shear cracks within the specimen always sheared in opposite directions. Shear cracks always initiated at the left-hand and right-hand corners of the inclusion boundary, and always propagated downwards in the direction shown by the arrows in Figure 4.6. As mentioned earlier, the upper and lower inclusion boundaries also sheared, regardless of inclusion material. This may be the result of tensile crack propagation along the interface and/or the magnitude of shear

stresses at the inclined interface. It was observed that shear crack initiation at an Ultracal inclusion occurred at about the specimen's maximum stress. Shear crack initiation typically occurred before the maximum stress of a specimen containing a plaster inclusion.

4.3.4 Diamond Inclusions

A summary of the crack sequences and relative stress levels for one-inch diamond inclusions is shown in Table 4.4. Debonding at the inclusion boundary was rarely seen prior to tensile crack initiation. The initiation of tensile cracks, however, typically led to significant (sometimes simultaneous) inclusion debonding. After tensile crack initiation, inclusions typically debonded completely from the surrounding matrix. This can be attributed to the inclusion geometry, as shearing along the boundary was commonly observed.

Tensile cracks typically initiated at the upper and lower tips of the inclusion, regardless of the inclusion material. The propagation of tensile cracks into the inclusion depended on the inclusion material. Tensile cracks typically initiated at the boundary and later propagated into a plaster inclusion. Regarding Ultracal inclusions, however, tensile cracks began to propagate along the inclusion boundary, and then extended into the inclusion (Figure 4.7). Shear cracks always initiated on both sides of the inclusion at the left and right boundary tip. The most common shearing pattern observed is shown in Figure 4.7 (i.e. both cracks shear in the same direction and in a similar orientation). It was also observed that shear crack initiation at an Ultracal inclusion occurred after the specimen's maximum stress. Regarding plaster inclusions, however, shear crack initiation occurred before the maximum stress.

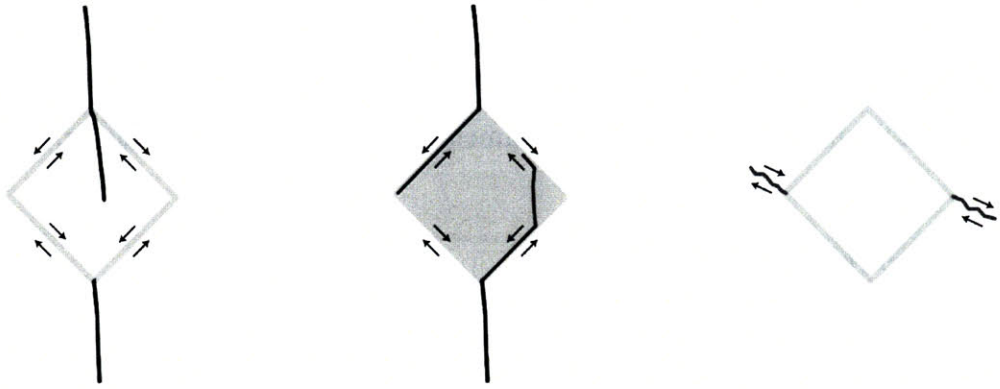

Figure 4.7 –Debonding, tensile crack initiation, and propagation at a one-inch diamond inclusion of plaster material (left), and Ultracal material (center), along with shear crack initiation at a typical inclusion (right). A summary of all crack sequences and relative stress levels is shown in Table 4.4.

4.3.4 Square Inclusions

A summary of the crack sequences and relative stress levels for one-inch square inclusions is shown in Table 4.4. Inclusion debonding seldom occurred at the boundary of a plaster inclusion prior to tensile crack initiation. Debonding occasionally occurred with an Ultracal inclusion; however, it occurred after tensile crack initiation. Moreover, tensile cracks always initiated at the pre-test surface cracks located within the Ultracal inclusion. Tensile cracks then continued to propagate along the existing pre-test surface cracks and eventually into the surrounding Hydrocal matrix. Tensile crack initiation occurred at various locations of the upper and lower plaster inclusion boundary, however. As the tensile crack began propagating into the Hydrocal matrix, the crack then also propagated into the inclusion without a significant change in direction.

Shear cracks typically did not initiate at the boundaries of a plaster inclusion, but did initiate at the Ultracal inclusions. When shear cracks initiated on both sides of the inclusion, the two shear cracks always sheared in opposite directions (as shown in Figure 4.8). Shear cracks usually initiated at the lower corners of the inclusion boundary. Shear crack initiation typically occurred before the specimen's maximum stress, regardless of inclusion material.

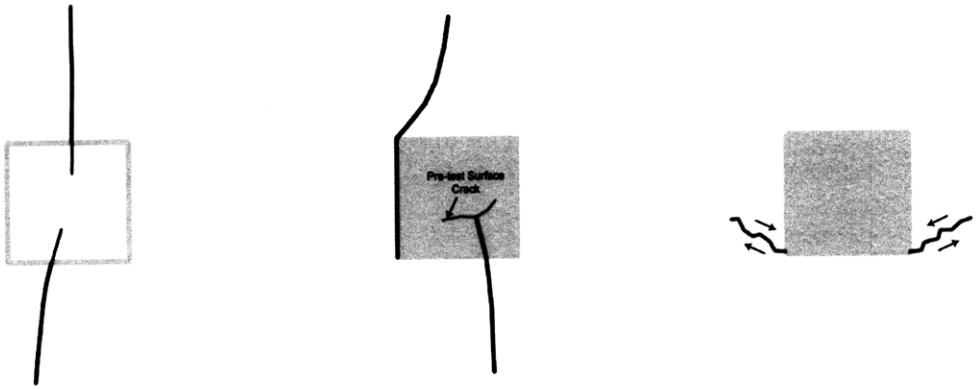

Figure 4.8 – Tensile crack initiation and propagation at a one-inch square inclusion of plaster material (left), and Ultracal material (center), along with shear crack initiation and propagation at an Ultracal inclusion (right). A summary of all crack sequences and relative stress levels is shown in Table 4.4.

4.3.5 Bowed Cracks

Tensile cracks did not always initiate at the inclusion boundary. On occasion, tensile cracks initiated at the upper or lower (loaded) specimen boundaries and propagated towards the other boundary; this commonly resulted in specimen detachment as buckling of the smaller specimen piece typically occurred. Sometimes as a tensile crack propagated adjacent to the inclusion it turned towards the inclusion, and then turned away again (Figure 4.9). These "bowed" tensile cracks typically initiated after a shear crack had initiated at the adjacent inclusion boundary, regardless of the inclusion material, but sometimes did occur when no noticeable shear cracks were observed (e.g., Figure 4.10). This occurred in all specimens containing various one-inch inclusions.

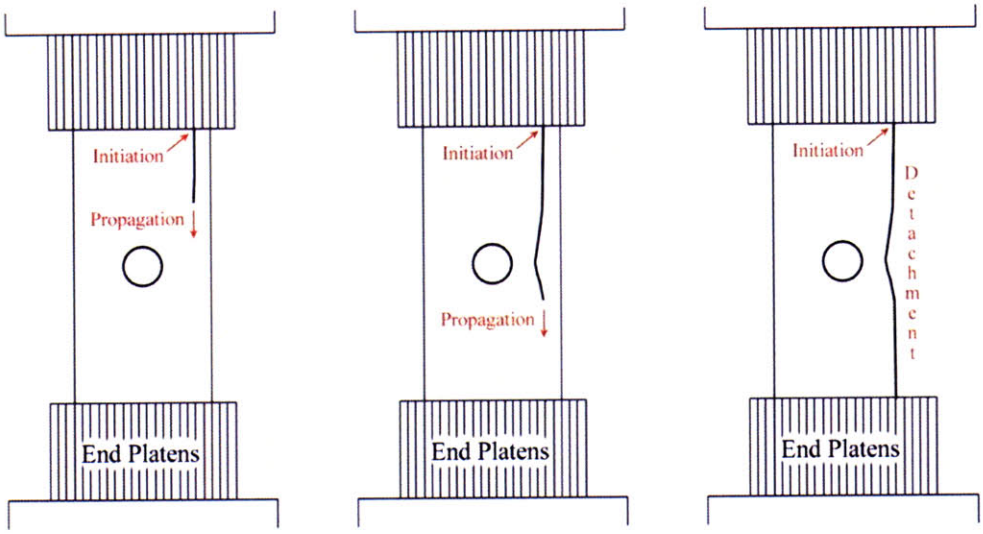

Figure 4.9 – Sketch showing the sequence of a typical "bowed" tensile crack.

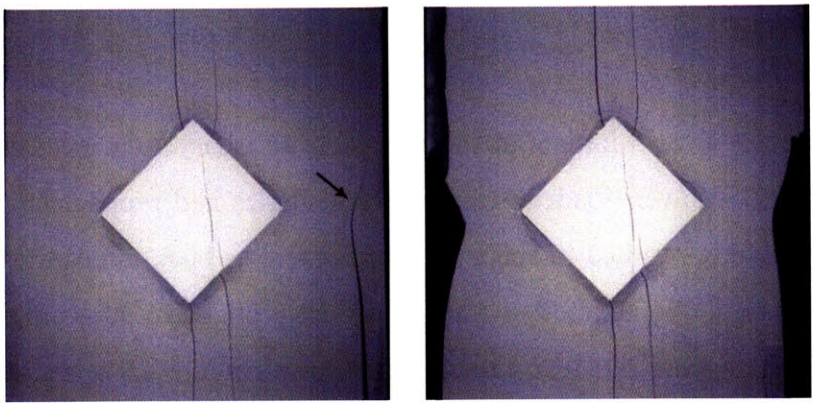

Figure 4.10 – Image taken from the experimental trial of DM-1-Pl depicting the described bowed crack (left) at the right specimen boundary that eventually led to the detachment of a specimen piece (right).

4.4 Crack Initiation and Propagation of Half-inch Inclusions

4.4.1 Circular Inclusions

A summary of the crack sequences and relative stress levels for half-inch circular inclusions is shown in Table 4.5. It should be noted that pre-test surface cracks were rarely seen with half-inch circular inclusions of either material. A significant amount of debonding occurred at both

inclusion types, unlike what was observed with the one-inch inclusions. It typically occurred prior to tensile crack initiation at an Ultracal inclusion boundary; whereas, debonding generally started simultaneously with tensile crack initiation at a plaster inclusion. Tensile crack initiation was also different between the two inclusion materials. Tensile cracks initiated at the boundary of a plaster inclusion, and then propagated into the surrounding matrix. The same tensile cracks then began to propagate into the inclusion, as long as debonding did not occur at the respective boundary point. The initiation of tensile cracks at Ultracal inclusions differed, however. It was common for tensile cracks to initiate just above, or below, the inclusion boundary (Figure 4.11). These tensile cracks propagated in both directions and eventually reached the inclusion boundary. Unlike the one-inch inclusion series, bowed cracks were not observed in specimens with half-inch circular inclusions.

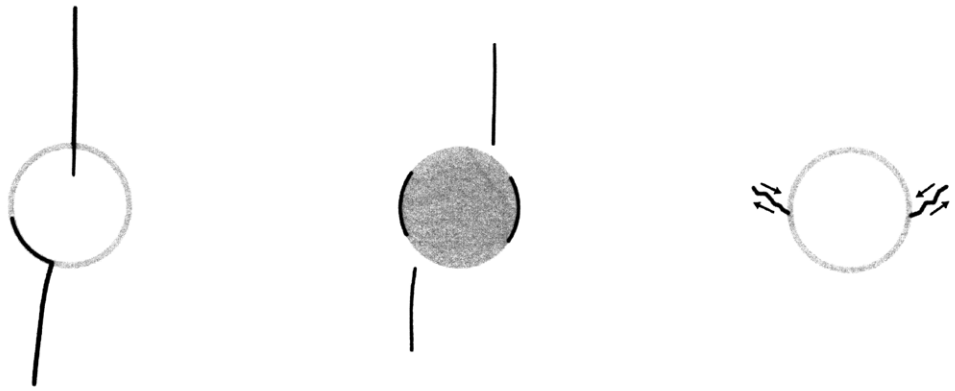

Figure 4.11 – Tensile crack initiation and propagation at a half-inch circular inclusion of plaster material (left), and Ultracal material (center), along with shear crack initiation and propagation at a typical inclusion (right). A summary of all crack sequences and relative stress levels is shown in Table 4.5.

Shear crack initiation typically occurred after the initiation of tensile cracks. As with one-inch inclusions, this always occurred at the left-hand and right-hand inclusion boundary. Shear cracks always initiated at both sides of the inclusion, regardless of the inclusion material. The two shear cracks always sheared in opposite directions (Figure 4.11). This observation is quite different from what was observed with the one-inch inclusions. Shear crack initiation at an Ultracal inclusion typically occurred after the specimen's maximum stress. Shear crack initiation at a plaster inclusion occurred before the maximum stress, however.

4.4.2 Square Inclusions

A summary of the crack sequences and relative stress levels for half-inch square inclusions is shown in Table 4.5. In contrast to what was observed at the boundary of one-inch inclusions, pre-test surface cracks were not seen with half-inch square inclusions of either material and debonding occurred frequently. Debonding always initiated at the left or right inclusion interface. Tensile cracks then initiated at the boundary corners where debonding had occurred, and then propagated away from the inclusion (Figure 4.12). Failure of the specimen occurred when other tensile cracks later initiated at the top or bottom (loaded) specimen boundaries. These other tensile cracks propagated towards the opposite specimen boundary, which typically resulted in specimen detachment (refer to Section 4.3.5). Bowed cracks were not observed in specimens containing half-inch square inclusions. Shear cracks were not common, which is again quite different from what was observed with the one-inch inclusions.

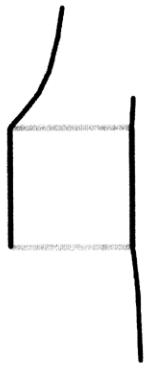

Figure 4.12 – Sketch depicting debonding and tensile crack initiation associated with a half-inch square inclusion. A summary of all crack sequences and relative stress levels is shown in Table 4.5.

4.5 Stress Analysis

4.5.1 Introduction

The previous sections of this chapter provided a qualitative interpretation of the fracture behavior associated with specimens containing single inclusions. An analysis of the quantitative data

collected during each test will now be presented. These data include the various stresses, strains, and stress ratios described in Chapter 3.

4.5.2 Maximum Stress

Each specimen was loaded until a maximum stress value was reached. In this study, the maximum stress is defined as the failure stress of the specimen. Two figures are presented below. Figure 4.13 plots the maximum stress for each specimen containing one-inch inclusions, while Figure 4.14 plots the maximum stress for each specimen containing half-inch inclusions.

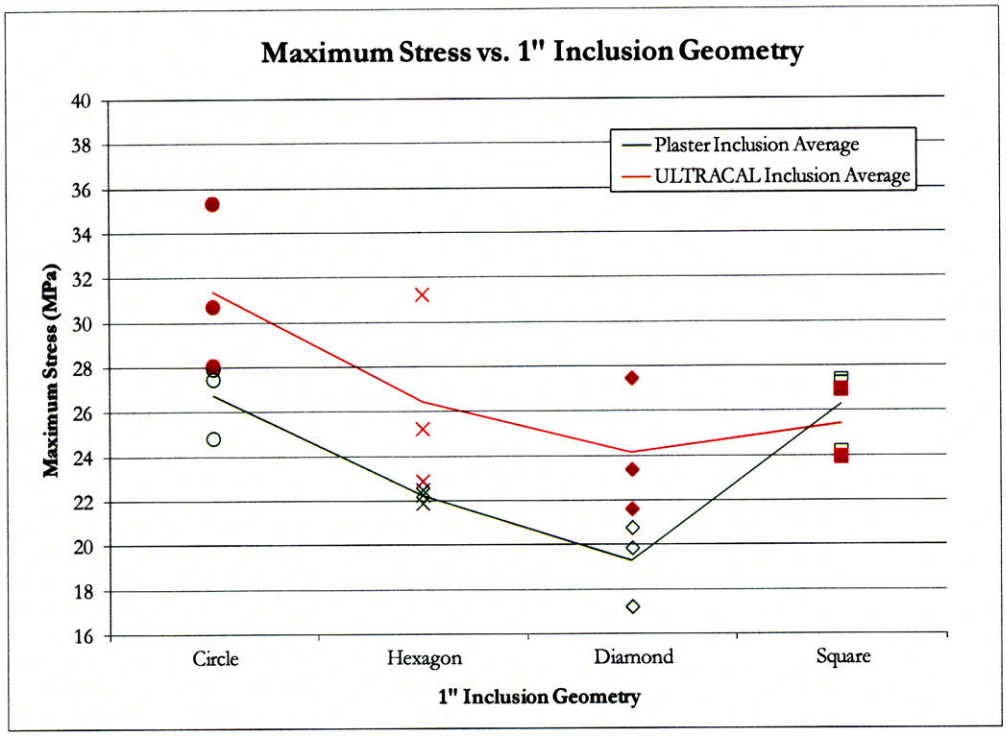

Figure 4.13 – Maximum stresses for specimens with one-inch inclusions. The solid points represent the values for the Ultracal inclusions, while the hollow points represent the values for the plaster inclusions. The lines connect the averages for each geometry and material type.

As shown in Figure 4.13, the maximum stress values for each of the four inclusion geometries are remarkably different. The circular inclusions have a higher average maximum stress value than the other geometries. There is then a significant decrease in the maximum stress of the

hexagon inclusions, followed by another decrease with the diamond inclusions. The average maximum stresses of the square inclusions, however, are approximately the same as the hexagon inclusions. It should be noted that there is substantially less scatter with the maximum stresses of one-inch square inclusions than the other geometries (refer to Figure 4.13). The specimens containing Ultracal inclusions typically sustained higher maximum stresses, with the exception of the square inclusions.

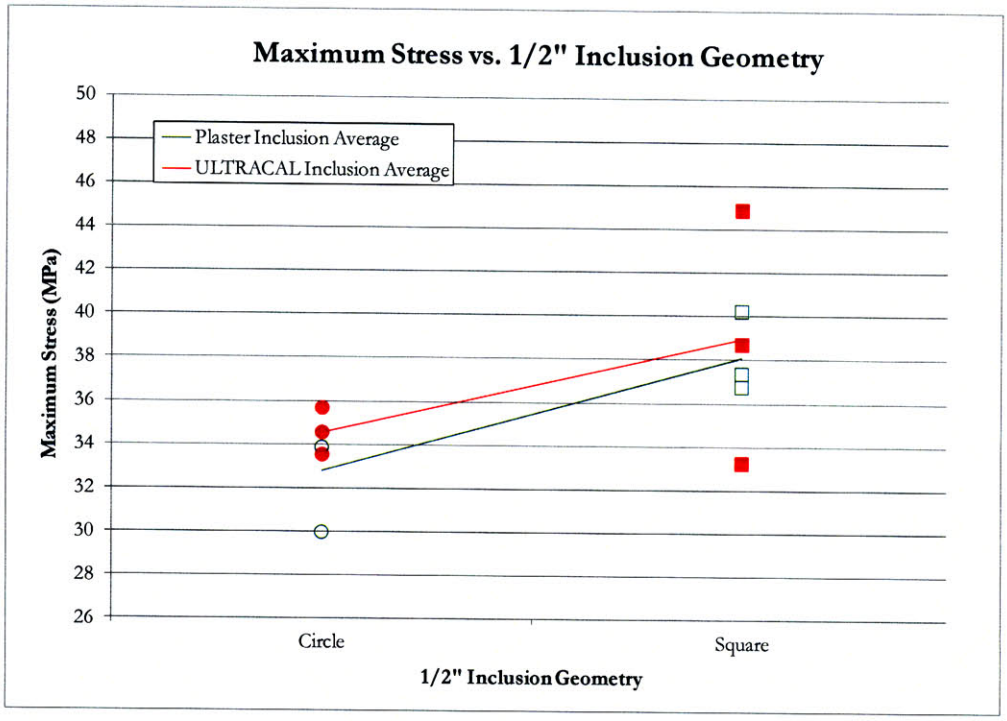

Figure 4.14 – Maximum stresses for specimens with half-inch inclusions. The solid points represent the values for the Ultracal inclusions, while the hollow points represent the values for the plaster inclusions. The lines connect the averages for each geometry and material type.

In contrast to what was observed with the one-inch inclusions, the average maximum stress of the half-inch circular inclusions is less than the square inclusions. Notice, however, that there is significant scatter associated with the stress values of the half-inch square inclusions. Regarding the circular inclusions, specimens containing Ultracal inclusions typically had a higher maximum stress. The same cannot be said of the square inclusions.

4.5.3 Crack Initiation Stress and Stress Ratio

As mentioned earlier in this chapter, tensile cracks always initiated before shear cracks. The stress at which this occurred for specimens containing a one-inch inclusion is plotted in Figure 4.15.

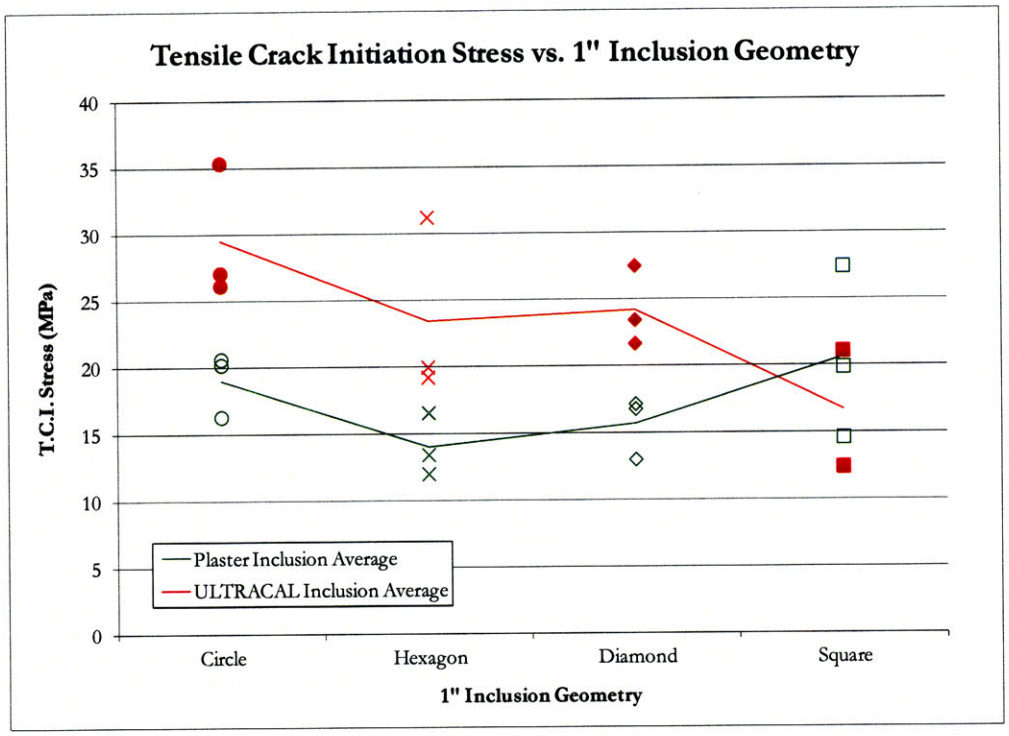

Figure 4.15 – Tensile crack initiation stresses for specimens with one-inch inclusions. The solid points represent the values for the Ultracal inclusions, while the hollow points represent the values for the plaster inclusions. The lines connect the averages for each geometry and material type.

For the most part, the averages for the inclusion geometries follow a similar trend as the maximum stress averages shown in Figure 4.13. With the exception of the square inclusions, there is a greater spread between the initiation stresses of plaster versus Ultracal inclusions. Comparison between Figure 4.15 and Figure 4.13 shows that tensile crack initiation occurred either at, or just before, failure for an Ultracal inclusion; whereas, it typically occurred before the failure of a specimen containing a plaster inclusion. This observation can be better distinguished in Figure 4.16, where the tensile crack initiation stress is normalized with the maximum stress.

Again, this specific observation is not applicable to the square inclusions. It should also be noted that hexagon inclusions also commonly contained pre-test surface cracks, and this may explain the low tensile crack initiation stress ratios in Figure 4.16.

As mentioned earlier, pre-test surface cracks may have resulted in premature tensile crack initiation. Table 4.1 lists the average tensile crack initiation stress ratios for one-inch inclusions that had visible surface cracks, compared to those that did not have visible surface cracks. A direct comparison can be made between the Ultracal, hexagon inclusions and the plaster, diamond inclusions. Notice the reduction in tensile crack initiation stress ratios for those specific specimens.

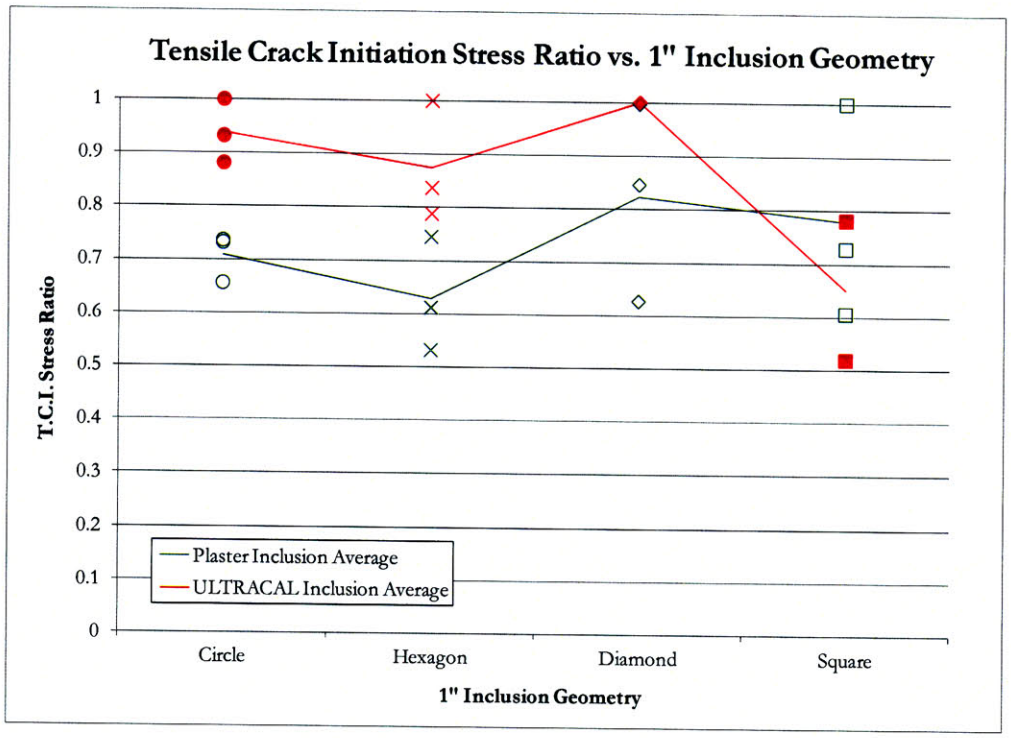

Figure 4.16 – Tensile crack initiation stress ratios for specimens with one-inch inclusions. The solid points represent the values for the Ultracal inclusions, while the hollow points represent the values for the plaster inclusions. The lines connect the averages for each geometry and material type.

		Circle	Hexagon	Diamond	Square
1" Inclusion	Plaster w/ surf. cracks	N/A	62.9%	**62.6%**	N/A
	Plaster w/o surf. cracks	70.9%	N/A	**92.1%**	66.7%
	Ultracal w/ surf. cracks	N/A	**81.3%**	N/A	64.9%
	Ultracal w/o surf. cracks	93.7%	**99.9%**	99.9%	N/A

Table 4.1 – A comparison of average tensile crack initiation ratios (reported in percentages) between one-inch inclusions containing surface cracks, versus no visible surface cracks. Note the differences between the Ultracal, hexagon inclusions and the plaster, diamond inclusions.

A similar comparison can be performed for the specimens containing half-inch inclusions. The tensile crack initiation stresses for half-inch inclusions are presented in Figure 4.17, while the initiation stress ratios are presented in Figure 4.18. Figure 4.14 shows that square inclusions typically had a higher maximum stress than the circular inclusions. Figure 4.18, however, illustrates that the average initiation stress ratios of both inclusions are about the same, although there is some scatter. There is no distinction between the plaster and Ultracal inclusions, unlike what was seen with the one-inch inclusions. Table 4.2 lists the average tensile crack initiation stresses for both the one-inch and half-inch inclusions.

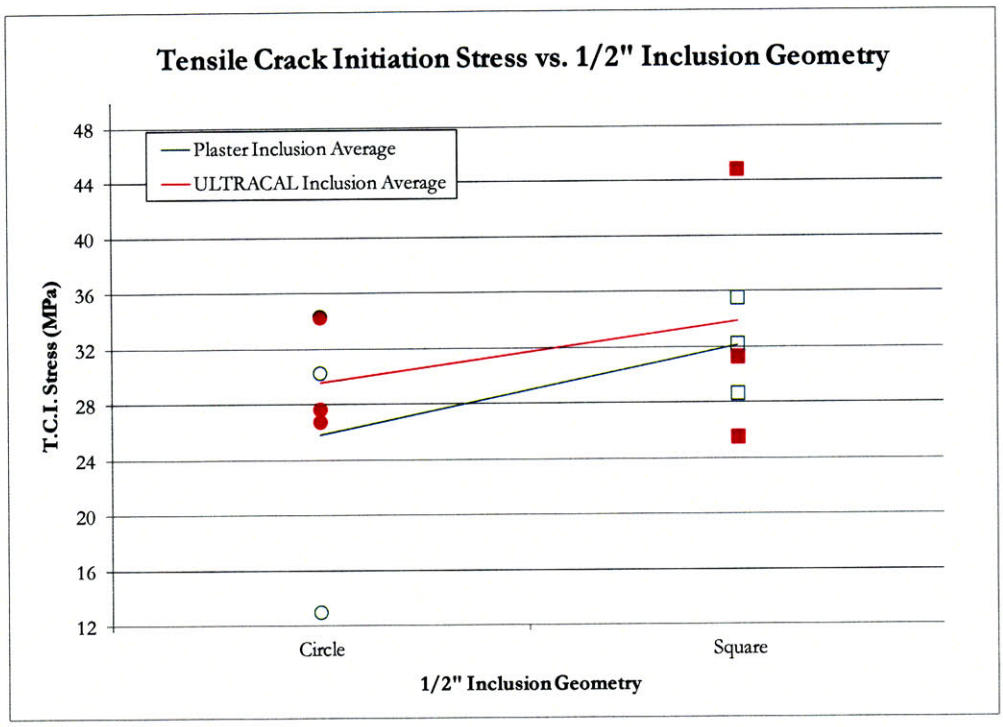

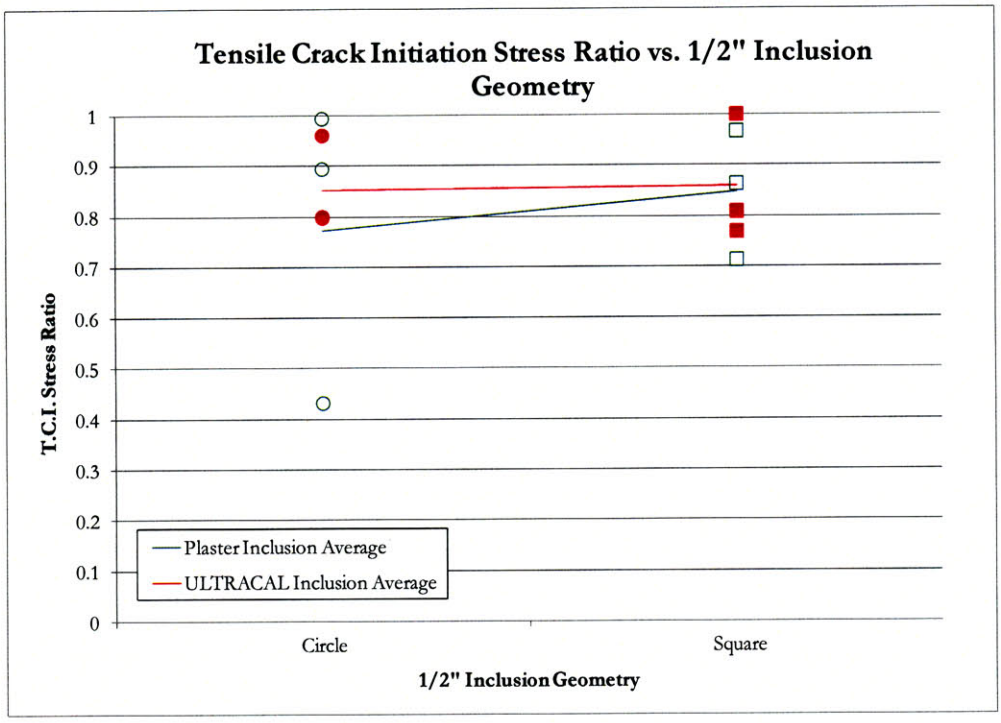

Figures 4.17 & 4.18 – Tensile crack initiation stresses (top) and initiation stress ratios (bottom) for specimens with half-inch inclusions. The solid points represent the values for the Ultracal inclusions, while the hollow points represent the values for the plaster inclusions. The lines connect the averages for each geometry and material type.

		Circle	Hexagon	Diamond	Square
1" Inclusion	Plaster	70.9%	62.9%	82.3%	77.8%
	Ultracal	93.7%	87.5%	99.9%	64.9%
1/2" Inclusion	Plaster	77.4%	-	-	84.8%
	Ultracal	85.3%	-	-	85.9%

Table 4.2 – Average tensile crack initiation ratios for the specimens containing one-inch inclusions. It should be noted that inclusions containing surface cracks were not excluded from the averages.

The shear crack initiation stresses for one-inch inclusions are presented in Figure 4.19, while the initiation stress ratios are presented in Figure 4.20. The pattern of the tensile crack initiation stress ratios (Figure 4.13) is very similar to the shear crack initiation stress values of Figure 4.19. Figure 4.20 shows that the average shear crack initiation stress ratios for all one-inch inclusion specimens are very close to one (i.e., shear cracks typically initiated close to failure). The shear crack initiation stresses for half-inch inclusions are presented in Figure 4.21, while the initiation stress ratios are presented in Figure 4.22. As mentioned earlier, shear cracks typically did not initiate at the square inclusions. Notice, however, that the ratios for half-inch circular inclusions are almost identical to the one-inch circular inclusion shear crack initiation ratios presented in Figure 4.20.

It should be noted that obtaining a stress value for the initiation of a shear crack is somewhat subjective. The high speed video camera used in this study could only record fracture events at the specimen surface. Therefore, spalling at the specimen surface was used as an indicator for shear crack initiation, which corresponds to previous experimental experience of the MIT rock mechanics group and appears to be a very good indicator (e.g., Wong, 2008). Spalling, however, is indicative of a compressive stress state but not necessarily a result of shear crack initiation or propagation. Nevertheless, shearing could definitely be seen with the high speed video camera, and assuming that shear and spalling initiate at the same stress level is an acceptable assumption.

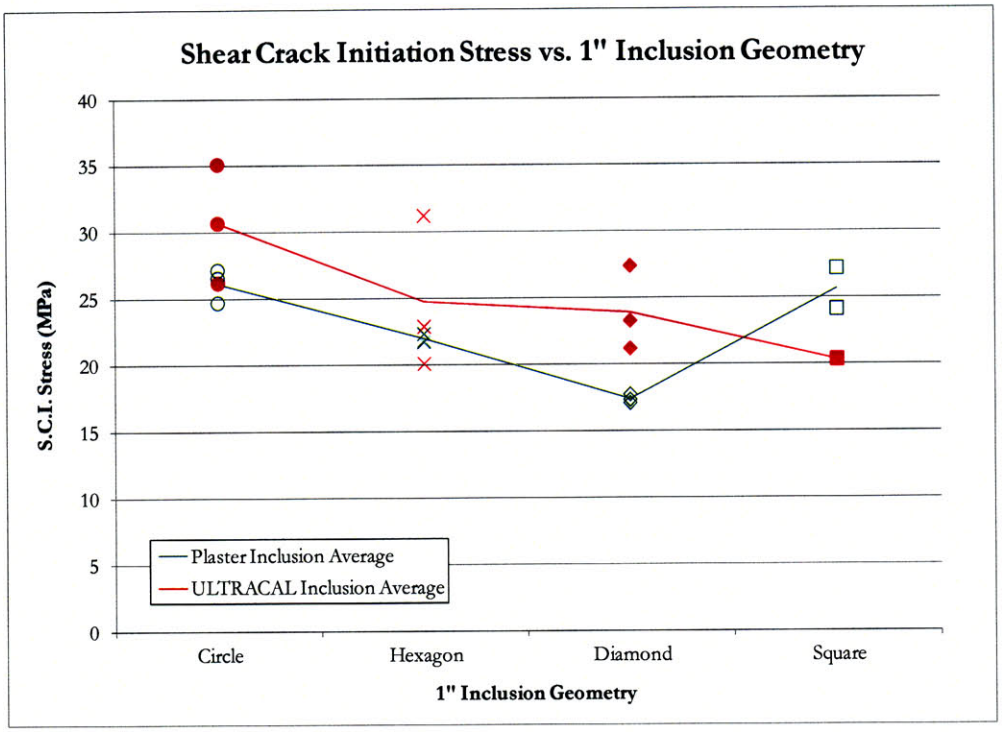

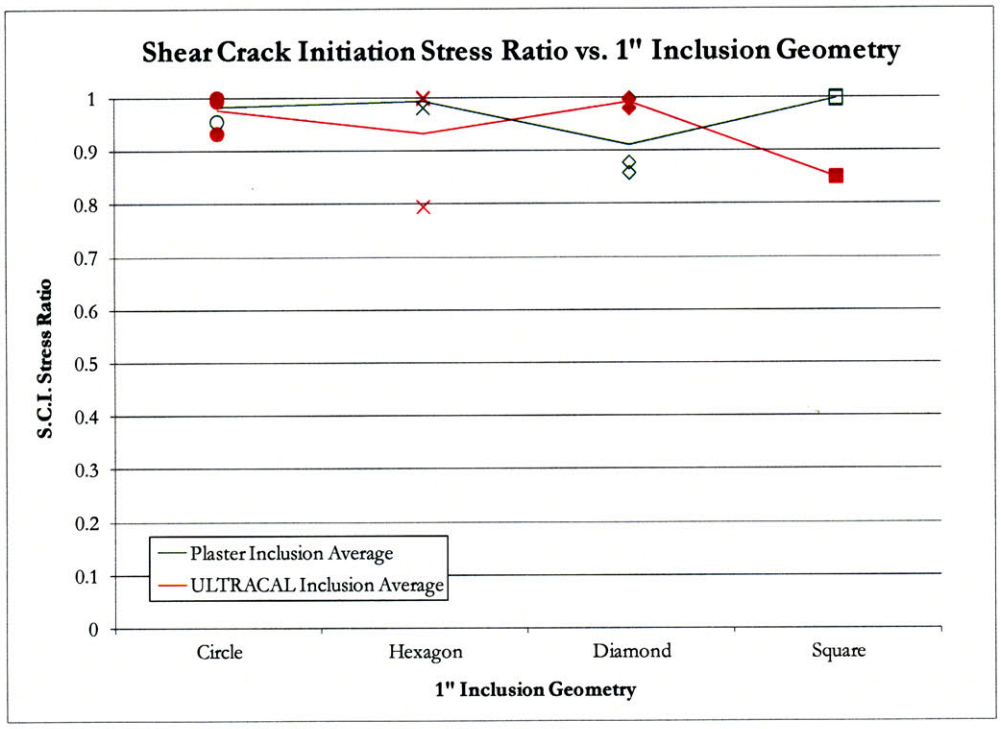

Figures 4.19 & 4.20 – Shear crack initiation stresses (top) and initiation stress ratios (bottom) for specimens with one-inch inclusions. The solid points represent the values for the Ultracal inclusions, while the hollow points represent the values for the plaster inclusions. The lines connect the averages for each geometry and material type.

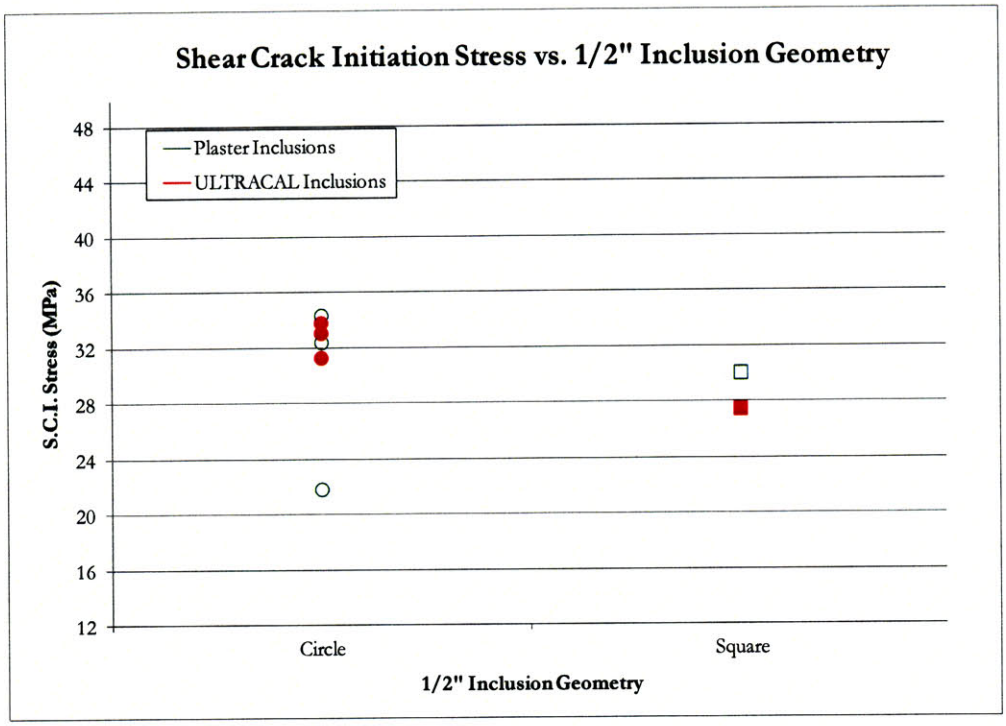

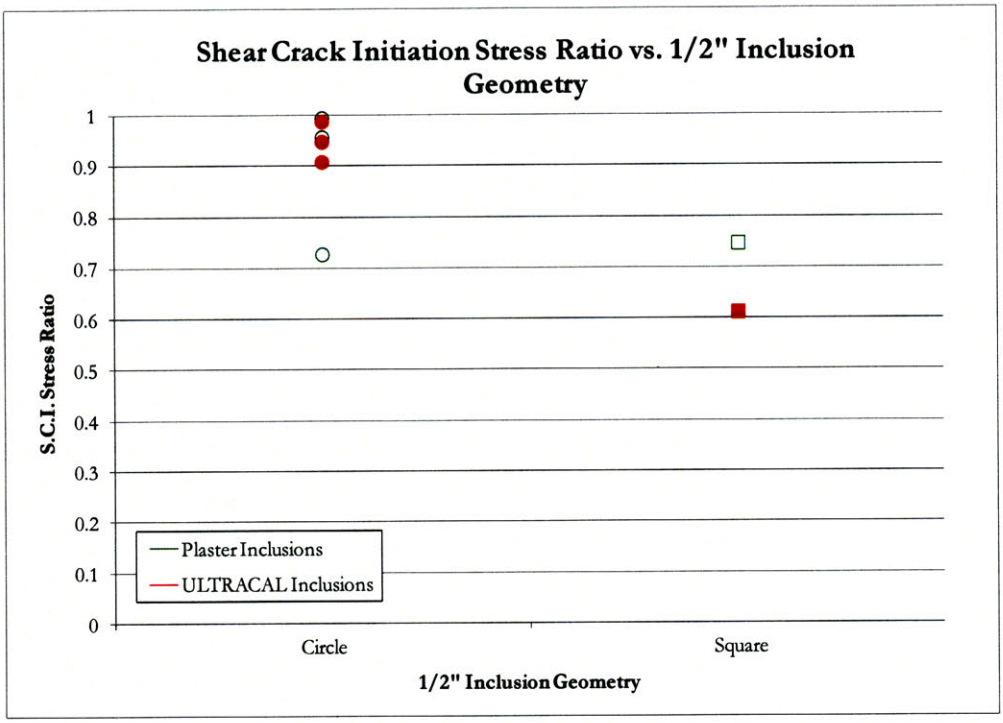

Figures 4.21 & 4.22 – Shear crack initiation stresses (top) and initiation stress ratios (bottom) for specimens with half-inch inclusions. The solid points represent the values for the Ultracal inclusions, while the hollow points represent the values for the plaster inclusions.

4.6 Conclusions

Several uniaxial compression tests were conducted on specimens containing single inclusions. These inclusions had various shapes, sizes, and stiffnesses. The observations made regarding the fracture behavior, as well as stress performance, for each specimen was discussed in this chapter.

4.6.1 Fracture Sequence Summary

Tables 4.3 through 4.5 present a summary of typical crack sequences and relative stress levels for each inclusion size, shape, and material. The relative stress level at each stage was calculated by normalizing the respective stress level with the maximum stress of the specimen. Only the specimens that exhibited the specific fracture pattern were included in the average that is reported in the top right-hand corner of every image. A ratio of the number of specimens that exhibited the trend to the total number of specimens is also reported in the bottom right-hand corner. It should be noted that crack patterns are symmetrical about the top and bottom, or left and right, interface unless otherwise noted. For example, Table 4.5 shows initial debonding on one-side of the plaster, half-inch square inclusion. This does not mean that debonding only occurred at the "right" interface boundary, but that it typically occurred only on one side.

4.6.2 Effect of Inclusion Geometry

The inclusion geometry had various effects on specimen performance. Debonding prior to tensile crack initiation was typically only observed with circular inclusions. More specifically, both one-inch and half-inch Ultracal, circular inclusions experienced extensive debonding prior to tensile crack initiation. This phenomenon may be explained by analyzing the stress concentration values at the inclusion interface. The closed form solutions presented in Section 2.4 are shown again in Figure 4.23. A circular, Ultracal inclusion can be compared to the rigid inclusion model. In this study, debonding was observed at the right and left inclusion interface. This may be a result of the radial tensile stresses that exist adjacent to the left and right rigid

inclusion interface shown in Figure 4.23. Tensile cracks then initiated at points on the inclusion boundary that experienced debonding.

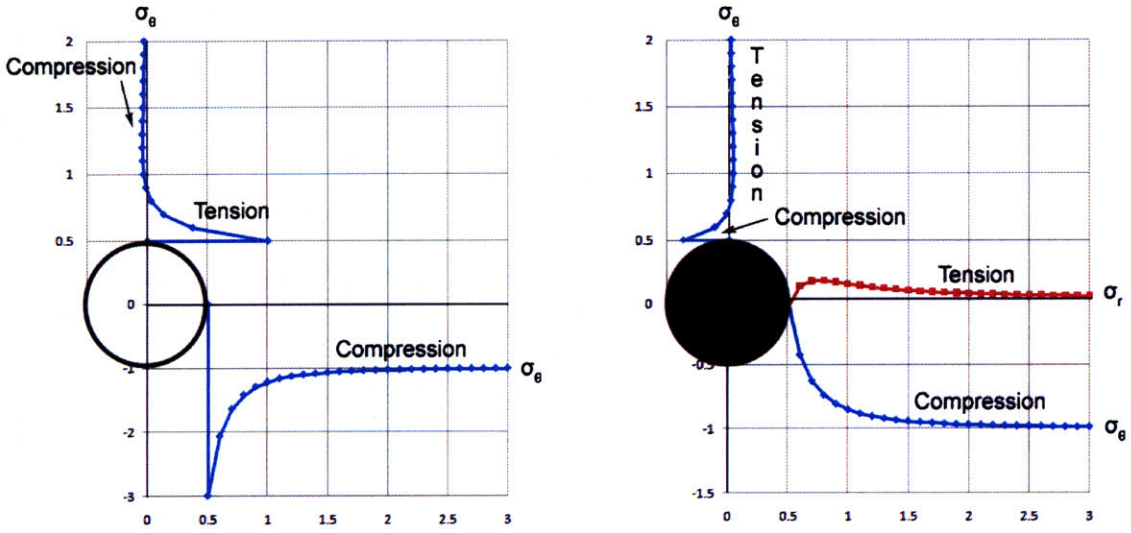

Figure 4.23 – Plots showing the stress concentration factors of a hole (left) and a rigid inclusion (right) cast within an infinite plate (for $\nu = 0.25$) subject to a far field uniaxial compressive stress in the vertical direction.

Whether the inclusion was debonded, or not, the location of tensile crack initiation depended on the inclusion shape. Diamond inclusions, for example, always experienced tensile crack initiation at the upper and lower points, regardless of material type (Table 4.4). Shear crack initiation also depended on inclusion geometry. Shear cracks typically initiated at the bottom corners of a square inclusion, but always initiated at the centers of the other inclusion shapes.

The shape of the inclusion also seemed to govern the extent of shearing at the inclusion interface, which typically occurred just before specimen failure (refer to Tables 4.3 and 4.4). The amount of debonding typically increased as the inclination of a respective inclusion interface increased with respect to the direction of applied load. Post-mortem investigations showed that diamonds experienced the most amount of debonding (100%), hexagons had moderate debonding (~75%), and circles and squares had the least amount of debonding (~50%).

The maximum stresses varied depending on the inclusion geometry. The maximum stress for a circular or square inclusion was about twenty to twenty-five percent higher than the diamond geometry, while the hexagon inclusions were somewhere in between (Figure 4.13). This may be a result of the described interface shearing observation described earlier.

4.6.3 Effect of Inclusion Size

The effects on the size of an inclusion have been studied for many decades. The results of this study essentially agree with those from the past. Specifically, the amount of pre-test surface cracks decreased as the inclusion size decreased. The likelihood that a one-inch inclusion contains more pre-test microcracks is high, since there is direct relationship between the volume of the inclusion and the formation of imperfections, or microcracks. Note a typical one-inch inclusion has four-times the volume of a half-inch inclusion. An increase in debonding was also observed as the inclusion size decreased. Debonding occurred at the same locations as with the one-inch inclusions (i.e., the left and right interface). This again agrees with the closed form solutions shown in Figure 4.23.

Tensile crack initiation occurred earlier at one-inch inclusions compared to half-inch inclusions. This may be a result of the increase in microcrack density as discussed in the previous paragraph. Tensile cracks generally initiated at the same location regardless of inclusion size. The initiation of shear cracks occurred less frequently as the inclusion size decreased. In general, the entire fracturing sequence occurred more instantaneously with half-inch inclusions than with one-inch inclusions. In other words, half-inch inclusions showed signs of fracture at 90% of maximum load, or later, whereas the range for one-inch inclusions was 63% to 99% (Tables 4.3 through 4.5). Also, the maximum stress for specimens containing square inclusions increased about fifty percent with a decrease in inclusion size, while the maximum stress for circular inclusions increased five to twenty percent.

4.6.4 Effect of Inclusion Material

The mechanical properties of both inclusion materials are listed in Table 3.1. It should be noted, however, that the mechanical properties of a half-inch inclusion and one-inch inclusion may be different. This may be a result of the difference between the intact area and volume of a one-inch inclusion compared to a half-inch inclusion. A one-inch inclusion has four-times the volume of a half-inch inclusion, but only has twice the contact surface area. Assuming that the Hydrocal matrix adsorbs an equal amount of water (per contact unit area) from the inclusion paste during pouring, more water (relative to the inclusion volume) was removed from the half-inch inclusion paste compared to the one-inch inclusion paste. Therefore, the half-inch inclusions might be somewhat stiffer than the one-inch inclusions. This hypothesis will need further investigation.

The stiffness of the inclusion relative to the surrounding matrix had various effects on the fracture behavior of the specimen. It appears that the extent of debonding typically increased as the stiffness of the inclusion increased. This supports the argument presented in the previous paragraph, since half-inch inclusions typically debonded more than one-inch inclusions. As discussed in Section 4.6.2, the debonding phenomenon may be explained by the closed form solutions presented in Figure 4.23.

Tensile crack initiation differed between plaster and Ultracal inclusions since debonding commonly occurred at Ultracal inclusions. Regarding Ultracal inclusions, primary tensile cracks (i.e., the first tensile cracks to initiate) typically initiated at areas of interface debonding. Secondary tensile cracks, which initiated after primary tensile cracks, also propagated into plaster inclusions more often than Ultracal inclusions. In some instances tensile cracks were observed initiating just above, or below, an Ultracal inclusion. According to the stress concentration factors presented in Figure 4.23, the rigid inclusion experiences a region of tensile stresses just above and below the inclusion and this may explain the phenomenon observed in this study. Shear crack initiation does not seem to be impacted by the stiffness of the inclusion, but this cannot be said with certainty since analytical data cannot be provided for reasons mentioned in Section 4.5.3.

For the most part, specimens containing Ultracal inclusions had a higher failure stress than plaster inclusions. Tensile cracks also initiated at plaster inclusions before Ultracal inclusions. According to Tables 4.3 through 4.5, the cracking sequences associated with one-inch Ultracal inclusions occurred "simultaneously" compared to plaster inclusions (i.e., typically all cracking processes occurred just before failure).

1" Inclusion Shape & Material		Initial Geometry	Typical Fracturing Sequence and Relative Stress Levels		
Circle	Plaster		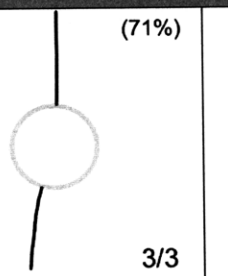	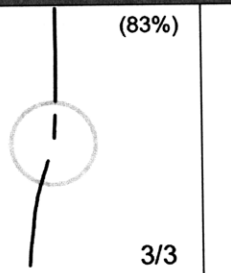	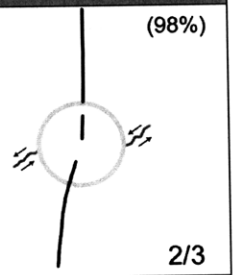
	Ultracal		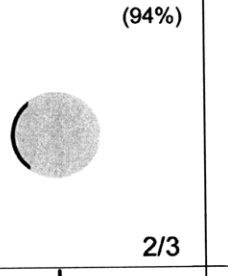	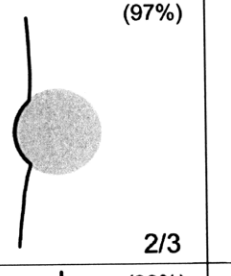	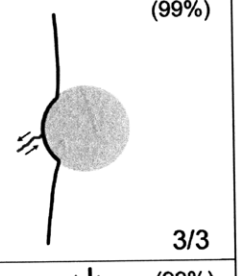
Hexagon	Plaster		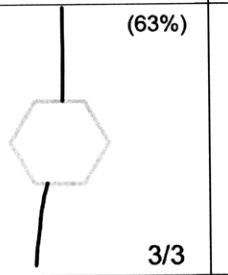	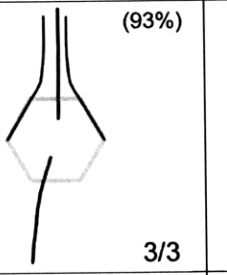	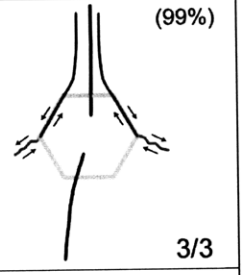
	Ultracal		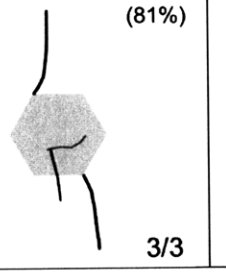	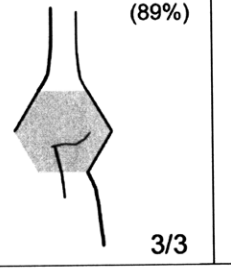	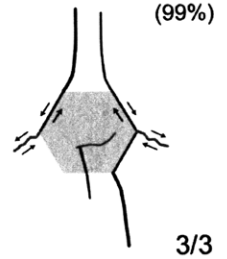

Table 4.3 – Crack sequences for the circle and hexagon one-inch inclusions (refer to Section 4.6.1 for details).

1" Inclusion Shape & Material		Initial Geometry	Typical Fracturing Sequence and Relative Stress Levels		
Diamond	Plaster		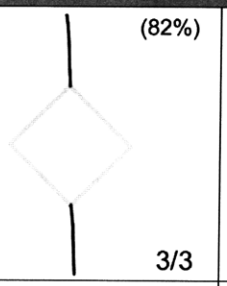	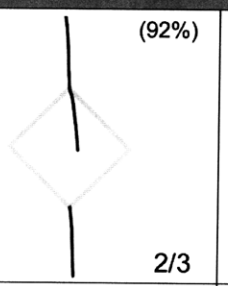	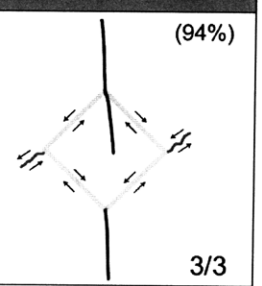
	Ultracal		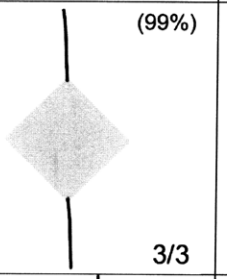	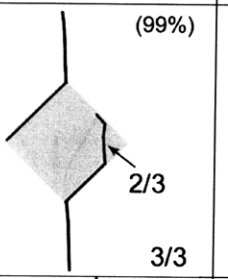	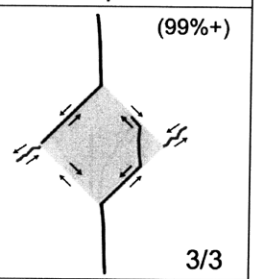
Square	Plaster		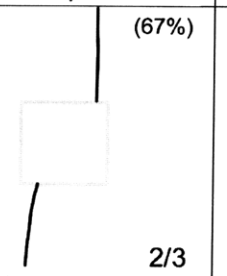	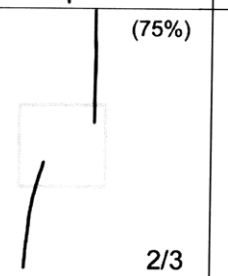	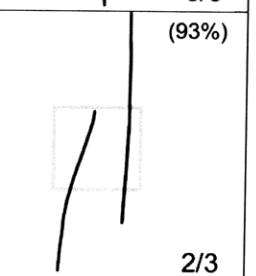
	Ultracal		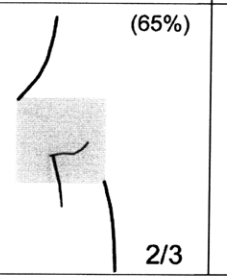	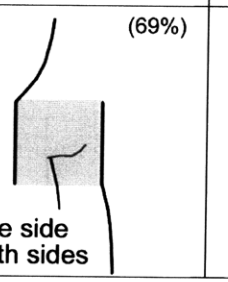	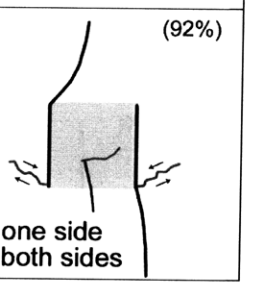

Table 4.4 – Crack sequences for the diamond and square one-inch inclusions (refer to Section 4.6.1 for details).

1/2" Inclusion Shape & Material		Initial Geometry	Typical Fracturing Sequence and Relative Stress Levels		
Circle	Plaster		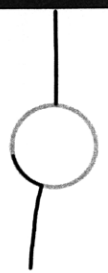 (94%) 2/3	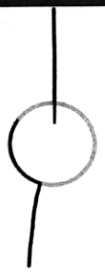 (95%) 2/3	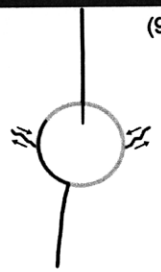 (98%) 3/3
	Ultracal		 (90%) 2/3	 (93%) 2/3	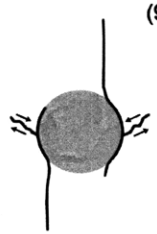 (95%) 3/3
Square	Plaster		 (99%+) 2/3	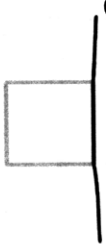 (99%+) 3/3	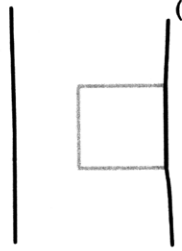 (99%+) 3/3
	Ultracal	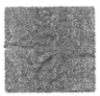	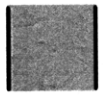 (94%) 2/3 one side 1/3 both sides	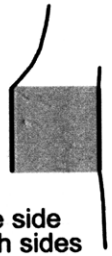 (95%) 2/3 one side 1/3 both sides	 (99%+) 2/3 one side 1/3 both sides

Table 4.5 – Crack sequences for the circle and square half-inch inclusions (refer to Section 4.6.1 for details).

CHAPTER 5 – Uniaxial Compression Tests of Specimens Containing Double Inclusions

5.1 Introduction

Unconfined uniaxial compression tests were performed on prismatic specimens containing two inclusions. These specimens were loaded until failure and similar observations were made as with the single inclusions. Of specific interest, however, is the coalescence behavior for the pair of inclusions. More specifically, the effects of inclusion inclination angle, inclusion material, and inclusion shape on the coalescence of an inclusion pair was studied. The results of these experiments are described in this chapter, while the detailed analyses can be found in Appendix D and Appendix E.

5.2 Experimental Details

In order to study the fracture behavior of two half-inch inclusions, two inclusion geometries were considered: square and circle. It would have been ideal that all four geometries tested in the one-inch inclusion series were also incorporated into the double inclusion series, but time constraints prevented this from happening. In order to create a systematic test series and possibly correlate the results of this study with those done by past MIT rock mechanics group members, the same geometric definitions were adopted in this study (Figure 5.1).

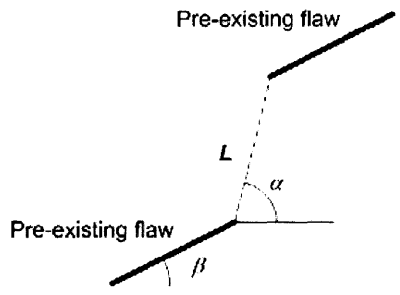

Figure 5.1 – Double flaw geometry defined by Wong (2008) which consists of an inclination angle (β), a bridging angle (α), and a ligament length (L).

An issue exists when trying to apply the geometric scheme in Figure 5.1 to two inherently different geometric shapes. The main goal in this study was to keep the ligament length constant (equal to 0.5", or 2a), especially since this seems to have affected the results reported by Maji and Shah (1989; 1990). The way the inclination angle was measured differed between the two geometries, as an entirely analogous way of defining β for circular and square inclusions would have transformed the "square" geometry into a "diamond" geometry at large β values. Only half-inch inclusions were used in this study so to be consistent with the 2a flaw geometries tested by the MIT rock mechanics group. The geometric definitions for both inclusion shapes are presented in Figure 5.2.

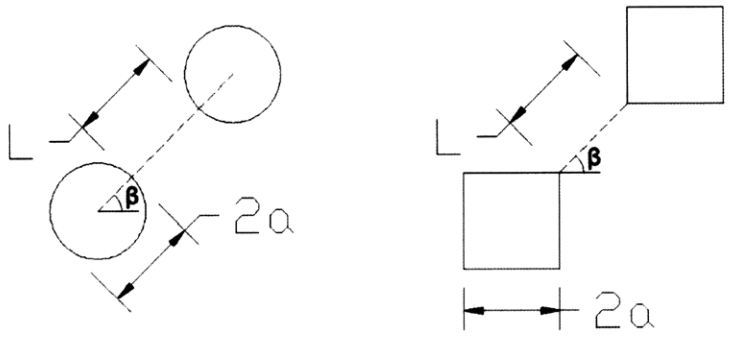

Figure 5.2 – Double inclusion geometries for the square and circle half-inch inclusions, which consist of an inclination angle (β) and a ligament length (L).

Only the inclination angle (β) and the inclusion material were varied in this test series. Regarding the circular inclusions, the inclination angle was defined as either 0°, 30°, or 60°. The square inclusions were cast in -45°, 30°, and 60° inclinations, but an additional inclination angle of 75° was also created to account for the geometric differences described in the previous paragraph. This resulted in fourteen unique geometries that are listed in Table 5.1, and depicted in Figure 5.3 in order to see the similarities and dissimilarities between the inclusion geometries.

Inclusion		Inclination Angle (β)			
		β =0° (circles) & β = -45° (squares)	β = 30° (circles) & β = 30° and 60° (squares)		β =60° (circles) & β = 75° (squares)
Circle	Plaster	CR(Pl)-0-0	CR(Pl)-30-0		CR(Pl)-60-0
	Ultracal	CR(Ul)-0-0	CR(Ul)-30-0		CR(Ul)-60-0
Square	Plaster	SQ(Pl)-45-0	SQ(Pl)-30-0	SQ(Pl)-60-0	SQ(Pl)-75-0
	Ultracal	SQ(Ul)-45-0	SQ(Ul)-30-0	SQ(Ul)-60-0	SQ(Ul)-75-0

Table 5.1 – The square and circle double inclusion geometries tested in this study. The geometries with inclination similarities are grouped into the same column (refer to Figure 5.3).

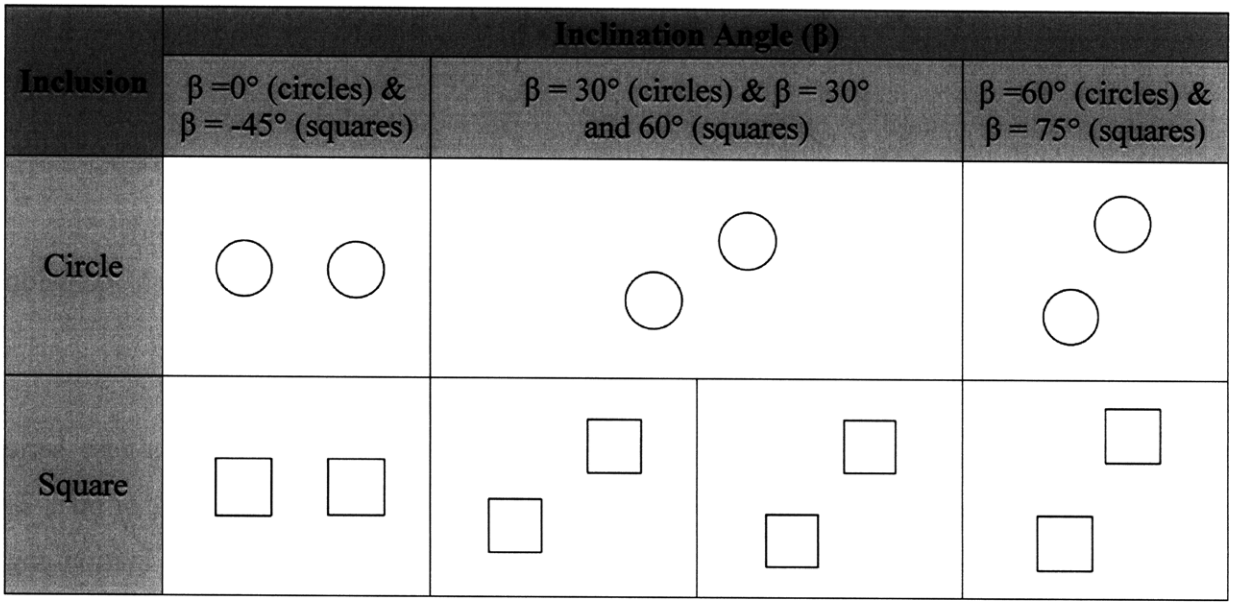

Figure 5.3 – Depiction of the square and circle double inclusion geometries.

5.3 Crack Initiation and Propagation

The cracking behavior of the circle and square double inclusion specimens was very similar to what was observed with the single inclusions (refer to Section 4.3). To summarize, tensile cracks first initiated at a plaster interface and then propagated into the surrounding matrix. As the load increased, the same tensile cracks propagated into the plaster inclusion. Regarding

Ultracal inclusions, tensile cracks commonly initiated at a debonded portion of the interface and then propagated into the surrounding matrix. On occasion tensile cracks initiated within the Ultracal inclusion, or just above and below the interface. Four basic tensile crack "types" initiated in this double inclusion study (Figure 5.4 and 5.5). The four crack types are defined as follows:

Type I – A tensile crack that propagates relatively straight.

Type II – A tensile crack that propagates with curvature.

Type III – A tensile crack that initiates at a pre-test surface crack.

Type IV – A tensile crack that initiates within the matrix.

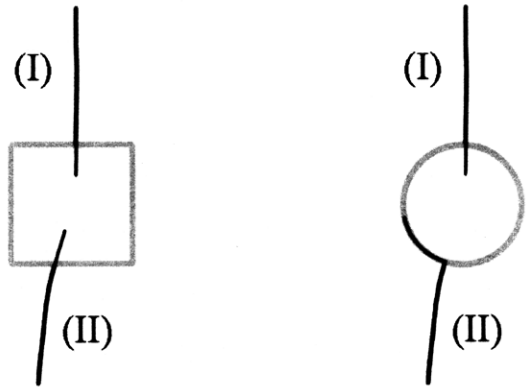

Figure 5.4 – Typical tensile crack initiation and propagation at a square (left) and circle (right) plaster inclusion.

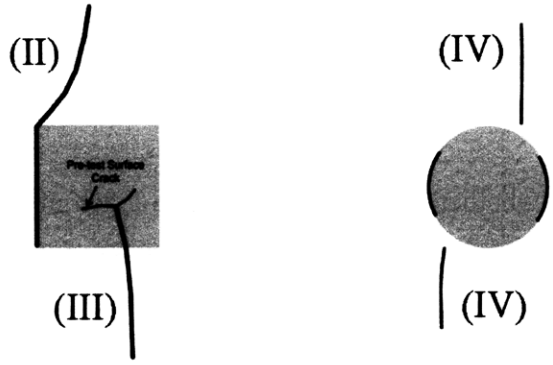

Figure 5.5 – Typical tensile crack initiation and propagation at a square (left) and circle (right) Ultracal inclusion.

The initiation of shear cracks was again similar to what was reported with the single half-inch inclusions (see Section 4.3). Shear cracks always initiated at the midpoints of the circular inclusions, while shear cracks only initiated at the corners of square inclusions. After initiation, shear cracks always propagated away from the inclusion. The propagation of shear cracks typically resulted in the coalescence of the inclusion pair, which will be discussed in detail in Section 5.4.

It was commonly observed that crack initiation started in one inclusion first, especially with the $\beta = 0°$ (circle) and $\beta = -45°$ (square) series. This inclusion typically had a pre-test surface crack, whereas the other did not (see Figure 5.6). Tensile cracks later initiated at the other inclusion after extensive cracking already occurred at the first inclusion.

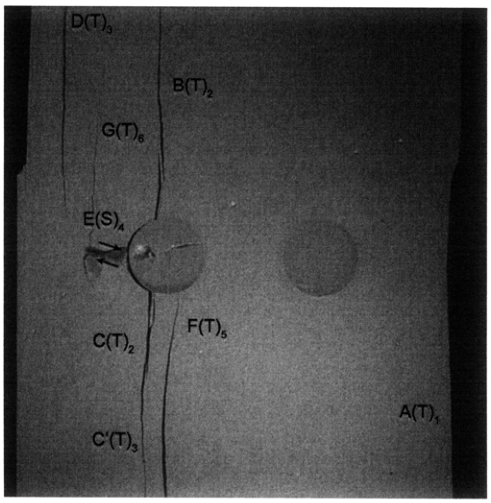

Figure 5.6 – A specimen containing two circular inclusions where extensive cracking occurred at the left-hand inclusion prior to the right-hand inclusion. Notice the surface crack located within the left-hand inclusion. Image taken from the analysis of specimen CR(Ul)-0-0A.

It is important to determine whether a previously initiated crack affected the coalescence of the inclusion pair. Typically, the overall cracking behavior associated with specimens of the same geometry was dissimilar. For this reason a table depicting general crack sequences is not presented, but comments will be made on those cracks preceding coalescence (Section 5.4).

5.4 Coalescence Behavior

5.4.1 Coalescence Categories

As mentioned in Chapter 2, Wong (2008) studied the coalescence behavior of flaw pairs in gypsum and marble. He used his definitions for the seven crack types (Figure 5.7) in order to report nine different coalescence patterns (Figure 5.8), which will also be used to describe the coalescence patterns observed in this study. A brief description of all nine coalescence categories is as follows:

Category 1 – No coalescence. Tensile and/or shear cracks initiate at the flaw tips, but coalescence does not occur.

Category 2 – Coalescence occurs in an indirect manner. Tensile and/or shear cracks initiate at the flaw tips and propagate away from the flaw pair. Two or more of these cracks then coalescence outside the bridging area.

Category 3 – Coalescence results from the propagation of one or two "type 2" shear cracks that previously initiated at the inner flaw tips. Type 2 cracks are coplanar with the existing flaw pair.

Category 4 – Coalescence results from the propagation of one or two "type 1" shear cracks that previously initiated at the inner flaw tips. Type 1 cracks are not coplanar with the existing flaw pair.

Category 5 – Coalescence results from one, or more, type 2 "S"-shaped shear cracks that initiate at the inner flaw tips, while type 2 tensile crack segments initiate in between the central bridging area.

Category 6 – One, or two, type 2 tensile cracks initiate independently at the inner flaw tips and propagate until coalescence.

Category 7 – Coalescence results from a single type 1 tensile wing crack that initiates at one inner flaw tip and propagates to the other flaw.

Category 8 – Coalescence results from one, or more, type 2 tensile cracks that initiate and coalesce with the flaw tips of the same side. This type 2 tensile crack(s) does not exhibit tensile wing crack behavior, and may contain short shear segments.

Category 9 – A single type 3 tensile crack initiates from one side of a flaw tip and coalesces with the other side of the opposite flaw. Type 3 cracks are commonly referred to as anti-wing cracks, and in this case may contain short shear cracking segments.

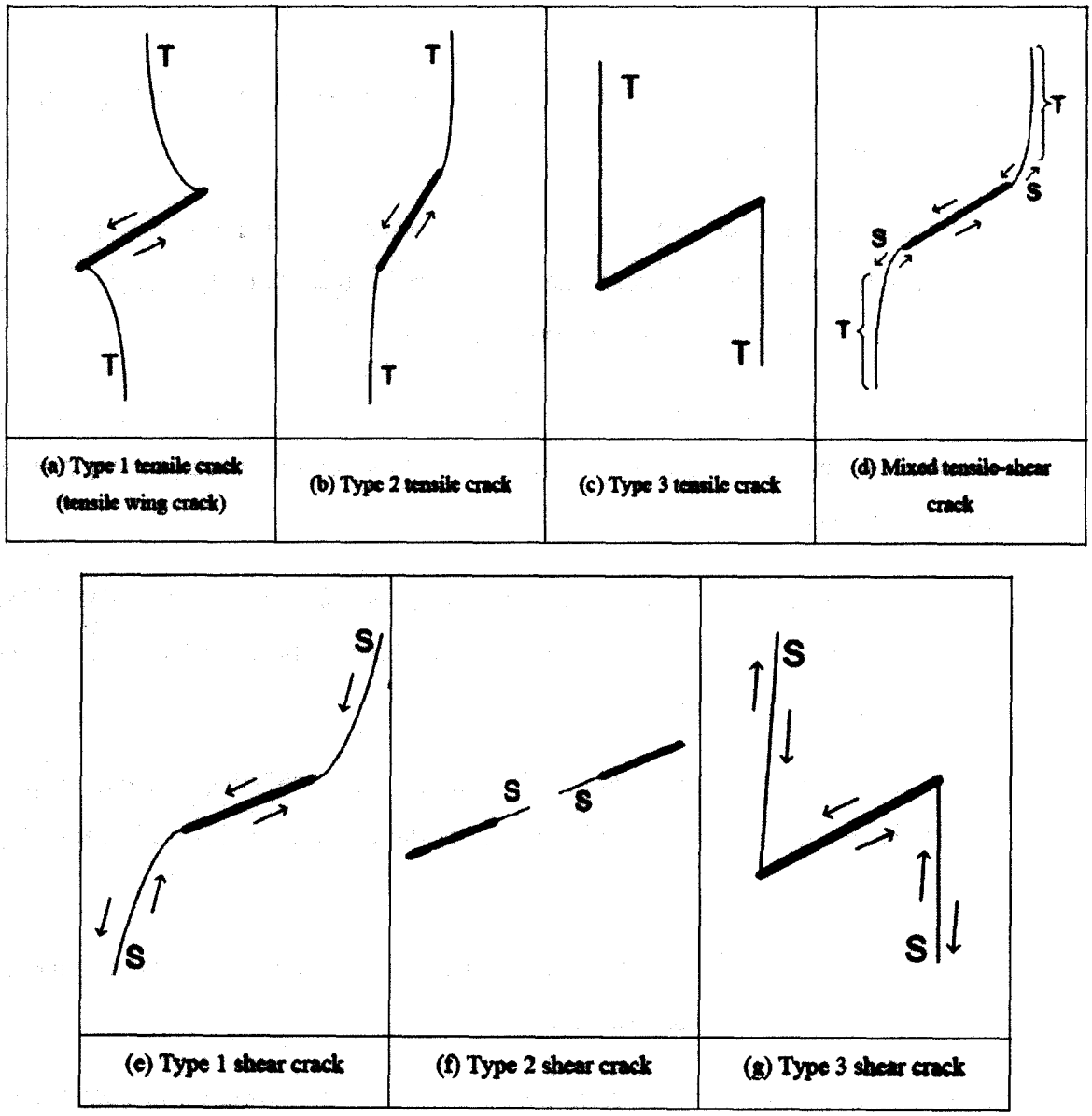

Figure 5.7 – The seven crack types associated with a single flaw (Wong, 2008).

Category	Coalescence patterns	Crack types involved
1	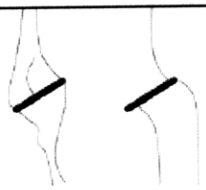	No coalescence
2	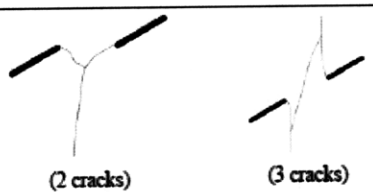	Indirect coalescence by two or multiple cracks (crack types vary)
3	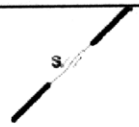	Type 2 S crack(s)
4	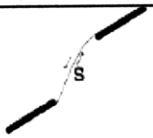	Type 1 S crack(s)
5	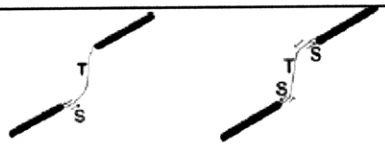	One or more type 2 S crack(s) and type 2 T crack segments between inner flaw tips
6		Type 2 T crack(s). There may be occasional short S segments present along the coalescence crack.
7	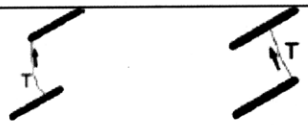	Type 1 T crack(s)
8		Flaw tips of the same side linked up by T crack(s) not displaying wing appearance (crack type not classified). There may be occasional short S segments present along the coalescence crack.
9		Type 3 T crack(s) linking right tip of the top flaw and left tip of the bottom flaw. There may be occasional short S segments present along the coalescence crack.

Figure 5.8 – The nine coalescence patterns reported by Wong (2008), where T = tensile and S = shear. Refer to Figure 5.7 for crack type descriptions.

5.4.2 Circular Inclusions

Detailed analyses of specimens with double circular inclusions are presented in Appendix D. A summary of the coalescence patterns observed in this experimental series is presented in Figure 5.9.

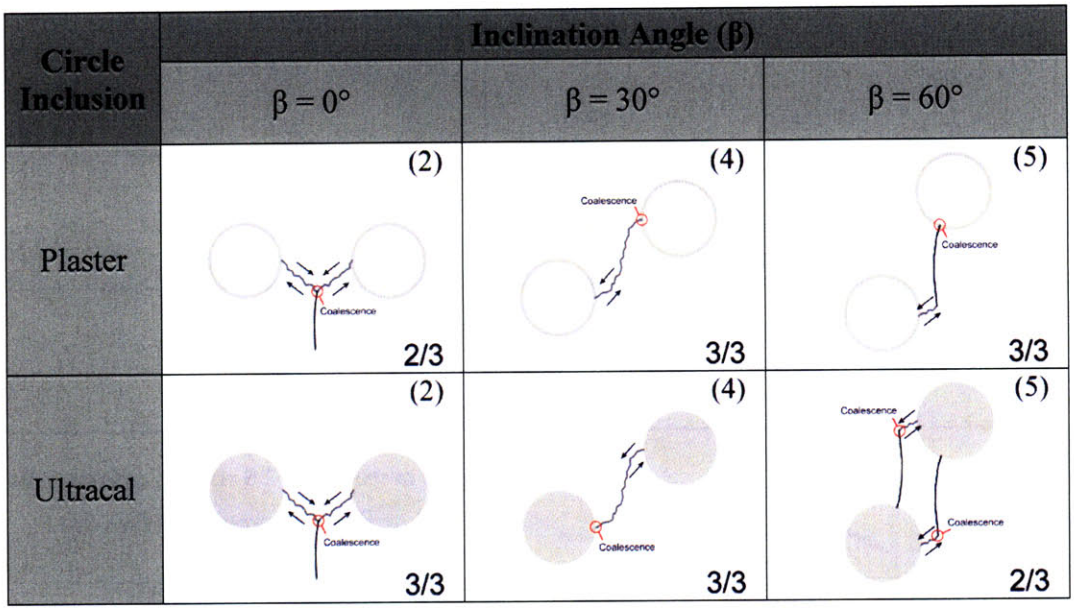

Figure 5.9 – Coalescence patterns for the double, circular inclusion series. The number in the top right-hand corner of each image represents the coalescence category (refer to Figure 5.8) observed, while the fraction in the bottom right-hand corner represents the number of specimens showing that particular behavior out of the number of specimens tested.

Regardless of the inclusion material, the $\beta = 0°$ series coalesced in a similar indirect manner; the dominant coalescence category was a (2). All three Ultracal specimens coalesced in this fashion, and two of the three plaster inclusions also coalesced in this way (the other plaster specimen did not coalesce). Typically, a shear crack initiated at one of the inner inclusion boundaries and propagated until a tensile crack initiated at the shear crack tip. Another shear crack then initiated at the other inner inclusion interface and propagated until its coalescence with the first shear crack. Primary tensile crack initiation did not appear to have a *direct* effect on coalescence, but the initiation of the first shear crack typically occurred at the same inclusion where primary

tensile crack initiation occurred (this will be defined as a *possible* effect on coalescence). This *possible* effect occurred in all specimens except one which contained Ultracal inclusions. In this specimen, shear crack initiation did not occur at the same inclusion as primary tensile crack initiation (defined as *no* effect on coalescence).

The $\beta = 30°$ series also coalesced in a similar manner regardless of inclusion material. The coalescence pattern for all six specimens was category (4). A single shear crack initiated at one of the inner inclusion interfaces and propagated in an "S"-shaped manner until its coalescence with the other inner inclusion boundary. In two out of three specimens with plaster inclusions, primary tensile crack initiation appeared to have *no* effect on coalescence. In the other specimen, and all three Ultracal specimens, primary tensile crack initiation had a *possible* effect on coalescence as the initiation of the first shear crack occurred at the same inclusion as primary tensile crack initiation.

A difference in coalescence patterns between inclusions of different material was observed for the $\beta = 60°$ series, although both showed category (5) coalescence. For the plaster series, all three specimens coalesced in the same way. A shear crack first initiated at the inner inclusion boundary of one inclusion and propagated in the direction of the other inclusion. A tensile crack then initiated at the tip of the shear crack and propagated until its coalescence with the other inclusion. Two out of three specimens containing Ultracal inclusions also coalesced in a similar manner, but typically coalescence occurred through two sets of cracks, as shown in Figure 5.9. The tensile cracks initiated first at the Ultracal inclusion boundary and propagated vertically towards the other inclusion. Shear cracks then initiated at the opposite inclusion interface and propagated until coalescence with the tensile cracks. The other specimen coalesced similar to the $\beta = 60°$ plaster inclusions series. In all specimens, the propagations of primary tensile cracks were *directly* involved in the coalescence of the inclusion pair (i.e., coalescence occurred along these primary tensile cracks).

	Inclination Angle	First (Primary) Cracks To Appear	***Effect of Primary Cracks on Coalescence	Coalescence Cracks
Plaster Inclusions	$\beta = 0°$	Type II (2/3) Unknown* (1/3)	Possible (2/3)	Category 2 (2/3) No Coalescence (1/3)
	$\beta = 30°$	Type II (2/3) Boundary** (1/3)	Possible (1/3) None (2/3)	Category 4 (3/3)
	$\beta = 60°$	Type II (3/3)	Direct (3/3)	Category 5 (3/3) – two cracks
Ultracal Inclusions	$\beta = 0°$	Type II (3/3)	Possible (2/3) None (1/3)	Category 2 (3/3)
	$\beta = 30°$	Type I (1/3) Type III (1/3) Type IV (1/3)	Possible (3/3)	Category 4 (3/3)
	$\beta = 60°$	Type II (1/3) Boundary** (2/3)	Direct (3/3)	Category 5 (1/3) – two cracks Category 5 (2/3) – four cracks

* Unknown due to error during test (see Appendix D).

** First crack initiated at the lower loaded specimen boundary and propagated towards an inclusion (refer to Appendix D).

*** A *possible* effect on coalescence is when the initiation of the first shear crack occurred at the same inclusion as primary tensile crack initiation, while a *direct* effect is when coalescence occurred along primary tensile cracks.

Table 5.2 – Summary of cracking behavior for the circular inclusion pair series. Numbers in parentheses represent the number of specimens that experienced that trait compared to the number of specimens tested.

5.4.3 Square Inclusions

Detailed analyses of specimens with double square inclusions are presented in Appendix E. A summary of the coalescence patterns observed in this experimental series is presented in Figure 5.10.

The coalescence patterns observed for the β = -45° series differed depending on inclusion material. The Ultracal inclusions all coalesced directly with a category (3) pattern. A single

shear crack initiated at the corner of one inclusion and propagated towards the opposite corner of the other inclusion. The plaster inclusions typically coalesced in an indirect manner (category 2). A shear crack initiated at one corner of an inclusion and propagated towards the other inclusion's opposite corner. A tensile crack then initiated at the shear crack tip while another shear crack initiated at the corner of the other inclusion. The third specimen with plaster inclusion coalesced in the same way as the Ultracal inclusions. Primary tensile crack initiation had a *possible* effect on coalescence in all specimens, since the initiation of the first shear crack always occurred at the same inclusion as primary tensile crack initiation.

Square Inclusion	Inclination Angle (β)			
	β = -45°	β = 30°	β = 60°	β = 75°
Plaster	(2) Coalescence 2/3	(4) Coalescence 1/3 (2/3 no coal.)	(3) Coalescence 1/3 (1/3 no coal.)	(5) Coalescence Coalescence 2/3
Ultracal	(3) Coalescence 3/3	(4) Coalescence 3/3	(3) Coalescence 2/3	(5) Coalescence Coalescence 2/3

Figure 5.10 – Coalescence patterns for the double, square inclusion series. The number in the top right-hand corner of each image represents the coalescence category observed, while the fraction in the bottom right-hand corner represents the number of specimens showing that behavior out of the number of specimens tested.

The specimens of the β = 30° series all coalesced in the same way regardless of inclusion material. Coalescence occurred through a single shear crack that initiated at one inner corner of an inclusion and propagated to the same inner corner of the other inclusion (category 4). Two out of the three plaster inclusions, however, did not coalesce at all. In these "non-coalescing" tests, tensile cracks typically initiated at one of the loaded specimen boundaries and propagated towards the other loaded boundary, which eventually resulted in detachment (Figure 5.11). Tensile cracks also initiated at the inclusion boundaries and propagated towards both loaded

specimen boundaries, which resulted in the splitting (and failure) of the specimen. Primary tensile crack initiation had a *possible* effect on coalescence in all specimens, except for one which contained Ultracal inclusions. In this specimen, shear crack initiation did not occur at the same inclusion as primary tensile crack initiation (i.e., *no* effect on coalescence).

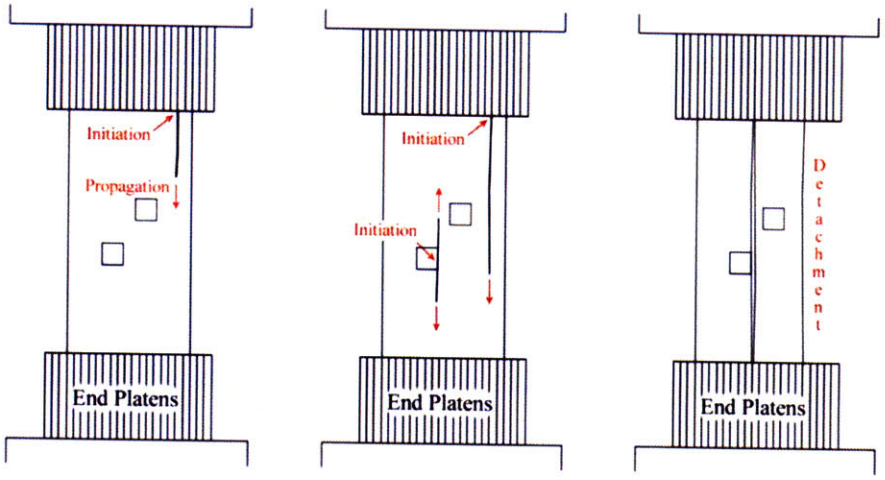

Figure 5.11 – Typical "no coalescence" sequence for the double, square inclusion series.

The $\beta = 60°$ series also coalesced in the same manner regardless of inclusion material. A single shear crack initiated at the innermost corner of one inclusion and propagated directly to the innermost corner of the opposite inclusion (category 3). The reason why this coalescence pattern is defined as category (3) versus category (4), is because (unlike the square and circular $\beta = 30°$ series) the shear crack propagated along the double inclusion's bridging area (refer to Figure 5.8 and Section 5.4.1). No coalescence occurred in one specimen containing plaster inclusions (refer to Figure 5.11), while coalescence occurred similarly to the $\beta = 75°$ plaster series in the other specimens. Two out of the three Ultracal inclusions coalesced as described, while the other specimen coalesced in the same way as the Ultracal $\beta = 30°$ series. Primary tensile cracks had a *possible* effect on coalescence in all three specimens containing Ultracal inclusions. Primary cracks had *no* effect in one specimen containing plaster inclusions, while a *direct* effect was observed in the other specimen that experienced coalescence.

As mentioned earlier, the $\beta = 75°$ series was cast in order to account for the inclination differences between the square and circular inclusions. As a result, the $\beta = 60°$ circular series and the $\beta = 75°$ square geometries are very similar in appearance (refer to Figure 5.3) and both

series have similar coalescence patterns. The coalescence of the $\beta = 75°$ square series can be described as category (5), and this occurred in two out of the three plaster and Ultracal specimens tested. A tensile crack initiated at an innermost inclusion corner and propagated vertically towards the other inclusion. A shear crack then typically initiated at the innermost corner of the opposite inclusion and propagated until its coalescence with the tensile crack. Occasionally, the shear crack initiated at the tensile crack tip and then propagated until its coalescence with the opposite inclusion interface. The third test with plaster and Ultracal inclusions did not coalesce (refer to Figure 5.11). In all coalescing specimens, the propagations of primary tensile cracks were *directly* involved in the coalescence of the inclusion pair.

	Inclination Angle	First (Primary) Cracks To Appear	Effect of Primary Cracks on Coalescence	Coalescence Cracks
Plaster Inclusions	$\beta = 0°$	Type I (2/3) Type II (1/3) Type IV (1/3)	Possible (2/3)	Category 2 (2/3) No Coalescence (1/3)
	$\beta = 30°$	Type I (3/3)	Possible (1/3)	Category 4 (1/3) No Coalescence (2/3)
	$\beta = 60°$	Type I (2/3) Type III (1/3)	Direct (1/3) None (1/3)	Category 3 (1/3) Category 4 (1/3) No Coalescence (1/3)
	$\beta = 75°$	Type II (2/3) Type III (1/3)	Direct (2/3)	Category 5 (2/3) – two cracks No Coalescence (1/3)
Ultracal Inclusions	$\beta = 0°$	Type II (1/3) Type III (1/3) Type IV (1/3)	Possible (3/3)	Category 3 (3/3)
	$\beta = 30°$	Type I (1/3) Type II (1/3) Type III (1/3)	Possible (2/3) None (1/3)	Category 4 (3/3)
	$\beta = 60°$	Type II (2/3) Type III (1/3)	Possible (3/3)	Category 3 (2/3) Category 4 (1/3)
	$\beta = 75°$	Type II (1/3) Type III (1/3) Type IV (1/3)	Direct (2/3)	Category 5 (2/3) – two cracks No Coalescence (1/3)

Table 5.3 – Summary of cracking behavior for the square inclusion pair series. Numbers in parentheses represent the number of specimens that experienced that trait compared to the number of specimens tested.

5.5 Stress Analysis

5.5.1 Introduction

The previous sections of this chapter provided a visual interpretation for the cracking behavior of specimens containing double inclusions. An analysis of the quantitative data collected during each test will now be presented. These data include the various stresses, strains, and stress ratios described in Chapter 3.

5.5.2 Maximum Stress

Each specimen was loaded until a maximum stress value was reached (i.e., failure). Two figures are presented below. Figure 5.12 plots the maximum stress for each specimen containing double circular inclusions, while Figure 5.13 plots the maximum stress for the double square inclusions.

As shown in Figure 5.12, there does not appear to be a correlation between the inclination angle of the circular inclusions and the maximum stress of the specimen. There is a slight increase in the average maximum stress for specimens with plaster inclusions as the inclination angle increases, however. Also with an increase of inclination angle, the average maximum stress for specimens with plaster inclusions was higher than that of Ultracal inclusions. Figure 5.13 shows that there is another complex relationship between the inclination angle of square inclusions and their specimen's respective maximum stress. Again, the specimens containing plaster inclusions had a higher average maximum stress compared to the Ultracal inclusions. The maximum stress for the Ultracal inclusions generally decreases as the inclination angle increase, except for $\beta = 75°$. This cannot be said of the plaster inclusions as no such relationship appears to exist.

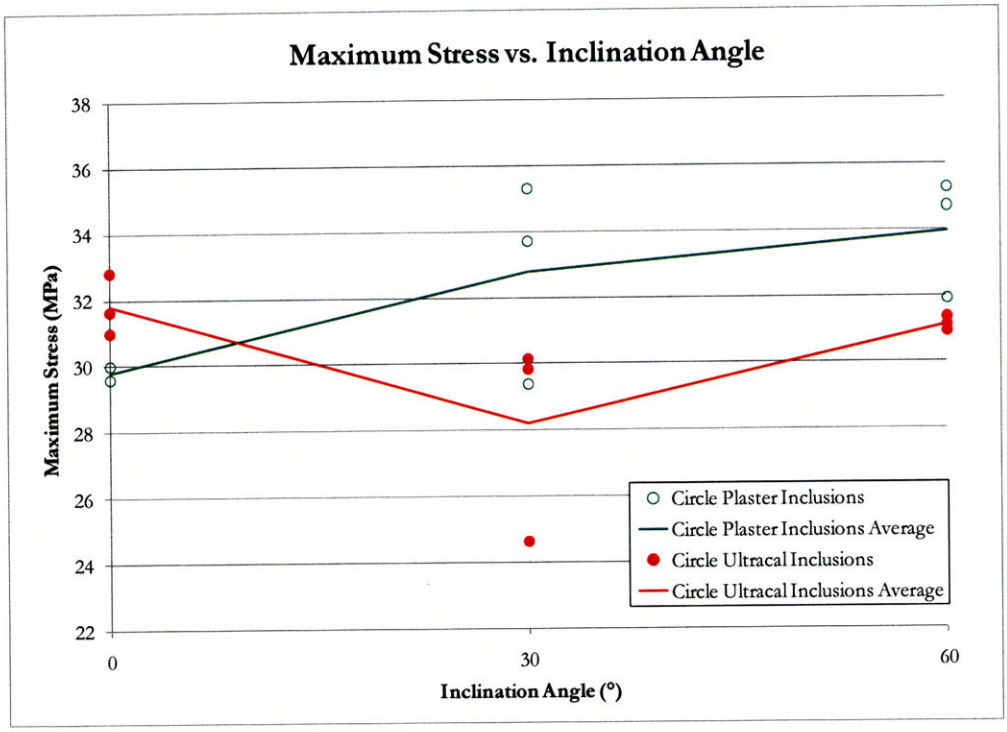

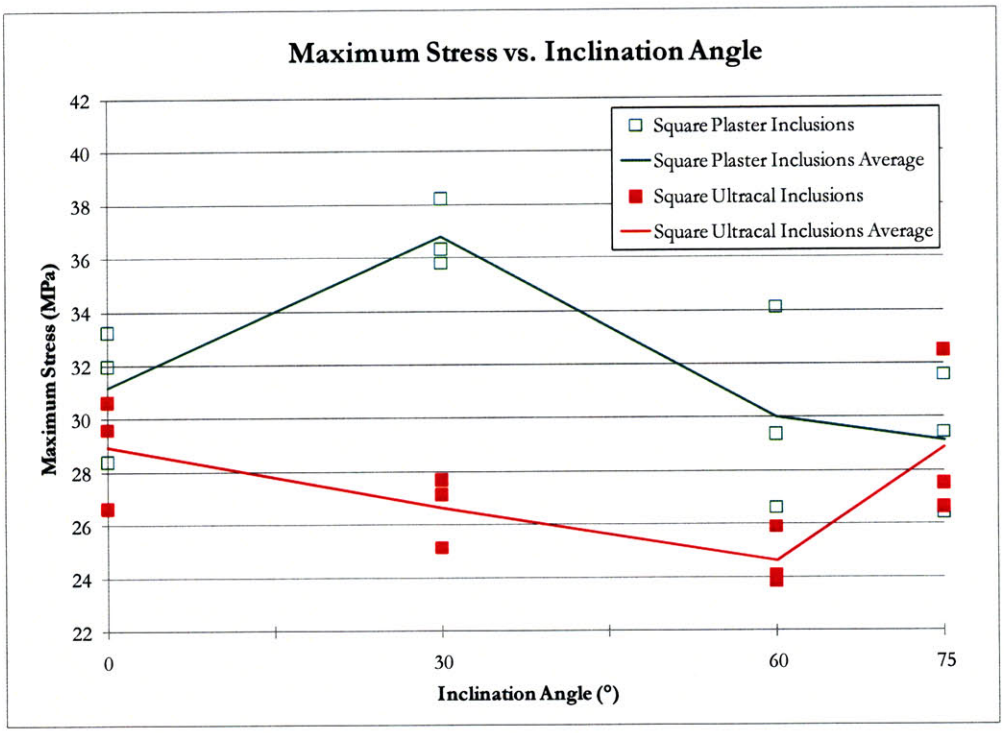

Figures 5.12 & 5.13 – Maximum stresses for the circular (top) and square (bottom) double inclusion series. The solid points represent the values for the Ultracal inclusions, while the hollow points represent the values for the plaster inclusions. The lines connect the averages for each inclination angle and material type.

The reason why the plaster inclusions had a higher average maximum stress compared to the Ultracal inclusions may be the result of pre-test surface cracks, which were more predominant in Ultracal inclusions. For example, all three specimens in the circular $\beta = 30°$ Ultracal series contained pre-test surface cracks, while the other two series ($\beta = 0°$ & $60°$) only had one specimen containing visible pre-test surface cracks. This may explain the drop in maximum stress shown in Figure 5.12. Also, all of the specimens in the circular $\beta = 0°$ plaster series contained pre-test surface cracks, which may explain the lower relative maximum stresses compared to the other plaster series in Figure 5.12. Regarding the square series, eleven out of twelve Ultracal specimens contained visible pre-test surface cracks, while only three out of the twelve plaster specimens contained surface cracks. Further investigation into the effects of surface cracks is still needed, however.

5.5.3 Crack Initiation Stress and Stress Ratio

The tensile crack initiation stresses for the double circular inclusions are presented in Figure 5.14. For the most part, the averages follow a similar trend as the maximum stress averages shown in Figure 5.12. Generally, tensile crack initiation occurred at Ultracal inclusions at lower stresses than plaster inclusions.

The tensile crack initiation stresses for the double square inclusions are presented in Figure 5.15. Again, a similar trend as for the maximum stress values of Figure 5.12 exists. Regarding the plaster inclusions, the tensile crack initiation stress increases slightly from 0 (i.e., $\beta = -45°$) to $\beta = 30°$; after $\beta = 30°$, there is a gradual decrease as the inclination angle increases. The opposite can be said of the Ultracal inclusions. The tensile crack initiation stress decreases as the inclination angle increases until $\beta = 60°$, then a sharp increase in tensile crack initiation stress is observed when $\beta = 75°$. In general, the tensile crack initiation stresses for the square Ultracal inclusions were much lower than the circular Ultracal inclusions. This again may be the result of pre-test surface cracks, which were dominant in square inclusions compared to circular inclusions.

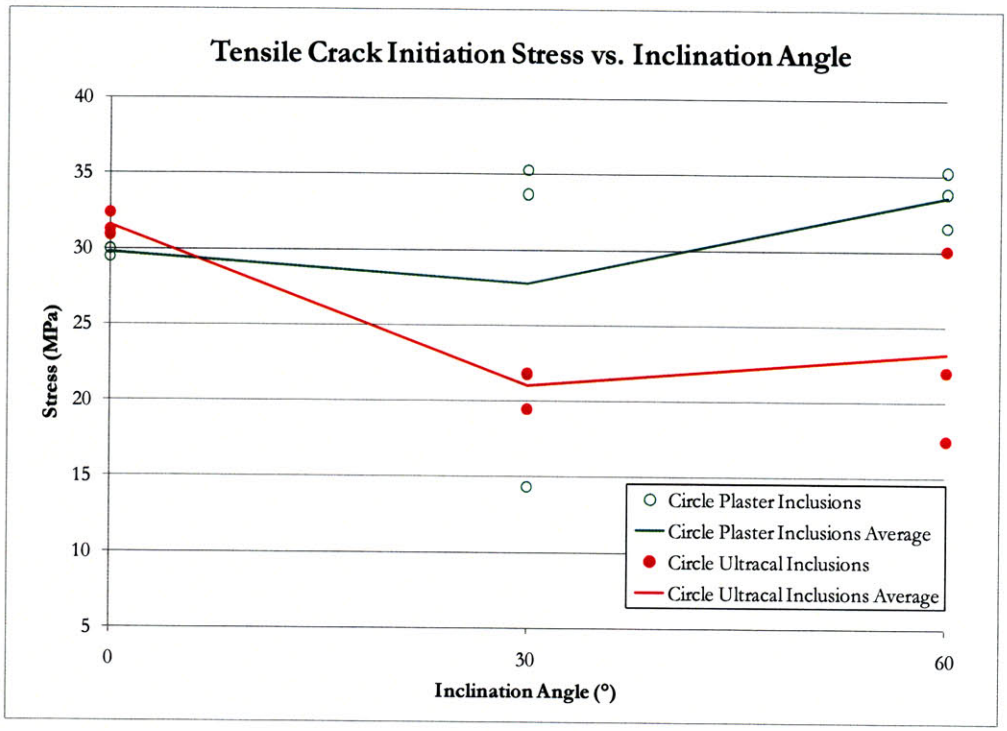

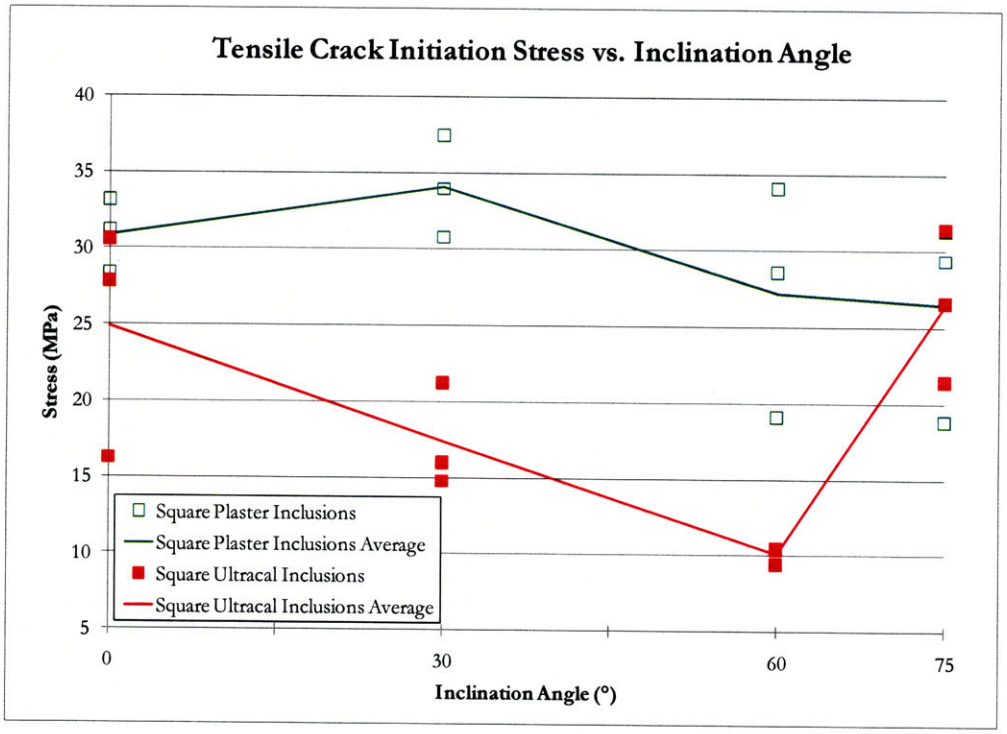

Figures 5.14 & 5.15 – Tensile crack initiation stresses for the circular (top) and square (bottom) double inclusion series. The solid points represent the values for the Ultracal inclusions, while the hollow points represent the values for the plaster inclusions. The lines connect the averages for each inclination angle and material type.

The tensile crack initiation stress ratios for both double inclusion shapes are presented in Figure 5.16 and 5.17. Tensile cracks typically initiated at lower stresses at Ultracal inclusions compared to plaster inclusions. By comparing Figures 5.16 and 5.17 to Figures 5.12 and 5.13, it appears that earlier tensile crack initiations resulted in a lower maximum stress of the respective specimens. The average tensile crack initiation ratios are presented in Table 5.4.

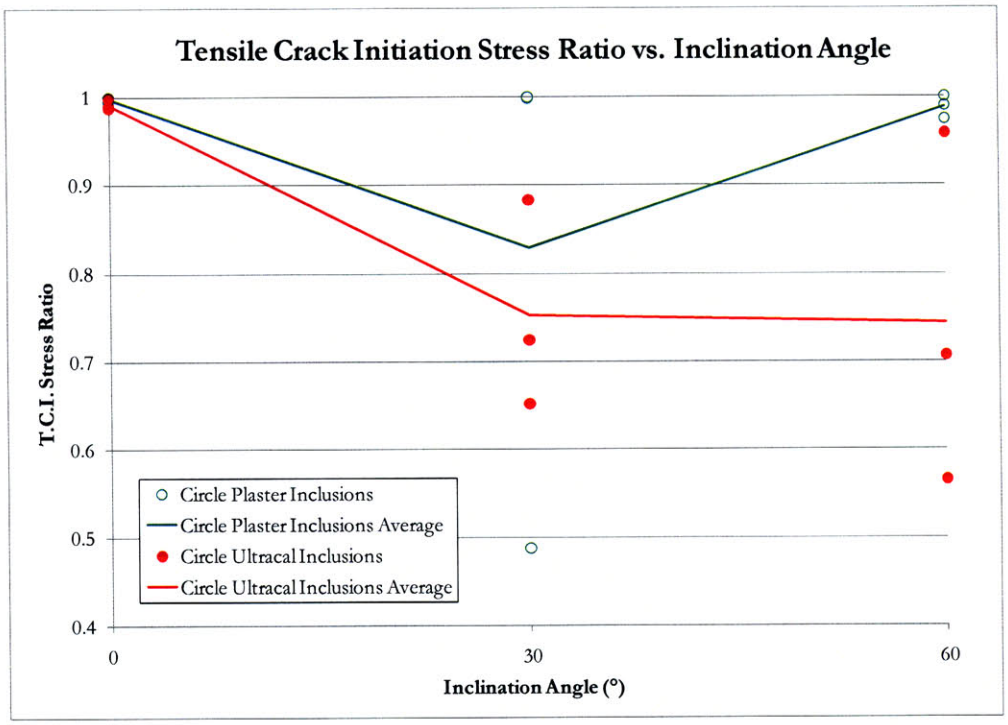

Figures 5.16 – Tensile crack initiation stress ratios for the circular, double inclusion series. The solid points represent the values for the Ultracal inclusions, while the hollow points represent the values for the plaster inclusions. The lines connect the averages for each inclination angle and material type.

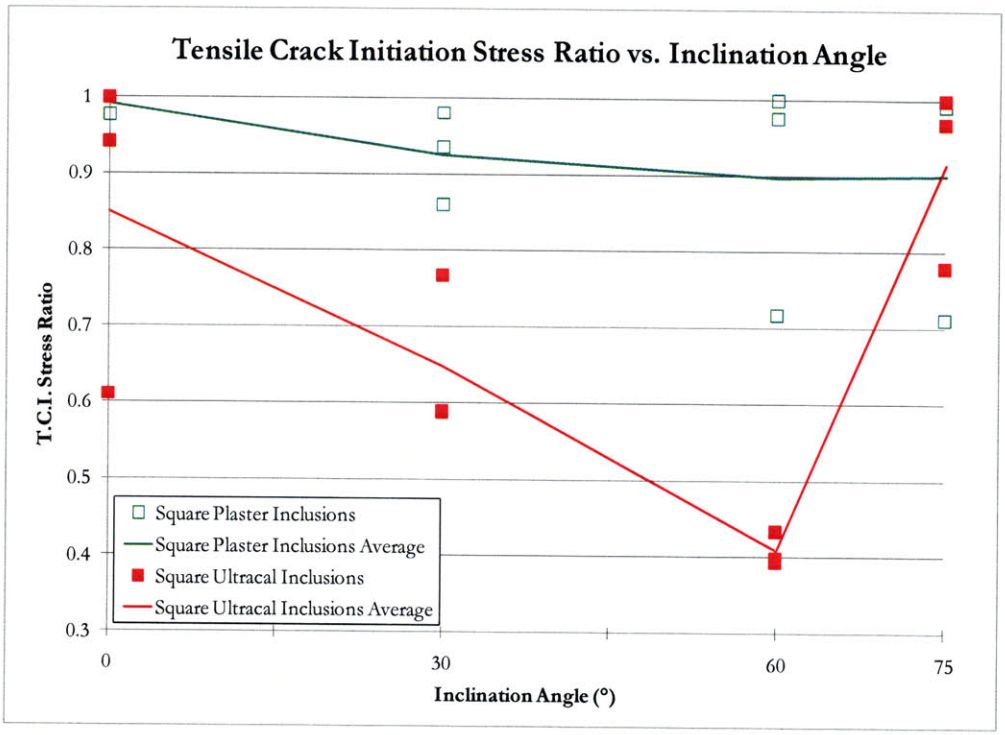

Figures 5.17 – Tensile crack initiation stress ratios for the square, double inclusion series. The solid points represent the values for the Ultracal inclusions, while the hollow points represent the values for the plaster inclusions. The lines connect the averages for each inclination angle and material type.

		β =0° (circles) & β = -45° (squares)	β = 30°	β = 60°	β = 75°
Circle	Plaster	99.8%	82.9%	98.8%	-
	Ultracal	99.2%	75.3%	74.3%	-
Square	Plaster	99.2%	92.6%	89.8%	90.1%
	Ultracal	85.1%	64.8%	40.9%	91.6%

Table 5.4 – Average tensile crack initiation ratios for the specimens containing double inclusions.

5.5.4 Coalescence Stress

The coalescence of the inclusion pairs typically occurred after the maximum stress of the specimen. Therefore, the coalescence strain ratios for both double inclusion shapes are presented in Figure 5.18 and 5.19. There is a notable difference between the circular coalescence strain ratios and the square strain ratios. The circular strain ratios, especially the Ultracal inclusions, increase slightly as the inclination angle increases. The ratios for the square inclusions, however, generally decrease as the inclination angle increases. There is a large decrease when $\beta = 60°$ for the Ultracal, square inclusions (the only instance when coalescence occurred prior to the specimen's maximum stress). The average coalescence strain ratios are presented in Table 5.5.

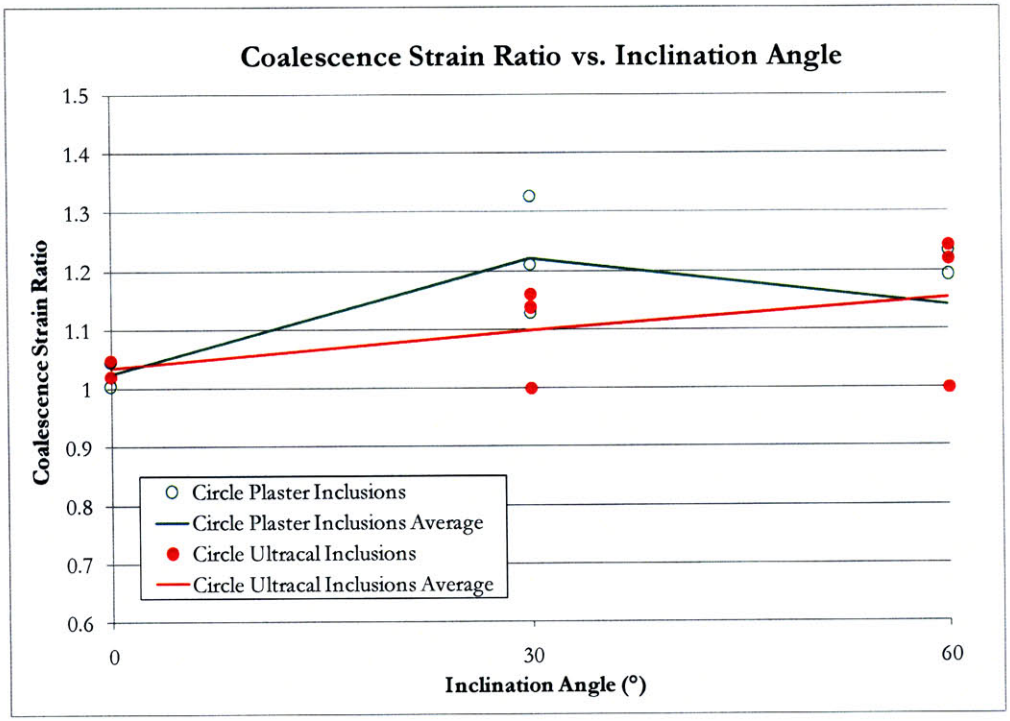

Figures 5.18 – Coalescence strain ratios for the circular, double inclusion series. The solid points represent the values for the Ultracal inclusions, while the hollow points represent the values for the plaster inclusions. The lines connect the averages for each inclination angle and material type.

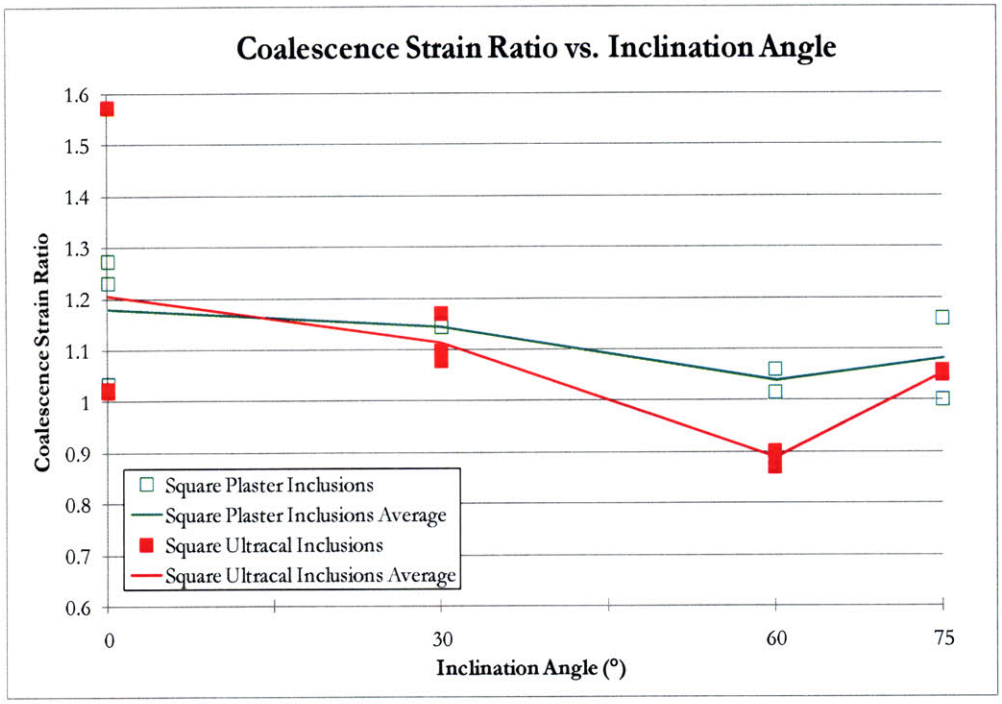

Figures 5.19 – Coalescence strain ratios for the square, double inclusion series. The solid points represent the values for the Ultracal inclusions, while the hollow points represent the values for the plaster inclusions. The lines connect the averages for each inclination angle and material type.

		β =0° (circles) & β = -45° (squares)	β = 30°	β = 60°	β = 75°
Circle	Plaster	102%	122%	114%	-
	Ultracal	103%	110%	115%	-
Square	Plaster	118%	114%	104%	108%
	Ultracal	120%	111%	88.9%	105%

Table 5.5 – Average coalescence strain ratios for the specimens containing double inclusions.

5.6 Conclusions

Several uniaxial compression tests were conducted on specimens containing double inclusions. These inclusions were either circular or square shaped, and of various stiffnesses. The observations made regarding the fracture behavior, as well as stress performance, for each specimen was discussed in this chapter.

Typically, the cracking processes associated with the double inclusion series were very similar to the half-inch, single inclusion series. Tensile cracks always initiated first and were then followed by the initiation of shear cracks at the inclusion boundary. The propagation of these shear cracks resulted in the coalescence of the inclusion pair. In many cases, the initiation of primary tensile cracks had some effect on coalescence. This effect was either *direct* (when coalescence involved a primary crack) or *possible* (when the coalescing crack initiated at the same inclusion as primary tensile crack initiation). Typically, a *direct* effect on coalescence only occurred for the circular $\beta = 60°$ series and the square $\beta = 75°$ series. *Possible* effects on coalescence were common in all other series. Table 5.6 presents a summary of the coalescence patterns observed in this study, along with the results presented by Wong (2008). It was determined that the coalescence patterns observed by Wong (2008) are also suitable for describing the coalescence patterns in this study.

A complex relationship exists between the maximum stress and tensile crack initiation stress of both circular and square inclusions. Specimens containing plaster inclusions typically had a higher maximum stress and tensile crack initiation stress. As mentioned previously, this is possibly a result of pre-test surface cracks located especially within square, Ultracal inclusions.

	PLASTER INCLUSIONS	ULTRACAL INCLUSIONS		PLASTER INCLUSIONS	ULTRACAL INCLUSIONS	Wong (2008)
β = 0°	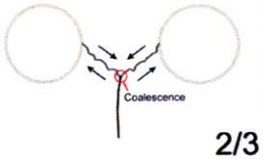 2/3	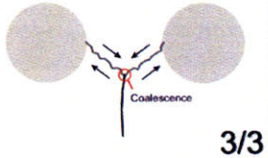 3/3	β = -45°	 2/3	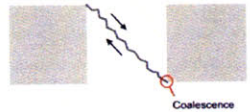 3/3	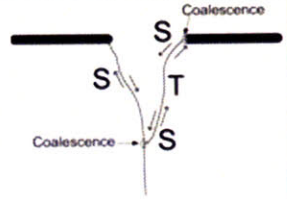 *(2 cracks)*
β = 30°	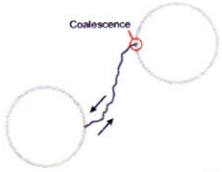 3/3	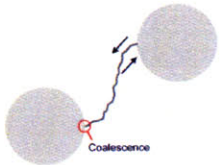 3/3	β = 30°	 1/3 (2/3 no coal.)	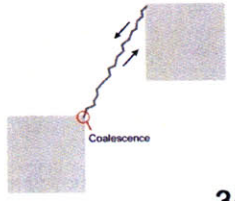 3/3	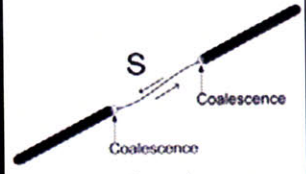 *(1 crack)*
			β = 60°	 1/3 (1/3 no coal.)	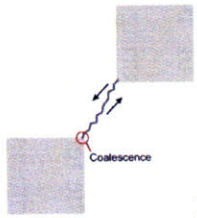 2/3	
β = 60°	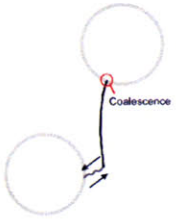 3/3	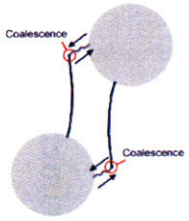 2/3	β = 75°	 2/3	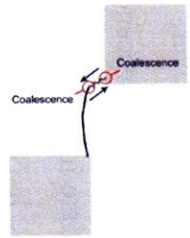 2/3	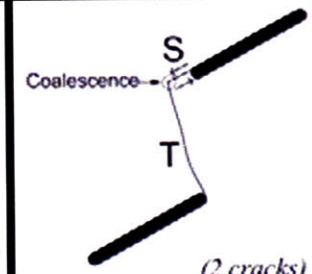 *(2 cracks)*

Table 5.6 – Sketch of the double inclusion coalescence patterns, compared to those reported by Wong (2008)

CHAPTER 6 – Summary, Conclusions, and Recommendations for Future Research

6.1 Introduction

The cracking behavior associated with a brittle material containing inclusions is very complicated. Moreover, the strength of brittle material is governed by the initiation, propagation, and coalescence of cracks during loading. This is a significant issue when these cracks initiate in tension since the tensile strength of a brittle material is very low. In the past, researchers have tried to experimentally (e.g., Zaitsev and Wittmann, 1981; Maji and Shah, 1989; 1990; Zhang and Gjørv, 1990; Aulia, 2000) and analytically (e.g., Zaitsev and Wittmann, 1981; Tasdemir et al., 1989) identify the various cracking processes associated with a brittle material containing inclusions. The purpose of this study was to observe the cracking processes associated with specimens of gypsum containing inclusions of different geometries, sizes, stiffnesses, and orientations.

This chapter will provide a summary of the experiments performed in this study (Section 6.2), compare the observations made in this study to previous studies (Section 6.3), and based on this, reach conclusions (Section 6.4). The latter allow one to identify where further work is needed in this research (Section 6.5).

6.2 Experimental Summary

6.2.1 Experimental Procedure

Unconfined, uniaxial compression tests were conducted on prismatic gypsum specimens containing either one, or two, inclusions. The dimensions of these specimens were roughly 6 inches (height) x 3 inches (width) x 1.25 inches (thickness). Inclusion size (one-inch or half-inch), shape (square, circle, hexagon, or diamond), strength, and stiffness were varied. These inclusions were made of plaster (lower strength and stiffness relative to the matrix) or Ultracal

(higher strength and stiffness relative to the matrix). During each test, high speed and real-time video were captured. Real-time video was recorded throughout the entire test, while the high speed video was only taken when a significant cracking event occurred (i.e., failure, coalescence, etc.). These recordings were used to visually analyze the cracking processes at the specimen surface. Load-displacement data were also acquired for each of the experiments, which were then synchronized with the video recordings in order to obtain a full account of crack initiation, propagation, and coalescence (if the latter is applicable). Comprehensive analyses for each specimen were then prepared, which can be found in Appendices B through E.

6.2.2 Single Inclusions

The first part of this study examined the cracking sequences associated with specimens containing single inclusions (Chapter 4). Figures 6.1 and 6.2 present a summary of typical crack sequences and relative stress levels for each inclusion size, shape, and material. The relative stress level at each stage was calculated by normalizing the respective stress level with the maximum stress of the specimen and is reported at the top right-hand corner of every image. A ratio of the number of specimens that exhibited the trend to the total number of specimens is also reported at the bottom of each image (for more details refer to Section 4.6.1).

To summarize, tensile cracks first initiated at the interface of a plaster inclusion and propagated into the surrounding matrix. As the load increased, the same tensile cracks then propagated into the inclusion. Regarding Ultracal inclusions, tensile cracks commonly initiated at a debonded portion of the interface and then propagated into the surrounding matrix; on occasion tensile cracks initiated just above and below the interface.

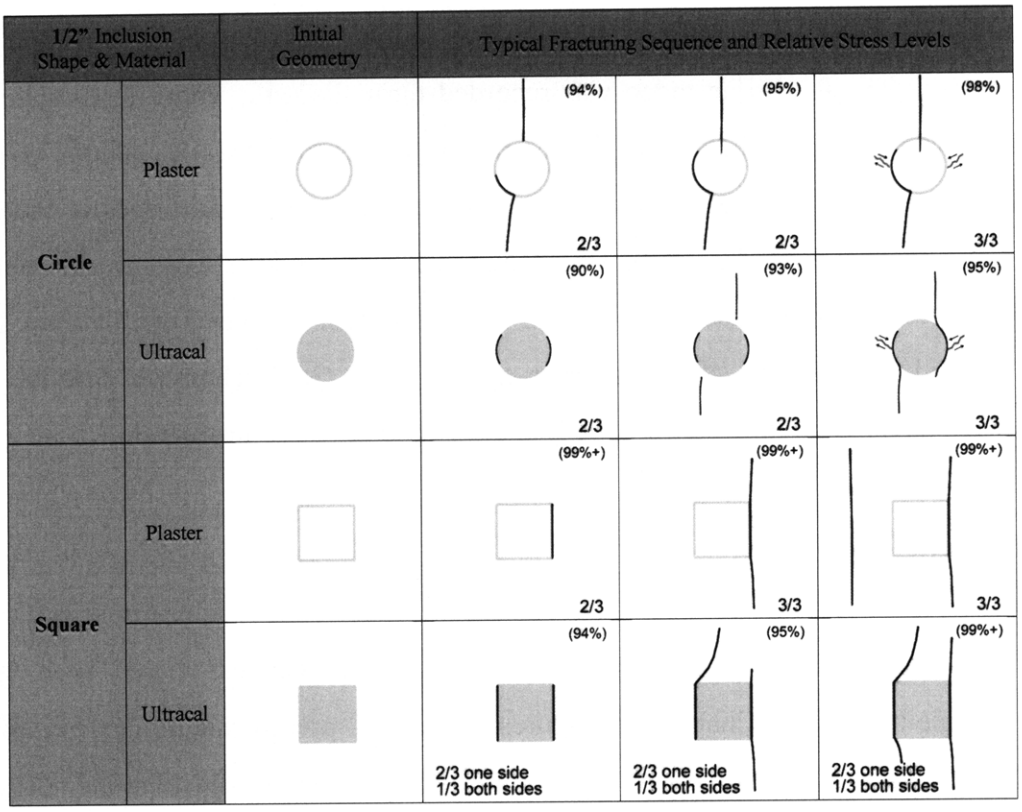

Figure 6.1 – Crack sequences for the single, half-inch inclusions (refer to Section 4.6.1 for details).

In addition to the effects caused by the strength (and stiffness) of an inclusion, the size and shape of an inclusion also had particular effects. Specifically, an increase in debonding was observed as the inclusion size decreased. Debonding occurred at the same locations (i.e., the left and right interface) for both sizes, however. Comparison between Figures 6.1 and 6.2 shows that tensile crack initiation was also affected by inclusion size, as it typically occurred at lower stress levels in specimens containing one-inch inclusions compared to half-inch inclusions. Shape had an effect on the location of tensile crack initiation. Diamond inclusions, for example, always experienced tensile crack initiation at the upper and lower interface points, regardless of material type (Figure 6.2).

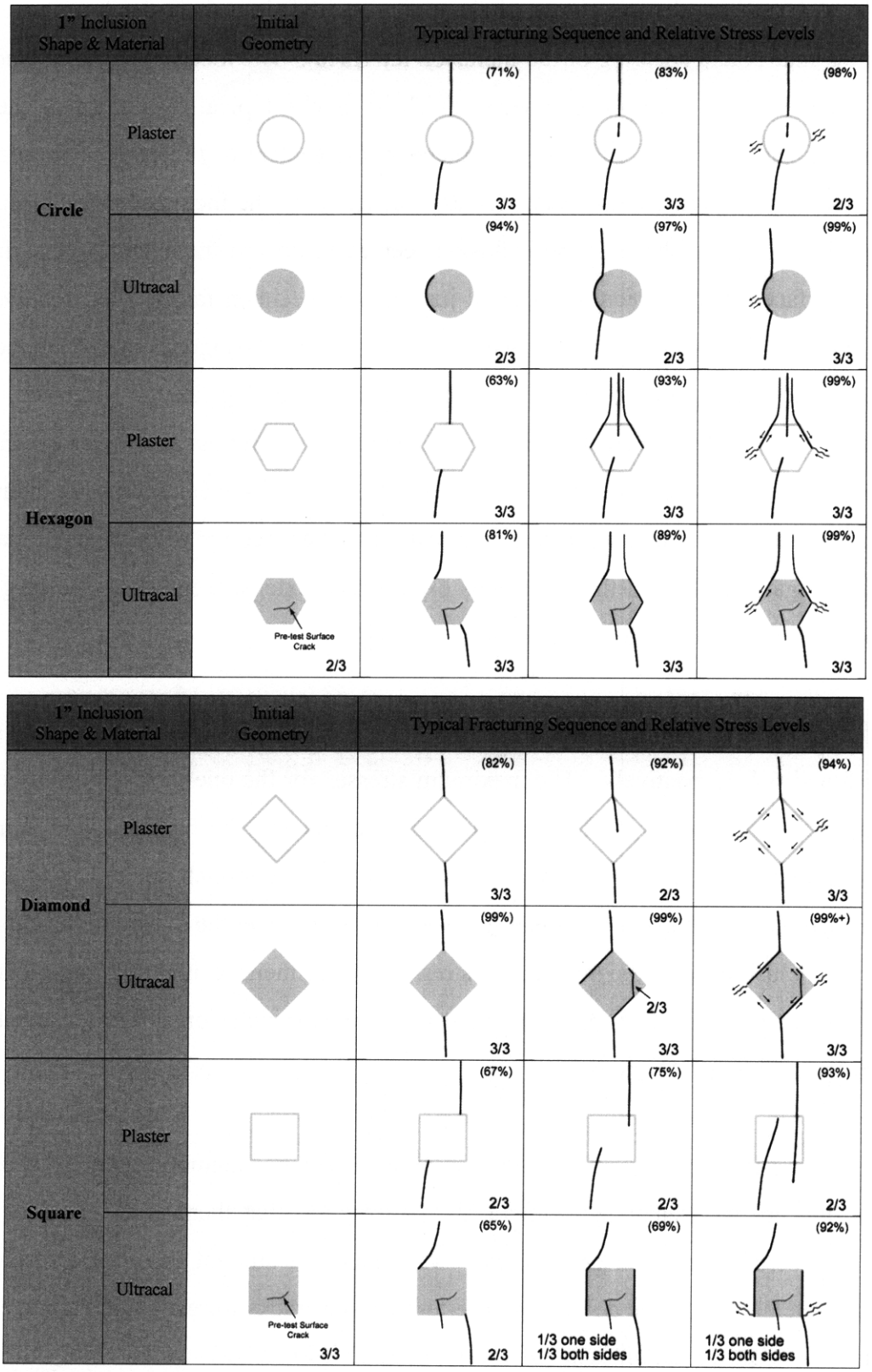

Figure 6.2 – Crack sequences for the single, one-inch inclusions (refer to Section 4.6.1 for details).

In addition to tensile cracks, two types of shearing occurred (i.e., shear crack propagation into the specimen matrix and shearing of the inclusion interface). The location of matrix shear crack initiation depended on inclusion geometry, as shear cracks typically initiated at the bottom corners of a square inclusion but always initiated at the centers of the other inclusion shapes. The initiation of shear cracks also occurred less frequently as the inclusion size decreased. As shown in Figure 6.2, the shape of the inclusion seemed to govern the extent of shearing at the inclusion interface, which typically occurred just before specimen failure (i.e., at 99% of max stress or later). Shearing at the interface was observed for hexagonal and diamond shaped inclusions. Regarding the diamond inclusion series, shearing at the interface occurred "simultaneously" with tensile crack initiation (and failure) at the upper and lower interface. The amount of debonding caused by shearing at the interface typically increased as the inclination of a respective inclusion interface increased with respect to the direction of the applied load. Post-mortem investigations showed that diamonds experienced extensive interface shearing (100%), while hexagons experienced moderate shearing (~75%).

The maximum stresses for specimens containing one-inch and half-inch inclusions are shown in Figures 6.3 and 6.4, respectively. The maximum stresses for the one-inch inclusion geometries were remarkably different, with the circular inclusions having the highest average maximum stress. Additionally, unlike what was observed with the one-inch inclusions, the average maximum stress for the half-inch circular inclusions was less than the square inclusions. With a decrease in inclusion size, the maximum stress for specimens containing square inclusions increased about fifty percent; the maximum stress for circular inclusions increased five to twenty percent (refer to Figures 6.3 and 6.4).

In this study pre-test surface cracks were common in square, diamond, and hexagon shaped inclusions, but not in circular inclusions (this may suggest that there is an effect of the non-uniformity of certain inclusion geometries). Moreover, the amount of pre-test surface cracks decreased as the inclusion size decreased. Pre-test surface cracks were assumed to have an effect on the tensile crack initiation stress of the specimen (refer to Table 6.1). Only the Ultracal, hexagon series and the plaster, diamond series had instances where surface cracking existed in some specimens but not in the others; in these cases there are clear differences between the

tensile crack initiation stress ratios (i.e., tensile crack initiation stress divided by the maximum stress of the respective specimen). A separate experimental investigation stills needs to be performed, however, in order to confirm these observations.

		Circle	Hexagon	Diamond	Square
1" Inclusion	Plaster w/ surf. cracks	N/A	62.9%	**62.6%**	N/A
	Plaster w/o surf. cracks	70.9%	N/A	**92.1%**	66.7%
	Ultracal w/ surf. cracks	N/A	**81.3%**	N/A	64.9%
	Ultracal w/o surf. cracks	93.7%	**99.9%**	99.9%	N/A

Table 6.1 – A comparison of average tensile crack initiation ratios (i.e., tensile crack initiation stress divided by the maximum stress of the specimen) between one-inch inclusions containing surface cracks, versus no visible surface cracks. Notice the tensile crack initiation stress differences in the Ultracal, hexagon inclusion series and the plaster, diamond inclusion series.

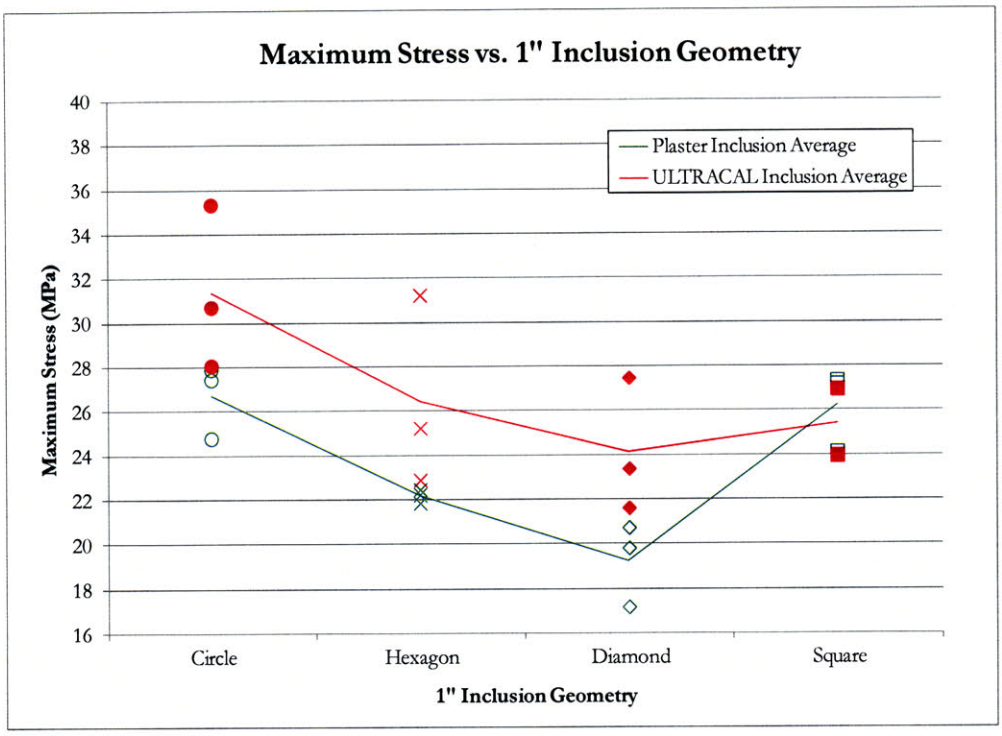

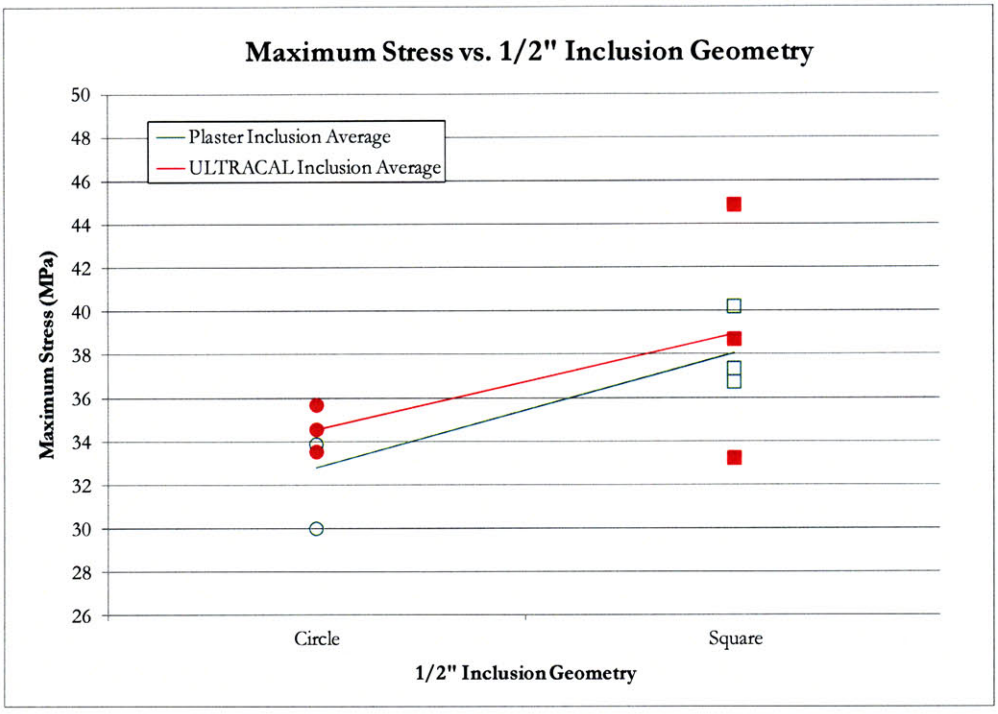

Figures 6.3 & 6.4 – Maximum stresses for the one-inch (top) and half-inch (bottom) inclusion series. The solid points represent the values for the Ultracal inclusions, while the hollow points represent the values for the plaster inclusions. The lines connect the averages for each geometry and material type.

6.2.3 Double Inclusions

The second part of this study examined the cracking sequences associated with specimens containing double inclusions. The size of these inclusions (half-inch) was the same for each specimen, while the shape was either circular or square. A visual (Figures 6.5 and 6.6) and descriptive (Tables 6.2 and 6.3) summary of typical coalescence patterns for each specimen geometry is presented. The number at the top right-hand corner of each image represents the coalescence category observed (refer to Section 5.4.1), while the fraction at the bottom right-hand corner represents the number of specimens showing that particular behavior out of the number of specimens tested.

Typically, the tensile cracking processes associated with the double inclusion series were very similar to the single inclusion series. Four basic tensile crack types were defined in this study as follows:

Type I – A tensile crack that propagates relatively straight,

Type II – A tensile crack that propagates with curvature,

Type III – A tensile crack that initiates at a pre-test surface crack,

Type IV – A tensile crack that initiates within the matrix.

One of these tensile crack types always initiated first, which was then followed by the initiation of matrix shear cracks at the inclusion boundary. The propagation of these shear cracks into the matrix resulted in the coalescence of the inclusion pair (either exclusively or in connection with tensile cracks, as described next). In many cases, the initiation of primary tensile cracks had some effect on coalescence. This effect was either *direct* (when the coalescence involved a primary crack) or *possible* (when the coalescing crack initiated at the same inclusion as primary tensile crack initiation). Typically, a *direct* effect on coalescence only occurred for the circular $\beta = 60°$ series and the square $\beta = 75°$ series. *Possible* effects on coalescence were common in all other series.

Circle Inclusion	Inclination Angle (β)		
	β = 0°	β = 30°	β = 60°
Plaster	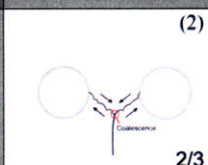 (2) 2/3	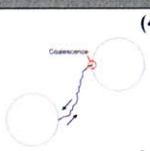 (4) 3/3	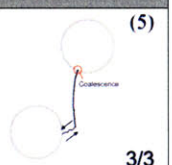 (5) 3/3
Ultracal	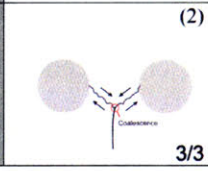 (2) 3/3	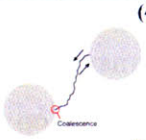 (4) 3/3	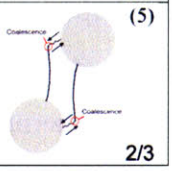 (5) 2/3

Figure 6.5 – Coalescence patterns for the circular inclusion pair series. The number in parenthesis represents the coalescence category observed (refer to Section 5.4.1), while the fraction represents the number of specimens showing that particular behavior out of the number of specimens tested.

	Inclination Angle	First (Primary) Cracks To Appear	***Effect of Primary Cracks on Coalescence	Coalescence Cracks
Plaster Inclusions	β = 0°	Type II (2/3) Unknown* (1/3)	Possible (2/3)	Category 2 (2/3) No Coalescence (1/3)
	β = 30°	Type II (2/3) Boundary** (1/3)	Possible (1/3) None (2/3)	Category 4 (3/3)
	β = 60°	Type II (3/3)	Direct (3/3)	Category 5 (3/3) – two cracks
Ultracal Inclusions	β = 0°	Type II (3/3)	Possible (2/3) None (1/3)	Category 2 (3/3)
	β = 30°	Type I (1/3) Type III (1/3) Type IV (1/3)	Possible (3/3)	Category 4 (3/3)
	β = 60°	Type II (1/3) Boundary** (2/3)	Direct (3/3)	Category 5 (1/3) – two cracks Category 5 (2/3) – four cracks

* Unknown due to error during test (see Appendix D).

** First crack initiated at the lower loaded specimen boundary and propagated towards an inclusion (refer to Appendix D).

*** A *possible* effect on coalescence is when the initiation of the first shear crack occurred at the same inclusion as primary tensile crack initiation, while a *direct* effect is when coalescence involved primary tensile cracks.

Table 6.2 – Summary of cracking behavior for the circular inclusion pair series. Numbers in parentheses represent the number of specimens that experienced that behavior compared to the number of specimens tested.

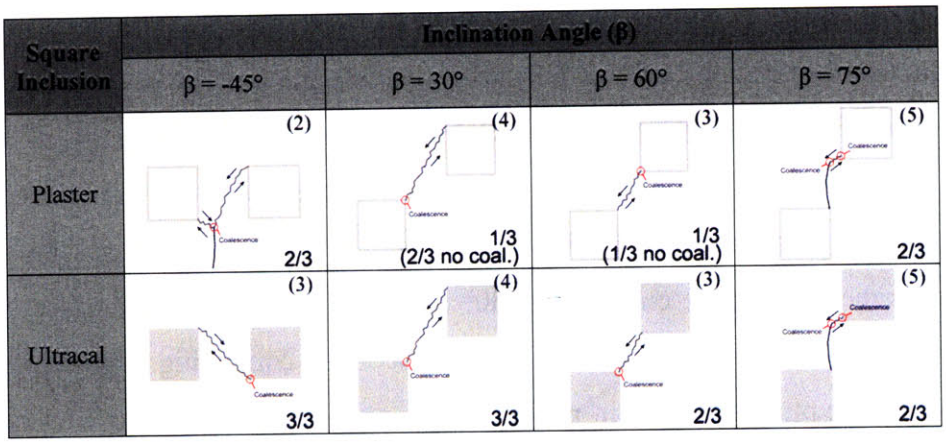

Figure 6.6 – Coalescence patterns for the square inclusion pair series. The number in parenthesis represents the coalescence category observed, while the fraction represents the number of specimens showing that particular behavior out of the number of specimens tested.

	Inclination Angle	First (Primary) Cracks To Appear	Effect of Primary Cracks on Coalescence	Coalescence Cracks
Plaster Inclusions	β = 0°	Type I (2/3) Type II (1/3) Type IV (1/3)	Possible (2/3)	Category 2 (2/3) No Coalescence (1/3)
	β = 30°	Type I (3/3)	Possible (1/3)	Category 4 (1/3) No Coalescence (2/3)
	β = 60°	Type I (2/3) Type III (1/3)	Direct (1/3) None (1/3)	Category 3 (1/3) Category 4 (1/3) No Coalescence (1/3)
	β = 75°	Type II (2/3) Type III (1/3)	Direct (2/3)	Category 5 (2/3) – two cracks No Coalescence (1/3)
Ultracal Inclusions	β = 0°	Type II (1/3) Type III (1/3) Type IV (1/3)	Possible (3/3)	Category 3 (3/3)
	β = 30°	Type I (1/3) Type II (1/3) Type III (1/3)	Possible (2/3) None (1/3)	Category 4 (3/3)
	β = 60°	Type II (2/3) Type III (1/3)	Possible (3/3)	Category 3 (2/3) Category 4 (1/3)
	β = 75°	Type II (1/3) Type III (1/3) Type IV (1/3)	Direct (2/3)	Category 5 (2/3) – two cracks No Coalescence (1/3)

Table 6.3 – Summary of cracking behavior for the square inclusion pair series. Numbers in parentheses represent the number of specimens that experienced that trait compared to the number of specimens tested.

A complex relationship exists between the maximum stresses of both circular and square inclusion pairs (refer to Figures 6.7 and 6.8). Specimens containing plaster inclusions typically had a higher maximum stress and tensile crack initiation stress (refer to Figures 5.14 & 5.15) compared to specimens containing Ultracal inclusions. As mentioned previously, this is possibly a result of pre-test surface cracks located especially within Ultracal inclusions. For example, all three specimens in the Ultracal, circular $\beta = 30°$ series contained pre-test surface cracks, while the other two series ($\beta = 0°$ & $60°$) only had one specimen containing visible pre-test surface cracks. This may explain the drop in maximum stress shown in Figure 6.7. Also, all of the specimens in the circular $\beta = 0°$ plaster series contained pre-test surface cracks, which may explain the lower relative maximum stresses compared to the other plaster series in Figure 6.7. Regarding the square series, eleven out of twelve Ultracal specimens contained visible pre-test surface cracks, while only three out of the twelve plaster specimens contained surface cracks. Further investigation into the effects of surface cracks is still needed, however.

A major difference between the double inclusion series and the single inclusion series was the significance of shear crack initiation at the inclusion interface and propagation into the matrix. For specimens containing single inclusions, shear crack propagation was a "randomly" occurring result of specimen failure. The extent and direction of shear crack propagation differed even with specimens of the same type. With the double inclusion series, however, shear crack initiation and propagation was consistent, common, and could be related to specific geometries. In order to study the various interaction effects of inclusions further, additional testing needs to be done.

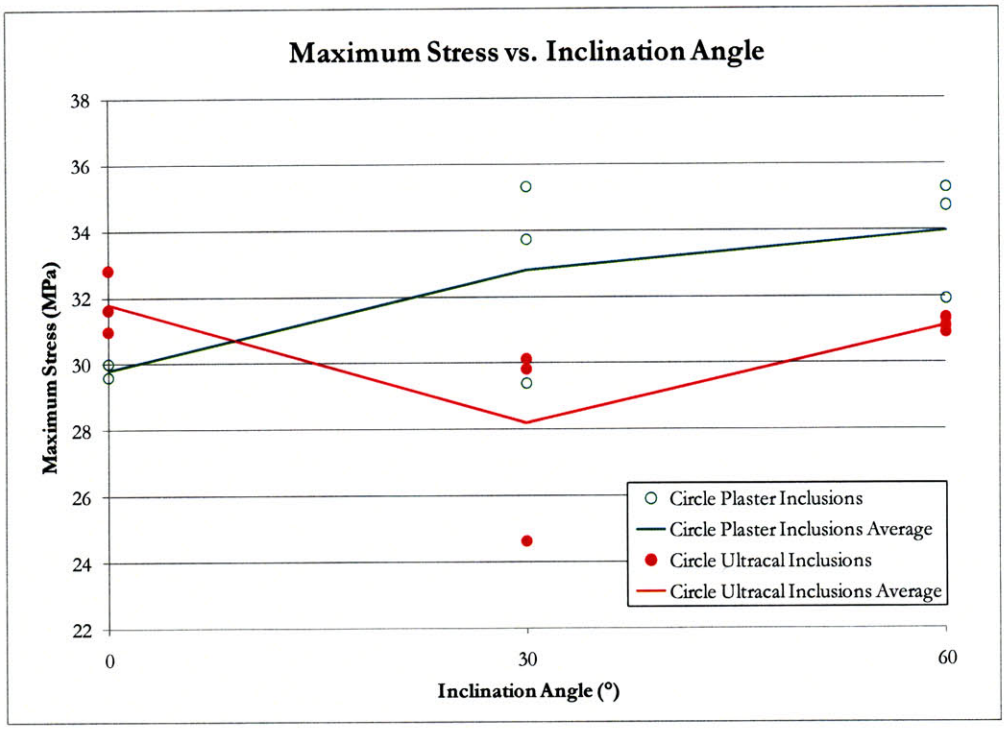

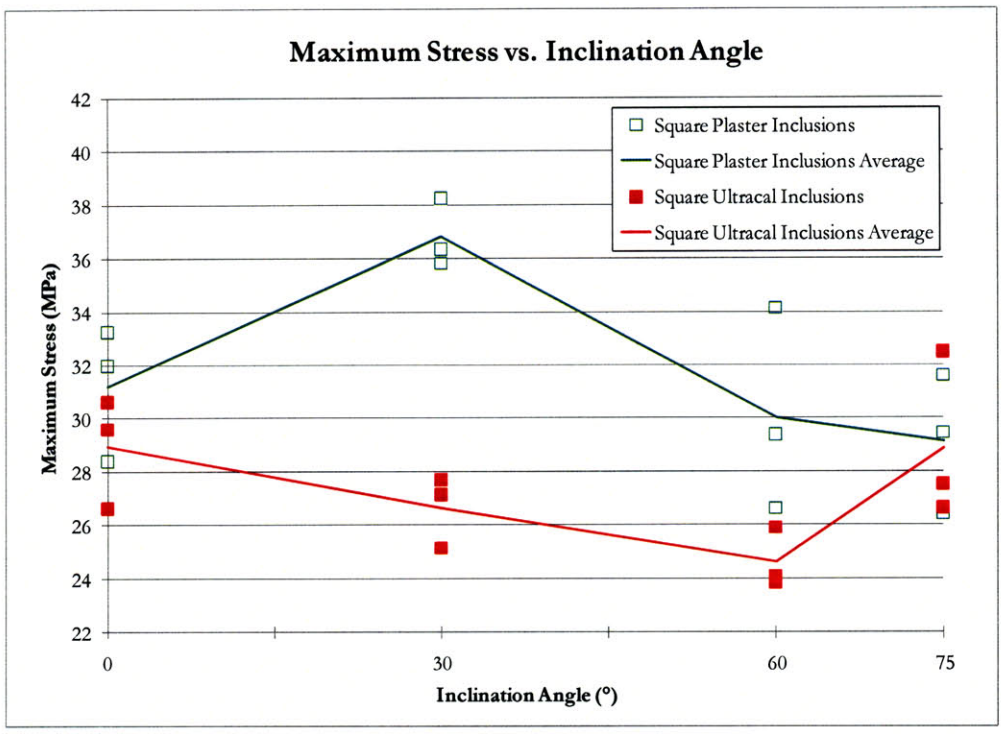

Figures 6.7 and 6.8 – Maximum stresses for the circular (top) and square (bottom) double inclusion series. The solid points represent the values for the Ultracal inclusions, while the hollow points represent the values for the plaster inclusions. The lines connect the averages for each inclination angle and material type.

6.3 Comparison with Previous Results

Various similarities exist between this study and others performed in the past. A review of the background chapter (Chapter 2) is presented below in bullet format. Comparisons with this study are also provided when possible (i.e., where similar observations were made). The research done by Maji and Shah (1989) contained many similarities to the work done in this study, and will therefore be discussed in detail at the end of the review.

- Zhang and Gjørv (1990) – performed SEM analyses on lightweight aggregate interfaces and concluded that as the porosity of the interface increased, so did the homogeneity of the interface (i.e., the quality of the bond).

- Lo and Cui (2004) – performed SEM analyses on aggregate interfaces of various strengths and concluded that lightweight aggregate have smaller interface thicknesses compared to normal-weight aggregate.

- Hansen (1958) & Neville (1997) – stated that the difference between the elastic constants of the matrix and aggregate had the greatest effect on the internal stress distribution of a composite material (assuming linear elastic behavior).

- Goodier (1933) – calculated closed form solutions to predict the stress concentration values surrounding a spherical particle within a matrix subjected to a far field compressive stress.

    → These same solutions were used in this study in order to explain the observed cracking processes, and were shown to describe the different cracking behavior well.

- Aulia (2000) – performed experiments on specimens where the elasticity modulus of the matrix (E_m) and aggregate (E_a) were either similar, or very different. When $E_m << E_a$ microcracking (which later propagated into the matrix) initiated at the top and bottom of the aggregate interfaces (i.e., parallel to the direction of compressive load). When $E_m \approx$

E_a microcracking (which later propagated into the matrix) initiated at the sides of the aggregate interfaces.

→ A comparison cannot be made with the $E_m \approx E_a$ series, but observations in this study disagree with the $E_m << E_a$ series as debonding typically initiated at the sides of a circular, Ultracal inclusion prior to tensile crack initiation. According to Aulia (2000) tensile cracks should initiate at the upper and lower boundaries of high-strength inclusions, though he does not provide detailed reasoning (refer to Section 2.4)

- Zaitsev and Wittmann (1981) – applied the sliding crack model to the analysis of a single polygon inclusion within a matrix subjected to a far field compressive load, in order to study crack propagation along the interface. They showed that an inclined interface microcrack will begin to propagate in shear due to normal stresses on the interface, but then at the ends of the interface the same crack will propagate into the matrix in tension (assuming that the tensile strength of the matrix is much lower than its compressive strength). A similar analysis for a matrix containing two polygonal inclusions was also performed. Crack propagation along the interface of a second inclusion was studied assuming a single tensile crack (from the first inclusion) results in the coalescence of the two inclusions.

  → Observations from the present hexagon and diamond one-inch inclusion series agree with the polygonal model proposed by Zaitsev and Wittmann (1981), as shearing along the inclined inclusion interfaces was commonly observed to occur "simultaneously" with tensile crack initiation.

  → Comparison with the polygonal inclusion pair model can be made, even though the assumption that coalescence occurs through a single tensile crack (which is what Zaitsev and Wittmann (1981) assumed) was not seen in this study. Typically, debonding was observed in this study when a tensile crack (that previously initiated from a shear crack) coalesced with the other inclusion boundary (refer to the circular $\beta = 60°$ series).

- Maji and Shah (1989) – performed experiments on specimens containing circular inclusion and void pairs, and made observations regarding the specimen's cracking and stress/strain behavior.

  → This previous study most closely resembles the work in this study and will, therefore, be compared in detail at the end of the review.

- Tasdemir et al. (1989) – incorporated the principles of mixed-mode fracture to a crack at a rectangular inclusion interface that refined the work done by Zaitsev and Wittmann (1981). The analytical results were confirmed through experiments where specimens containing single rectangular inclusions were cast at various inclination angles. The results showed that the specimen's debonding, initiation, and failure stress decreased as the inclusion's inclination angle increased (where horizontal = 0° and the maximum inclination angle ≈ 72°).

  → Comparison can be made for the present square and diamond inclusion series, as the diamond inclusions had an interface inclination angle of 45°, while the square inclusions had an interface inclination angle of 0°. The average failure stress for the one-inch, diamond inclusion series was lower than the square series (regardless of inclusion material). The average tensile crack initiation stress for the plaster, diamond inclusion series was also lower compared to the plaster, square series. However, the Ultracal, square series had a lower average tensile crack initiation stress compared to the Ultracal, diamond series (as mentioned earlier, this is likely a result of pre-test surface cracking).

- Maji et al. (1991) - performed experiments that verified the analytical work done by Tasdemir et al. (1989) and showed that the initiation of cracks at a rectangular inclusion interface was not purely tensile, but mixed-mode (tensile behavior dominated, however).

  → Observations from the one-inch diamond inclusion series showed that shearing at the inclined interface occurred "simultaneously" with tensile crack initiation at the upper and lower interface.

Maji and Shah (1989) first created prismatic concrete specimens containing circular, limestone inclusion pairs. Two series of specimens were created with one-inch and half-inch inclusions. Maji and Shah (1989) reported that interface cracks typically propagated along the entire one-inch limestone inclusion before propagating into the concrete matrix (Figure 6.9). These interface cracks initiated at about thirty percent of the peak load. Maji and Shah (1989) also noted that interface cracking initiated at various points around the inclusions. This suggests that the interface cracks may not be purely tensile in nature, since initiation did not exclusively occur at the right and left inclusion boundary. In this study, however, interface debonding only occurred partially (prior to tensile crack initiation) and initiated at about ninety percent of the peak load (refer to Section 6.2.1). Just prior to failure, Maji and Shah (1989) observed diagonal cracking that commonly coalesced with previously initiated vertical matrix cracks (refer to Figure 6.9). These diagonal cracks typically initiated at the sides of the inclusion boundary, and post-mortem investigations showed that many of these cracks did not extend entirely through the specimen.

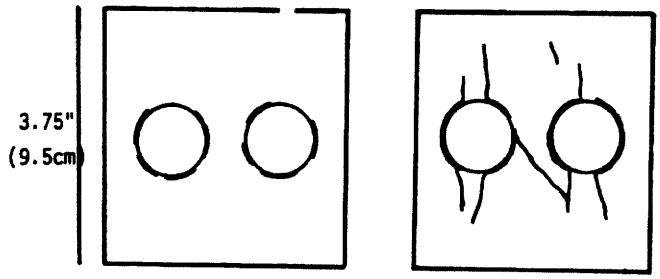

Figure 6.9 – Sketch of bond crack initiation in a specimen containing one-inch inclusions (left) and of the same specimen just prior to failure (right) (Maji and Shah, 1989).

Regarding the half-inch limestone inclusions, Maji and Shah (1989) reported that no interface and negligible matrix cracking occurred. The cracking associated with the half-inch inclusion series observed in this study, however, was quite extensive. It should be noted that the ligament length of Maji and Shah's (1989) half-inch inclusion series was an inch longer than their one-inch series (Figure 6.10). Emphasis was placed in this study on maintaining a constant ligament length (0.5") for all specimens containing double inclusions. Wong (2008) showed that an increase in ligament length decreased flaw interaction effects, and the same effect likely occurred in the case of Maji and Shah (1989).

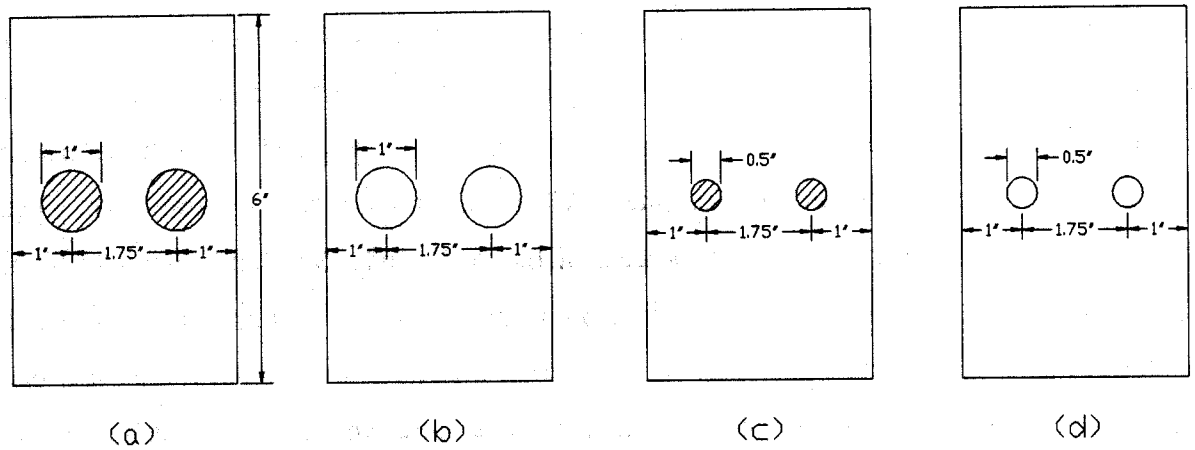

Figure 6.10 – The specimen geometries tested by Maji and Shah (1989): (a) 1" diameter limestone inclusion, (b) 1" diameter hole, (c) ½" diameter limestone inclusion, (d) ½" diameter hole.

Maji and Shah (1989) then created prismatic concrete specimens containing circular, one-inch and half-inch holes. These specimens behaved differently than the specimens containing inclusions. Matrix cracking always initiated at the top and bottom of the holes, and propagated in the same fashion as the specimens containing inclusions. These specimens also experienced minor diagonal cracking, and failed when the spalling of specimen pieces occurred at one of the boundaries. The half-inch specimens failed at a higher stress, which again may be a result of the different ligament lengths between the two geometries. These observations correspond well with the observations from this study. The plaster inclusion series behaved quite similarly, especially regarding the location of tensile crack initiation and the occurrence of detachment at the specimen boundaries that resulted in failure.

There are three main differences between the experimental work done by Maji and Shah (1989) and this study. They cast limestone inclusions within a concrete matrix. It can be assumed that the mechanical properties of limestone and a typical concrete mortar are different; Maji and Shah (1989) do not provide any details on their material's mechanical properties, however. In this study, gypsum material was used for both the matrix and inclusions. Secondly, the specimen matrices in this study were submerged in water prior to inclusion casting in order to improve the quality of the interface (refer to Section 3.3.3). Maji and Shah (1989) cast their specimens using conventional methods (i.e., the matrix paste was cast around dry inclusions). Maji and Shah

(1989) also used holographic interferometry to capture cracking processes, while this study used a high speed video system. An issue with the holographic interferometry system is that an incremental loading rate had to be used in order to capture images, while the HSV system used in this study allowed for a constant loading rate.

6.4 Conclusions

Many advances have been made in studying the cracking behavior associated with materials containing inclusions. This study consisted of an experimental series that considered the effects of inclusion shape, size, stiffness, and strength. While past researchers have performed experimental and analytical studies with the same motives, none have made such extensive efforts as this study. Four different inclusion shapes (square, circle, hexagon, and diamond) were considered in this study to analyze the cracking behavior of a specimen containing a single inclusion. Other researchers, however, were limited to either rectangular or circle inclusions. Moreover, no other researchers until this study, with the exception of Maji and Shah (1989), have systematically studied the interaction effects of an inclusion pair (with different shapes and stiffnesses) set at various geometries.

Debonding (prior to tensile crack initiation) was found to be minor in all cases of this study, but was slightly more extensive at the interfaces of half-inch inclusions compared to the one-inch inclusions. When debonding initiated in this study, it typically occurred only at the right and left inclusion boundaries. Other researchers such as Maji and Shah (1989), Tasdemir et al. (1990), and Maji et al. (1991) all observed extensive interface debonding prior to tensile crack initiation, however. Although it was believed to be attributed to the difference in the mechanical properties of material between this study and others, along with specimen preparation methods, additional experimental work needs to be performed. Moreover, a microscopic analysis (such as the ones performed by Zhang and Gjørv (1990), and Lo and Cui (2004)) may contribute to understanding this phenomenon.

Stress distributions were calculated in an attempt to explain the observed cracking processes (specifically debonding and tensile crack initiation) for inclusions of different strengths and

stiffnesses. The results of these closed formed solutions tend to agree with the results observed in this study. Figure 6.11 shows the stress concentration factors associated with a hole (E = 0) and a rigid inclusion (E = ∞) set in an infinite plate subject to a vertical far field uniaxial compressive stress. Both the tangential stress (σ_θ) and radial stress (σ_r) concentration factors are plotted. It is assumed that the Poisson's ratio (ν) of the plate is 0.25.

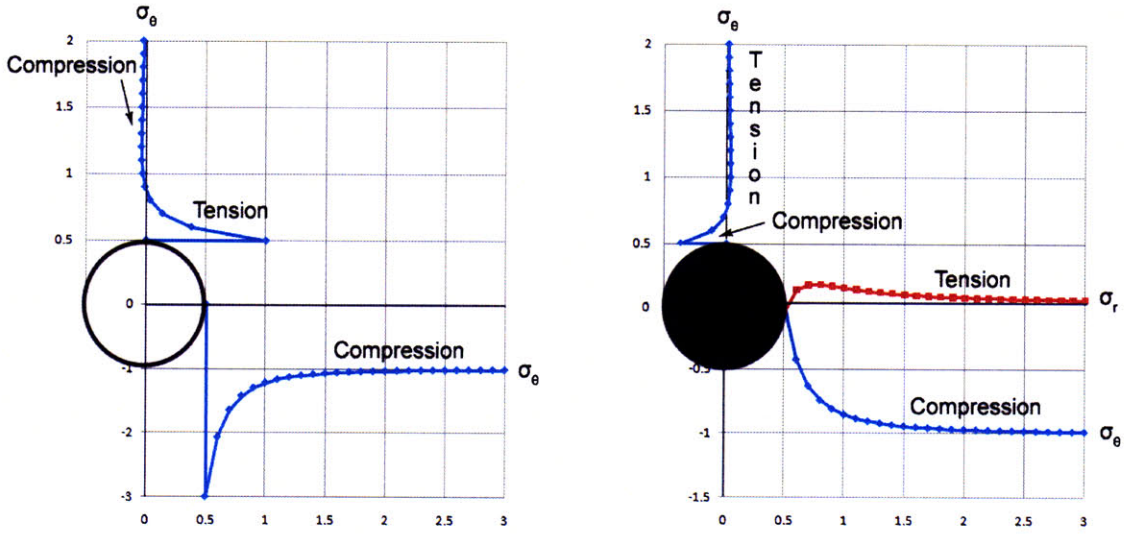

Figure 6.11 – Plots showing the tangential (σ_t) and radial (σ_r) stress concentration factors for a hole (left) and a rigid inclusion (right) cast within an infinite plate (for ν = 0.25) subject to a far field uniaxial compressive stress (σ_o) in the vertical direction.

According to Figure 6.11, the matrix containing a hole experiences high tangential compressive stresses ($\sigma_c = 3\sigma_o$) at the right and left interface, and moderate tensile stresses ($\sigma_t = -\sigma_o$) at the top and bottom interface. Transition into a compressive stress then occurs further above and below the hole. The matrix containing a rigid inclusion experiences different stress concentrations. The top and bottom interface experiences compressive tangential stresses ($\sigma_c \approx 0.38\sigma_o$), but a transition into tensile stresses then occurs at about a distance of half the inclusion's radius from the interface. Both the radial and tangential stresses are also plotted for the sides of the rigid inclusion. Notice how the tangential stresses are compressive, while the radial stresses are tensile.

The closed form solutions can be compared to the cracking behavior observed in this study. Figure 6.12 compares the cracking patterns for the Ultracal, circular inclusions to the "rigid inclusion" model shown in Figure 6.11. As mentioned earlier, debonding (prior to tensile crack initiation) only occurred at the sides of the inclusion interface. This agrees with the presence of tensile radial stresses at the sides of the rigid inclusion model. Since the tensile strength of gypsum is about a tenth of its compressive strength, tensile debonding might initiate first. It was observed that tensile crack initiation occurred in the matrix (above and below the inclusion) in some specimens containing half-inch inclusions. The plot in Figure 6.12 agrees with this observation as tensile tangential stresses occur just above and below the inclusion.

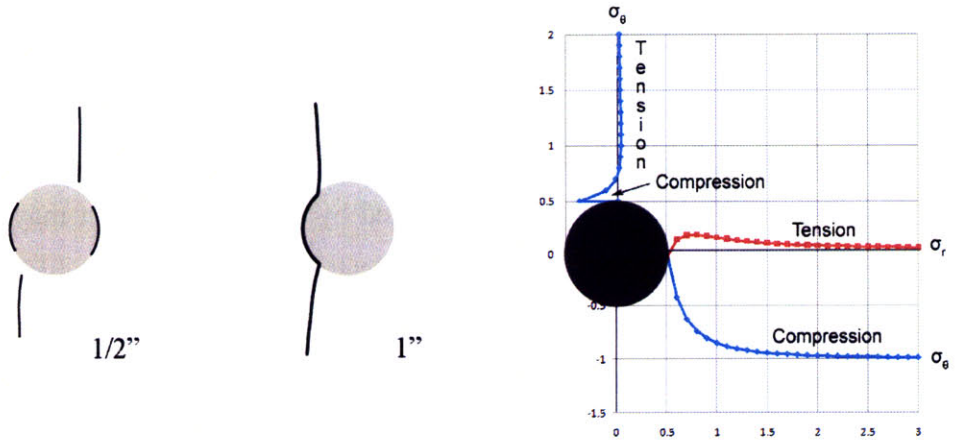

Figure 6.12 – A comparison of the Ultracal, circular inclusions to the plot showing the tangential (σ_t) and radial (σ_r) stress concentration factors for the rigid inclusion in Figure 6.11.

The tendency for tensile crack initiation at the upper and lower interface of plaster inclusions may also be explained through comparison to the "hole" model (Figure 6.13). According to the closed form solutions, the magnitude of tangential tensile stresses at these locations is relatively high. Again, since the tensile strength of a typical gypsum material is about a tenth of its compressive strength, the assumption that tensile cracks should initiate at the top or bottom of the interface can be made. This may also explain why tensile cracks initiated at plaster inclusions at lower stresses compared to the Ultracal inclusions, since a high tensile stress concentration may exist just above and below the plaster inclusion compared to the rigid (Ultracal) inclusion model.

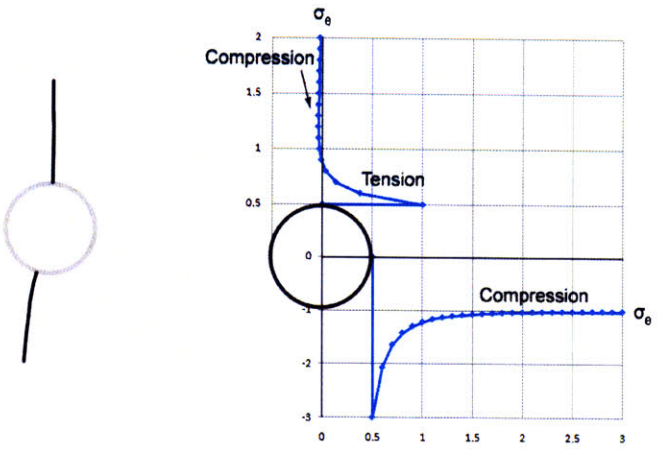

Figure 6.13 – A comparison of the plaster, circular inclusions to the plot showing the tangential (σ_t) stress concentration factors for the model containing a hole in Figure 6.11.

Interestingly, these closed form solutions (along with the observations from this study) do not agree with the tensile crack initiation results reported by Aulia (2000), but may agree with the work done by Maji and Shah (1989). Aulia (2000) stated that when large differences between E_m and E_a exist, as for the case of a high-strength concrete ($E_m << E_a$), microcracking will occur at the top and bottom interface. He also states that when the differences between E_m and E_a are small, microcracking will occur at the interface sides. Aulia (2000) did not provide sound reasoning to back up his theory (as discussed in Section 2.4), other than the fact that the theory agreed with his experimental work. Aulia (2000) did not cast specimens containing single inclusions, however, but mortar specimens containing numerous inclusions. The experimental work performed by Maji and Shah (1989) may agree to some extent with the tensile crack initiation predictions from the closed form solutions, considering they reported that typically the entire inclusion debonded prior to tensile crack initiation. Therefore, the specimen may be compared to the model containing a hole (used as this study's plaster model), which might explain why tensile crack initiation commonly occurred at the top and bottom of the debonded interfaces

The initiation of shear cracks (that propagated into the matrix) at an inclusion boundary was not reported by any other researcher prior to this study. The propagation of shear cracks was a common observation that resulted in the coalescence of all specimens containing inclusion pairs.

As mentioned earlier, Maji and Shah (1989) commonly observed the initiation of "diagonal" cracks at the sides of the inclusion interface. Maji and Shah (1989), however, did not report the nature (tensile/shear) of these diagonal cracks. Based on the results from this study, these diagonal cracks may have been shear cracks. One of the indicators used to determine the initiation and propagation of shear cracks in this study was surface spalling, which would explain Maji and Shah's (1989) post-mortem observations regarding diagonal cracks not extending through the entire specimen.

In this study, interface shearing typically initiated at the inclined boundary of hexagon and diamond inclusions. The results from Zaitsev and Wittmann (1981) and Maji et al. (1990) essentially agree with the observations from this study. Zaitsev and Wittman (1981) attributed this phenomenon to the presence of normal stresses on the inclined interface, and used it as a fundamental assumption for their analytical work. Maji et al. (1991) experimentally determined that the initiation of a crack at an inclined interface (that had previously experienced extensive debonding) was in mixed-mode and may explain why tensile crack initiation and interface shearing occurred "simultaneously" in this study.

Regarding specimens containing two inclusions, the coalescence patterns observed in this study can to some extent be compared to the results of Wong (2008) for specimens containing a flaw pair. The results of this study match those reported by Wong (2008) quite well (refer to Figure 6.14). For example, the horizontal inclusion pair (square and circle) and the horizontal, coplanar flaw pair geometries reported by Wong (2008) both coalesced indirectly along two or more cracks. The experimental series performed by Maji and Shah (1989) on horizontal inclusion pairs also agrees with the results from this study, as both studies observed that the horizontal inclusion pair typically coalesced indirectly (Figures 6.5 and 6.9). The analytical study performed by Zaitsev and Wittman (1981) can also be compared to this study. As mentioned earlier, Zaitsev and Wittman (1981) assumed that coalescence only occurred along a single tensile crack as they were only analyzing overlapping inclusion pairs. In this study, however, coalescence never occurred through a single tensile crack; this may be explained by the fact that no specimens containing overlapping inclusions were tested in this study. In some specimens where the inclusion inclination angle was large, however, the propagation of tensile cracks

(which previously initiated at a shear crack) resulted in coalescence. Figure 6.15 presents a visual comparison of the coalescence patterns observed by Zaitsev and Wittman (1981), Wong (2008), and this study. To fully confirm the similarities, it will be necessary to test specimens containing overlapping inclusion geometries.

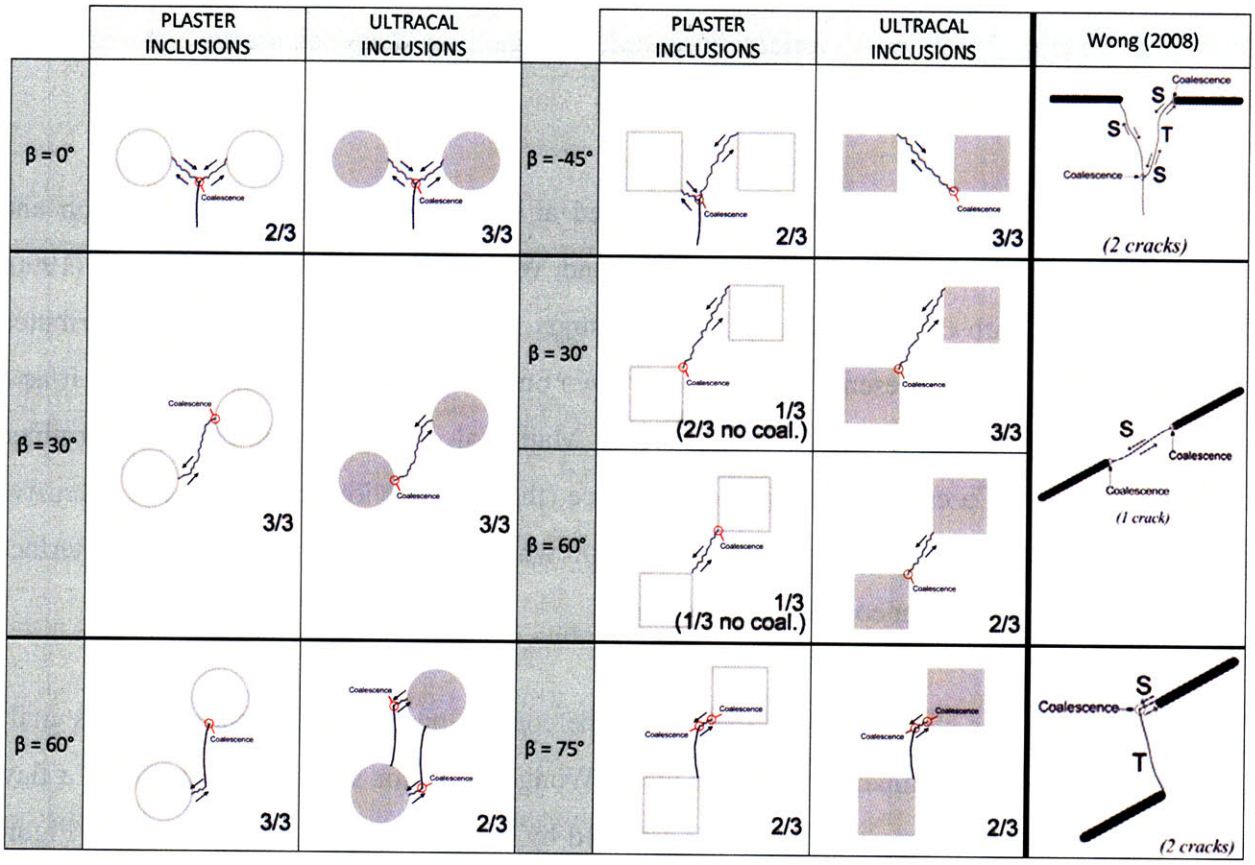

Figure 6.14 – Sketch of the double inclusion coalescence patterns from this study, compared to those reported by Wong (2008).

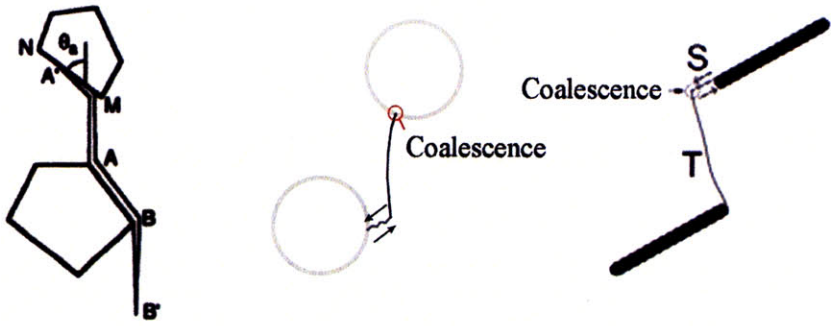

Figure 6.15 – A comparison of the coalescence patterns observed by Zaitsev and Wittmann (1981) (left), this study (center), and Wong (2008) (right).

6.5 Recommendations for Future Research

The experimental work performed by Maji and Shah (1989), Tasdemir et al. (1989), and Maji et al. (1991) provide a good framework for this area of research. Their selections of specimen material (especially inclusion shape and strength) were limited, however, due to fabrication issues. For this reason, this study utilized material that can be easily cast. This allowed us to create many different inclusion shapes, sizes, and strengths. Further experimental work is still needed, considering most brittle material contain numerous inclusions. There are several variables that affect the interaction effects of inclusions within a material. For example, comparison between the results by Maji and Shah (1989) and this study show that the ligament length of an inclusion pair may have a major effect. This study was limited to observing the cracking behavior of specimens containing only two inclusions. Therefore, more experimental work still needs to be done on specimens containing several inclusions, in order to understand which variables (both geometric and mechanical) have the most effect on the performance of material containing inclusions.

Boundary conditions will always exist that define what is feasible in an experimental sense. The analytical work done by Zaitsev and Wittmann (1981) and Aulia (2000) provide a good basis in attempting to understand the cracking complexities associated with a heterogeneous material. Since composite materials contain numerous inclusions of various shapes, sizes, and strengths

numerical modeling may be the only way in truly understanding how inclusions behave within a matrix.

In addition to studying cracking behavior associated with inclusions, the goal of this study was to provide the background for future work in formulating predictive models on the behavior of materials with inclusions. This study only provided the basis for this area of research, however. Additional testing is needed in order to further augment this background and to draw definitive conclusions regarding the behavior of a brittle material containing inclusions:

- Complete the half-inch, single inclusion series by testing specimens containing half-inch hexagon and diamond inclusions. Specifically, two series of specimens need to be created (one containing a plaster inclusion, and the other containing an Ultracal inclusion).

- Complete the double inclusion series by testing specimens containing hexagon and diamond inclusion pairs. Particularly, two series of specimens containing an Ultracal and plaster inclusion pair will need to be tested. These specimens are to first be tested at the same inclination angles as the square and circular series. Additional specimens containing inclusions of all four shapes then need to be tested at different (preferably larger) inclination angles in order to study the effects of overlapping inclusion pairs.

- Perform a macroscopic investigation (unconfined compression testing) on inclusions themselves, in order to determine their mechanical properties with certainty.

- Perform a microscopic investigation on the interface of various inclusions prior to, and after, testing (in order to study any possible precursors to interface debonding and crack initiation). Such investigations need to also be performed for cracking at different stages of propagation.

CHAPTER 7 – References

Anderson, T.L. (2005) *Fracture Mechanics: Fundamentals and Applications*, Edition 3, CRC Press, Boca Raton, FL.

Ashby, M.F. and Hallam, S.D. (1986) the failure of brittle solids containing small cracks under compressive stress states. *Acta Metall.*, 34, pp. 497-510.

Ashby, M.F. and Sammis. (1990) The damage mechanics of brittle solids in compression, *Pure Appl. Geophys.*, 133, pp 489-521.

Aulia, T.B. (2000) Strain localization and fracture energy of high-strength concrete under uniaxial compression, *LACER No. 5*, pp. 221-240.

Barenblatt, G.I. (1962) The mathematical theory of equilibrium cracks in brittle fracture. *Advances in Applied Mechanics*, Vol. VII, Academic Press, NY, pp. 55-109.

Bienawski. (1967) Mechanisms of brittle fracture of rock, part II – experimental studies, *Int. J. Rock. Mech. Min. Sci.*, Vol. 4, pp. 407-423.

Bobet, A. (1997) *Fracture Coalescence in Rock Materials: Experimental Observations and Numerical Predictions*, Sc.D. Thesis, Massachusetts Institute of Technology.

Bobet, A. and Einstein, H.H. (1998a) Fracture coalescence in rock-type materials under uniaxial and biaxial compression. *Int. J Rock Mech Min Sci*, 35(7), pp. 863-88.

Bobet, A. and Einstein, H.H. (1998b) Numerical modeling of fracture coalescence in a model rock material. *Int. J. Fracture*, 92, pp. 221-252.

Brace, W.F. and Bombolakis, E.G. (1963) A note on brittle crack growth in compression, *J. Geophys Res*, 68(12), pp. 3709-3713.

Chaker and Barquins. (1996) Sliding effect on branch cracks, *Phys. Chem. Earth*, 21(4), pp. 319-323.

Chen, G., Kemeny, J.M. and Harpalani, S. (1995) Fracture propagation and coalescence in marble plates with pre-cut notches under compression, In L.R. Myer, N.G.W. Cook, R.E. Goodman & C.F. Tsang (Eds). *Symposium on Fractured and Jointed Rock Mass*, Lake Tahoe, CA, pp. 435- 439.

Costin, L.S. (1985) Damage mechanics in the post-failure region. *Mech. Mat.* 4, pp. 149-160.

Cottrell, B. and Rice, J.R. (1980) Slightly curved or kinked cracks, *International Journal of Fracture*, 16(2), pp. 155-169.

De Ra, G. (2000) *Physical mechanisms controlling the pre-failure stress-strain behavior of frozen sand*, ScD Thesis, Massachusetts Institute of Technology, Cambridge, MA.

Dugdale, D.S. (1960) Yielding in steel sheets containing slits, *Journal of the Mechanics and Physics of Solids*, 8, pp. 100-104.

Einstein, H.H. and Hirschfeld R.C. (1973) Model studies on mechanics of jointed rocks, *ASCE Journal of the Geotechnical Division*, Vol. 99, SM3.

Einstein, H.H., Nelson, R.A., Bruhn, R.W. and Hirschfeld, R.C. (1969) Model studies of jointed rock behavior, *Proc. 11th Symposium on Rock Mechanics*, pp. 83-103.

Erdogan, F. and Sih, G.C. (1963) On the crack extension in plates under plane loading and transverse shear, *Journal of Basic Engineering*, 85, pp. 305-321.

Friedman, M., Handin, J. and Alani, G. (1972) Fracture energy of rocks. *Int. J. Rock. Mech. Min. Sci.*, 9, pp. 757-766.

Germanovich, L.N. and Dyskin, A.V. (2000) Fracture mechanisms and instability of openings in compression, *Int. J. Rock. Mech. Min. Sci.*, 37, pp. 263-284.

Goodier, J.N. (1933) Concentration of stress around spherical and cylindrical inclusions and flaws, J. Appl. Mech., 1, pp. 39-44.

Gramberg, J. (1965) Axial cleavage fracturing, a significant process in mining and geology, *Engineering Geology*, 1(1), pp. 31-72.

Griffith, A.A. (1920) The phenomenon of rupture and flow in solids. *Philosophical Transactions*, Series A, 221, pp. 163-198.

Grübl, P. (1979) Druckfestigkeit von leichbeton mit geschlossenem gefüge, *Beton*, 3(29), pp. 91-95.

Hansen, T.C. (1958) Creep of Concrete, *Swedish Cement and Concrete Research Institute*, Bulletin No. 33, 48 p.

Hillerborg, A., Modeer, M., and Petersson, P.E. (1976) Analysis of crack formation and crack growth in concrete by means of fracture mechanics and finite elements, *Cement and Concrete Research,* 6, pp. 773-782.

Hillerborg, A. (1991) Application of the fictitious crack model to different materials, *International Journal of Fracture*, 51, pp. 95-102.

Hoek and Bieniawski. (1965) Brittle fracture propagation in rock under compression, *Int. J. of Fracture Mechanics*, Vol. 1, pp 137-155.

Horii, H. & Nemat-Nasser, S. (1985) Compression-induced microcrack growth in brittle solids: Axial splitting and shear failure. *Journal of Geophysical Research*, 90 (B4), pp. 3105-3125.

Horii, H. & Nemat-Nasser, S. (1986) Brittle failure in compression: splitting, faulting, and brittle-ductile transition, *Phil. Transactions Royal Soc. London*, A319, pp. 337-374.

Huang J.F., Chen G.L., Zhao Y.H. and Wang R. (1990) An experimental study of the strain field development prior to failure of a marble plate under compression. *Tectonophysics*, Vol. 175, pp. 283-290.

Hussain, M.A., Pu, S.L. and Underwood, J. (1974) Strain energy release rate for a crack under combined mode I and mode II. *Fract Anal ASTM STP* 560, pp. 2–28.

Inglis, C.E. (1913) Stresses in a plate due to the presence of cracks and sharp corners. *Inst. Naval Architecture, London*, 55, pp. 219-230.

Ingraffea, A. and Wawrzynek, P.A. (2001) *Encyclopedia of Materials: Science and Technology*, pp. 1745-1750.

Irwin, G.R. (1957) Analysis of stresses and strains near the end of a crack traversing a plate. *Journal of Applied Mechanics*, 24, pp. 361-364.

Kachanov. (1985) A simple technique of stress analysis in elastic solids with many cracks, *Int. J. Fracture*, 28, R11 - R19.

Kemeny, J.M. and Cook, N.G.W. (1987) Crack models for the failure of rocks in compression. In *Proc. 2nd Int. Conf. on Constitutive Laws for Engineering Materials*, Tucson, Arizona.

Kemeny, J.M. and Cook, N.G.W. (1991) Micromechanics of deformation in rocks, *Toughening Mechanisms in Quasi-Brittle Materials*, edited by Shah, Kluwer Academic, Norwell, USA, pp. 155-188.

Ko, T.Y., Einstein, H.H. and Kemeny, J. (2006) Crack coalescence in brittle material under cyclic loading. Golden Rocks 2006, *Proc. of the 41st U.S. Symposium on Rock Mechanics (USRMS): "50 Years of Rock Mechanics - Landmarks and Future Challenges"*, Golden, Colorado, June 17- 21, ARMA/USRMS 06-930.

Lajtai. (1971) A theoretical and experimental evaluation of the Griffith theory of brittle fracture, *Tectonophysics*, 11, pp. 129-156.

Li, Y.P., Chen, L.Z. and Wang, Y.H. (2005) Experimental research on pre-cracked marble under compression, *International Journal of Solids and Structures*, 42, pp. 2505-2516.

Lo, T.Y. and Cui, H.Z. (2004) Effect of porous lightweight aggregate on strength of concrete, *Materials Letters*, 58, pp. 916-919.

Maji, A.K. and Shah, S.P. (1989) Application of acoustic emission and laser holography to study microfracture in concrete, *Nondestructive Testing*, ACI SP-112, edited by Lew, H.S., American Concrete Institute, Detroit, MI, pp. 83-109.

Maji, A.K. and Shah, S.P. (1990) Mixed mode fracture in compression, *Analysis of Concrete Structures by Fracture Mechanics,* edited by Elfgren, L. and Shah, S.P., Chapman and Hall, New York, NY, pp. 55-68.

Maji, A.K., Tasdemir, M.A., and Shah, S.P. (1991) Mixed mode crack propagation in quasi brittle material, *Engineering Fracture Mechanics*, 38(2/3), pp. 1058-1076.

Martinez, A.R. (1999) *Fracture coalescence in natural rock*, MSc Thesis, Massachusetts Institute of Technology, 341 p.

Melville, P.H. (1977) Fracture mechanics of brittle materials in compression, *Int. J. Frac.*, 13, pp. 532-534.

Miller, J.T. (2008) *Crack coalescence in granite*, MSc Thesis, Massachusetts Institute of Technology, 474 p.

Mitsui, K., Li, Z., Lange, D.A., and Shah, S.P. (1994) Relationship between microstructure and mechanical properties of the paste-aggregate interface, *ACI Materials Journal*, 91(1), pp. 30-39.

Motoyama, H. and Hirschfeld, R.C. (1971) The effect of joint configurations on the strength and deformability of model rock masses, Final Report, Federal Railroad Administration, Department of Transportation, Washington, D.C. 20591, 183 p.

Moss, W.C. and Gupta, Y.M. (1982) A constitutive model describing dilatancy and cracking in brittle rocks. *Journal of Geophysical Research,* 87 (B4), pp. 2985-2998.

Mughieda, O. and Alzo'ubi, A.K. (2004) Fracture mechanics of offset rock joints – a laboratory investigation, *Geotechnical and Geological Engineering*, 22, pp. 545-562.

Nelson, R.A. (1968) *Modeling a jointed rock mass*, MSc Thesis, Massachusetts Institute of Technology, 218 p.

Nemat-Nasser and Horii. (1982) Compression-induced non-planar crack extension with application to splitting, exfoliation, and rockburst, *J. Geophys. Res.*, 87(8), pp 6805-6821.

Nesetova and Lajtai. (1973) Fracture from compressive stress concentrations around elastic flaws, *Int J. Rock Mech. Min. Sci. & Geomech. Abstr.*, 10, pp. 265-284.

Neville, A.M. (1997) Aggregate bond and modulus of elasticity of concrete, *ACI Materials Journal*, 94(1), pp. 71-74.

Petit, J. and Barquins, M. (1988) Can natural faults propagate under Mode II conditions?, *Tectonics*, 7(6), pp. 1246-1265.

Reyes, O. (1987) *Numerical modeling of fracture propagation in tension softening materials*, S.M. Thesis, Massachusetts Institute of Technology, Cambridge, MA.

Reyes, O. (1991) *Experimental study and analytic modeling of compressive fracture in brittle materials*, Ph.D. Thesis, Massachusetts Institute of Technology, Cambridge, MA.

Reyes, O. and Einstein, H.H. (1991) Failure mechanism of fractured rock – a fracture coalescence model, *Proceedings of the 7th International Congress of Rock Mechanics*, Aachen, Germany, 1, pp. 333-340.

Sagong, M. (2001) The study of the fracture of multiple flaw specimens, *Ph.D. Thesis*, Purdue University, Indiana.

Sagong, M. and Bobet, A. (2002) Coalescence of multiple flaws in a rock-model material in uniaxial compression, *Int. J. Rock. Mech. Min. Sci.*, 39, pp. 229-241.

Segall, P. and Pollard, D.D. (1983) Nucleation and growth of strike slip faults in granite, *J. Geophys Res*, 88, pp. 555-568.

Shah, S. P. (1995) *Fracture mechanics of concrete: applications of fracture mechanics to concrete, rock and other quasi-brittle materials*, edited by Shah, S.P., Swartz, S.E., Ouyang, C., Wiley, New York, 552 p.

Shen, B., Stephansson, O., Einstein, H.H. and Ghahreman, B. (1995) Coalescence of fractures under shear stress experiments, *J. Geophys Res*, 100(6), pp. 5975-90.

Sih, G.C. (1973) Some basic problems in fracture mechanics and new concepts, *Engineering Fracture Mechanics,* 5, pp. 365–377.

Sih, G.C. (1974) Strain-energy-density factor applied to mixed mode crack problems, *International Journal of Fracture*, 10(3), pp. 305-321.

Tasdemir, M.A., Maji, A.K. and Shah, S.P. (1990) Crack propagation in concrete under compression, *Journal of Engineering Mechanics*, 116(5), pp. 1058-1076.

Taylor, M.A. and Broms, B.B. (1964) Shear bond strength between coarse aggregate and cement paste or mortar, *ACI J.*, Proc., 61(8), pp. 937-957.

Wang, E.Z. and Shrive, N.G. (1995) Brittle fracture in compression: mechanics, models and criteria, *Engineering Fracture Mechanics*, 52(6), pp. 1107 – 1126.

Wong, L.N.Y. (2008) Crack coalescence in molded gypsum and Carrara Marble, PhD Thesis, Massachusetts Institute of Technology, Cambridge, MA 2008. 876 p.

Wong, L.N.Y. and Einstein, H.H. (2009) Using high speed video imaging in the study of cracking processes in rock, *Geotechnical Testing Journal*, 32(2).

Wong, R.H.C. and Chau, K.T. (1998) Crack coalescence in a rock-like material containing two cracks, *Int. J. Rock. Mech. Min. Sci.*, 35(2), pp. 147-164.
Zaitsev, Y.B. and Wittmann, F.H. (1981) Simulation of crack propagation and failure of concrete, *Materials and Structures*, 14(83), pp. 357-365.

Zaitsev, Y.B. (1983) Crack propagation in a composite material, *Fracture Mechanics of Concrete*, edited by Wittmann, F.H. Elsevier Science, Amsteram, pp. 251-299.

Zhang, M.H. and Gjørv O.E. (1990) Microstructure of the interfacial zone between lightweight aggregate and cement paste, *Cement and Concrete Research*, 20(4), pp. 610-618.

APPENDIX A – Testing Equipment Caveats

A.1 Introduction

The three sections of this appendix are intended to present the apparatus used for specimen testing, along with various issues that were encountered during testing. The first section will present a general description of the equipment and setup profile used for experimental testing. The second section will introduce problems that were encountered during testing; these issues, and their respective solutions, will be discussed in section three.

A.2 General Description of Loading Equipment and Setup Profile

All testing was performed with a Baldwin 200 kip Loading Frame that was controlled by a computer software program called MTestW (Version M 9.0.7i) created by ADMET. This loading frame is connected to a hydraulic system that produces the required pressure. The hydraulic system contains two valves referred to as the "servo" and "dump" valve. The servo valve controls the inflow of hydraulic fluid into the piston of the Baldwin frame; whereas, the dump valve controls the outflow of hydraulic fluid. When a specimen is loaded, the hydraulic pump passes the fluid through the servo valve at a user specified rate. When unloading a specimen the servo valve is shut and the dump valve is opened. The oil then flows through the dump valve and back into the reservoir. This is a cyclical process that occurs each time a specimen is tested. Only one valve can be opened at one time (i.e. there is never a scenario when both valves are partly, or fully, open).

The user setup profile within the MTestW software contains various input parameters that the user can modify. There is a section within the setup profile that controls the rate at which the hydraulic pump operates, which is called the "servo profile". The servo profile contains the specific loading scheme that will run during the test (Figure A.1). For example, in Figure A.1 there are three different loading rates that the user has specified.

There are four parameters for each loading rate (refer to Figure A.1). The first one, which is denoted with an encircled number one, is referred to as the control channel. The user can define this as either load, position, or stress controlled. The second, which is the control rate, can be set in units per second, or per minute. The third is the end channel, which can be defined as load, position, time, stress, or none regulated. The end channel serves as the boundary condition for each loading rate; once the end channel has been exceeded, the next loading rate commences. For example, in Figure A.1 the second loading rate (0.0003 in/sec) will begin when the load exceeds 1000 pounds. The fourth parameter, which is the log channel, defines how often data is recorded.

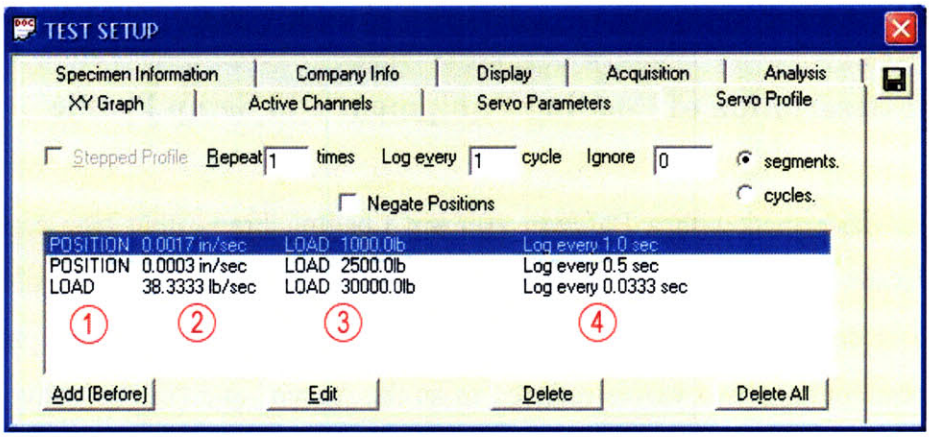

Figure A.1 – The servo profile section within the setup profile used for experimental testing.

A.3 Encountered Testing Issues

There were two major issues that were encountered during different tests. The first occurred when the hydraulic pump shut off during the middle of a test run, and then suddenly turned back on several moments later.

The second issue occurred during the end of a test. The MTestW software has a "go home" feature that allows the user to send the loading table back to its pre-test zero value. This process, which is controlled by the hydraulic dump valve, is required for the removal of the specimen after testing. On several occasions the table began to lower, start rising again, and then lowers to

the zero-value. This proved to be quite dangerous to the user as the failed specimen would get reloaded during the removal process.

A.4 Remediation of Testing Issues

Regarding the first issue, we learned that the entire campus was experiencing electrical problems that same day. The exact cause of this issue has not been understood, nor has it recurred again. The second issue was related to the setup profile used during testing. There is a section of the setup profile that controls the "go home" rate (Figure A.3).

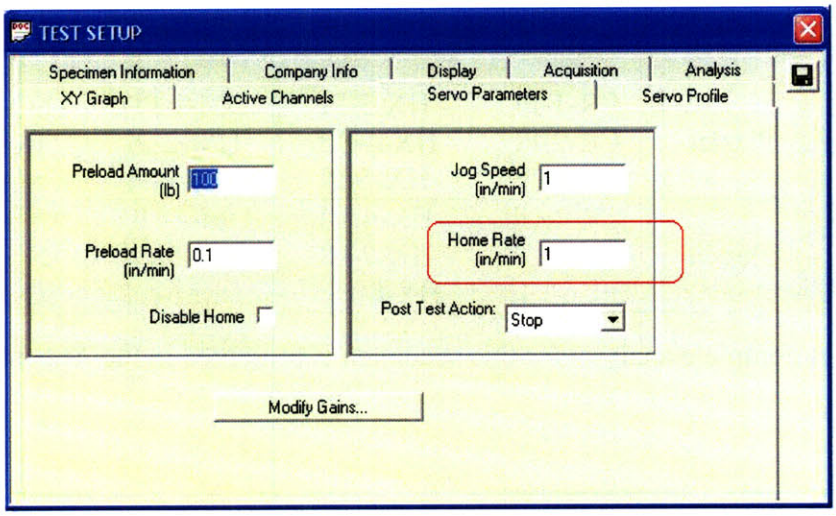

Figure A.3 - The servo parameters section located within the setup profile used for experimental testing.

As shown in Figure A.3, the home rate value was set at 1 in/min. It was determined that the dump valve lowers the piston at a constant maximum rate of roughly 5 in/min. The home rate set within the setup profile created a conflict within the hydraulic system. When the user selected the "go home" option, the dump valve switched on and lowered the table at 5 in/min. However, the software recognized that this is greater than the home rate specified within the setup file and turned on the servo valve in order to bring the table back to the position it should be at. This issue was resolved by selecting a home rate within the setup profile that is greater than the dump valve can operate at (i.e., 10 in/min).

APPENDIX B – One-inch Single Inclusions

This appendix contains the detailed analyses for specimens with single, one-inch inclusions. Four different inclusion geometries were tested (circle, hexagon, diamond, and square) with either an Ultracal or plaster inclusion; one complete analysis for each specimen type is presented, while summaries for the other specimens are provided. For a complete summary of results, refer to Section 4.3. A list of tested specimens is summarized below.

		Circle	Hexagon	Diamond	Square
1" Inclusion	Plaster	CR-1-Pl CR-2-Pl CR-3-Pl*	HX-3-Pl HX-4-Pl* HX-5-Pl	DM-1-Pl* DM-2-Pl DM-3-Pl	SQ-4-Pl* SQ-5-Pl SQ-7-Pl
	Ultracal	CR-4-Ul CR-5-Ul CR-6-Ul*	HX-6-Ul HX-7-Ul HX-8-Ul*	DM-4-Ul* DM-5-Ul DM-6-Ul	SQ-8-Ul SQ-9-Ul SQ-10-Ul*

* A complete analysis for this specimen is presented in the Appendix.

SUMMARY

Specimen Number: CR-1-PI (20080601)

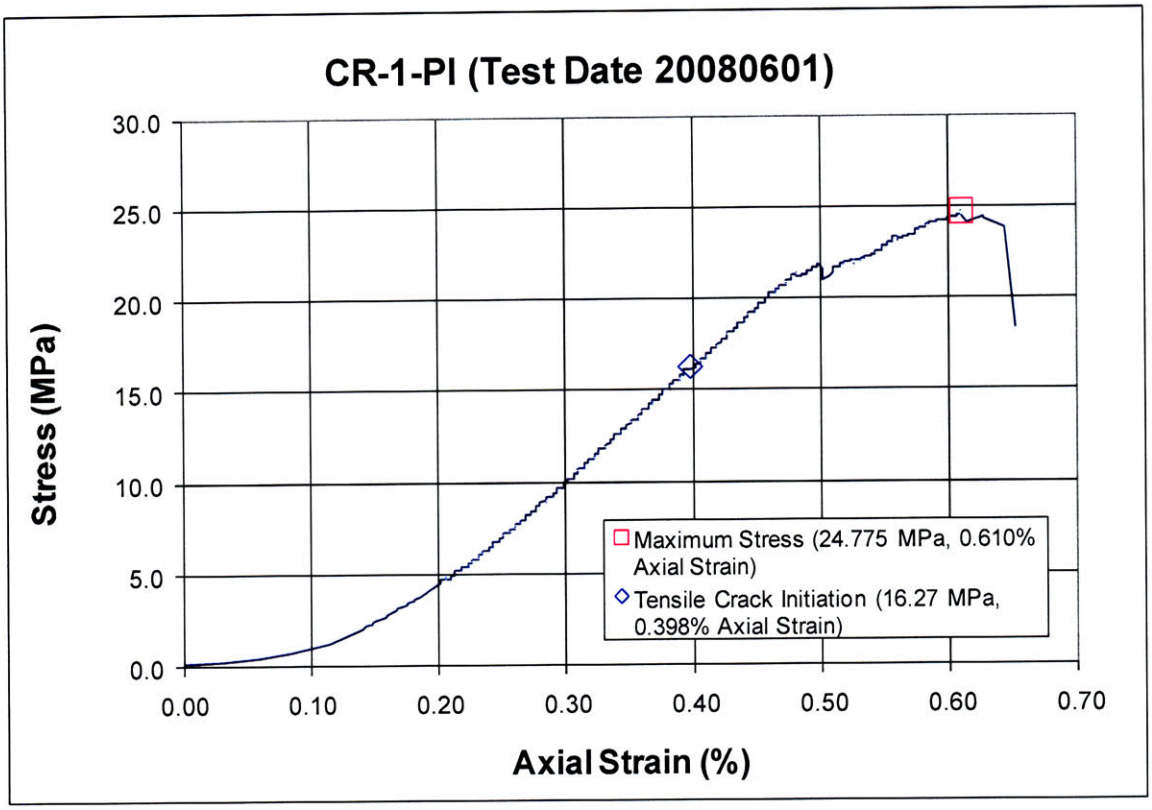

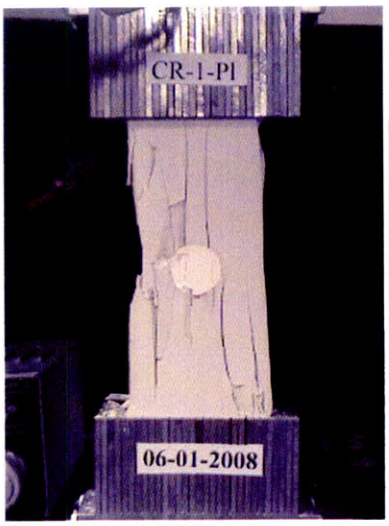

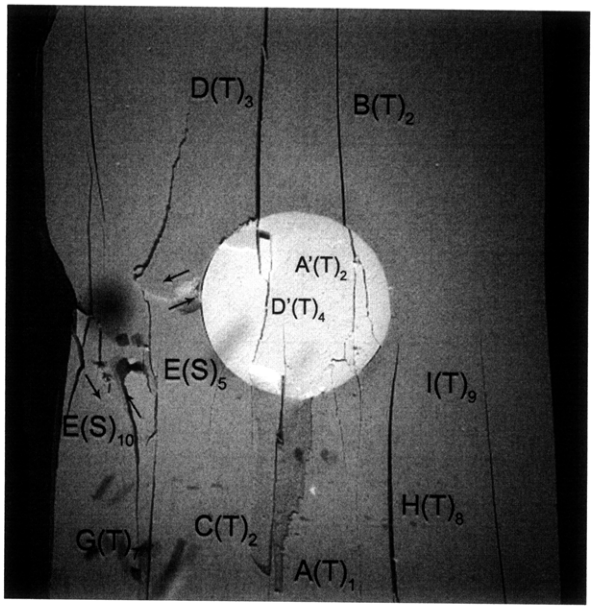

(Recorded by High Speed Video System)

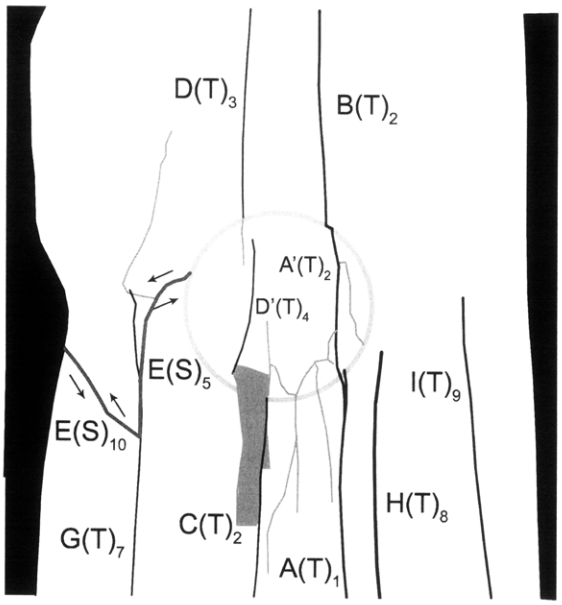

(- MPa) - Ultimate Failure
Time: 5 minutes & 13.165 seconds
HS Image # - 3053

Shear crack (E) begins to propagate upwards and shear in an opposite direction after its coalescence with tensile crack (G).

Shear crack (E) then coalesces with the left-hand specimen boundary.

SUMMARY

Specimen Number: CR-2-PI (20080601)

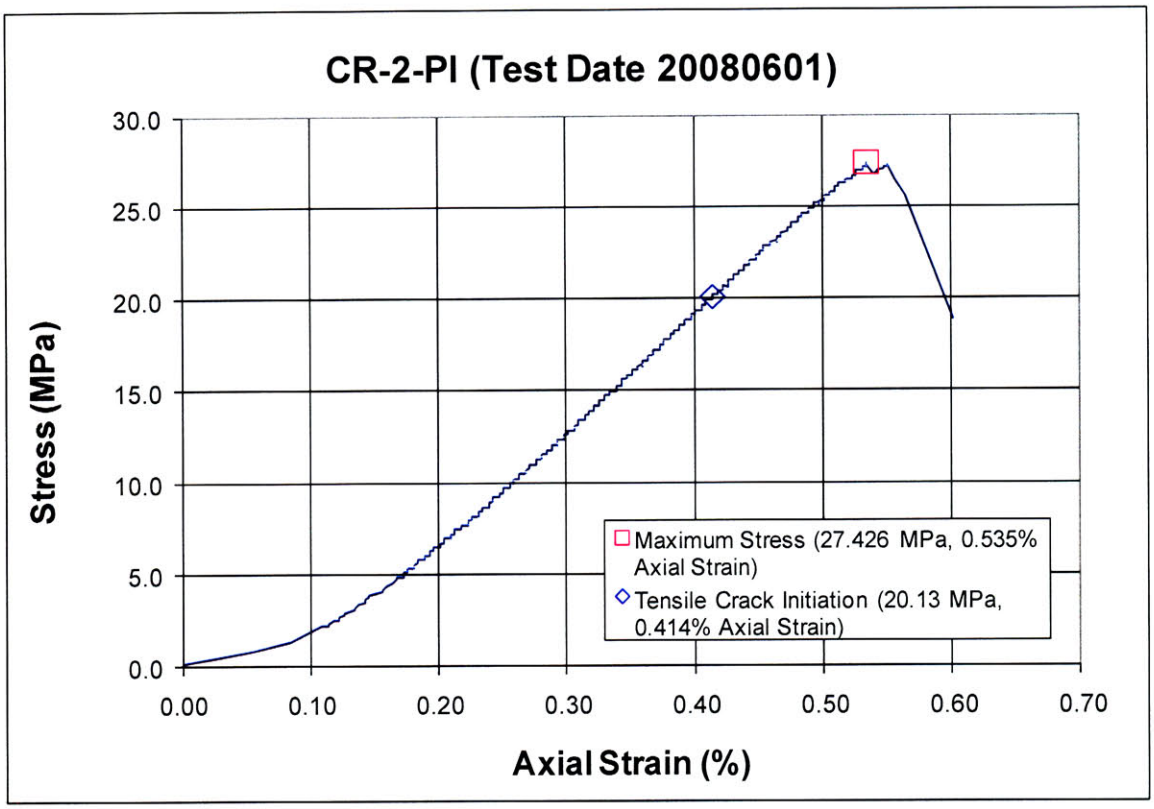

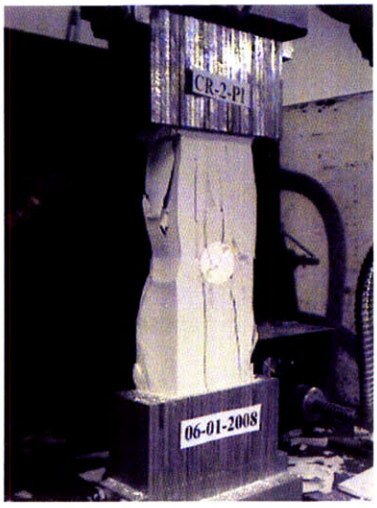

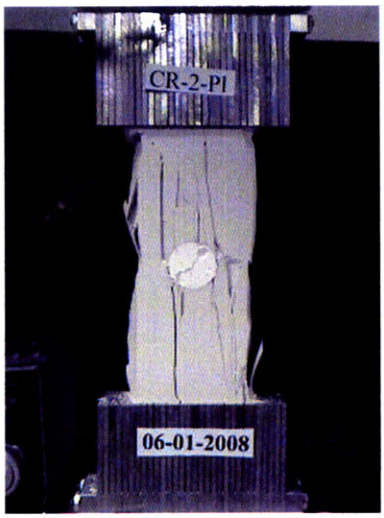

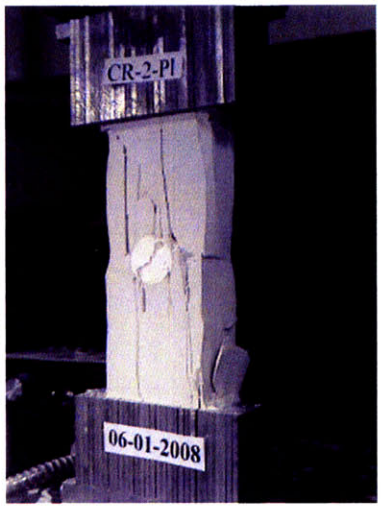

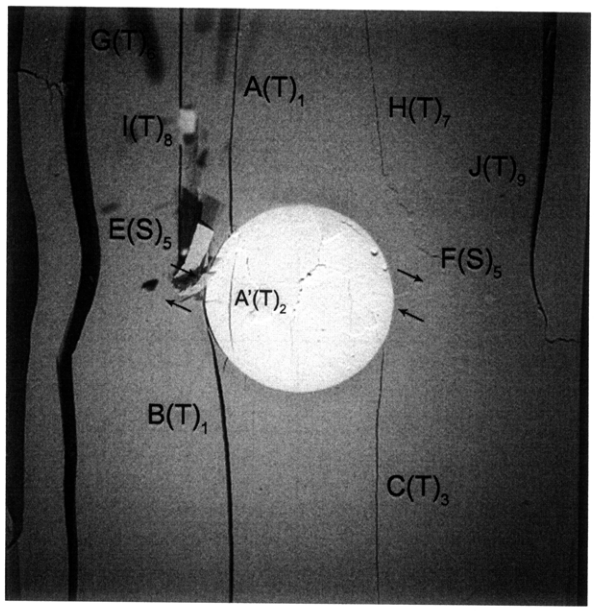

(Recorded by High Speed Video System)

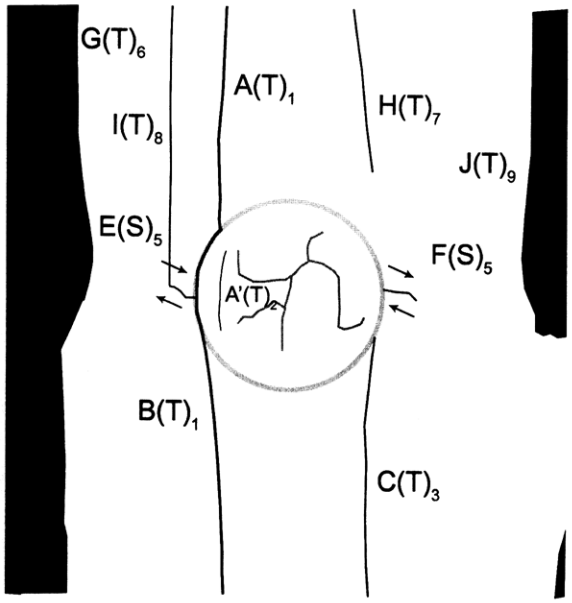

(27.02 MPa)
Time: 5 minutes & 42.996 seconds
HS Image # - 2442

A new tensile crack (J) initiates at the upper specimen boundary and propagates until its coalescence with the right-hand specimen boundary, which results in the detachment of another large specimen piece.

Specimen Number: CR-3-PI (20080601)

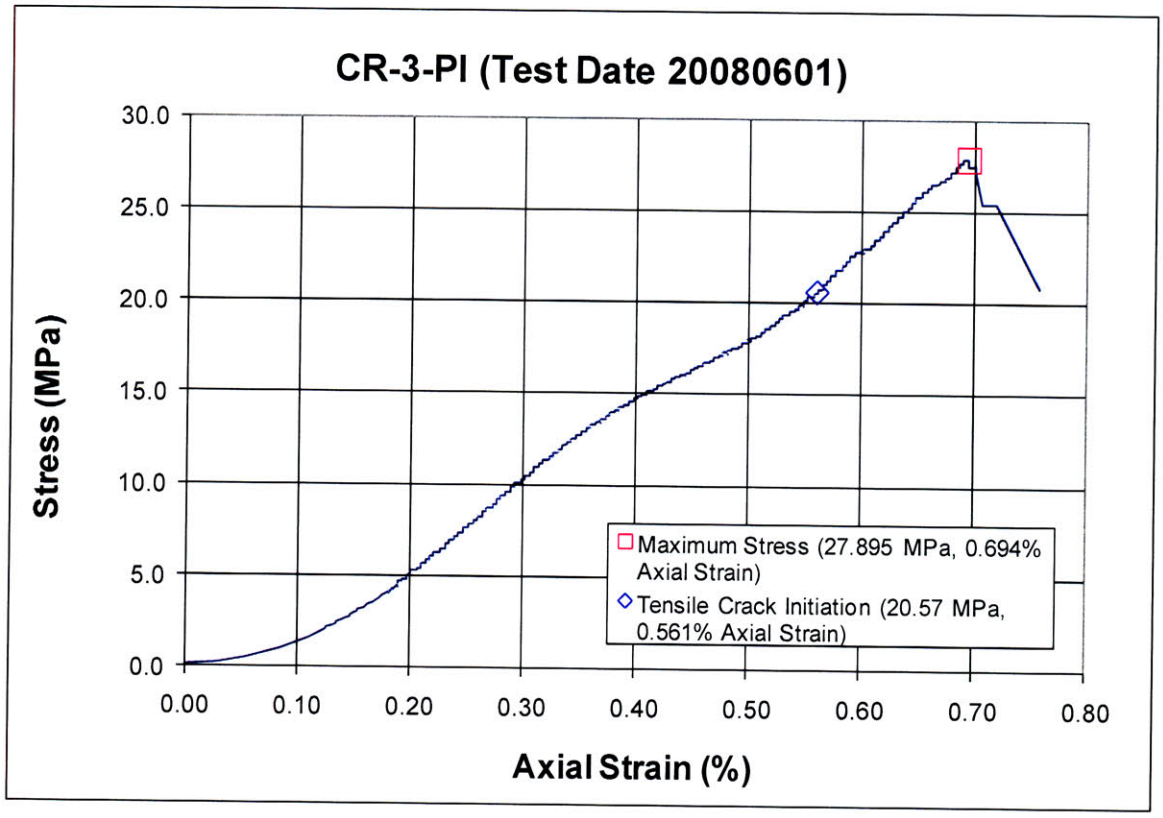

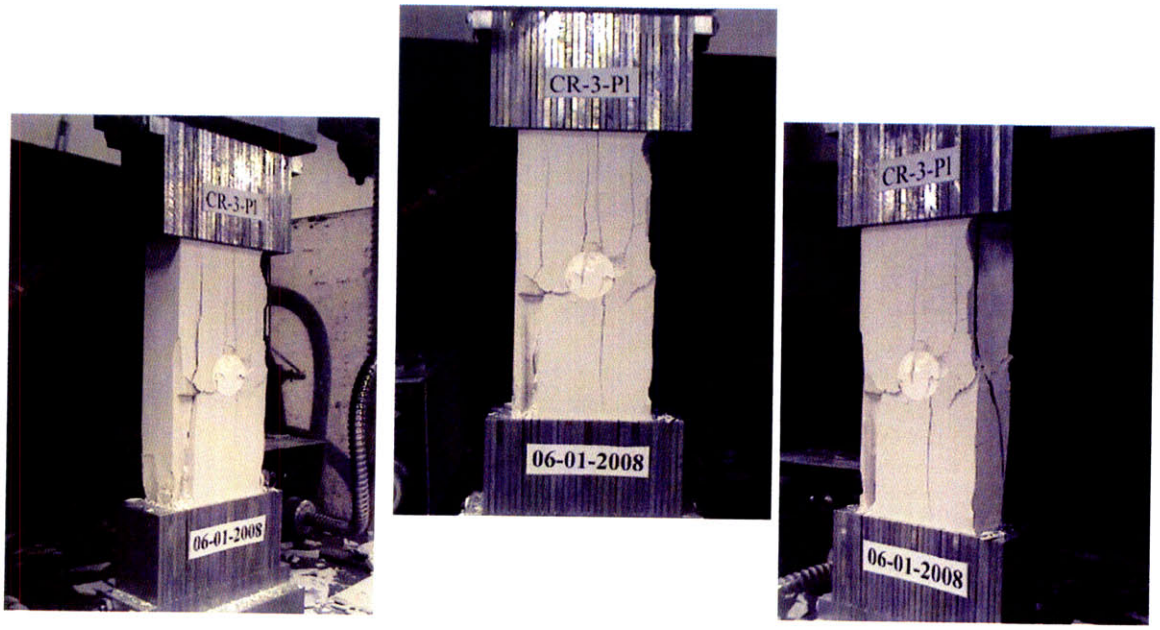

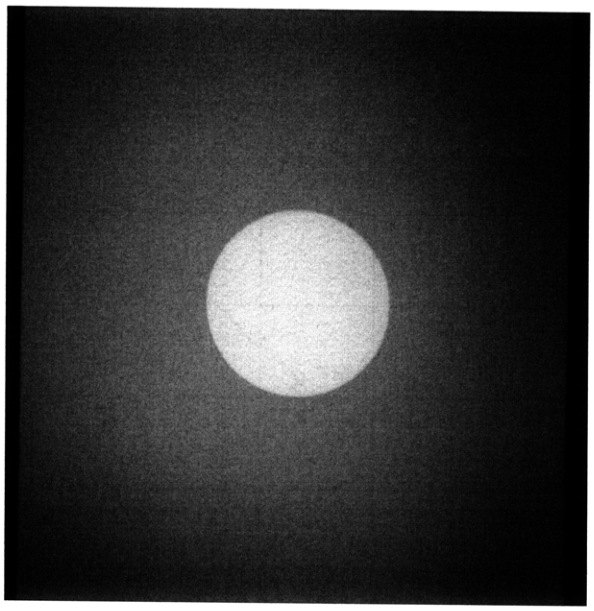

(Recorded by High Speed Video System)

Initial Inclusion Geometry:
CIRCLE – Plaster Material

Inclusion **less** stiff than matrix.

High Speed Camera Frame Rate:
5000 pps

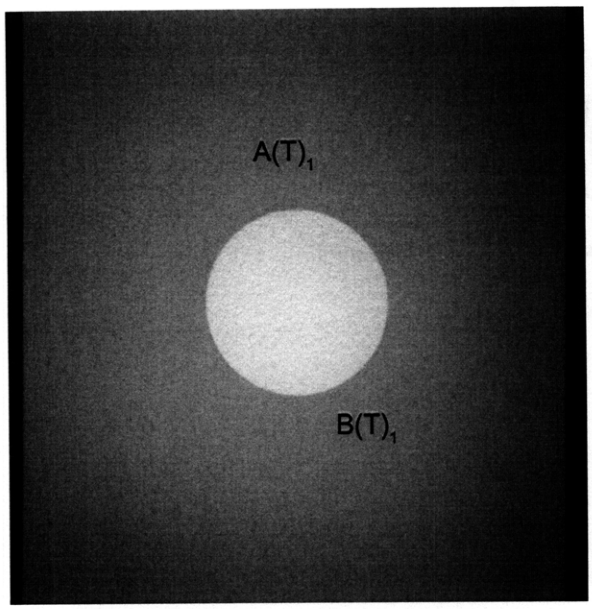

(Recorded by High Speed Video System)

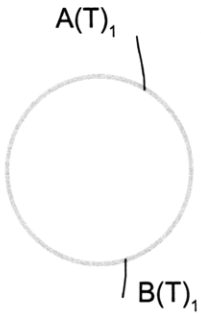

(20.57 MPa)

- Tensile Crack Initiation

Time: 4 minutes & 8.76 seconds

Tensile crack (A) initiates at the upper inclusion boundary and propagates towards the upper specimen boundary.

Tensile crack (B) initiates at the lower inclusion boundary and propagates towards the lower specimen boundary.

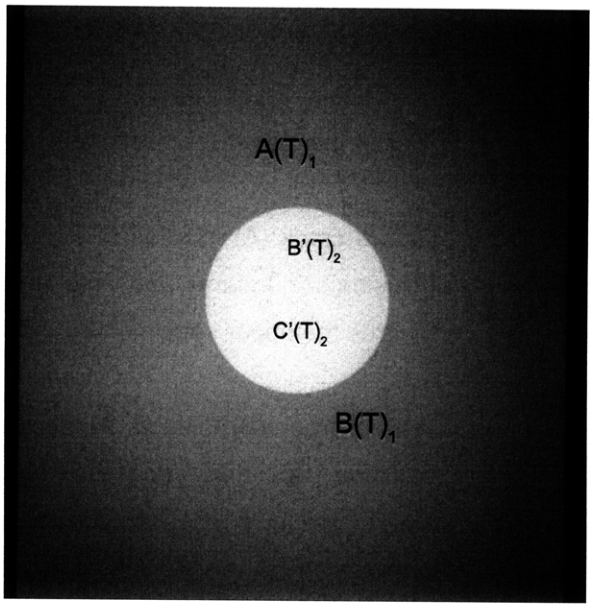

(Recorded by High Speed Video System)

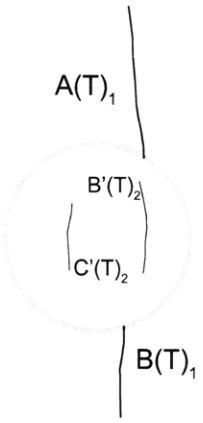

(22.26 MPa)

Time: 4 minutes & 32.96 seconds

As the apertures of tensile cracks (A&B) increase, two new tensile cracks (B'&C') initiate within the inclusion.

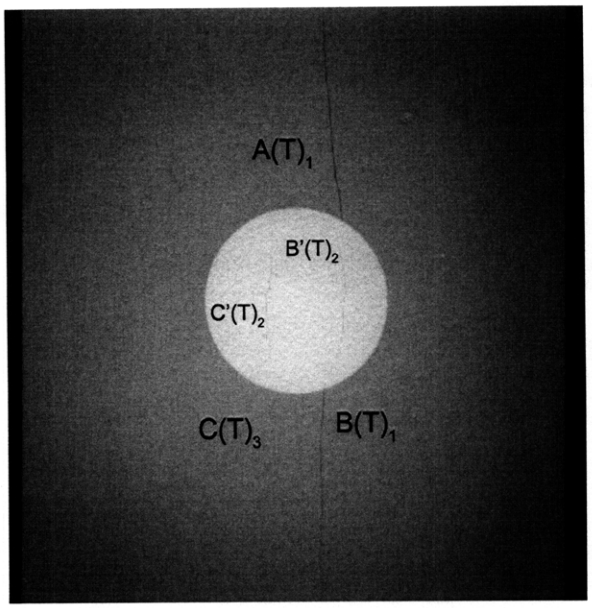

(Recorded by High Speed Video System)

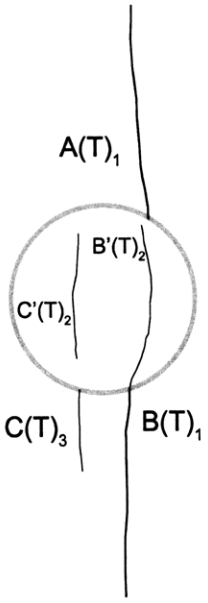

(22.94 MPa)
Time: 4 minutes & 42.79 seconds

With an increase in loading, tensile crack (B') propagates towards the lower inclusion boundary and coalesces with tensile crack (B).

A new tensile crack (C) initiates at the lower inclusion boundary and propagates downwards.

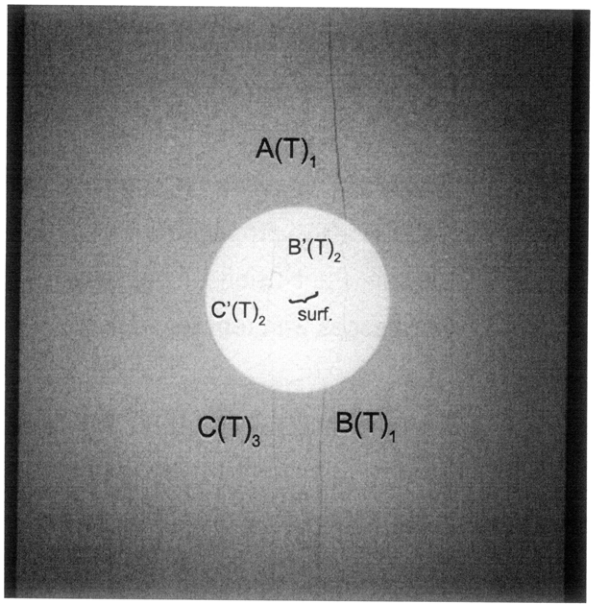

(Recorded by High Speed Video System)

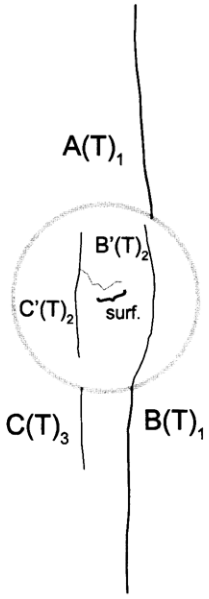

(23.27 MPa)

Time: 4 minutes & 47.27 seconds

A surface crack (surf.) initiates at tensile crack (C') and propagates towards tensile crack (B').

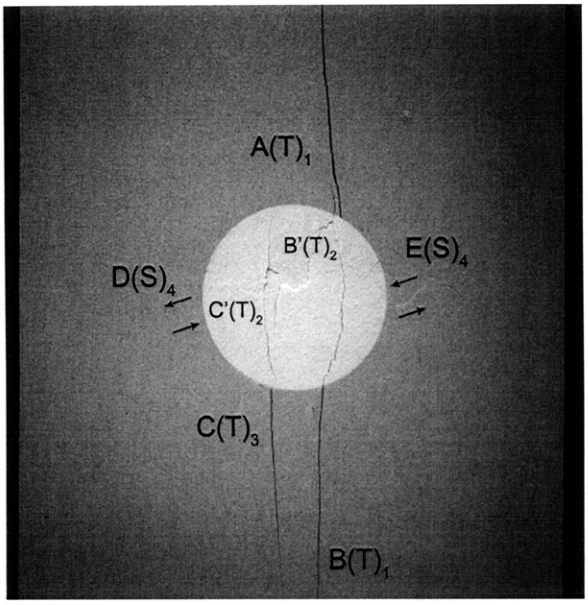

(Recorded by High Speed Video System)

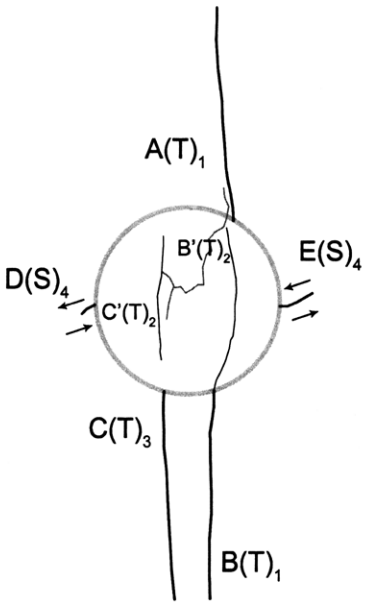

(26.63 MPa)
Time: 5 minutes & 35.45 seconds

Shear cracks (D&E) initiate at the inclusion boundary and propagate away from the inclusion.

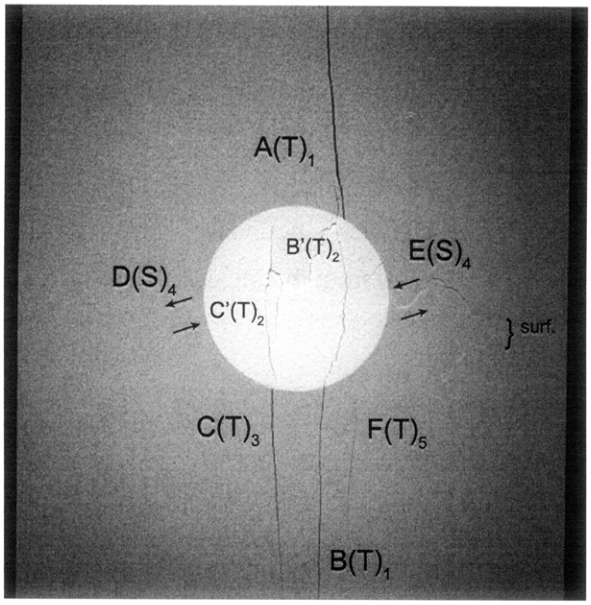

(Recorded by High Speed Video System)

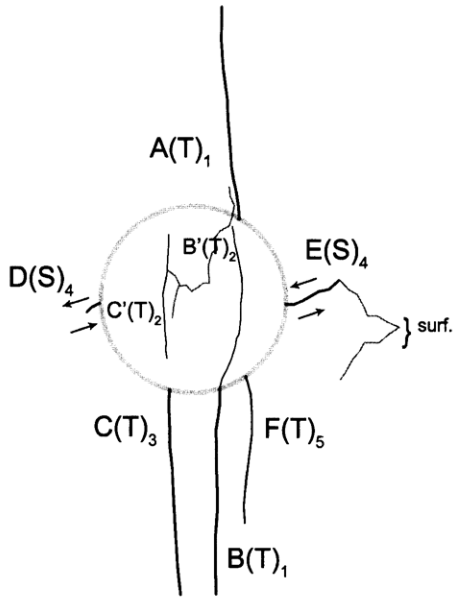

(27.895 MPa) [Max. Stress]
- FAILURE

Time: 5 minutes & 53.346 seconds

HS Image # - 3692

A new tensile crack (F) initiates at the lower inclusion boundary and propagates downwards.

A surface crack (surf.) initiates at shear crack (E).

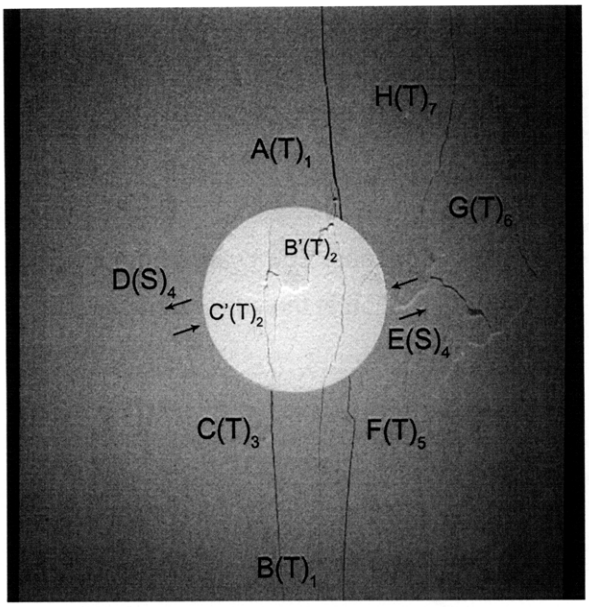

(Recorded by High Speed Video System)

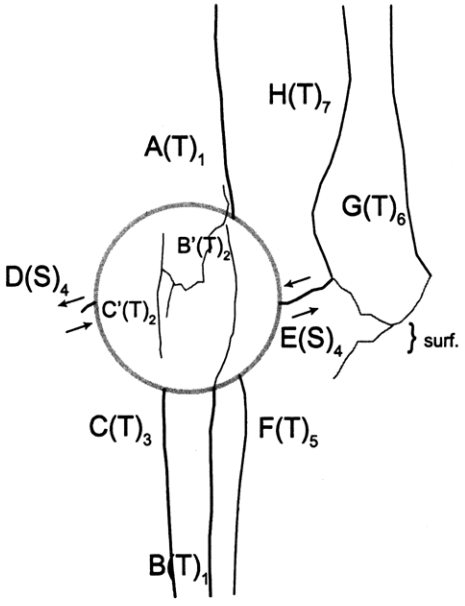

(27.25 MPa)
Time: 5 minutes & 53.682 seconds
HS Image # - 3144

Tensile crack (G) initiates at surface crack (surf.) and propagates towards the upper specimen boundary.

Tensile crack (H) then initiates at the upper specimen boundary and propagates until its coalescence with shear crack (E).

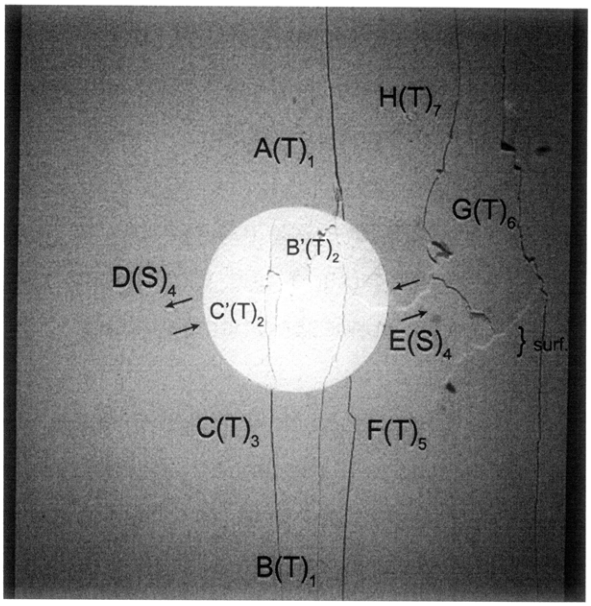

(Recorded by High Speed Video System)

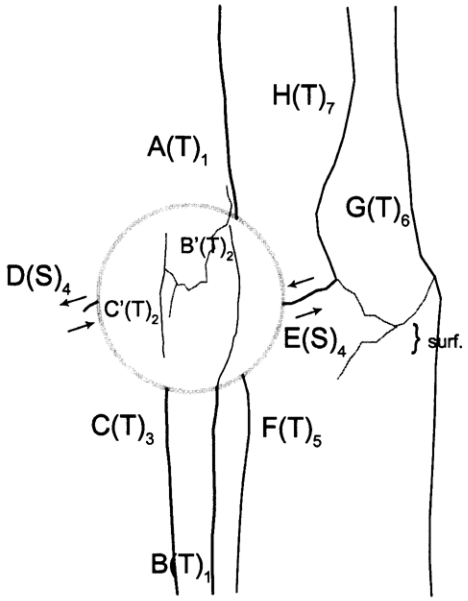

(25.43 MPa)
Time: 5 minutes & 53.712 seconds
HS Image # - 2994

Tensile crack (G) begins to also propagate downwards from its point of initiation at the surface crack (surf.).

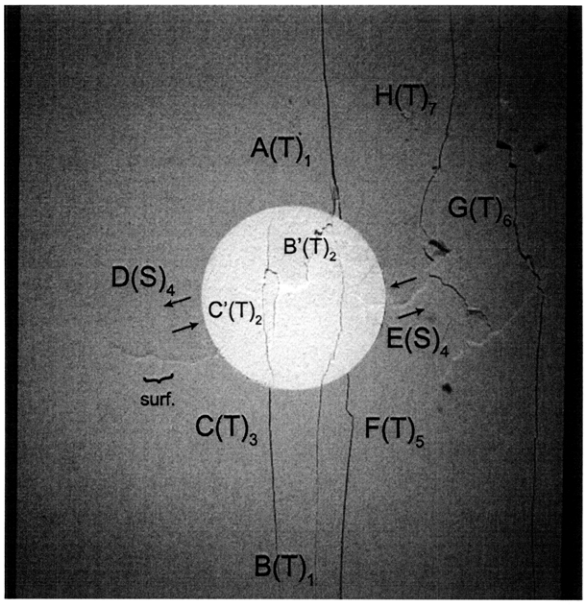

(Recorded by High Speed Video System)

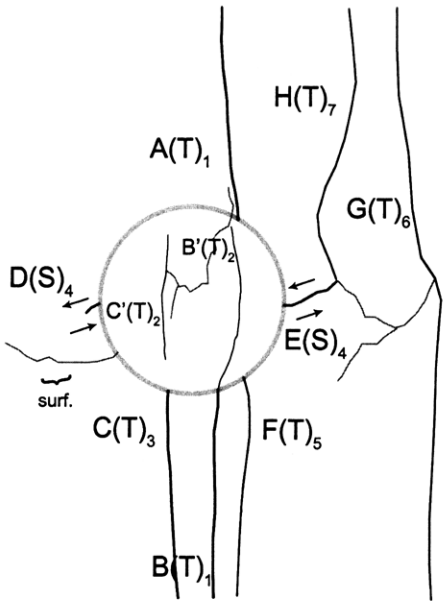

(25.43 MPa)
Time: 5 minutes & 53.724 seconds
HS Image # - 2934

A new surface crack (surf.) initiates at the left-hand inclusion boundary and propagates towards the left-hand specimen boundary.

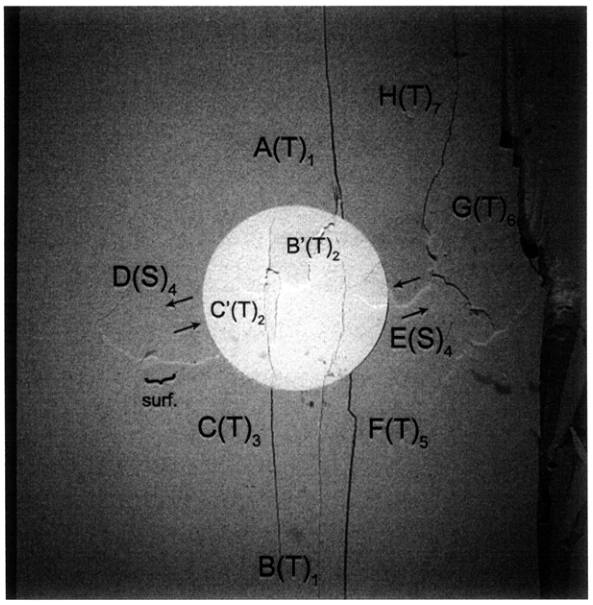

(Recorded by High Speed Video System)

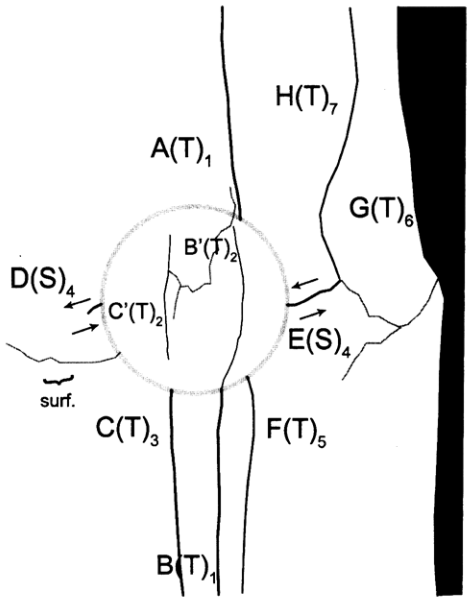

Time: 5 minutes & 53.788 seconds
HS Image # - 2612

The propagation of tensile crack (G) results in the detachment of a large specimen piece at the right-hand specimen boundary post failure.

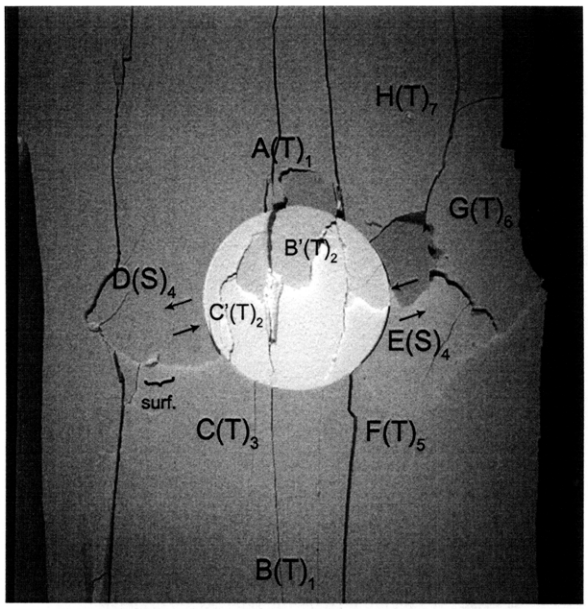

(Recorded by High Speed Video System)

(0 MPa) – Final Picture

Time: 5 minutes & 54.179 seconds

HS Image # - 661

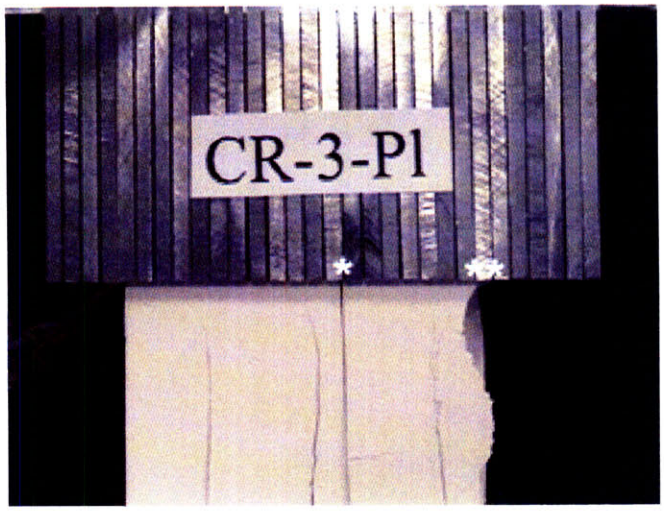	Upper edge of the specimen. The cracks marked with a (*) coincide with the openings between the teeth of the brush platen.
	Lower edge of the specimen. The cracks marked with a (*) coincide with the openings between the teeth of the brush platen.

SUMMARY

Specimen Number: CR-4-UI (20080601)

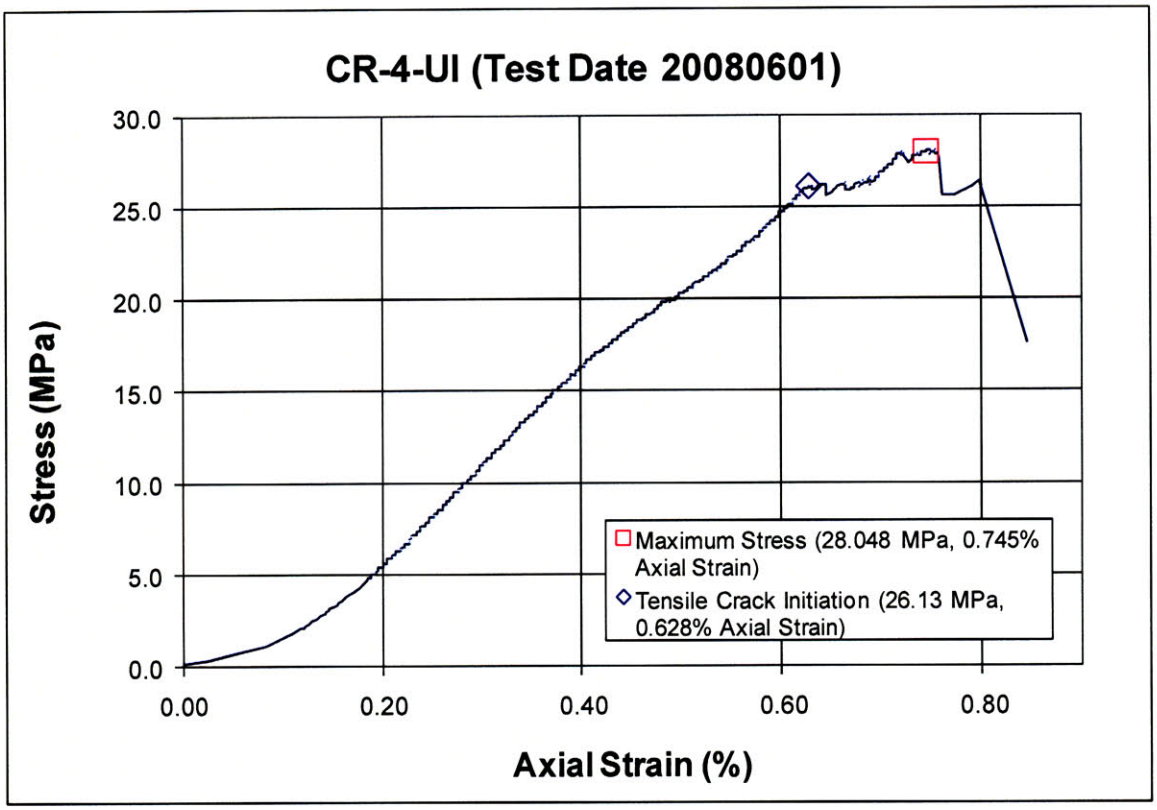

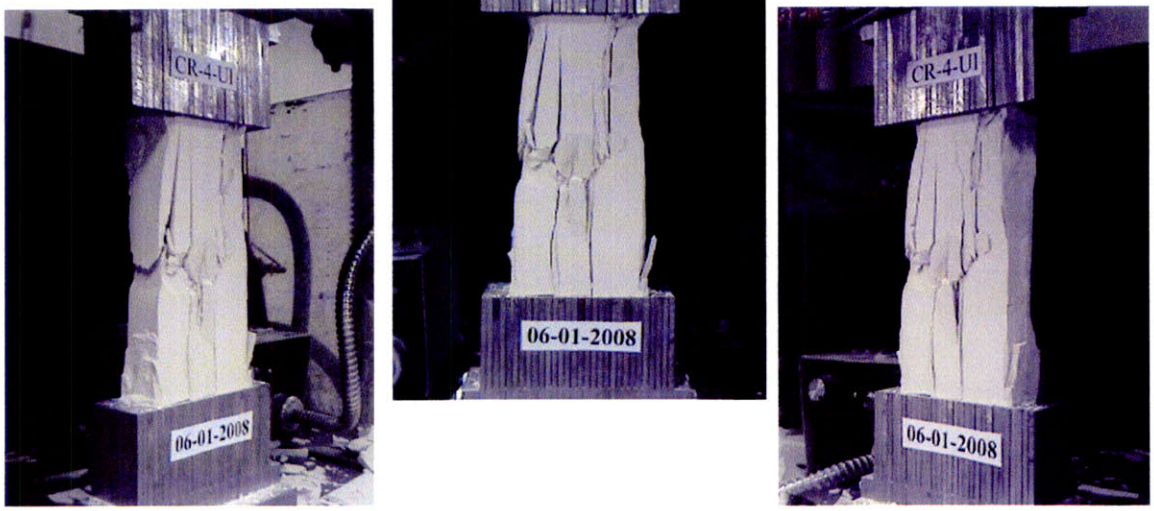

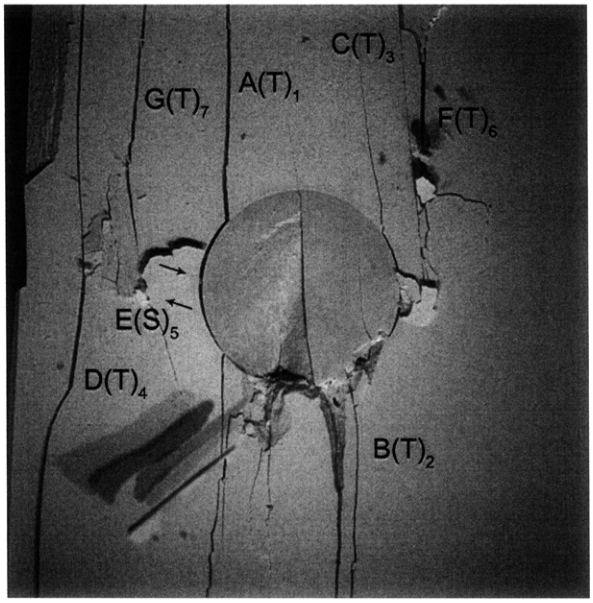

(Recorded by High Speed Video System)

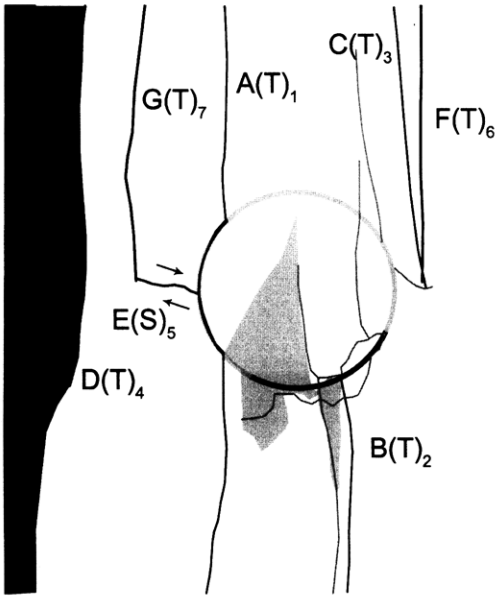

(26.06 MPa)
Time: 5 minutes & 55.159 seconds
HS Image # - 2158

Tensile crack (D) propagates until its coalescence with the lower specimen boundary, which results in the detachment of a large specimen piece.

SUMMARY

Specimen Number: CR-5-UI (20080601)

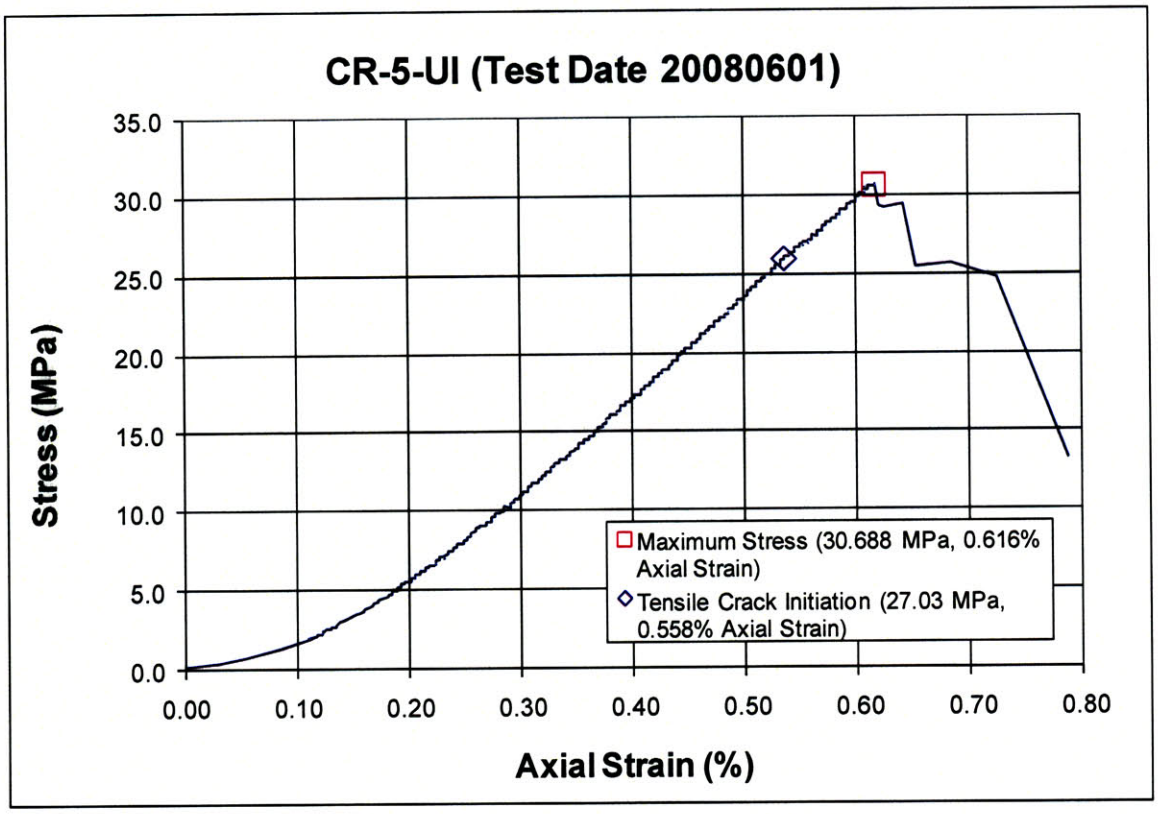

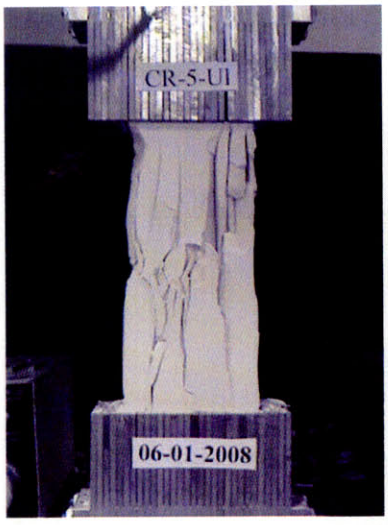

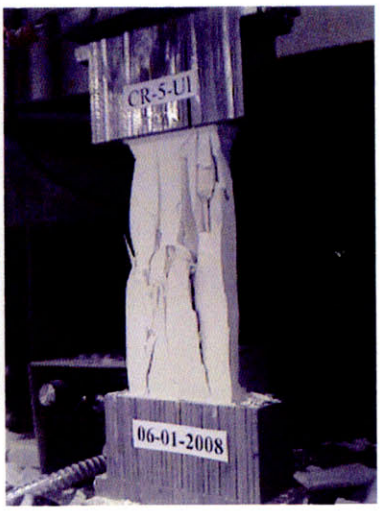

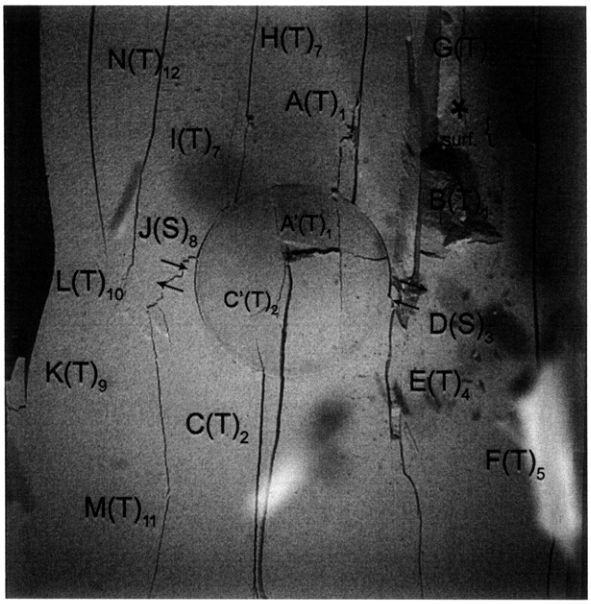

(Recorded by High Speed Video System)

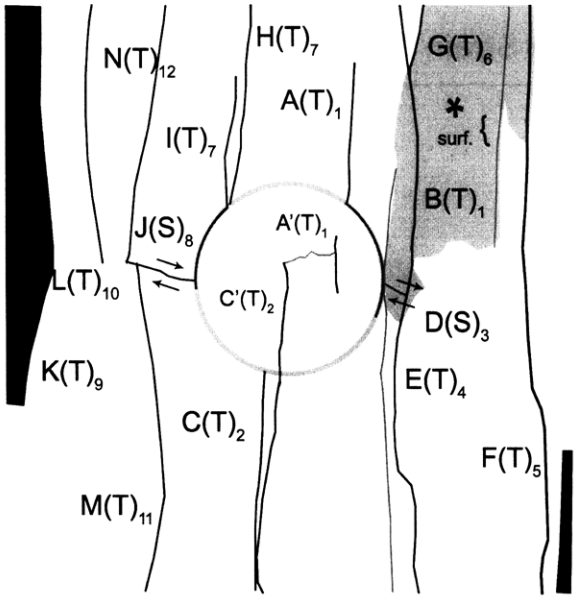

(20.87 MPa)
Time: 6 minutes & 35.022 seconds
HS Image # - 2441

Tensile crack (L) initiates at the upper specimen boundary and propagates downwards.

As shear crack (J) continues to propagate towards the left-hand specimen boundary, tensile crack (M) initiates at shear crack (J) and propagates downwards.

Tensile crack (N) then initiates at shear crack (J) and propagates upwards.

Specimen Number: CR-6-UI (20080601)

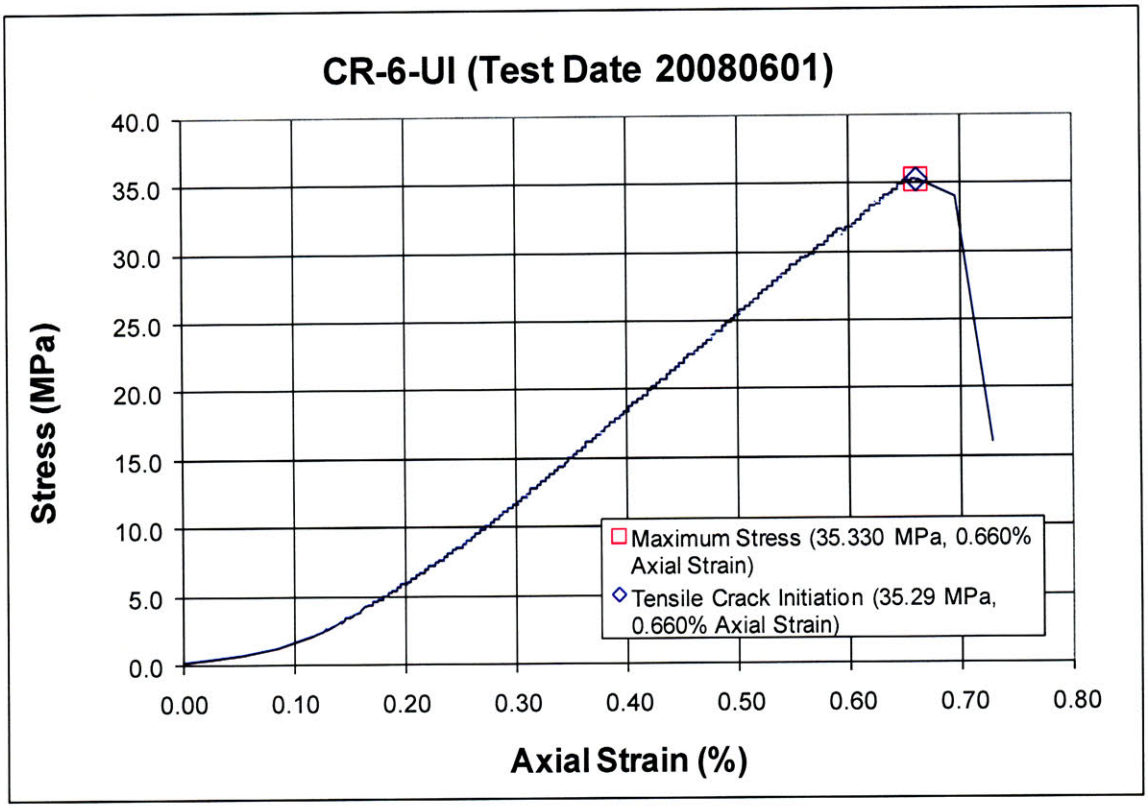

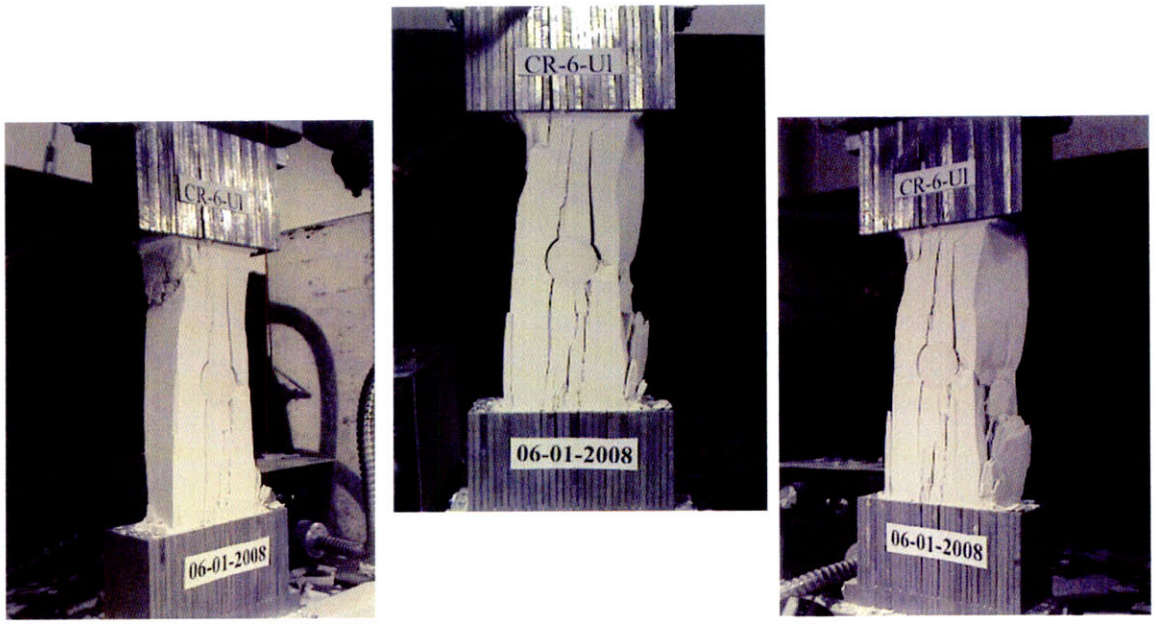

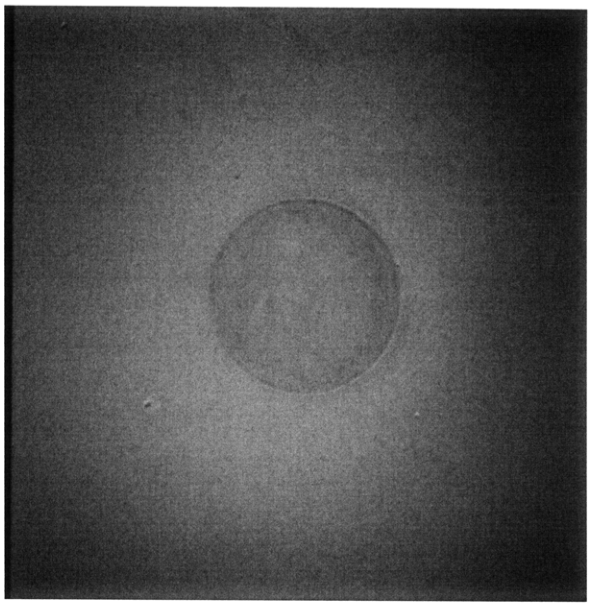

(Recorded by High Speed Video System)

Initial Inclusion Geometry:
CIRCLE – Ultracal Material

Inclusion **more** stiff than matrix.

High Speed Camera Frame Rate:
5000 pps

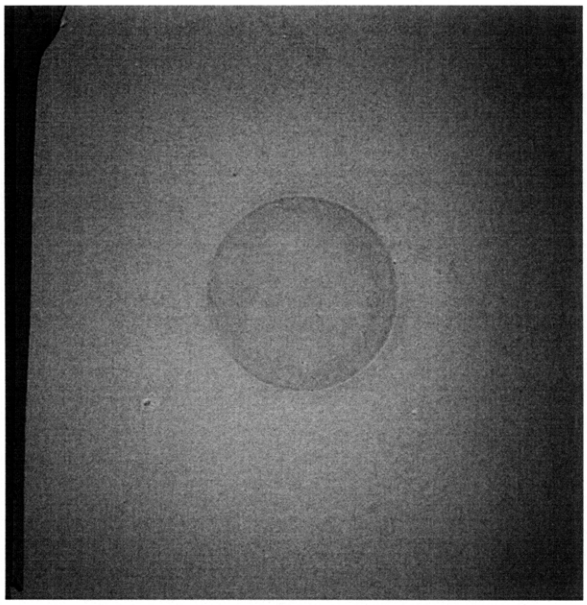

(Recorded by High Speed Video System)

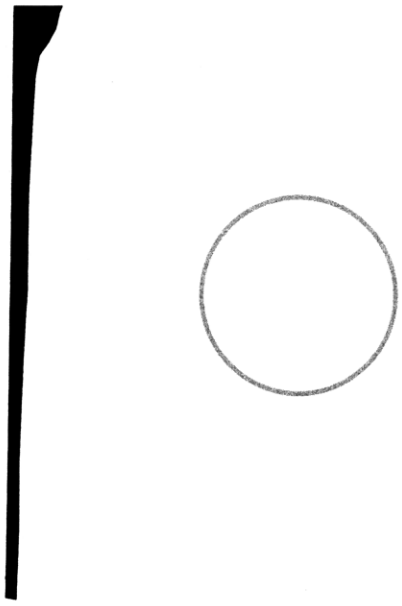

(35.330 MPa) [Max. Stress]
Time: 7 minutes & 36.956 seconds

Prior to tensile crack initiation at the inclusion boundary, a large piece of specimen detaches from the left-hand specimen boundary.

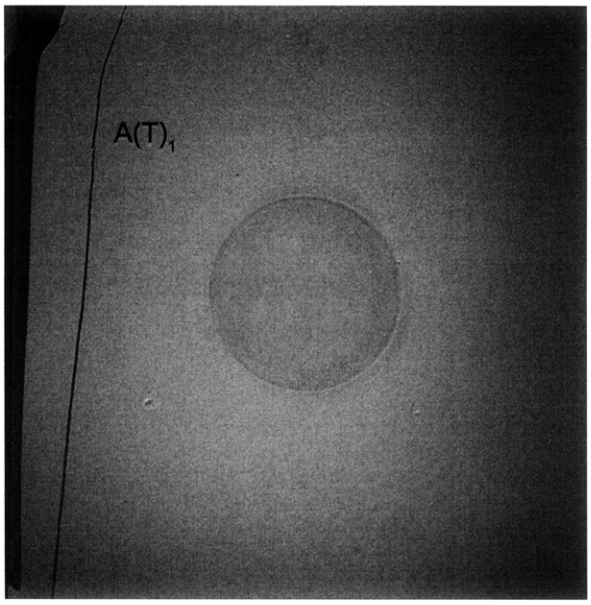

(Recorded by High Speed Video System)

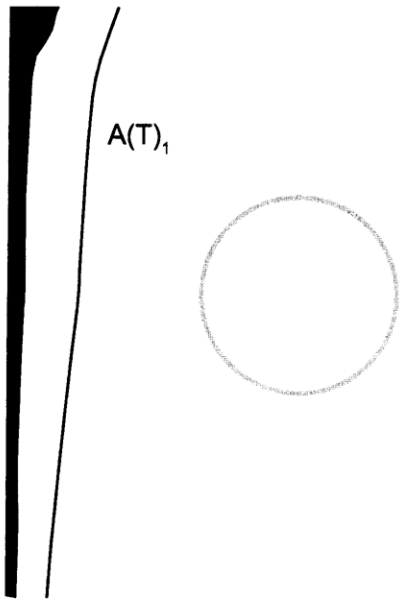

(35.29 MPa)
Time: 7 minutes & 37.190 seconds
HS Image # - 2464

Tensile crack (A) initiates at the upper specimen boundary and propagates down towards the lower specimen boundary.

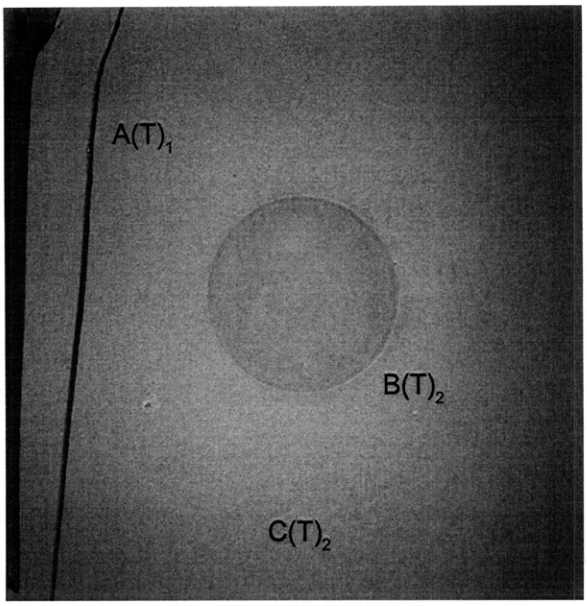

(Recorded by High Speed Video System)

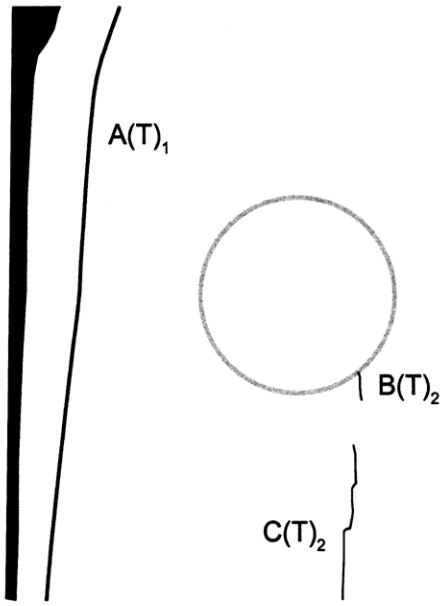

(35.29 MPa)

- Tensile Crack Initiation

Time: 7 minutes & 37.190 seconds

HS Image # - 2463

Tensile crack (B) initiates at the lower inclusion boundary and propagates downwards.

Tensile crack (C) initiates at the lower specimen boundary and propagates towards the inclusion.

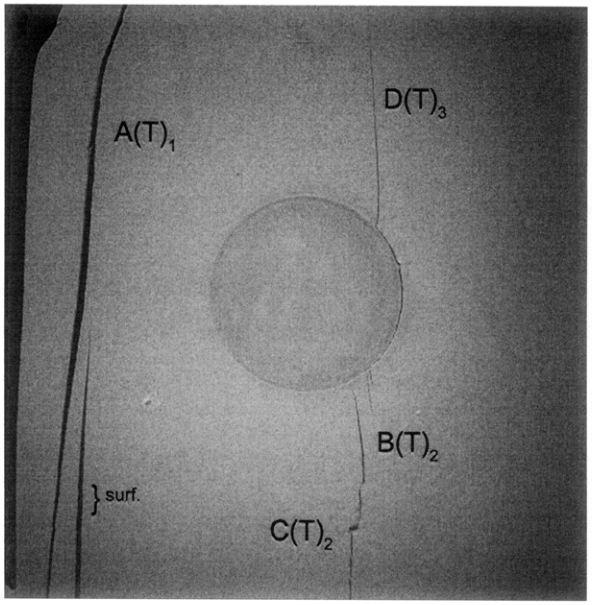

(Recorded by High Speed Video System)

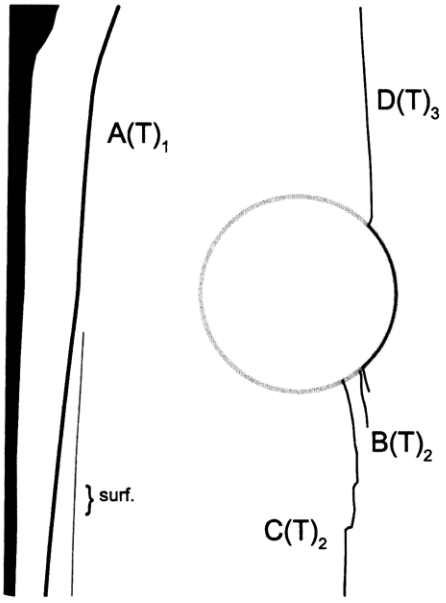

(35.28 MPa)
Time: 7 minutes & 37.191 seconds
HS Image # - 2462

Tensile crack (D) initiates at the upper inclusion boundary and propagates towards the upper specimen boundary. It also begins to propagate around the right-hand inclusion boundary and into the surrounding matrix, adjacent to tensile crack (B).

A surface crack (surf.) initiates at the lower specimen boundary and propagates adjacent to tensile crack (A).

Tensile crack (C) coalesces with the lower inclusion boundary.

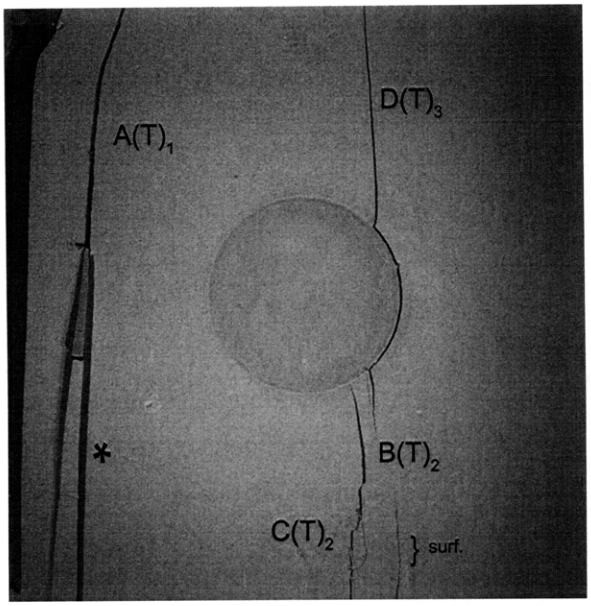

(Recorded by High Speed Video System)

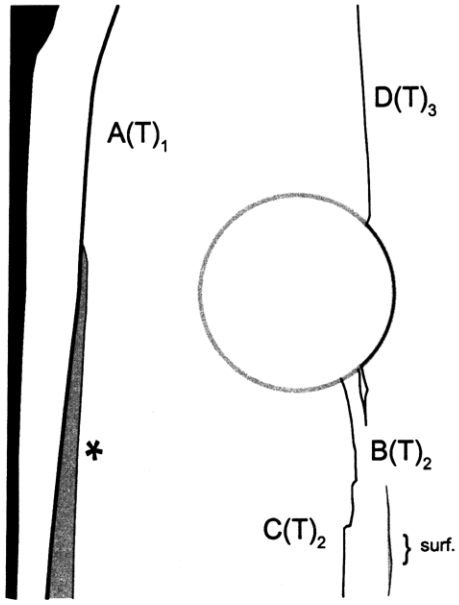

(35.26 MPa)
Time: 7 minutes & 37.191 seconds
HS Image # - 2459

The previously initiated surface crack (*) coalesces with tensile crack (A), which results in surficial detachment from the specimen.

Tensile crack (D) coalesces with tensile crack (B) just below the inclusion boundary.

A new surface crack (surf.) initiates at the lower specimen boundary and propagates upwards.

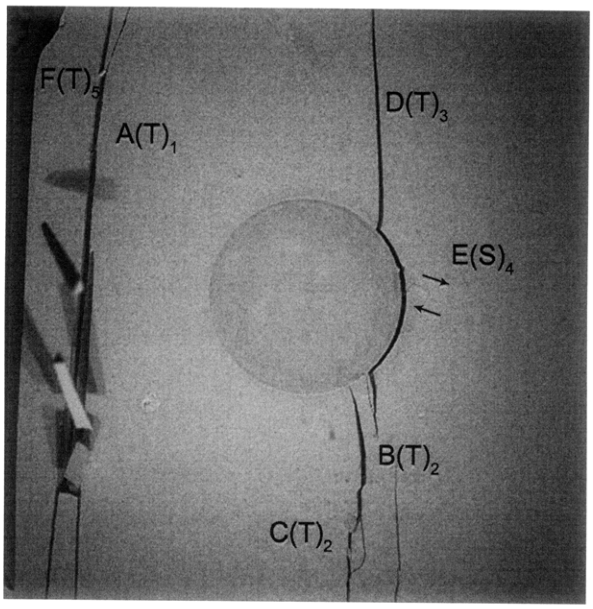

(Recorded by High Speed Video System)

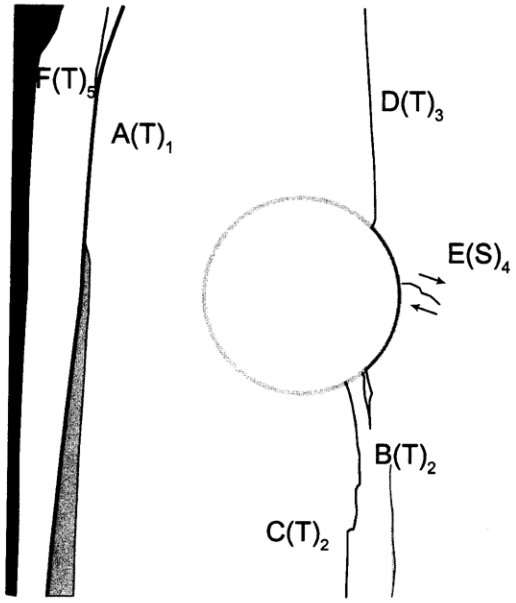

(35.09 MPa)
Time: 7 minutes & 37.196 seconds
HS Image # - 2434

Shear crack (E) initiates at the right-hand inclusion boundary and propagates away from the inclusion.

A new tensile crack (F) initiates at the upper specimen boundary and propagates until its coalescence with tensile crack (A).

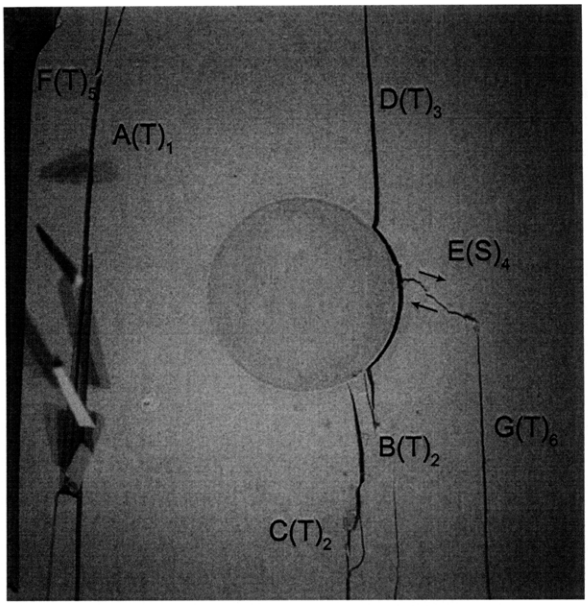

(Recorded by High Speed Video System)

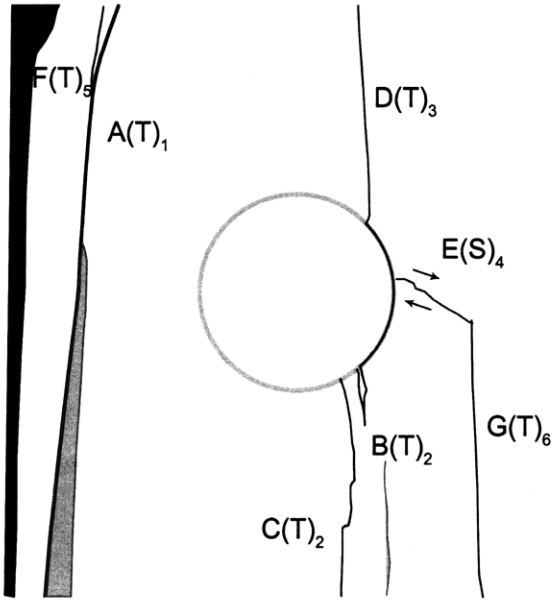

(35.07 MPa)
Time: 7 minutes & 37.197 seconds
HS Image # - 2431

Tensile crack (G) initiates at the lower specimen boundary and propagates until its coalescence with shear crack (E).

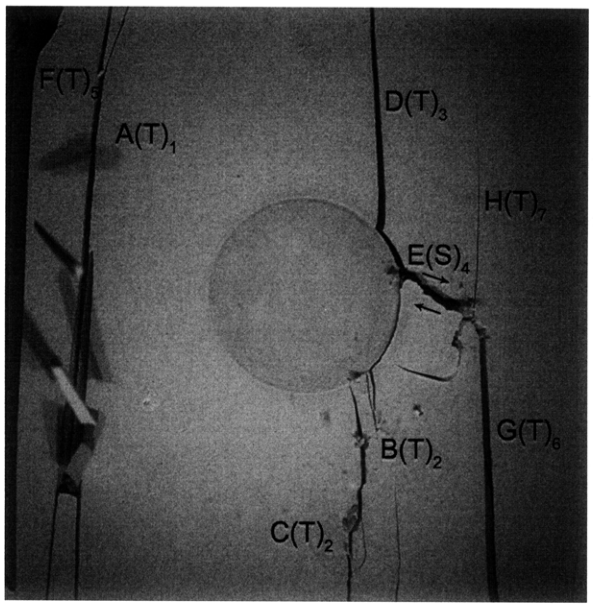

(Recorded by High Speed Video System)

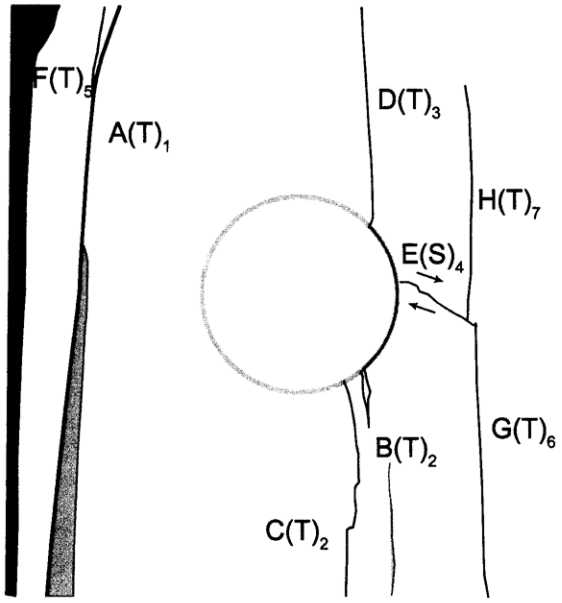

(35.06 MPa)
Time: 7 minutes & 37.197 seconds
HS Image # - 2429

Tensile crack (H) initiates at shear crack (E) and propagates upwards.

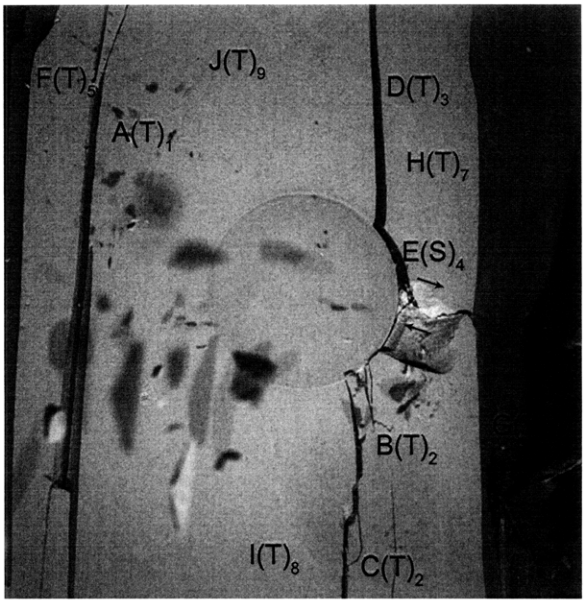

(Recorded by High Speed Video System)

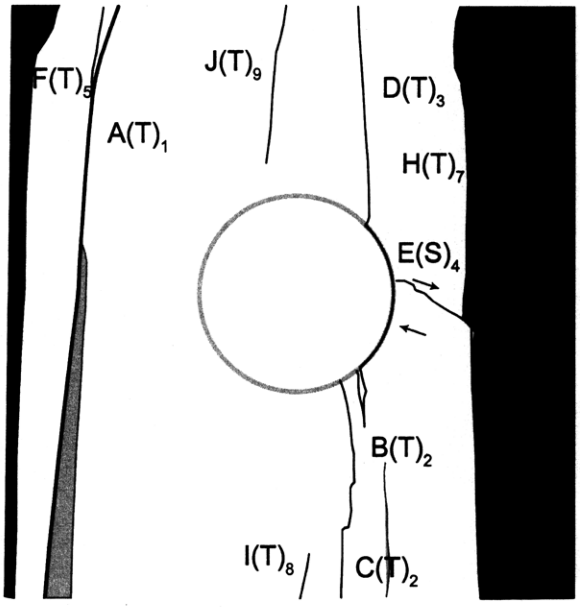

(- MPa)
Time: 7 minutes & 37.328 seconds
HS Image # - 1775

The propagation of tensile crack (H) results in the detachment of a large specimen piece at the right-hand specimen boundary.

A new tensile crack (I) initiates at the lower specimen boundary and propagates upwards.

Tensile crack (J) then initiates at the upper specimen boundary and propagates towards the inclusion.

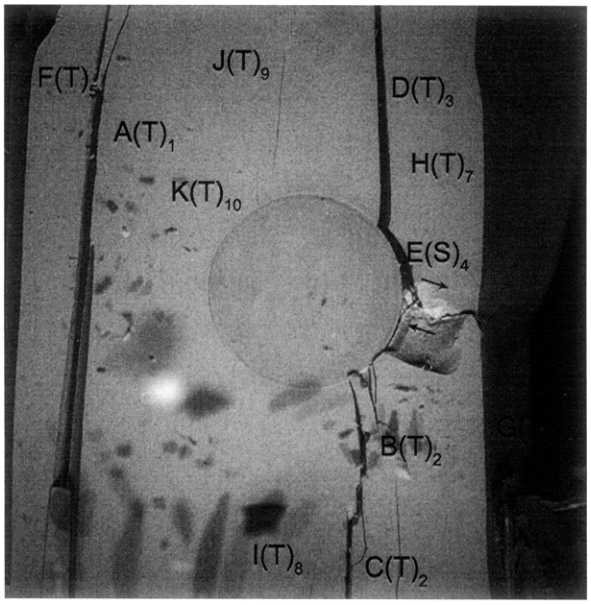

(Recorded by High Speed Video System)

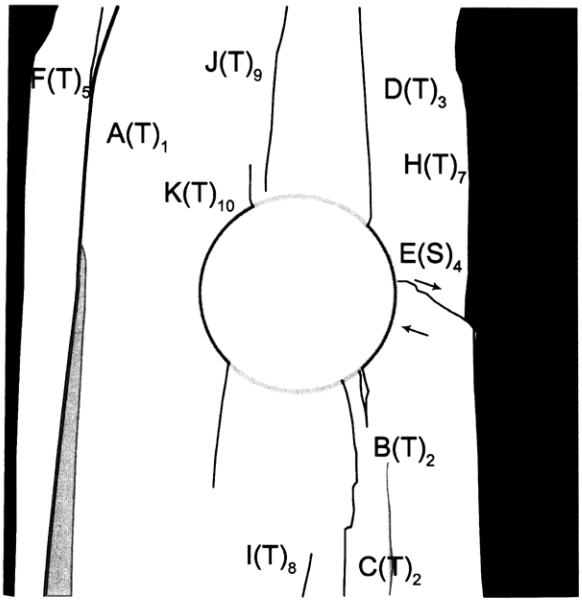

(- MPa)
Time: 7 minutes & 37.342 seconds
HS Image # - 1703

Tensile crack (K) initiates at the upper inclusion boundary and propagates upwards. It also begins to propagate around the left-hand inclusion boundary and into the surrounding matrix.

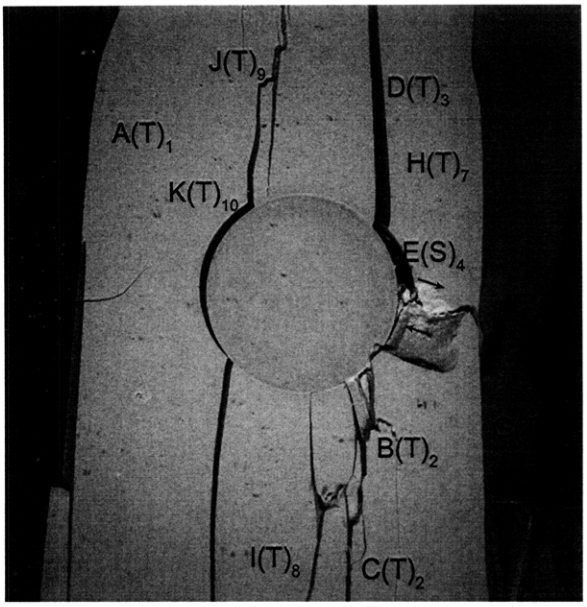

(Recorded by High Speed Video System)

(0 MPa) – Final Picture

Time: 7 minutes & 37.683 seconds

HS Image # - 1

	Upper edge of the specimen. The cracks marked with a (*) coincide with the openings between the teeth of the brush platen.
	Lower edge of the specimen. The cracks marked with a (*) coincide with the openings between the teeth of the brush platen.

SUMMARY

Specimen Number: HX-3-PI (20080412)

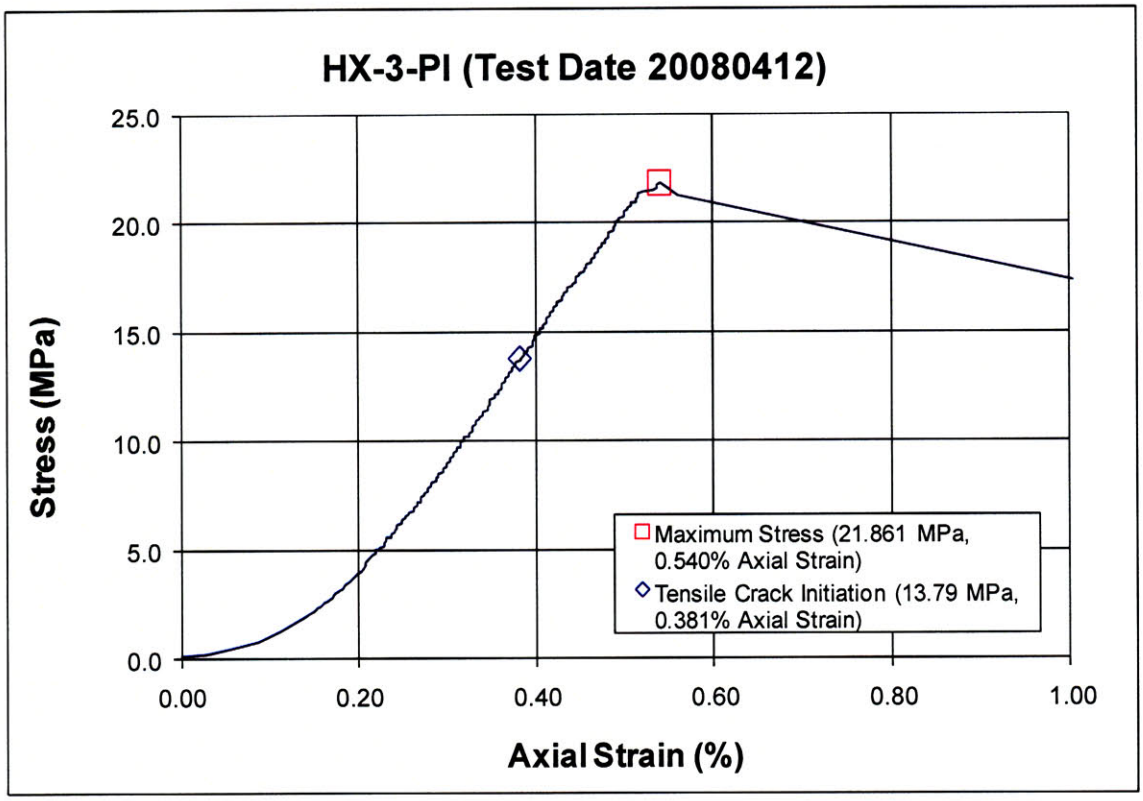

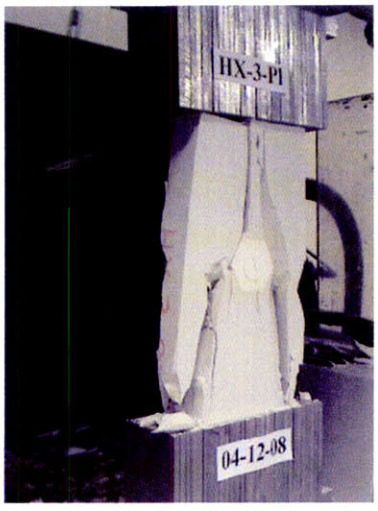

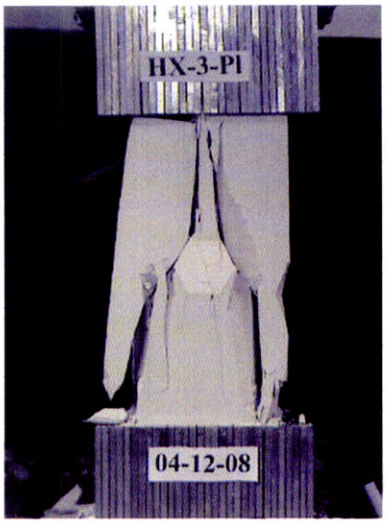

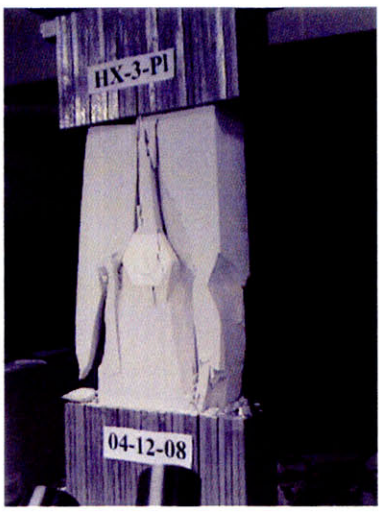

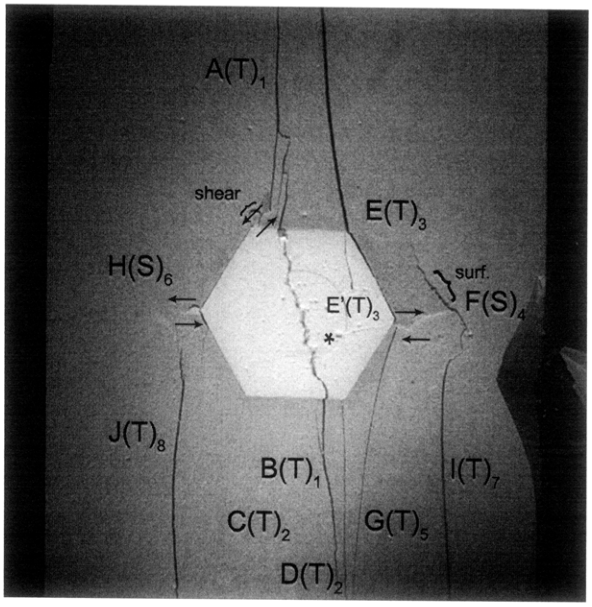

(Recorded by High Speed Video System)

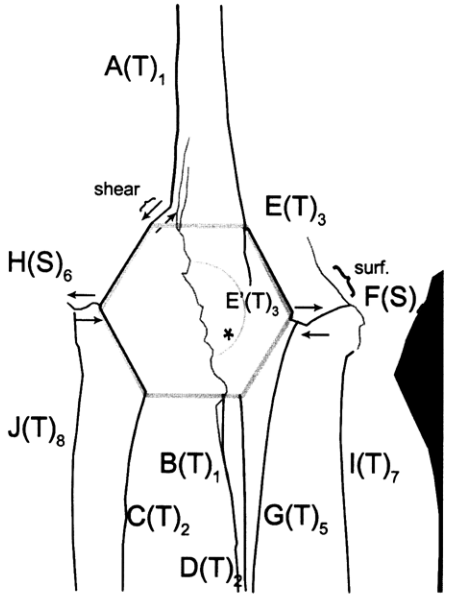

(21.861 MPa)
Time: 4 minutes & 29.001 seconds
HS Image # - 2354

A new tensile crack (J) initiates at the lower specimen boundary and propagates upwards until it coalesces with shear crack (H) post failure.

Specimen Number: HX-4-PI (20080412)

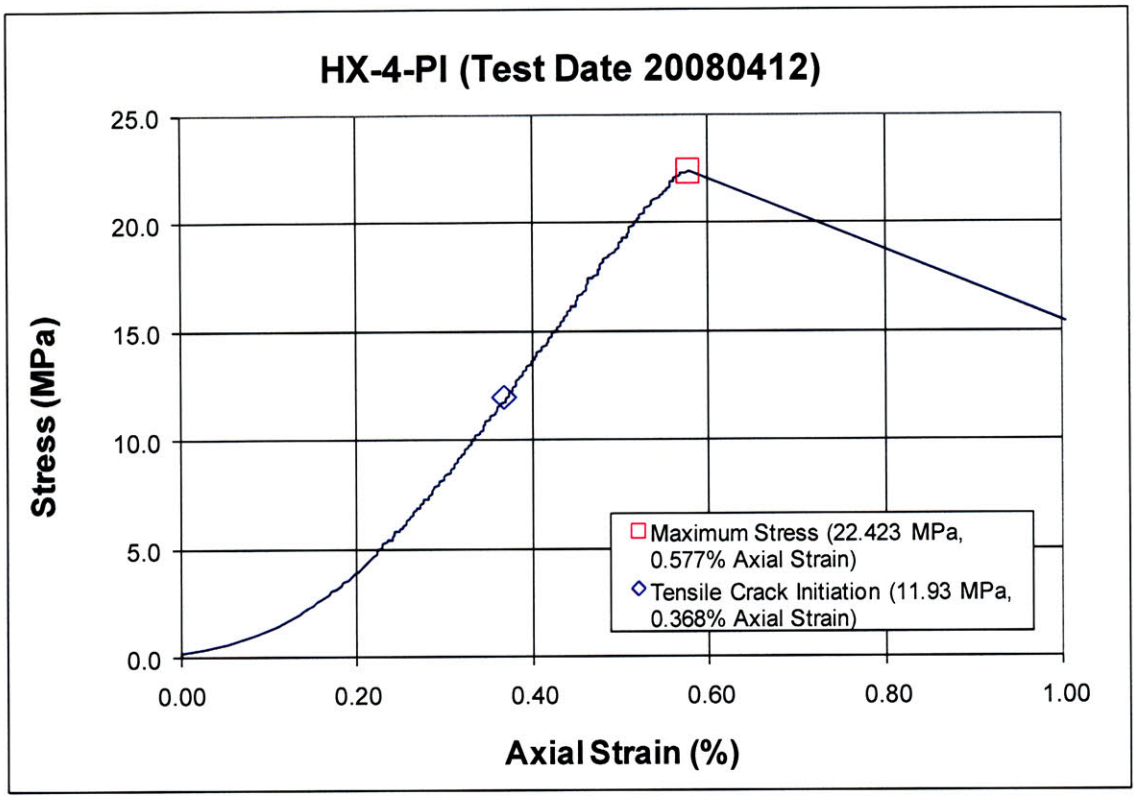

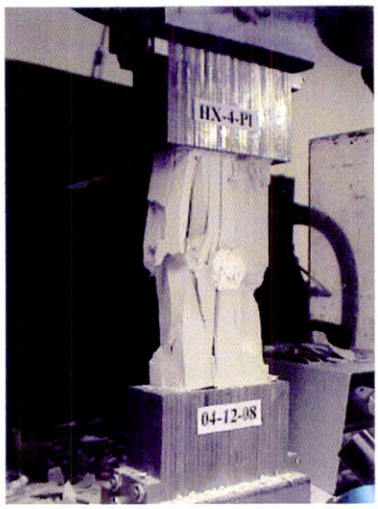

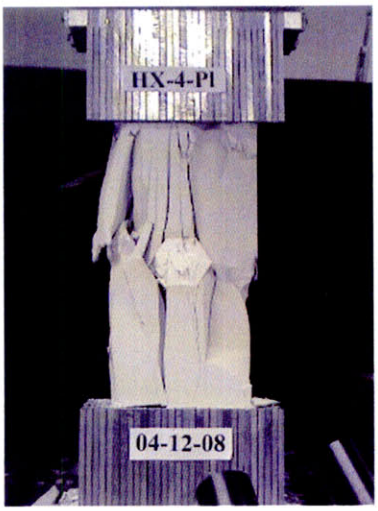

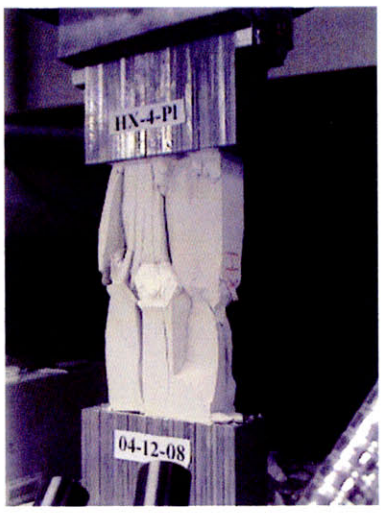

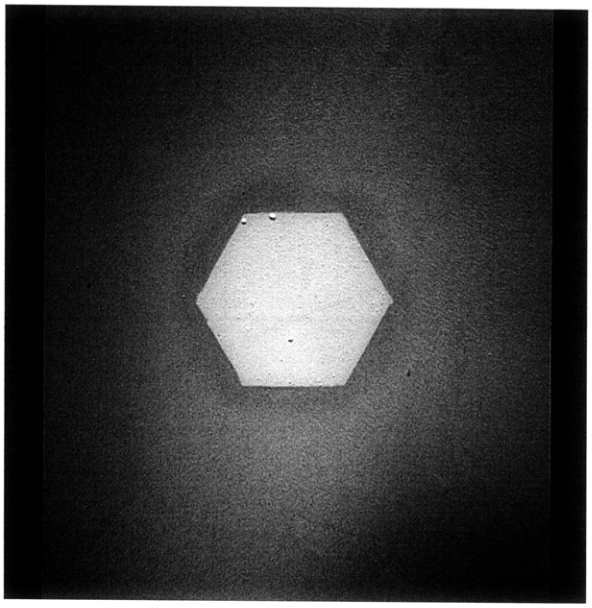

(Recorded by High Speed Video System)

Initial Inclusion Geometry:
HEXAGON – Plaster Material

Inclusion **less** stiff than matrix.

High Speed Camera Frame Rate:
5000 pps

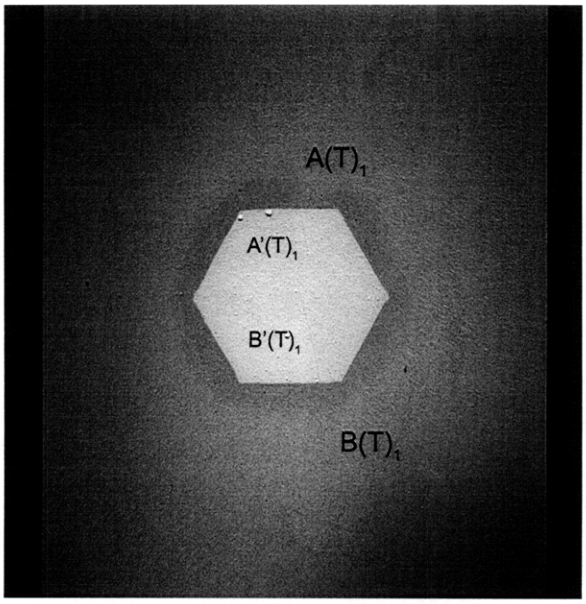

(Recorded by High Speed Video System)

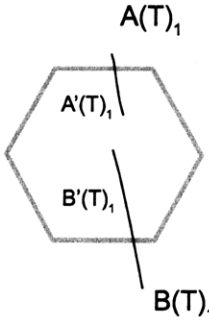

(11.93 MPa)

– Tensile Crack Initiation

Time: 2 minutes & 9 seconds

Tensile cracks (A,A',B&B') develop at the inclusion boundary.

Tensile crack (A) forms at the upper inclusion boundary and propagates away from the inclusion. It is believed that tensile crack (A') propagates into the inclusion just afterwards, though the high speed footage was inconclusive.

Tensile crack (B) forms at the lower inclusion boundary and propagates away from the inclusion. It is also believed that tensile crack (B') propagates into the inclusion just afterwards, though the high speed footage was inconclusive.

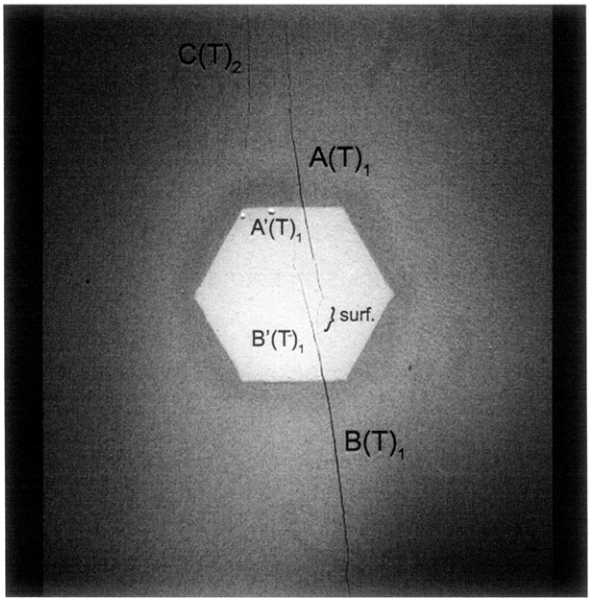

(Recorded by High Speed Video System)

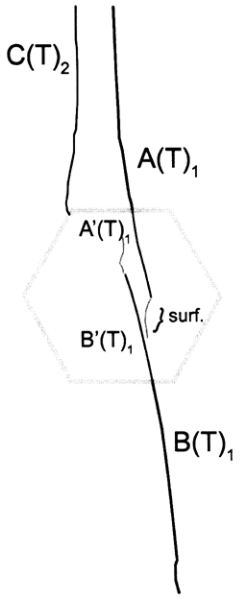

(18.59 MPa)
Time: 3 minutes & 44 seconds

As the apertures of tensile cracks (A,A',B&B') increase, surface cracks (surf.) initiate from the tips of tensile cracks (A'&B') within the inclusion.

A new tensile crack (C) initiates at the upper specimen boundary and propagates downwards until it coalesces with the upper left-hand inclusion boundary.

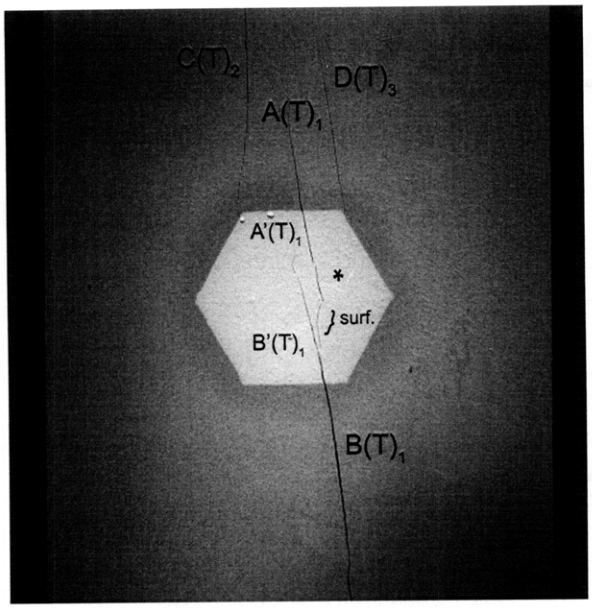

(Recorded by High Speed Video System)

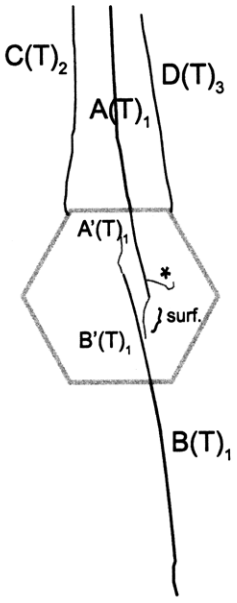

(21.04 MPa)
Time: 4 minutes & 19 seconds

A new surface crack (*) initiates from tensile crack (A') within the inclusion.

A new tensile crack (D) initiates at the upper right-hand inclusion boundary and propagates towards the upper specimen boundary.

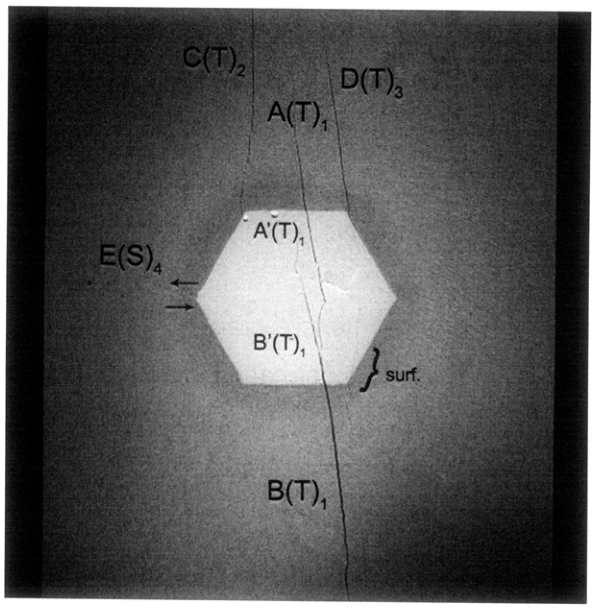

(Recorded by High Speed Video System)

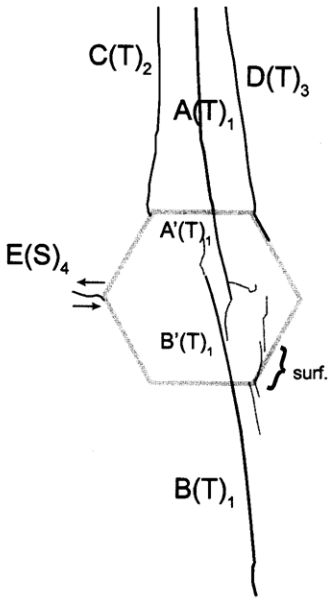

(22.40 MPa)
Time: 4 minutes & 39.620 seconds
HS Image # - 5404

A new shear crack (E) initiates at the left-hand inclusion boundary and propagates towards the left-hand specimen boundary.

New surface cracks (surf.) initiate at the lower right-hand inclusion boundary.

Tensile crack (D) begins to propagate around the right-hand inclusion boundary.

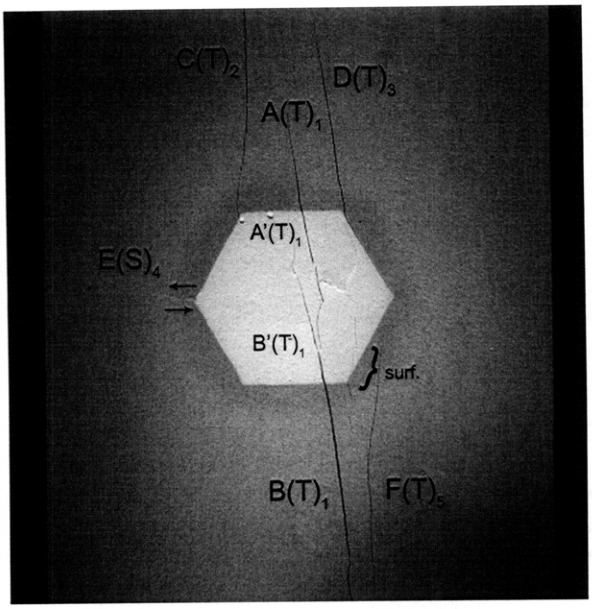

(Recorded by High Speed Video System)

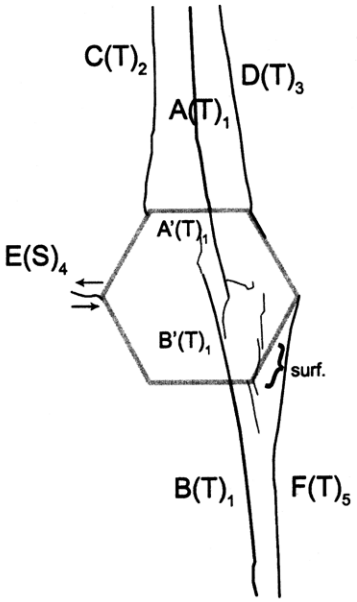

(22.42 MPa)
Time: 4 minutes & 39.999 seconds
HS Image # - 3507

A new tensile crack (F) initiates at the lower specimen boundary and propagates until it intersects the right-hand inclusion boundary.

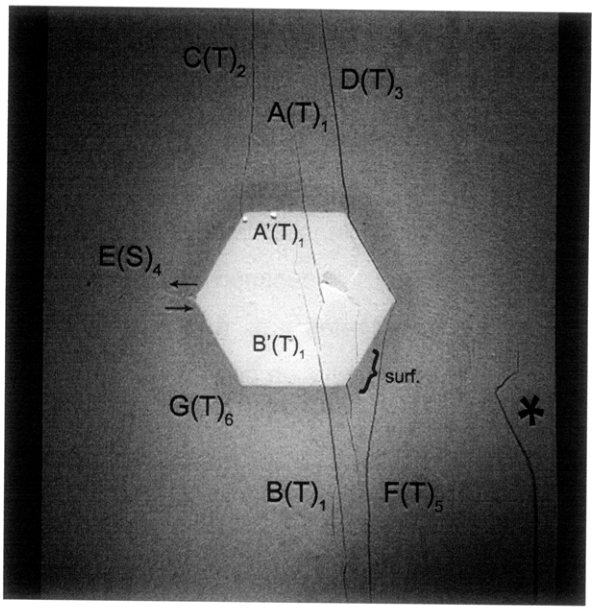

(Recorded by High Speed Video System)

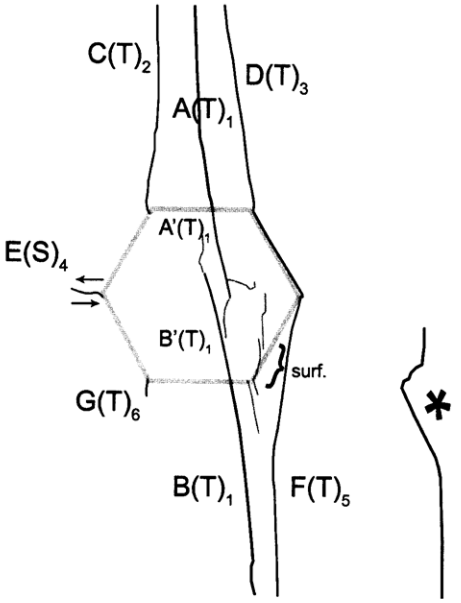

22.423 MPa [Max. Stress] – FAILURE
Time: 4 minutes & 40 seconds
HS Image # - 3505

Tensile crack (D) completely propagates around the right-hand inclusion boundary and coalesces with tensile crack (F).

A large piece of specimen (*) begins to detach from the lower right-hand specimen boundary.

A new tensile crack (G) initiates at the lower left-hand inclusion boundary and propagates downwards.

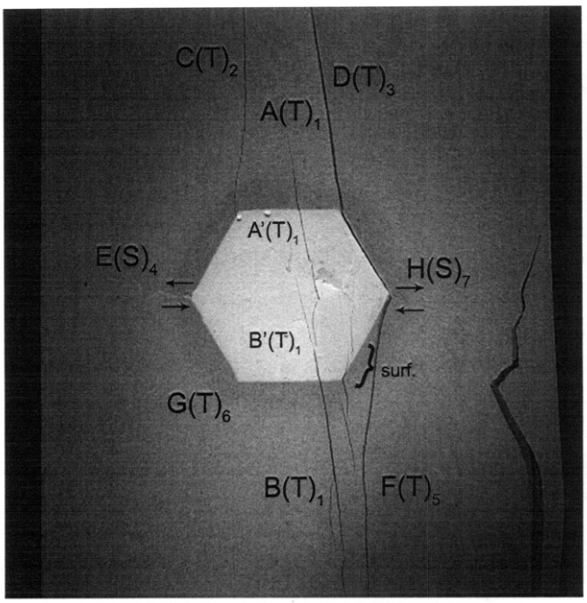

(Recorded by High Speed Video System)

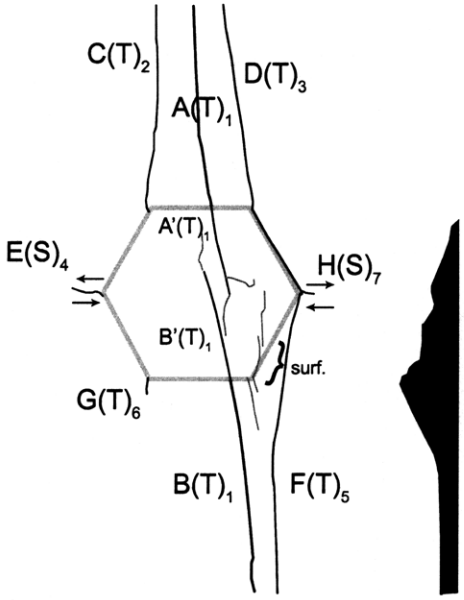

Time: 4 minutes & 40.003 seconds
HS Image # - 3488

The large piece of specimen completely detaches from the right-hand specimen boundary.

As the apertures of tensile cracks (D&F) increase, shear crack (H) initiates at the right-hand inclusion boundary and propagates towards the right-hand specimen boundary.

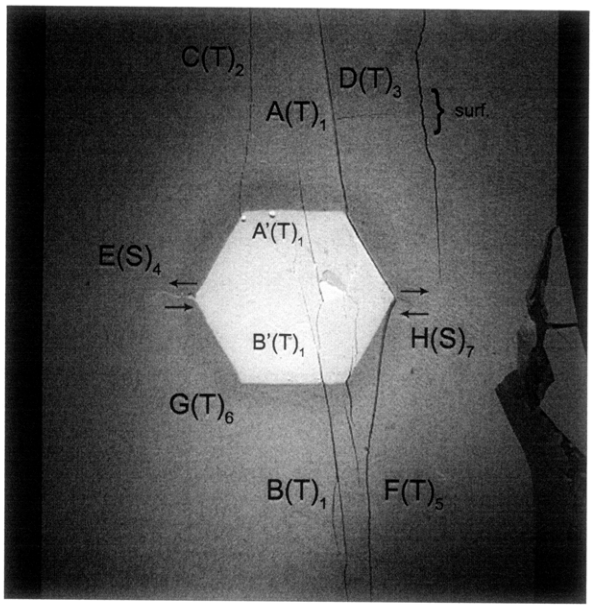

(Recorded by High Speed Video System)

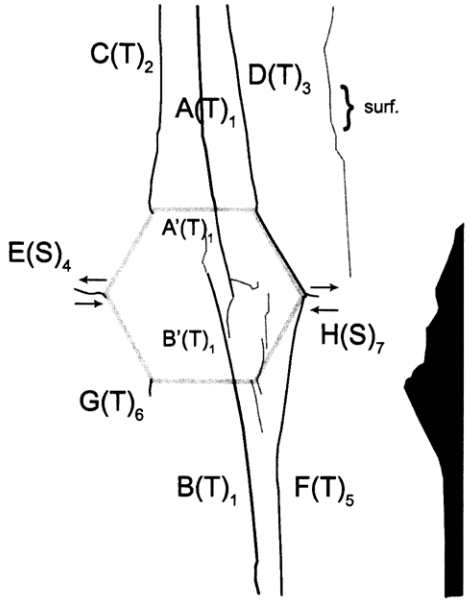

Time: 4 minutes & 40.006 seconds
HS Image # - 3474

A new surface crack (surf.) initiates at the upper specimen boundary and propagates towards shear crack (H).

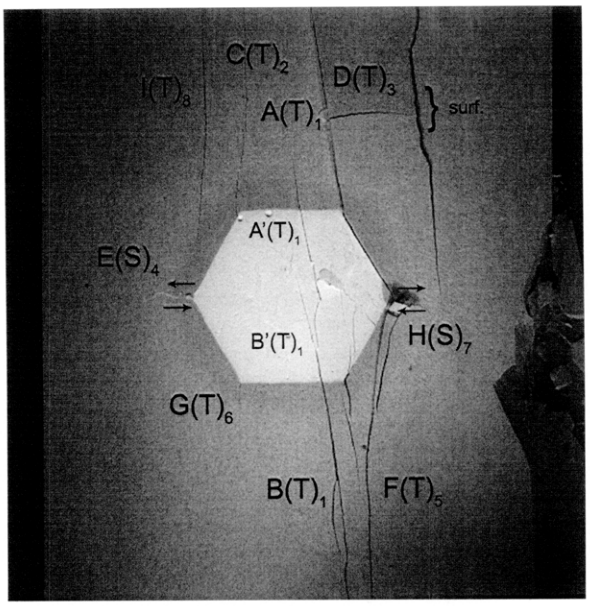

(Recorded by High Speed Video System)

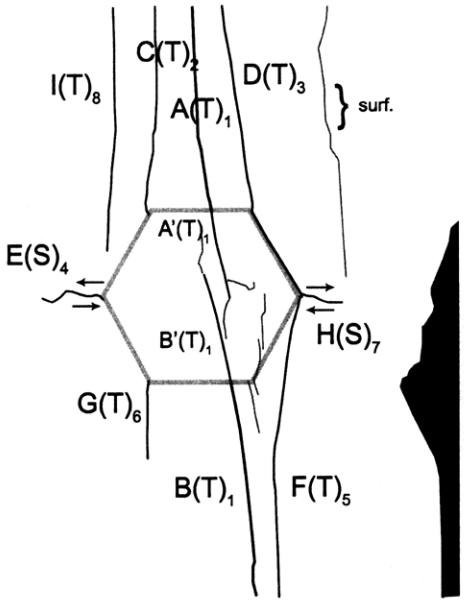

Time: 4 minutes & 40.010 seconds
HS Image # - 3455

A new tensile crack (I) initiates at the upper specimen boundary and propagates towards shear crack (E).

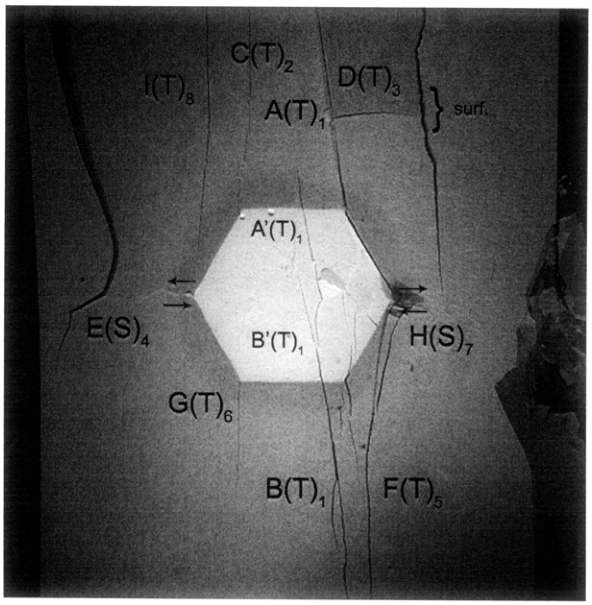

(Recorded by High Speed Video System)

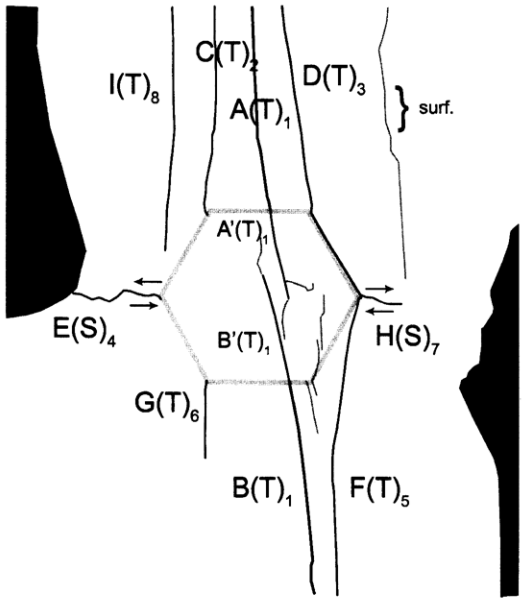

Time: 4 minutes & 40.011 seconds
HS Image # - 3448

A large piece of specimen detaches from the upper left-hand specimen boundary.

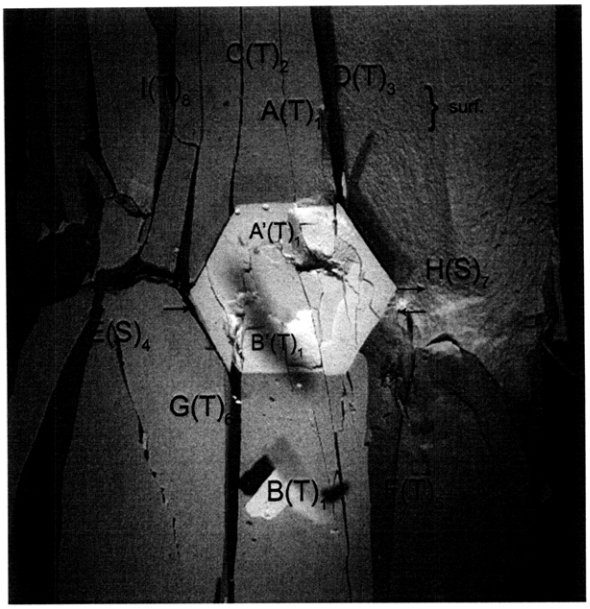

(Recorded by High Speed Video System)

(0 MPa – Final Picture)
HS Image # - 1213

A good view of the propagation of shear crack (H) can be seen in this picture.

	Upper edge of the specimen. The cracks marked with a (*) coincide with the openings between the teeth of the brush platen.
	Lower edge of the specimen. The cracks marked with a (*) coincide with the openings between the teeth of the brush platen.

SUMMARY

Specimen Number: HX-5-PI (20080517)

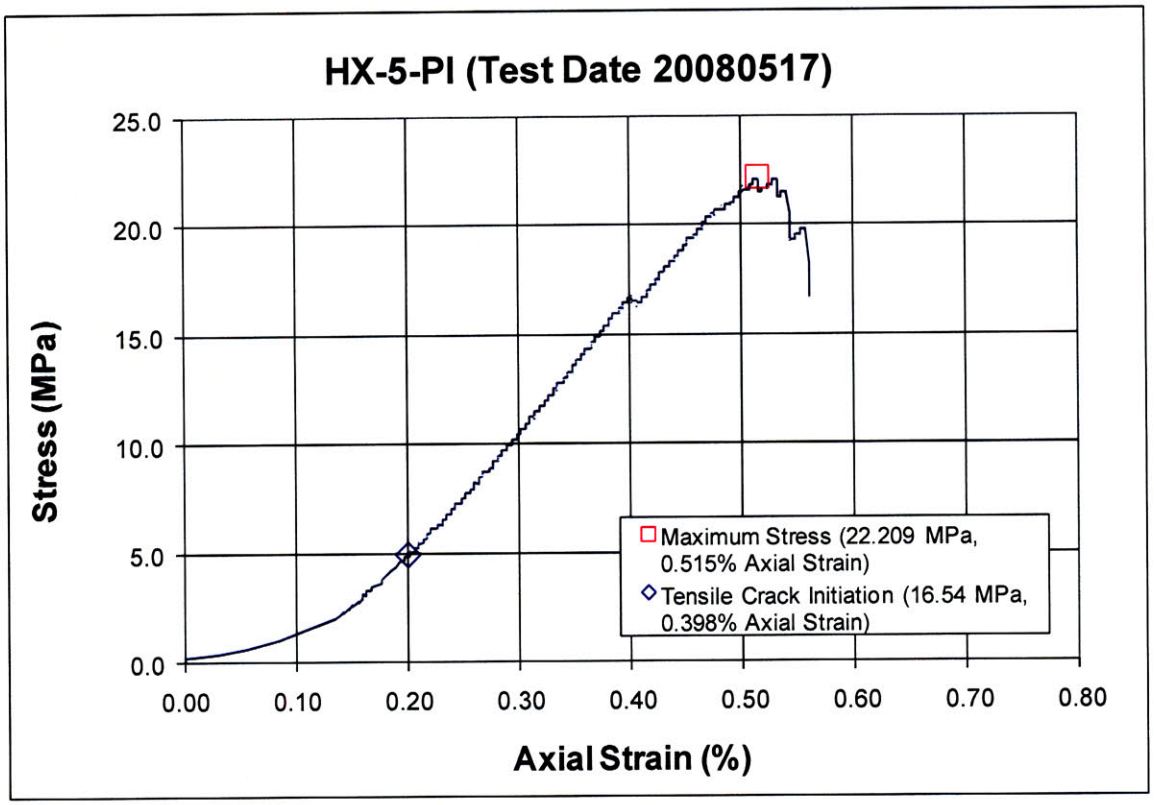

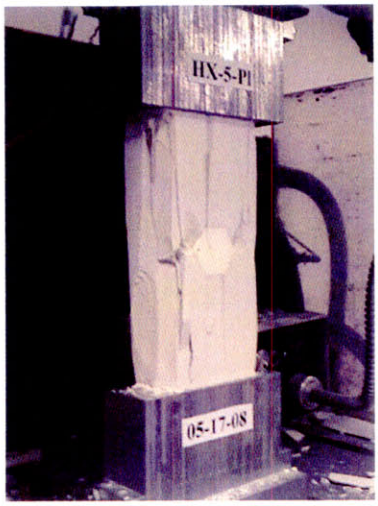

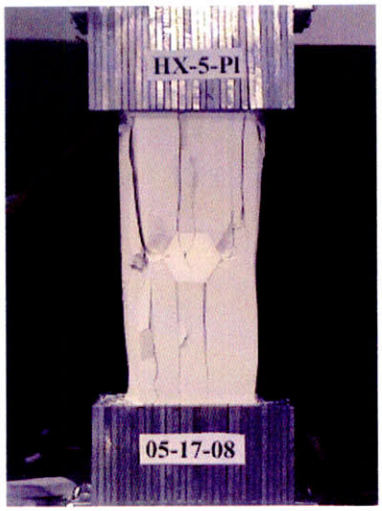

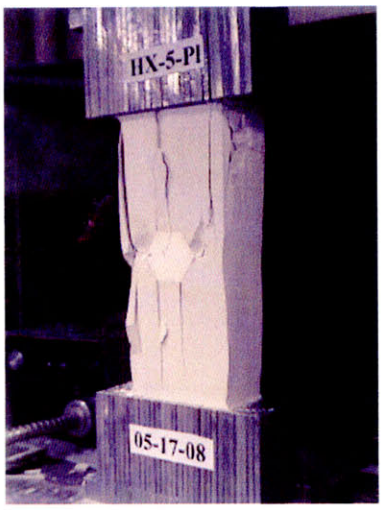

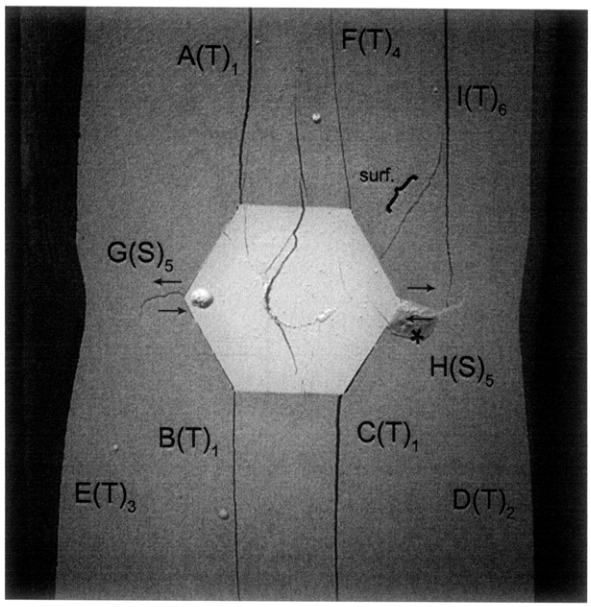

(Recorded by High Speed Video System)

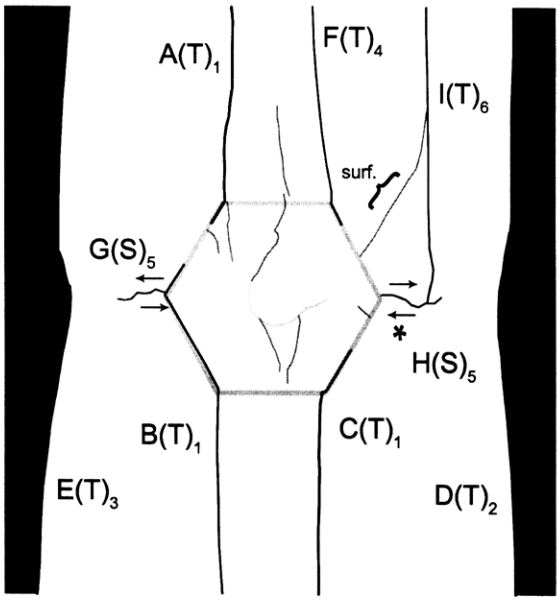

(19.21 MPa) – Post Failure
Time: 8 minutes & 28.1 seconds

A new tensile crack (I) initiates at the upper specimen boundary and propagates until it coalesces with shear crack (H). Surface spalling (*) occurs adjacent to shear crack (H).

A new surface crack (surf.) initiates at the inclusion boundary and coalesces with tensile crack (I).

SUMMARY

Specimen Number: HX-6-UI (20080518)

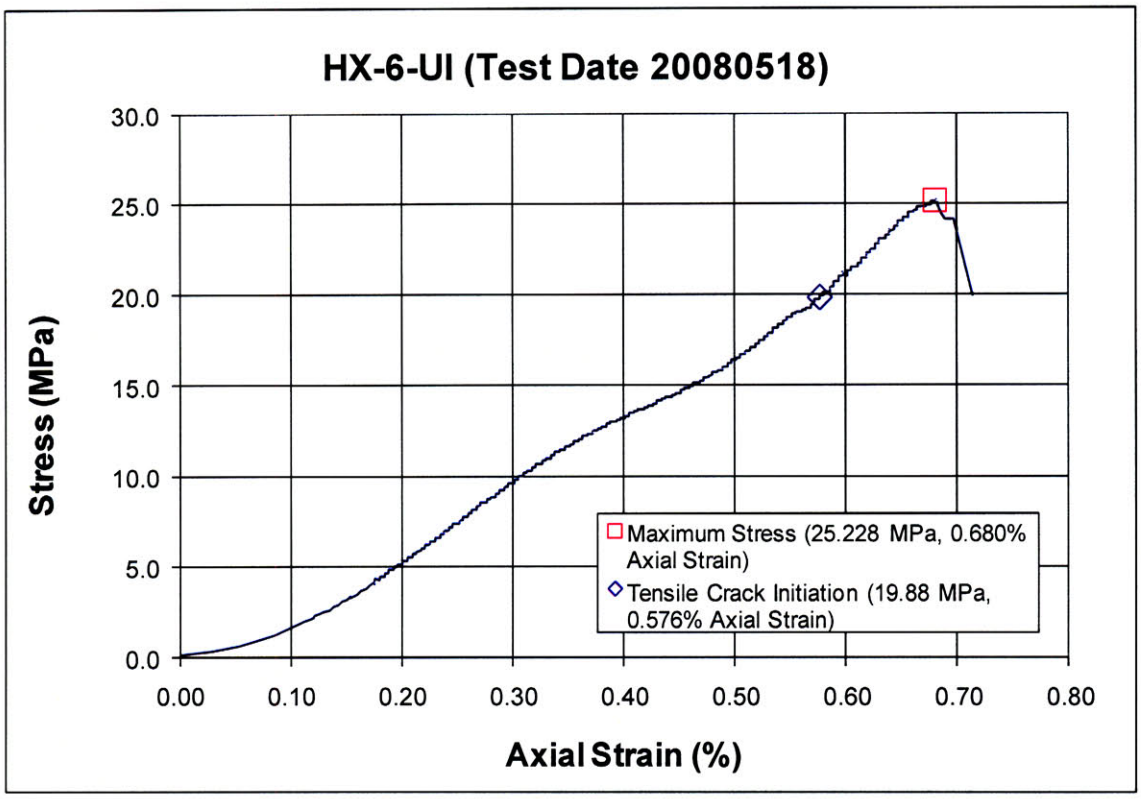

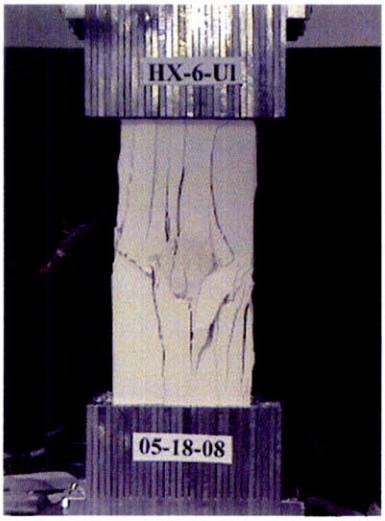

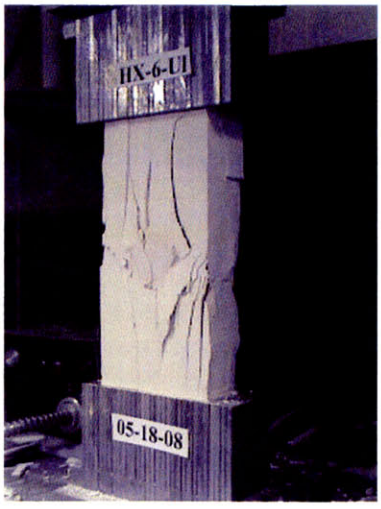

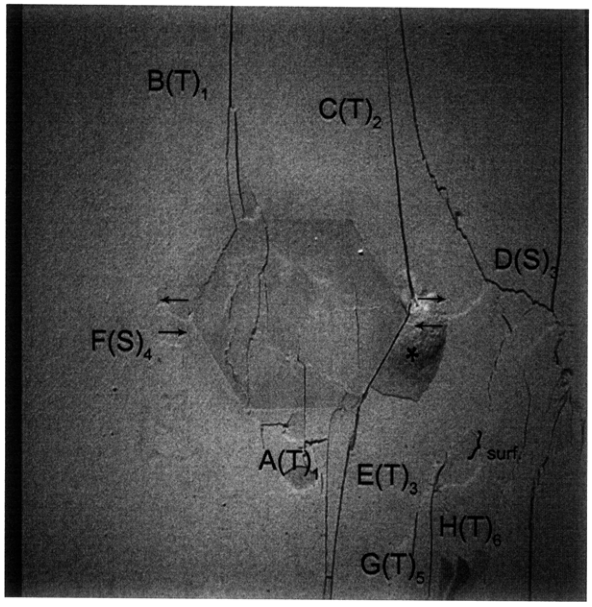

Time: 5 minutes & 16.144 seconds
HS Image # - 3246

Shear crack (D) coalesces with the right-hand specimen boundary.

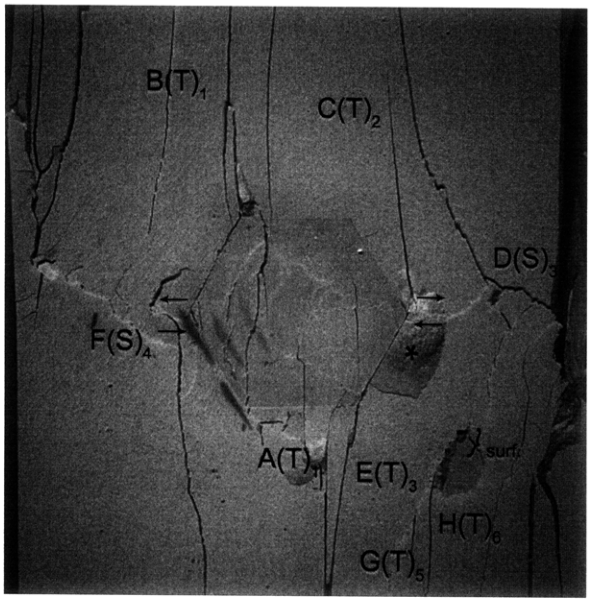

(Recorded by High Speed Video System)

Time: 5 minutes & 16.249 seconds
HS Image # - 2724

Shear crack (F) coalesces with the left-hand specimen boundary.

SUMMARY

Specimen Number: HX-7-UI (20080518)

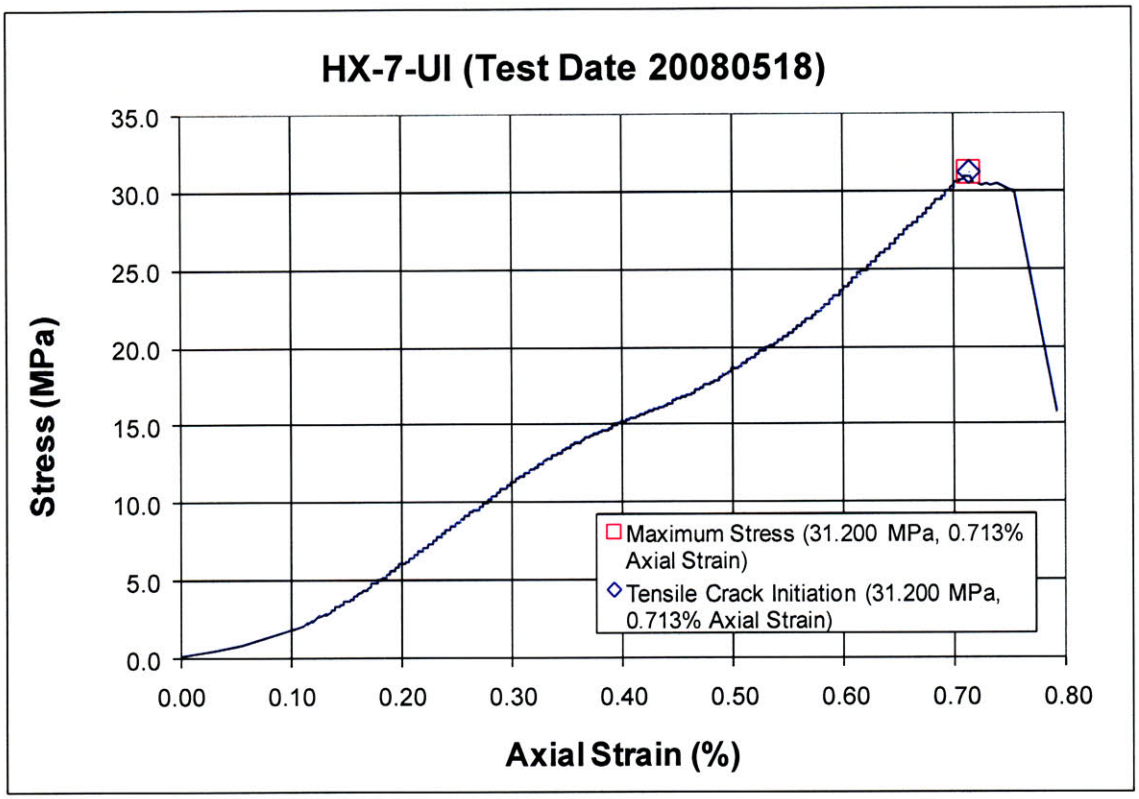

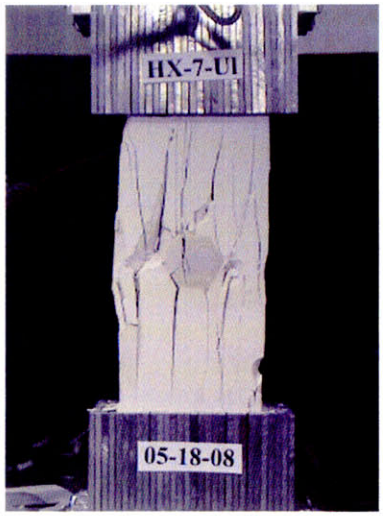

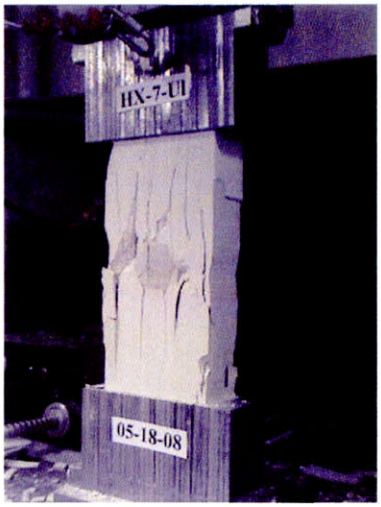

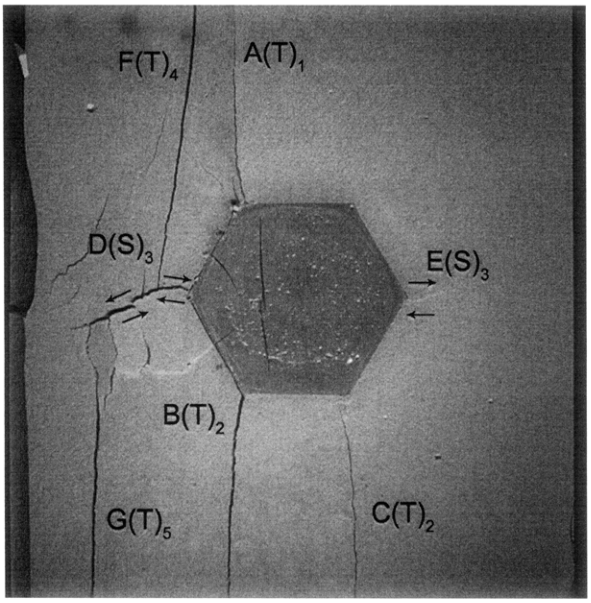

(30.40 MPa) – Ultimate Failure
Time: 6 minutes & 36.027 seconds
HS Image # - 3144

Surface spalling initiates adjacent to shear crack (D).

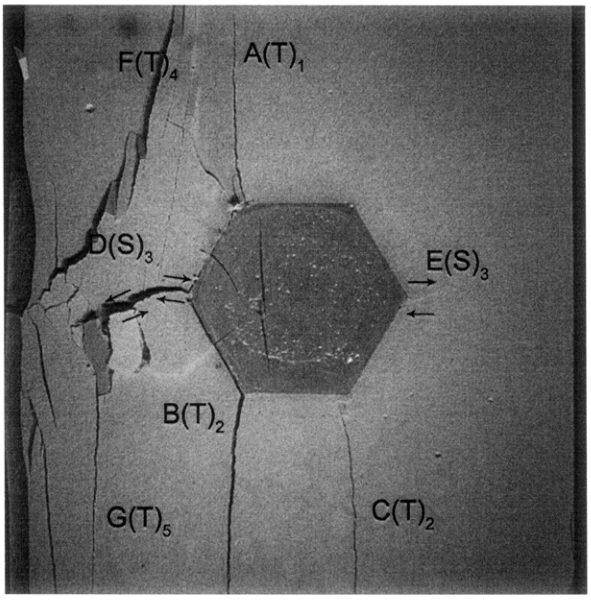

(Recorded by High Speed Video System)

Time: 6 minutes & 36.027 seconds
HS Image # - 3141

Shear crack (D) coalesces with the left-hand specimen boundary.

Specimen Number: HX-8-UI (20080518)

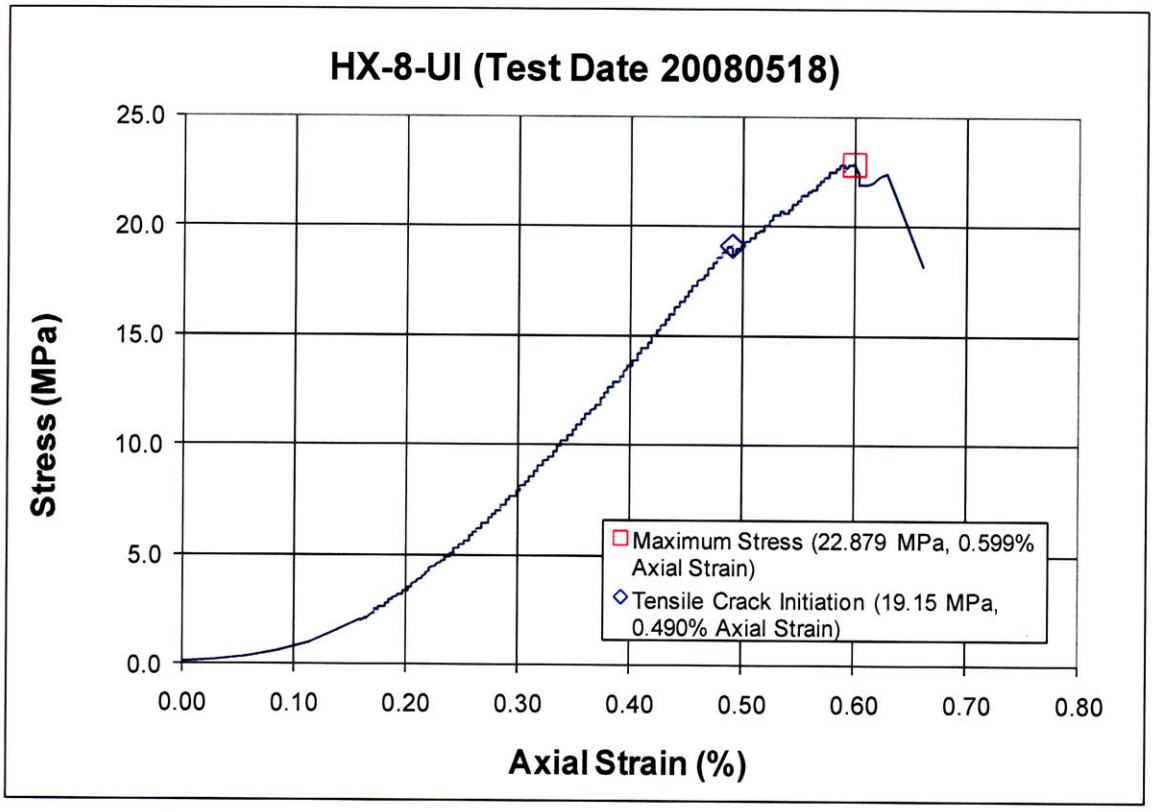

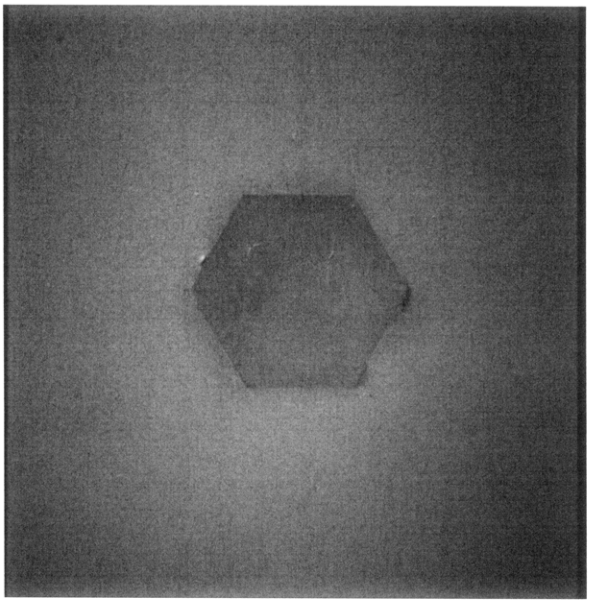

(Recorded by High Speed Video System)

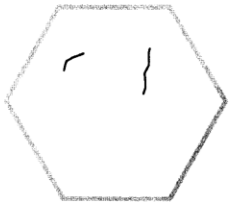

Initial Inclusion Geometry:
HEXAGON – Ultracal Material

Inclusion **more** stiff than matrix.

Initial surface cracks present prior to testing.

High Speed Camera Frame Rate:
5000 pps

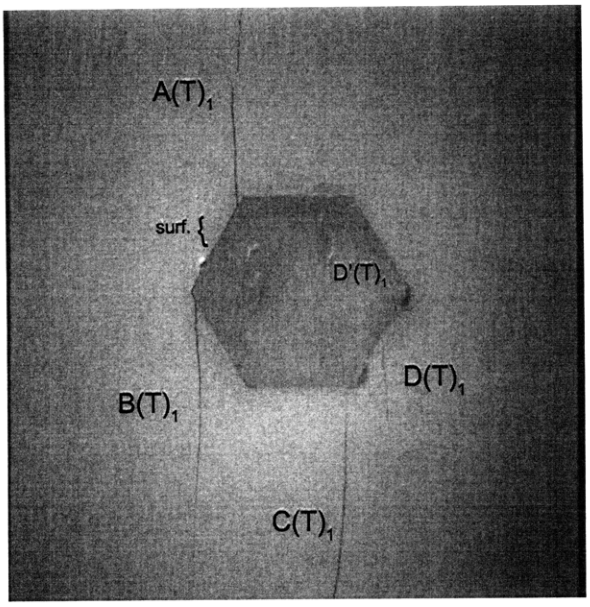

(Recorded by High Speed Video System)

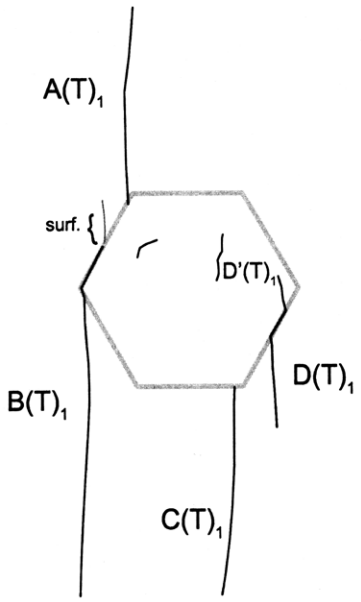

(19.15 MPa)

– Tensile Crack Initiation

Time: 4 minutes & 4.434 seconds

Tensile crack (A) initiates at the upper specimen boundary and propagates until its coalescence with the upper left-hand inclusion boundary.

Tensile crack (B) initiates at the left-hand inclusion boundary and propagates towards the lower specimen boundary. Tensile crack (B) also begins to propagate around the left-hand inclusion boundary. A surface crack (surf.) also initiates from the upper left-hand inclusion boundary.

Tensile cracks (C&D) initiate at the inclusion boundary and propagate towards the lower specimen boundary. Tensile crack (D) begins to propagate around the right-hand inclusion boundary and into the inclusion, which will be referred to as tensile crack (D').

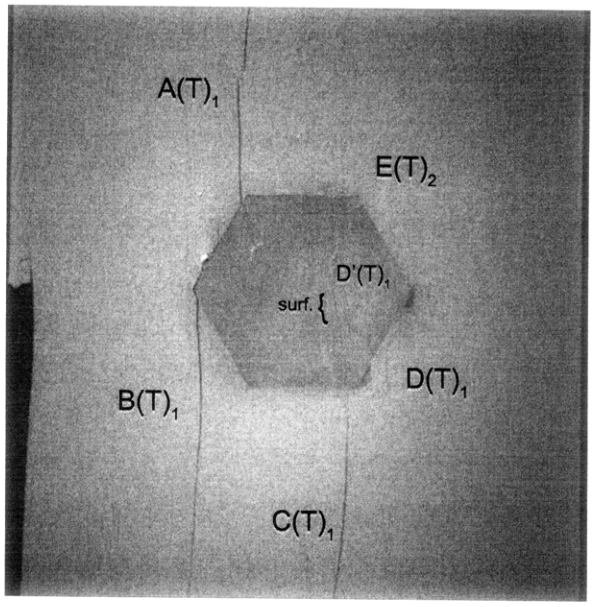

(Recorded by High Speed Video System)

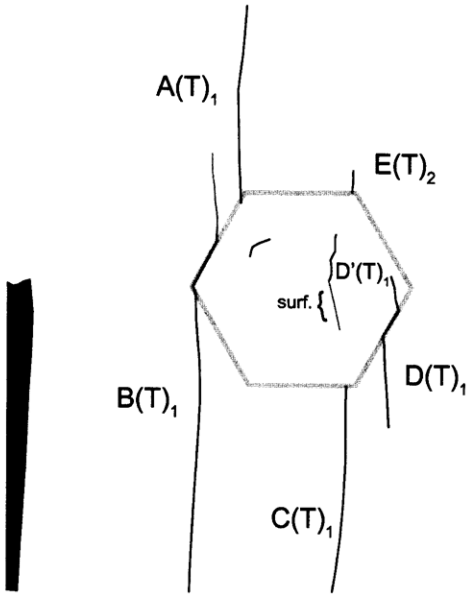

(19.82 MPa)
Time: 4 minutes & 13.734 seconds

Prior to the capture of this image, a large piece of specimen detaches from the left boundary.

Tensile crack (E) initiates from the upper right-hand inclusion boundary and propagates towards the upper specimen boundary.

A new surface crack (surf.) initiates from a pre-test surface crack within the inclusion.

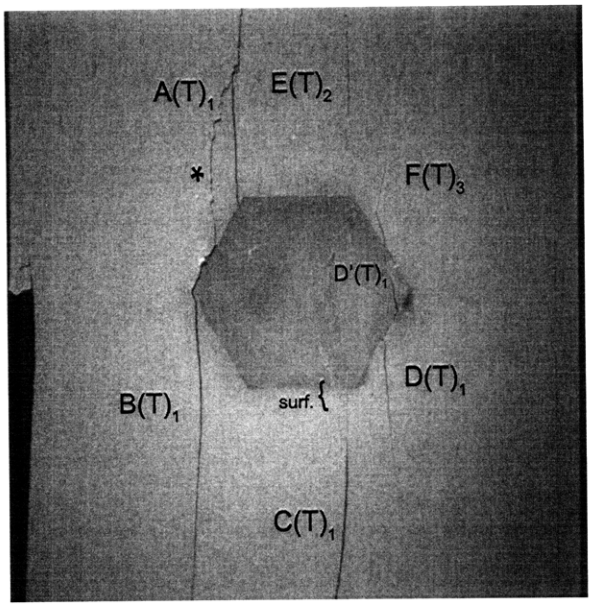

(Recorded by High Speed Video System)

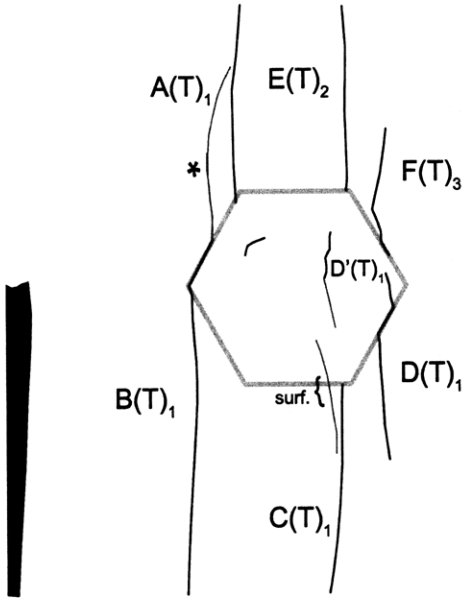

(20.22 MPa)
Time: 4 minutes & 19.776 seconds

A previously initiated surface crack (*) coalesces with tensile crack (A). A new surface crack (surf.) also initiates at lower the inclusion boundary.

A new tensile crack (F) initiates at the right-hand inclusion boundary and propagates upwards.

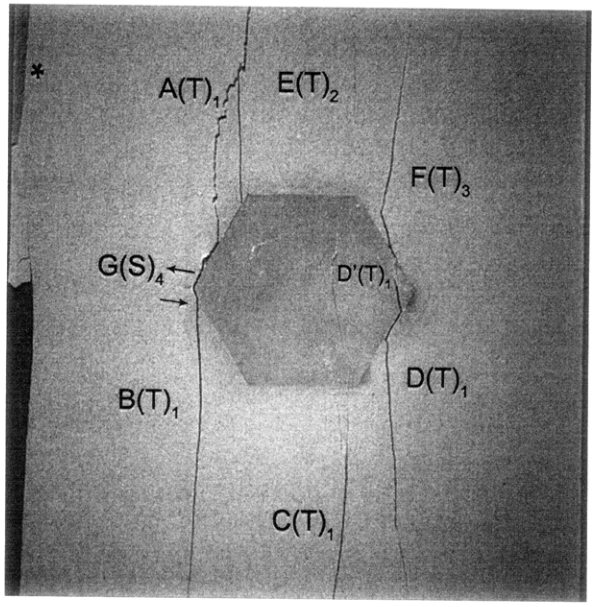

(Recorded by High Speed Video System)

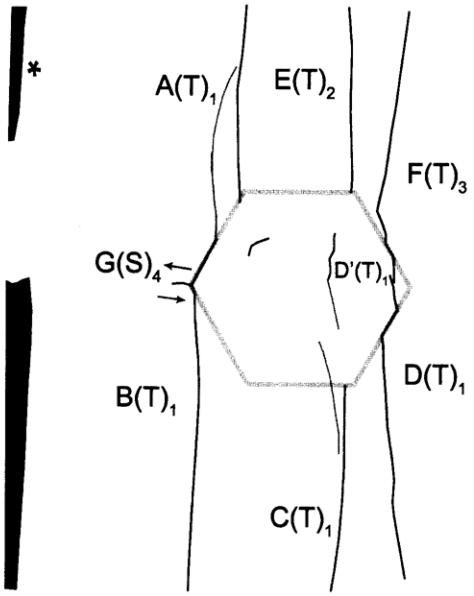

(22.84 MPa)
Time: 4 minutes & 57.732 seconds
HS Image # - 5404

Prior to the capture of this image, another piece of specimen (*) detaches from the upper left-hand specimen boundary.

With an increase in loading, tensile crack (F) coalesces with tensile crack (D').

Shear crack (G) initiates at the left-hand inclusion boundary and propagates away from the inclusion.

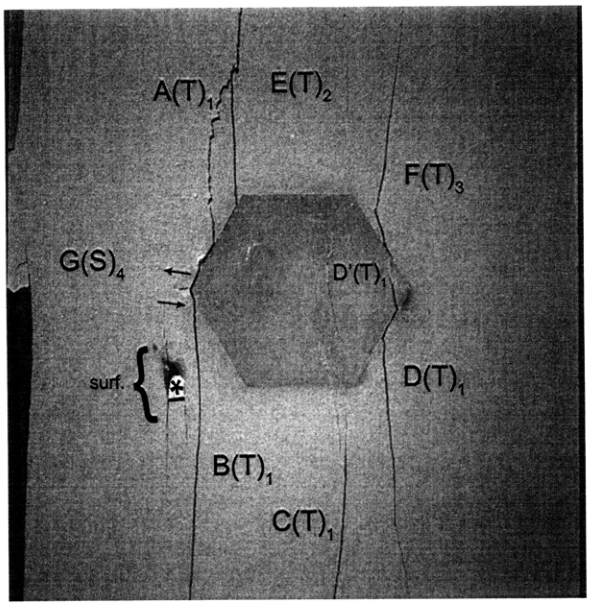

(Recorded by High Speed Video System)

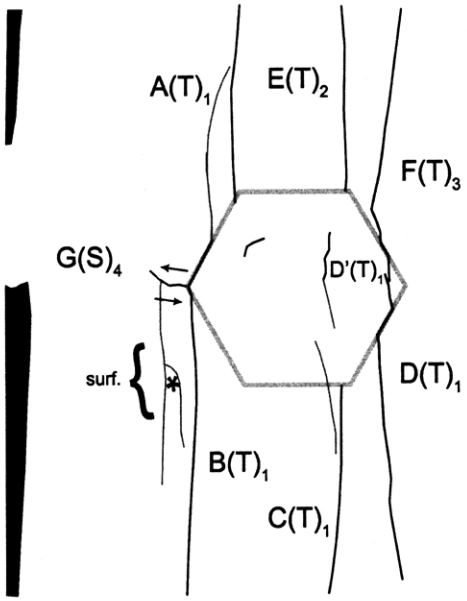

(22.879 MPa) – [Max. Stress]
Time: 4 minutes & 58.122 seconds
HS Image # - 3455

As shear crack (G) propagates towards the left-hand specimen boundary, a surface crack (surf.) initiates and propagates downwards. The surface crack (surf.) then bifurcates, which causes the detachment (*) of a surficial piece of specimen.

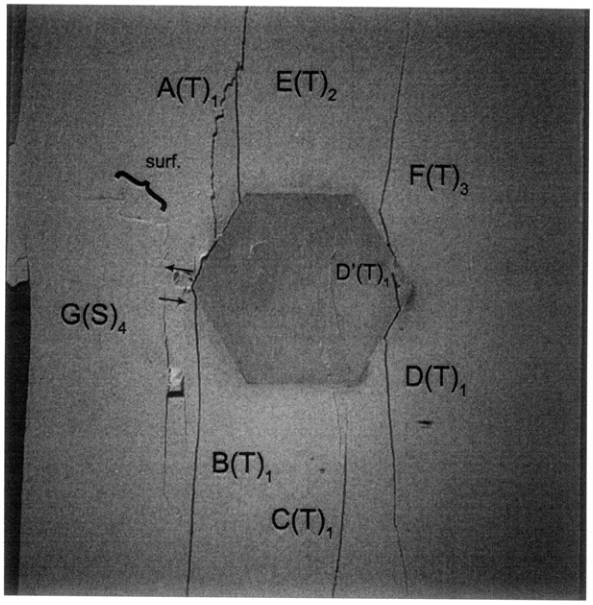

(Recorded by High Speed Video System)

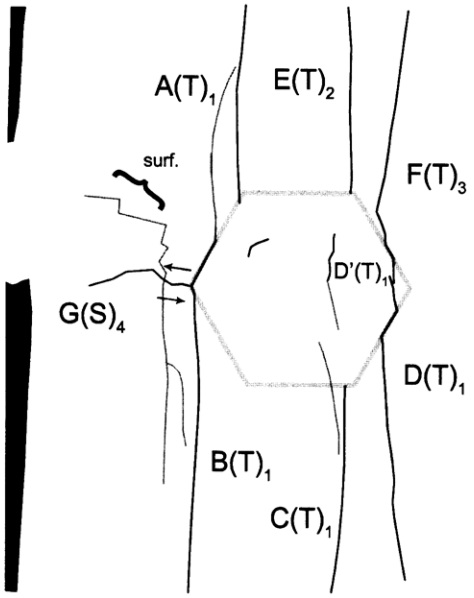

(22.46 MPa)
Time: 4 minutes & 58.185 seconds
HS Image # - 3138

As shear crack (G) continues to propagate towards the left-hand specimen boundary, a new surface crack (surf.) initiates.

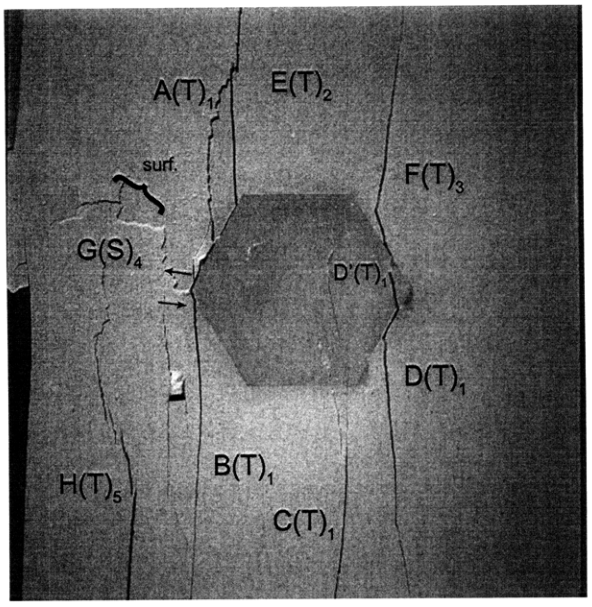

(Recorded by High Speed Video System)

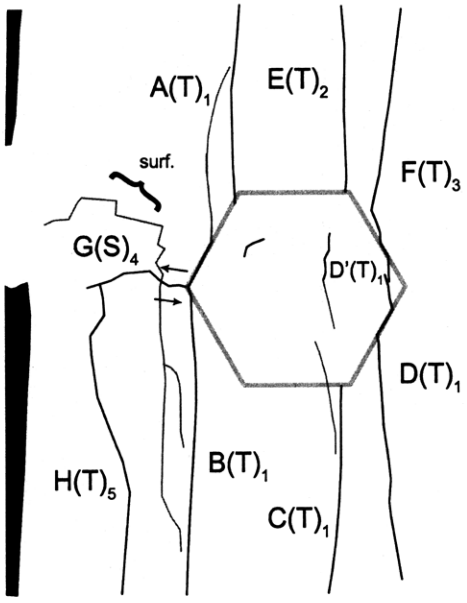

(22.26 MPa)
Time: 4 minutes & 58.353 seconds
HS Image # - 2299

A new tensile crack (H) initiates at the lower specimen boundary and propagates until its coalescence with shear crack (G).

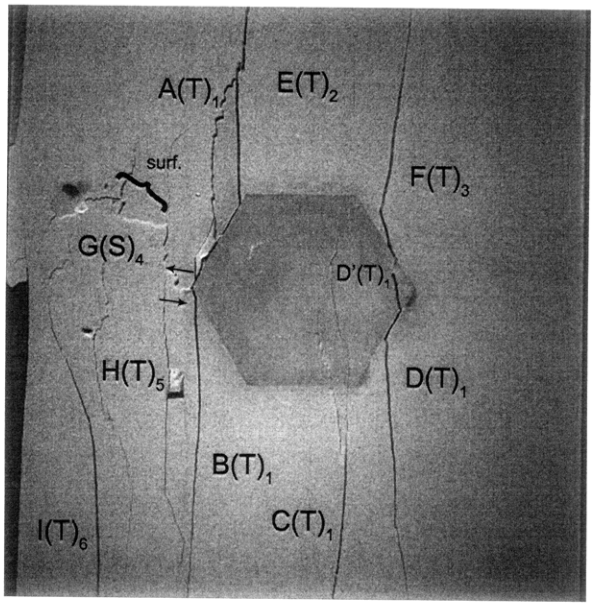

(Recorded by High Speed Video System)

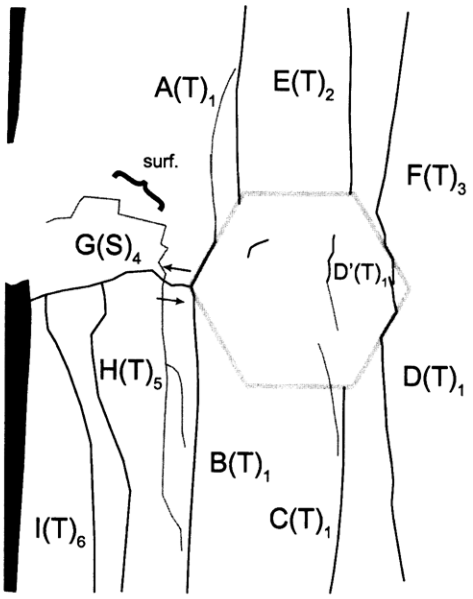

(22.28 MPa) – Ultimate Failure
Time: 4 minutes & 58.356 seconds
HS Image # - 2283

A new tensile crack (I) initiates at the lower specimen boundary and propagates until its coalescence with shear crack (G).

Shear crack (G) coalesces with the left-hand specimen boundary.

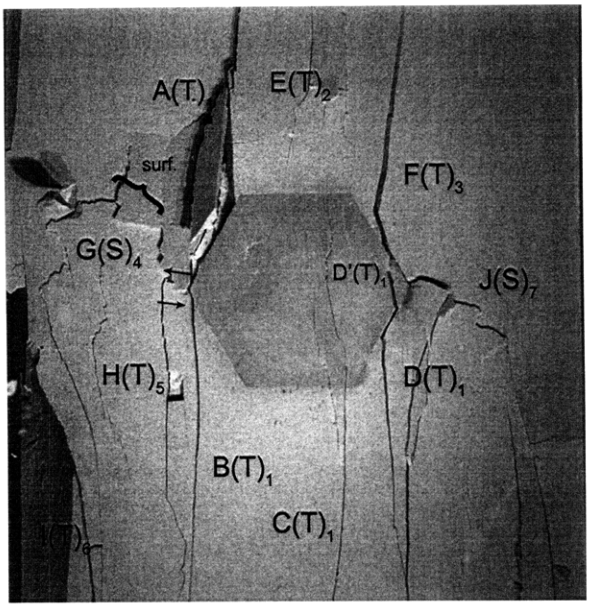

(21.83 MPa)
Time: 4 minutes & 58.409 seconds
HS Image # - 2022

A new shear crack (J) initiates at the right-hand inclusion boundary, and coalesces with the right-hand specimen boundary post failure.

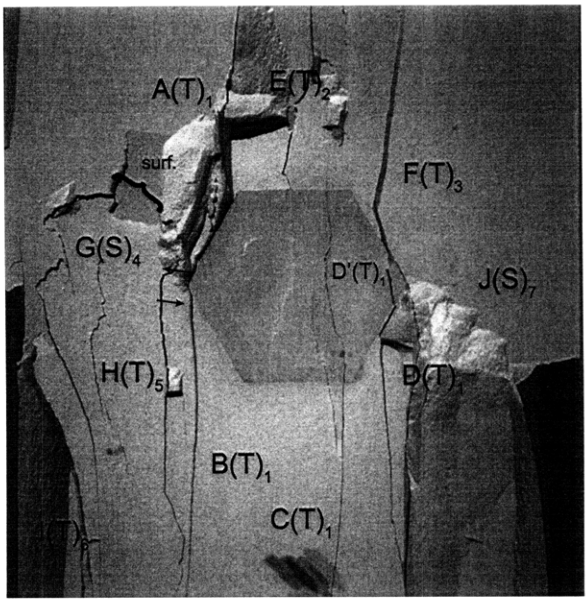

(Recorded by High Speed Video System)

(0 MPa – Final Picture)
HS Image # - 588

A good view of shear crack (J) can be seen in this picture.

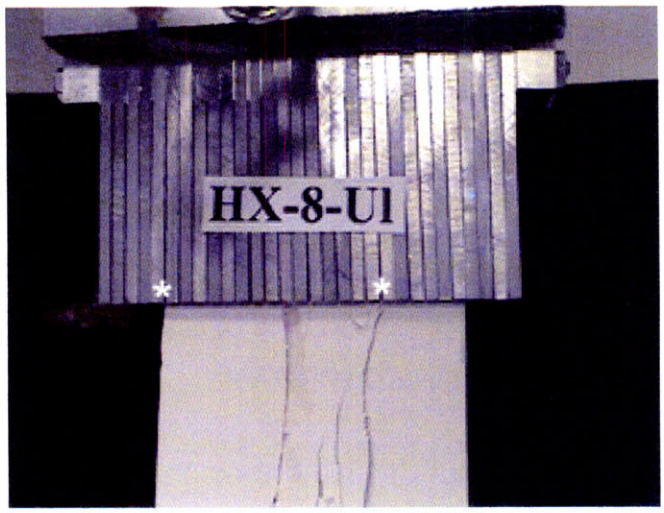	Upper edge of the specimen. The cracks marked with a (*) coincide with the openings between the teeth of the brush platen.
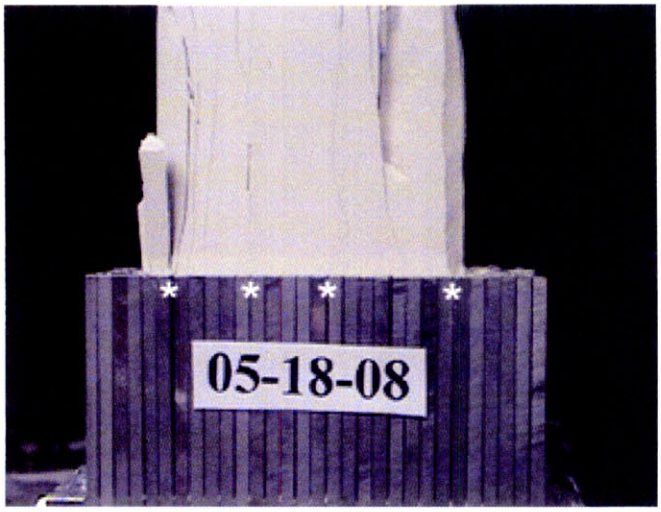	Lower edge of the specimen. The cracks marked with a (*) coincide with the openings between the teeth of the brush platen.

Specimen Number: DM-1-PI (20080601)

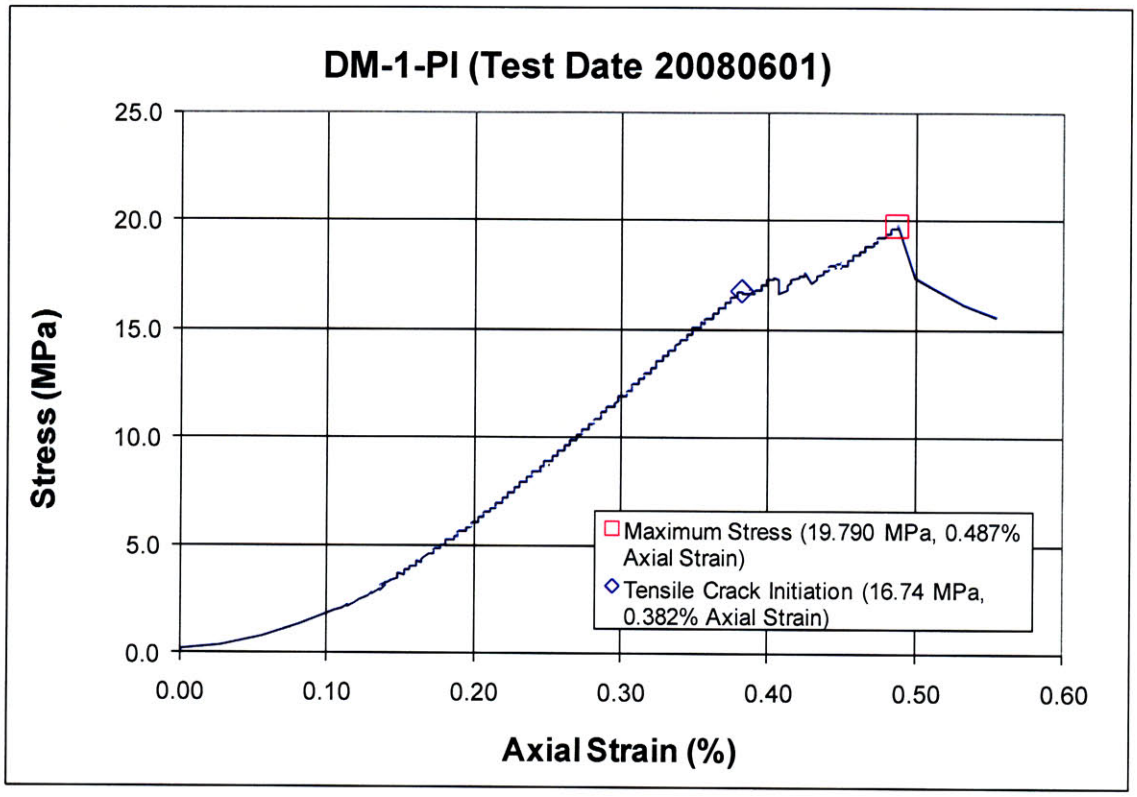

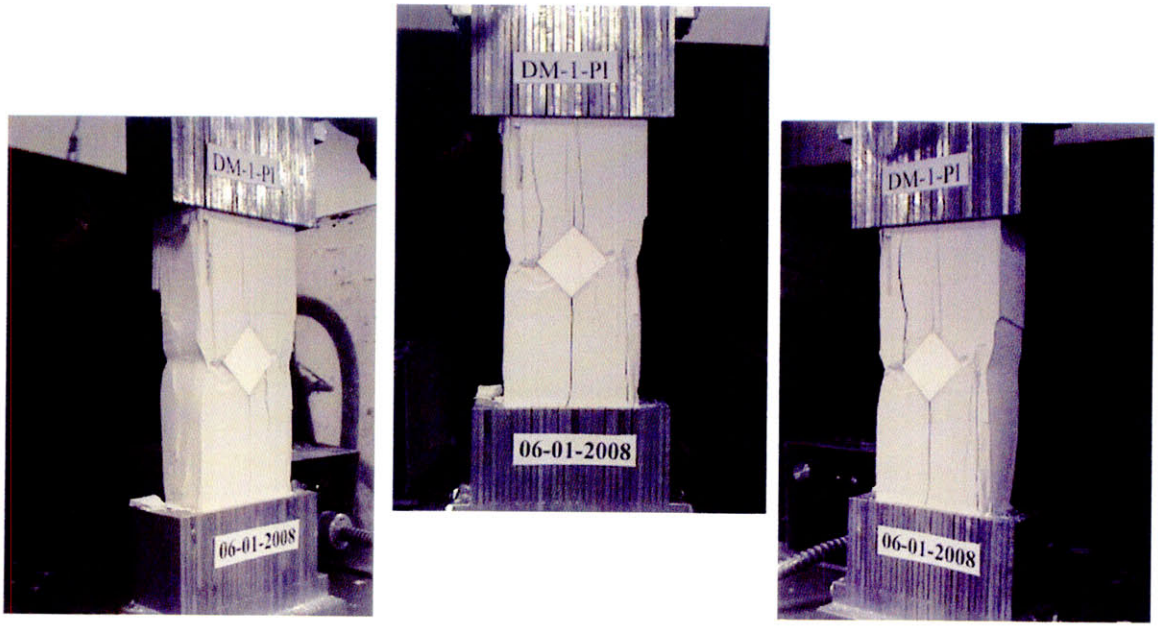

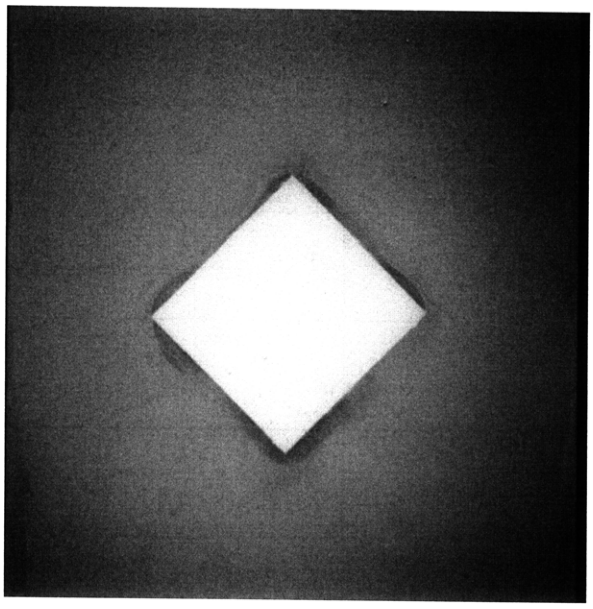

(Recorded by High Speed Video System)

Initial Inclusion Geometry:
DIAMOND – Plaster Material

Inclusion **less** stiff than matrix.

High Speed Camera Frame Rate:
5000 pps

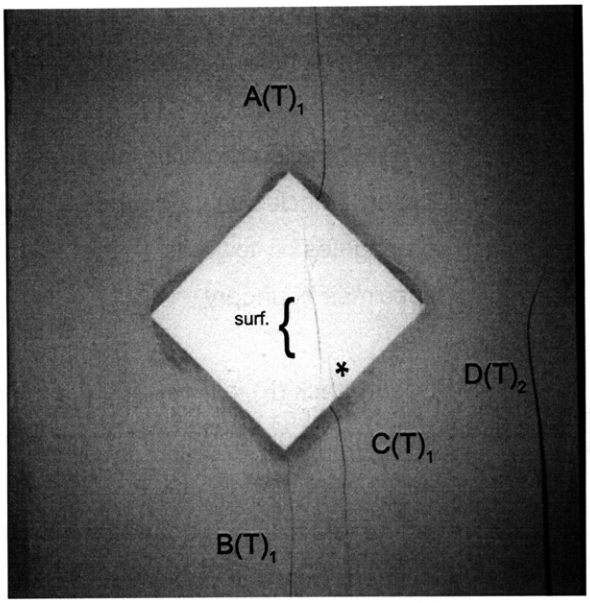

(Recorded by High Speed Video System)

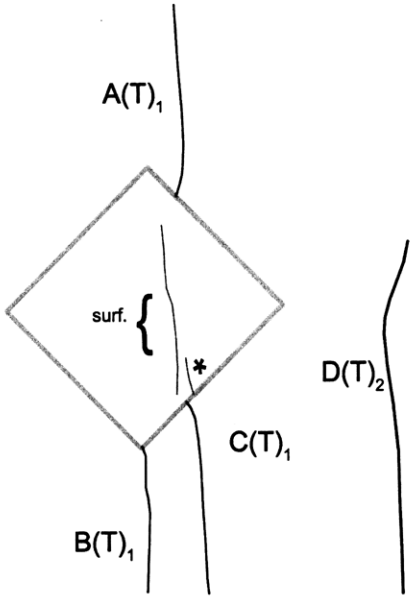

(16.74 MPa)

– Tensile Crack Initiation

Time: 3 minutes & 16.49 seconds

Tensile crack (A) initiates at the upper inclusion boundary and propagates towards the upper specimen boundary. Tensile cracks (B&C) initiate at the lower inclusion boundary and propagate towards the lower specimen boundary.

Surface crack (surf.) initiates within the inclusion, while surface crack (*) initiates at the lower inclusion boundary and propagates into the inclusion.

Tensile crack (D) then initiates at the lower specimen boundary and propagates upwards.

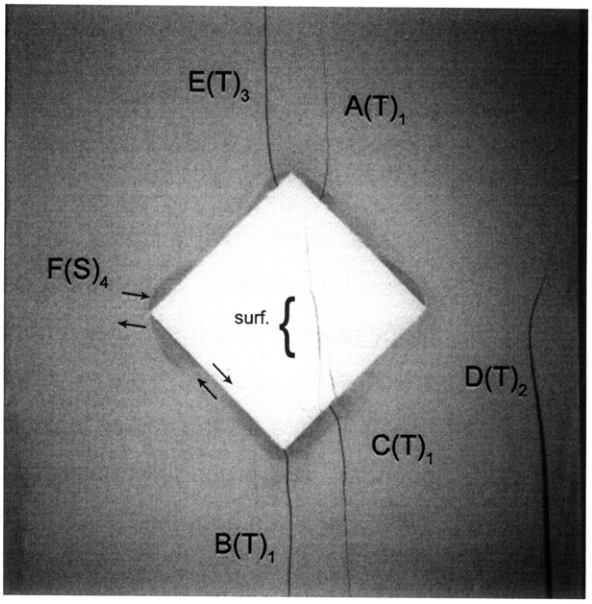

(Recorded by High Speed Video System)

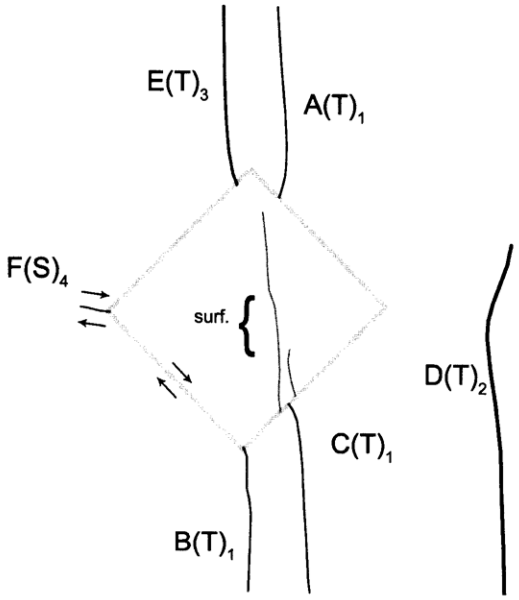

(17.36 MPa)
Time: 3 minutes & 25.92 seconds

A new tensile crack (E) initiates at the upper inclusion boundary and propagates towards the upper specimen boundary.

Shear crack (F) initiates at the left-hand inclusion boundary and propagates away from the inclusion. The lower left-hand inclusion boundary debonds in shear from the specimen, as shown by the arrows.

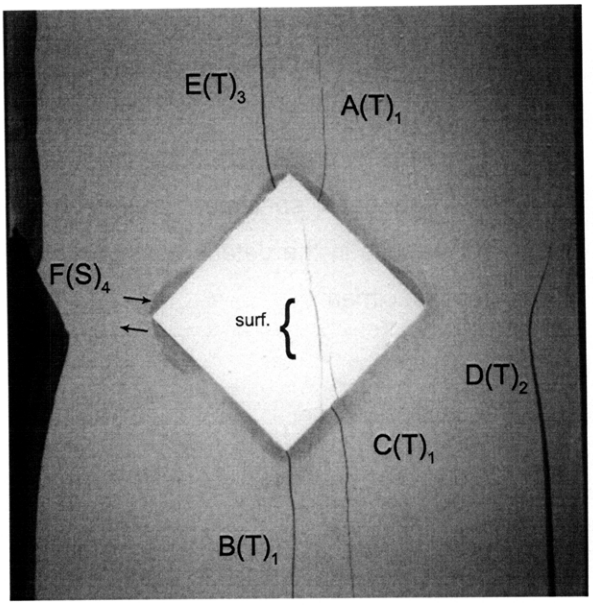

(Recorded by High Speed Video System)

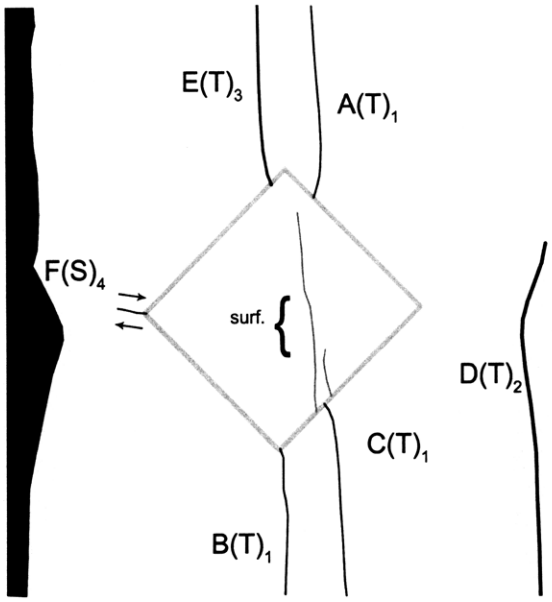

(17.56 MPa)
Time: 3 minutes & 28.34 seconds

A large piece of specimen detaches from the left-hand specimen boundary.

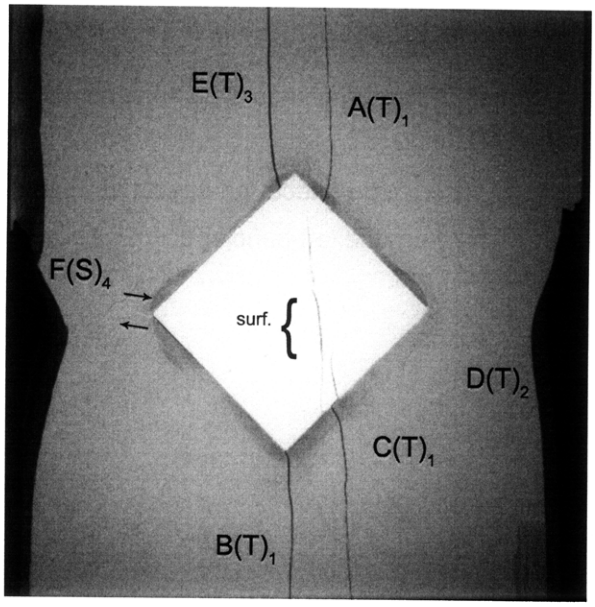

(Recorded by High Speed Video System)

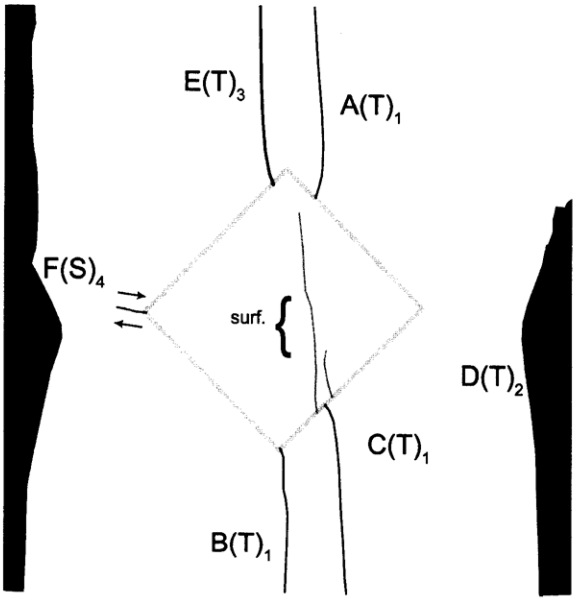

(18.08 MPa)
Time: 3 minutes & 35.58 seconds

Tensile crack (D) coalesces with the right-hand specimen boundary, which results in the detachment of a piece of specimen.

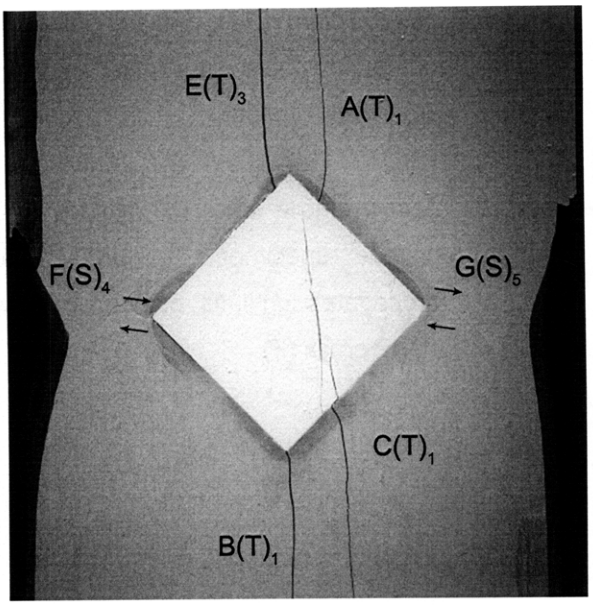

(Recorded by High Speed Video System)

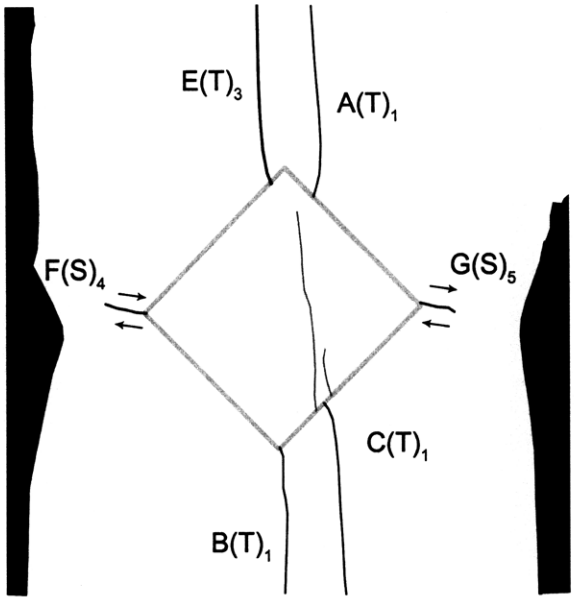

(19.75 MPa)
Time: 3 minutes & 59.95 seconds
HS Image # - 5404

A new shear crack (G) initiates at the right-hand inclusion boundary and propagates away from the inclusion.

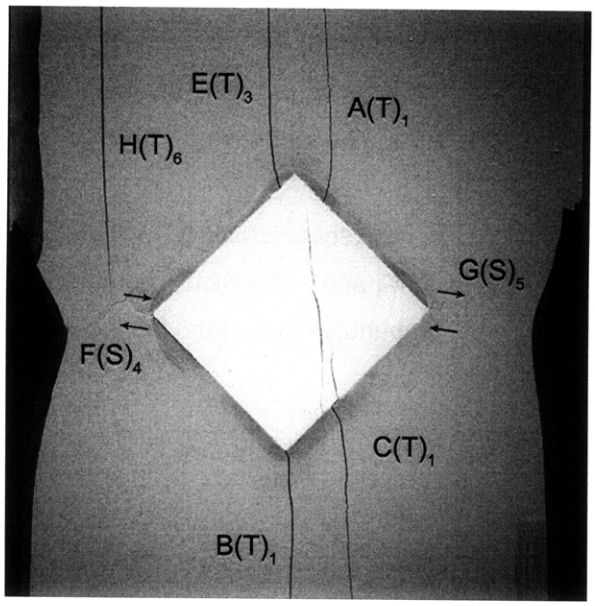

(Recorded by High Speed Video System)

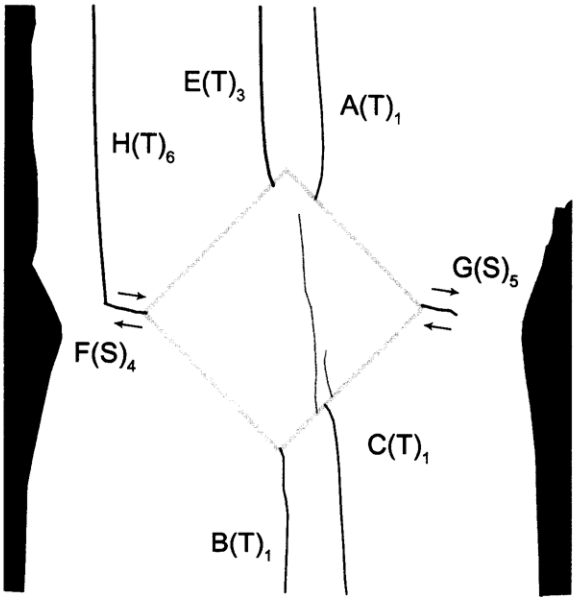

(19.790 MPa) [Max. Stress] - FAILURE
Time: 4 minutes & 0.314 seconds
HS Image # - 3588

A new tensile crack (H) initiates at the upper specimen boundary and propagates until its coalescence with shear crack (F).

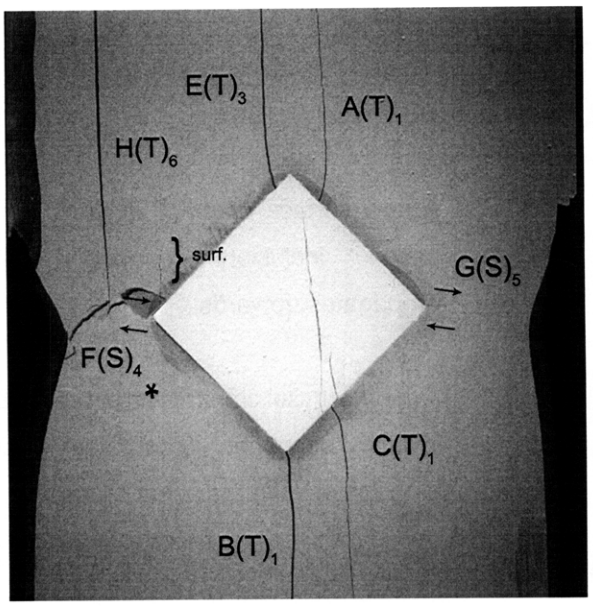

(Recorded by High Speed Video System)

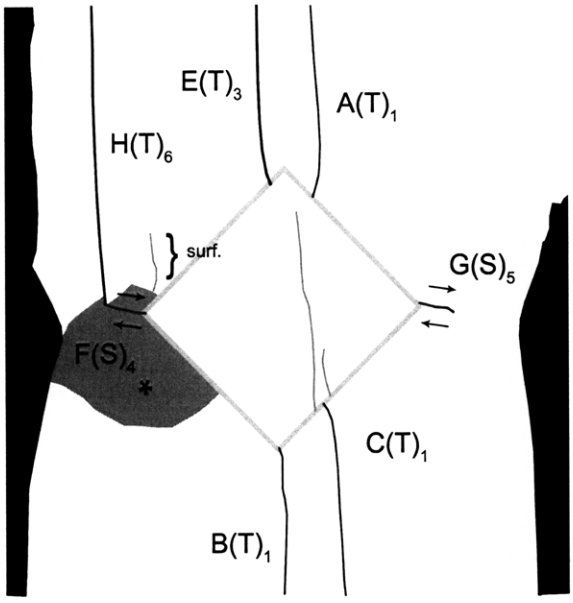

(19.789 MPa)
Time: 4 minutes & 0.314 seconds
HS Image # - 3587

As a result of shear crack (F), a large surficial piece (*) detaches from the specimen.

A new surface crack (surf.) initiates at the inclusion boundary and propagates upwards.

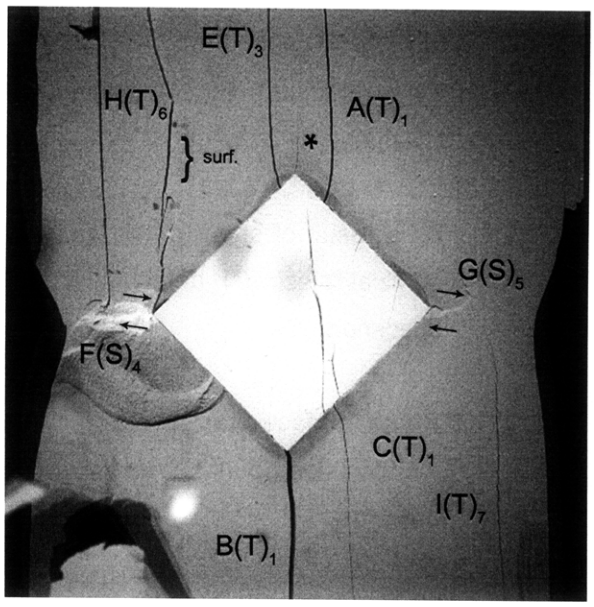

(Recorded by High Speed Video System)

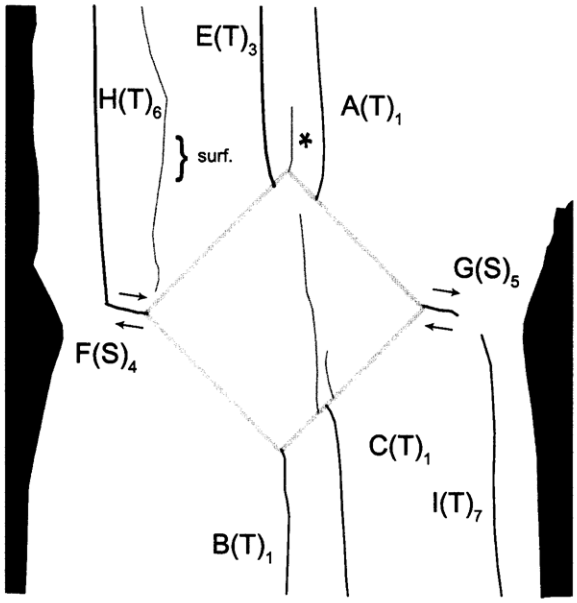

(- MPa)
Time: 4 minutes & 0.479 seconds
HS Image # - 2764

A new surface crack (*) initiates at the upper inclusion boundary and propagates upwards.

A new tensile crack (I) initiates at the lower specimen boundary and propagates towards shear crack (G).

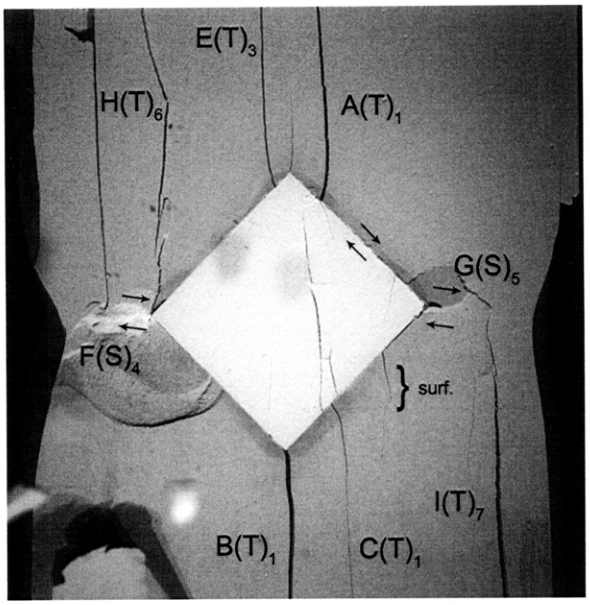

(Recorded by High Speed Video System)

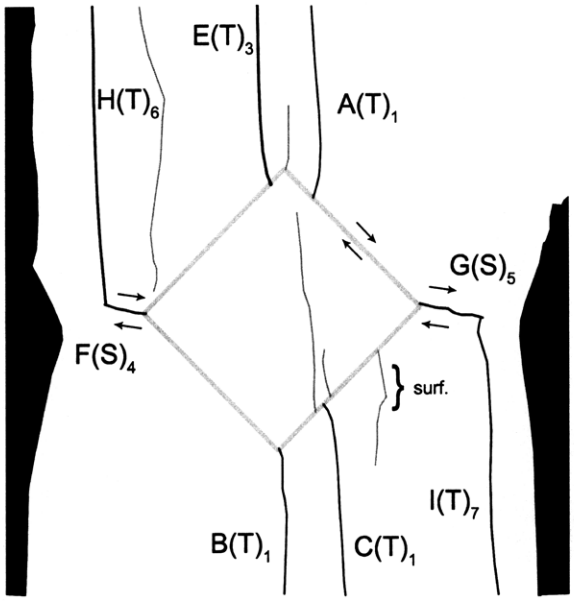

(- MPa)
Time: 4 minutes & 0.479 seconds
HS Image # - 2763

Tensile crack (I) propagates until its coalescence with shear crack (G).

A new surface crack (surf.) initiates at the lower right-hand inclusion boundary.

The upper-right hand inclusion boundary debonds in shear from the specimen, as shown by the arrows.

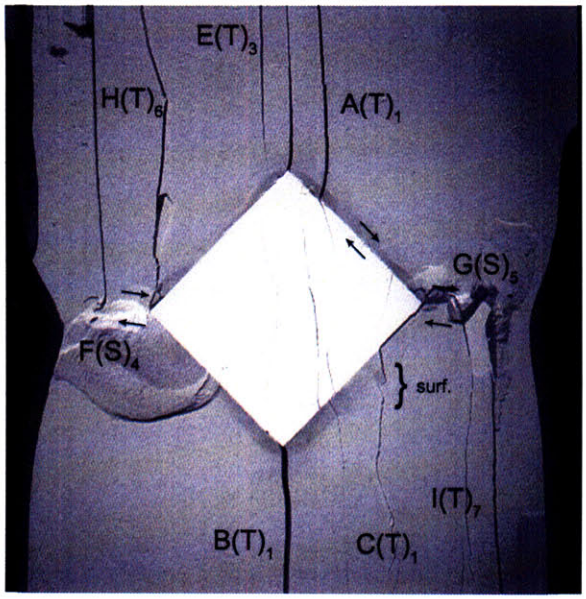

(Recorded by High Speed Video System)

(0 MPa – Final Picture)

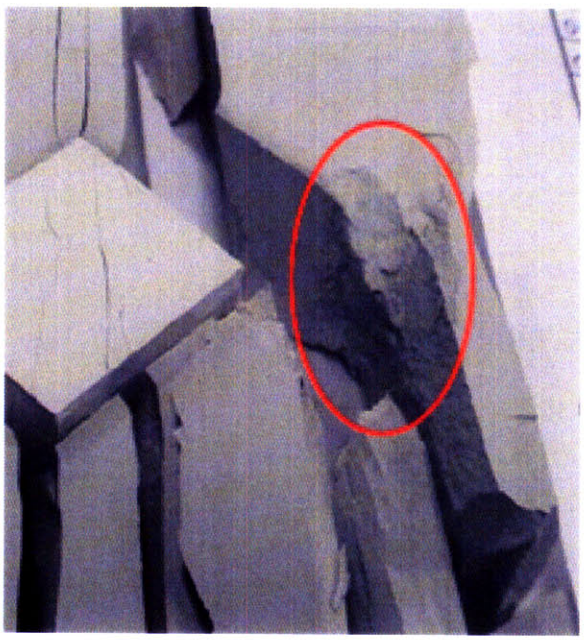

A good view of shear crack (G) can be seen in this post-testing picture.

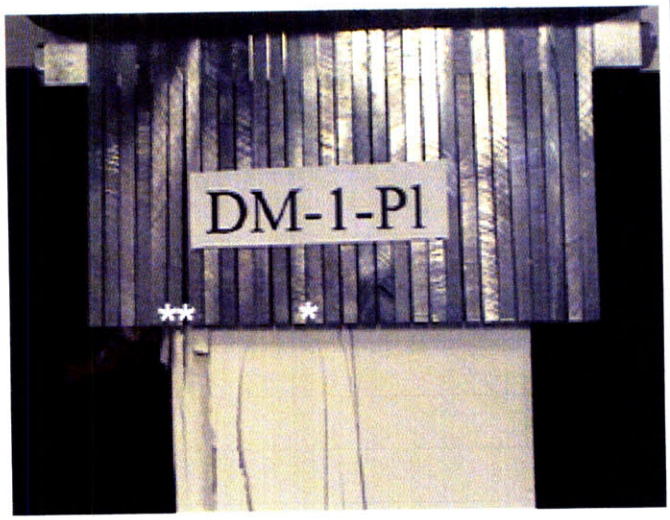	Upper edge of the specimen. The cracks marked with a (*) coincide with the openings between the teeth of the brush platen.
	Lower edge of the specimen. The cracks marked with a (*) coincide with the openings between the teeth of the brush platen.

SUMMARY

Specimen Number: DM-2-PI (20080601)

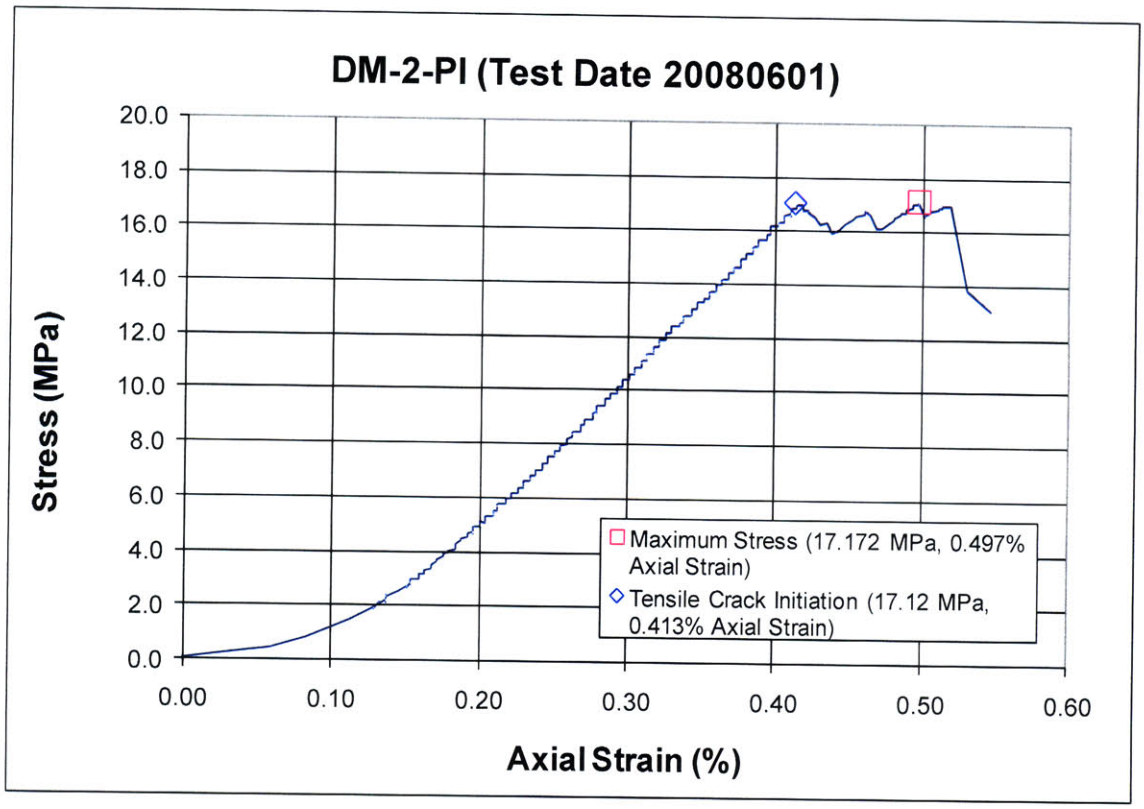

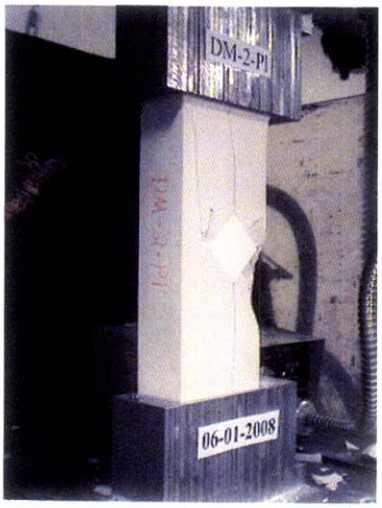

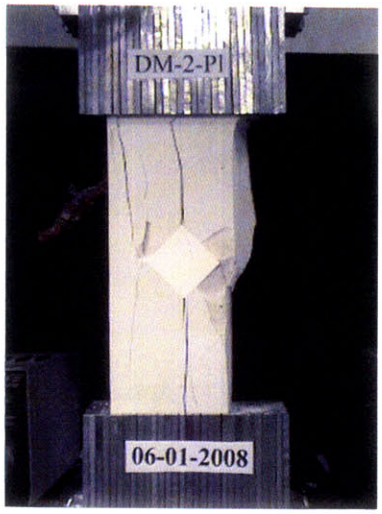

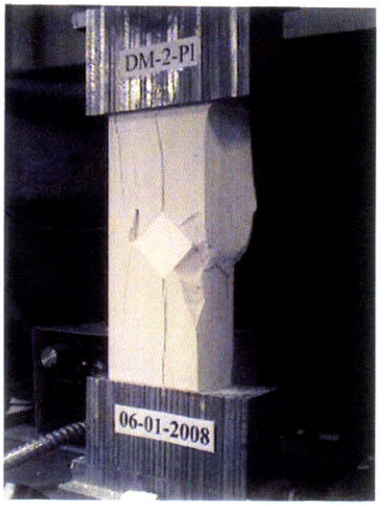

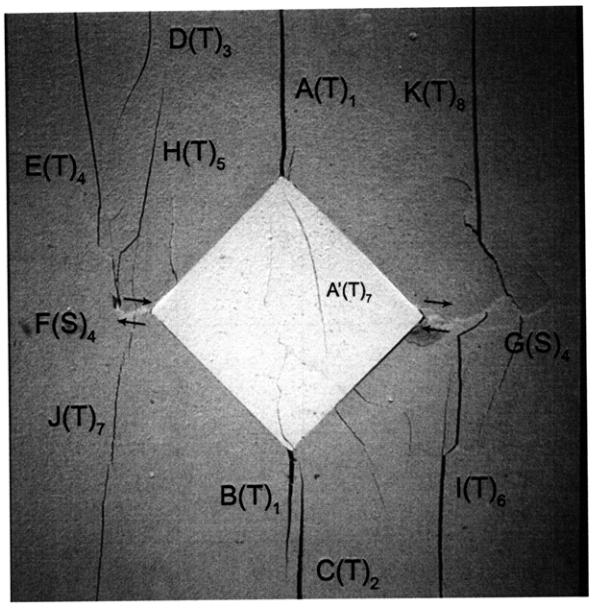

(Recorded by High Speed Video System)

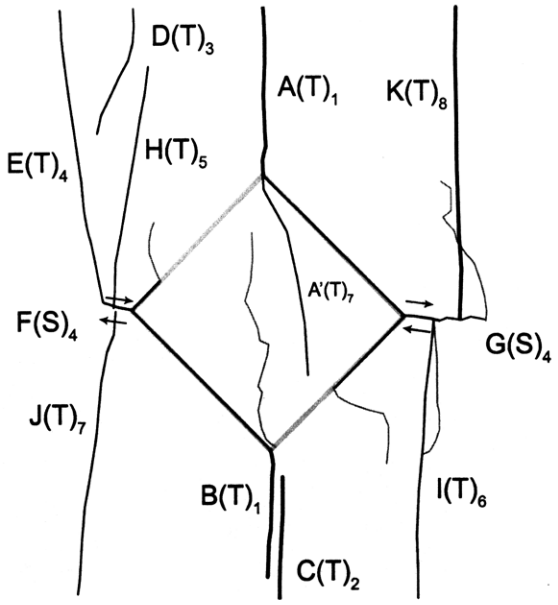

(- MPa)

Time: 3 minutes & 23.74 seconds

HS Image # - 2134

A new tensile crack (K) initiates at the upper specimen boundary and propagates until its coalescence with shear crack (G). This results in the ultimate failure of the specimen.

SUMMARY

Specimen Number: DM-3-PI (20080601)

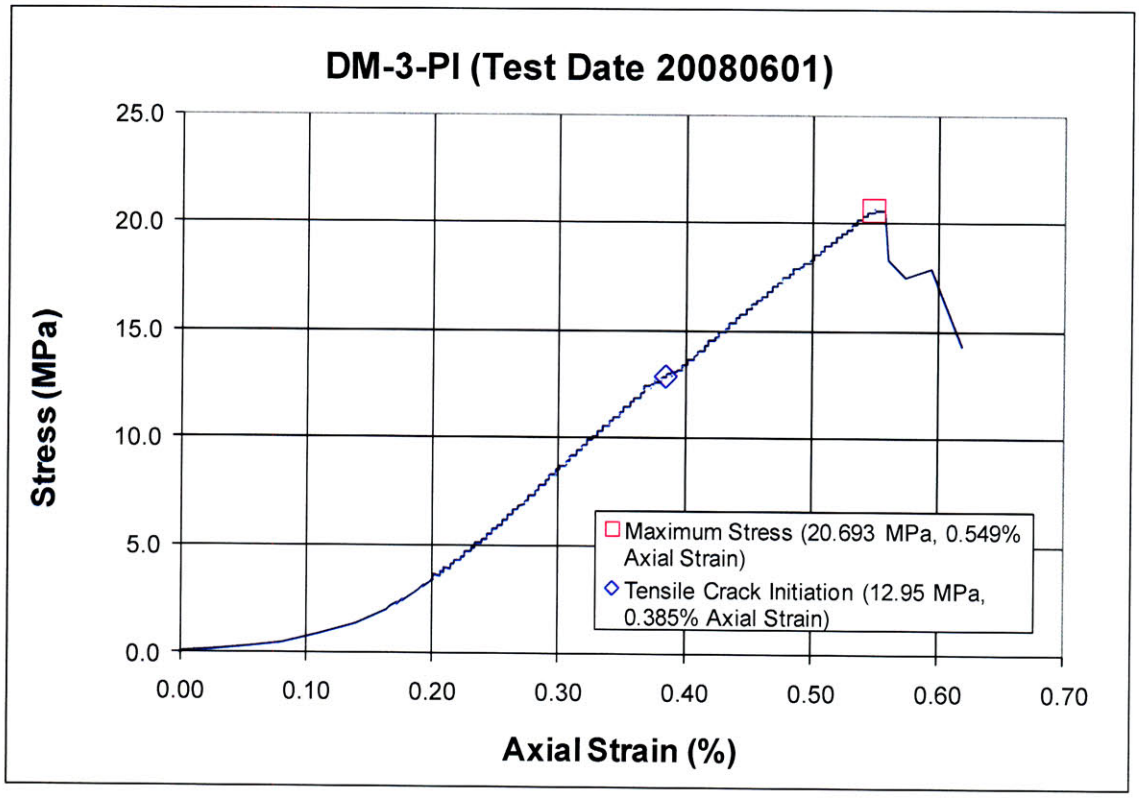

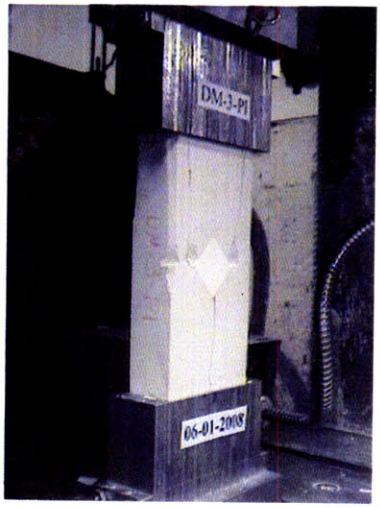

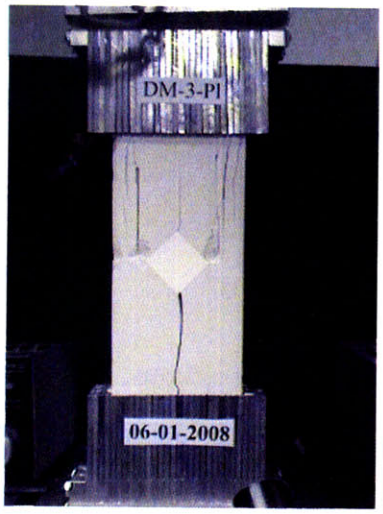

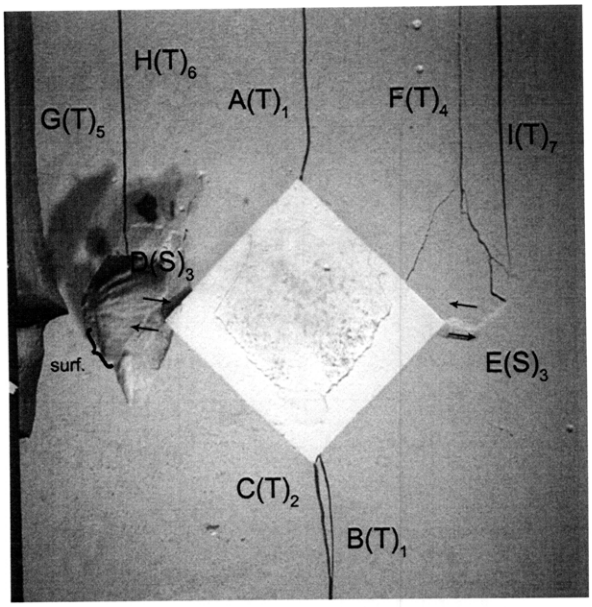

(Recorded by High Speed Video System)

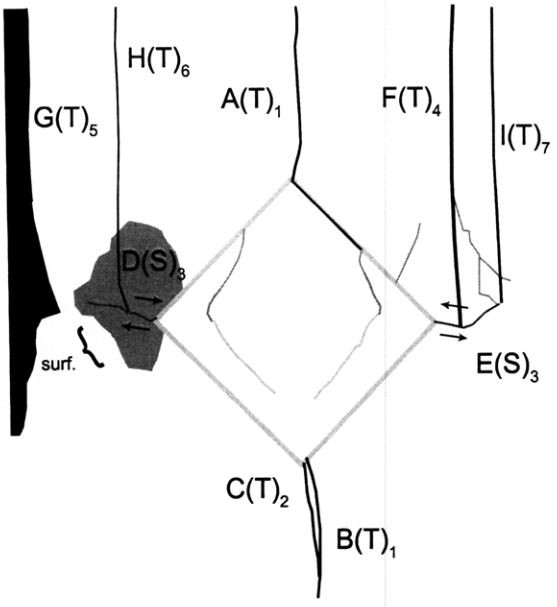

(14.36 MPa)
Time: 4 minutes & 13.162 seconds
HS Image # - 2594

A new tensile crack (I) initiates at the upper specimen boundary and propagates downwards until its coalescence with shear crack (E).

Specimen Number: DM-4-UI (20080601)

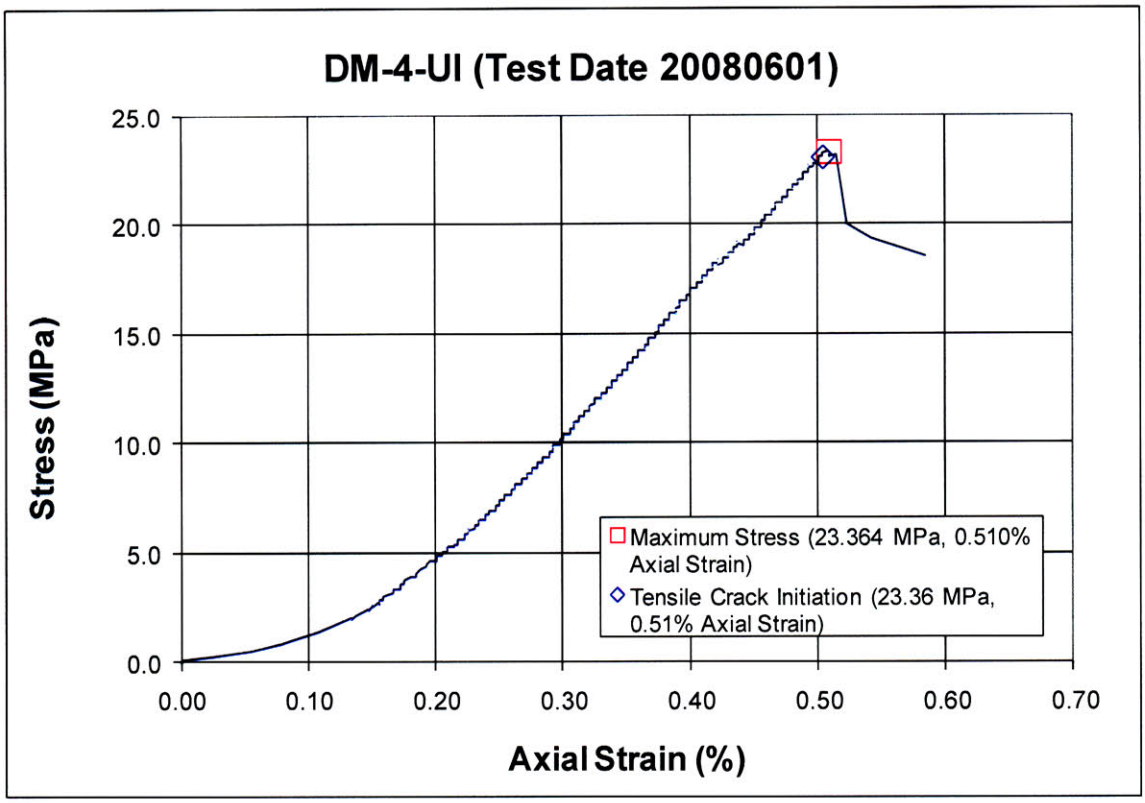

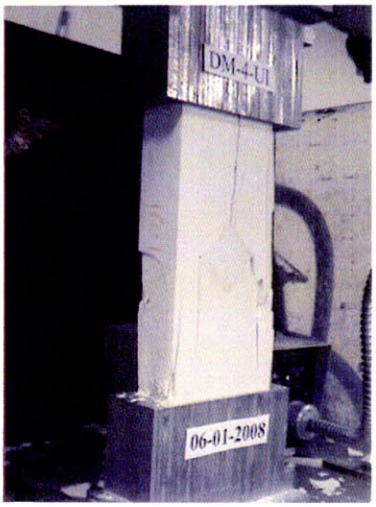

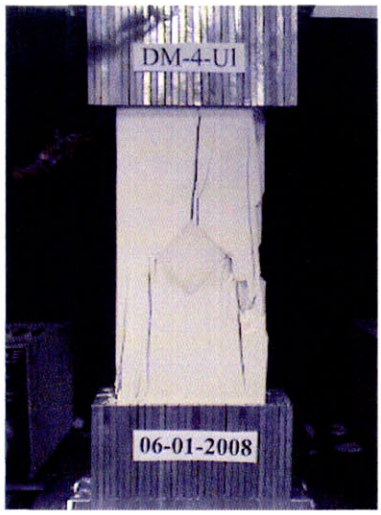

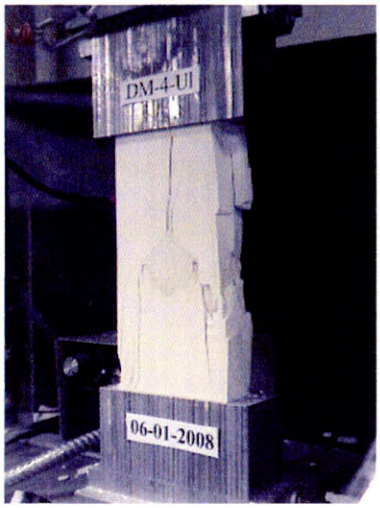

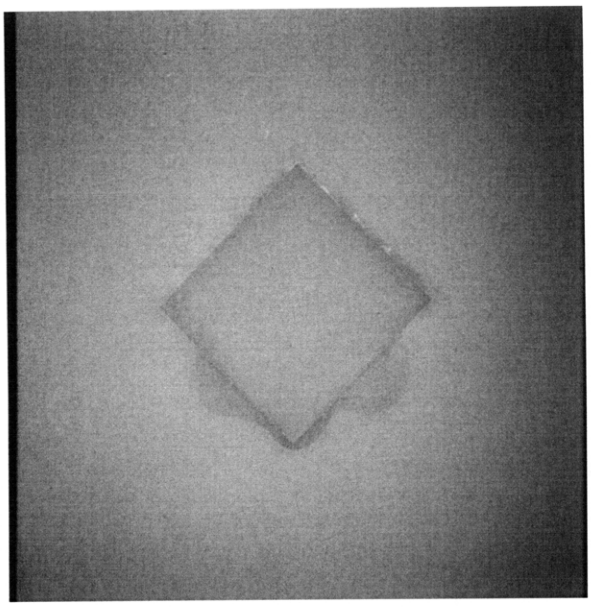

(Recorded by High Speed Video System)

Initial Inclusion Geometry:
DIAMOND – Ultracal Material

Inclusion **more** stiff than matrix.

High Speed Camera Frame Rate:
5000 pps

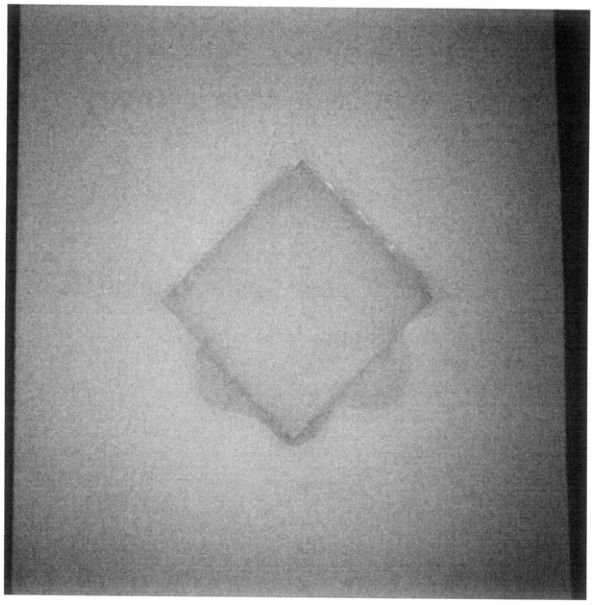

(Recorded by High Speed Video System)

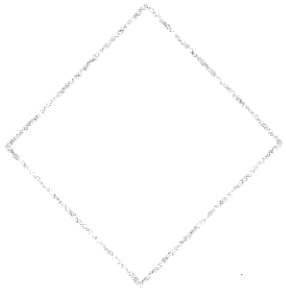

(18.39 MPa)
Time: 3 minutes & 39.60 seconds

Prior to tensile crack initiation, a large piece of specimen detaches from the right-hand specimen boundary.

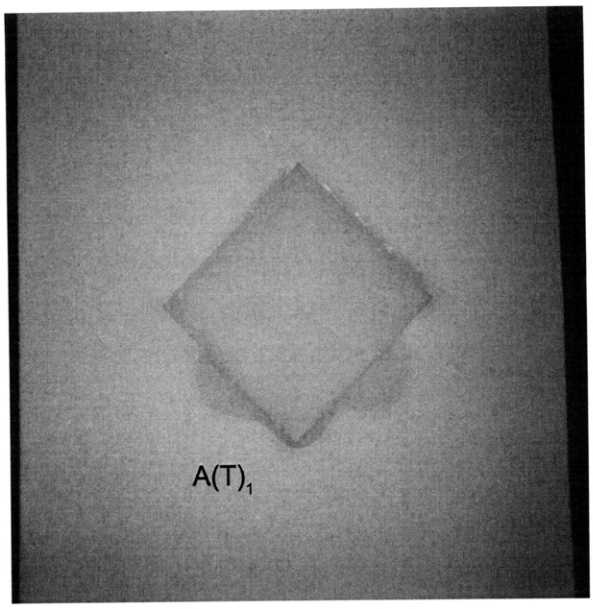

(Recorded by High Speed Video System)

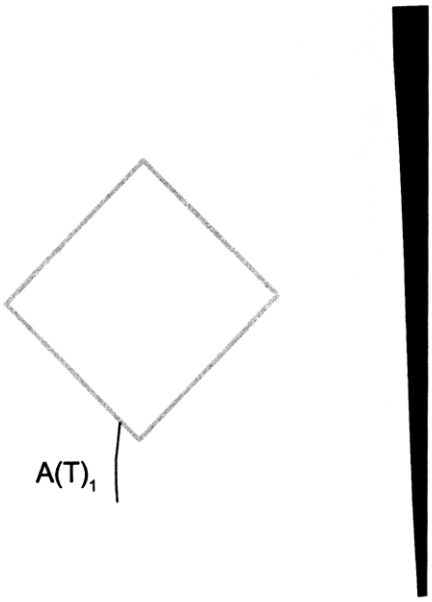

(23.12 MPa)

- Tensile Crack Initiation

Time: 4 minutes & 46.57 seconds

Tensile crack (A) initiates at the lower inclusion boundary and propagates towards the lower specimen boundary.

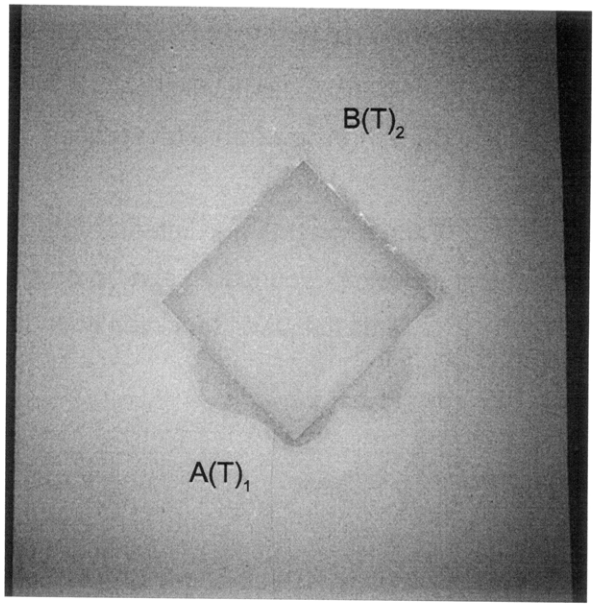

(Recorded by High Speed Video System)

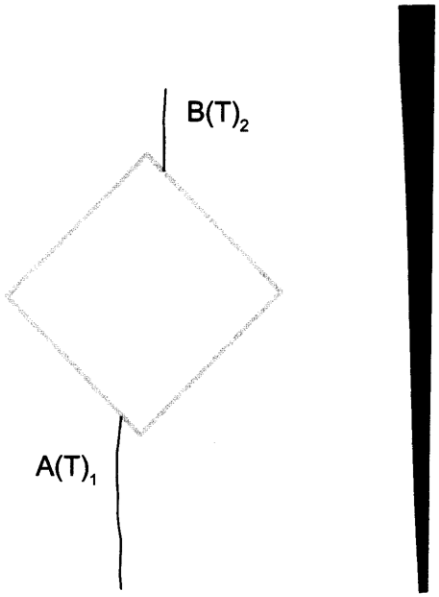

(23.09 MPa)
Time: 4 minutes & 50.697 seconds
HS Image # - 3824

As the aperture of tensile crack (A) increases, a new tensile crack (B) initiates at the upper inclusion boundary and propagates upwards.

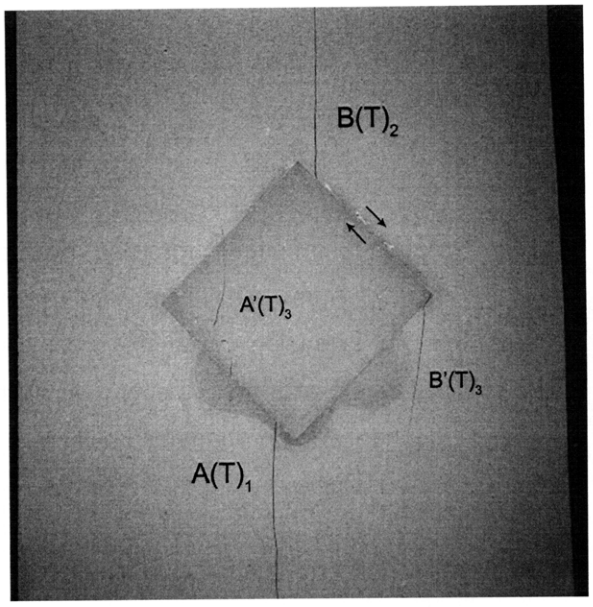

(Recorded by High Speed Video System)

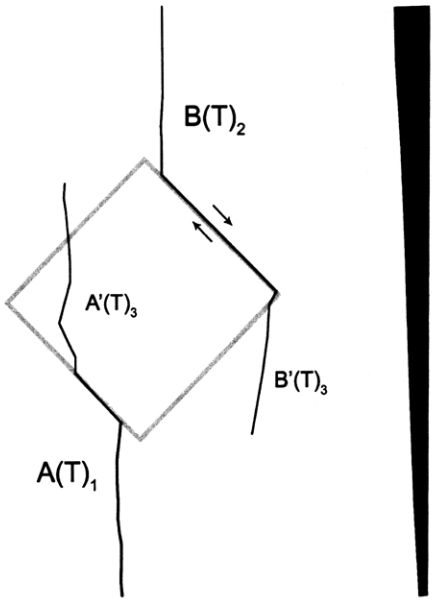

(23.09 MPa)
Time: 4 minutes & 50.697 seconds
HS Image # - 3822

Tensile crack (A) propagates around the lower left-hand inclusion boundary and propagates into, and then out of, the inclusion. This portion of tensile crack (A) will be referred to as tensile crack (A').

The upper right-hand inclusion boundary debonds in shear from the hydrocal matrix. A new tensile crack (B') initiates at the right-hand inclusion boundary and propagates downwards.

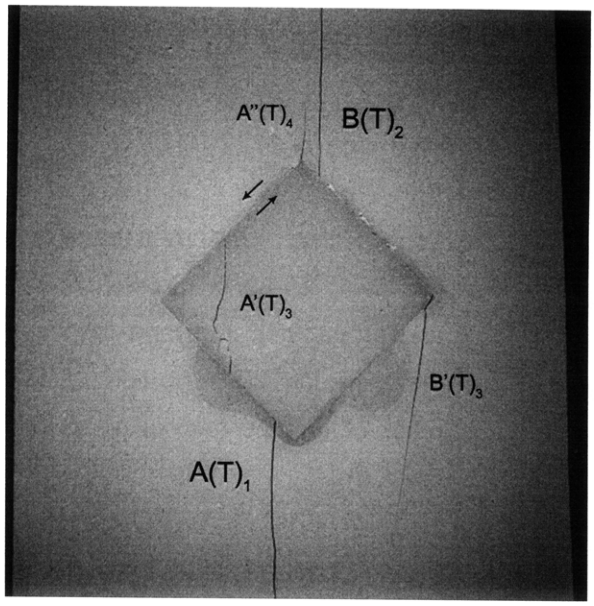

(Recorded by High Speed Video System)

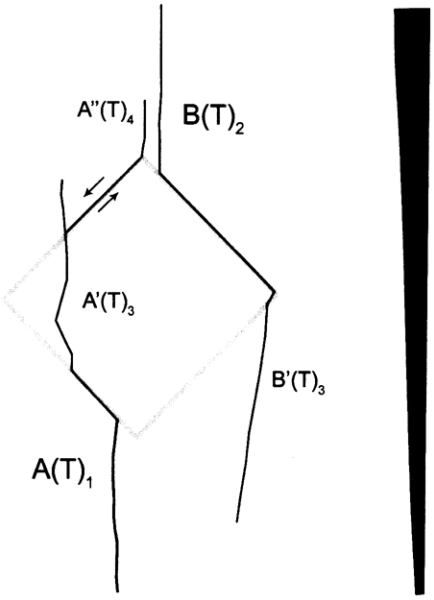

(23.09 MPa)
Time: 4 minutes & 50.698 seconds
HS Image # - 3821

The upper left-hand inclusion boundary debonds in shear from the hydrocal matrix. A new tensile crack (A''), which is an extension of tensile crack (A'), initiates at the upper inclusion boundary and propagates upwards.

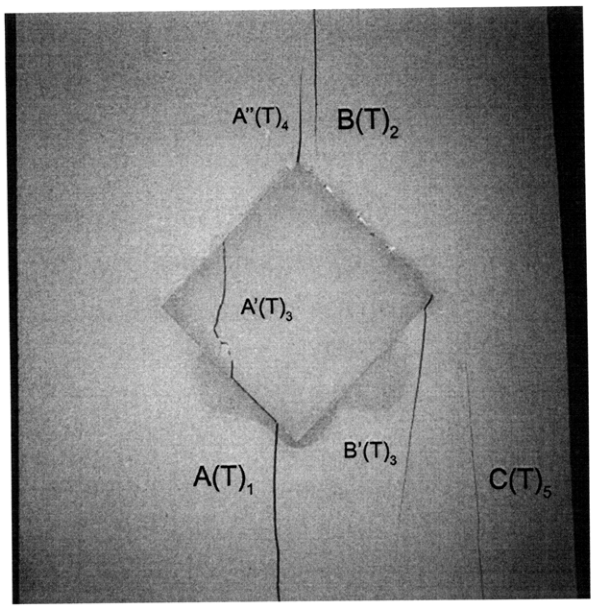

(Recorded by High Speed Video System)

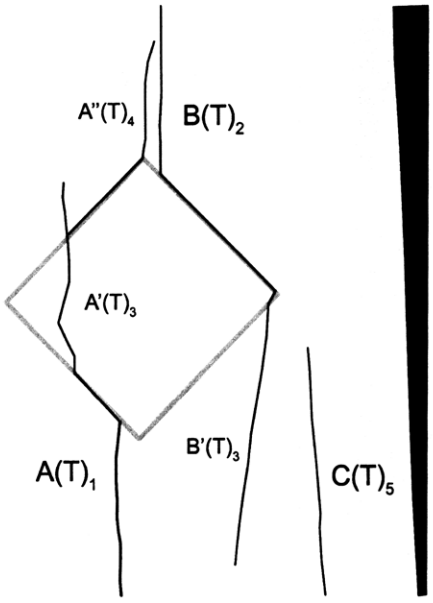

(23.09 MPa)
Time: 4 minutes & 50.698 seconds
HS Image # - 3818

A new tensile crack (C) initiates at the lower specimen boundary and propagates upwards.

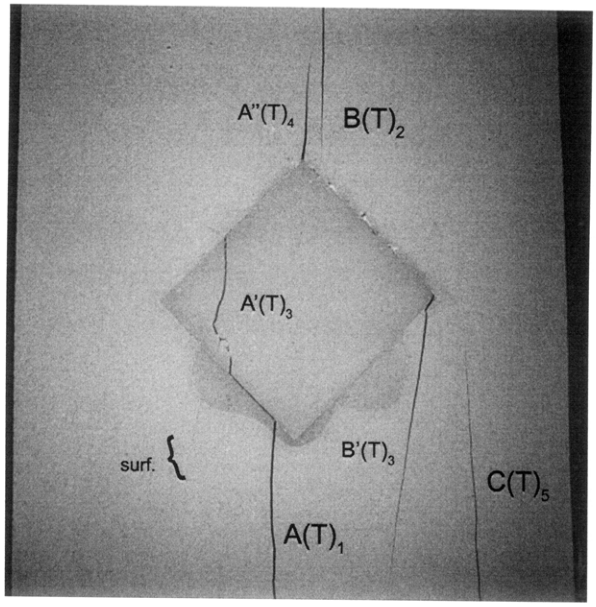

(Recorded by High Speed Video System)

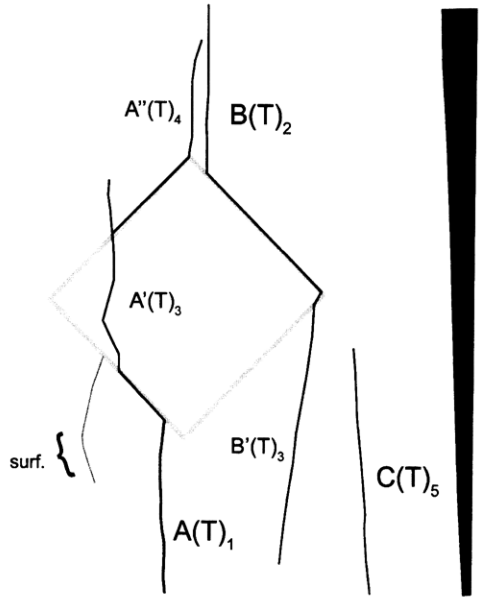

(23.09 MPa)
Time: 4 minutes & 50.700 seconds
HS Image # - 3809

A surface crack (surf.) initiates at the lower left-hand inclusion boundary and propagates towards tensile crack (A).

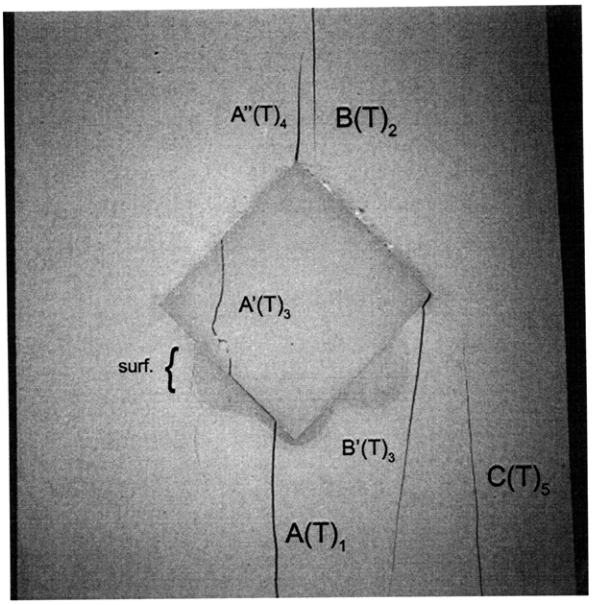

(Recorded by High Speed Video System)

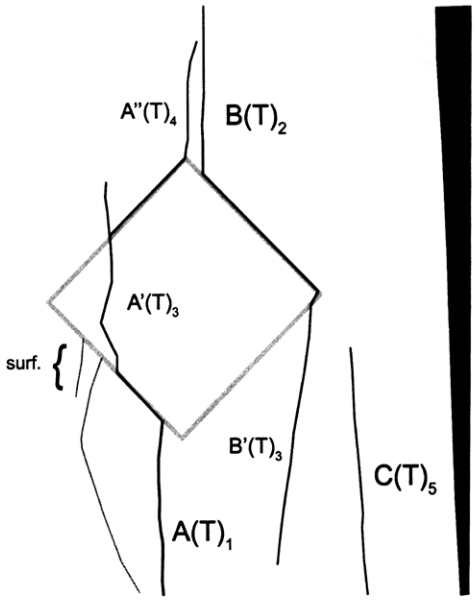

(23.09 MPa)
Time: 4 minutes & 50.705 seconds
HS Image # - 3785

A new surface crack (surf.) initiates at the lower left-hand inclusion boundary and propagates downwards.

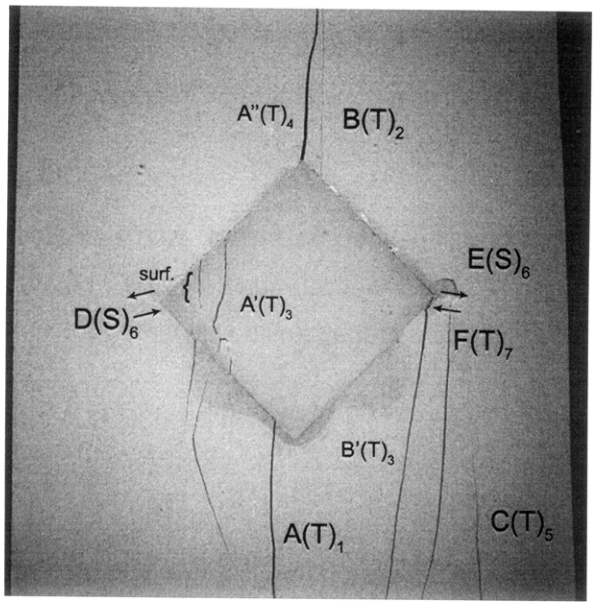

(Recorded by High Speed Video System)

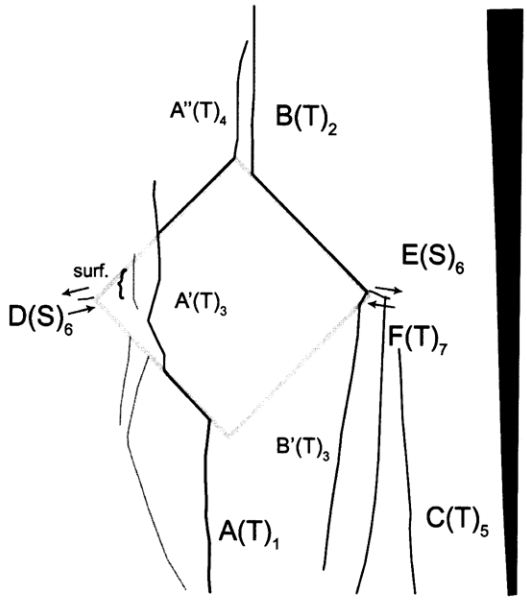

(23.24 MPa) – Ultimate Failure
Time: 4 minutes & 50.784 seconds
HS Image # - 3389

Shear cracks (D&E) initiate at the inclusion boundary and propagate away from the inclusion.

A new tensile crack (F) initiates at the lower specimen boundary and propagates until its coalescence with shear crack (E).

A new surface crack (surf.) initiates at the upper left-hand inclusion boundary and propagates into the inclusion.

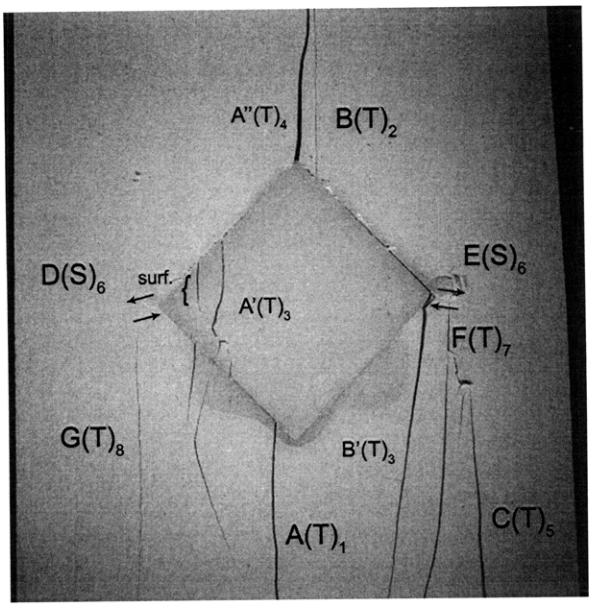

(Recorded by High Speed Video System)

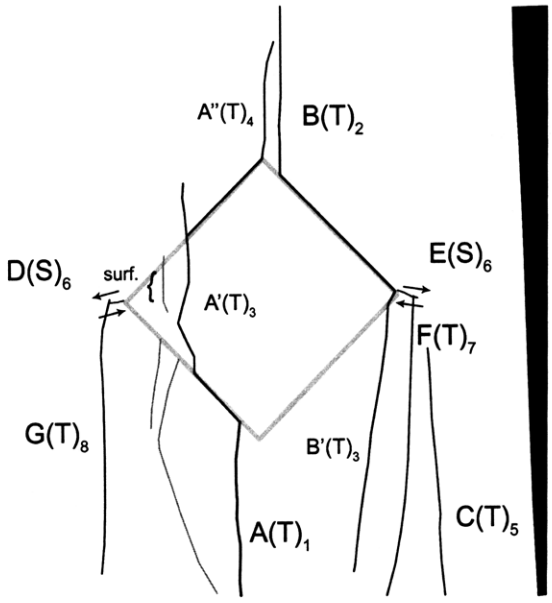

(23.13 MPa)
Time: 4 minutes & 50.785 seconds
HS Image # - 3383

A new tensile crack (G) initiates at the lower specimen boundary and propagates until its coalescence with shear crack (D).

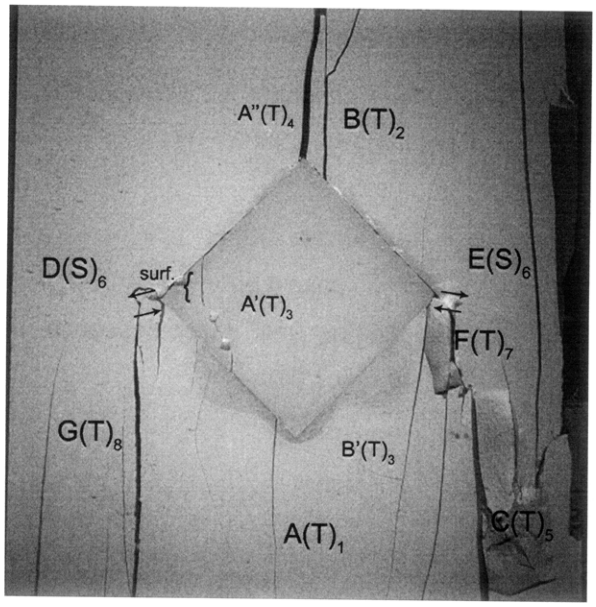

(Recorded by High Speed Video System)

(0 MPa) – Final Picture

Time: 4 minutes & 50.973 seconds

HS Image # - 2445

	Upper edge of the specimen. The cracks marked with a (*) coincide with the openings between the teeth of the brush platen.
	Lower edge of the specimen. The cracks marked with a (*) coincide with the openings between the teeth of the brush platen.

SUMMARY

Specimen Number: DM-5-UI (20080601)

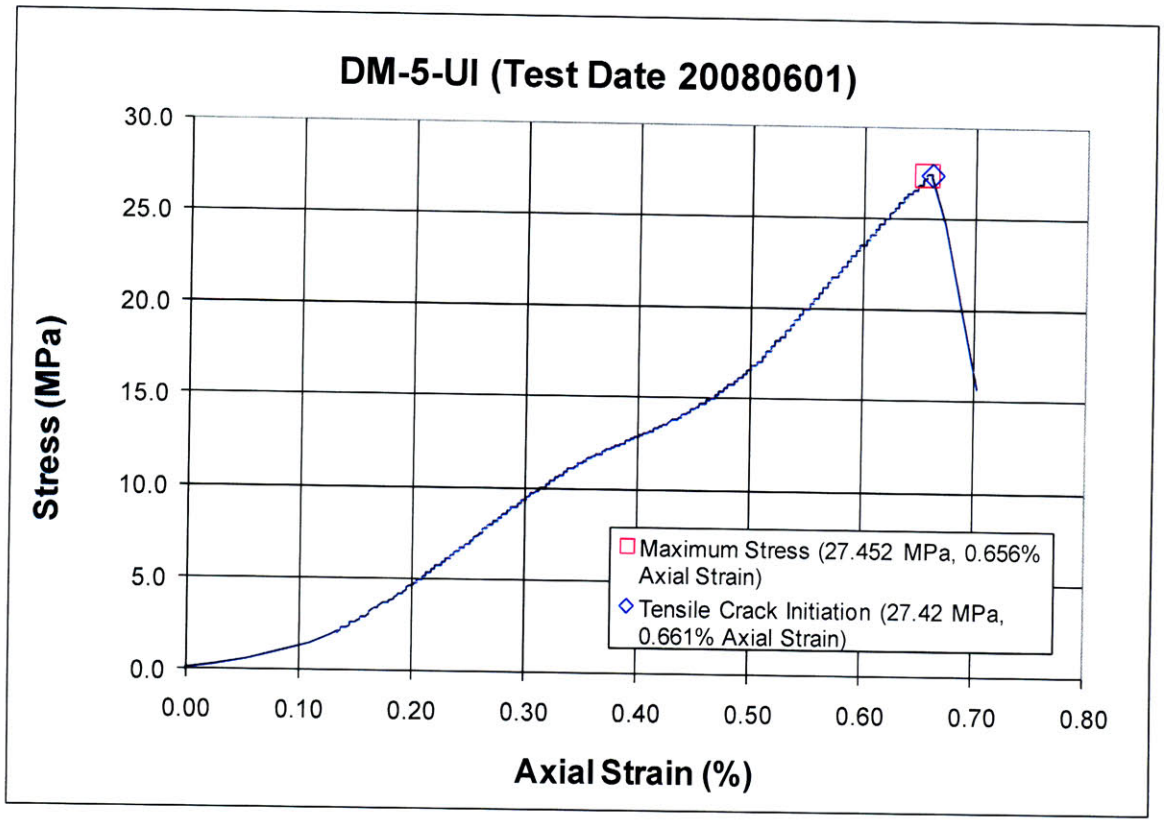

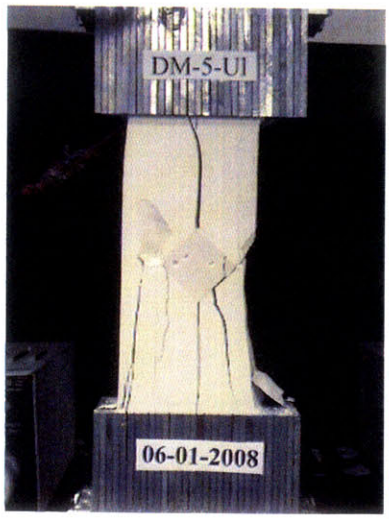

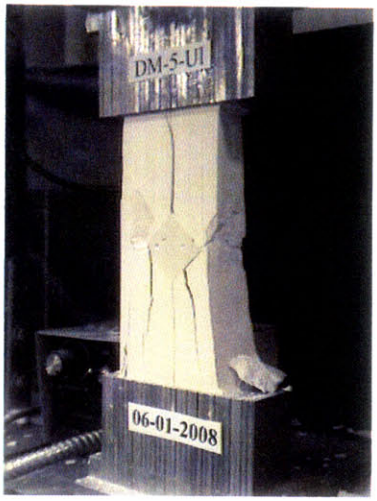

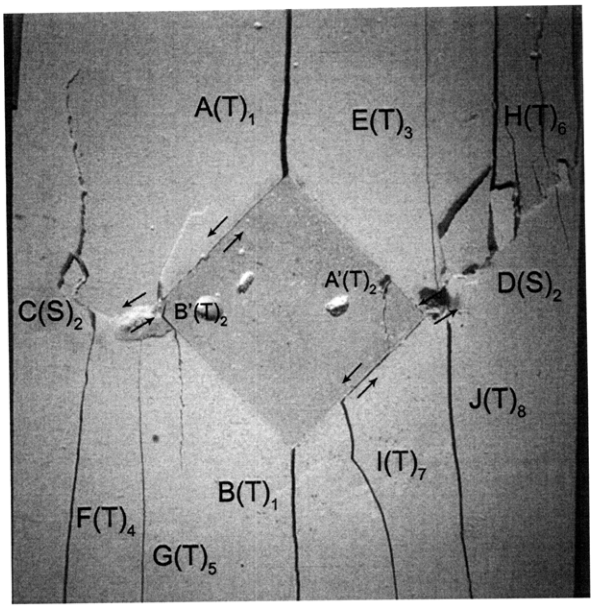

(Recorded by High Speed Video System)

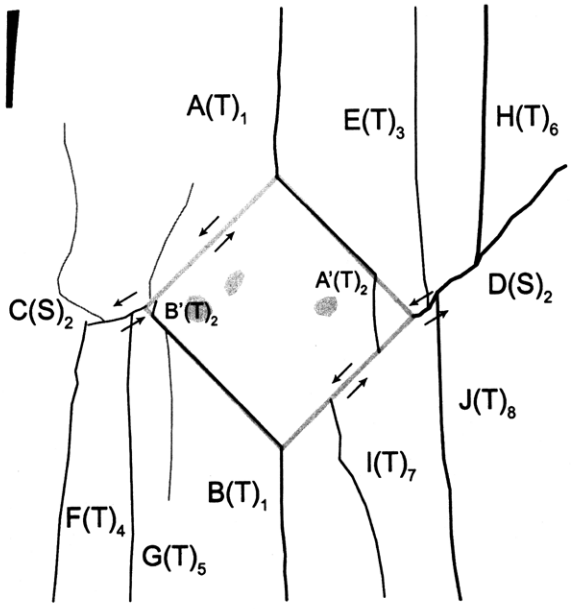

(22.561 MPa) – Ultimate Failure
Time: 5 minutes & 48.877 seconds
HS Image # - 3063

As shear crack (D) coalesces with the right-hand specimen boundary, a new tensile crack (J) initiates at shear crack (D) and propagates towards the lower specimen boundary.

SUMMARY

Specimen Number: DM-6-UI (20080601)

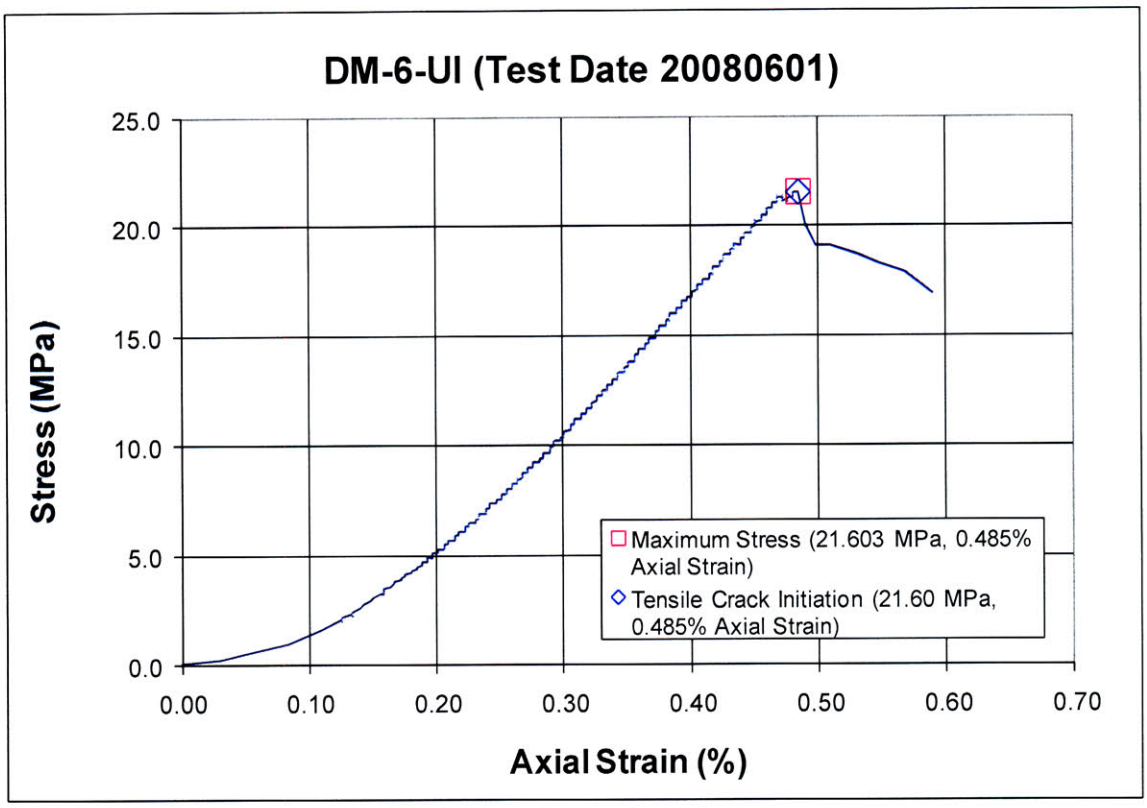

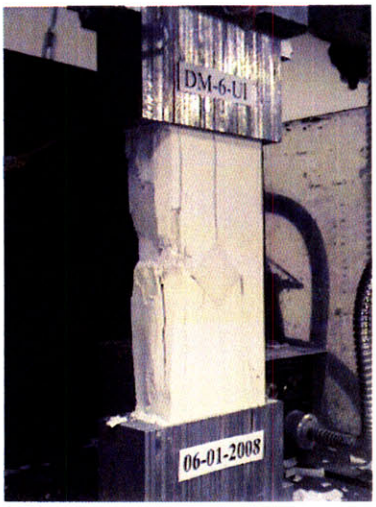

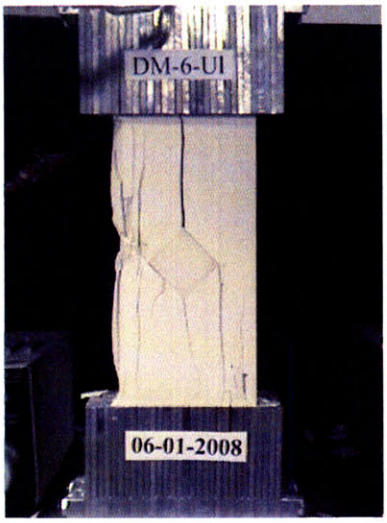

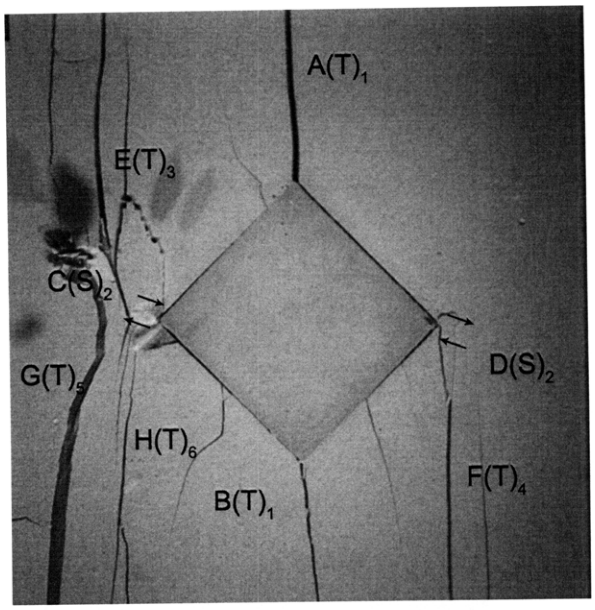

(Recorded by High Speed Video System)

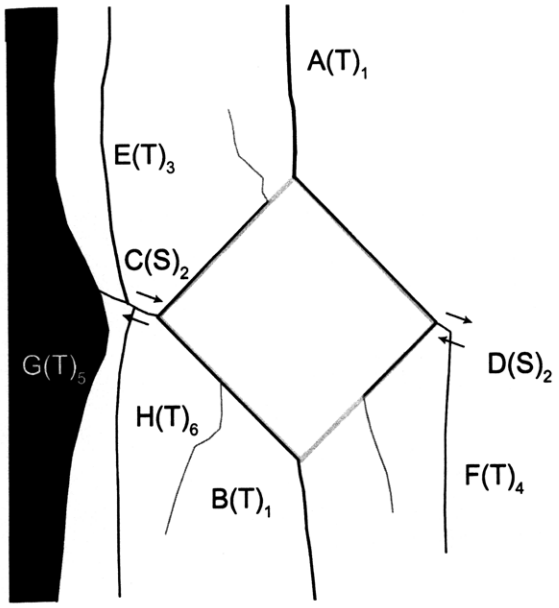

(17.033 MPa) – Ultimate Failure
Time: 4 minutes & 23.098 seconds
HS Image # - 2065

Shear crack (C) propagates until its coalescence with tensile crack (G).

Tensile crack (G) continues to propagate until its coalescence with the upper specimen boundary.

Specimen Number: SQ-4-PI (20080412)

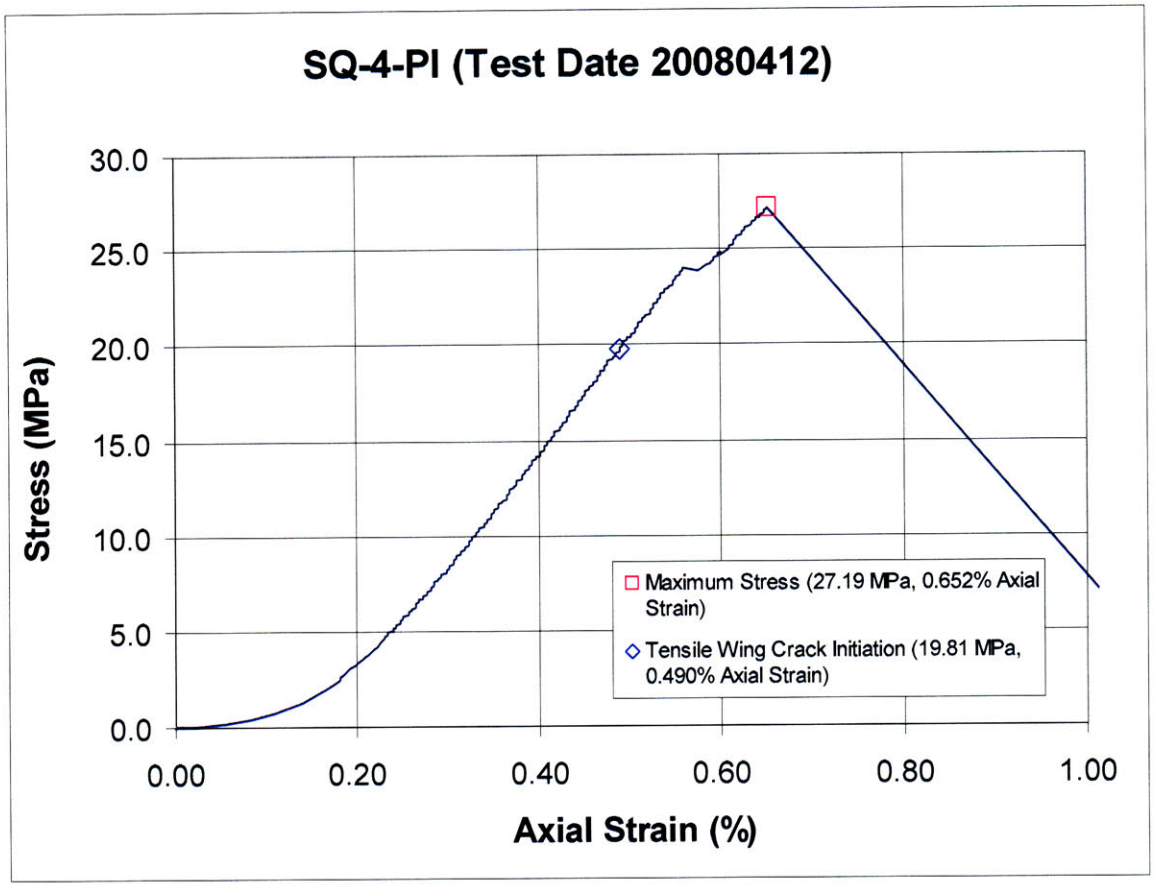

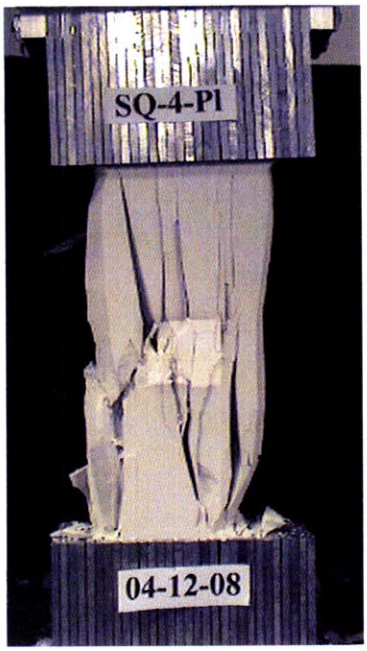

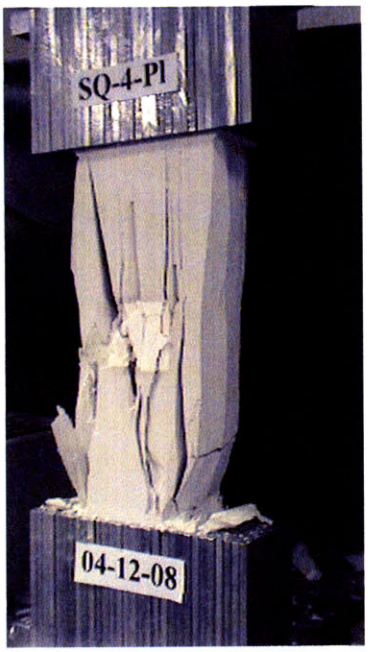

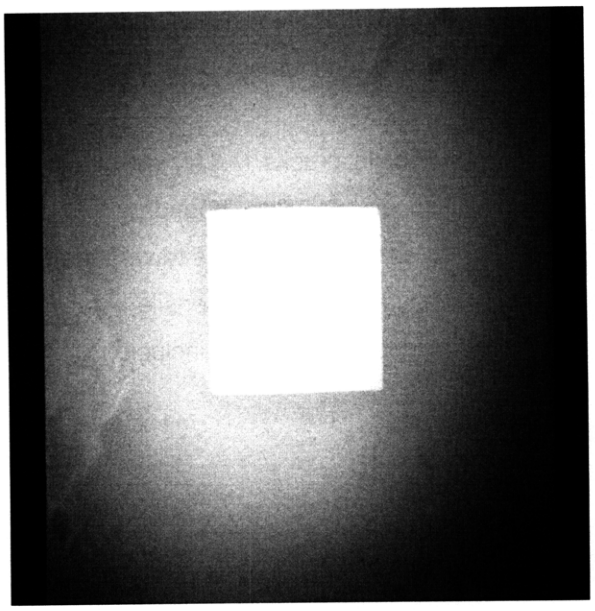

(Recorded by High Speed Video System)

Initial Inclusion Geometry:
SQUARE – Plaster Material

Inclusion **less** stiff than matrix.

High Speed Camera Frame Rate:
5000 pps

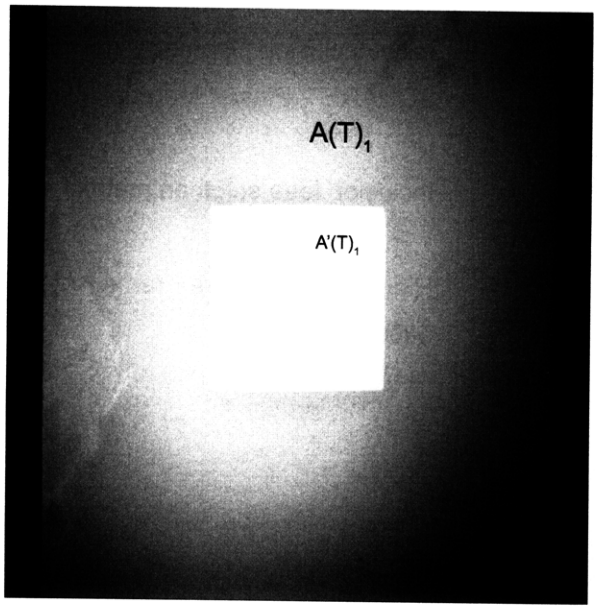

(Recorded by High Speed Video System)

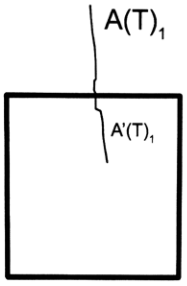

(19.81 MPa – Tensile Crack Initiation)
Time: 4 minutes & 0 seconds

Tensile cracks (A&A') develop at the upper inclusion boundary. Tensile crack (A) propagates toward the upper boundary, while tensile crack (A') propagates into the inclusion.

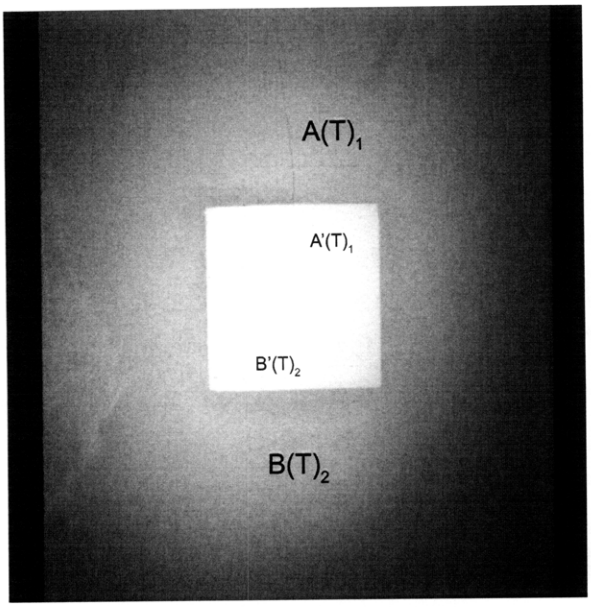

(Recorded by High Speed Video System)

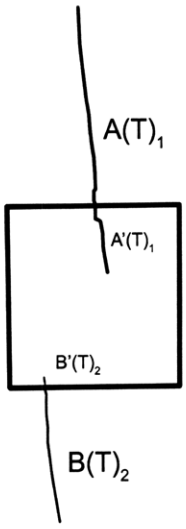

(20.51 MPa)
Time: 4 minutes & 10 seconds

As the aperture of tensile cracks (A&A') increase, tensile crack (A) propagates further towards the upper boundary.

New tensile cracks (B&B') develop at the lower inclusion boundary. Tensile crack (B) propagates toward the lower boundary, while tensile crack (B') propagates into the inclusion.

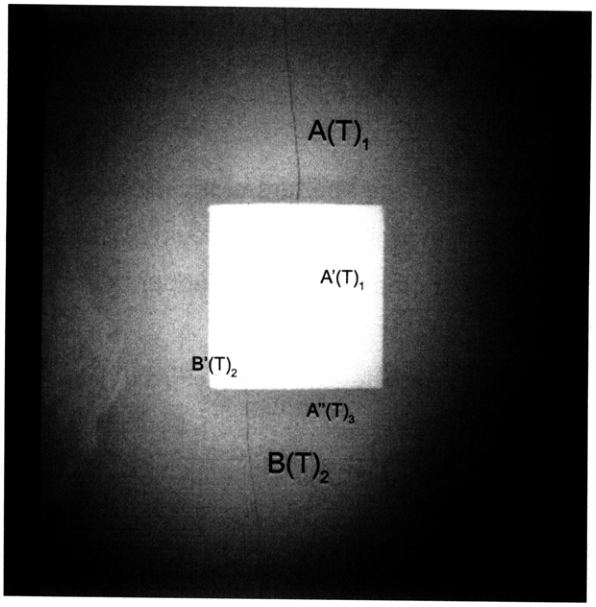

(Recorded by High Speed Video System)

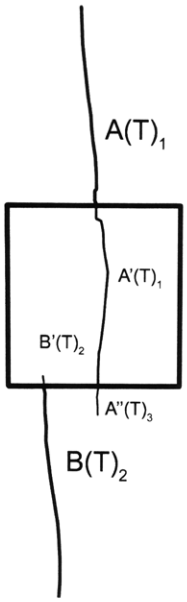

(21.63 MPa)
Time: 4 minutes & 26 seconds

As the apertures of tensile cracks (A&B) increase, tensile crack (A') propagates through the inclusion and intersects with lower inclusion boundary. This causes the formation of tensile crack A'' at the lower inclusion boundary, which begins to propagate towards the lower boundary.

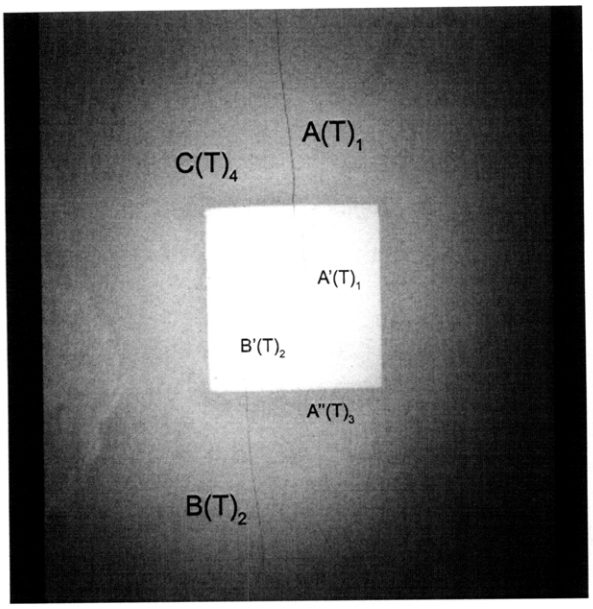

(Recorded by High Speed Video System)

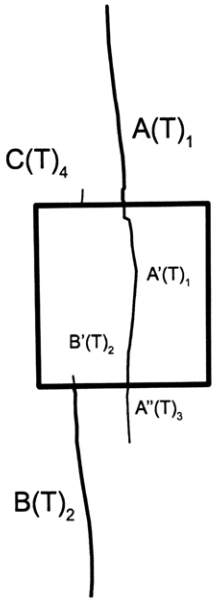

(22.58 MPa)
Time: 4 minutes & 40 seconds

As the apertures of tensile cracks (A'&A") increase, tensile crack (A") continues to propagate toward the lower boundary.

A new tensile crack (C) forms at the upper inclusion boundary.

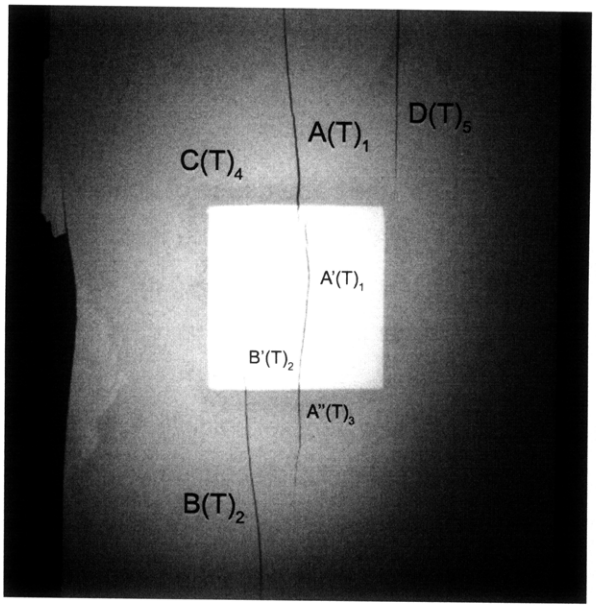

(Recorded by High Speed Video System)

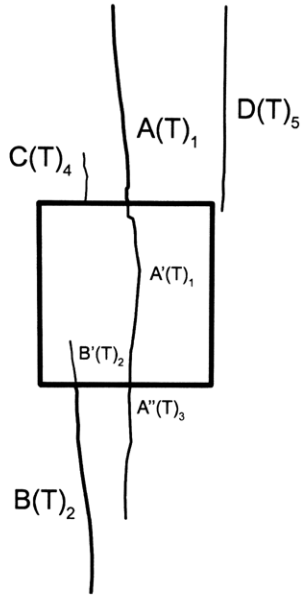

(23.85 MPa)
Time: 4 minutes & 58 seconds

Prior to the capture of this image, a large piece of the specimen breaks off from the left side.

This causes the apertures of tensile cracks (A,A',A'',B,&B'') to increase, and leads to the propagation of tensile cracks (A''&C).

A new tensile crack (D) develops from the upper boundary and propagates towards the upper right-hand corner of the inclusion.

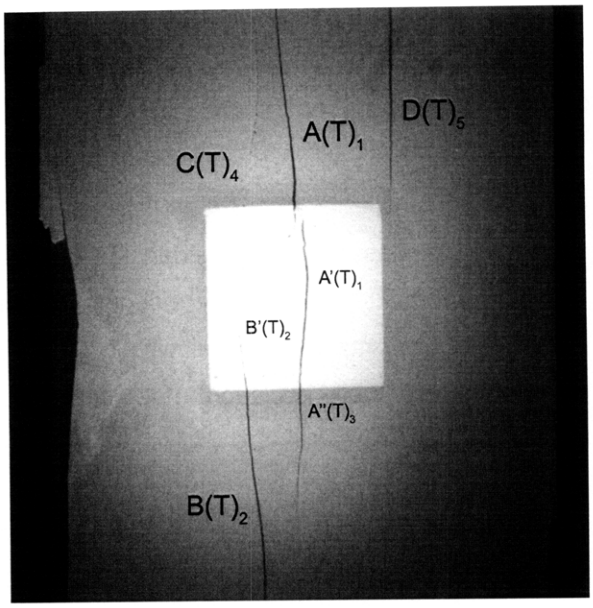

(Recorded by High Speed Video System)

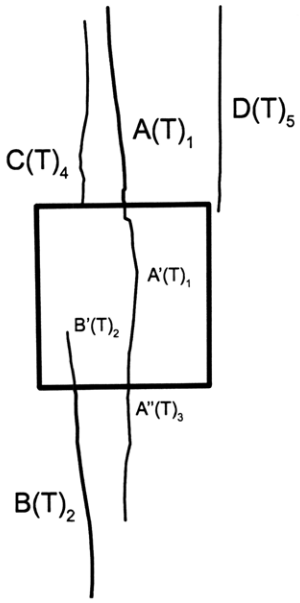

(26.21 MPa)
Time: 5 minutes & 32 seconds

With an increase in loading, tensile crack (B') continues to propagate into the inclusion, while tensile crack (C) continues to propagate towards the upper boundary.

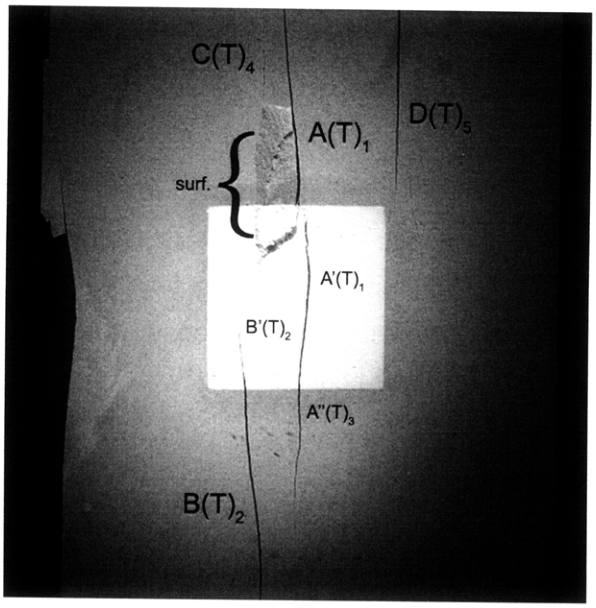

(Recorded by High Speed Video System)

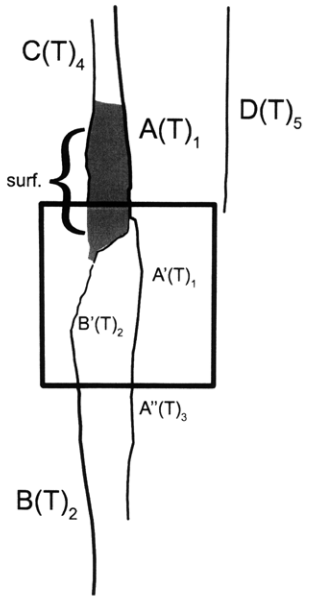

(27.156 MPa)
Time: 5 minutes & 46.567 seconds
HS Image # - 5404

Tensile crack (B') propagates until it coalesces with an extension of tensile crack (A). This induces surface cracking, designated with a "{", which eventually leads to the detachment of a surface piece.

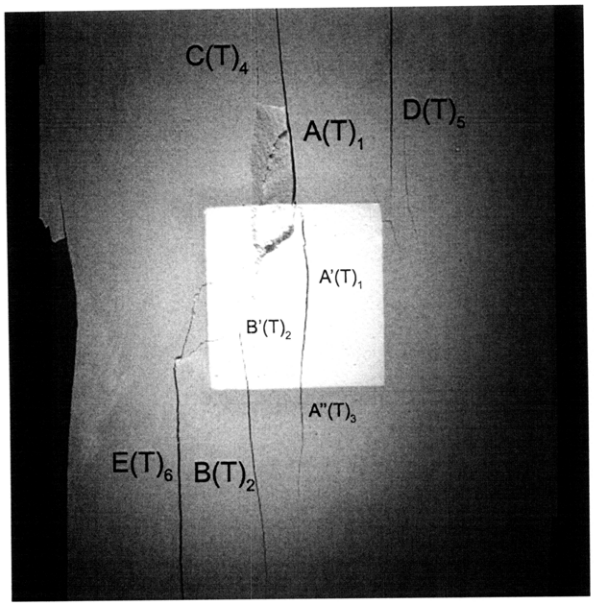

(Recorded by High Speed Video System)

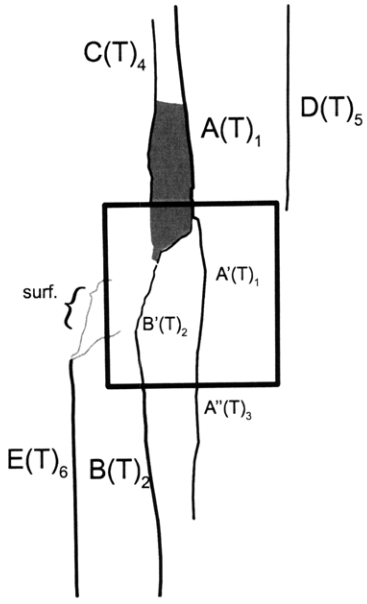

(27.185 MPa)
Time: 5 minutes & 46.996 seconds
HS Image # - 3258

A new tensile crack (E) develops from the lower boundary and propagates up until it coalesces with two surface cracks adjacent to the inclusion.

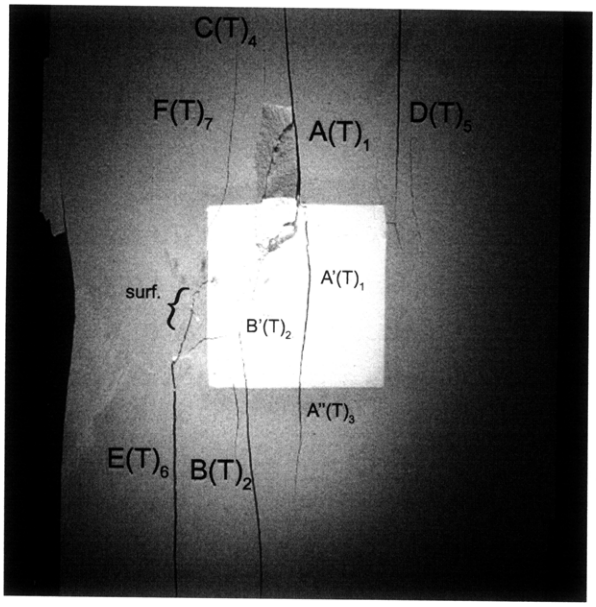

(Recorded by High Speed Video System)

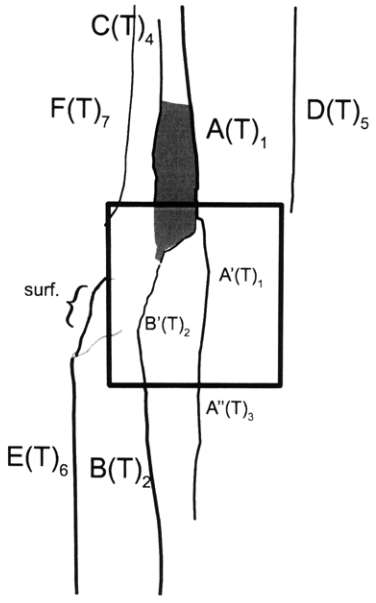

(27.185 MPa)
Time: 5 minutes & 46.999 seconds
HS Image # - 3244

Tensile crack (E) propagates beneath a surface crack until it intersects the inclusion boundary. A new tensile crack (F) forms in the top left-hand corner of the inclusion.

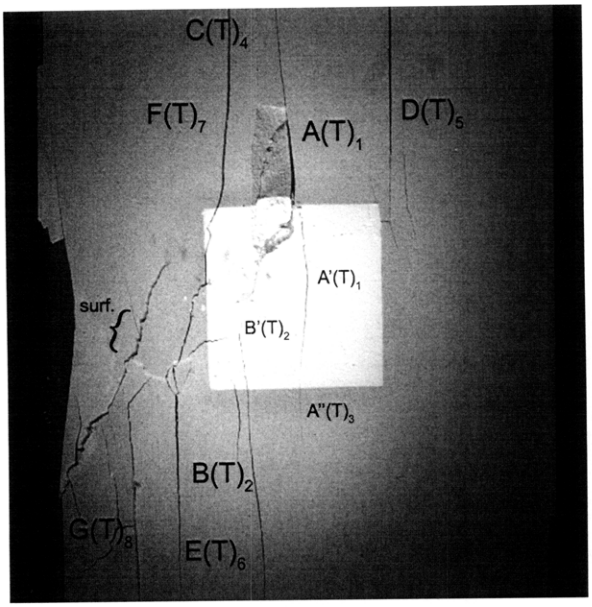

(Recorded by High Speed Video System)

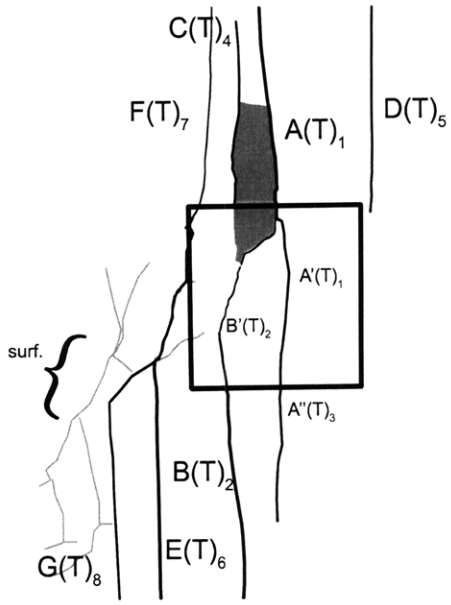

(27.185 MPa [Max Stress] – FAILURE)
Time: 5 minutes & 47 seconds
HS Image # - 3239

A new tensile crack (G) forms and coalesces with tensile crack (E). This causes several surface cracks to develop. Tensile crack (E) continues to propagate and coalesces with tensile crack (F). This induces ultimate failure.

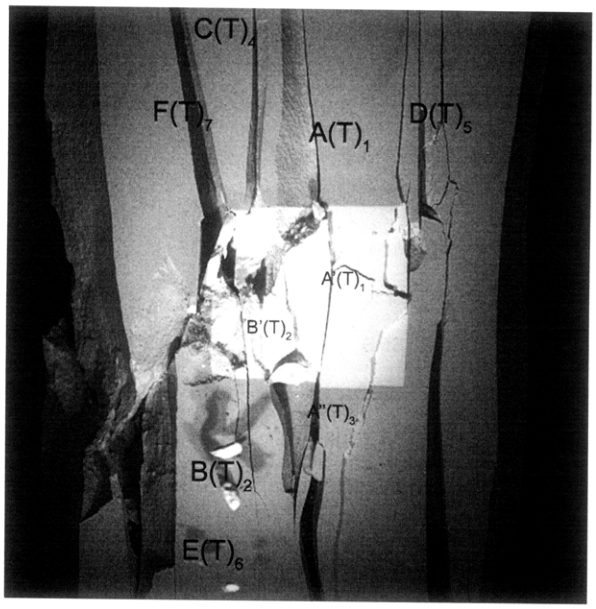

(Recorded by High Speed Video System)

(0 MPa – Final Picture)

HS Image # - 1299

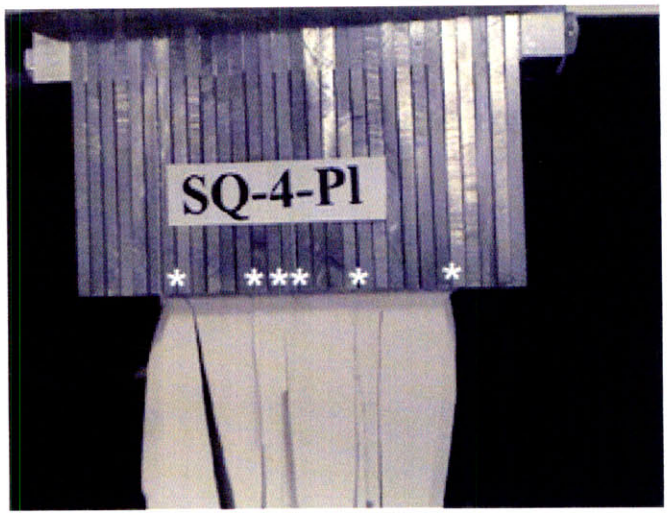	Upper edge of the specimen. The cracks marked with a (*) coincide with the openings between the teeth of the brush platen.
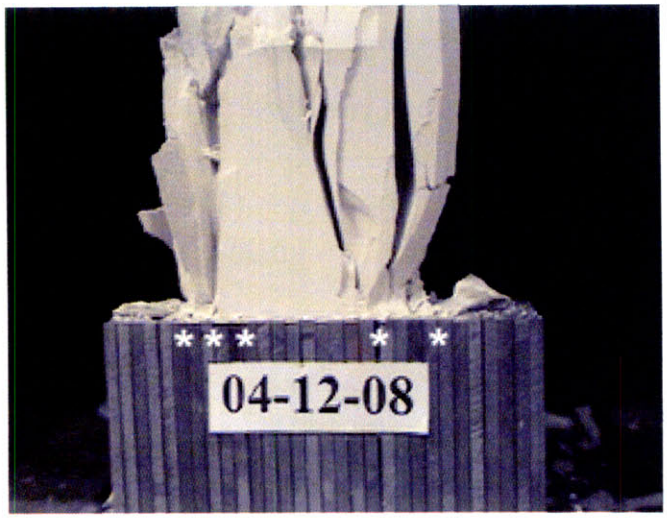	Lower edge of the specimen. The cracks marked with a (*) coincide with the openings between the teeth of the brush platen.

SUMMARY

Specimen Number: SQ-5-PI (20080412)

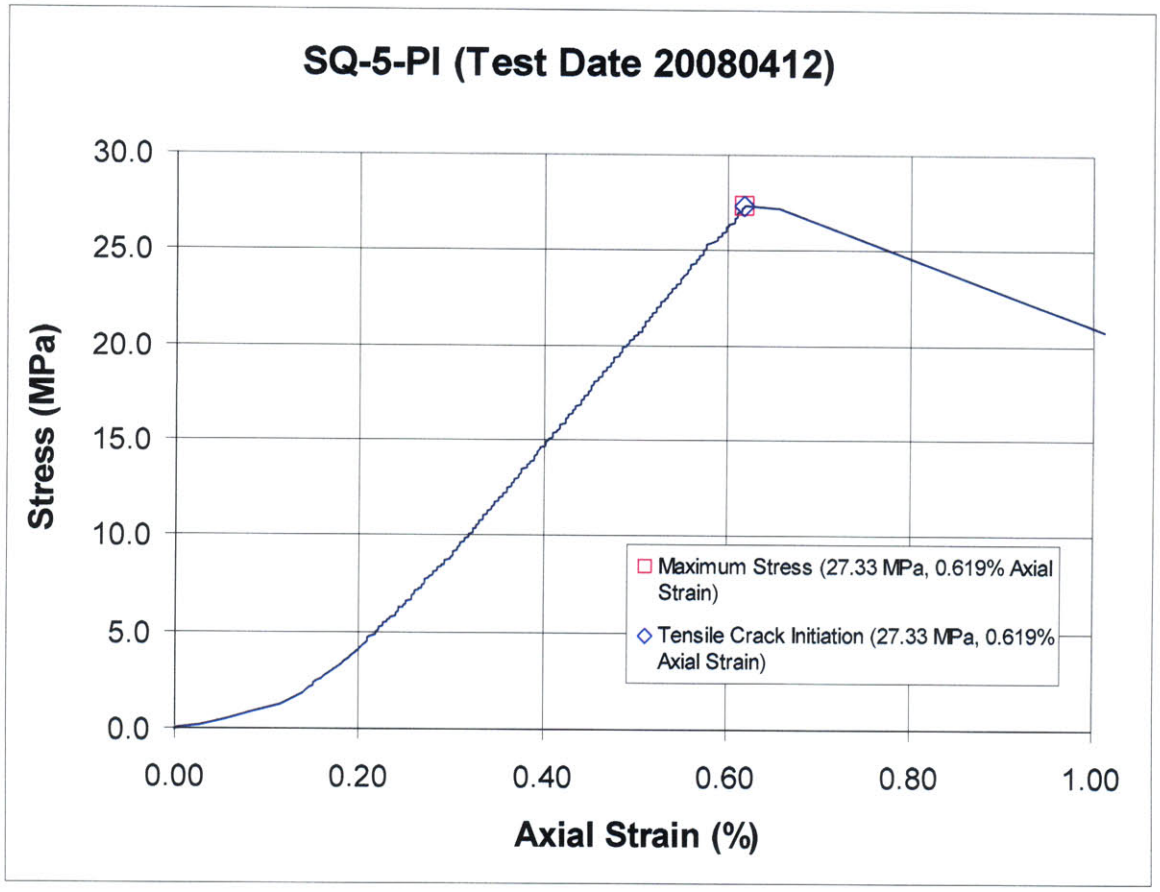

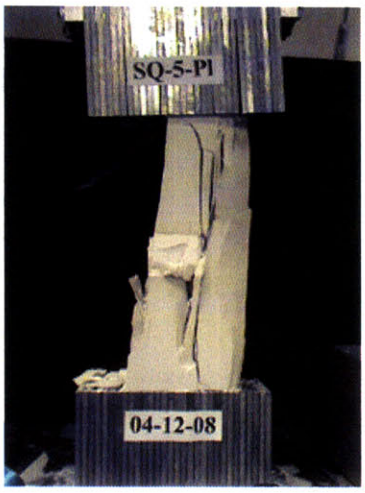

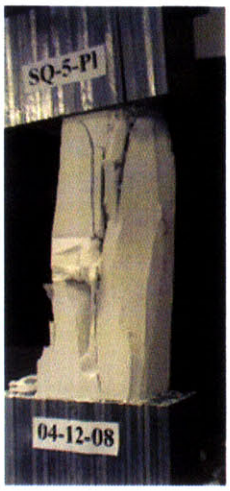

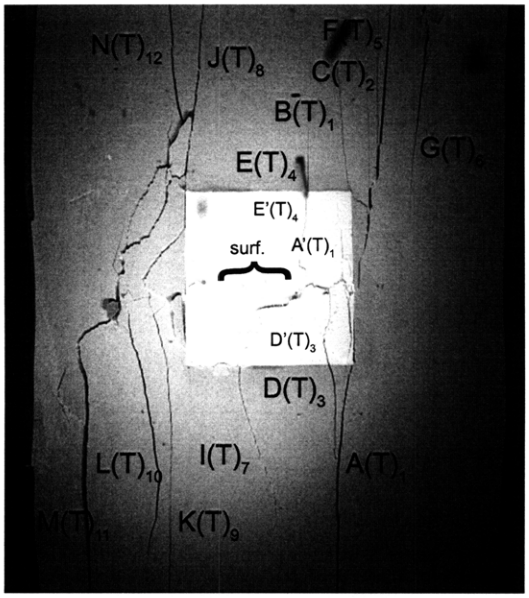

(Recorded by High Speed Video System)

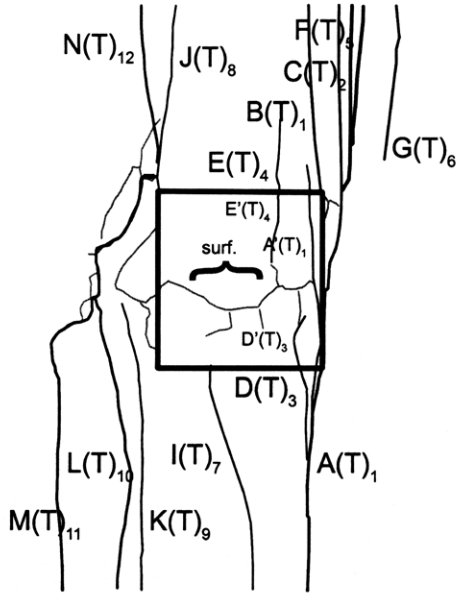

(27.268 MPa – Ultimate Failure)
Time: 5 minutes & 52.627 seconds
HS Image # - 2270

As tensile crack (L) continues to propagate, a new tensile crack (N) forms and propagates towards the upper specimen boundary. This results in ultimate failure.

SUMMARY

Specimen Number: SQ-7-PI (20080517)

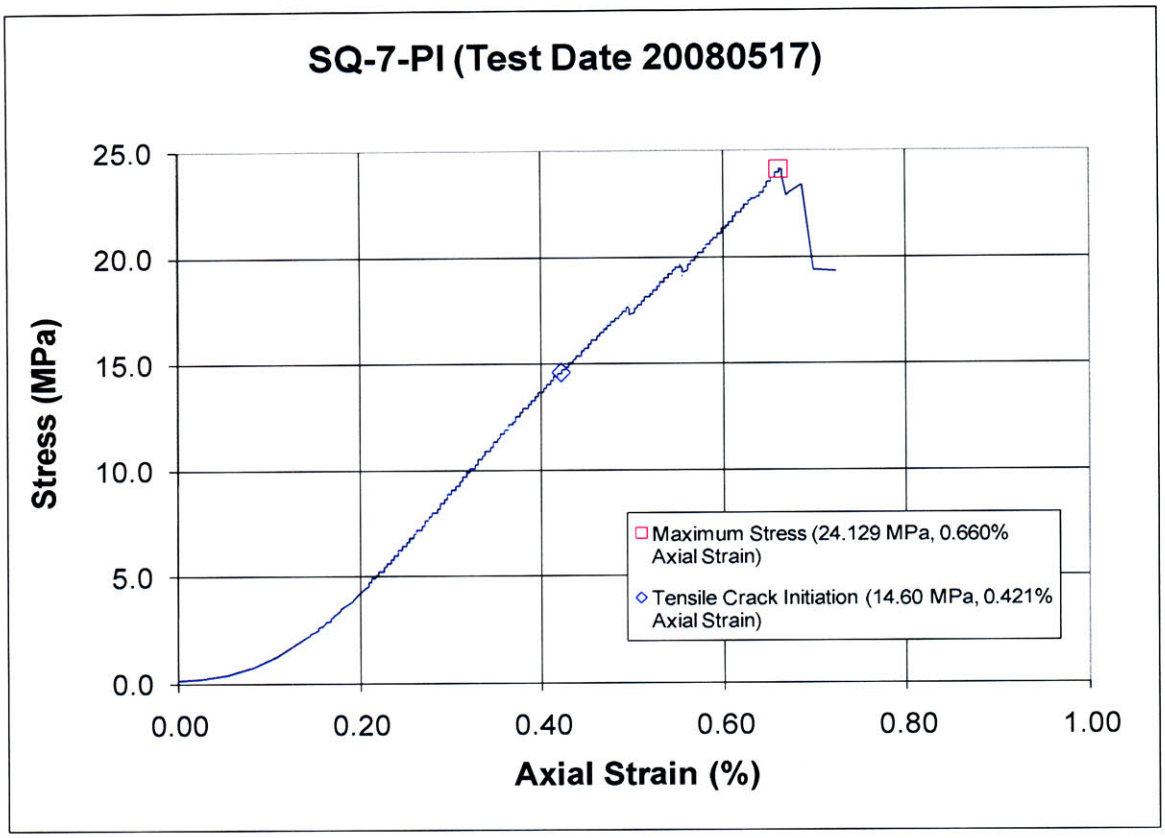

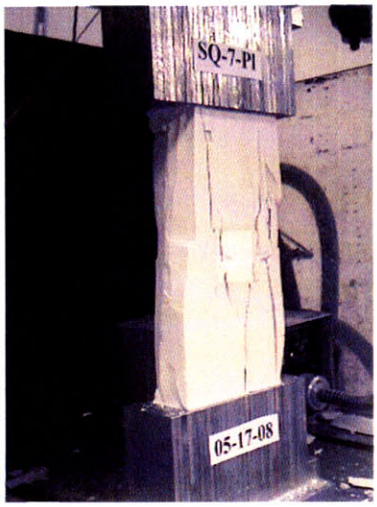

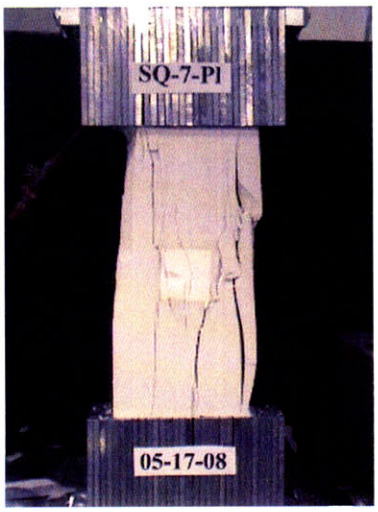

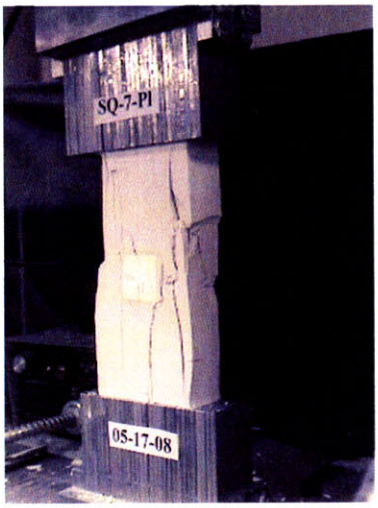

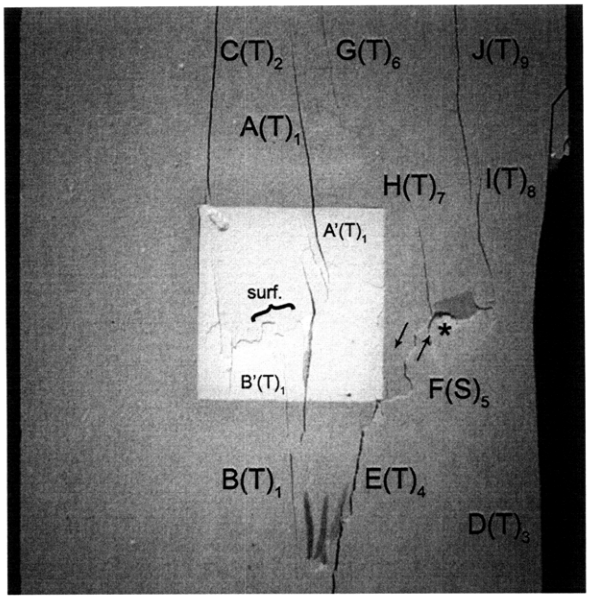

(Recorded by High Speed Video System)

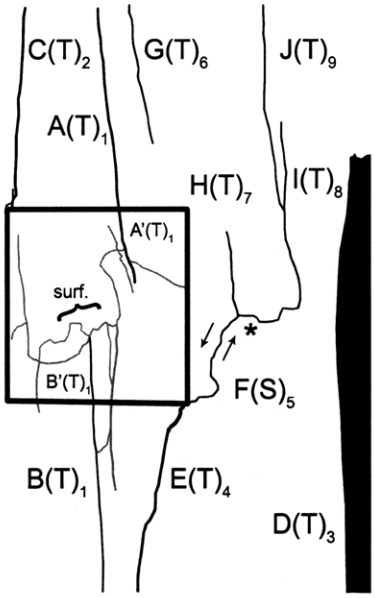

24.129 MPa [Max. Stress] – FAILURE
Time: 5 minutes & 0.840 seconds
HS Image # - 1697

Tensile crack (J) coalesces with tensile crack (I), which results in failure.

SUMMARY

Specimen Number: SQ-8-UI (20080517)

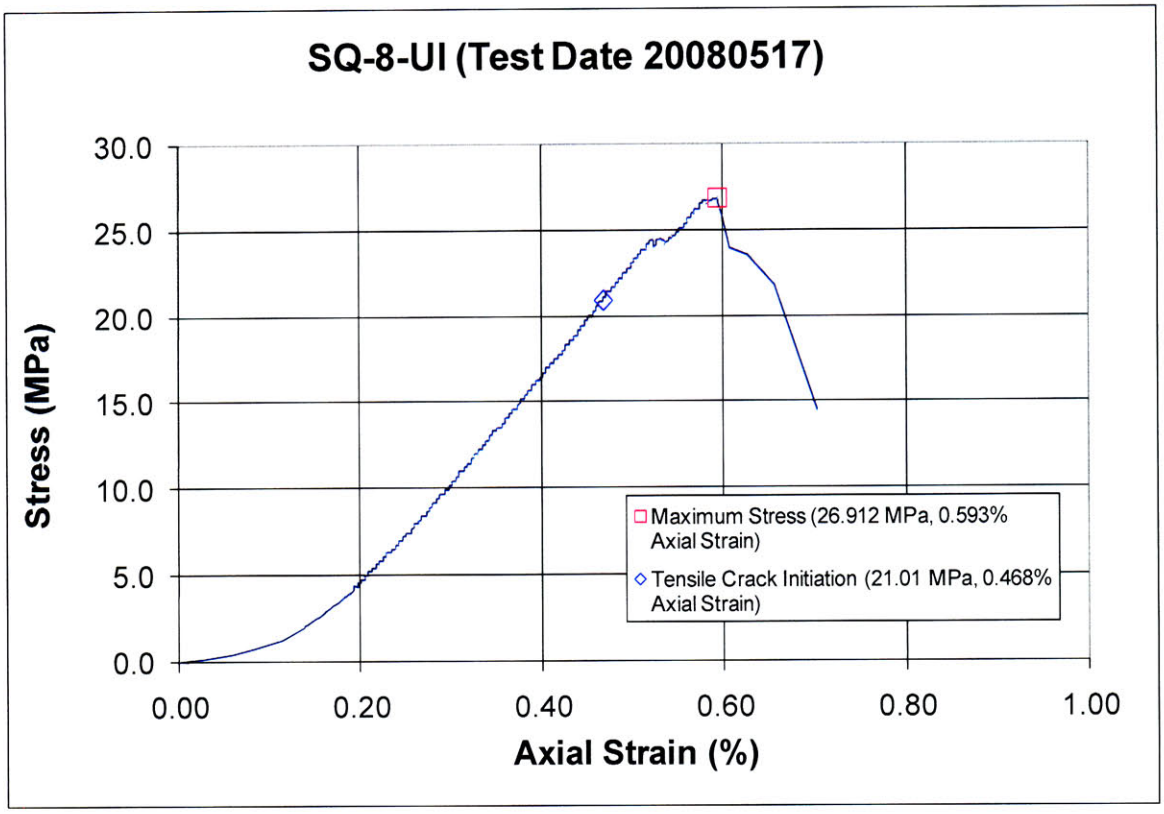

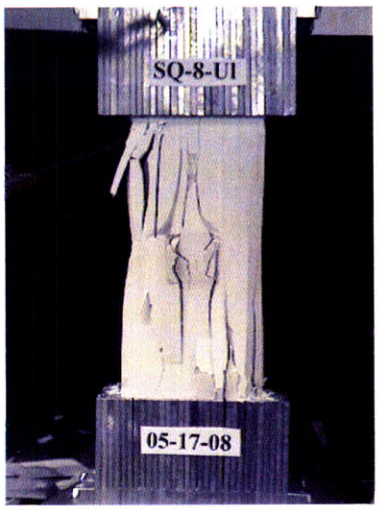

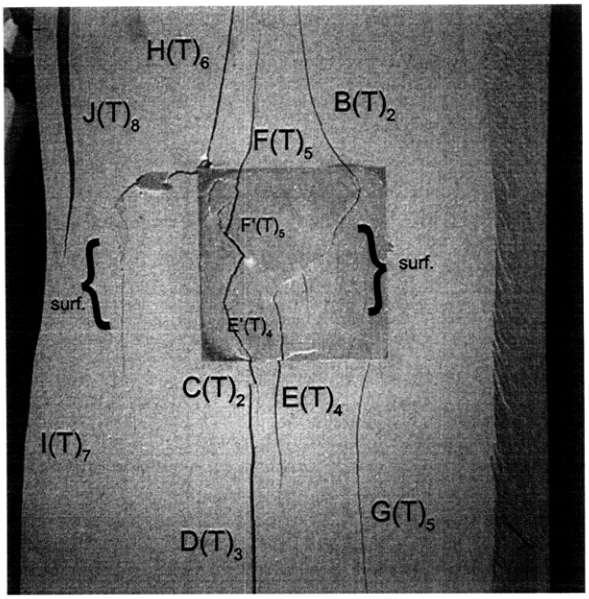

(Recorded by High Speed Video System)

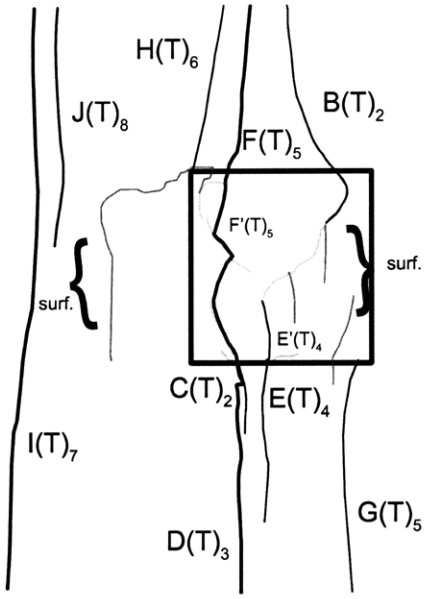

26.912 MPa [Max. Stress] – FAILURE
Time: 5 minutes & 37.360 seconds
HS Image # - 2268

Tensile crack (F') coalesces with tensile crack (C) and then with tensile crack (D), which causes the failure of the specimen.

SUMMARY

Specimen Number: SQ-9-UI (20080517)

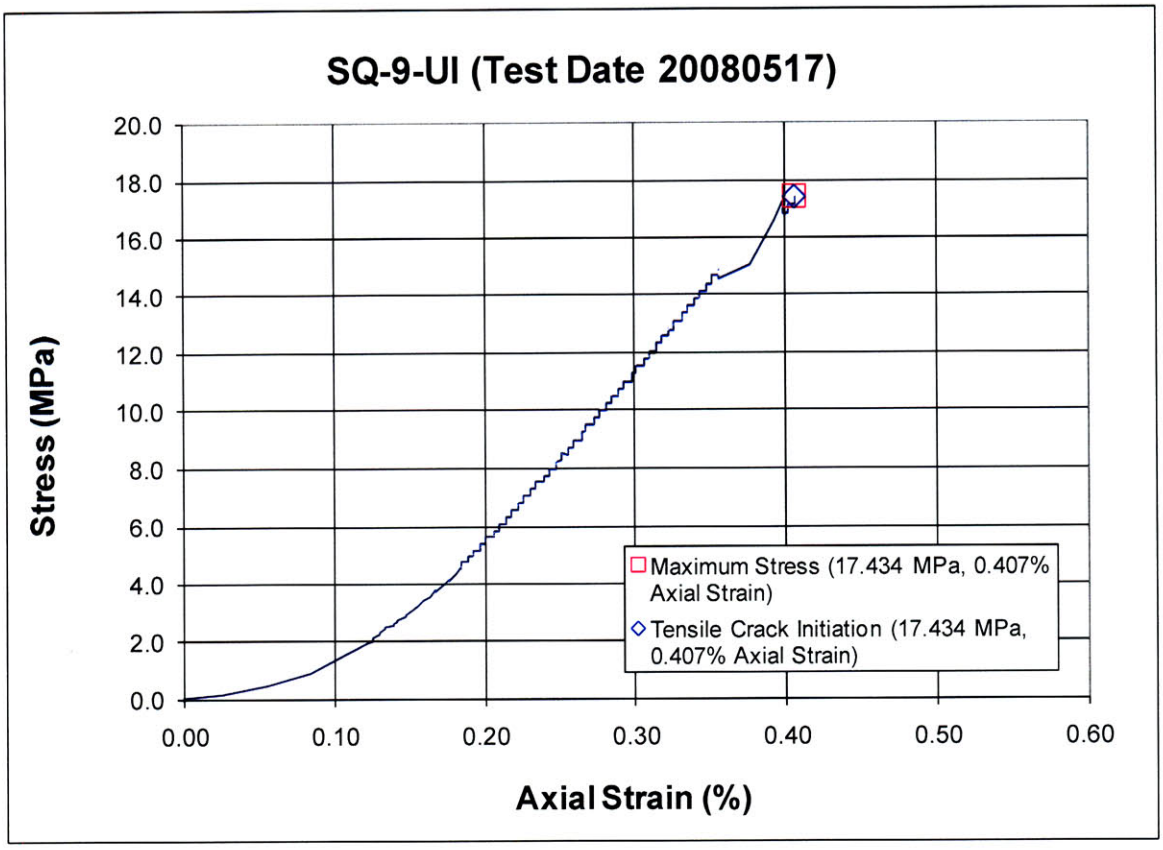

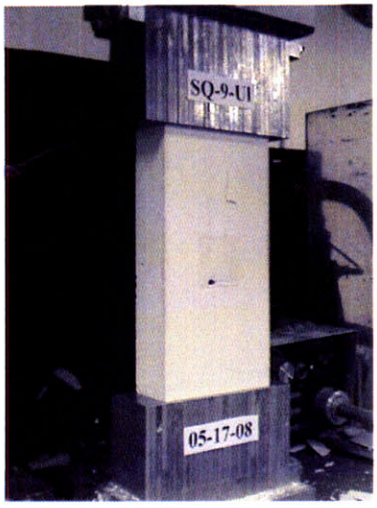

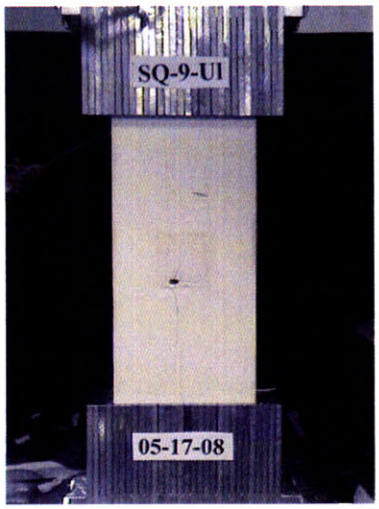

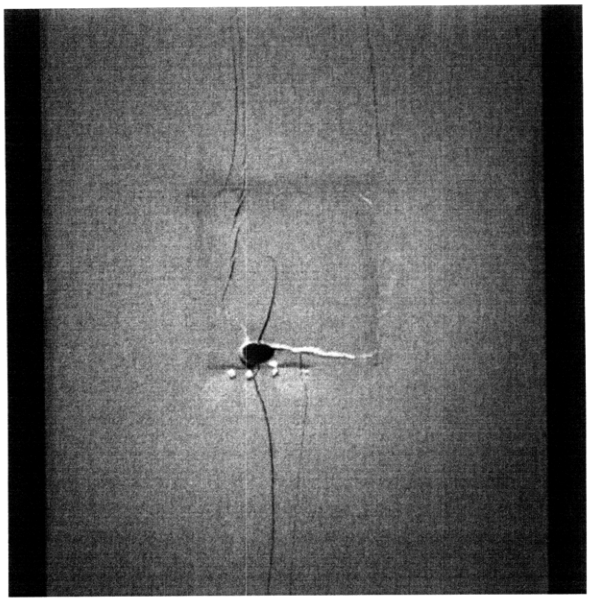

(Recorded by High Speed Video System)

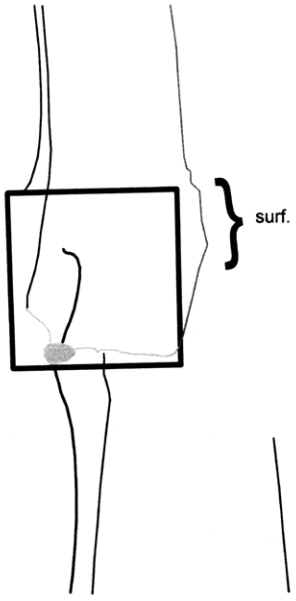

(17.434 MPa)
Time: 4 minutes & 19.84 seconds

Prior to tensile crack initiation, an error within the loading machine. This caused the hydraulic pump to stall for a prolonged period of time (as seen in the stress/strain curve). The cracks depicted in the figure occurred "simultaneously" as a result of the erratic loading rate.

Specimen Number: SQ-10-UI (20080518)

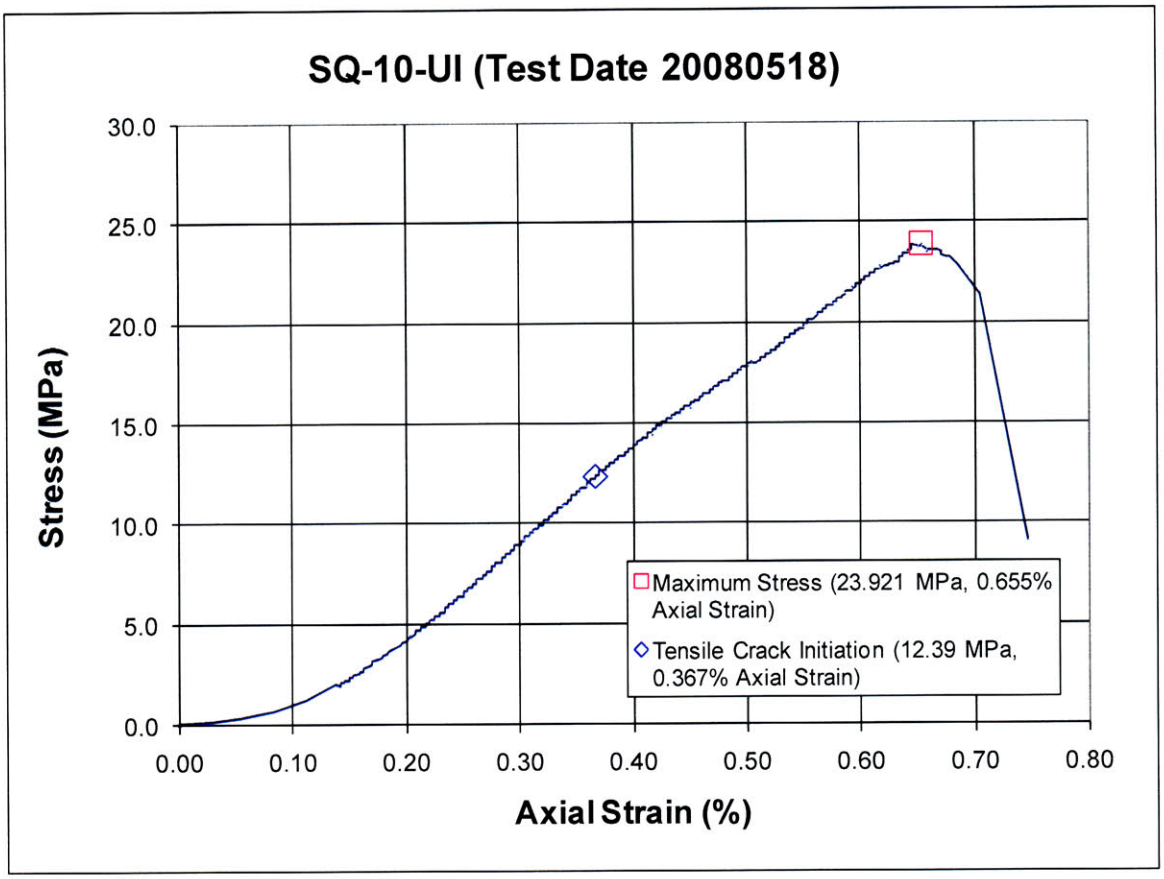

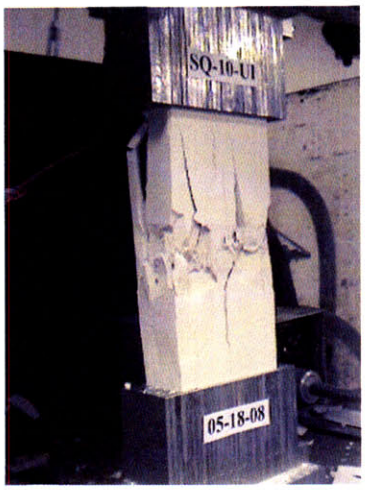

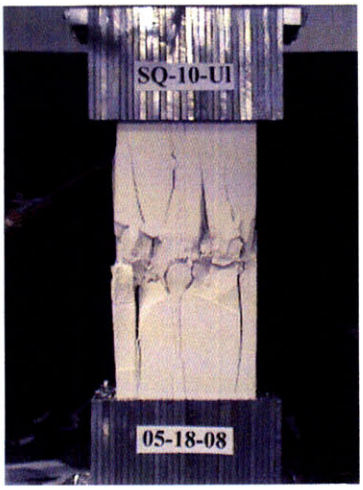

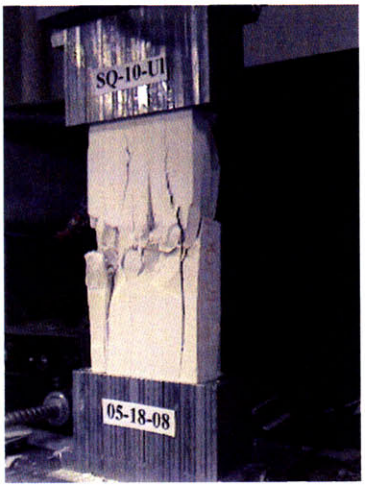

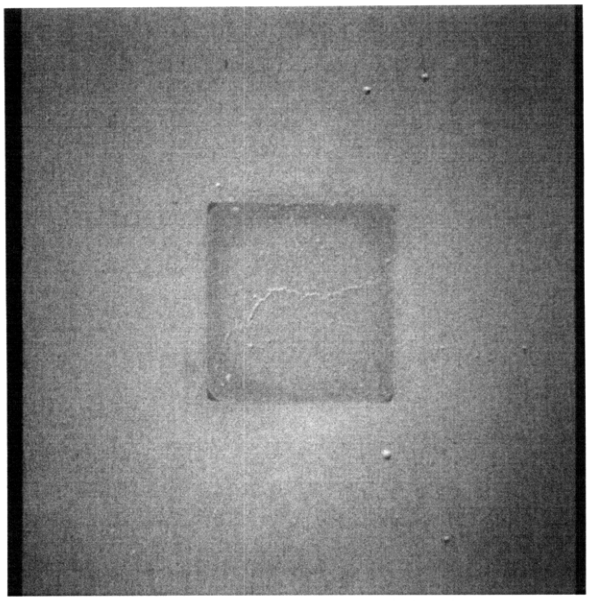

(Recorded by High Speed Video System)

Initial Inclusion Geometry:
SQUARE – Ultracal Material

Inclusion **more** stiff than matrix.

Initial surface cracks present prior to testing.

High Speed Camera Frame Rate:
5000 pps

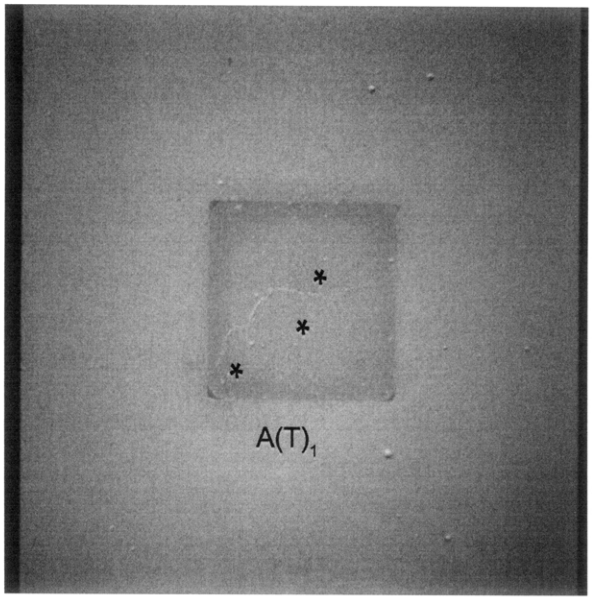

(Recorded by High Speed Video System)

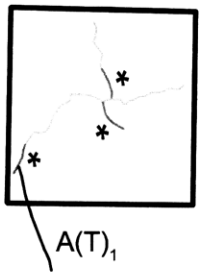

(12.39 MPa)

– Tensile Crack Initiation

Time: 2 minutes & 13.7 seconds

As new surface cracks (*) propagate from the initial surface cracks, a tensile crack (A) propagates from a new surface crack, intersects the inclusion boundary, and continues to propagate downwards into the surrounding hydrocal matrix.

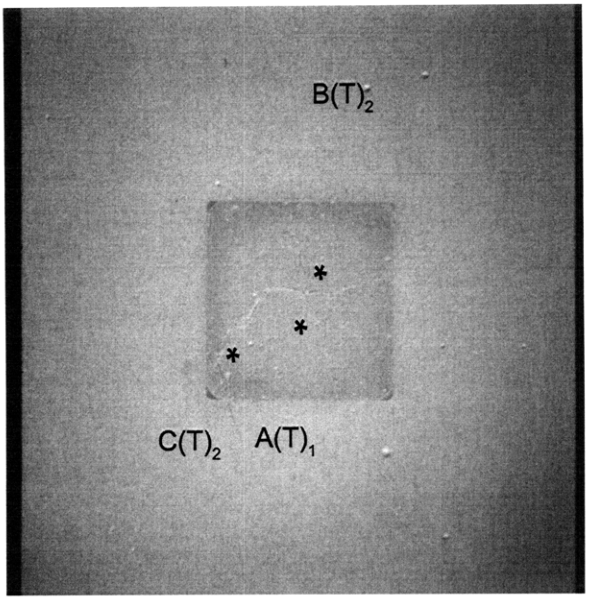

(Recorded by High Speed Video System)

(14.40 MPa)
Time: 2 minutes & 42.7 seconds

Two new tensile cracks (B&C) initiate at the inclusion boundary. Tensile crack (B) propagates from the upper inclusion boundary, and then coalesces with the initial surface crack within the inclusion. Tensile crack (C) propagates from the lower left-hand corner of the inclusion boundary.

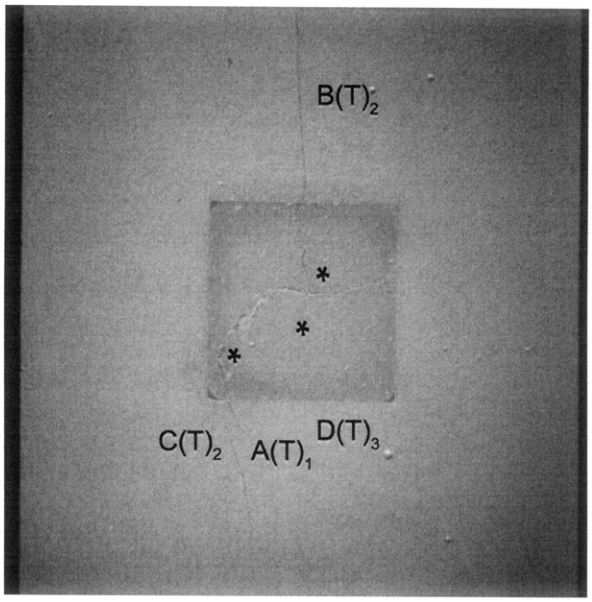

(Recorded by High Speed Video System)

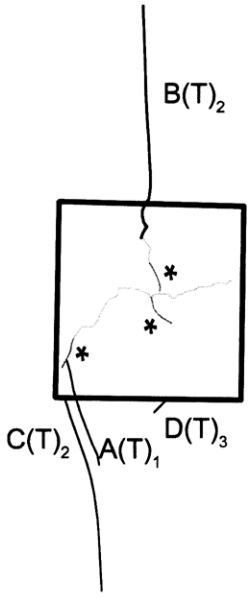

(15.68 MPa)
Time: 3 minutes & 1.2 seconds

Tensile cracks (B&C) propagate to the upper and lower specimen boundary, respectively. A new tensile crack (D) propagates from the lower inclusion boundary.

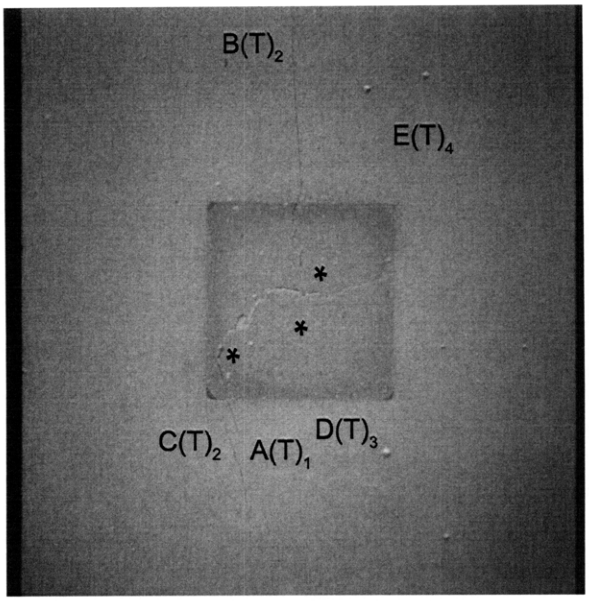

(Recorded by High Speed Video System)

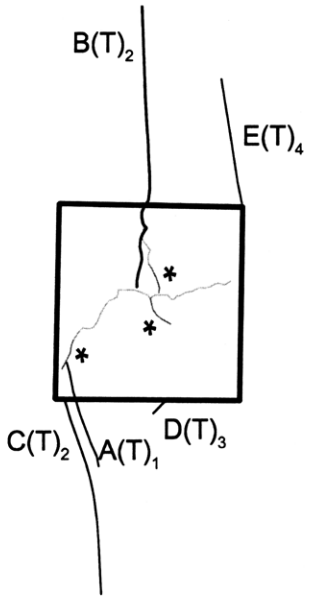

(16.57 MPa)
Time: 3 minutes & 13.7 seconds

As tensile crack (B) propagates until its coalescence with the central initial surface crack within the inclusion, a new tensile crack (E) propagates from the upper right-hand inclusion boundary.

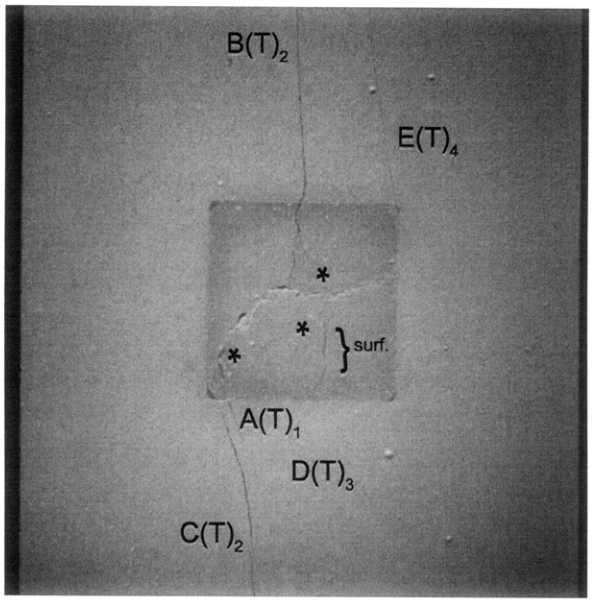

(Recorded by High Speed Video System)

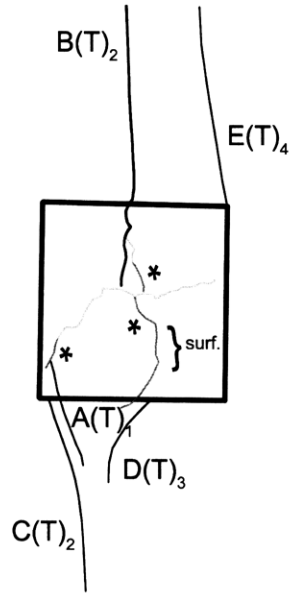

(18.29 MPa)
Time: 3 minutes & 38.598 seconds

As tensile cracks (D&E) propagate with an increase in loading, a previous surface crack (*), now referred to as (surf.), propagates past the inclusion boundary and into the surrounding hydrocal matrix.

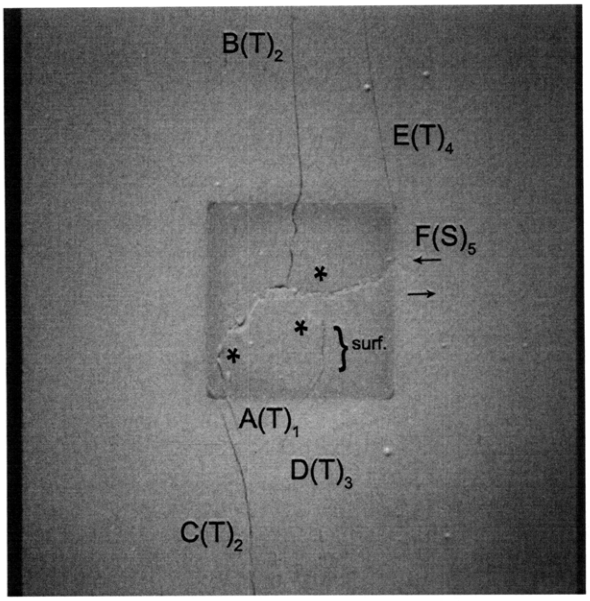

(Recorded by High Speed Video System)

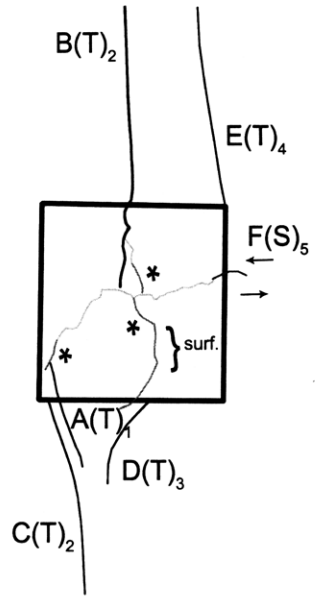

(20.34 MPa)
Time: 4 minutes & 8.1 seconds

A shear crack (F) propagates from the right-hand side of the inclusion, into the surrounding hydrocal matrix.

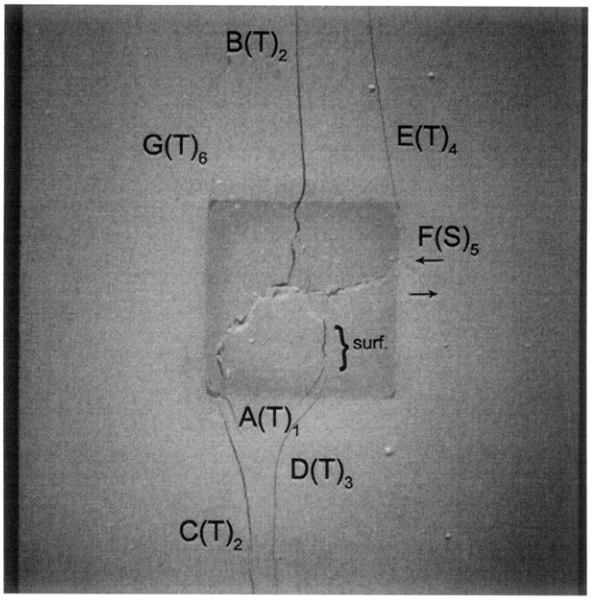

(Recorded by High Speed Video System)

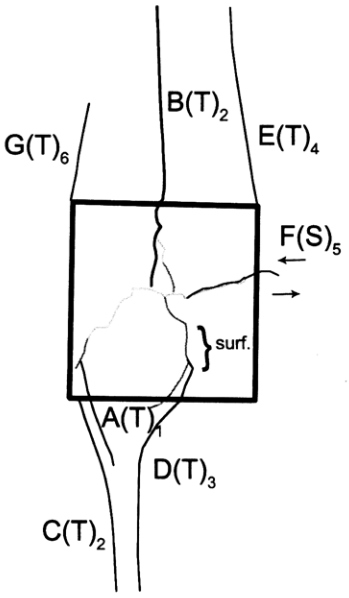

(22.93 MPa)
Time: 4 minutes & 45.3 seconds

Tensile crack (D) coalesces with a surface crack (surf.) within the inclusion. A new tensile crack (G) propagates from the upper left-hand inclusion boundary.

Small patches of spalling form adjacent to the central surface crack within the inclusion, as a result of shear crack (F) propagating into the inclusion through the central surface crack.

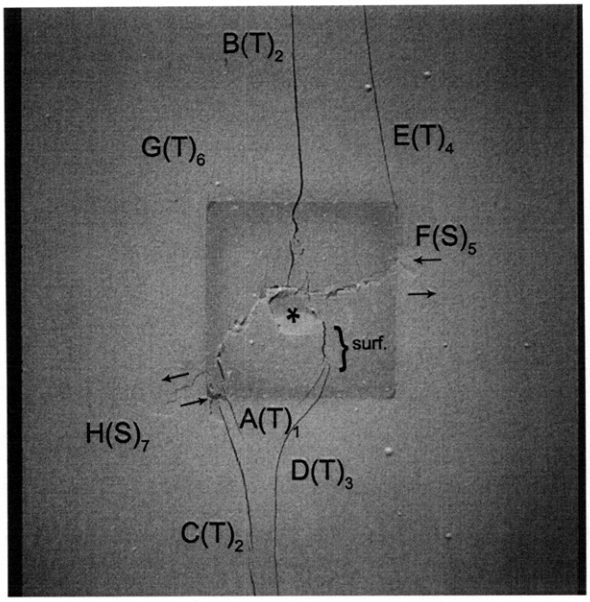

(Recorded by High Speed Video System)

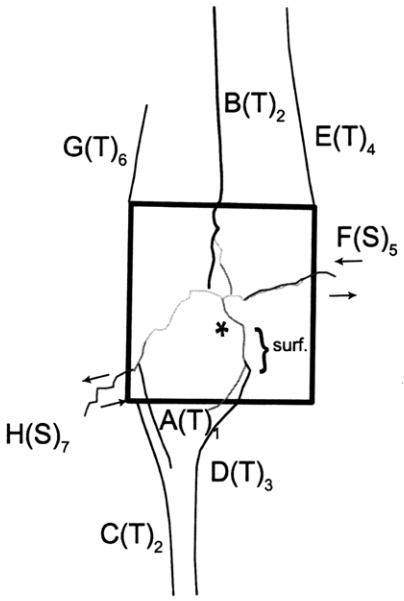

(23.68 MPa)
Time: 4 minutes & 58.927 seconds
HS Image # - 5404

A new shear crack (H) propagates from the lower left-hand side of the inclusion into the surrounding hydrocal matrix. As a result, a larger piece of spalling (*) forms.

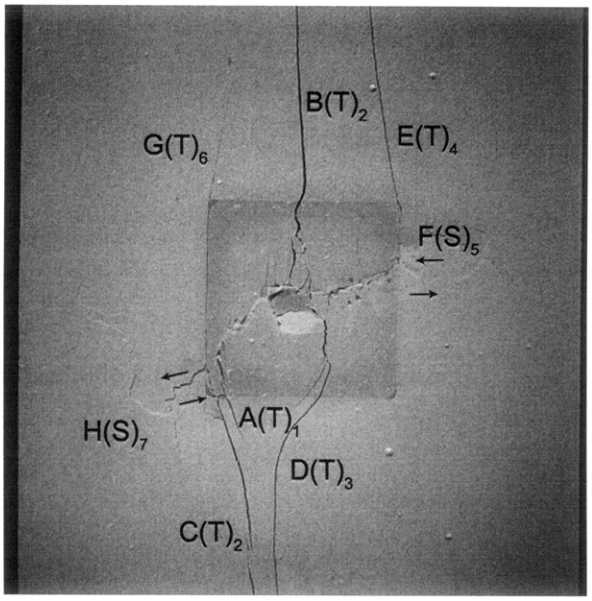

(Recorded by High Speed Video System)

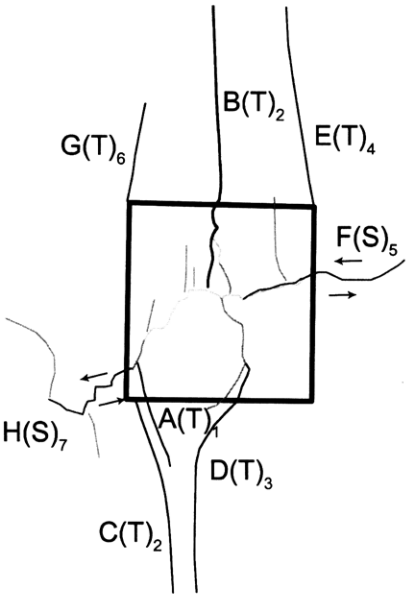

(23.82 MPa)
Time: 4 minutes & 59.407 seconds
HS Image # - 3004

Tensile crack (G) propagates down through the left-hand inclusion boundary.

As both shear cracks (F&H) propagate towards their respective specimen boundaries, surface cracking propagates from the shear cracks.

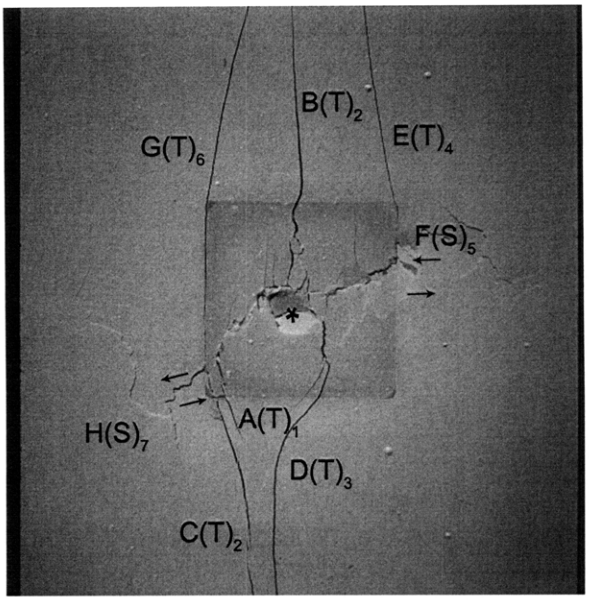

(Recorded by High Speed Video System)

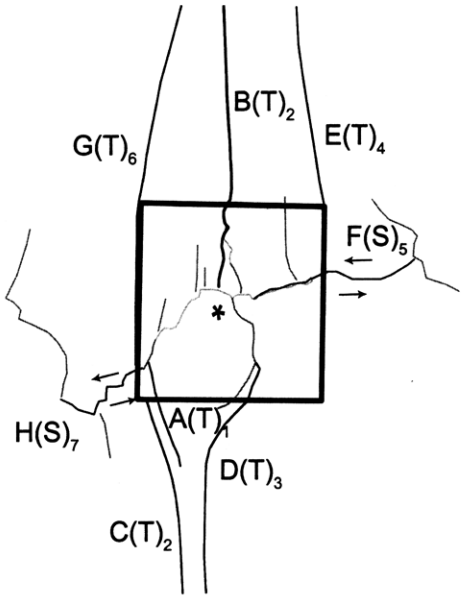

(23.89 MPa)
Time: 4 minutes & 59.589 seconds
HS Image # - 2095

Tensile crack (G) continues to propagate down through the left-hand inclusion boundary, until it coalesces with shear crack (H).

Surface cracking increases around both shear cracks (F&H).

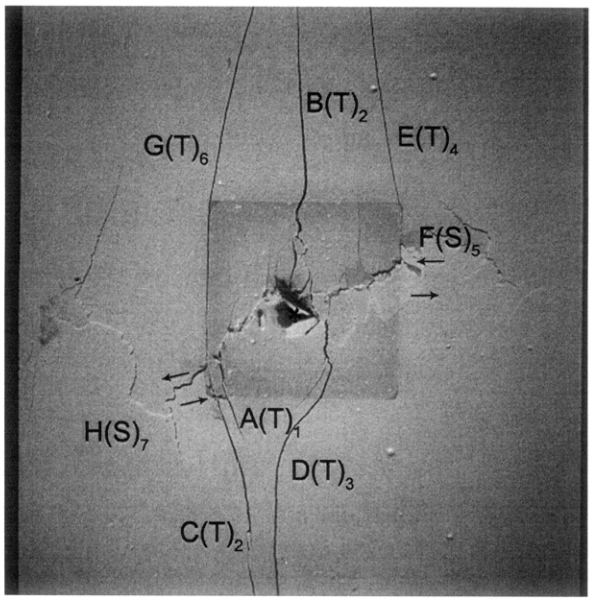

(Recorded by High Speed Video System)

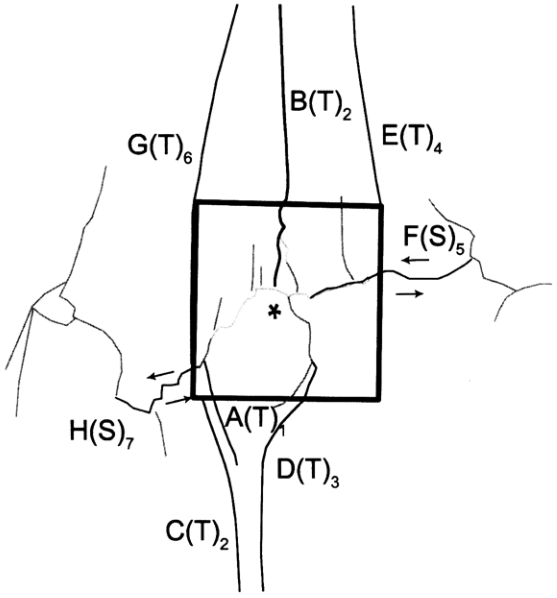

(23.90 MPa)
Time: 4 minutes & 59.601 seconds
HS Image # - 2035

The surface cracks that propagated from shear crack (H) coalesce with the left-hand specimen boundary.

As surface spalling (*) detaches from the specimen face, other larger pieces of surface spalling form adjacent to the initial surface crack located within the inclusion.

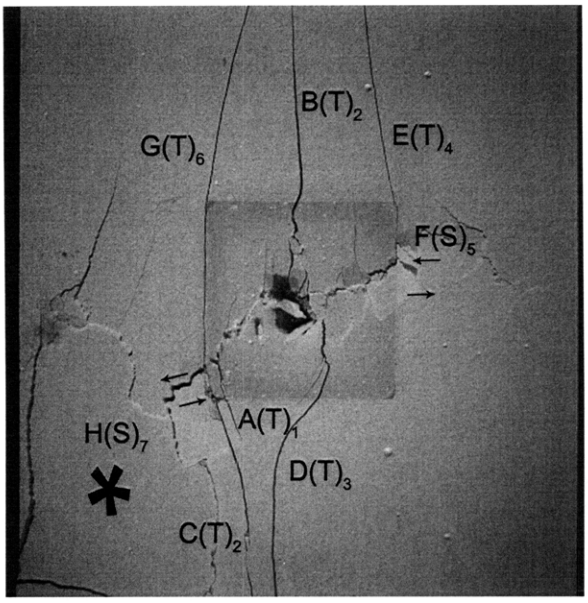

(Recorded by High Speed Video System)

(23.90 MPa)
Time: 4 minutes & 59.605 seconds
HS Image # - 2015

As the surface cracks coalesce with one another, a large piece of specimen (*) detaches from the face.

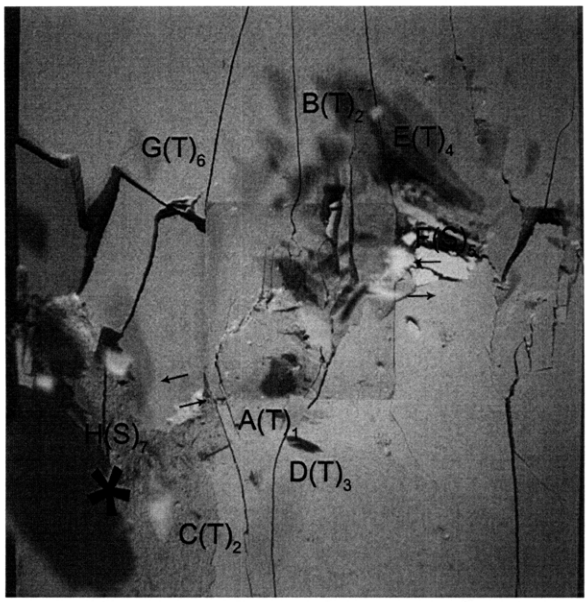

(Recorded by High Speed Video System)

23.921 MPa [Max. Stress] – FAILURE
Time: 4 minutes & 59.646 seconds
HS Image # - 1807

Both shear cracks (F&H) coalesce with their respective boundaries.

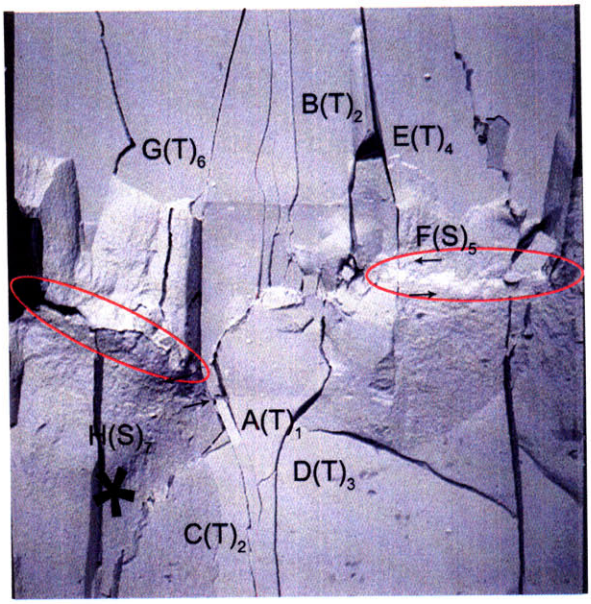

(Recorded by High Speed Video System)

(0 MPa – Final Picture)

HS Image # - 510

The true paths of shear cracks (F&H) can be seen in this picture.

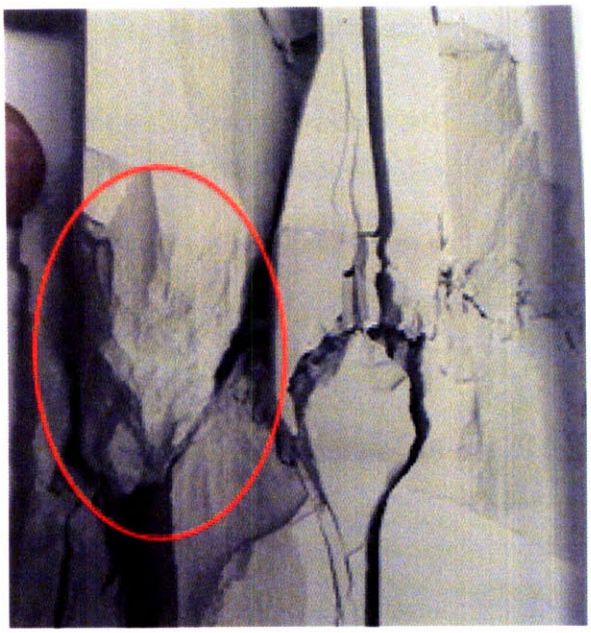

(Recorded by Camcorder)

A good post-test view of shear crack (H) can be seen in this picture.

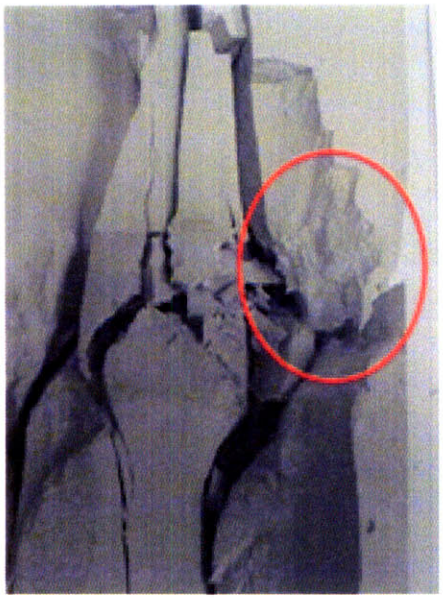

(Recorded by Camcorder)

A good post-test view of shear crack (F) can be seen in this picture.

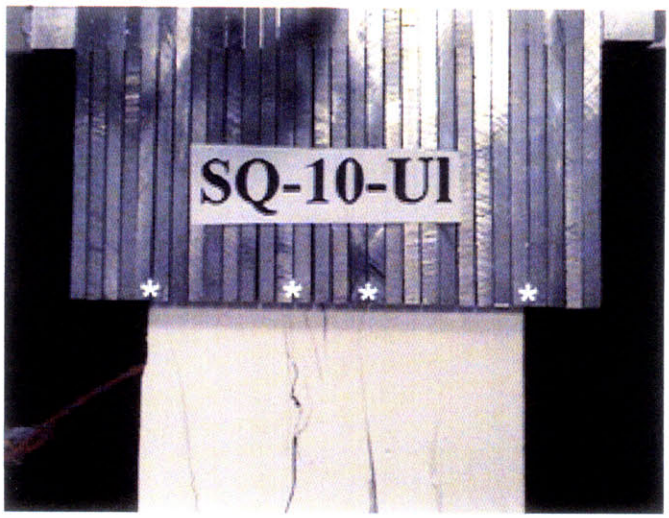	Upper edge of the specimen. The cracks marked with a (*) coincide with the openings between the teeth of the brush platen.
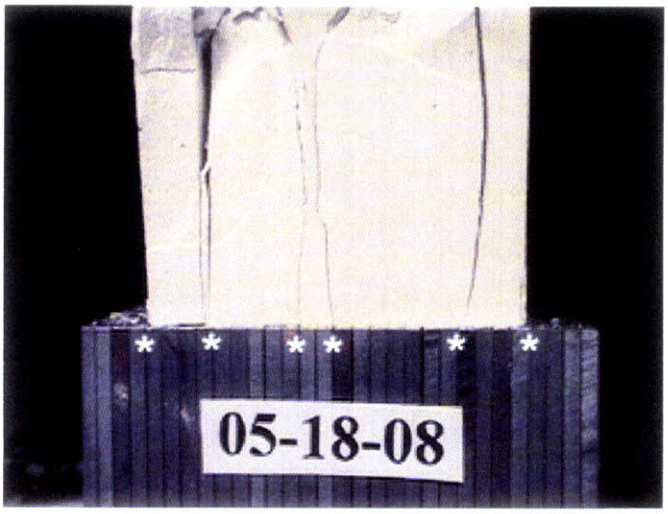	Lower edge of the specimen. The cracks marked with a (*) coincide with the openings between the teeth of the brush platen.

APPENDIX C – Half-inch Single Inclusions

This appendix contains the detailed analyses for specimens with single, half-inch inclusions. Two different inclusion geometries were tested (circle and square) with either an Ultracal or plaster inclusion; one complete analysis for each specimen type is presented, while only summaries of the other specimens are presented. For a complete summary of results, refer to Section 4.4. A list of tested specimens is summarized below.

		Circle	Square
1/2" Inclusion	Plaster	CR(Pl)-A CR(Pl)-B CR(Pl)-C*	SQ(Pl)-A SQ(Pl)-B* SQ(Pl)-C
	Ultracal	CR(Ul)-A CR(Ul)-B CR(Ul)-C*	SQ(Ul)-A* SQ(Ul)-B SQ(Ul)-C

* A complete analysis for this specimen is presented in the Appendix.

SUMMARY

Specimen Number: CR(PI)-A (20080828)

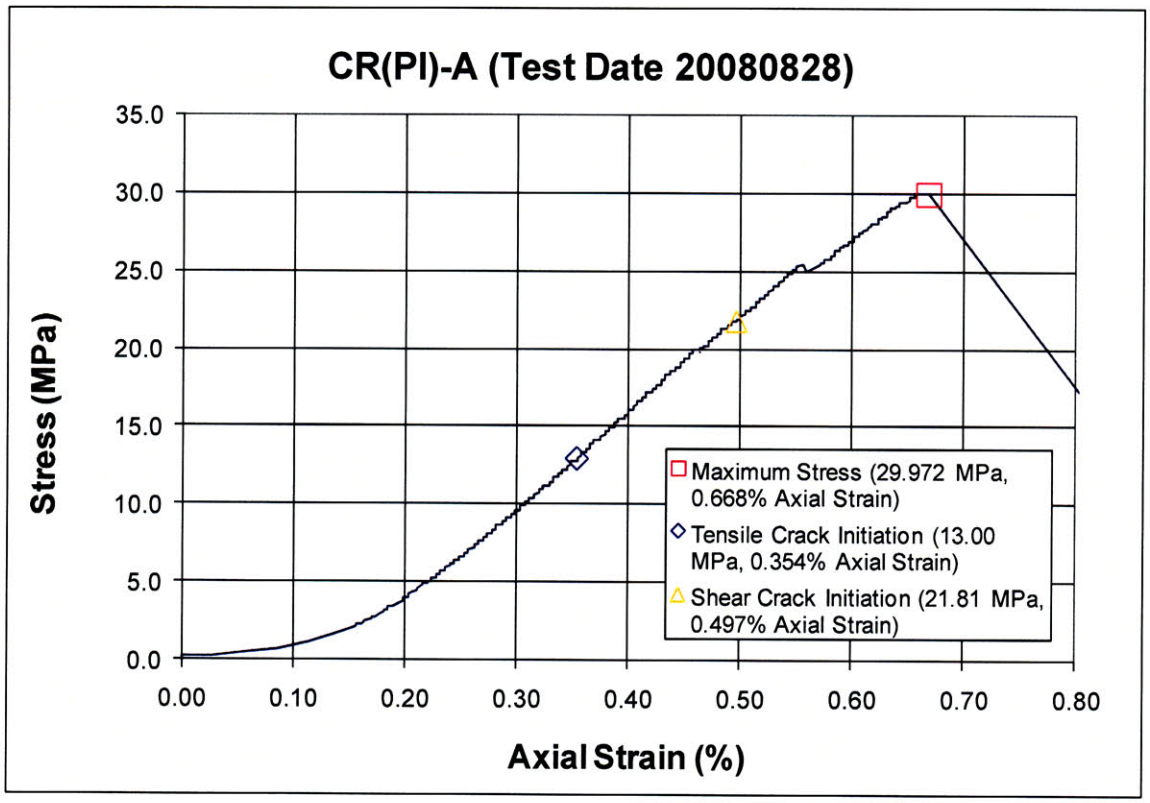

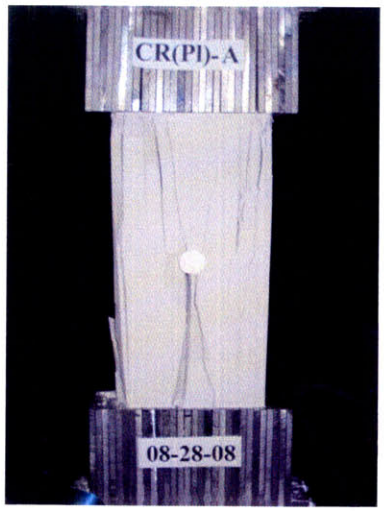

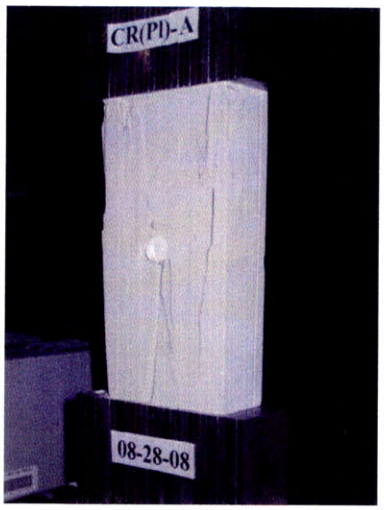

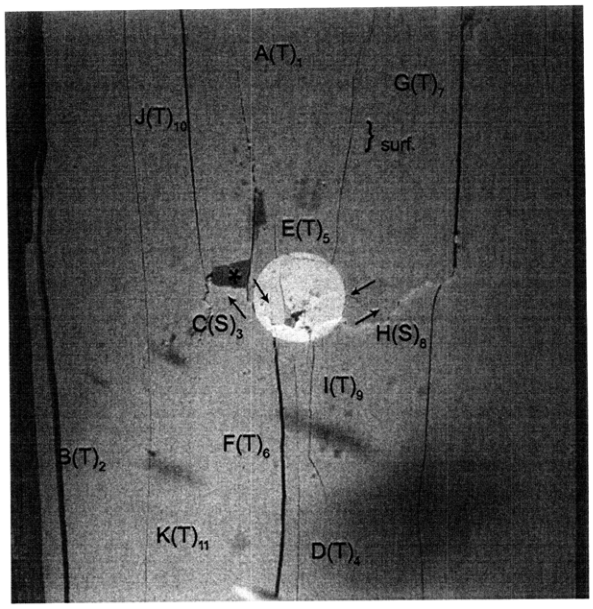

(Recorded by High Speed Video System)

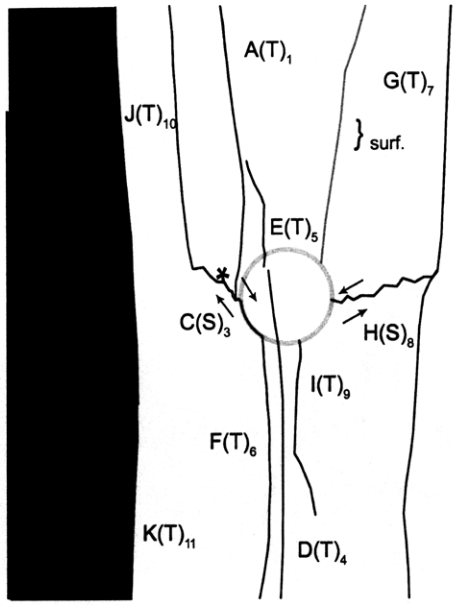

(21.11 MPa)
Time: 6 minutes & 18.909 seconds
HS Image # - 2564

Tensile crack (G) continues to propagate downwards, after its coalescence with shear crack (H).

Shear crack (C) then continues to propagate, until its coalescence with tensile crack (J). Spalling (*) initiates adjacent to shear crack (C).

SUMMARY

Specimen Number: CR(PI)-B (20090117)

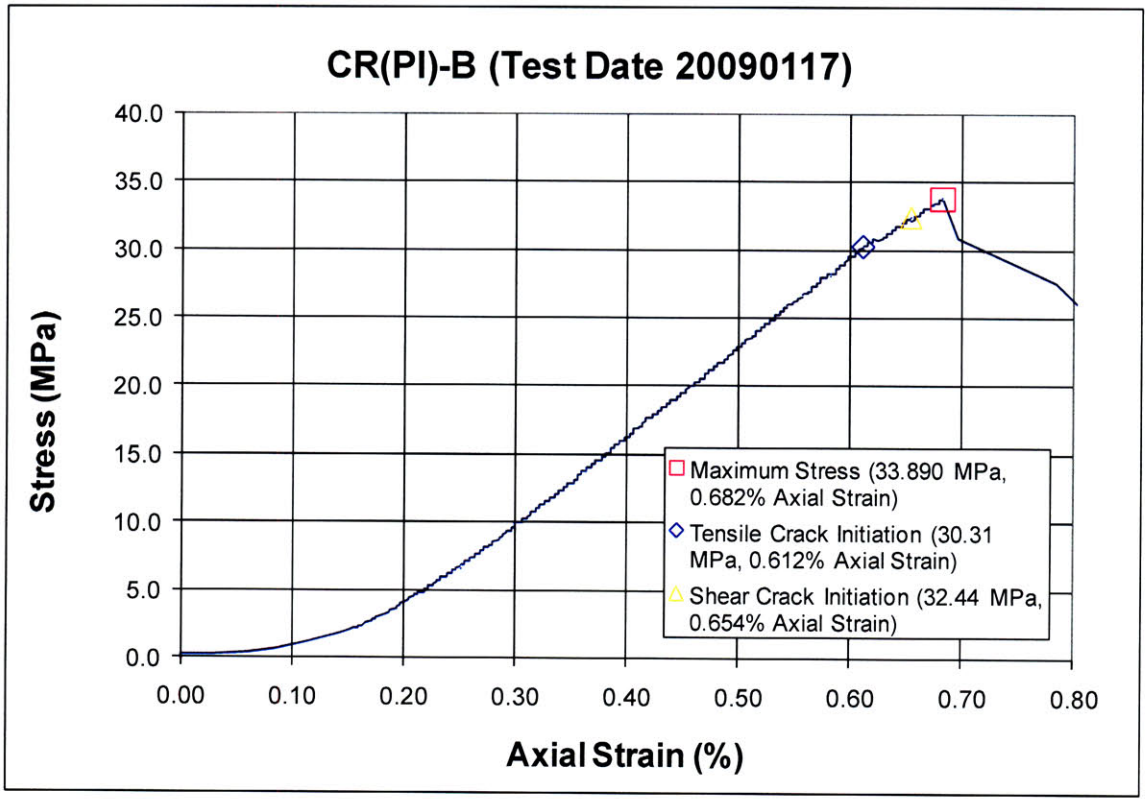

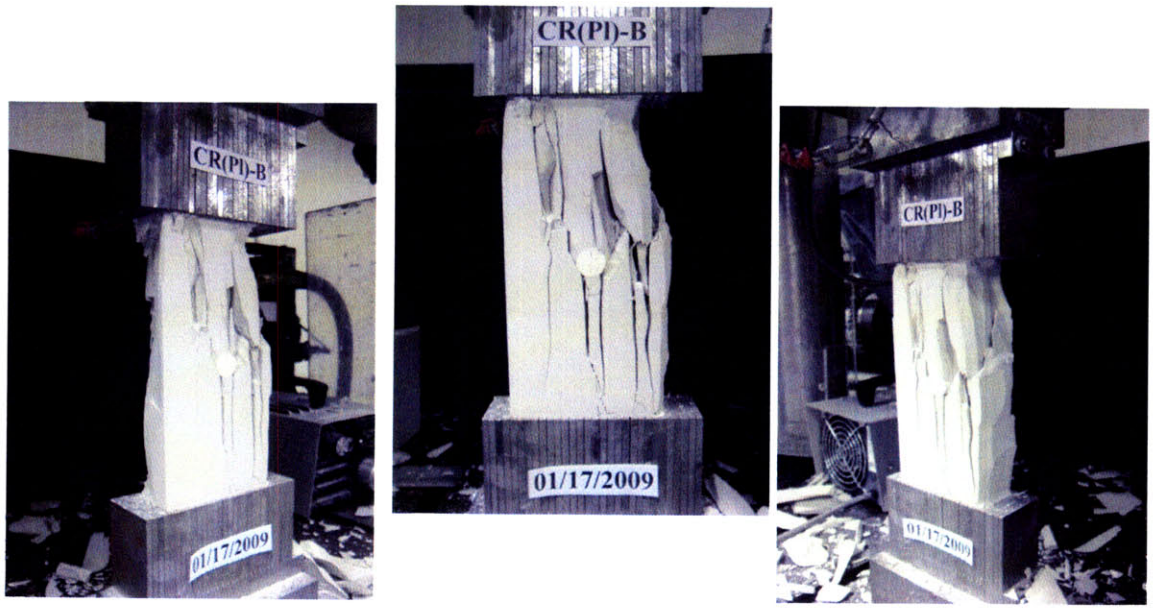

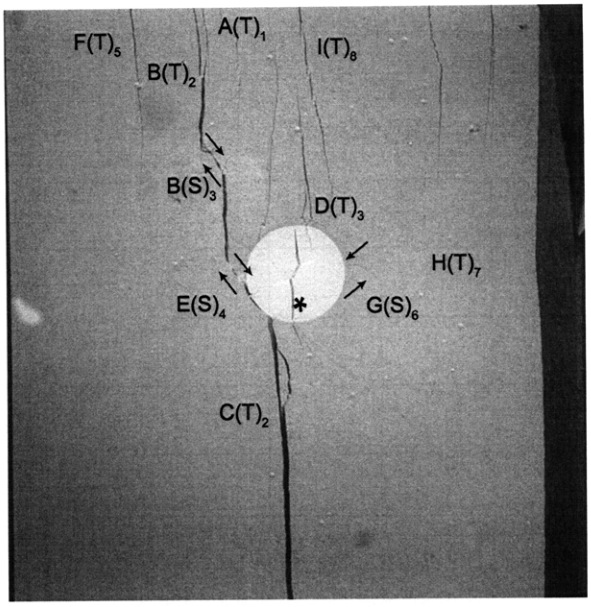

(Recorded by High Speed Video System)

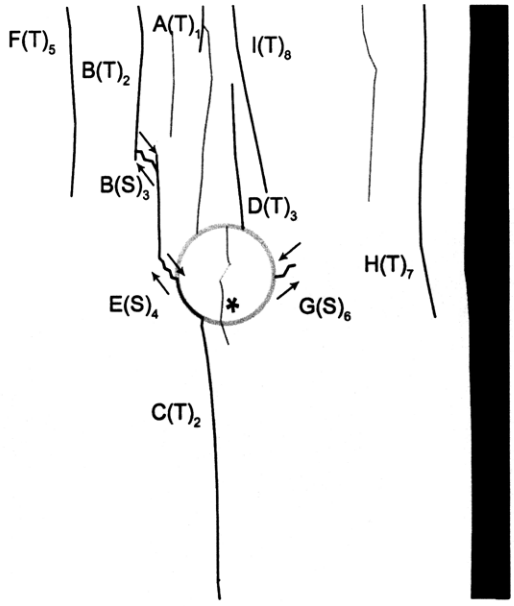

(18.97 MPa)
Time: 7 minutes & 7.617 seconds
HS Image # - 2972

As the surface "wing" cracks associated with the pre-test surface crack continue to propagate, one of the wing cracks (*) begins to propagate into the surrounding Hydrocal matrix.

Tensile crack (I) then initiates at the upper specimen boundary and propagates downwards.

Specimen Number: CR(PI)-C (20090117)

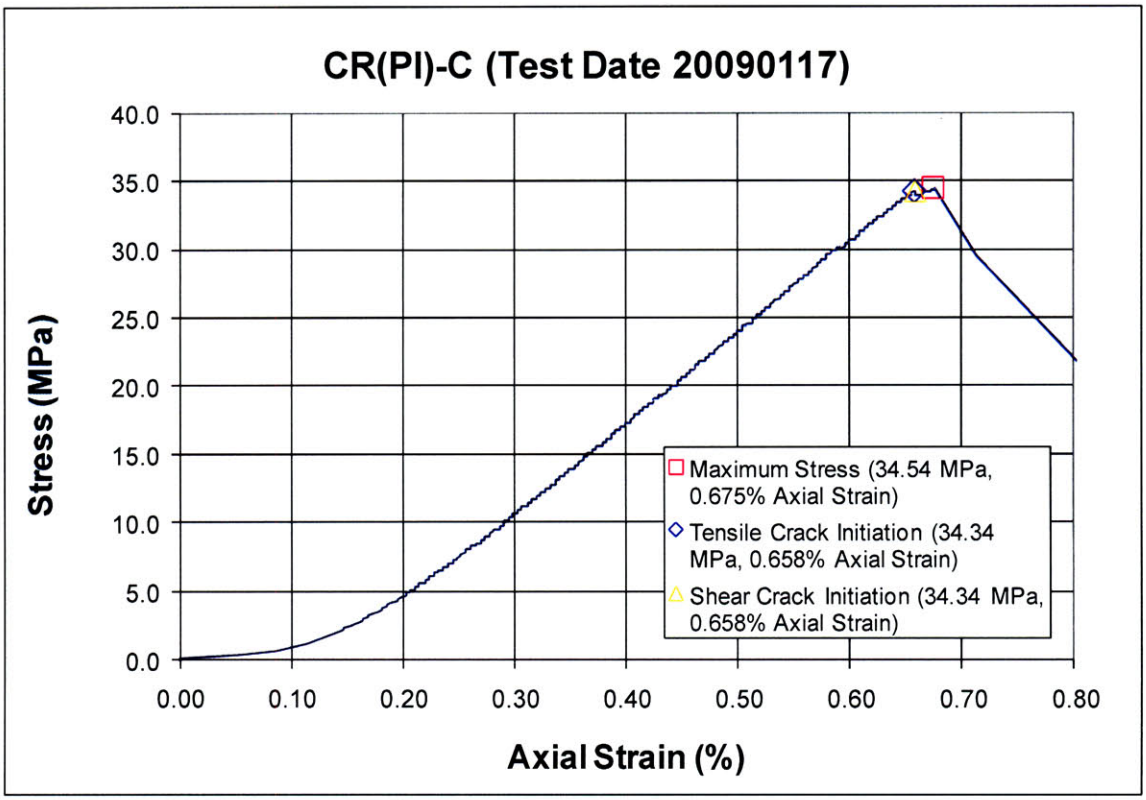

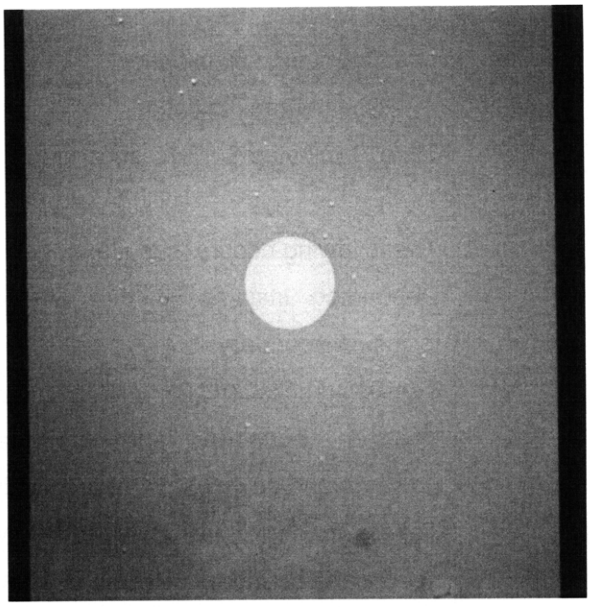

(Recorded by High Speed Video System)

Initial Inclusion Geometries:
CIRCLE – Plaster Material

Inclusion **less** stiff than matrix.

High Speed Camera Frame Rate:
5000 pps

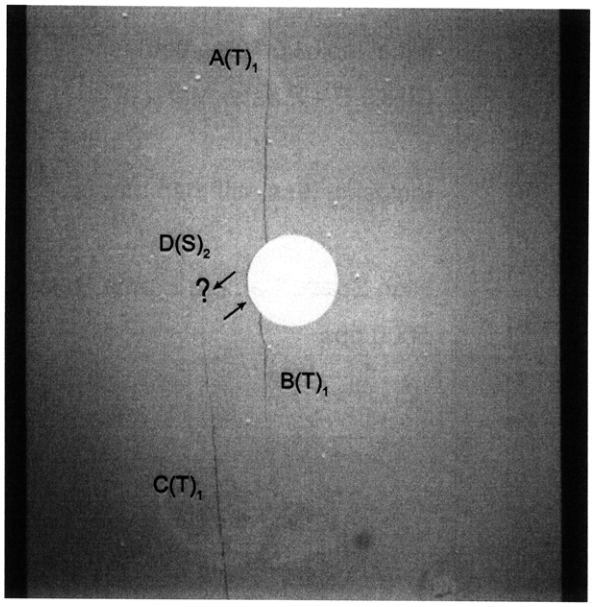

(Recorded by High Speed Video System)

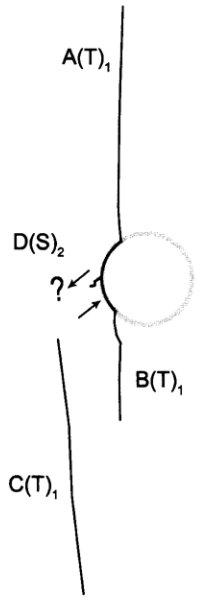

(34.34 MPa)

- Tensile Crack Initiation
- Shear Crack Initiation

Time: 7 minutes & 12.70 seconds

The following occurs "simultaneously": Debonding initiates at the left-hand inclusion boundary.

Tensile cracks (A&B) initiate at the inclusion boundary and propagate upwards and downwards, respectively.

Tensile crack (C) initiates at the lower specimen boundary and propagates upwards.

Shear crack (D) initiates at the inclusion boundary. Based on previous trends, it is assumed that shear crack (D) then propagates towards tensile crack (C) in the direction indicated, though it could not be confirmed.

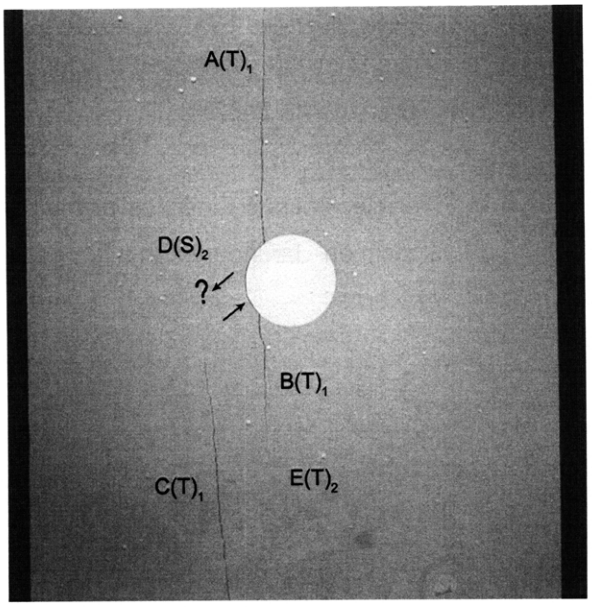

(Recorded by High Speed Video System)

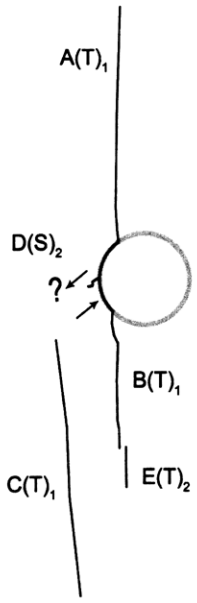

(34.54 MPa) [Max. Stress]
Time: 7 minutes & 15.492 seconds

Tensile crack (E) initiates adjacent to tensile crack (B).

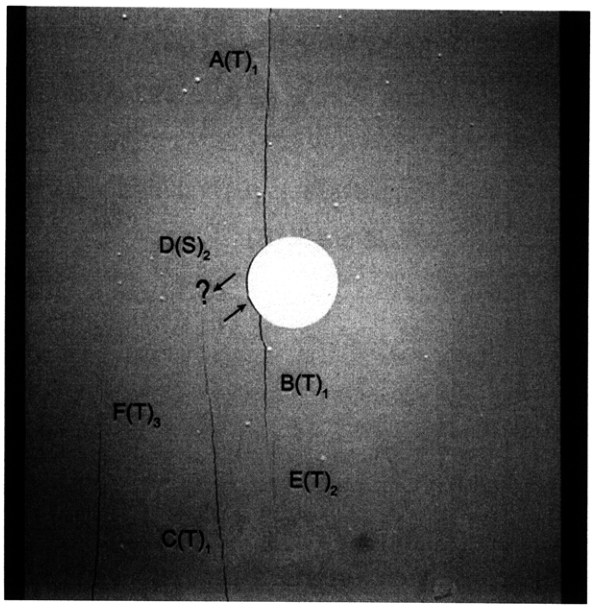

(Recorded by High Speed Video System)

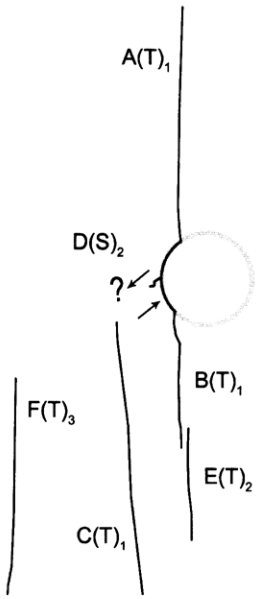

(34.20 MPa)
Time: 7 minutes & 15.499 seconds
HS Image # - 3482

Tensile crack (F) initiates at the lower specimen boundary and propagates upwards.

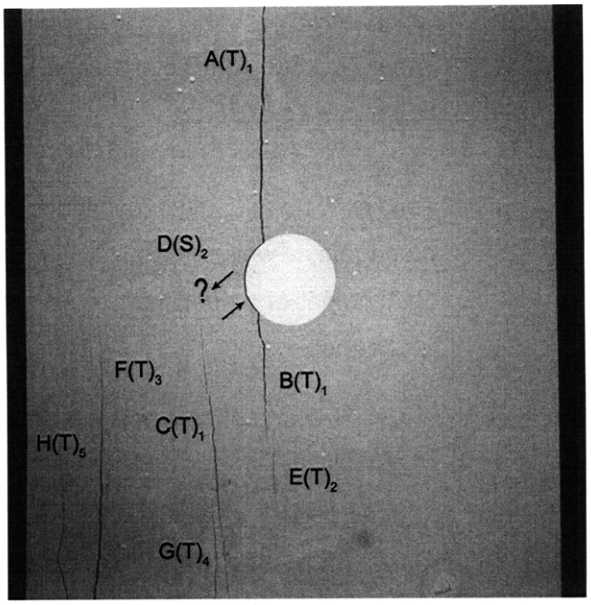

(Recorded by High Speed Video System)

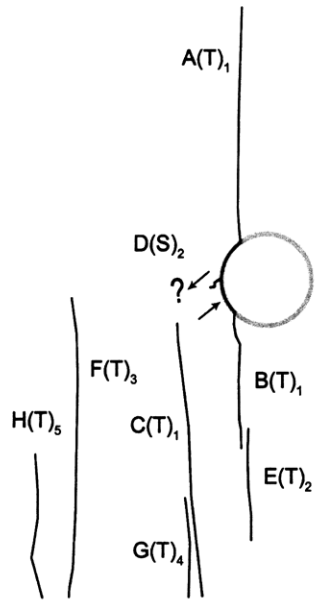

(34.06 MPa)
Time: 7 minutes & 15.501 seconds
HS Image # - 3468

Tensile crack (G) initiates at the lower specimen boundary and propagates upwards adjacent to tensile crack (C).

Tensile crack (H) then initiates at the lower specimen boundary and propagates upwards.

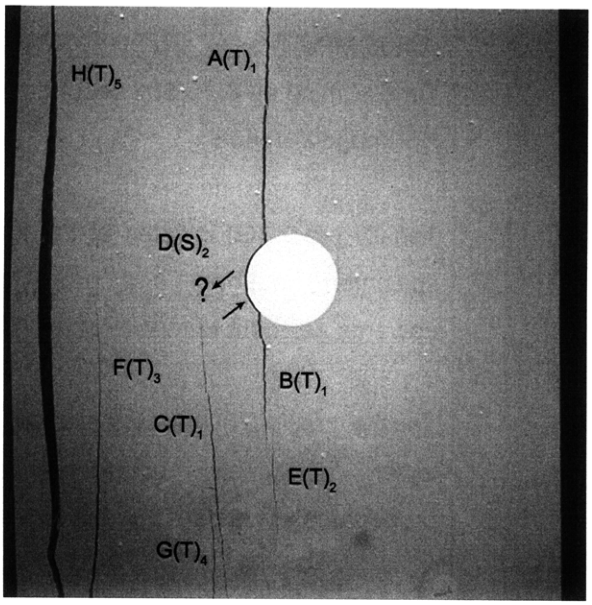

(Recorded by High Speed Video System)

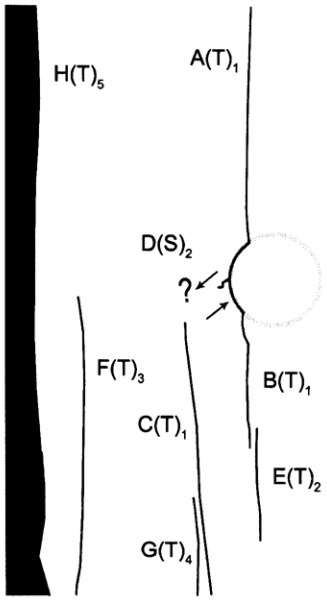

(33.92 MPa)
Time: 7 minutes & 15.504 seconds
HS Image # - 3455

Tensile crack (H) continues to propagate, which results in the detachment of a specimen piece at the left boundary.

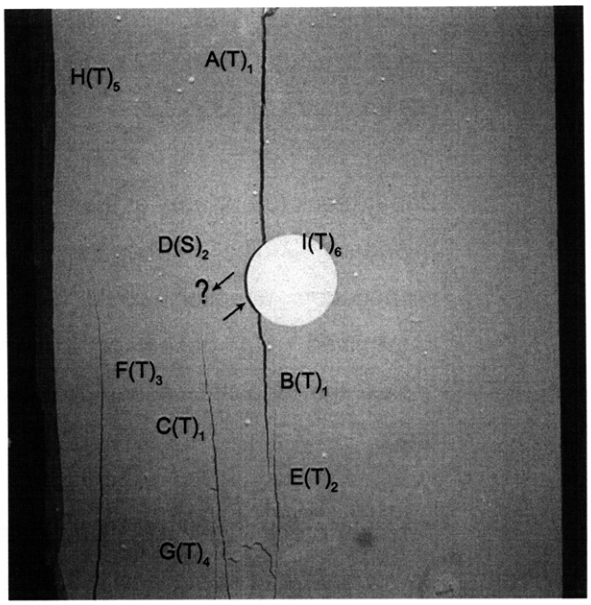

(Recorded by High Speed Video System)

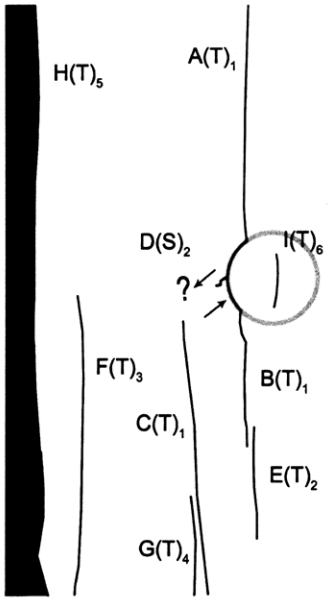

(31.38 MPa)
Time: 7 minutes & 15.553 seconds
HS Image # - 3208

Tensile crack (I) initiates within the inclusion.

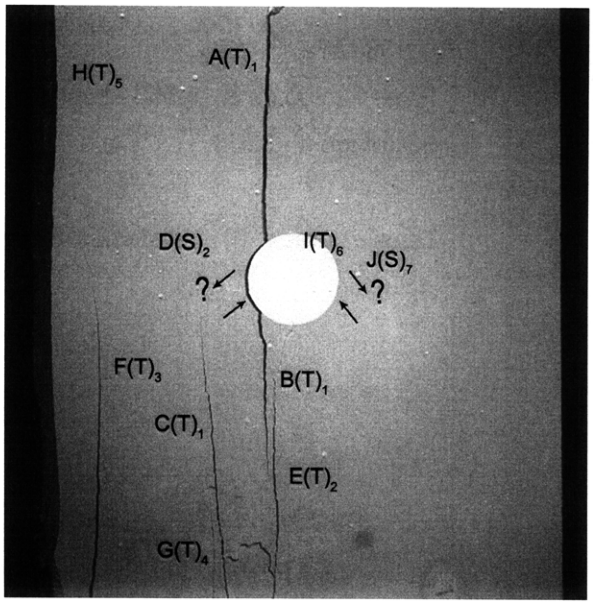

(Recorded by High Speed Video System)

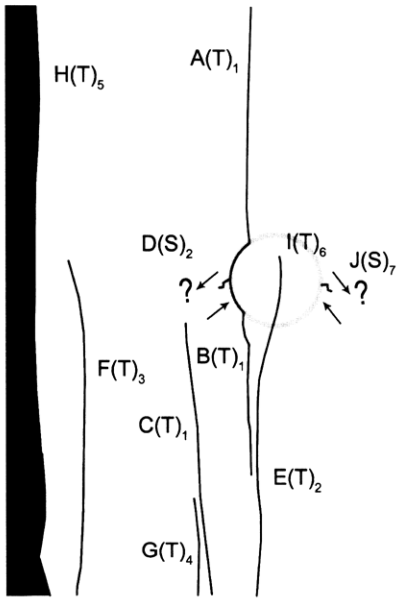

(30.92 MPa)
Time: 7 minutes & 15.562 seconds
HS Image # - 3163

Shear crack (J) initiates at the inclusion boundary. The shearing and propagation direction could not be determined, but based on previous trends the depicted assumption was made.

Tensile crack (I) then propagates downwards and coalesces with tensile crack (E).

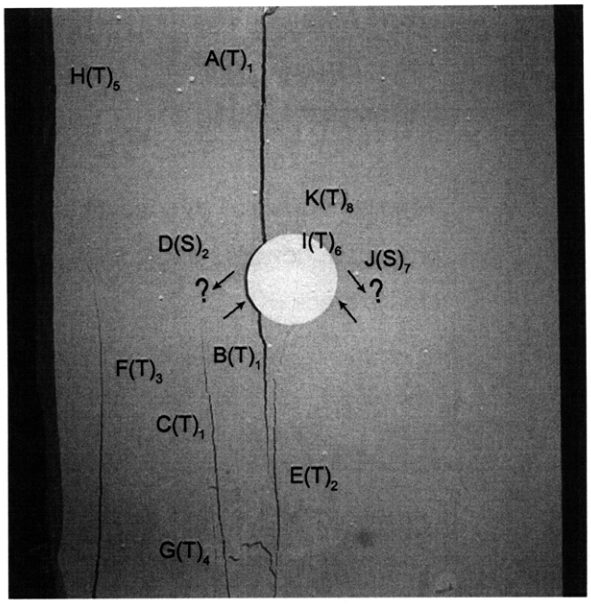

(Recorded by High Speed Video System)

(30.63 MPa)
Time: 7 minutes & 15.568 seconds
HS Image # - 3135

Tensile crack (K) initiates at the inclusion boundary and propagates upwards.

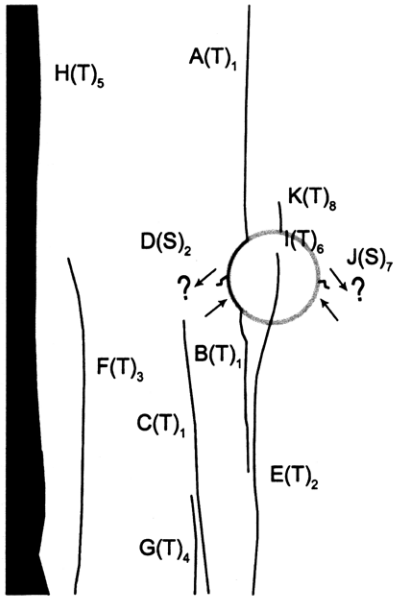

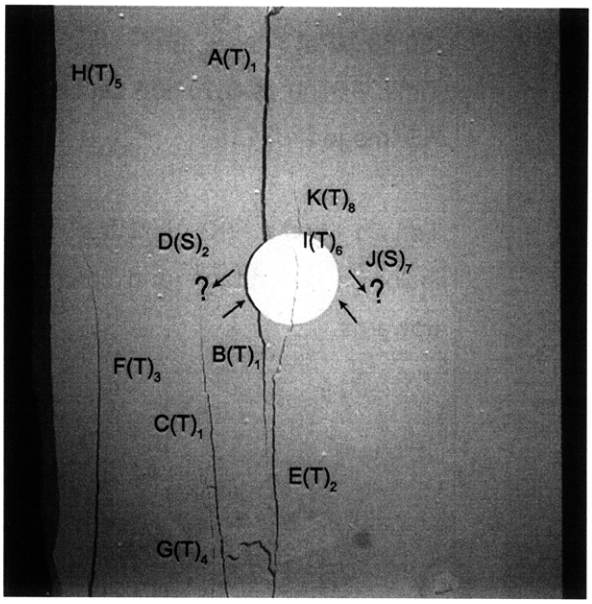

(Recorded by High Speed Video System)

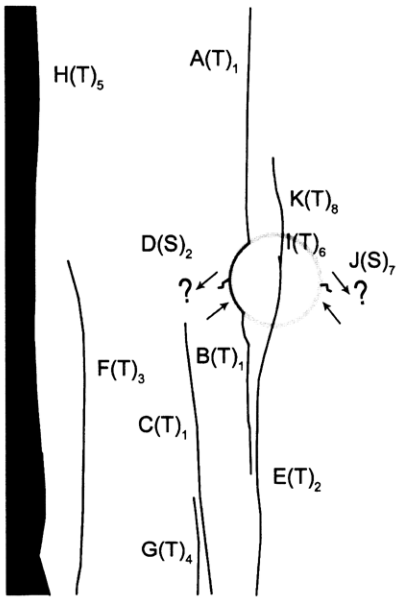

(28.15 MPa)
Time: 7 minutes & 15.597 seconds
HS Image # - 2991

Tensile crack (I) continues to propagate upwards and coalesces with tensile crack (K).

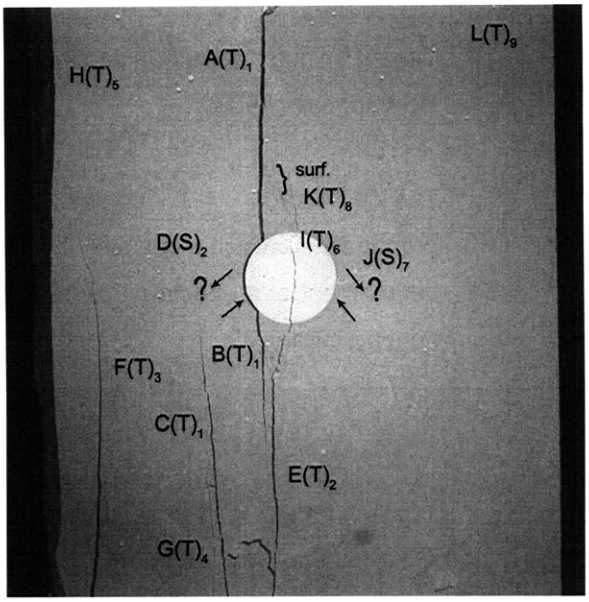

(Recorded by High Speed Video System)

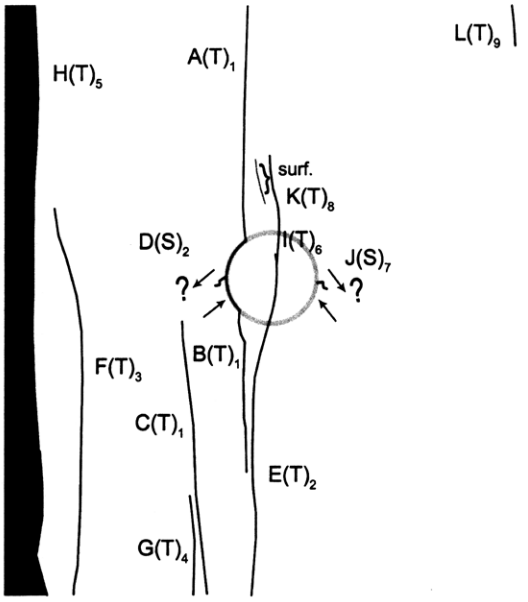

(27.98 MPa)
Time: 7 minutes & 15.598 seconds
HS Image # - 2986

Tensile crack (L) initiates at the upper specimen boundary and propagates downwards. Surface crack (surf.) initiates "simultaneously" with the initiation of tensile crack (L).

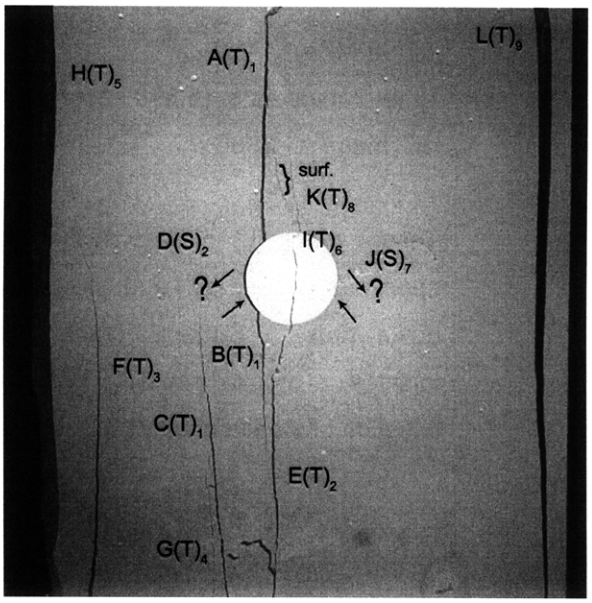

(Recorded by High Speed Video System)

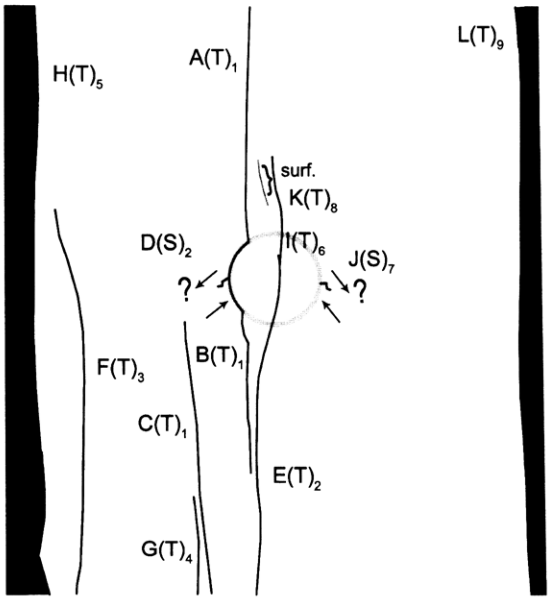

(27.88 MPa)
Time: 7 minutes & 15.598 seconds
HS Image # - 2983

Tensile crack (L) continues to propagate, which results in the detachment of a specimen piece at the right boundary.

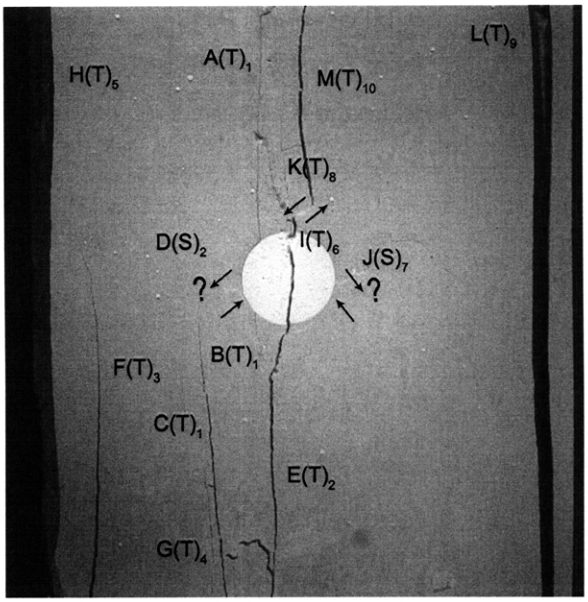

(Recorded by High Speed Video System)

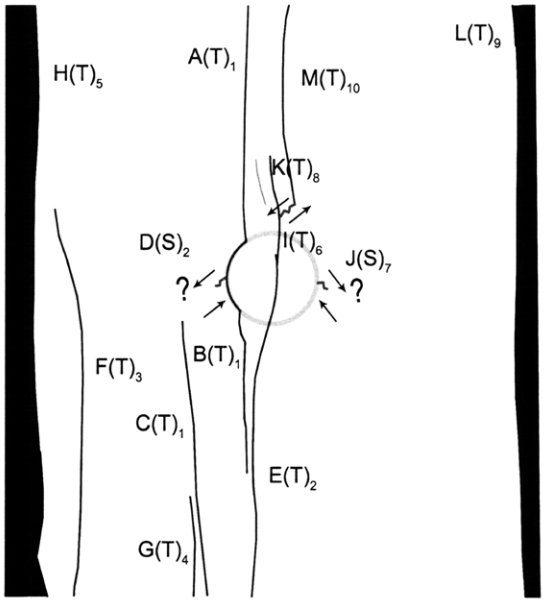

(27.85 MPa)
Time: 7 minutes & 15.599 seconds
HS Image # - 2982

Tensile crack (M) initiates at the upper specimen boundary and propagates downwards, until its coalescence with tensile crack (K) in shear.

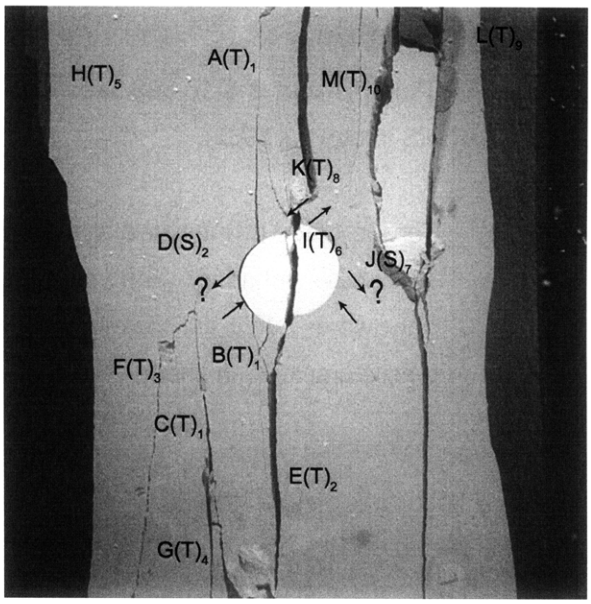

(Recorded by High Speed Video System)

(0 MPa) – Final Picture

Time: 7 minutes & 16.063 seconds

HS Image # - 661

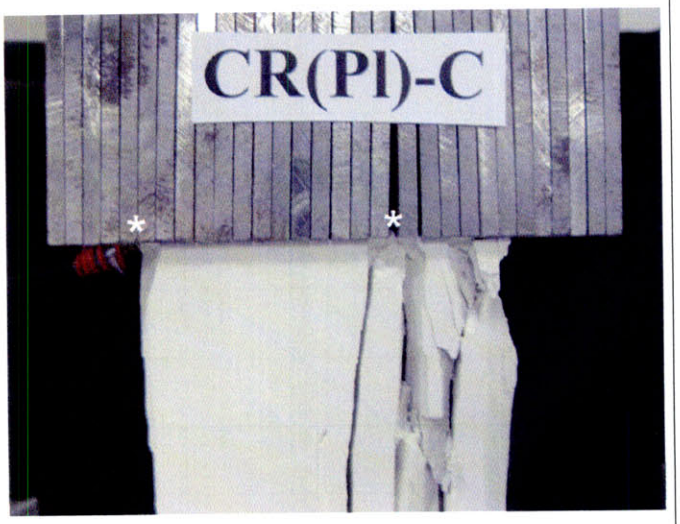	Upper edge of the specimen. The cracks marked with a (*) coincide with the openings between the teeth of the brush platen.
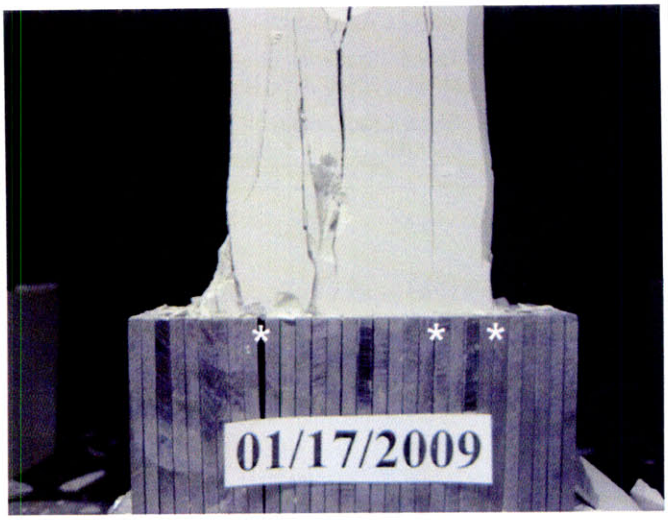	Lower edge of the specimen. The cracks marked with a (*) coincide with the openings between the teeth of the brush platen.

SUMMARY

Specimen Number: CR(UI)-A (20080828)

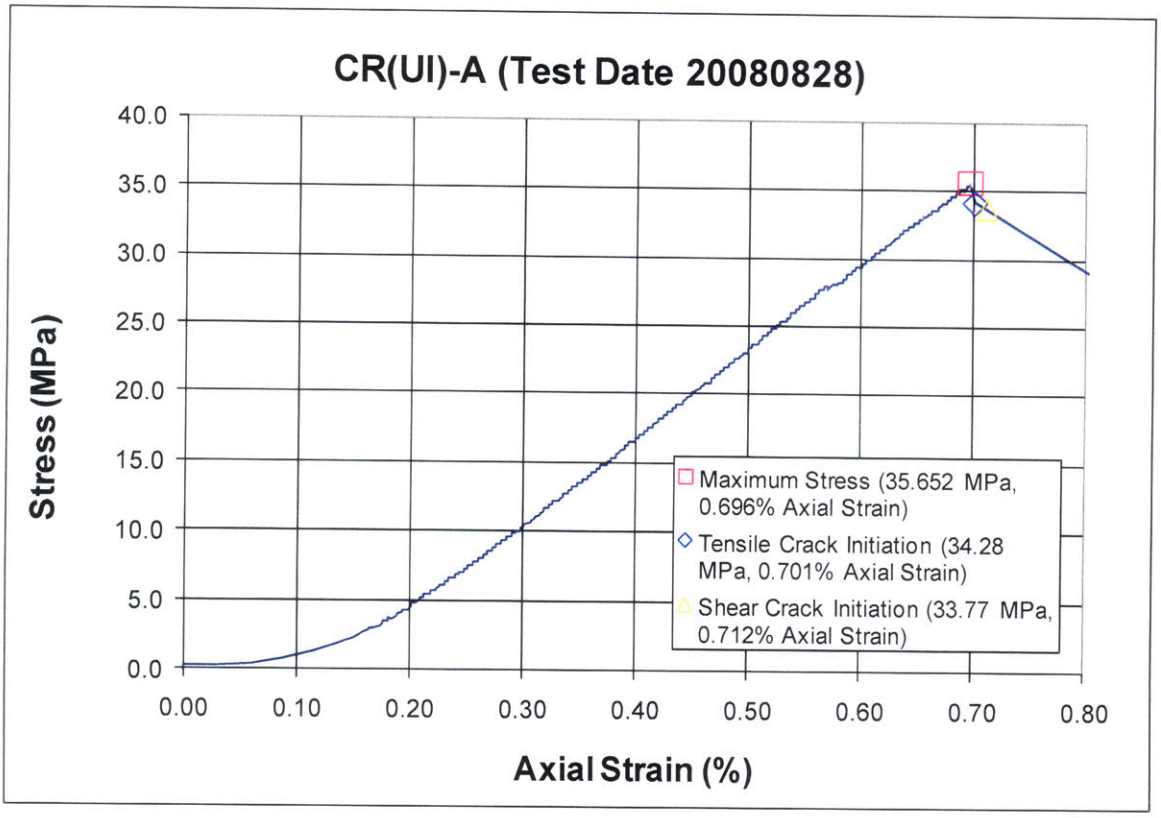

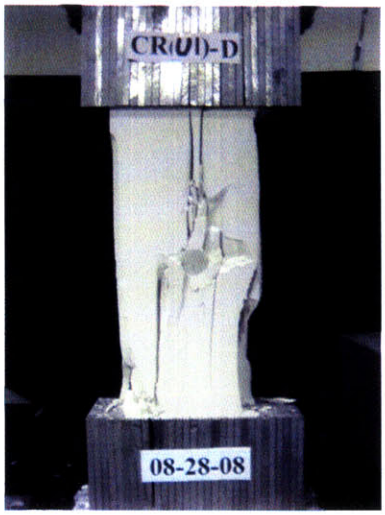

Specimen labeled as CR(UI)-D for the experiment

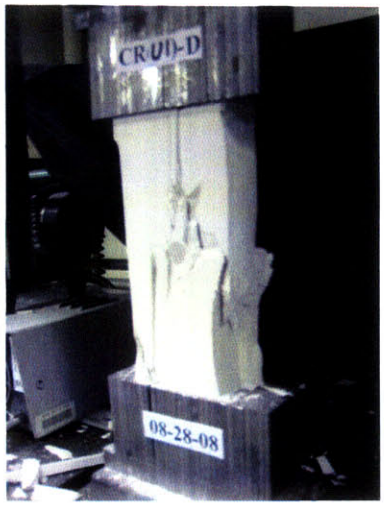

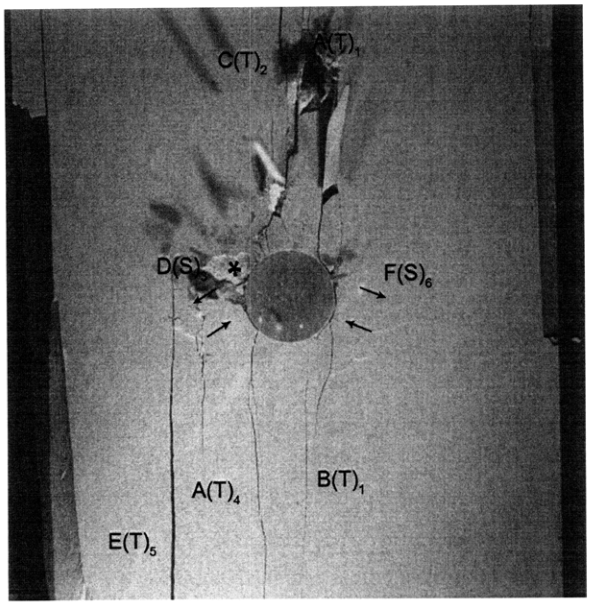

(Recorded by High Speed Video System)

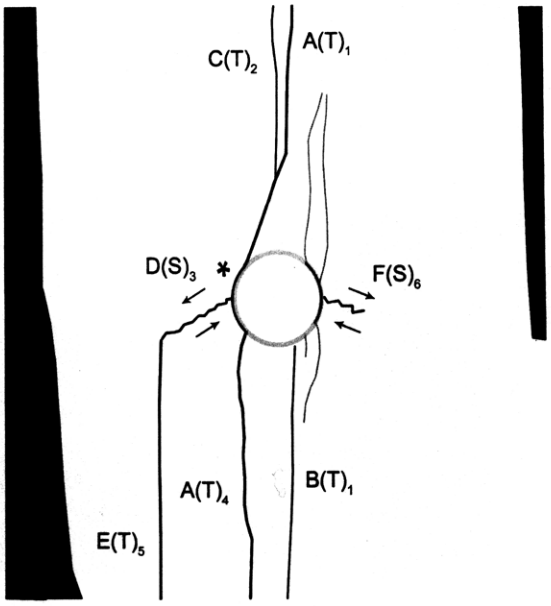

(31.69 MPa)
Time: 7 minutes & 39.808 seconds
HS Image # - 2303

Shear crack (F) initiates at the right-hand inclusion boundary and propagates downwards.

Spalling (*) occurs adjacent to shear crack (D).

SUMMARY

Specimen Number: CR(UI)-B (20080828)

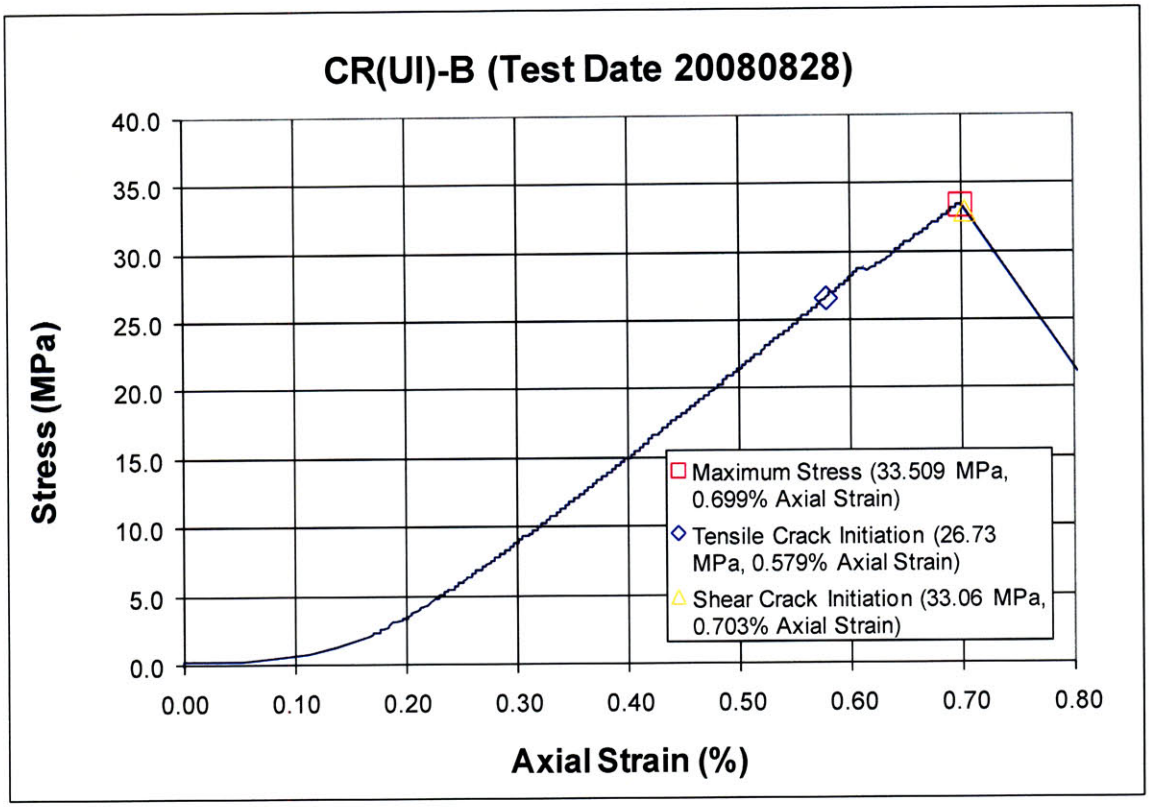

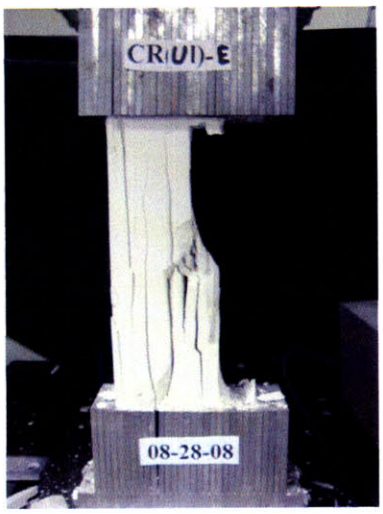

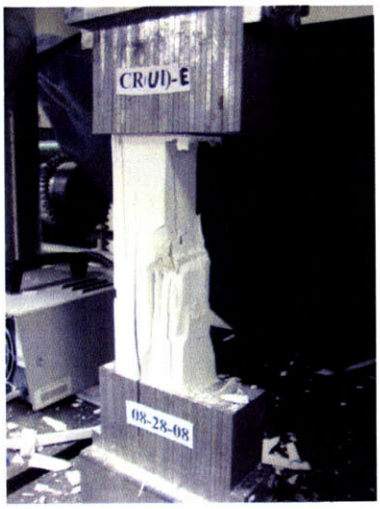

Specimen labeled as CR(UI)-E for the experiment

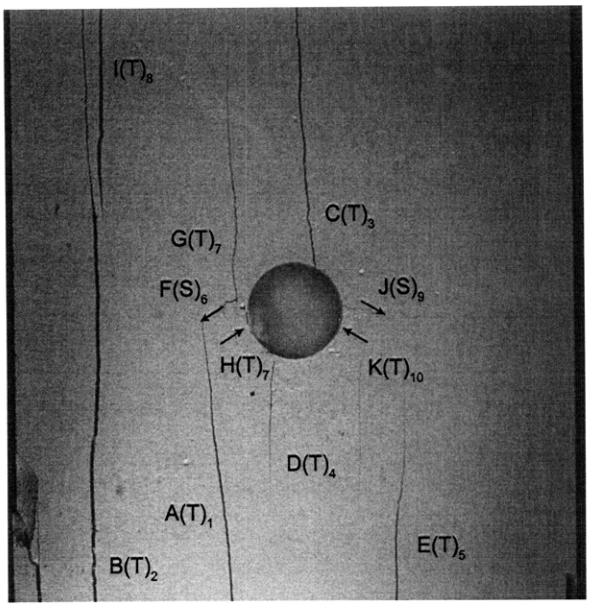

(Recorded by High Speed Video System)

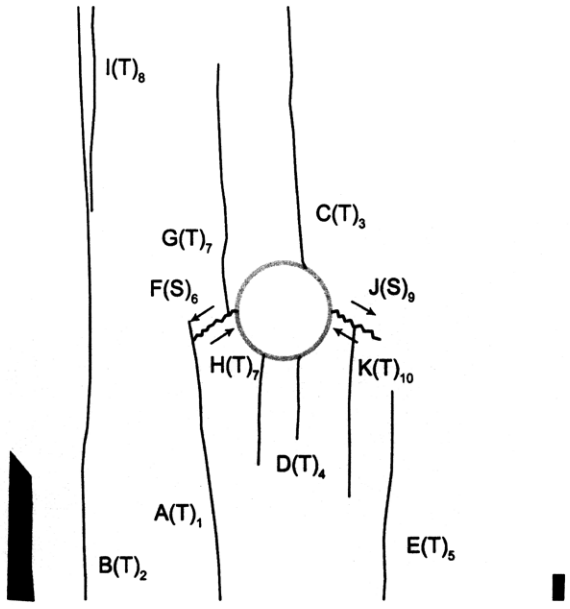

(29.85 MPa)
Time: 7 minutes & 7.295 seconds
HS Image # - 2909

Tensile crack (K) initiates at shear crack (J) and propagates downwards.

Specimen Number: CR(UI)-C (20090117)

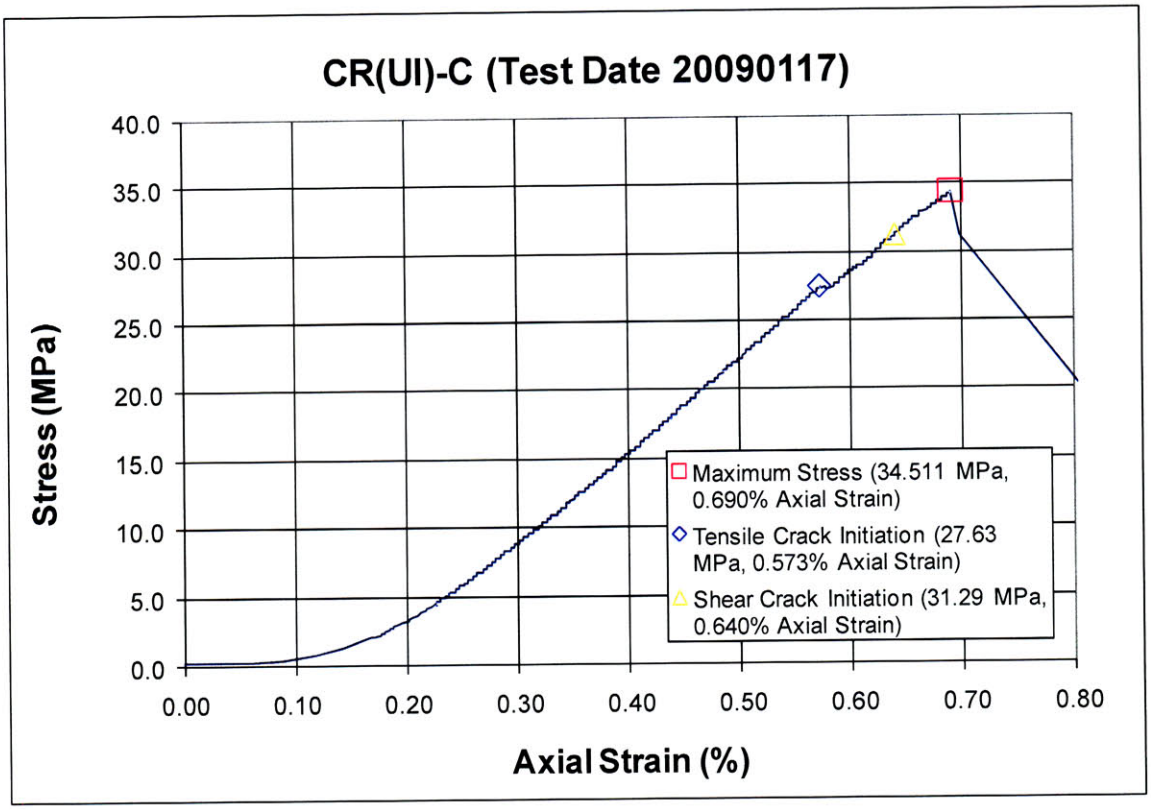

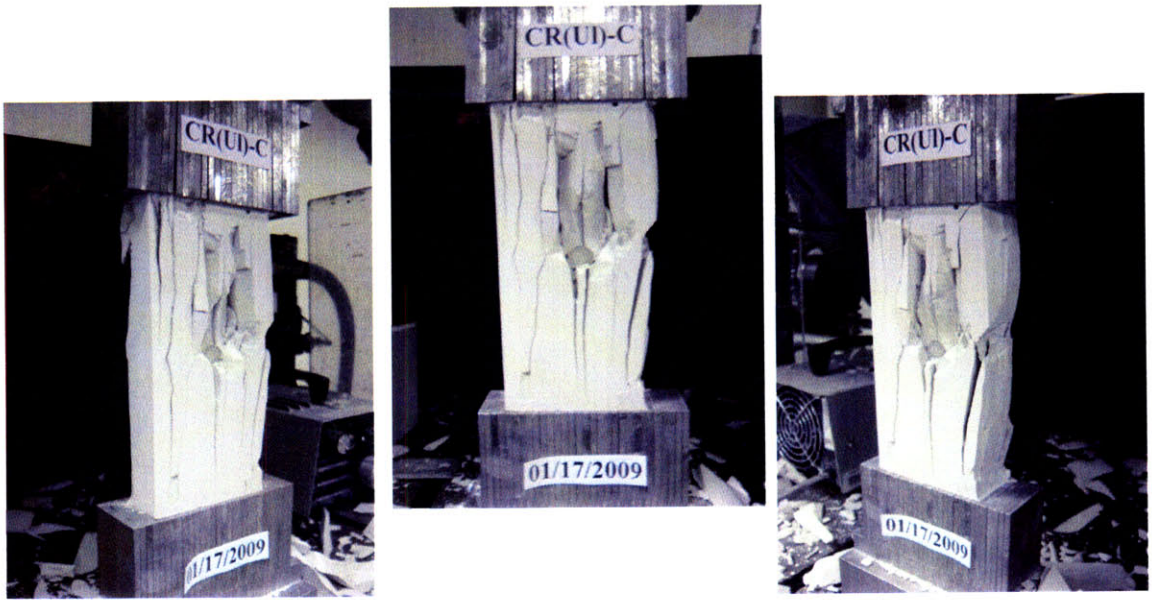

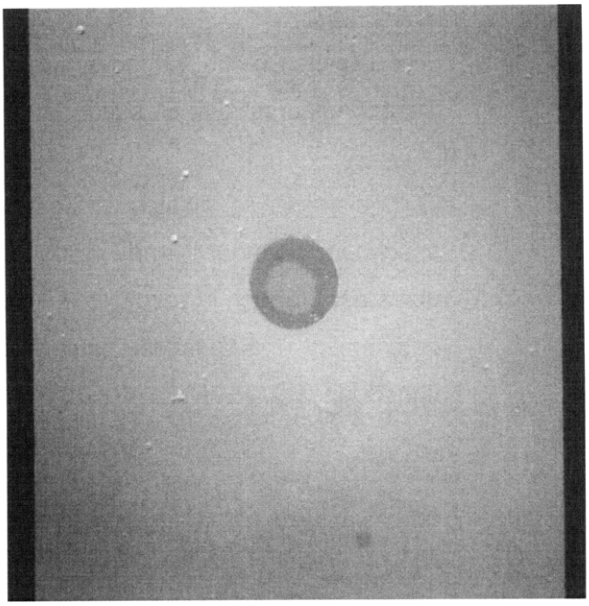

(Recorded by High Speed Video System)

Initial Inclusion Geometries:
CIRCLE – Ultracal Material

Inclusion **more** stiff than matrix.

High Speed Camera Frame Rate:
5000 pps

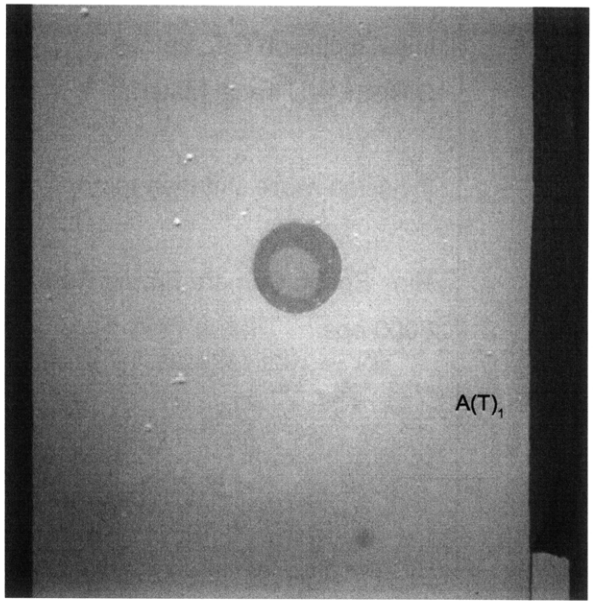

(Recorded by High Speed Video System)

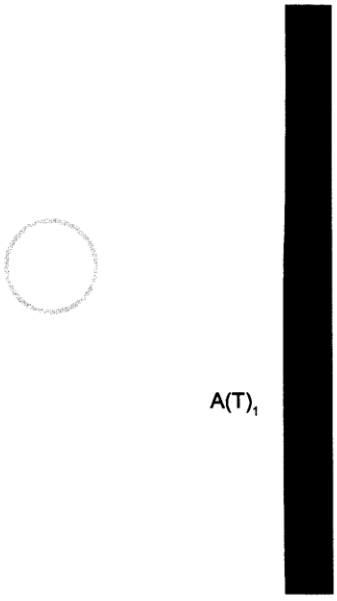

(27.63 MPa)

– Tensile Crack Initiation

Time: 5 minutes & 42.81 seconds

Tensile crack (A) initiates at the lower specimen boundary and propagates upwards, which results in the detachment of a specimen piece at the right boundary.

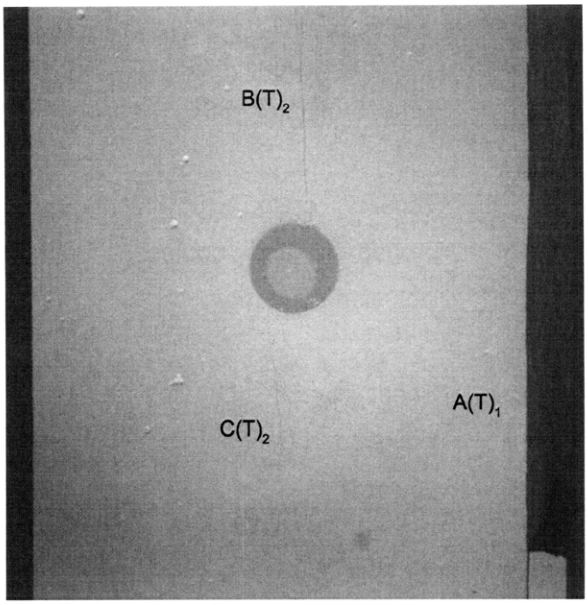

(Recorded by High Speed Video System)

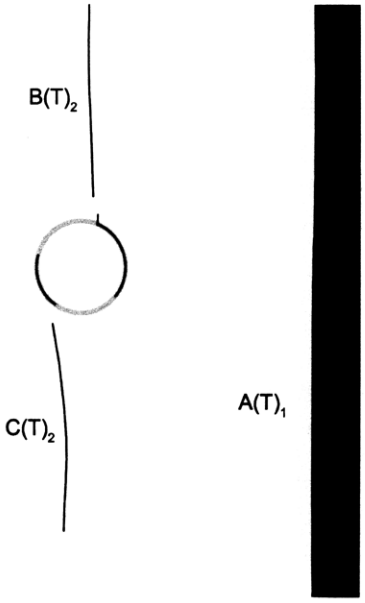

(29.08 MPa)
Time: 6 minutes & 3.23 seconds

The following occurs "simultaneously":

As debonding initiates at the right-hand and left-hand inclusion boundary, tensile cracks (B&C) initiate above and below the inclusion, respectively. Tensile cracks (B&C) propagate towards their respective specimen boundaries.

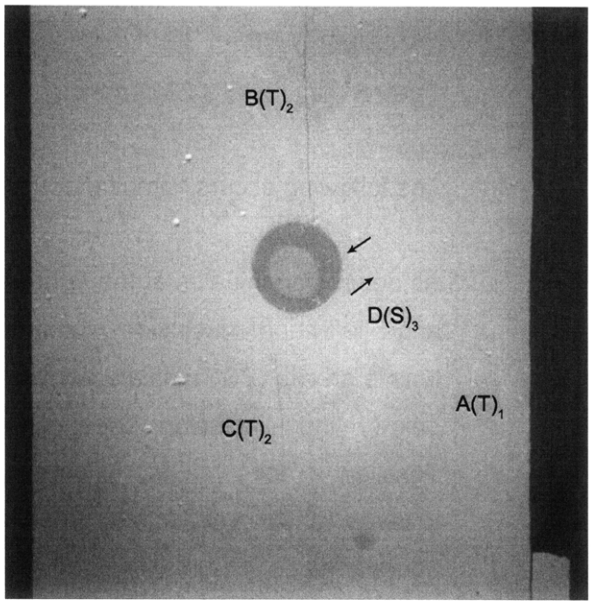

(Recorded by High Speed Video System)

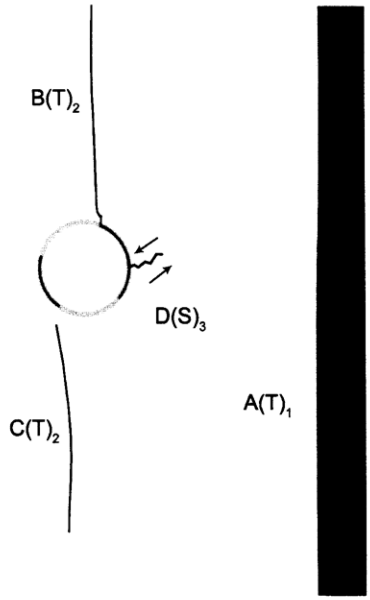

(31.29 MPa)

- Shear Crack Initiation

Time: 6 minutes & 34.61 seconds

Tensile crack (B) continues to propagate and coalesces with the inclusion boundary.

Shear crack (D) initiates at the inclusion boundary and propagates upwards.

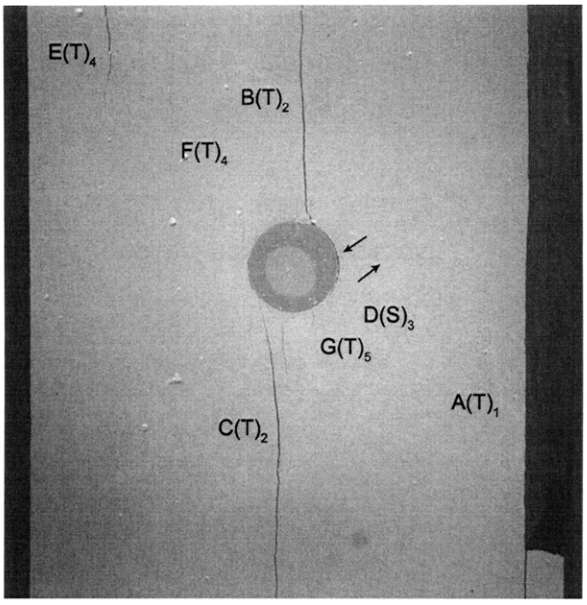

(Recorded by High Speed Video System)

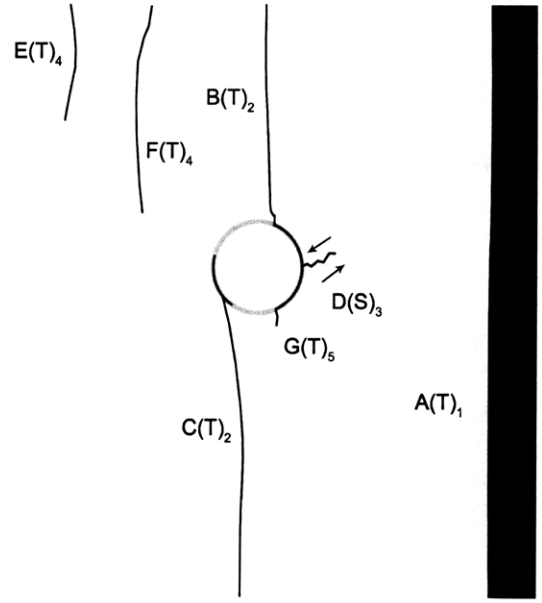

(34.511 MPa) [Max. Stress]
Time: 7 minutes & 19.832 seconds

Tensile cracks (E&F) initiate at the upper specimen boundary and propagate downwards.

Tensile crack (C) then continues to propagate and coalesces with the inclusion boundary.

Tensile crack (G) then initiates at the inclusion boundary and propagates downwards.

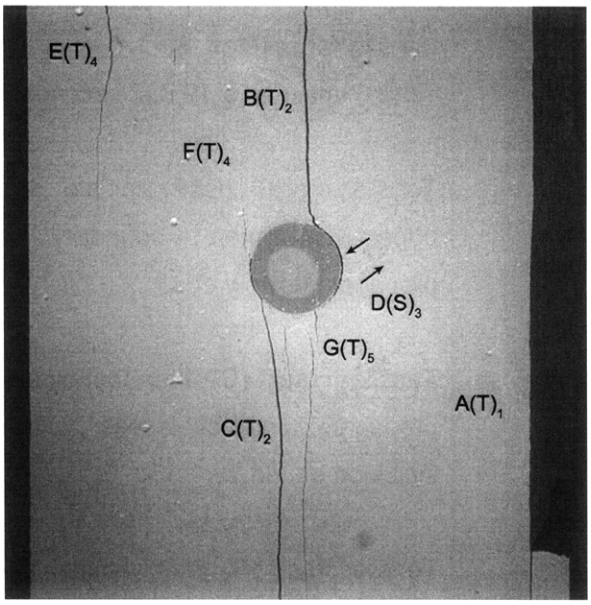

(Recorded by High Speed Video System)

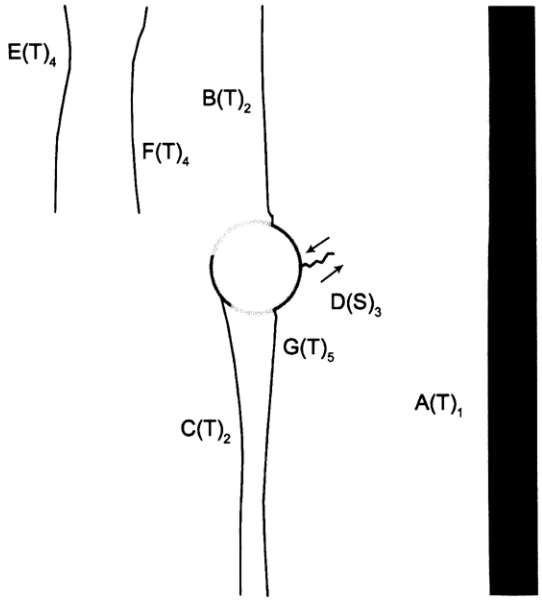

(21.75 MPa)
Time: 7 minutes & 20.275 seconds
HS Image # - 2891

Tensile crack (G) continues to propagate towards the lower specimen boundary.

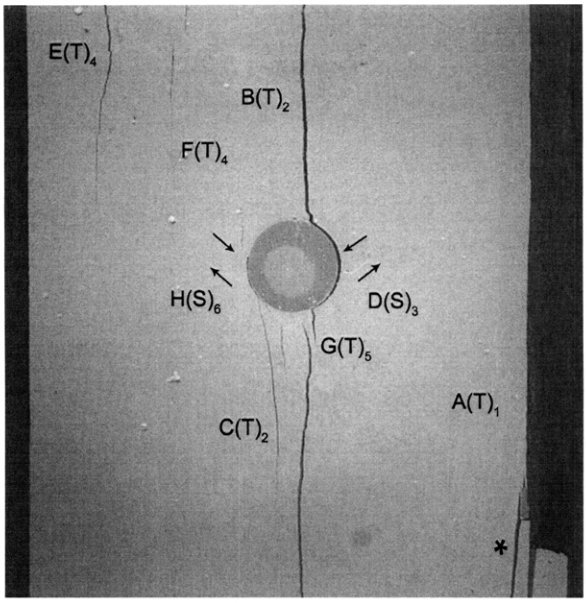

(Recorded by High Speed Video System)

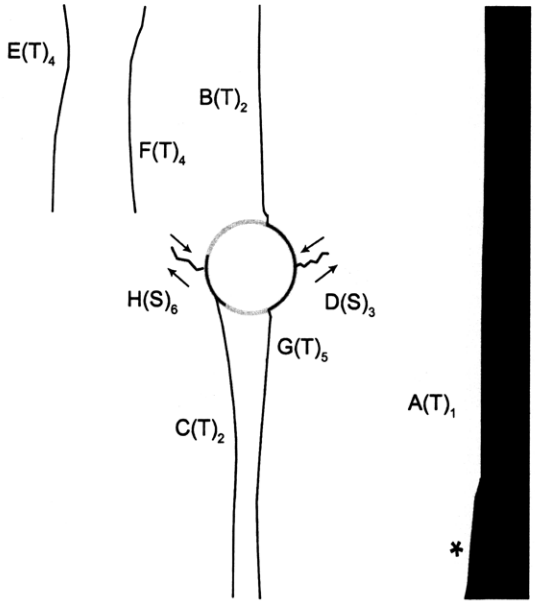

(21.47 MPa)
Time: 7 minutes & 20.276 seconds
HS Image # - 2884

Another piece of specimen detaches (*) from the lower right boundary.

Shear crack (H) then initiates at the inclusion boundary and propagates upwards.

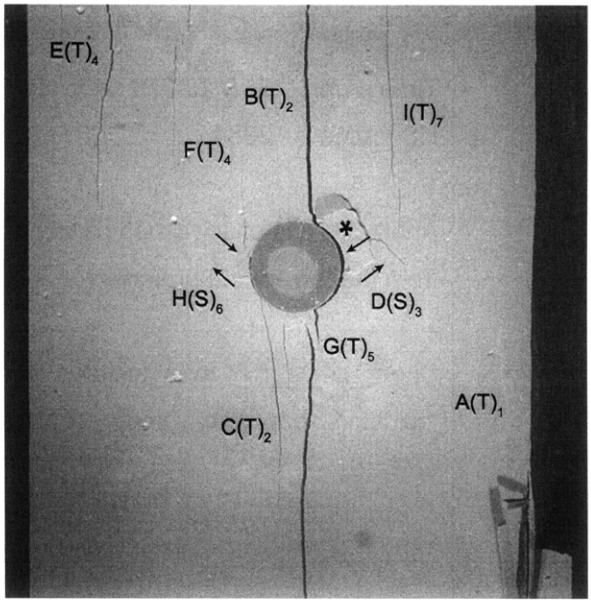

(Recorded by High Speed Video System)

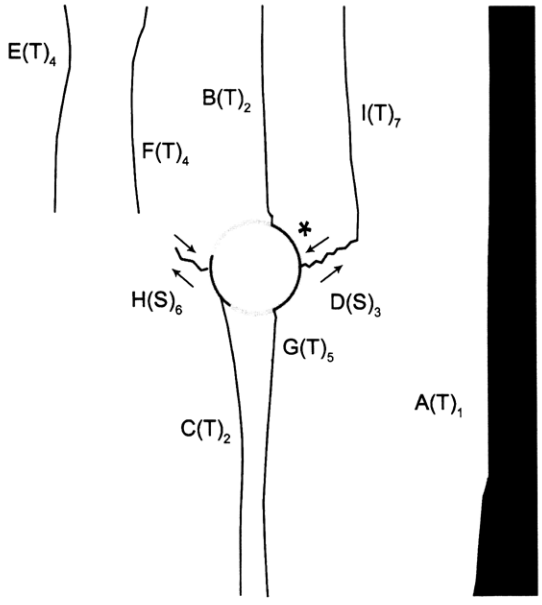

(20.19 MPa)
Time: 7 minutes & 20.282 seconds
HS Image # - 2853

Spalling (*) occurs adjacent to shear crack (D).

As shear crack (D) continues to propagate, tensile crack (I) initiates at shear crack (D) and propagates upwards.

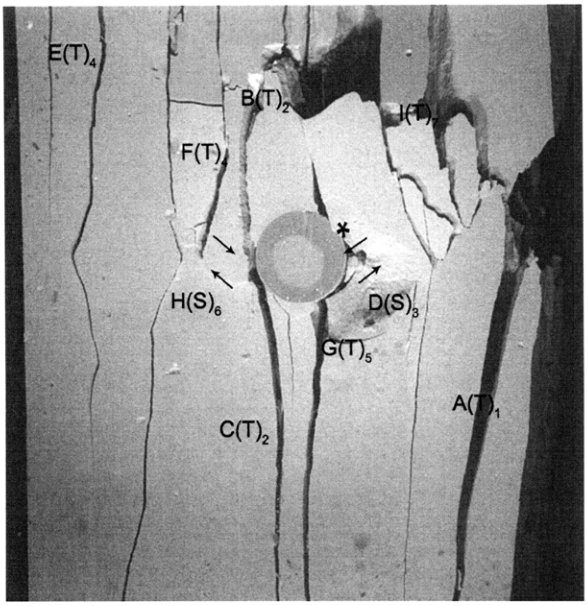

(Recorded by High Speed Video System)

(0 MPa) – Final Picture

Time: 7 minutes & 20.802 seconds

HS Image # - 257

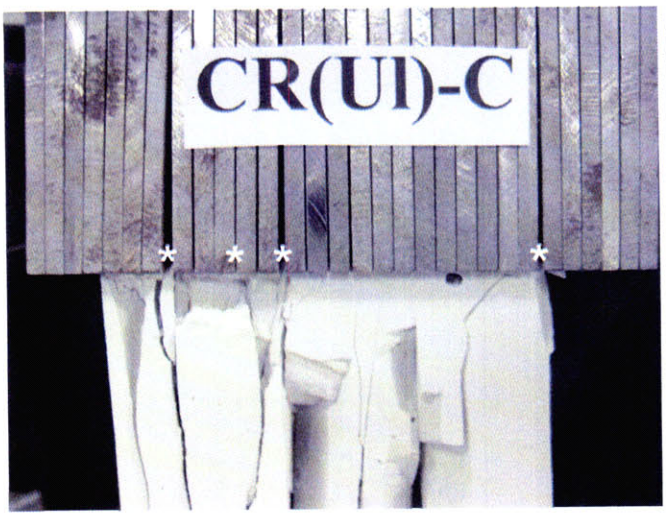	Upper edge of the specimen. The cracks marked with a (*) coincide with the openings between the teeth of the brush platen.
	Lower edge of the specimen. The cracks marked with a (*) coincide with the openings between the teeth of the brush platen.

SUMMARY

Specimen Number: SQ(PI)-A (20090117)

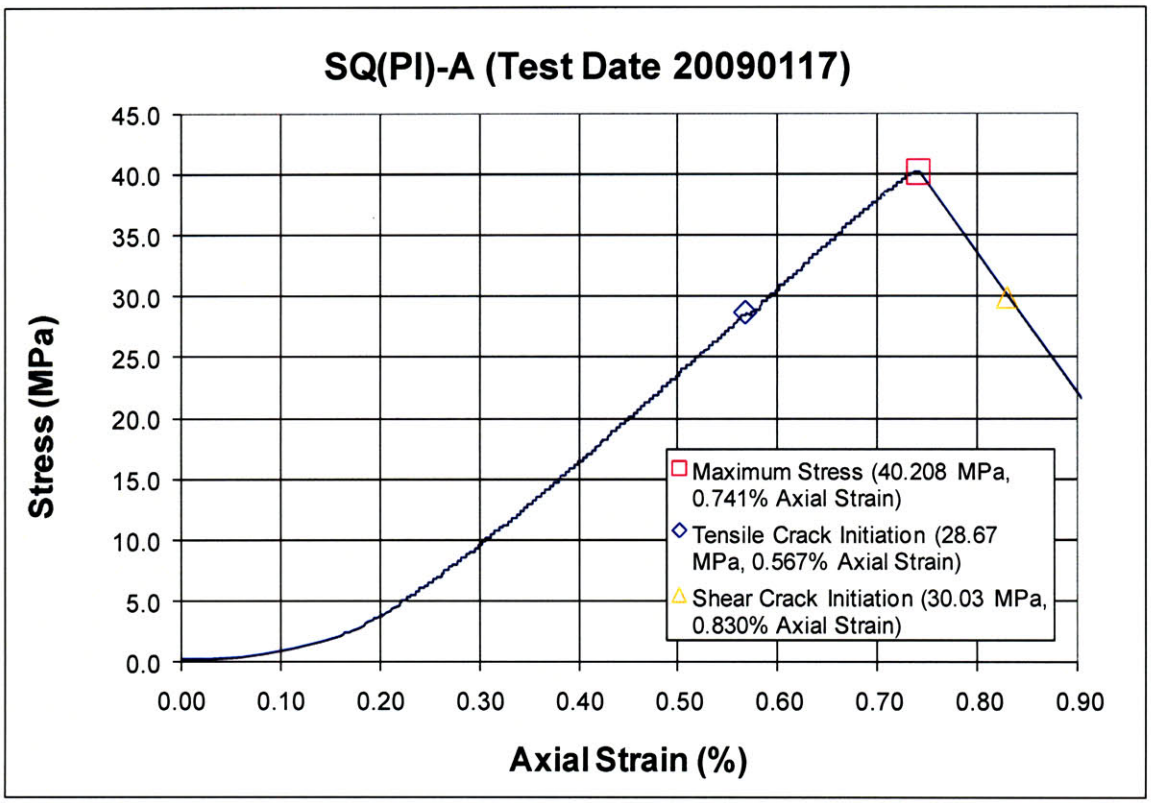

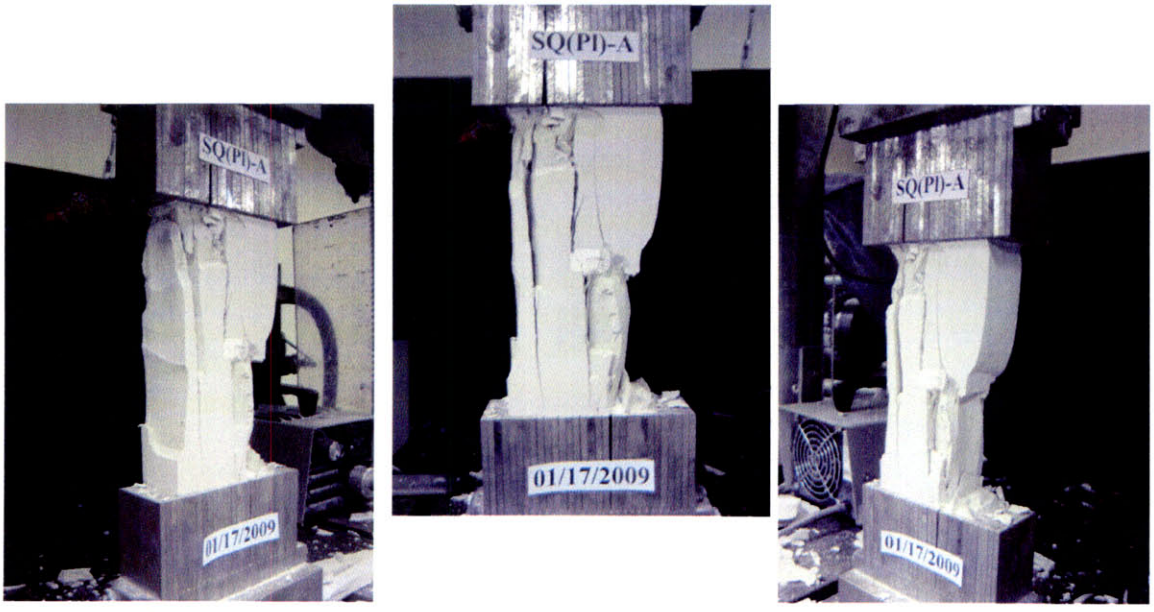

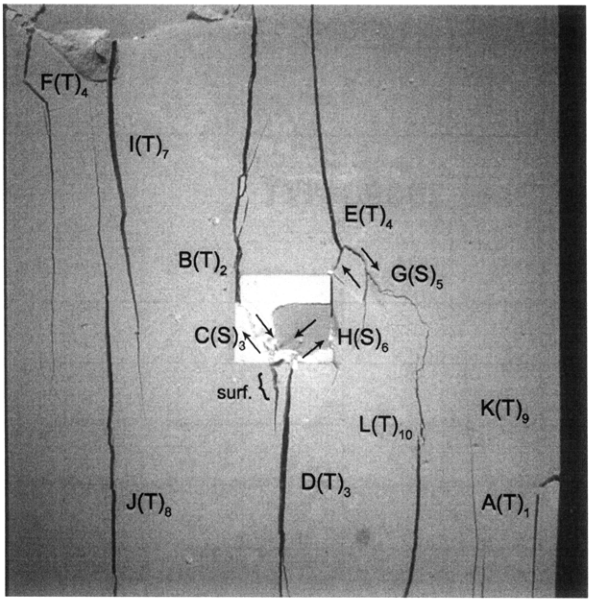

(Recorded by High Speed Video System)

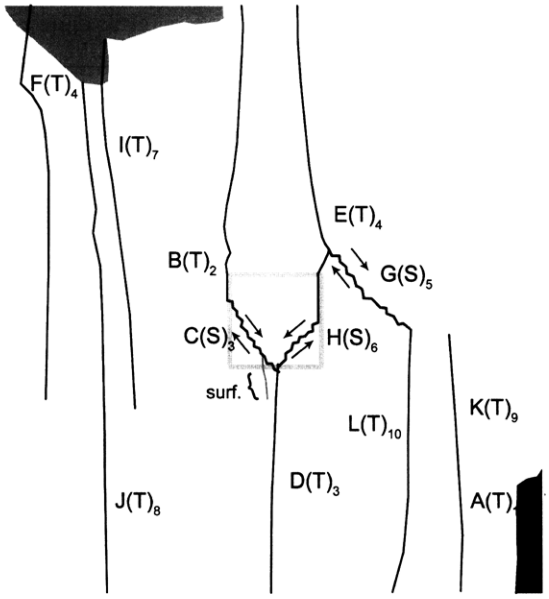

(29.32 MPa)
Time: 8 minutes & 40.561 seconds
HS Image # - 3252

As shear crack (G) continues to propagate, tensile crack (L) initiates at the lower specimen boundary and coalesces with shear crack (G).

Specimen Number: SQ(PI)-B (20090117)

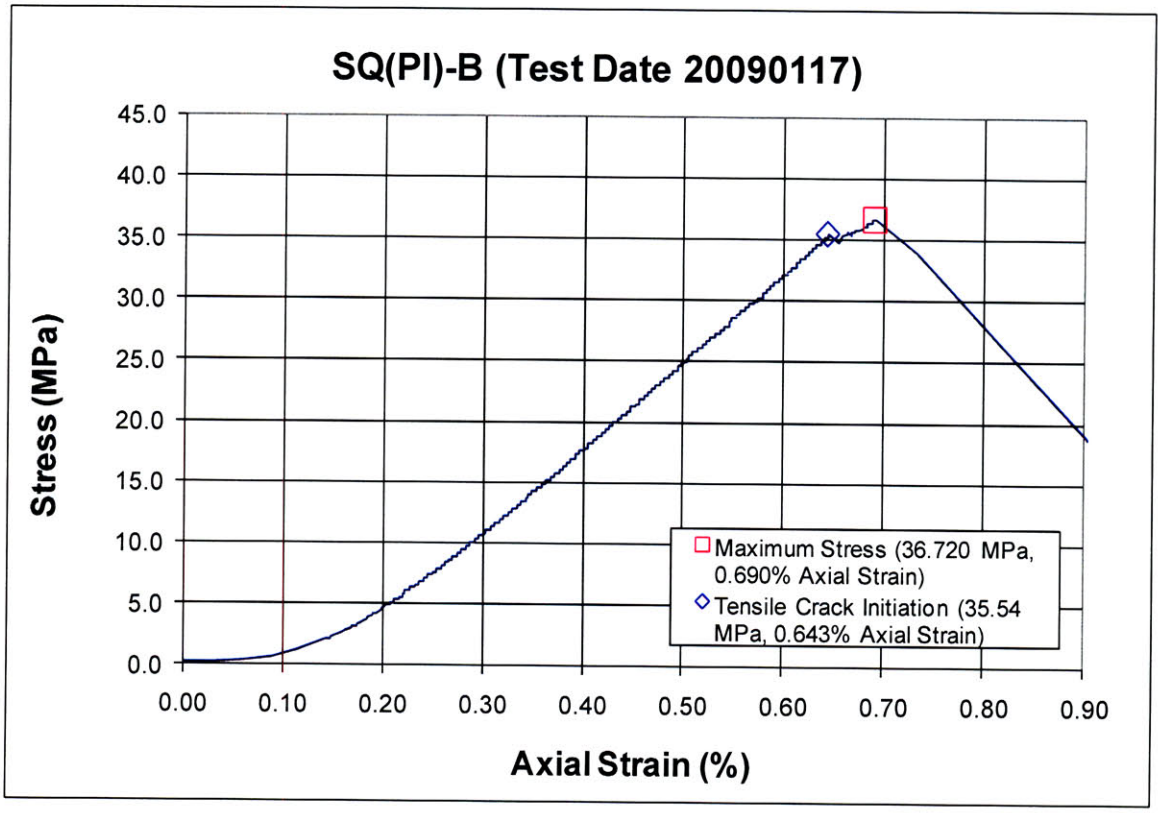

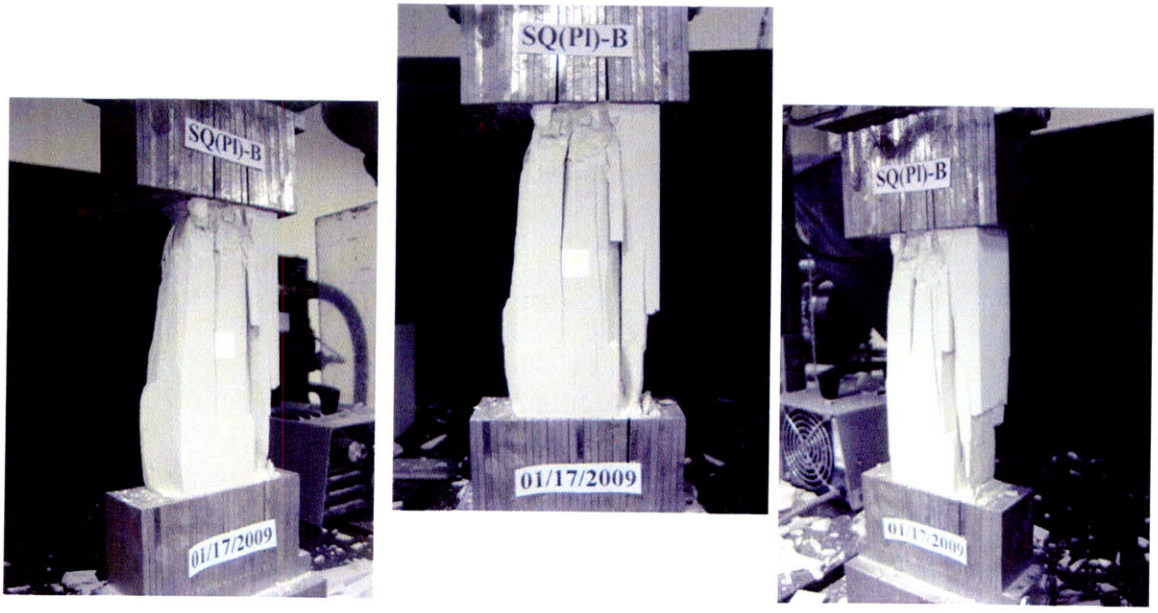

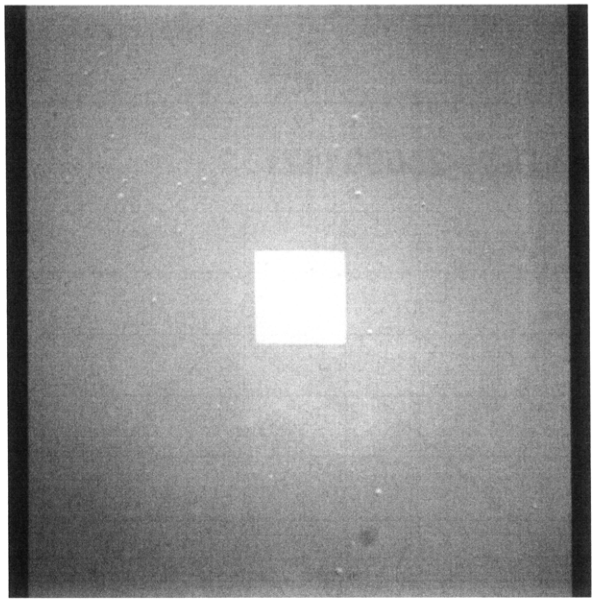

(Recorded by High Speed Video System)

Initial Inclusion Geometries:
SQUARE – Plaster Material

Inclusion **less** stiff than matrix.

High Speed Camera Frame Rate:
5000 pps

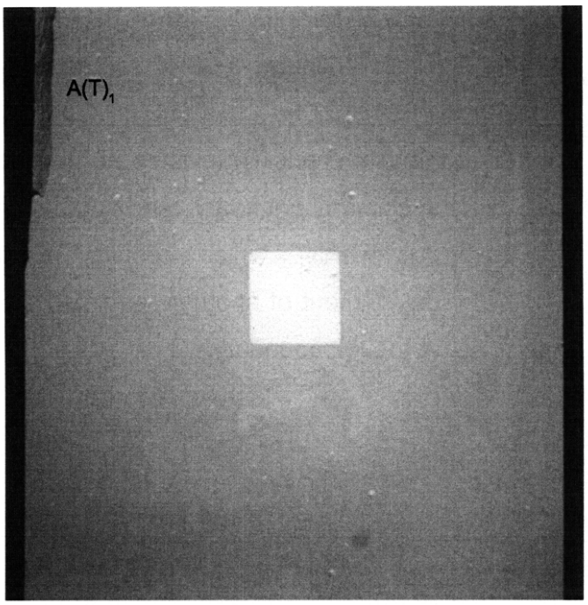

(Recorded by High Speed Video System)

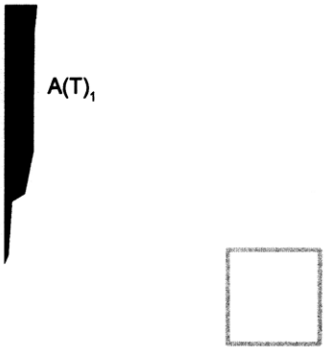

(35.54 MPa)

- Tensile Crack Initiation

Time: 7 minutes & 34.00 seconds

Tensile crack (A) initiates at the upper specimen boundary and propagates downwards, which results in the detachment of a large specimen piece at the upper left boundary.

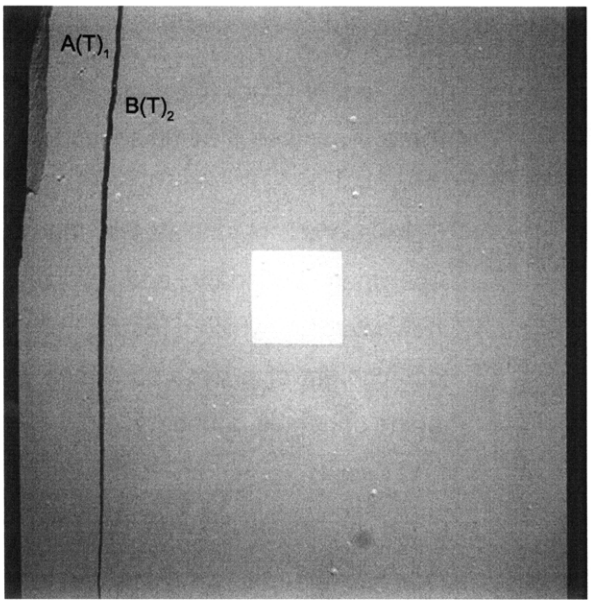

(Recorded by High Speed Video System)

(36.720 MPa) [Max. Stress]
Time: 7 minutes & 50.43 seconds

Tensile crack (B) initiates at the upper specimen boundary and propagates downwards, which results in the detachment of another specimen piece at the left boundary.

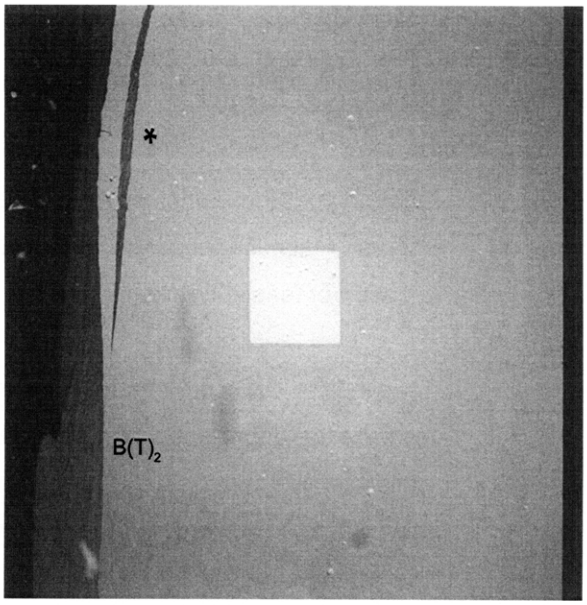

(Recorded by High Speed Video System)

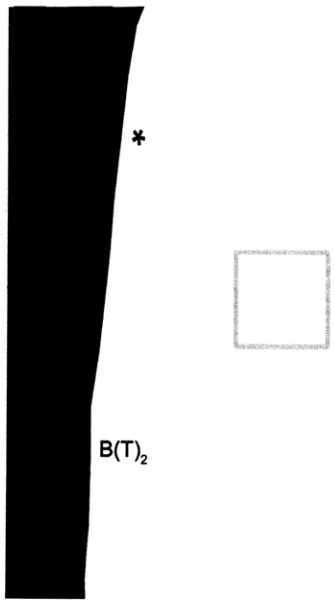

(33.95 MPa)
Time: 7 minutes & 50.628 seconds
HS Image # - 4262

Another piece of specimen detaches (*) from the left boundary prior to tensile crack initiation at the inclusion boundary.

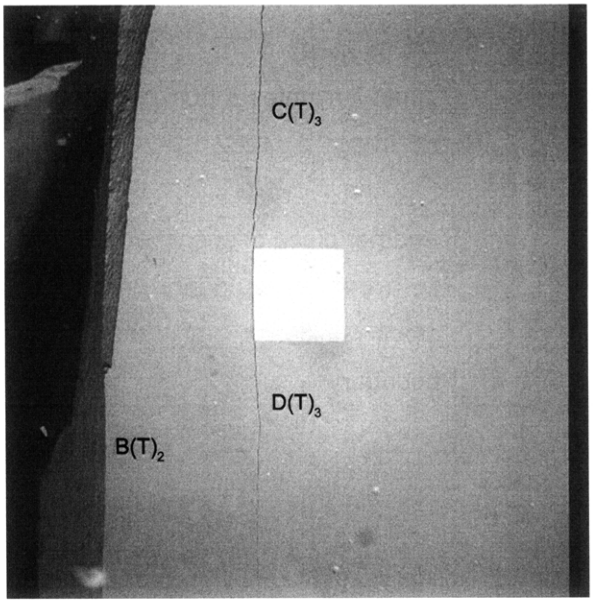

(Recorded by High Speed Video System)

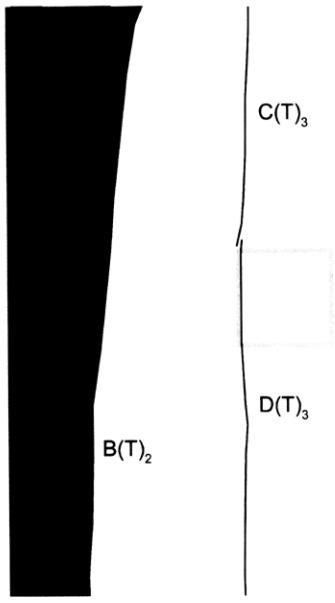

(26.47 MPa)
Time: 7 minutes & 50.664 seconds
HS Image # - 4080

Debonding at the inclusion boundary occurs "simultaneously" with the initiation of tensile cracks (C&D).

Tensile crack (C) propagates upwards towards the upper specimen boundary, while tensile crack (D) propagates downwards towards the lower specimen boundary.

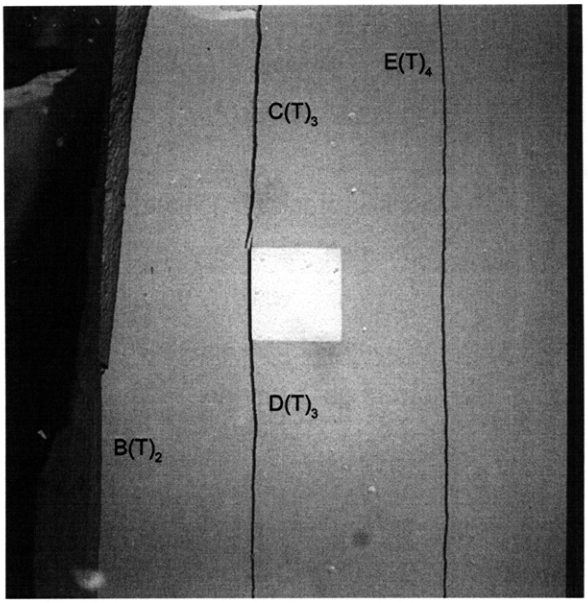

(Recorded by High Speed Video System)

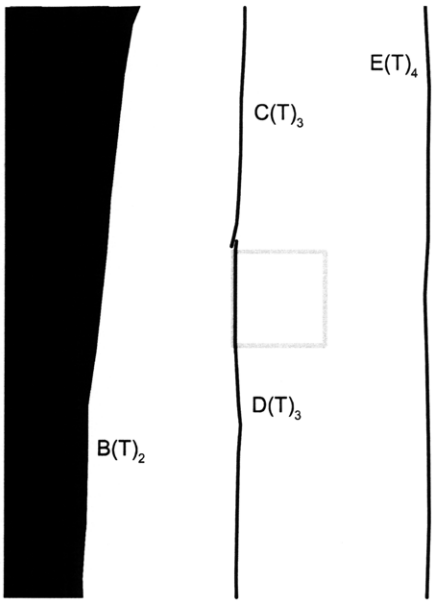

(26.34 MPa)
Time: 7 minutes & 50.665 seconds
HS Image # - 4077

Tensile crack (E) initiates at the upper specimen boundary and propagates downwards.

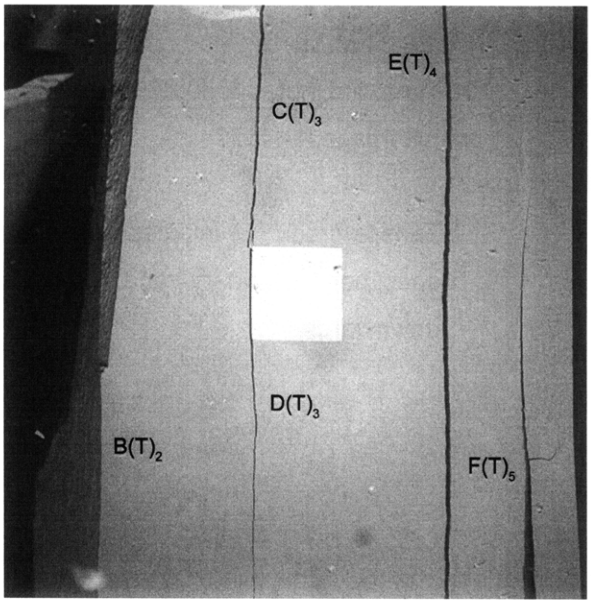

(Recorded by High Speed Video System)

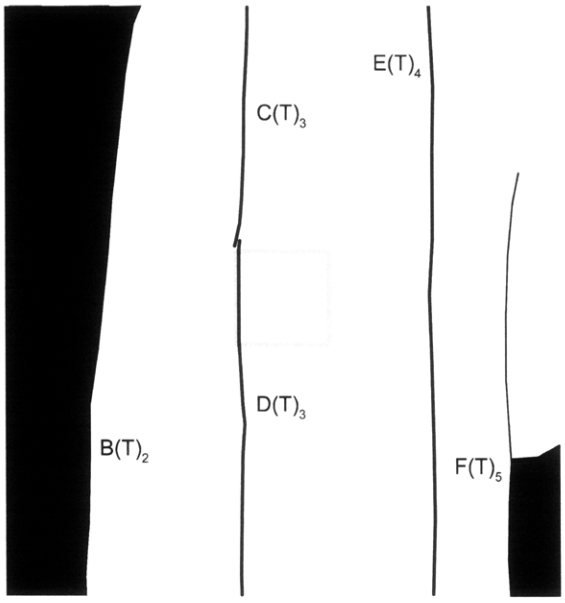

(26.22 MPa)
Time: 7 minutes & 50.666 seconds
HS Image # - 4074

Tensile crack (F) initiates at the lower specimen boundary and propagates upwards, which results in the detachment of a specimen piece at the lower right boundary.

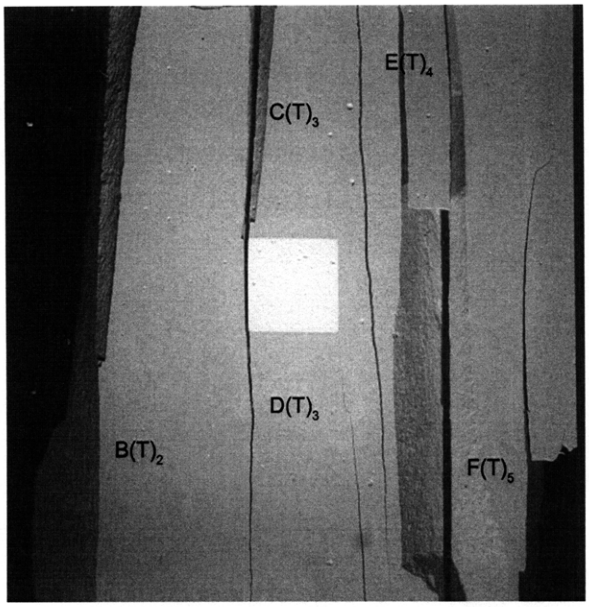

(Recorded by High Speed Video System)

(0 MPa) – Final Picture

Time: 7 minutes & 51.389 seconds

HS Image # - 459

	Upper edge of the specimen. The cracks marked with a (*) coincide with the openings between the teeth of the brush platen.
	Lower edge of the specimen. The cracks marked with a (*) coincide with the openings between the teeth of the brush platen.

SUMMARY

Specimen Number: SQ(PI)-C (20090117)

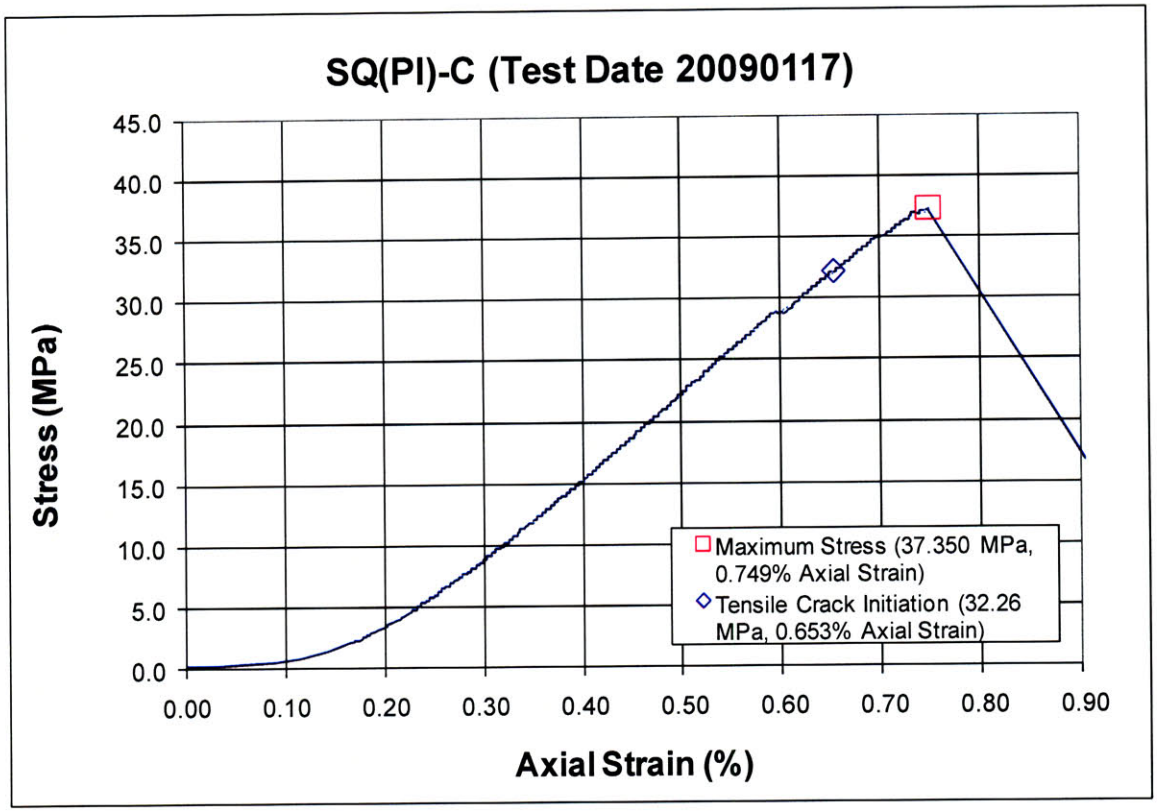

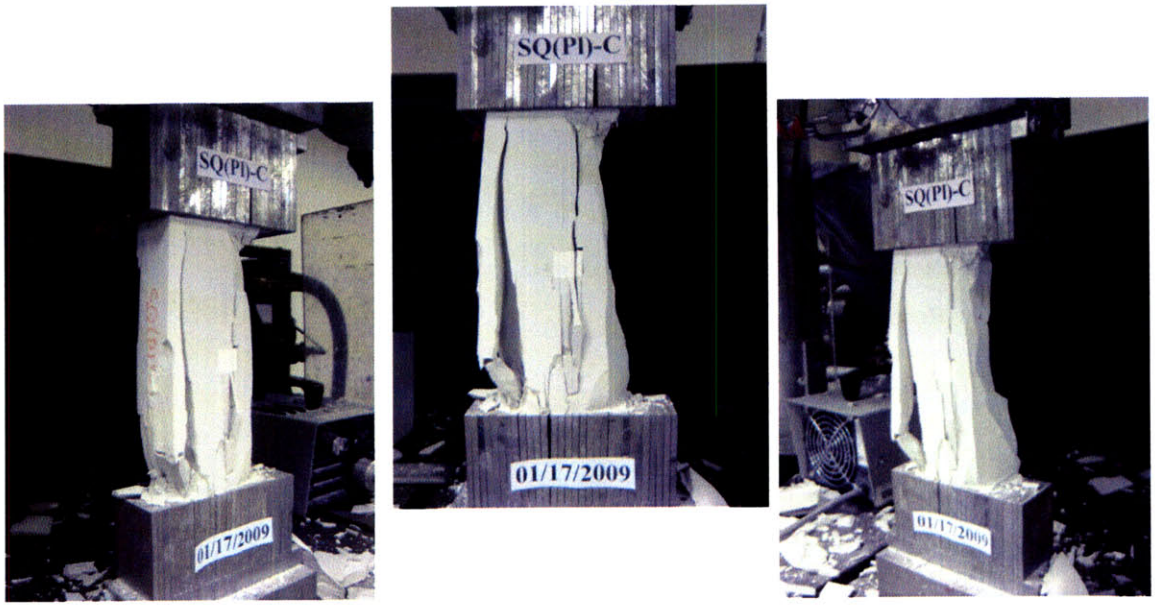

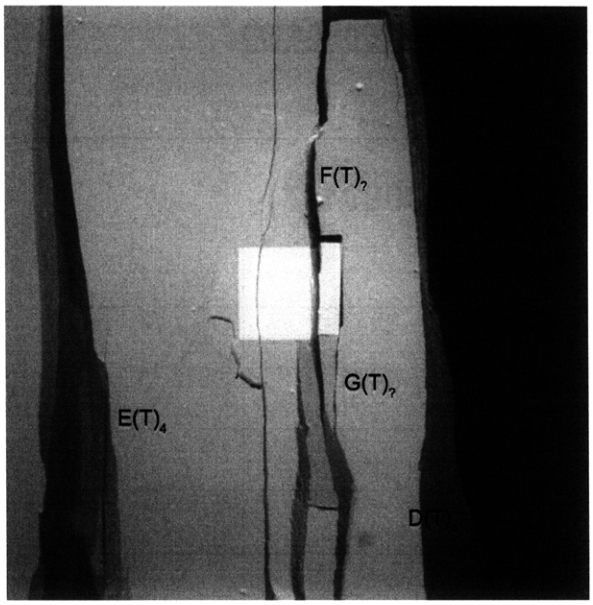

(Recorded by High Speed Video System)

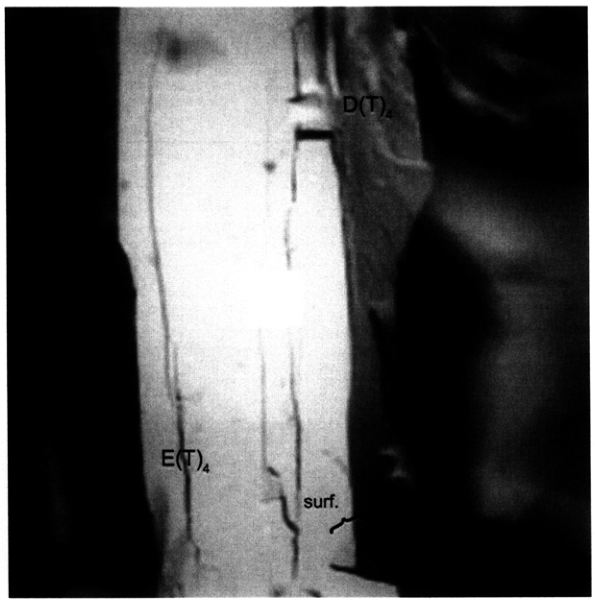

(Recorded by Camcorder)

(0 MPa) – Final Picture
Time: 7 minutes & 59.85 seconds

Based on post-mortem pictures, it is assumed that tensile crack (F) initiates at the lower specimen boundary and propagates upwards through the inclusion.

Based on previous trends, it is also assumed that debonding initiates at the right-hand inclusion boundary, and then tensile crack (G) initiates at the inclusion boundary and propagates downwards.

Specimen Number: SQ(UI)-A (20090117)

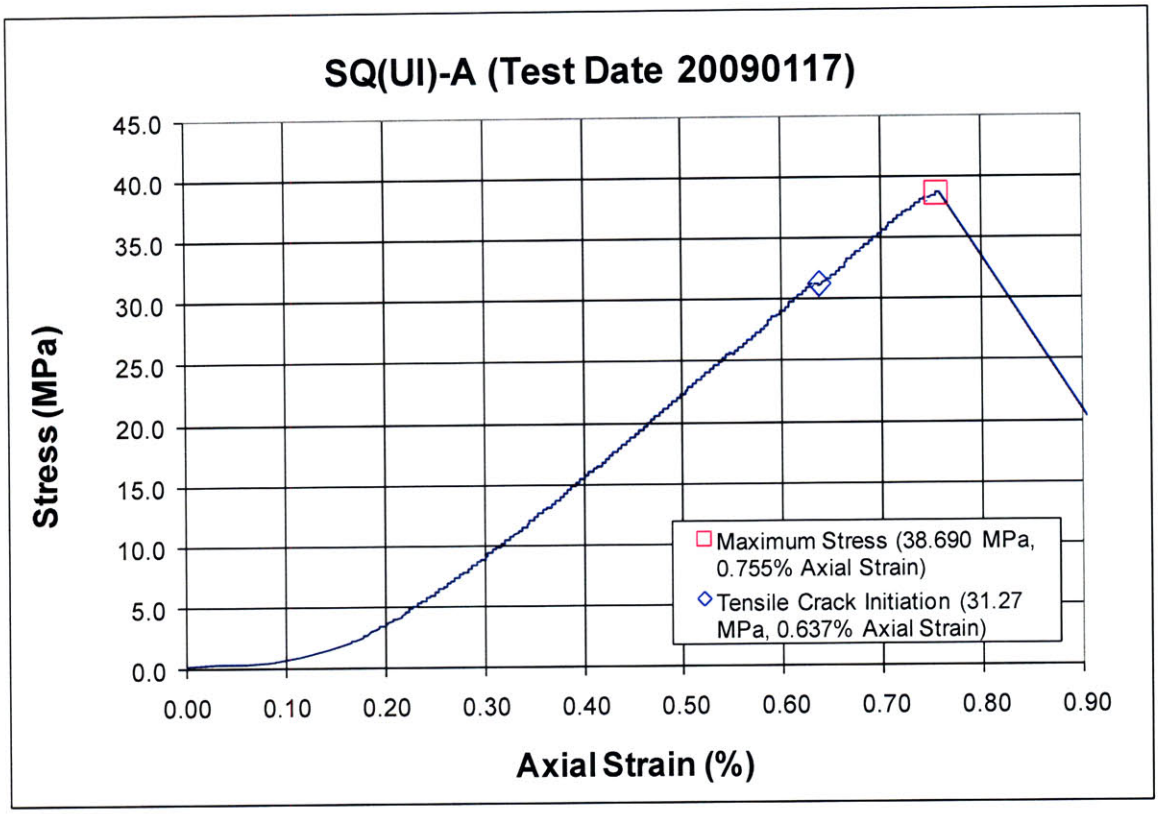

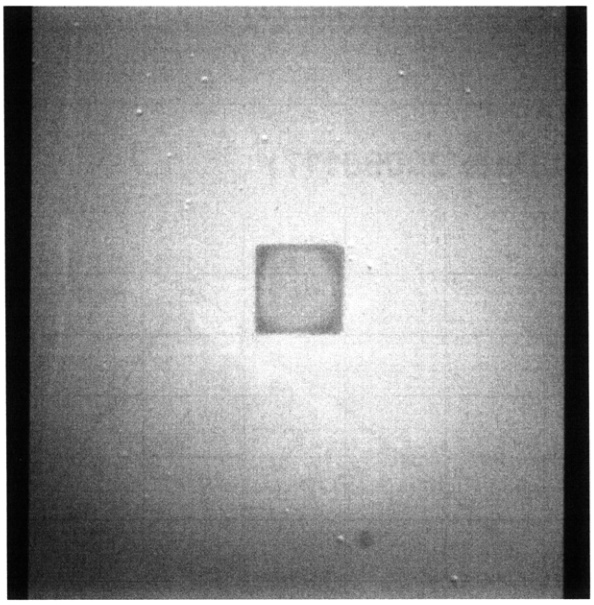

(Recorded by High Speed Video System)

Initial Inclusion Geometries:
SQUARE – Ultracal Material

Inclusion **more** stiff than matrix.

High Speed Camera Frame Rate:
5000 pps

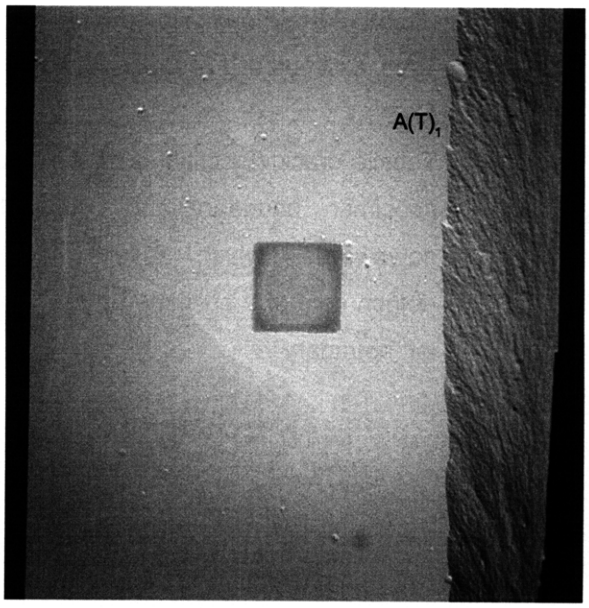

(Recorded by High Speed Video System)

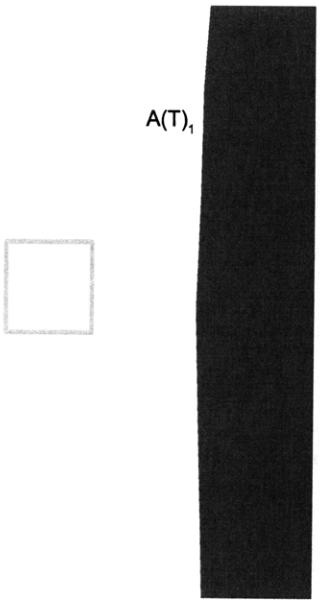

(31.27 MPa)

- Tensile Crack Initiation

Time: 6 minutes & 39.06 seconds

Tensile crack (A) initiates at the upper specimen boundary and propagates downwards, which results in the detachment of a large specimen piece at the right boundary.

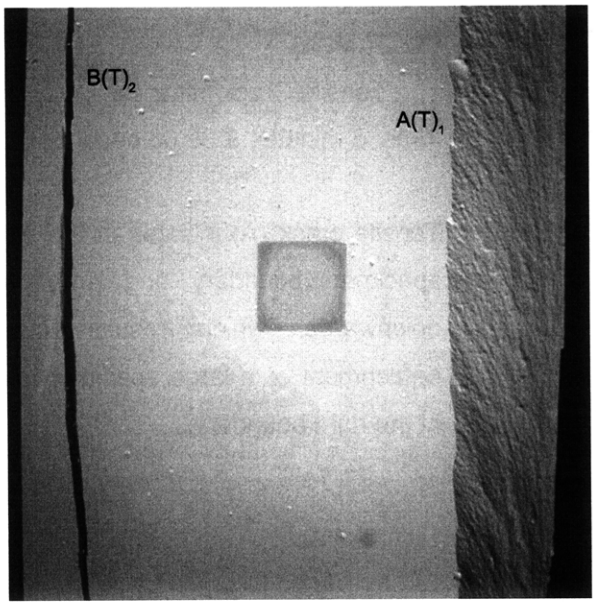

(Recorded by High Speed Video System)

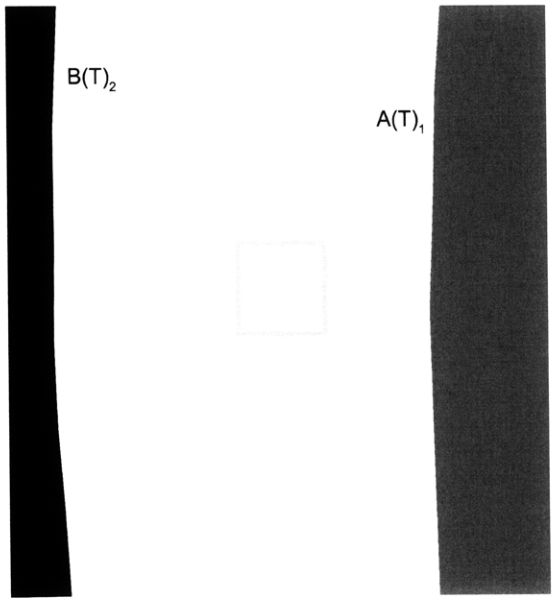

(38.690 MPa) [Max. Stress]
Time: 8 minutes & 24.048 seconds

Tensile crack (B) initiates at the upper specimen boundary and propagates downwards, which results in the detachment of a specimen piece at the left boundary.

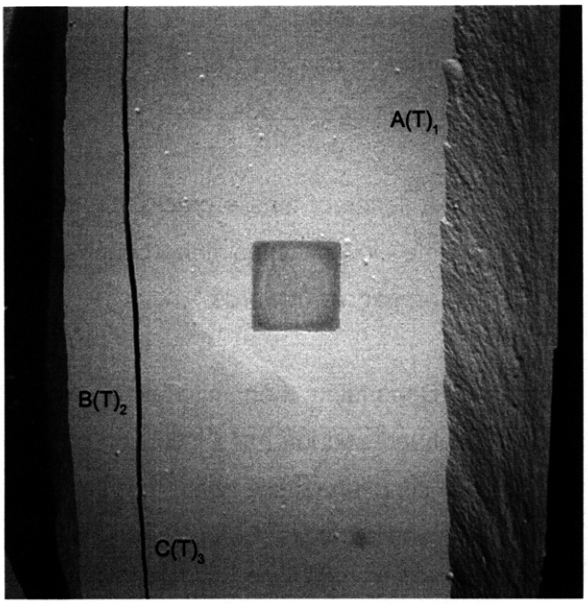

(Recorded by High Speed Video System)

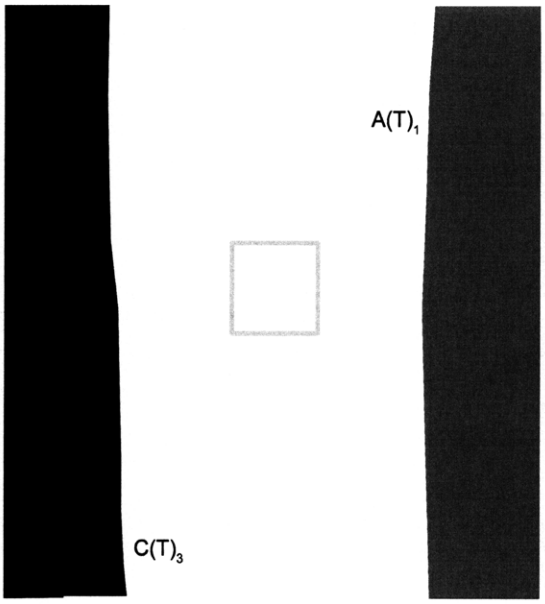

(21.91 MPa)
Time: 8 minutes & 24.205 seconds
HS Image # - 3391

Tensile crack (C) initiates at the lower specimen boundary and propagates upwards, which results in additional detachment at the left boundary.

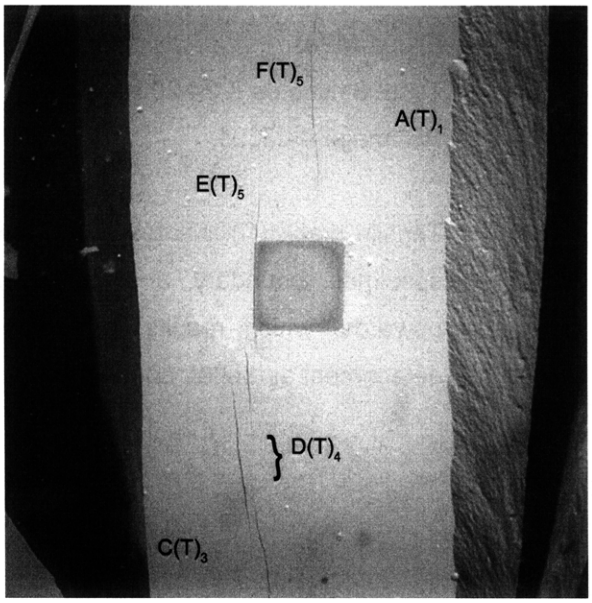

(Recorded by High Speed Video System)

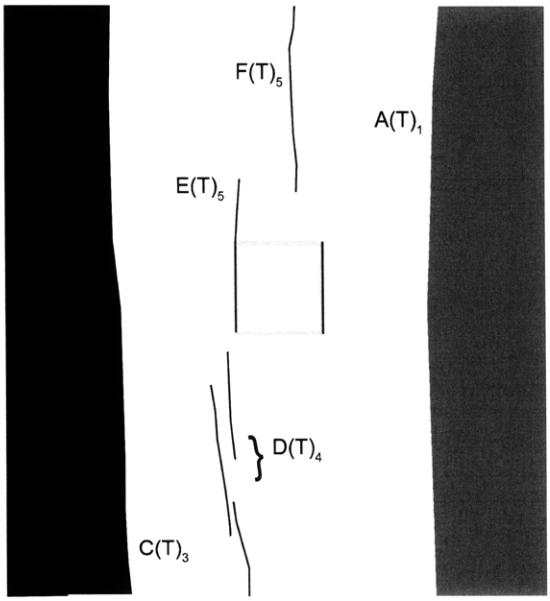

(19.03 MPa)
Time: 8 minutes & 24.214 seconds
HS Image # - 3344

A series of tensile cracks (D) initiate at the lower specimen boundary and propagate upwards.

Debonding then initiates at the right-hand and left-hand inclusion boundary, "simultaneously" with the initiation of tensile cracks (E&F).

The initiation point of tensile crack (F) was not determined. It either initiated at the upper specimen boundary and propagated downwards, or initiated just above the inclusion boundary and propagated upwards.

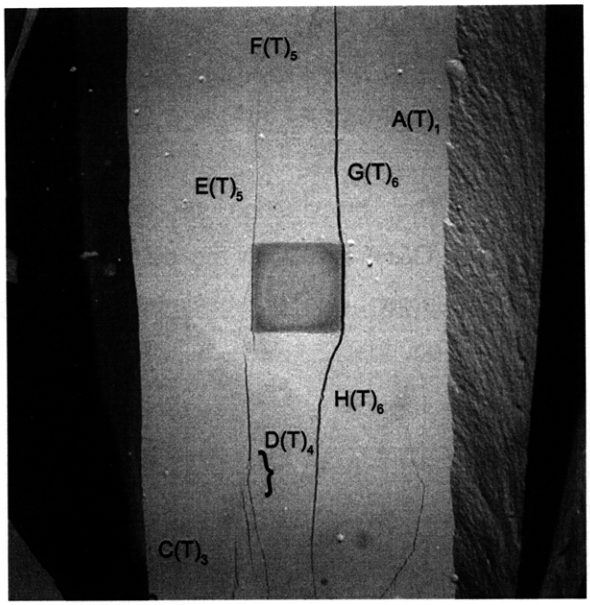

(Recorded by High Speed Video System)

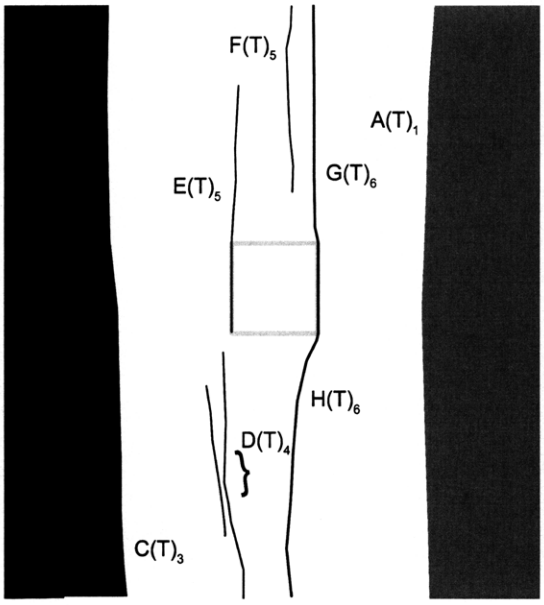

(18.97 MPa)
Time: 8 minutes & 24.214 seconds
HS Image # - 3343

Tensile cracks (G&H) initiate at the inclusion boundary and propagate upwards and downwards, respectively.

Two segments of tensile crack (D) continue to propagate and coalesce.

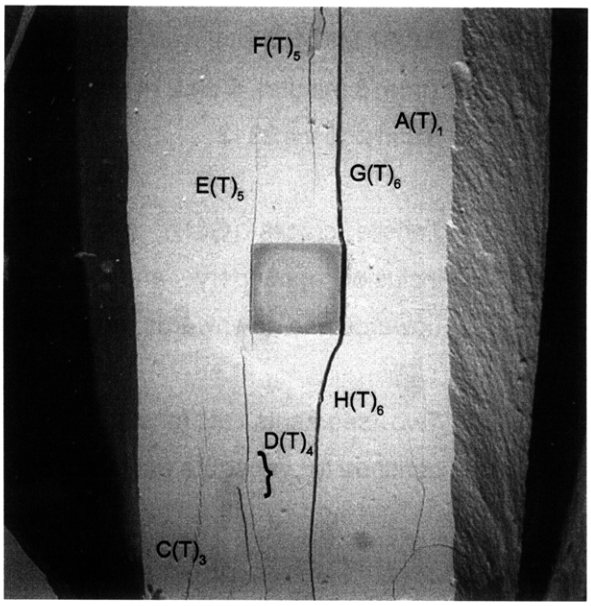

(Recorded by High Speed Video System)

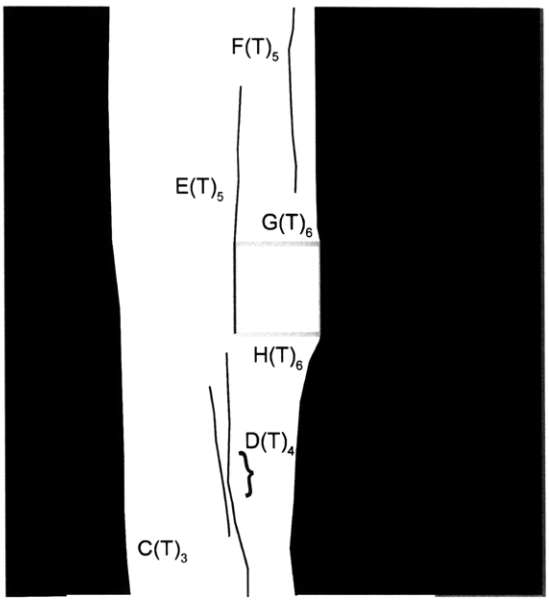

(18.85 MPa)
Time: 8 minutes & 24.215 seconds
HS Image # - 3341

The propagation of tensile cracks (G&H) results in the detachment of a large piece of specimen at the right boundary.

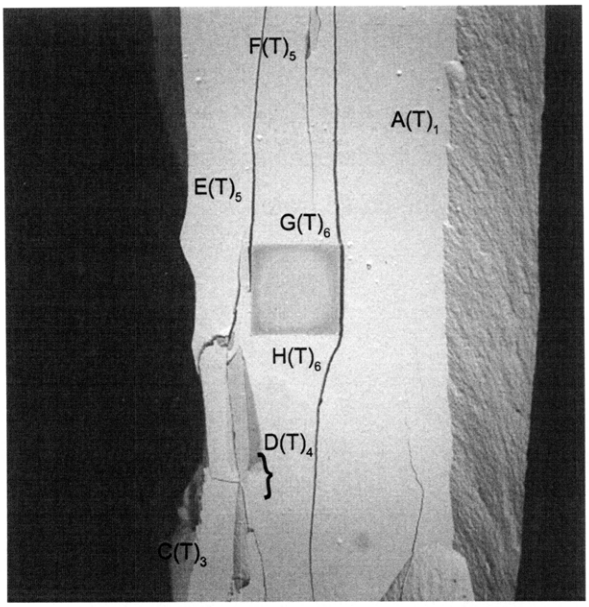

(Recorded by High Speed Video System)

(0 MPa) – Final Picture

Time: 8 minutes & 24.515 seconds

HS Image # - 1838

	Upper edge of the specimen. The cracks marked with a (*) coincide with the openings between the teeth of the brush platen.
	Lower edge of the specimen. The cracks marked with a (*) coincide with the openings between the teeth of the brush platen.

SUMMARY

Specimen Number: SQ(UI)-B (20090117)

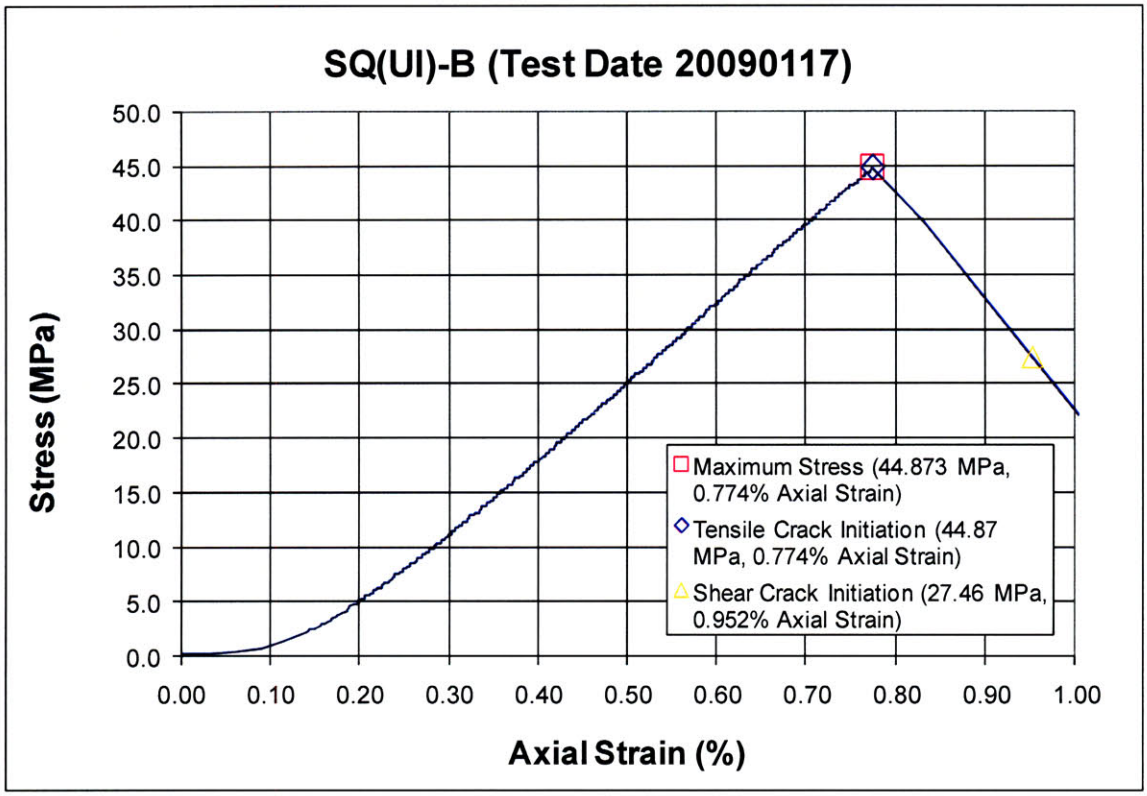

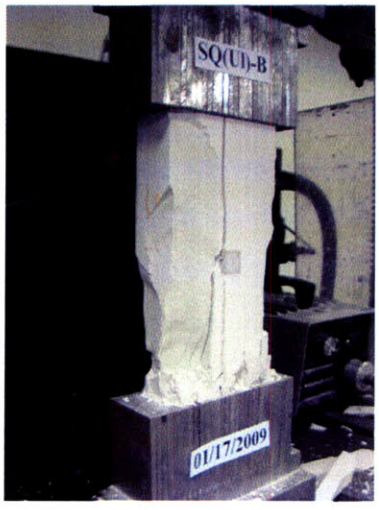

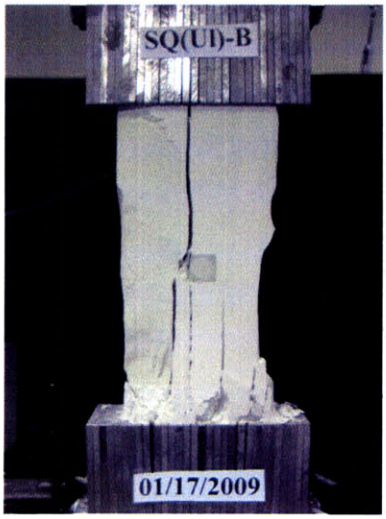

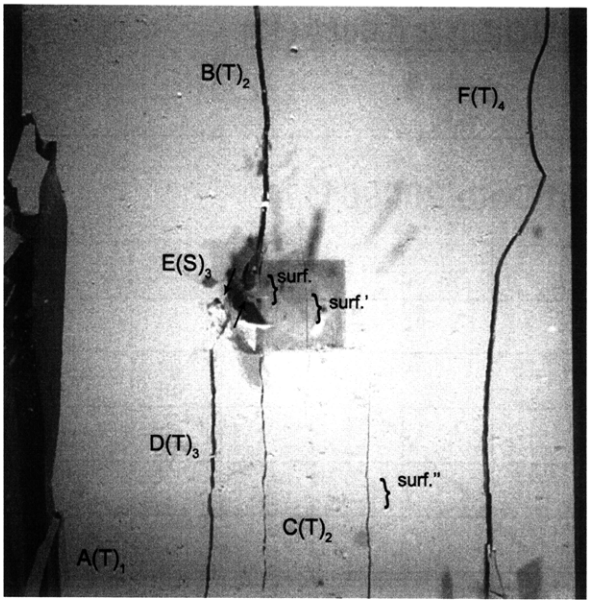

(Recorded by High Speed Video System)

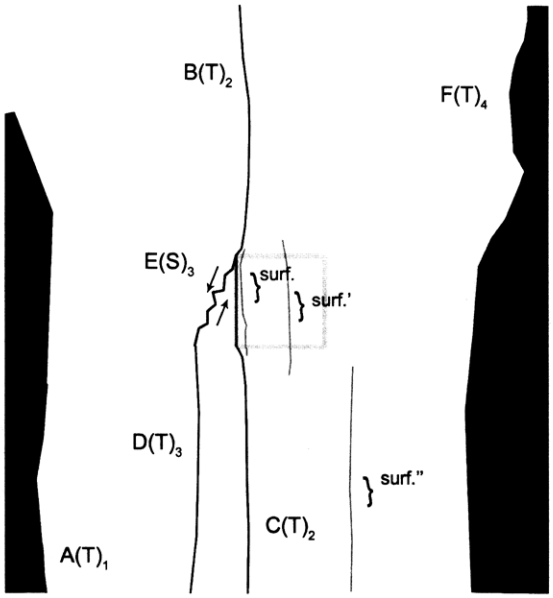

(26.79 MPa)
Time: 9 minutes & 46.085 seconds
HS Image # - 3344

Tensile crack (F) initiates at the lower specimen boundary and propagates upwards, which results in the detachment of a specimen piece at the right boundary.

Surface crack (surf.") then initiates at the lower specimen boundary and propagates upwards.

SUMMARY

Specimen Number: SQ(UI)-C (20090117)

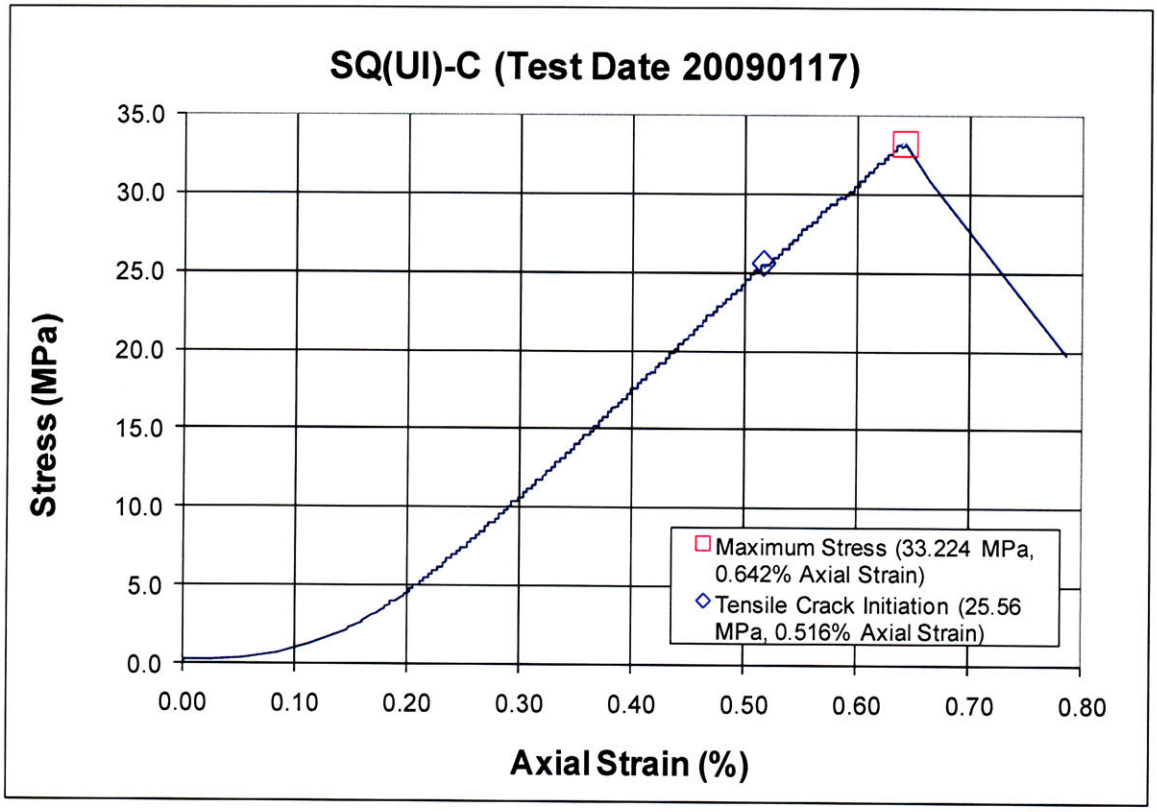

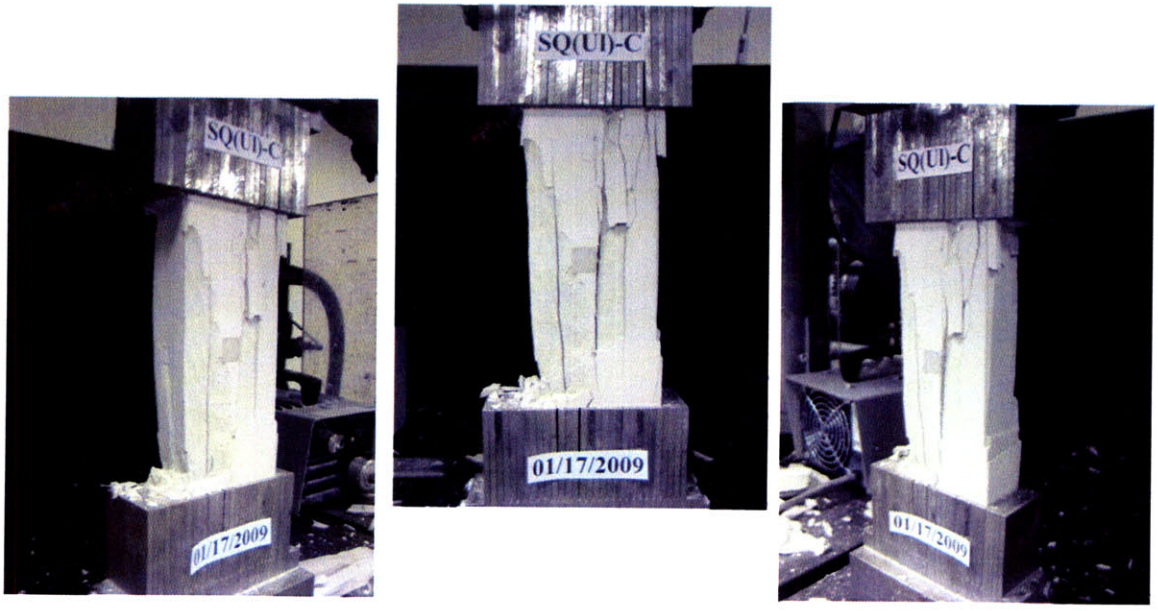

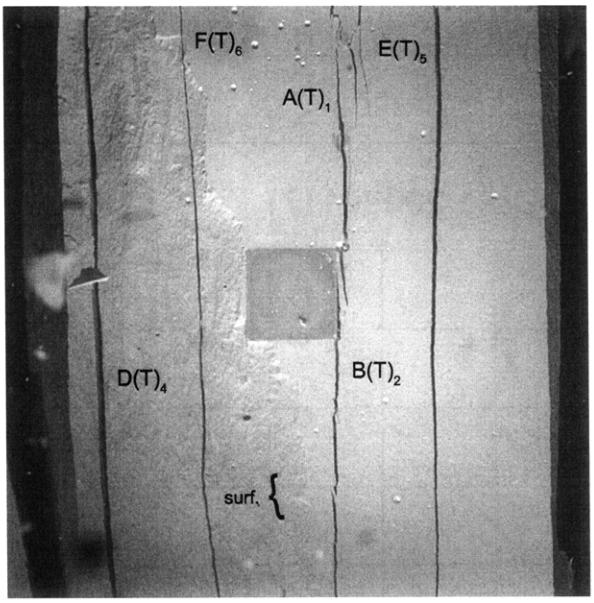

(Recorded by High Speed Video System)

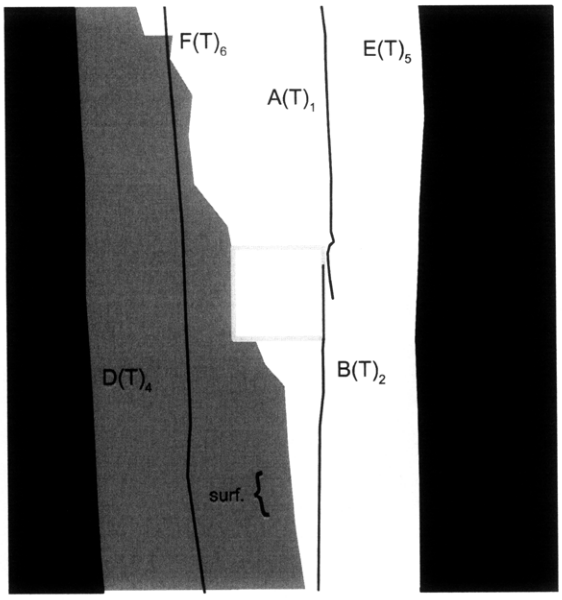

(24.65 MPa)
Time: 6 minutes & 58.478 seconds
HS Image # - 2413

Tensile crack (F) initiates at the lower specimen boundary and propagates upwards.

APPENDIX D – Circular, Half-inch Inclusion Pairs

This appendix contains the detailed analyses for specimens with circular, half-inch inclusion pairs. These specimens contained either an Ultracal, or plaster, inclusion pair. One complete analysis for every geometric series is presented, while only summaries of the other specimens are presented. For a complete summary of results, refer to Chapter 5. A list of tested specimens is summarized below.

		$\beta = 0°$	$\beta = 30°$	$\beta = 60°$
Circular Inclusions	Plaster	CR(Pl)-0-0A CR(Pl)-0-0B CR(Pl)-0-0C*	CR(Pl)-30-0A CR(Pl)-30-0B* CR(Pl)-30-0C	CR(Pl)-60-0A CR(Pl)-60-0B* CR(Pl)-60-0C
	Ultracal	CR(Ul)-0-0A CR(Ul)-0-0B CR(Ul)-0-0C*	CR(Ul)-30-0A* CR(Ul)-30-0B CR(Ul)-30-0C	CR(Ul)-60-0A CR(Ul)-60-0B CR(Ul)-60-0C*

* A complete analysis for this specimen is presented in the Appendix.

SUMMARY

Specimen Number: CR(PI)-0-0B (20080812)

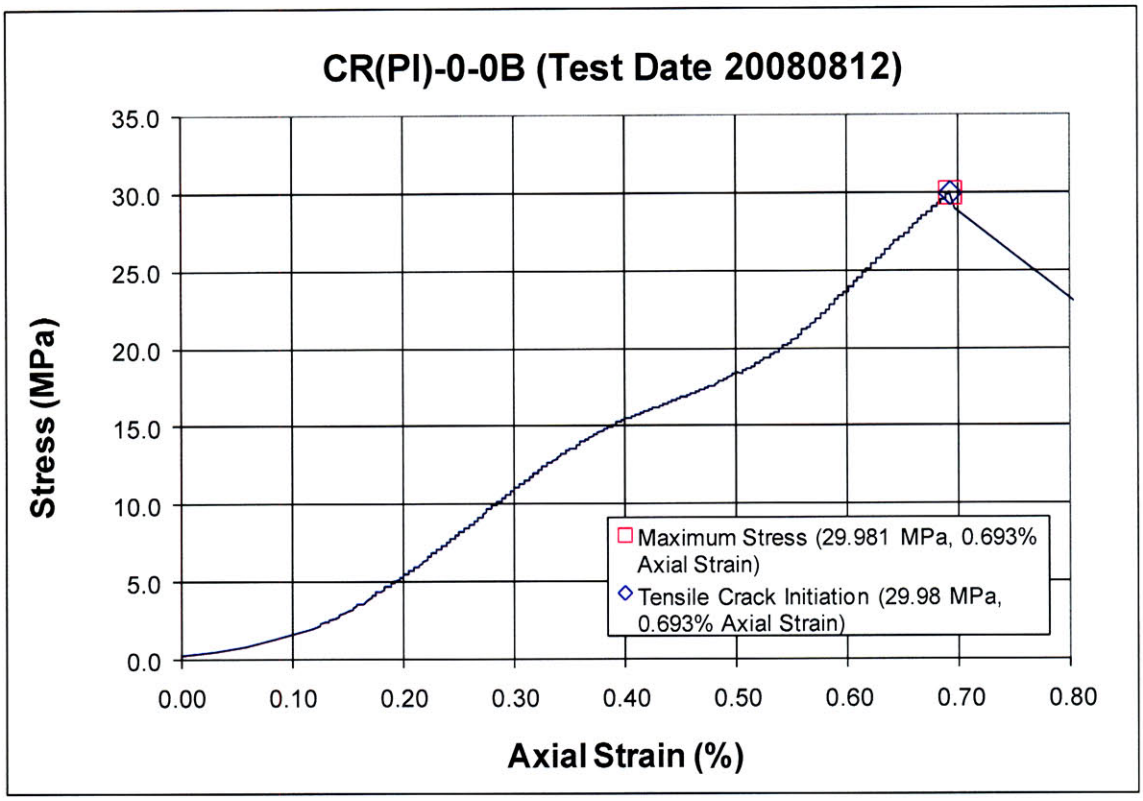

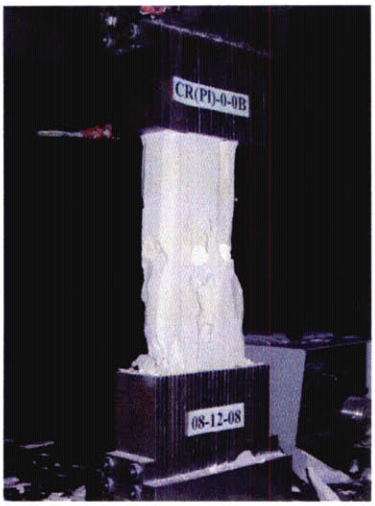

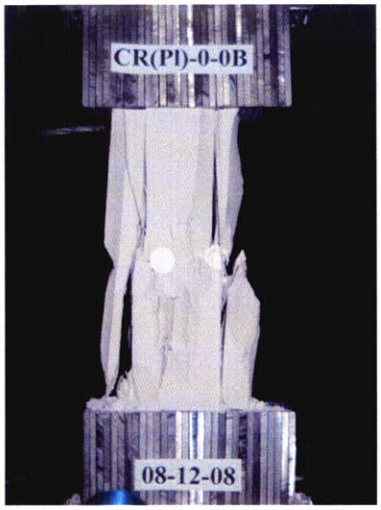

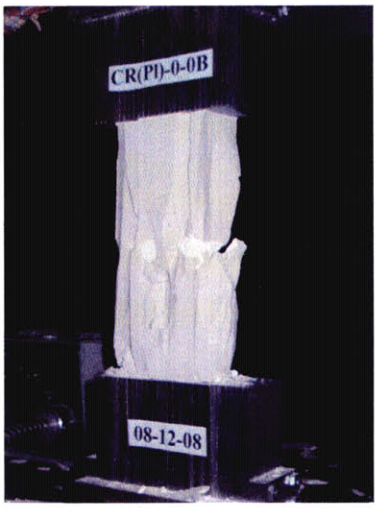

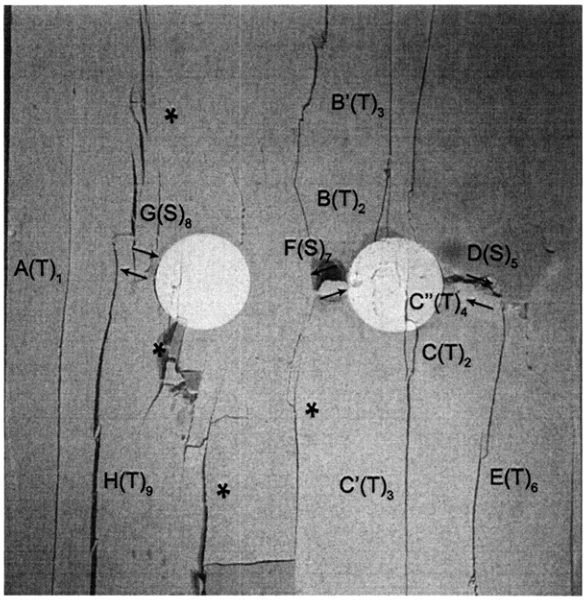

(Recorded by High Speed Video System)

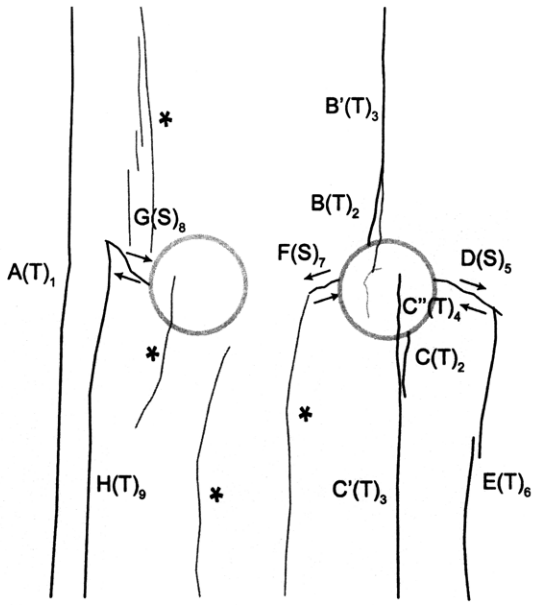

(29.12 MPa)
Time: 6 minutes & 26.576 seconds
HS Image # - 3336

Shear crack (G) initiates at the left-hand inclusion boundary and propagates away from the inclusion.

Tensile crack (H), which appears to be en echelon in nature, initiates at the lower specimen boundary and propagates until its coalescence with shear crack (G).

Specimen Number: CR(PI)-0-0C (20080812)

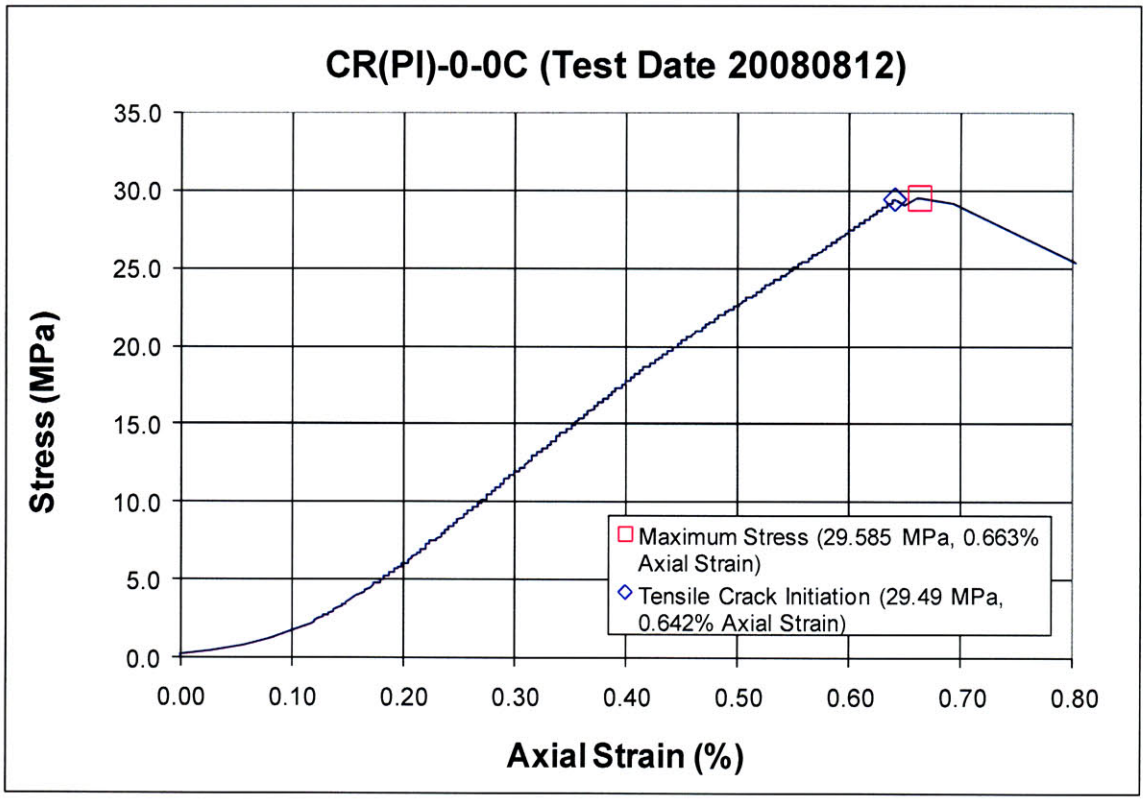

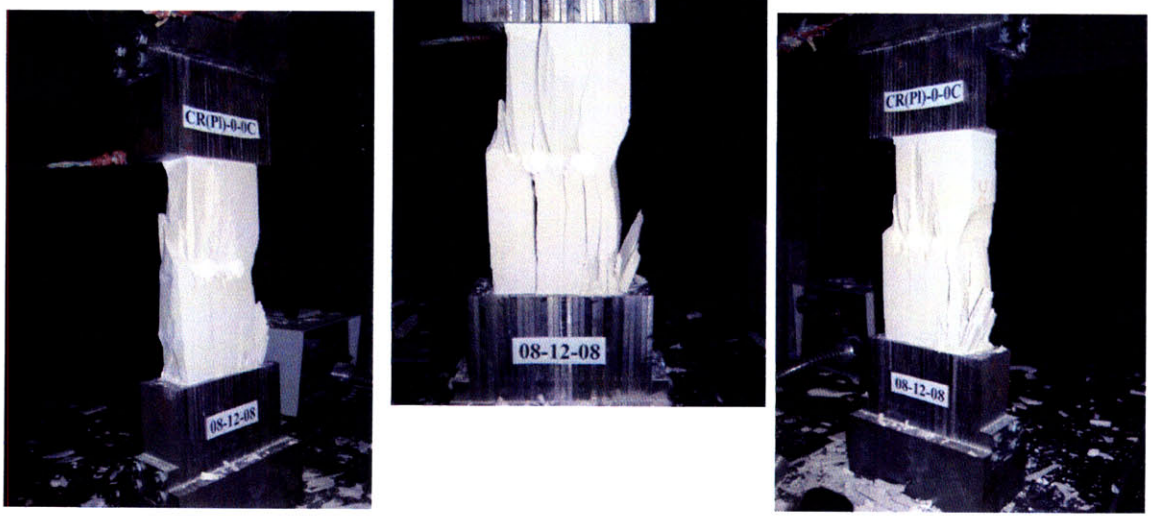

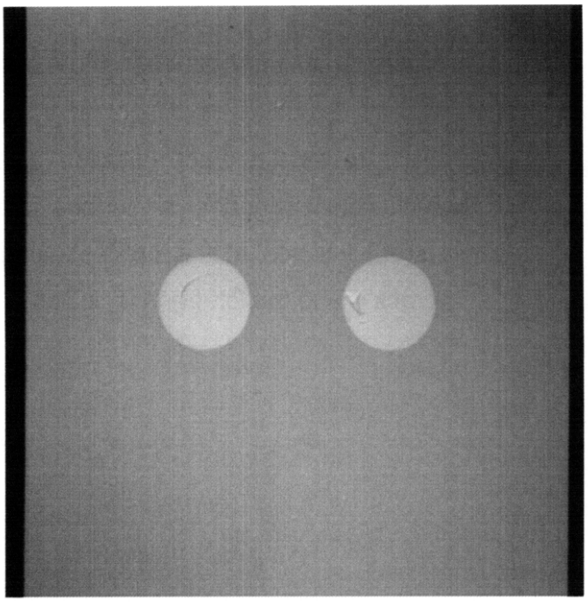

(Recorded by High Speed Video System)

Initial Inclusion Geometries:
CIRCLES – Plaster Material

Inclusion **less** stiff than matrix.

Initial surface crack present prior to testing within the left-hand inclusion.

High Speed Camera Frame Rate:
5000 pps

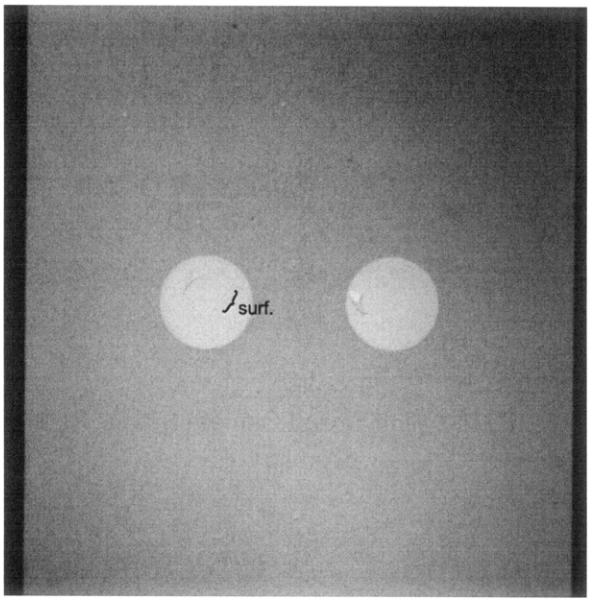

(Recorded by High Speed Video System)

surf.

(26.48 MPa)
Time: 5 minutes & 33.432 seconds

Prior to tensile crack initiation at the inclusion boundary, a surface crack (surf.) initiates at the pre-test surface crack within the left-hand inclusion.

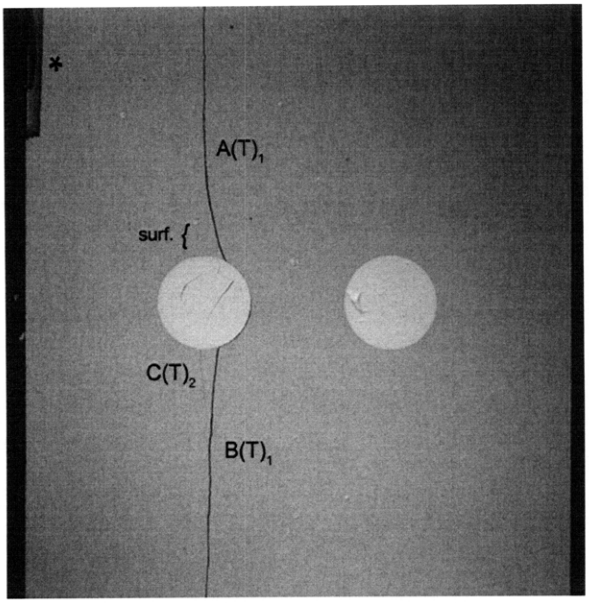

(Recorded by High Speed Video System)

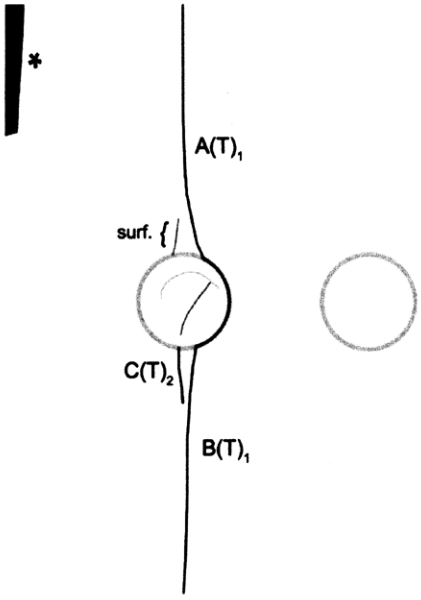

(29.49 MPa)

- Tensile Crack Initiation

Time: 6 minutes & 18.68 seconds

Tensile crack (A) initiates at the upper boundary of the left-hand inclusion and propagates upwards. Tensile crack (B) initiates at the lower boundary of the left-hand inclusion and propagates downwards. Tensile cracks (A&B) coalesce by propagating around the right-hand inclusion boundary.

A small piece of specimen then detaches from the upper left-hand specimen boundary. Tensile crack (C) initiates at the lower boundary of the left-hand inclusion, while a surface crack (surf.) initiates at the upper inclusion boundary.

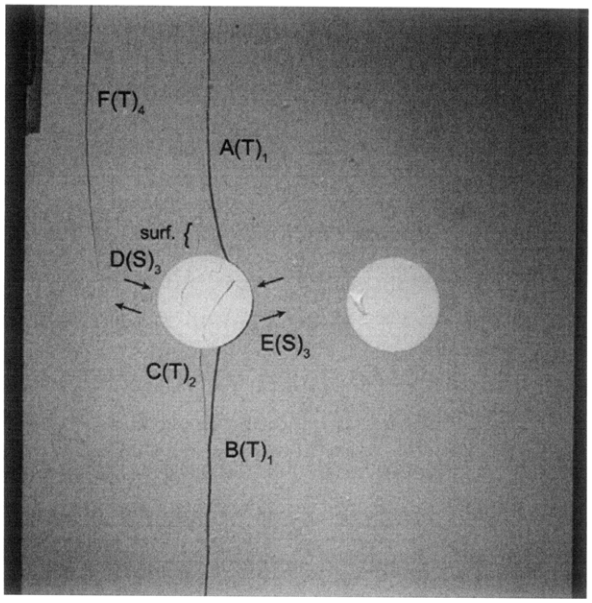

(Recorded by High Speed Video System)

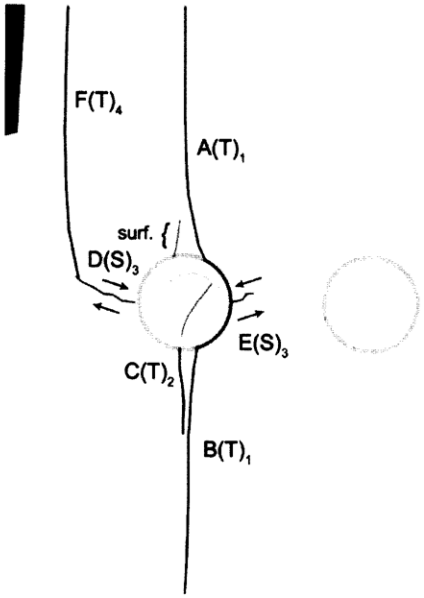

(29.585 MPa) [Max. Stress] - FAILURE
Time: 6 minutes & 19.182 seconds
HS Image # - 3426

Shear cracks (D&E) initiate at the boundary of the left-hand inclusion and propagate away from the inclusion.

Tensile crack (F) then initiates at the upper specimen boundary and propagates until its coalescence with shear crack (D).

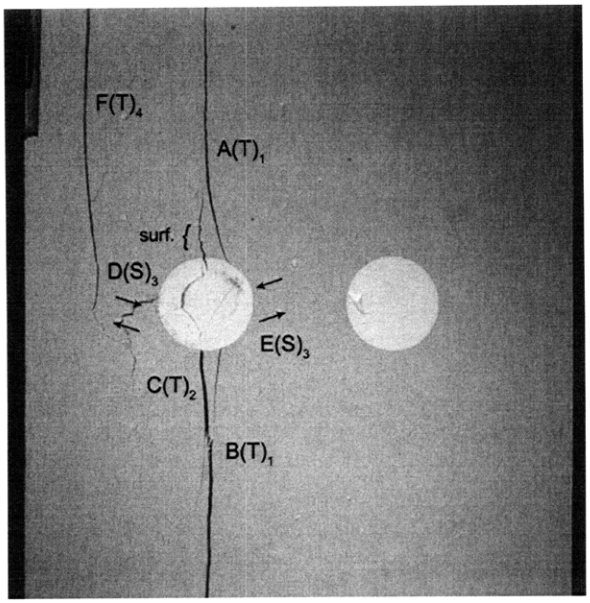

(Recorded by High Speed Video System)

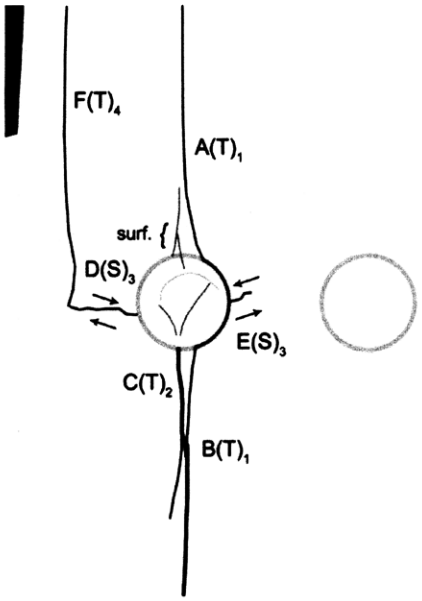

(29.24 MPa)
Time: 6 minutes & 19.425 seconds
HS Image # - 2212

Tensile crack (C) coalesces with tensile crack (B), which results in the increase of the apertures of tensile cracks (B&C).

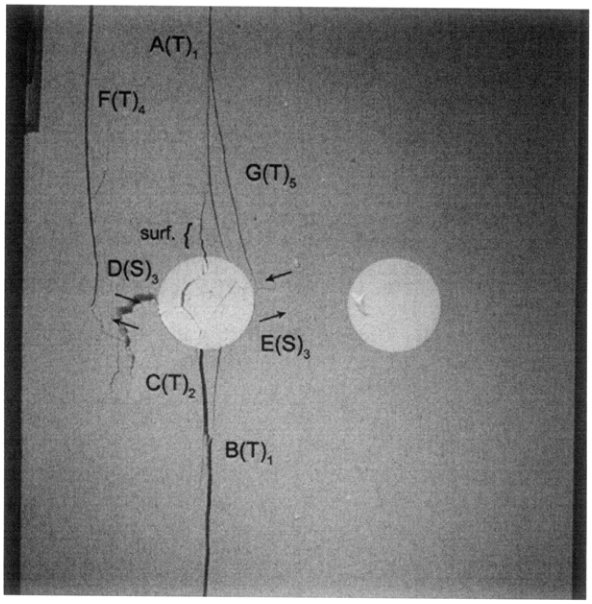

(Recorded by High Speed Video System)

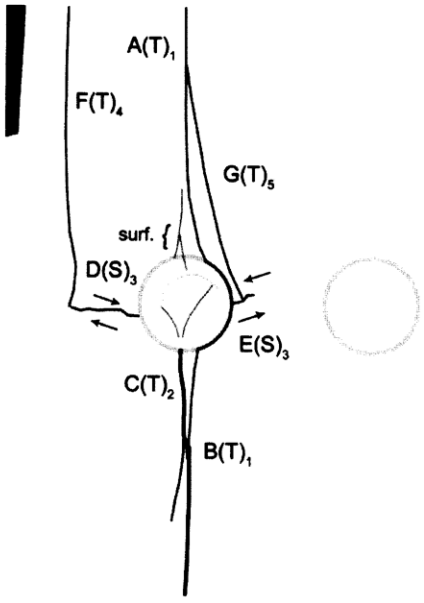

(28.06 MPa)
Time: 6 minutes & 19.450 seconds
HS Image # - 2090

Tensile crack (G) initiates at shear crack (E) and propagates until its coalescence with tensile crack (A).

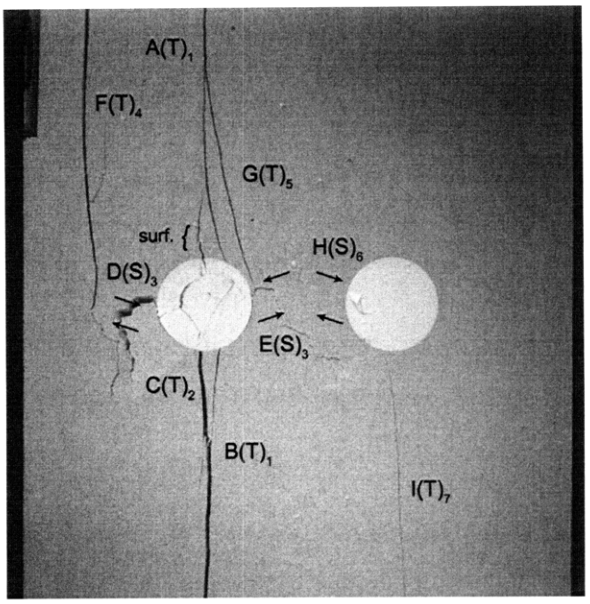

(Recorded by High Speed Video System)

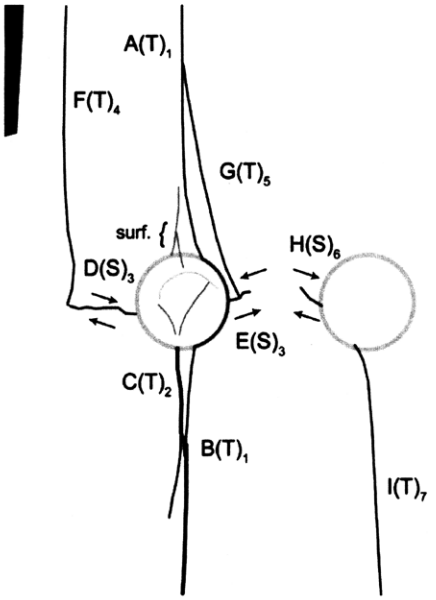

(28.04 MPa)
Time: 6 minutes & 19.450 seconds
HS Image # - 2089

Shear crack (H) initiates at the left-hand boundary of the right-hand inclusion.

Tensile crack (I) initiates at the lower boundary of the right-hand inclusion and propagates downwards.

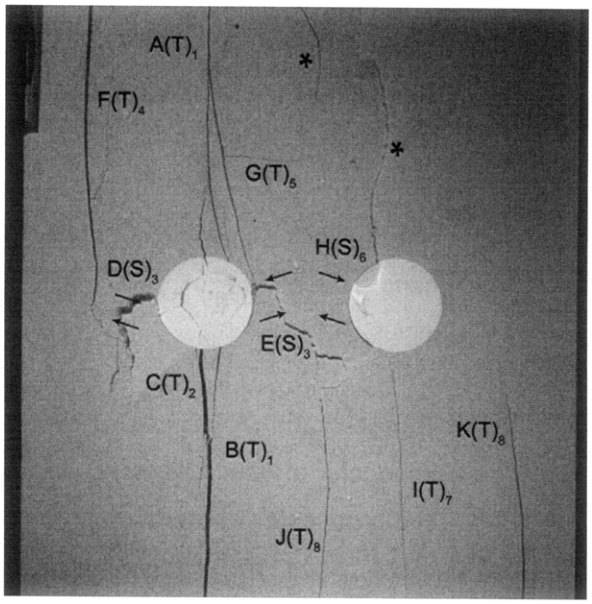

(Recorded by High Speed Video System)

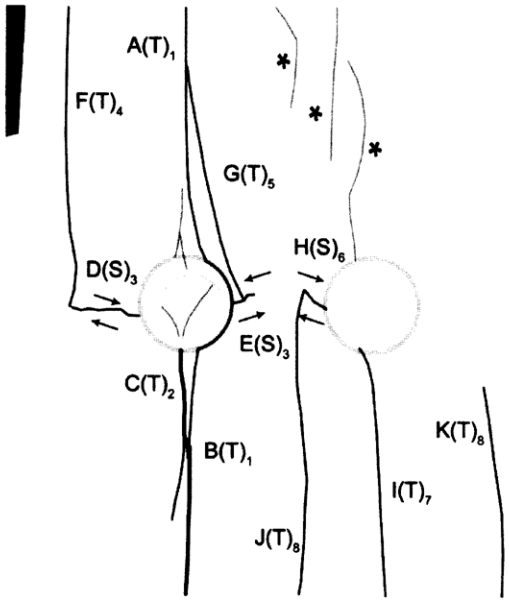

(28.03 MPa)
Time: 6 minutes & 19.450 seconds
HS Image # - 2088

Tensile crack (J) initiates at shear crack (H) and propagates downwards.

Tensile crack (K) initiates at the lower specimen boundary and propagates upwards.

Surface cracking (*) initiates at the upper face of the specimen.

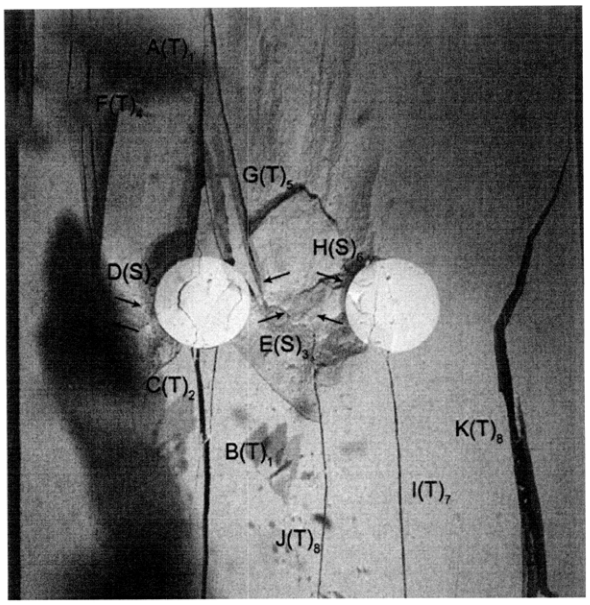

(Recorded by High Speed Video System)

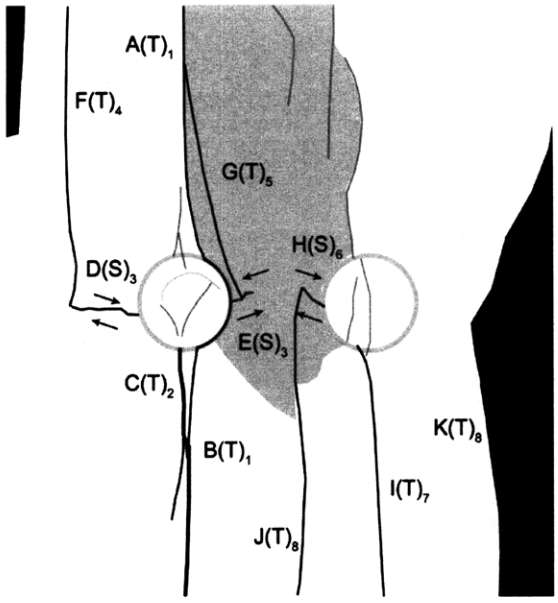

(20.07 MPa)
Time: 6 minutes & 19.556 seconds
HS Image # - 1558

A large piece of material detaches from the specimen face, as a result of the previously initiated surface cracking.

Tensile crack (K) propagates until its coalescence with the right-hand specimen boundary, which results in the detachment of a specimen piece.

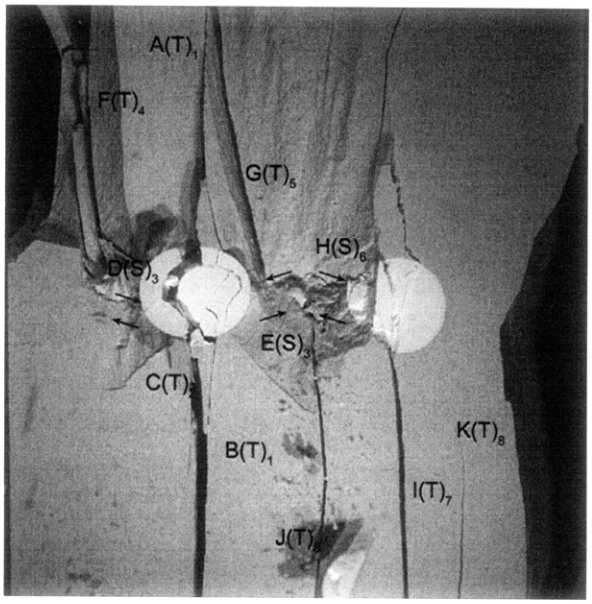

(Recorded by High Speed Video System)

(0 MPa) – Final Picture
Time: 6 minutes & 19.867 seconds
HS Image # - 1

Shear cracks (E&H) coalesce after failure.

	Upper edge of the specimen. The cracks marked with a (*) coincide with the openings between the teeth of the brush platen.
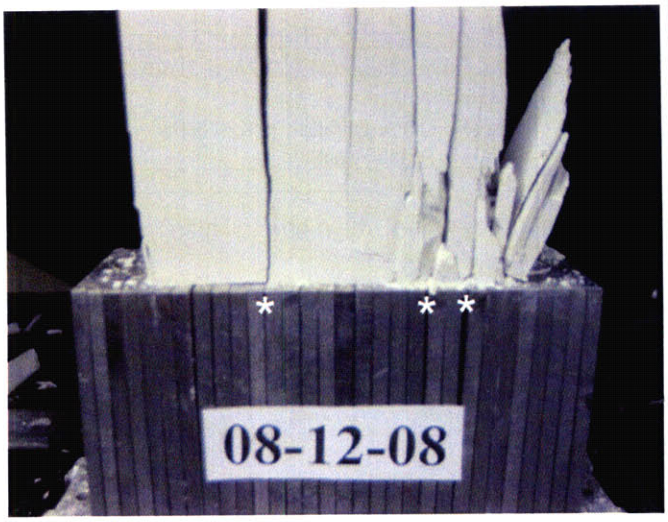	Lower edge of the specimen. The cracks marked with a (*) coincide with the openings between the teeth of the brush platen.

SUMMARY

Specimen Number: CR(UI)-0-0A (20080812)

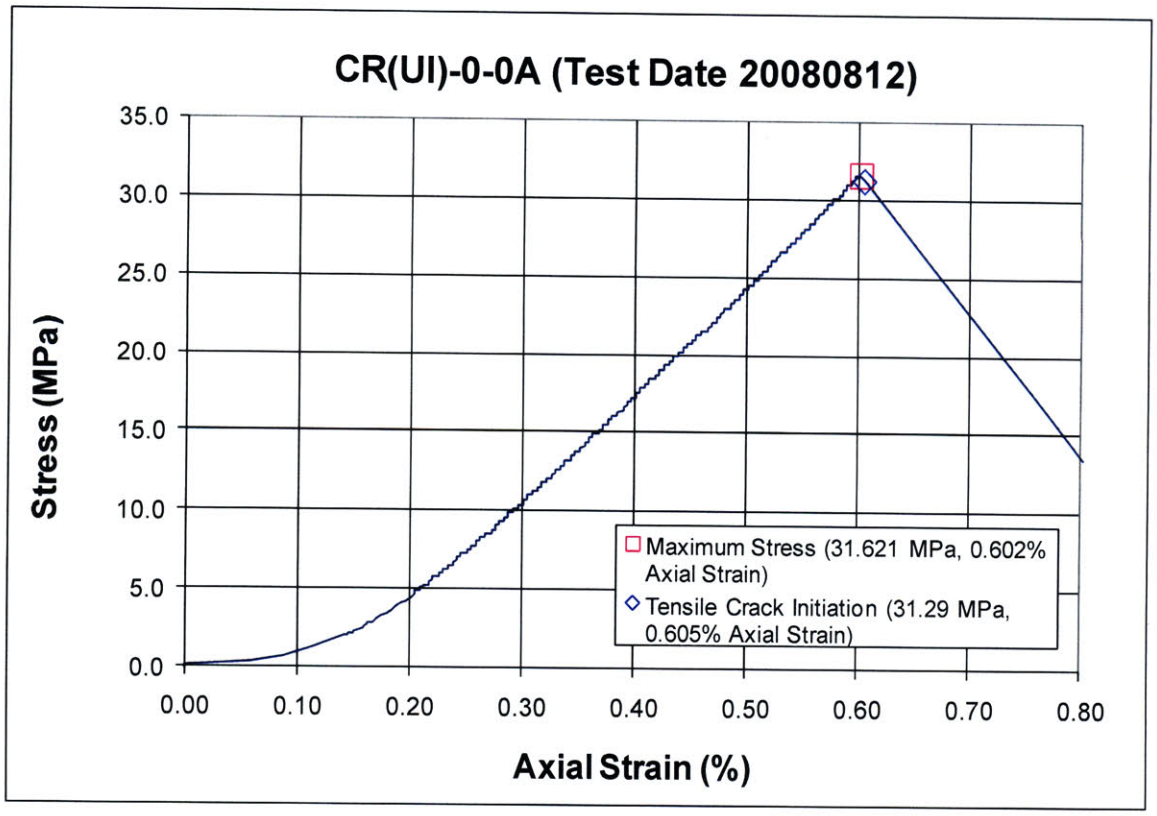

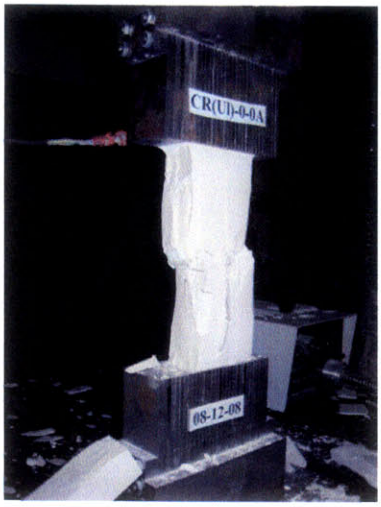

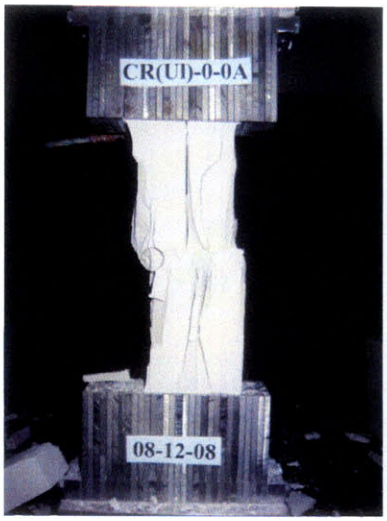

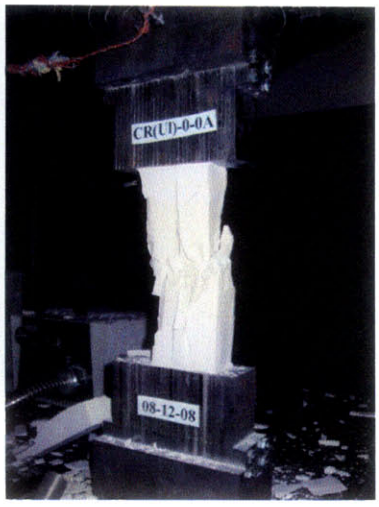

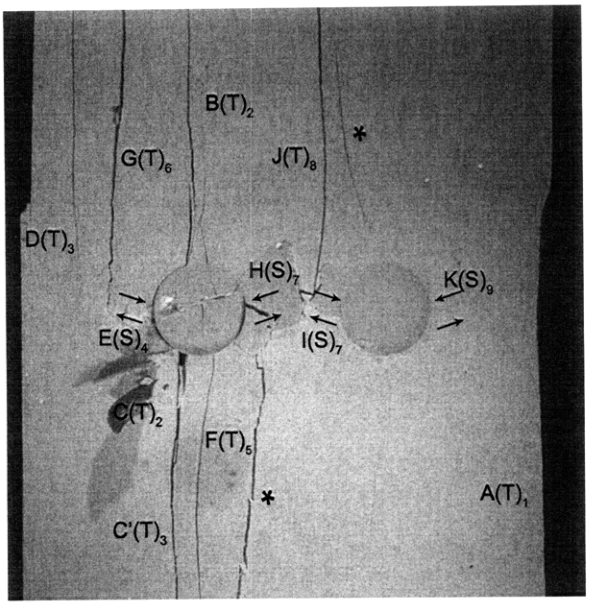

(Recorded by High Speed Video System)

(28.95 MPa)
Time: 6 minutes & 42.586 seconds
HS Image # - 2069

Shear cracks (H&I) propagate until their coalescence with tensile crack (J).

Shear crack (K) initiates at the boundary of the right-hand inclusion and propagates towards the right-hand specimen boundary.

Surface cracks (*) also initiate on the specimen face. The lower surface crack (*) appears to be en echelon in form.

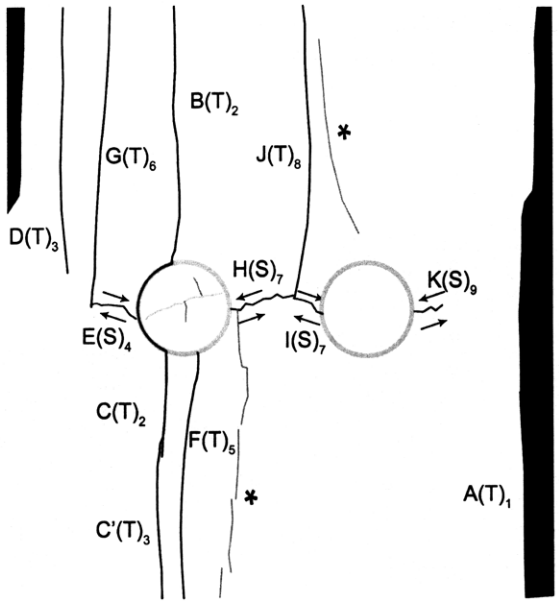

SUMMARY

Specimen Number: CR(UI)-0-0B (20080812)

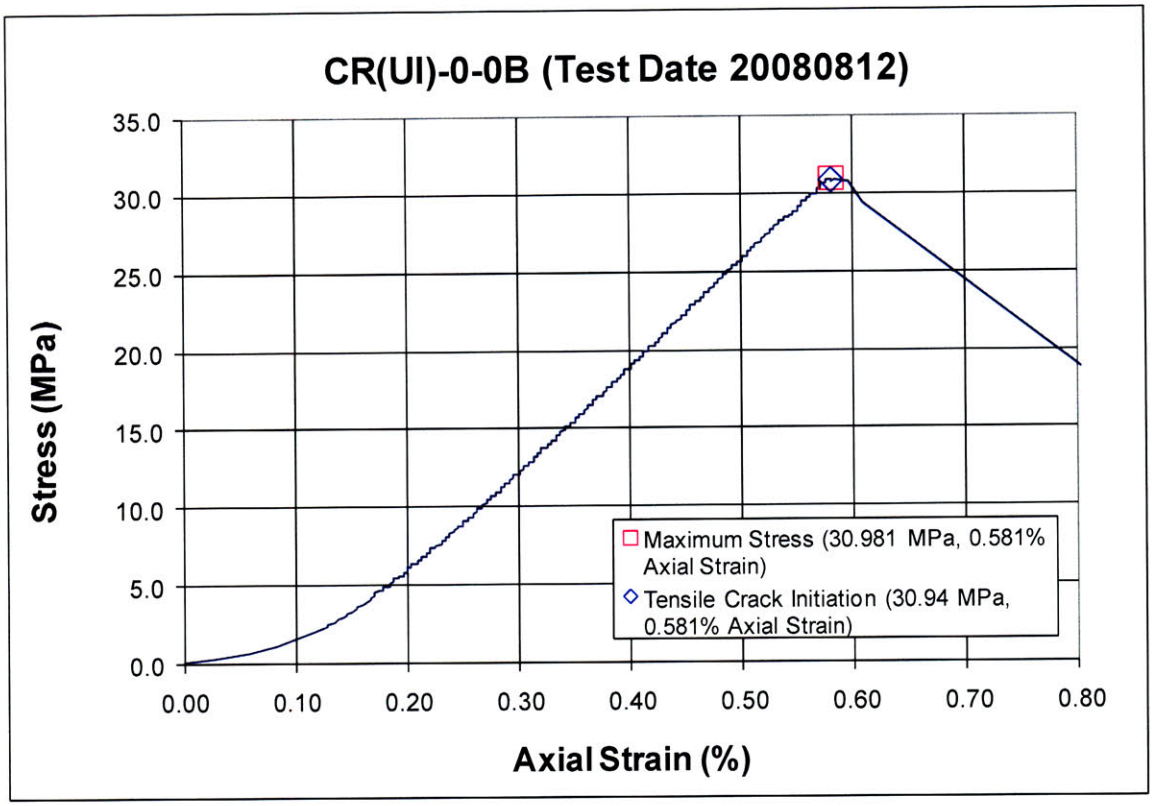

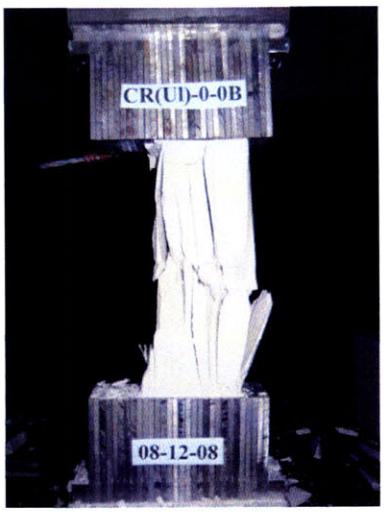

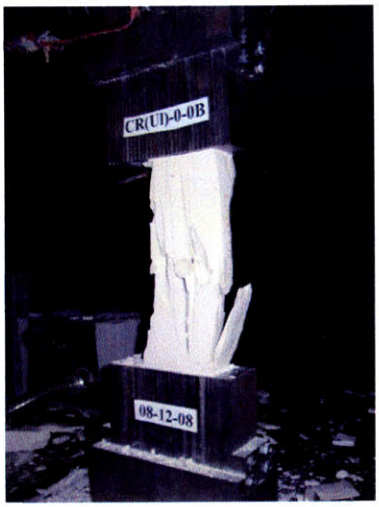

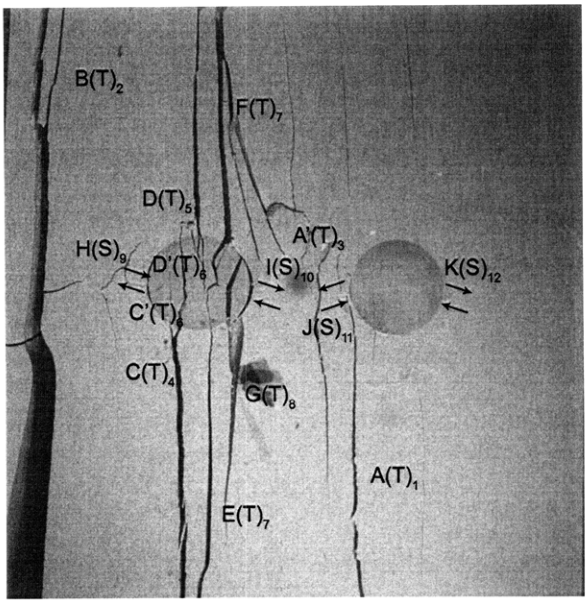

(Recorded by High Speed Video System)

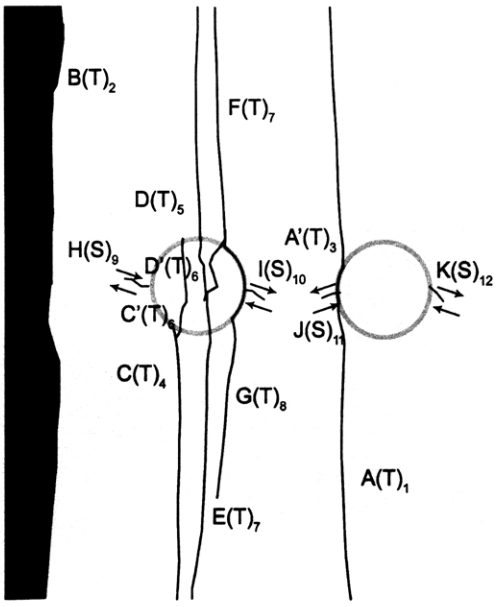

(30.93 MPa) – Ultimate Failure
Time: 6 minutes & 37.618 seconds
HS Image # - 1929

The coalescence of tensile crack (B) with the lower specimen boundary results in the detachment of a piece of specimen.

Shear crack (K) initiates at the boundary of the right-hand inclusion and propagates away from the inclusion.

Specimen Number: CR(UI)-0-0C (20080812)

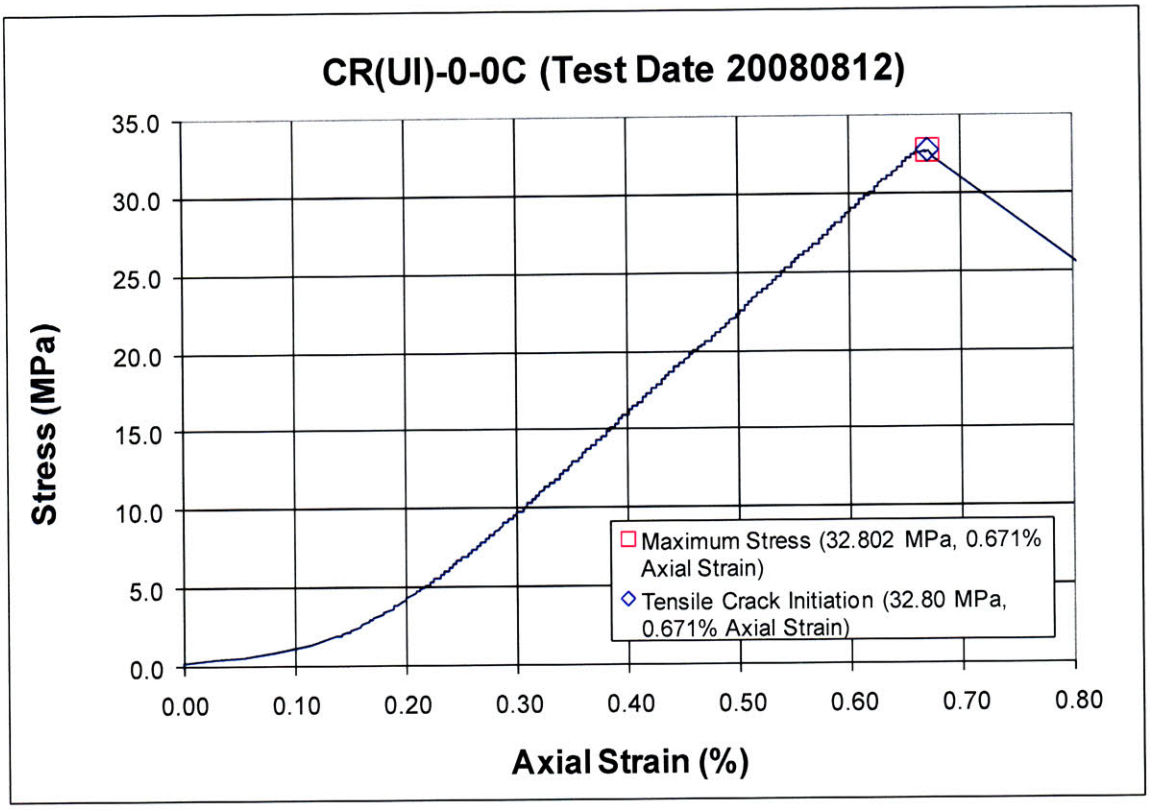

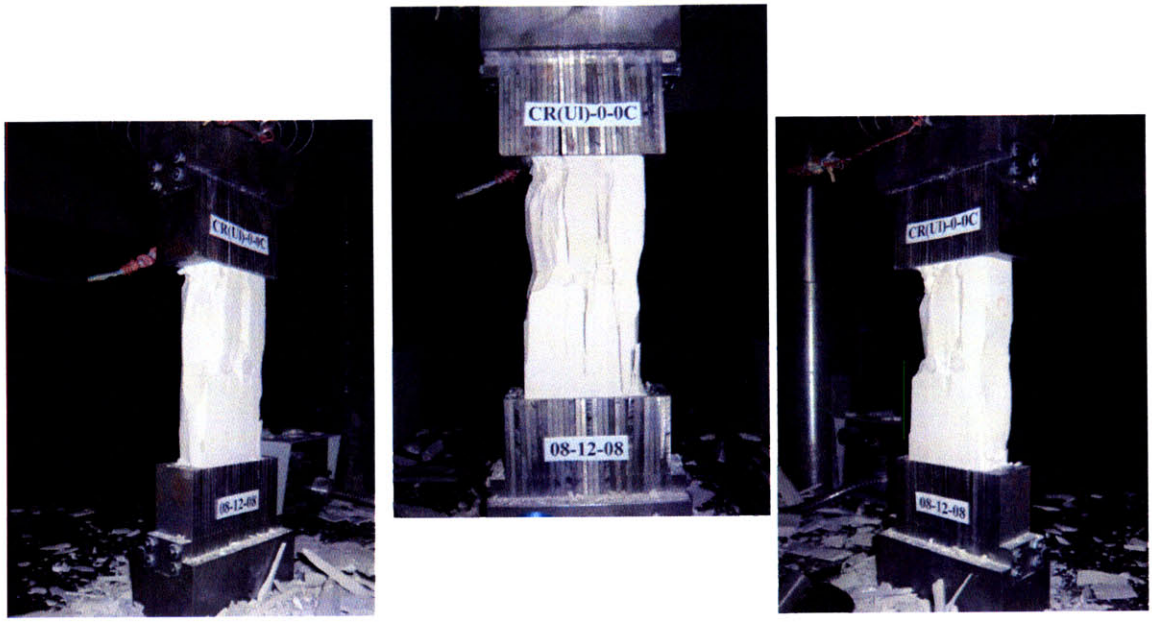

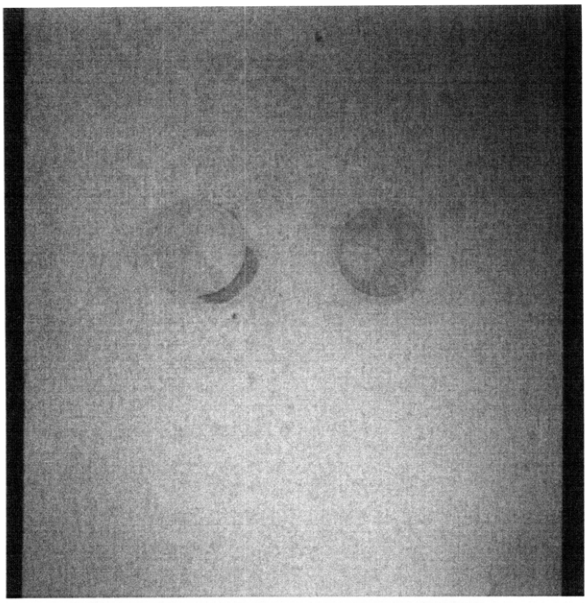

(Recorded by High Speed Video System)

Initial Inclusion Geometries:
CIRCLES – Ultracal Material

Inclusion **more** stiff than matrix.

High Speed Camera Frame Rate:
5000 pps

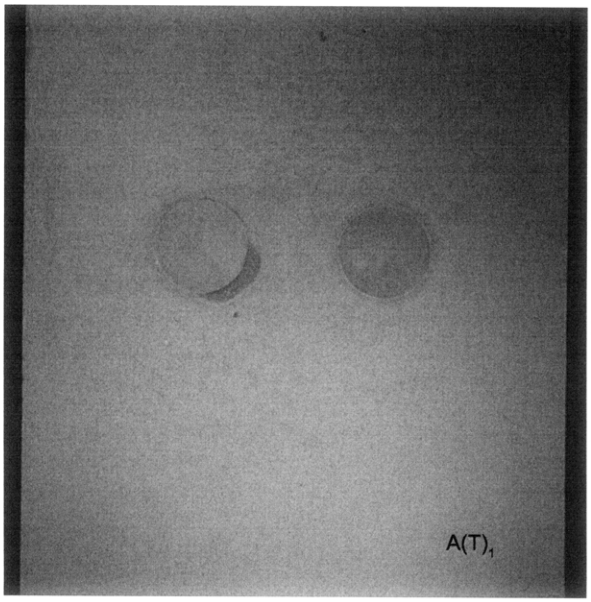

(Recorded by High Speed Video System)

A(T)1

(32.802 MPa) [Max. Stress]
Time: 7 minutes & 7.334 seconds

Prior to tensile crack initiation at the inclusion boundary, a tensile crack (A) initiates at the lower specimen boundary and propagates upwards.

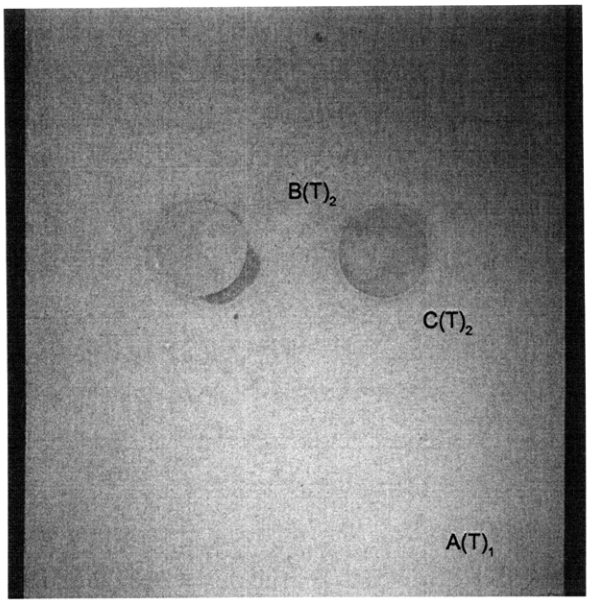

(Recorded by High Speed Video System)

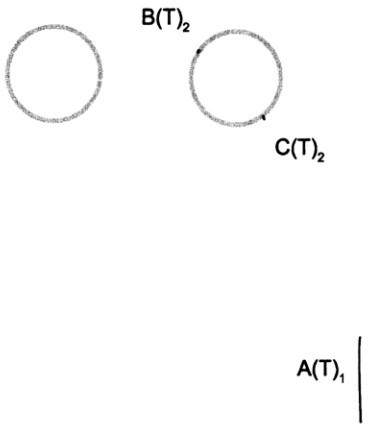

(32.38 MPa)

- Tensile Crack Initiation

Time: 7 minutes & 7.586 seconds

HS Image # - 3786

Tensile cracks (B&C) initiate at the boundary of the right-hand inclusion.

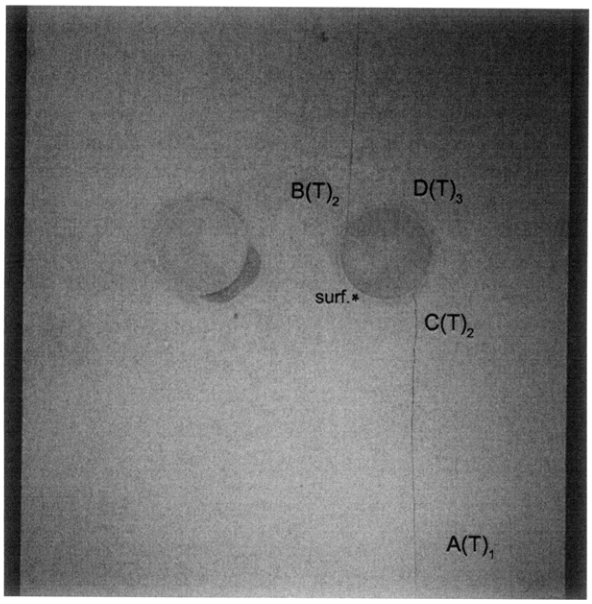

(Recorded by High Speed Video System)

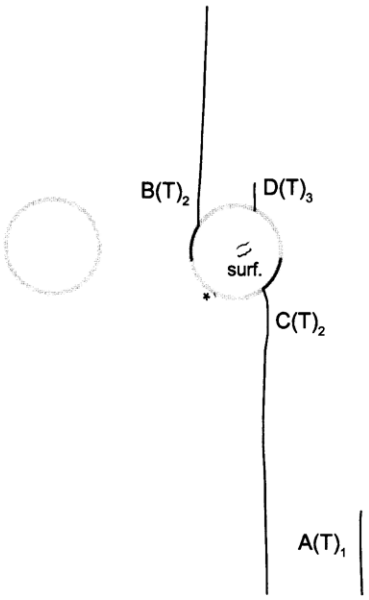

(32.37 MPa)
Time: 7 minutes & 7.586 seconds
HS Image # - 3785

As tensile cracks (B&C) propagate towards their respective boundaries, tensile crack (D) initiates at the boundary of the right-hand inclusion. A surface crack (*) then initiates at the lower boundary of the right-hand inclusion.

Tensile cracks (B&C) begin propagating along the boundary of the right-hand inclusion.

A surface crack (surf.) also initiates within the right-hand inclusion.

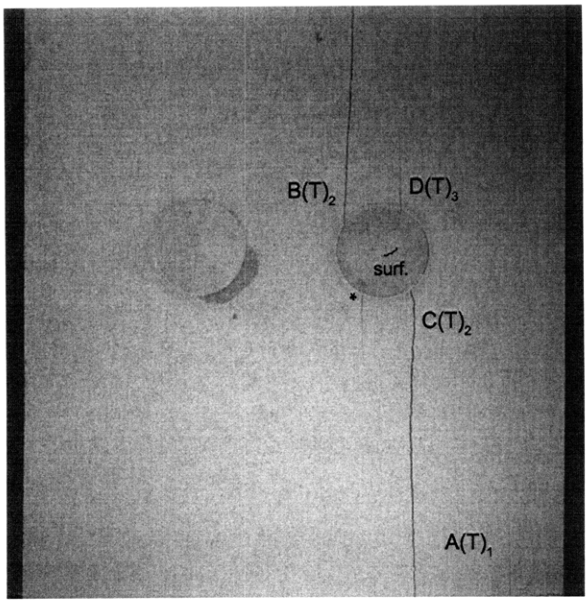

(Recorded by High Speed Video System)

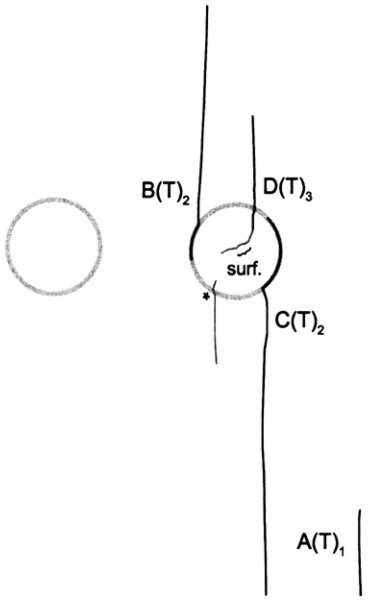

(32.35 MPa)
Time: 7 minutes & 7.586 seconds
HS Image # - 3784

Tensile crack (D) begins to propagate into the inclusion, until its coalescence with surface crack (surf.). Surface crack (*) also begins to propagate into the right-hand inclusion.

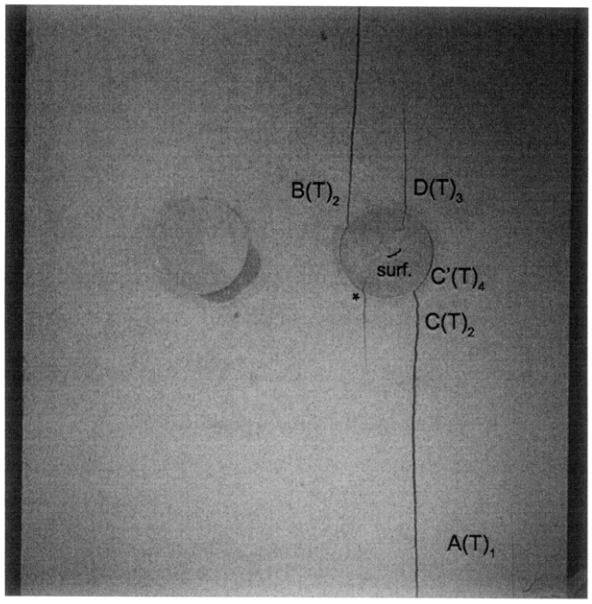

(Recorded by High Speed Video System)

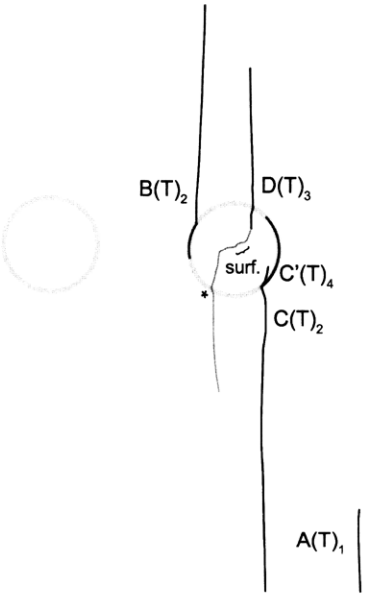

(16.68 MPa)
Time: 7 minutes & 7.785 seconds
HS Image # - 2789

Surface crack (*) continues to propagate into the right-hand inclusion until its coalescence with surface crack (surf.).

Tensile cracks (C') initiates at the right-hand inclusion boundary and propagates into the inclusion.

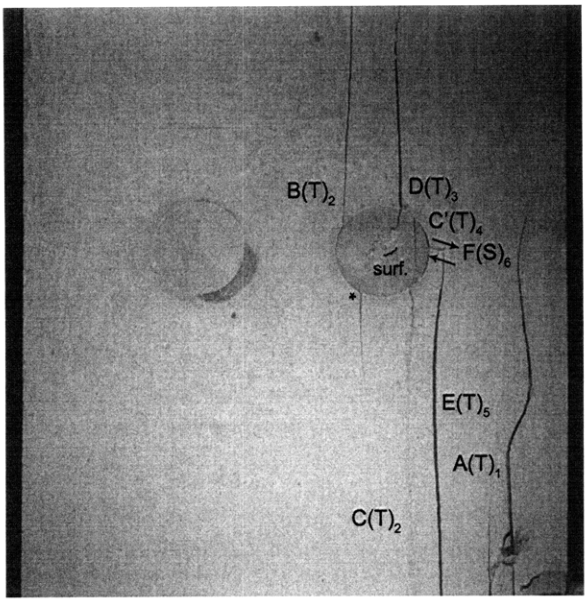

(Recorded by High Speed Video System)

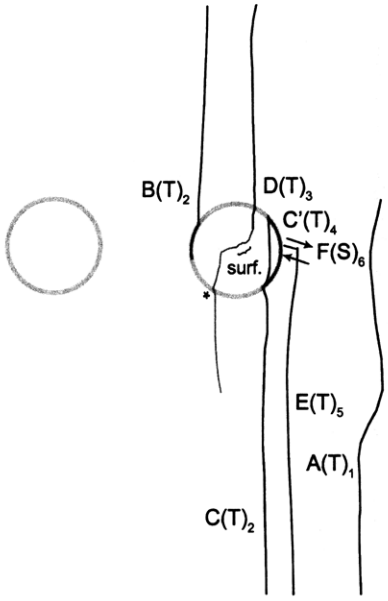

(15.89 MPa)
Time: 7 minutes & 7.795 seconds
HS Image # - 2739

Tensile crack (A) continues to propagate upwards and curves away as it propagates adjacent to the right-hand inclusion.

Tensile crack (E) then initiates at the lower specimen boundary and propagates upwards adjacent to the right-hand inclusion. This initiates shear crack (F) which propagates until its coalescence with tensile crack (E).

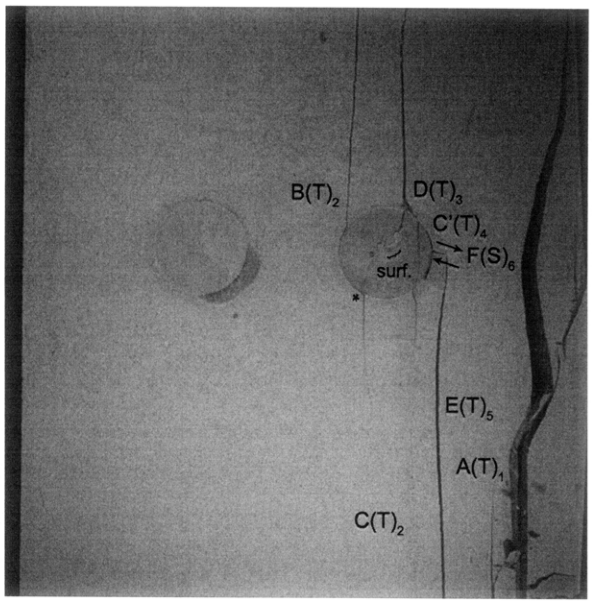

(Recorded by High Speed Video System)

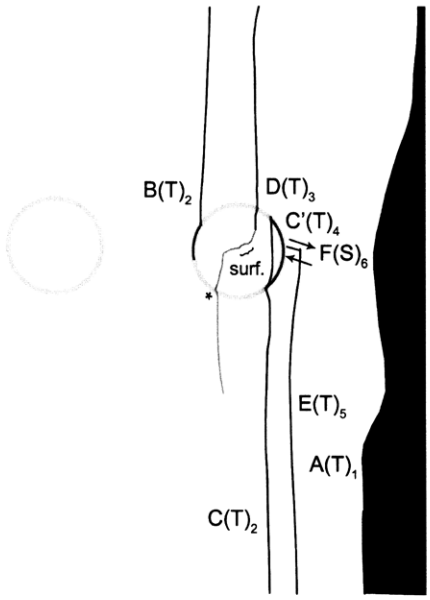

(15.83 MPa)
Time: 7 minutes & 7.796 seconds
HS Image # - 2735

The propagation of tensile crack (A) results in the detachment of a specimen piece from the right-hand boundary.

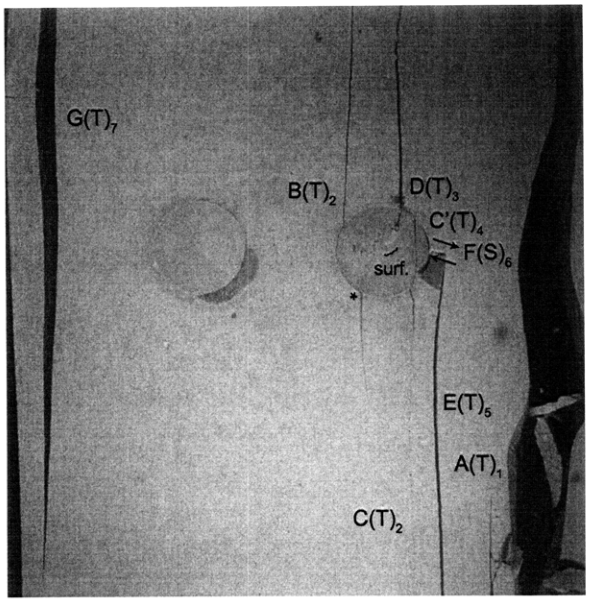

(Recorded by High Speed Video System)

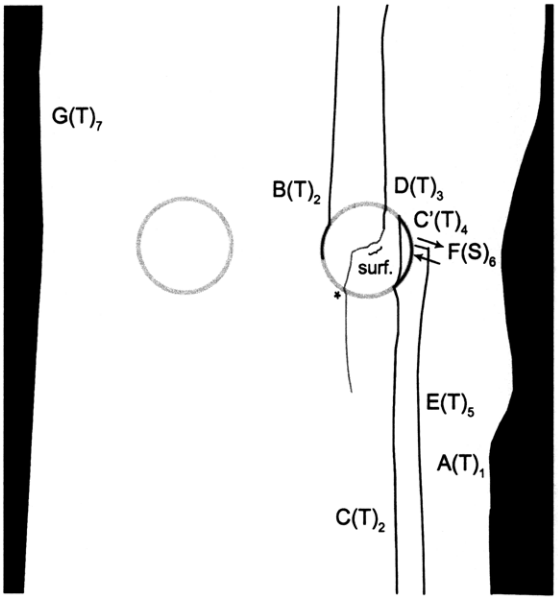

(15.68 MPa)
Time: 7 minutes & 7.798 seconds
HS Image # - 2726

Tensile crack (G) initiates at the upper specimen boundary and propagates, which results in the detachment of a specimen piece from the left-hand boundary.

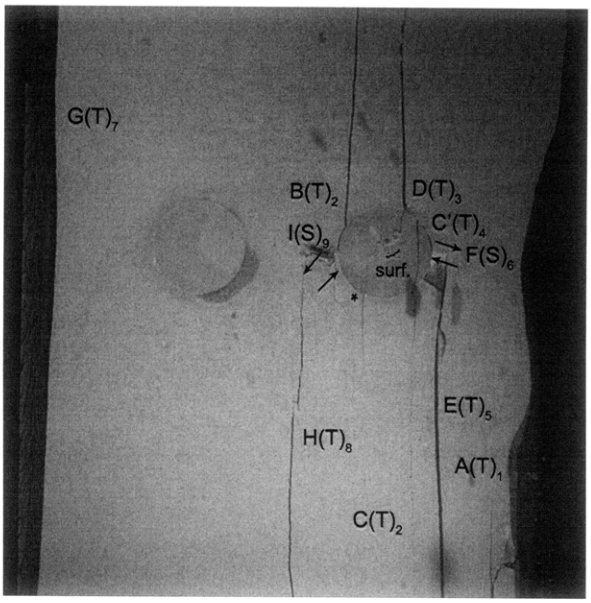

(Recorded by High Speed Video System)

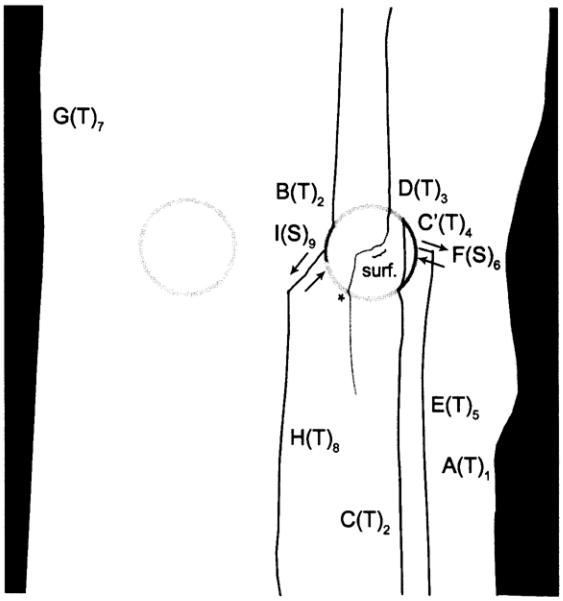

(13.42 MPa)
Time: 7 minutes & 7.827 seconds
HS Image # - 2582

Tensile crack (H) initiates from the lower specimen boundary and propagates upwards.

Shear crack (I) initiates at the boundary of the right-hand inclusion and propagates until its coalescence with tensile crack (H).

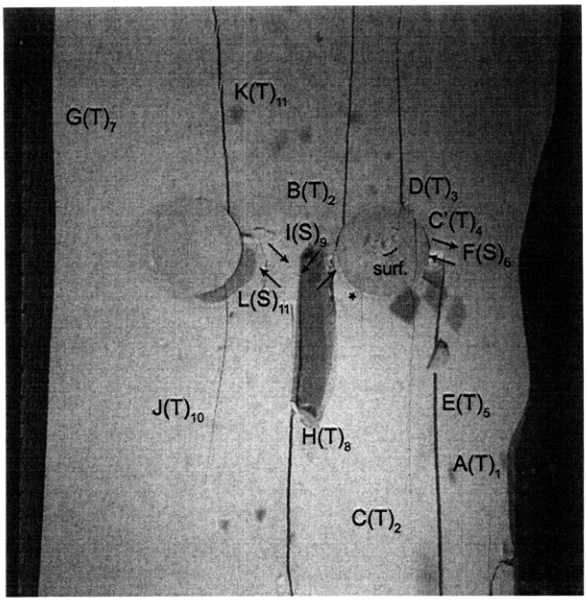

(Recorded by High Speed Video System)

(13.13 MPa)
Time: 7 minutes & 7.830 seconds
HS Image # - 2564

Tensile crack (J) initiates at the boundary of the left-hand inclusion and propagates downwards.

En echelon tensile crack (K) then initiates at the upper boundary and propagates downwards and along the inclusion boundary. Shear crack (L) also initiates at the boundary of the left-hand inclusion and propagates until its coalescence with tensile crack (H) and shear crack (I).

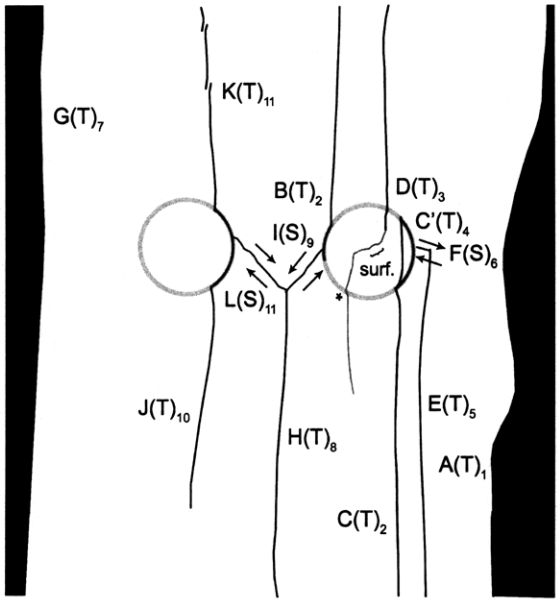

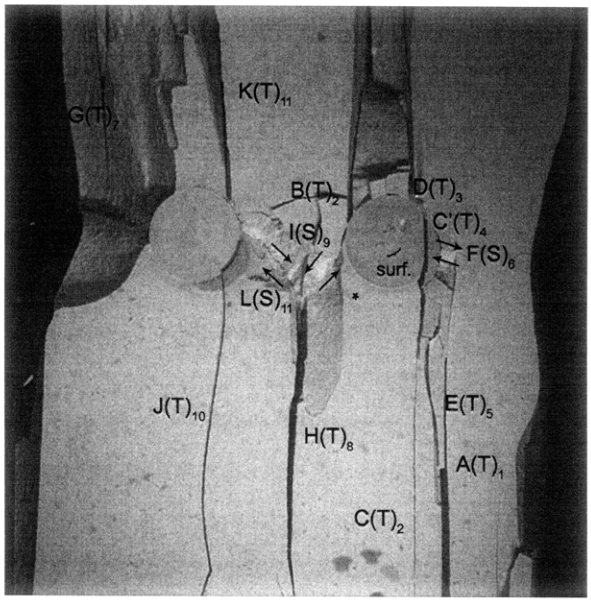

(Recorded by High Speed Video System)

(0 MPa) – Final Picture

Time: 7 minutes & 8.343 seconds

HS Image # - 1

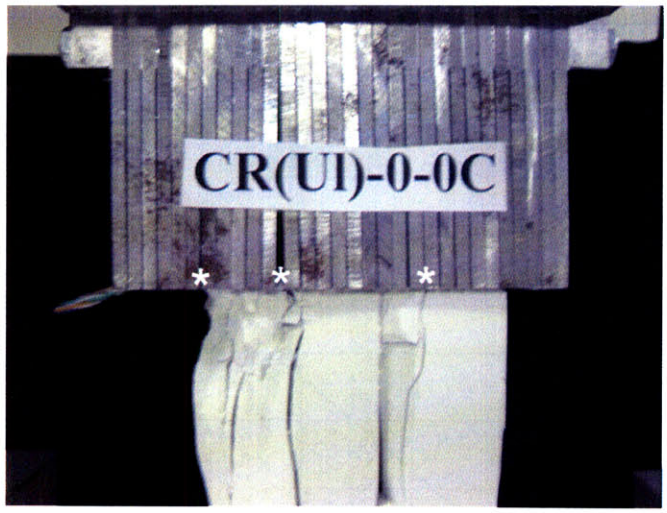	Upper edge of the specimen. The cracks marked with a (*) coincide with the openings between the teeth of the brush platen.
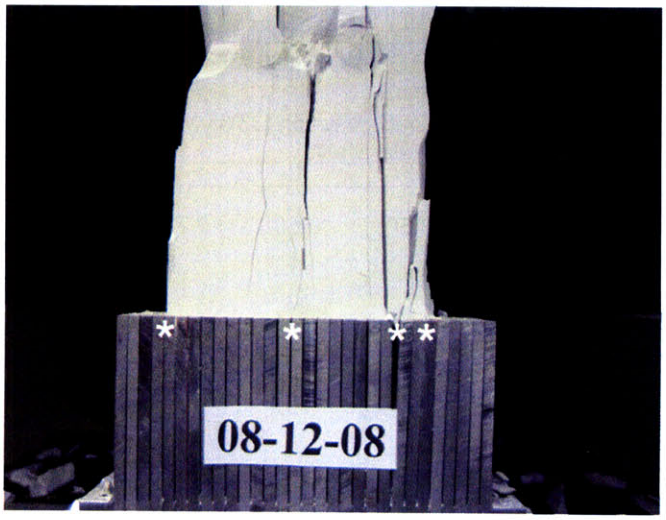	Lower edge of the specimen. The cracks marked with a (*) coincide with the openings between the teeth of the brush platen.

SUMMARY

Specimen Number: CR(PI)-30-0A (20080926)

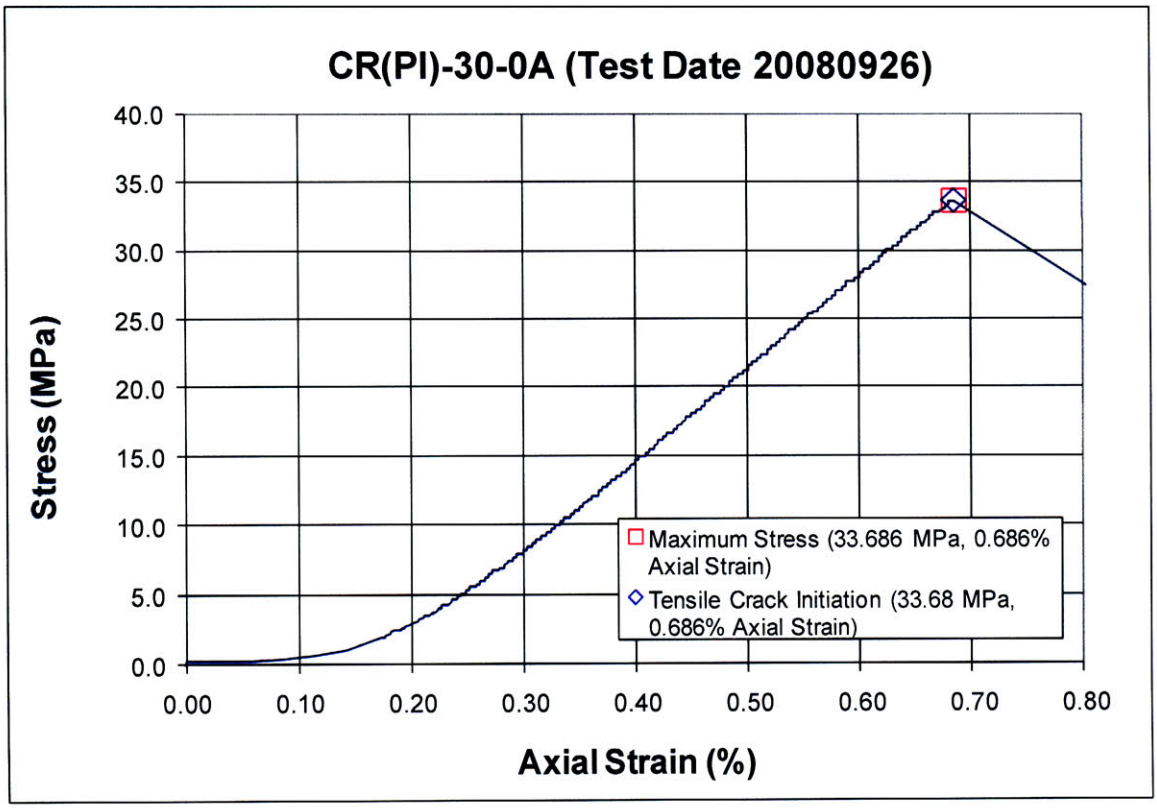

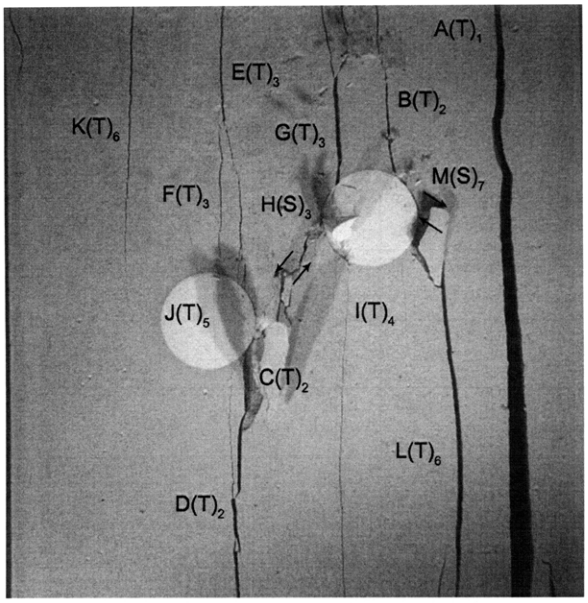

(Recorded by High Speed Video System)

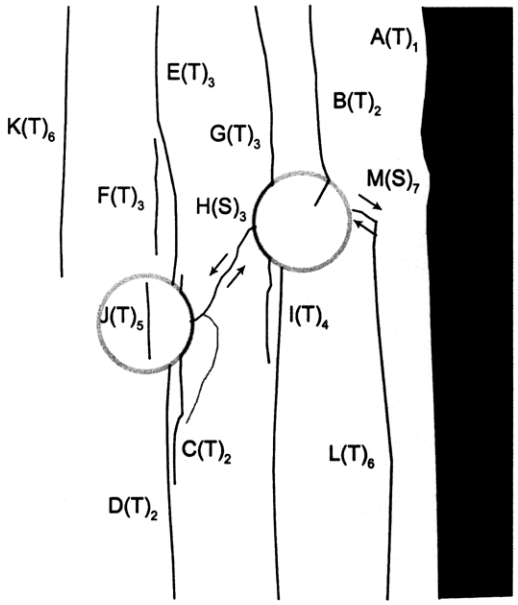

(21.37 MPa)
Time: 7 minutes & 16.339 seconds
HS Image # - 5187

The propagation of tensile crack (A) results in the detachment of a large piece of specimen from the right boundary.

Specimen Number: CR(PI)-30-0B (20080926)

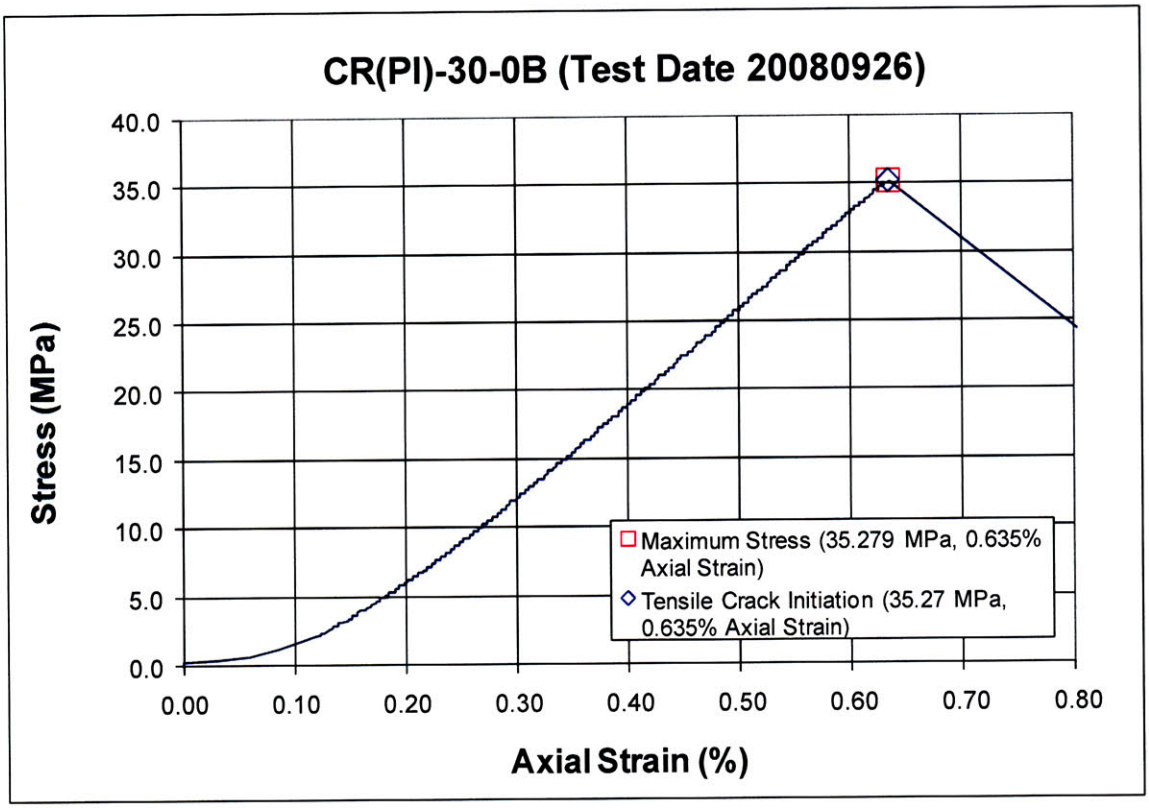

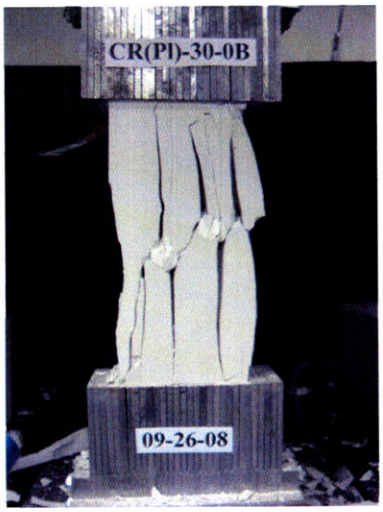

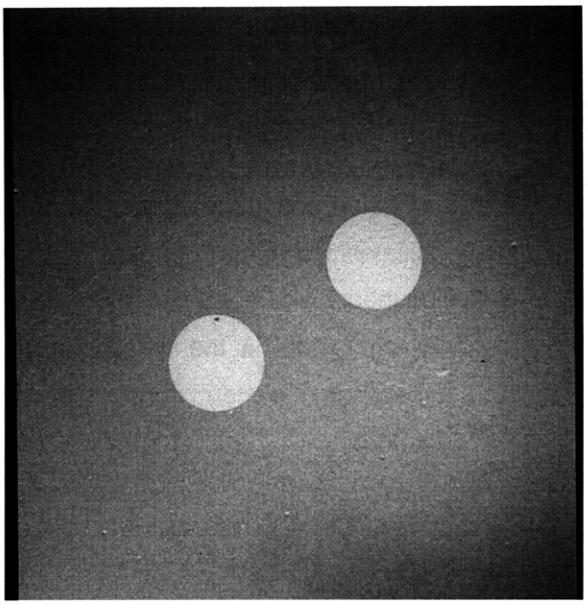

(Recorded by High Speed Video System)

Initial Inclusion Geometries:
CIRCLES – Plaster Material

Inclusions **less** stiff than matrix.

High Speed Camera Frame Rate:
5000 pps

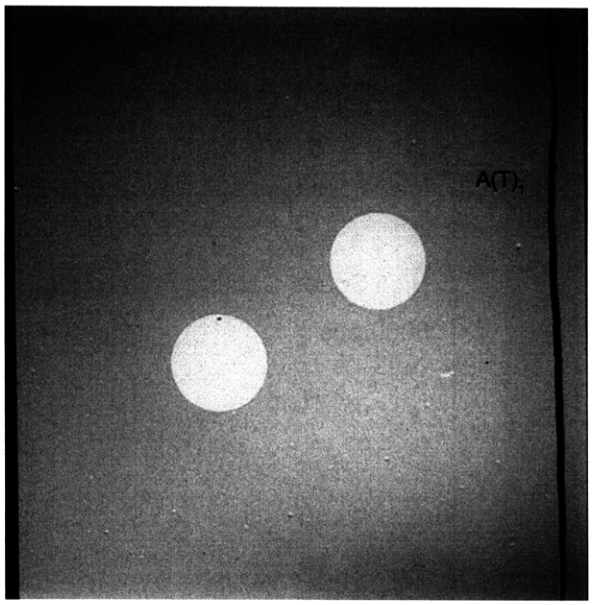

(Recorded by High Speed Video System)

(35.279 MPa) [Max. Stress]
Time: 7 minutes & 33.36 seconds

Prior to tensile crack initiation at the inclusion boundaries, tensile crack (A) initiates at the upper specimen boundary and propagates downwards, which results in the detachment of a specimen piece from the right boundary.

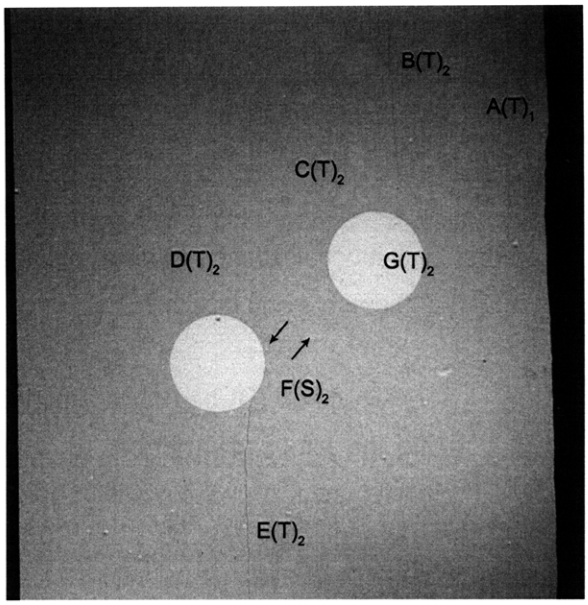

(Recorded by High Speed Video System)

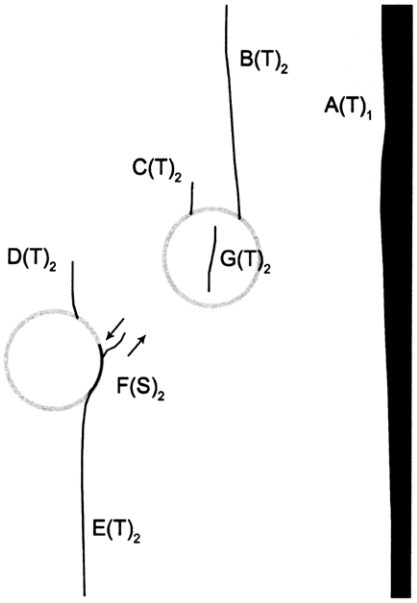

(35.27 MPa)

- Tensile Crack Initiation

Time: 7 minutes & 33.694 seconds

Tensile cracks (B,C,D,E,F&G) initiate simultaneously.

Tensile cracks (B&C) initiate at the boundary of the right-hand inclusion and propagate upwards.

Tensile cracks (D&E) initiate at the boundary of the left-hand inclusion and propagate away from the inclusion. Tensile crack (E) also begins to propagate along the boundary of the left-hand inclusion.

Shear crack (F) initiates at the boundary of the left-hand inclusion and propagates upwards towards the right-hand inclusion.

Tensile crack (G) initiates within the right-hand inclusion and propagates downwards.

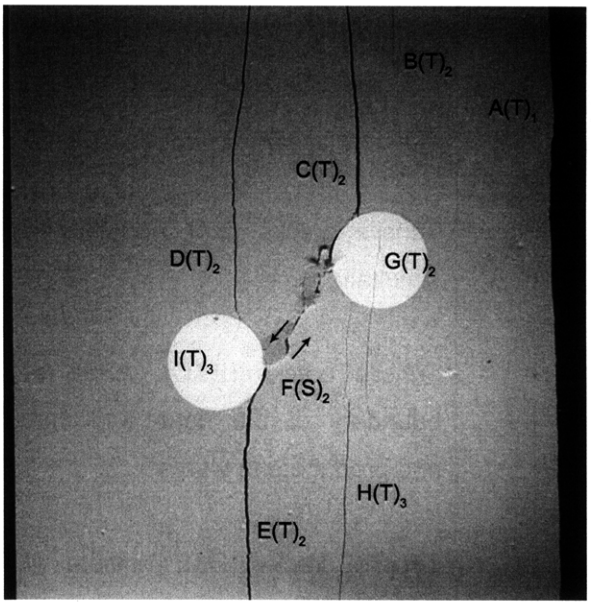

(Recorded by High Speed Video System)

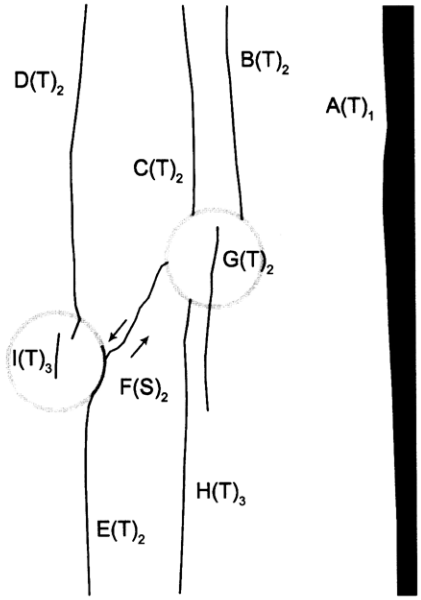

(26.60 MPa) – Ultimate Failure
Time: 7 minutes & 33.694 seconds
HS Image # - 2276

Shear crack (F) continues to propagate until its coalescence with the boundary of the right-hand inclusion.

Tensile crack (D) begins to propagate into the left-hand inclusion, as a new tensile crack (I) initiates within the left-hand inclusion.

Tensile crack (H) initiates at the boundary of the right-hand inclusion and propagates downwards.

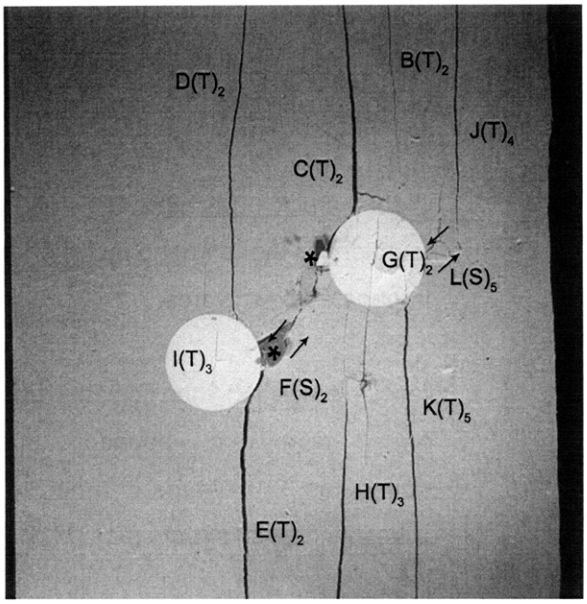

(Recorded by High Speed Video System)

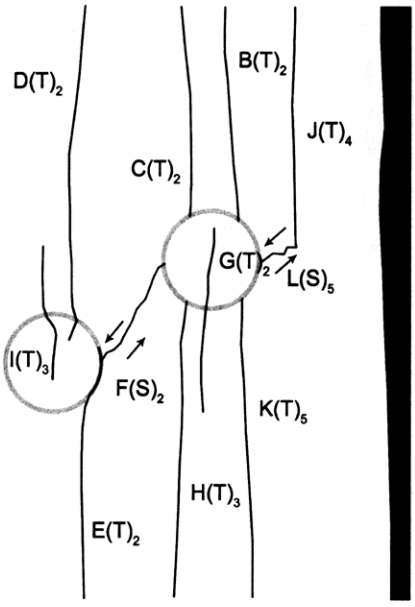

(26.56 MPa)
Time: 7 minutes & 33.695 seconds
HS Image # - 2274

Tensile crack (J) initiates at the upper specimen boundary and propagates downwards. Shear crack (L) then initiates at the boundary of the right-hand inclusion and propagates until its coalescence with tensile crack (J).

Tensile crack (K) initiates at the boundary of the right-hand inclusion and propagates downwards.

Spalling (*) occurs adjacent to shear crack (F).

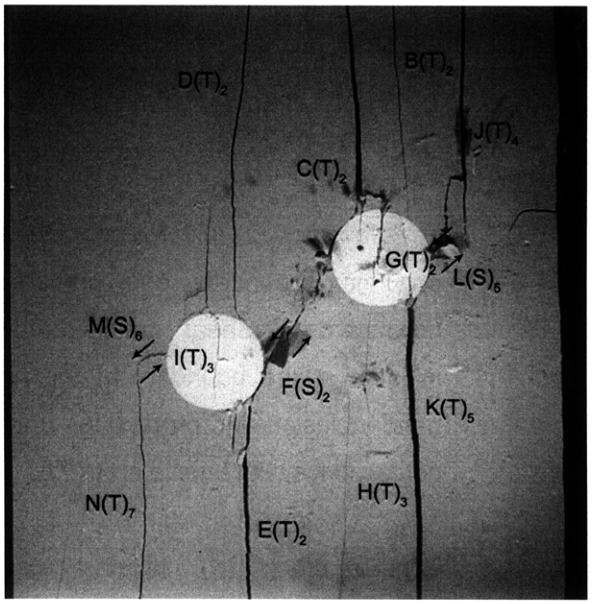

(Recorded by High Speed Video System)

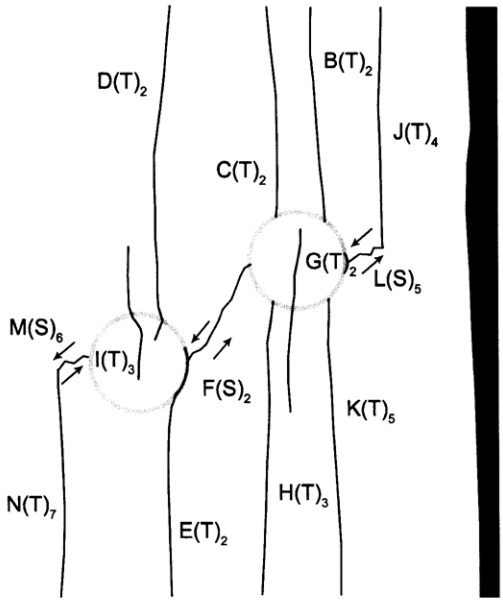

(26.46 MPa)
Time: 7 minutes & 33.696 seconds
HS Image # - 2269

Shear crack (M) initiates at the boundary of the left-hand inclusion and propagates downwards.

Tensile crack (N) then initiates at the lower specimen boundary and propagates upwards until its coalescence with shear crack (M).

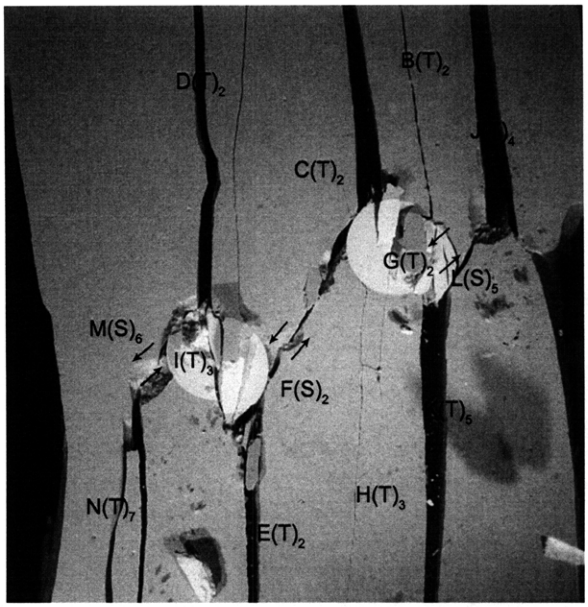

(Recorded by High Speed Video System)

(0 MPa) – Final Picture

Time: 7 minutes & 34.149 seconds

HS Image # - 1

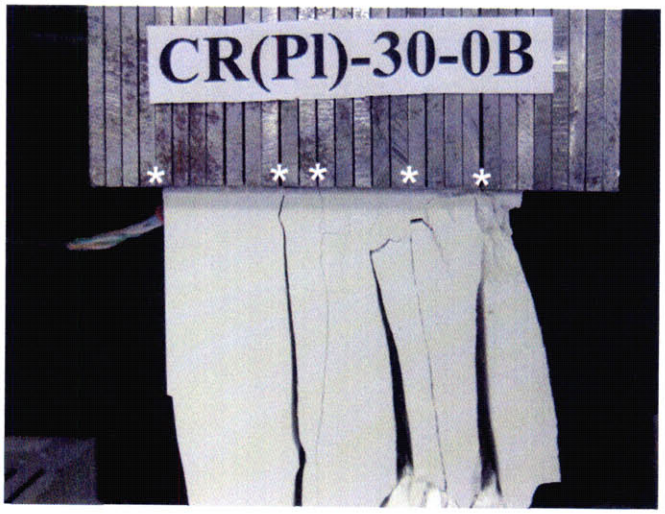	Upper edge of the specimen. The cracks marked with a (*) coincide with the openings between the teeth of the brush platen.
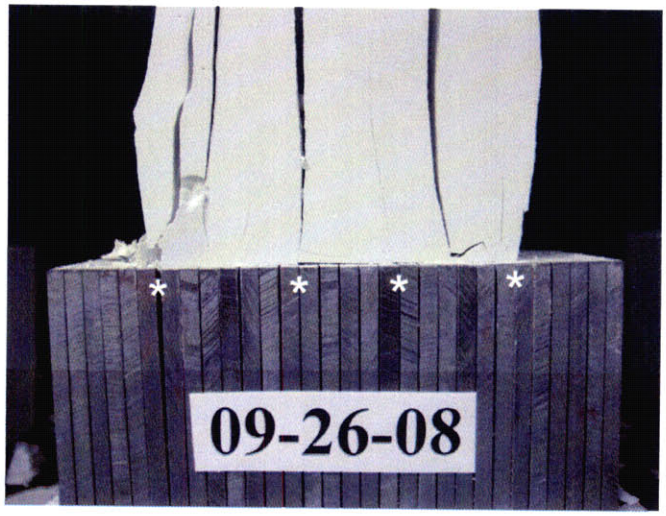	Lower edge of the specimen. The cracks marked with a (*) coincide with the openings between the teeth of the brush platen.

SUMMARY

Specimen Number: CR(PI)-30-0C (20080926)

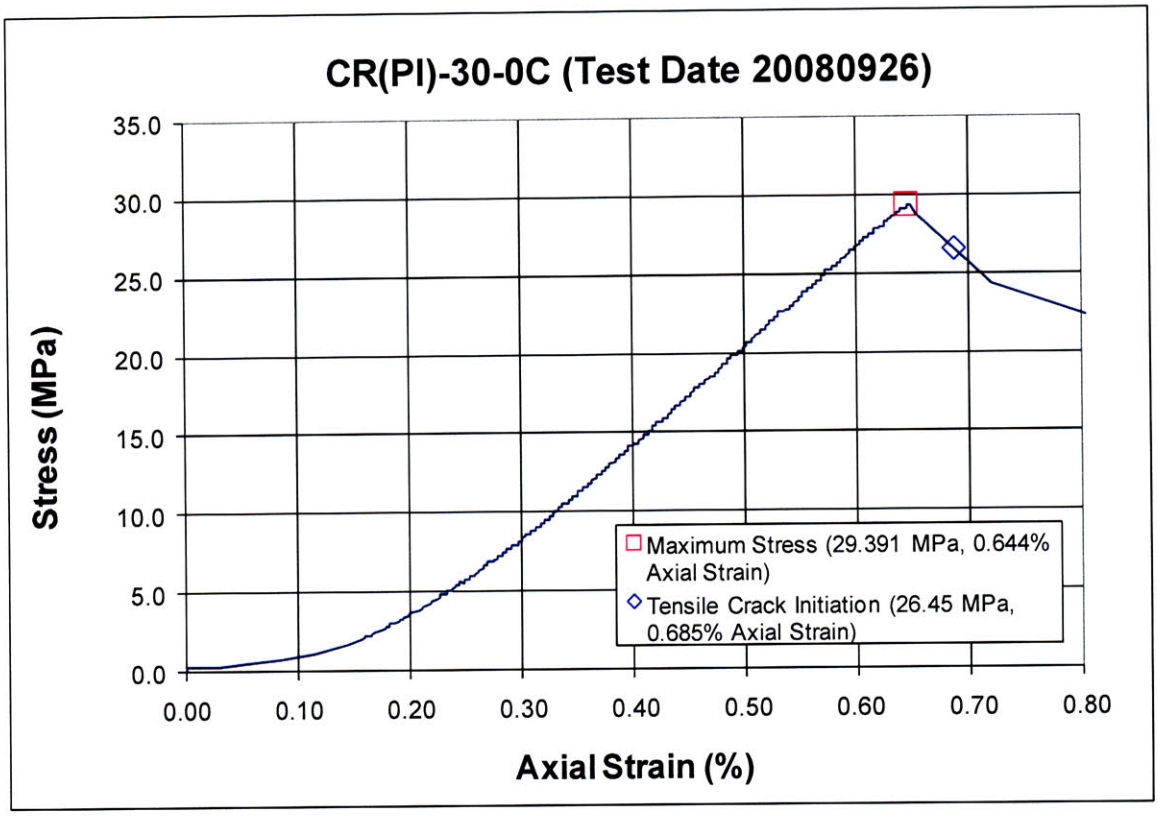

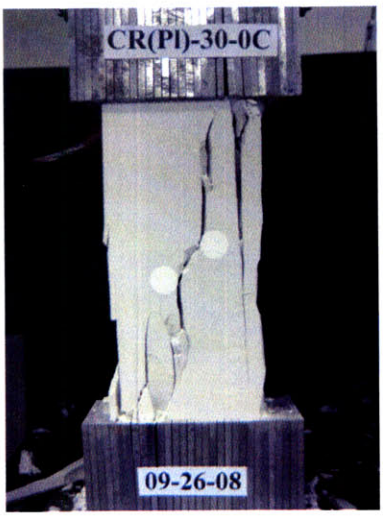

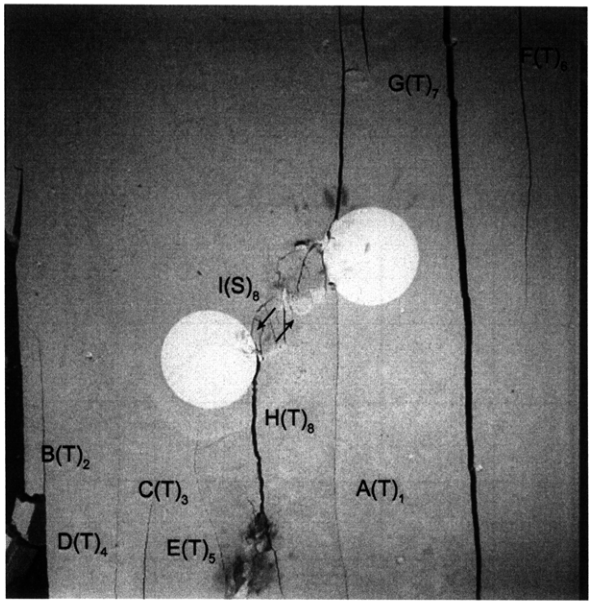

(Recorded by High Speed Video System)

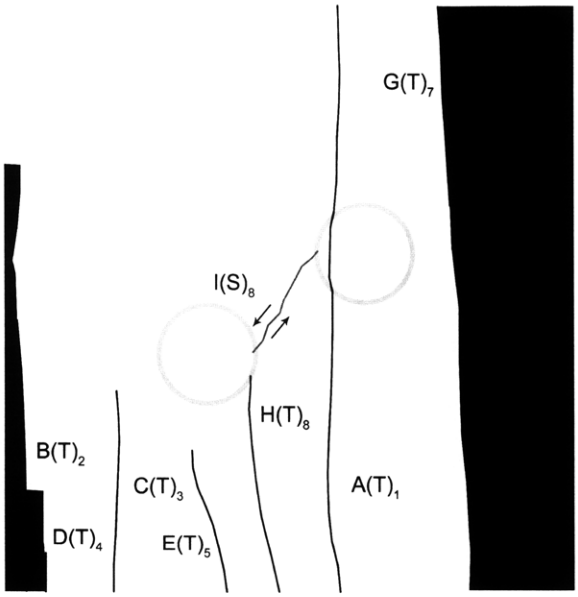

(24.10 MPa)
Time: 6 minutes & 14.477 seconds
HS Image # - 3091

The propagation of tensile crack (G) results in the detachment of a large specimen piece from the right boundary.

Specimen Number: CR(UI)-30-0A (20080926)

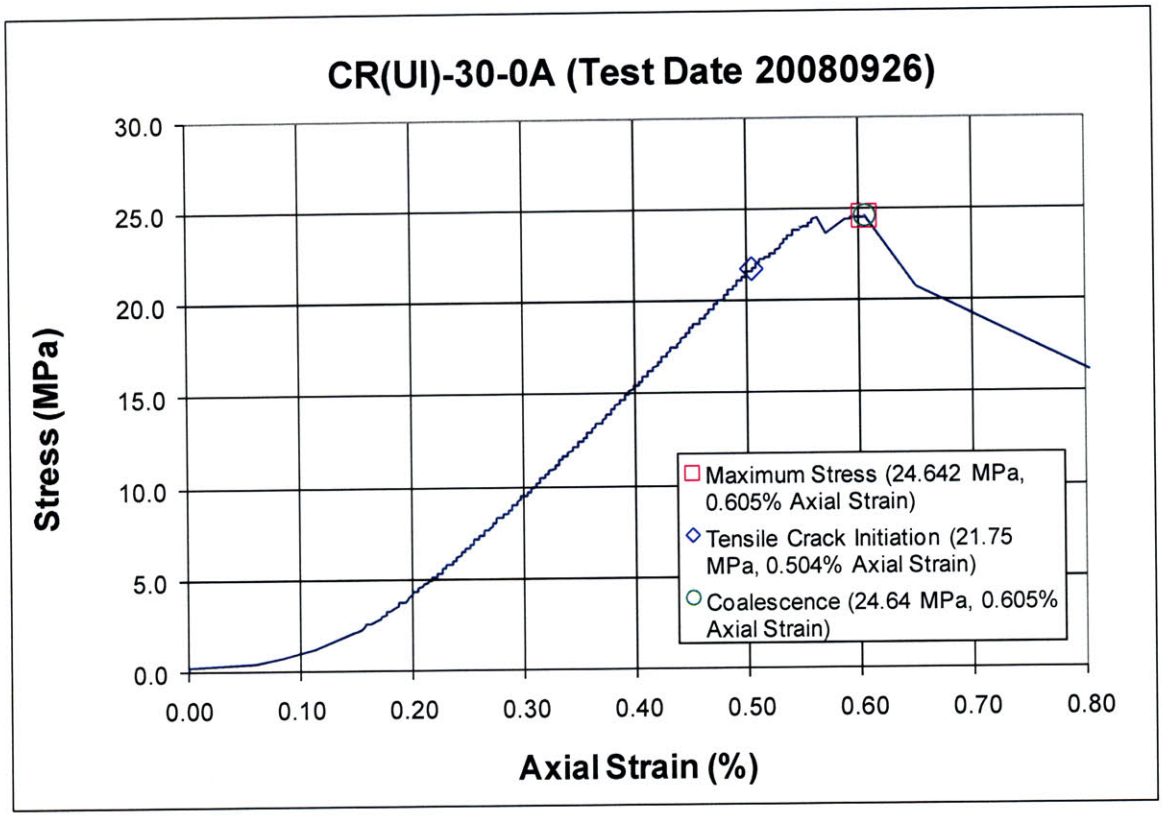

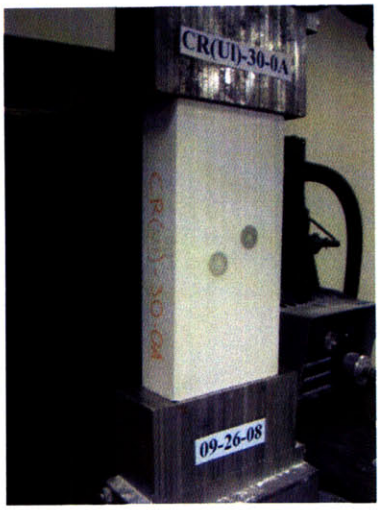

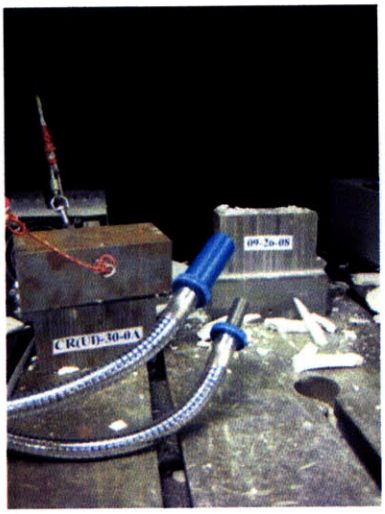

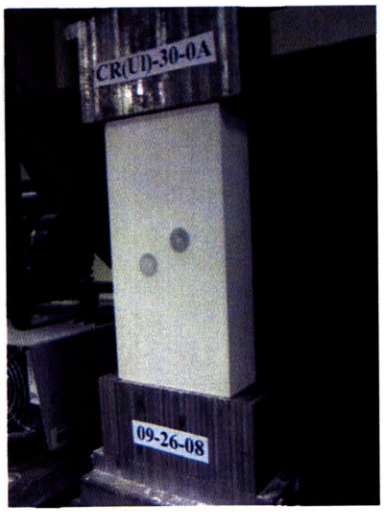

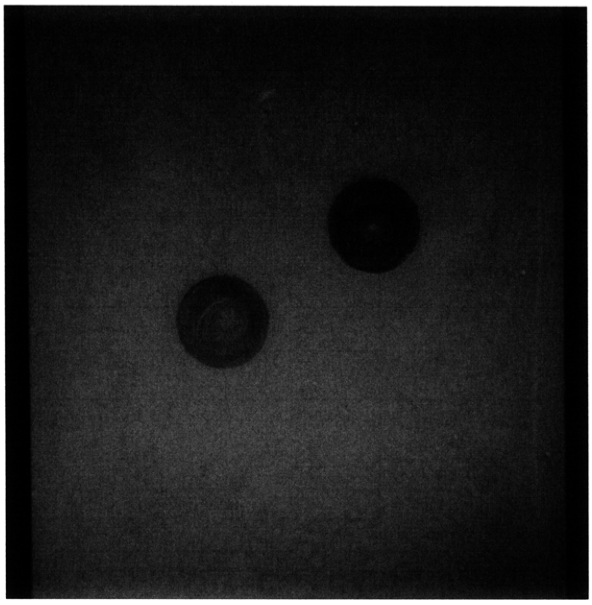

(Recorded by High Speed Video System)

Initial Inclusion Geometries:
CIRCLES – Ultracal Material

Inclusions **more** stiff than matrix.

Initial surface crack present, prior to testing, within left-hand inclusion.

High Speed Camera Frame Rate:
5000 pps

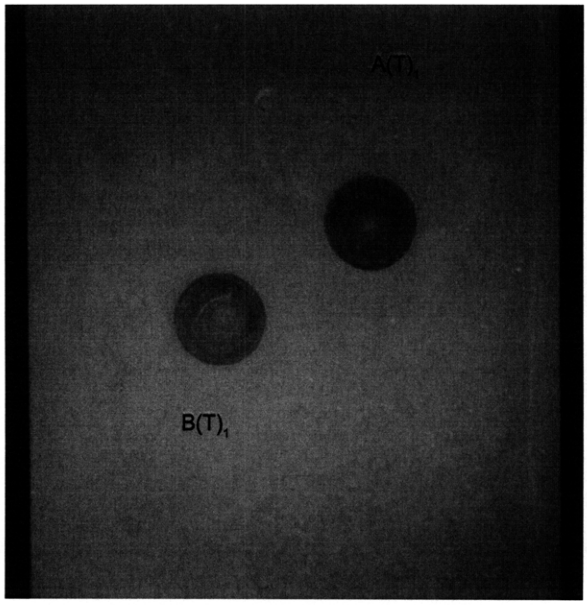

(Recorded by High Speed Video System)

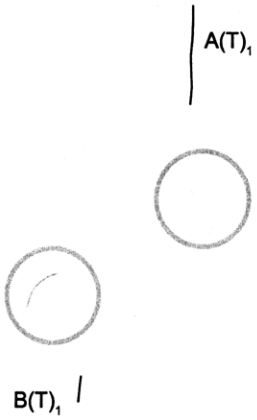

(21.75 MPa)

- Tensile Crack Initiation

Time: 4 minutes & 19.48 seconds

Tensile cracks (A&B) initiate within the hydrocal matrix. Tensile crack (A) initiates above the right-hand inclusion, while tensile crack (B) initiates below the left-hand inclusion.

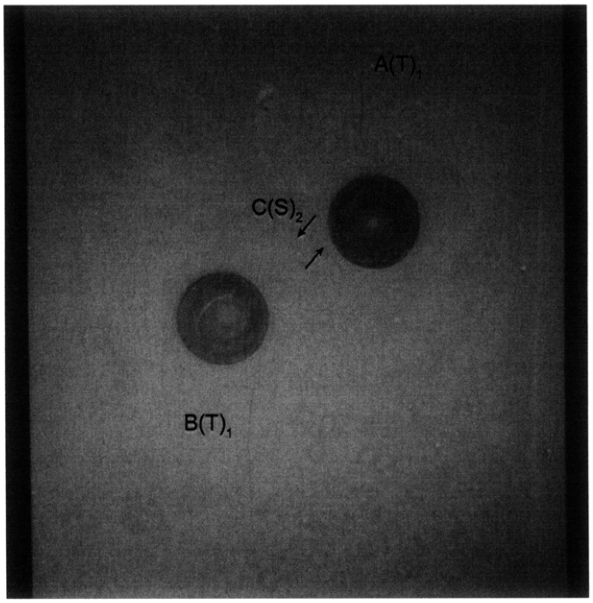

(Recorded by High Speed Video System)

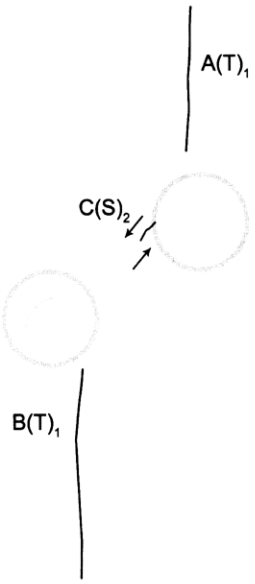

(23.47 MPa)
Time: 4 minutes & 43.48 seconds

Shear crack (C) initiates at the boundary of the right-hand inclusion and propagates downwards towards the left-hand inclusion.

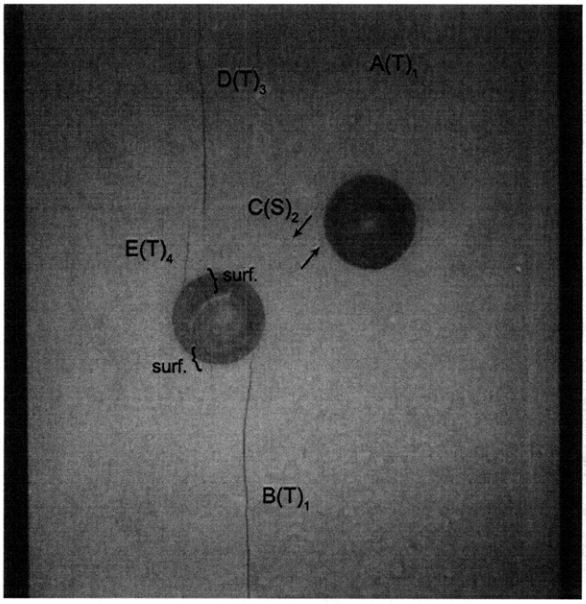

(Recorded by High Speed Video System)

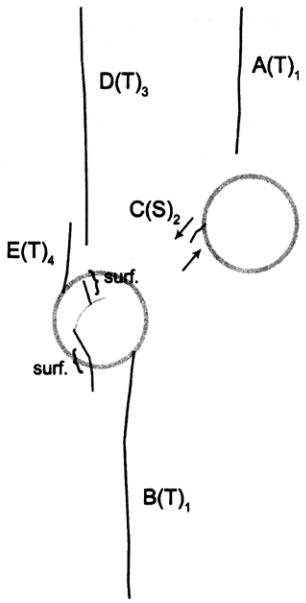

(24.01 MPa)
Time: 4 minutes & 50.98 seconds

Tensile crack (D) initiates within the matrix, above the left-hand inclusion, and propagates upwards.

Tensile crack (E) then initiates at the boundary of the left-hand inclusion and also propagates upwards. Surface cracks (surf.) initiate at the pre-test surface crack within the left-hand inclusion and propagate away from the inclusion.

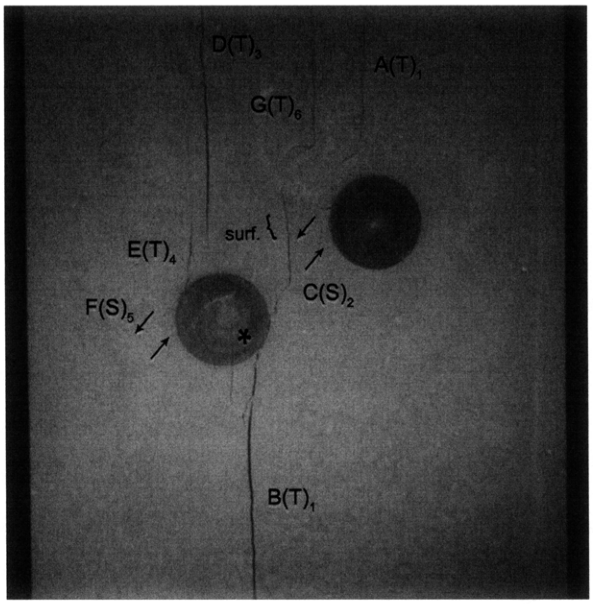

(Recorded by High Speed Video System)

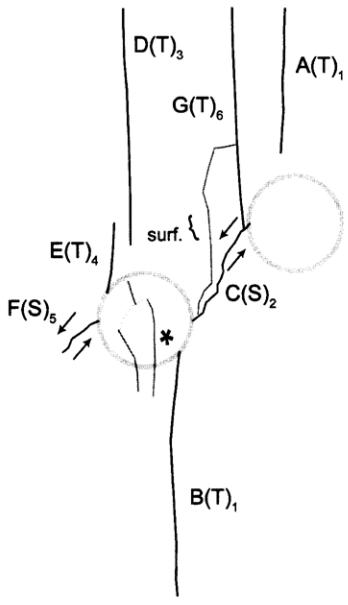

(24.64 MPa) [Max. Stress]

- Ultimate Failure

Time: 5 minutes & 0.228 seconds

Surface crack (surf.) initiates at shear crack (C) and propagates upwards.

Shear crack (C) then continues to propagate until its coalescence with the boundary of the left-hand inclusion.

Surface crack (*) initiates at the pre-test surface crack within the left-hand inclusion.

Shear crack (F) initiates at the boundary of the left-hand inclusion and propagates downwards towards the left specimen boundary.

Tensile crack (G) then initiates at shear crack (C) and propagates upwards.

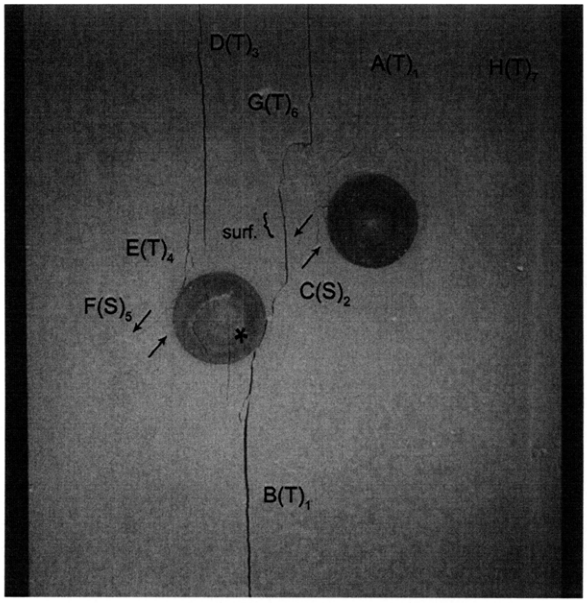

(Recorded by High Speed Video System)

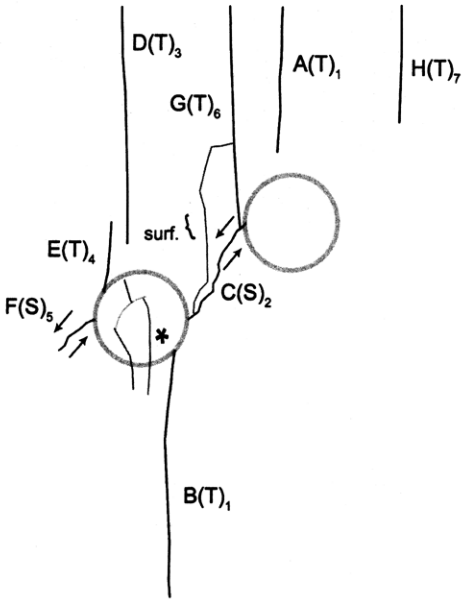

(23.07 MPa)
Time: 5 minutes & 0.328 seconds
HS Image # - 3789

Tensile crack (H) initiates at the upper specimen boundary and propagates downwards.

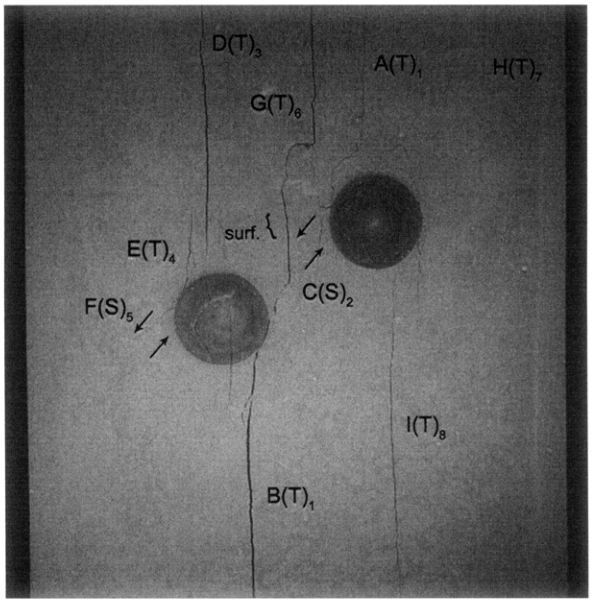

(Recorded by High Speed Video System)

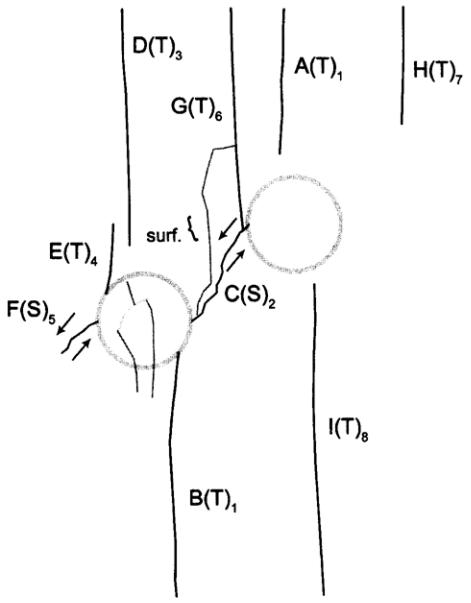

(23.07 MPa)
Time: 5 minutes & 0.328 seconds
HS Image # - 3788

Tensile crack (I) initiates below the right-hand inclusion and propagates downwards.

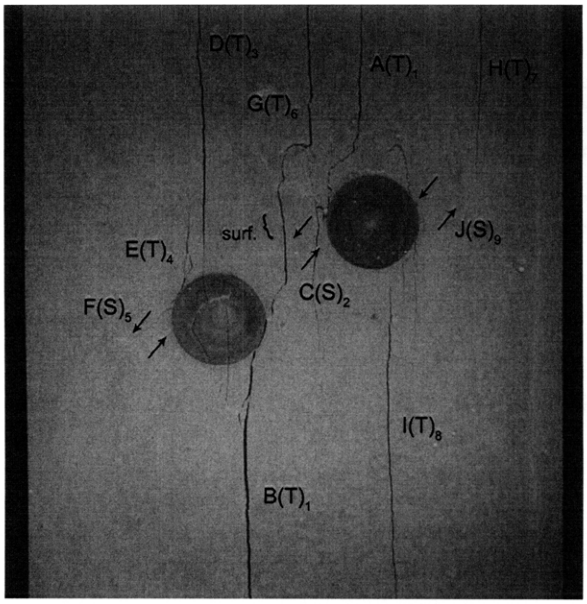

(Recorded by High Speed Video System)

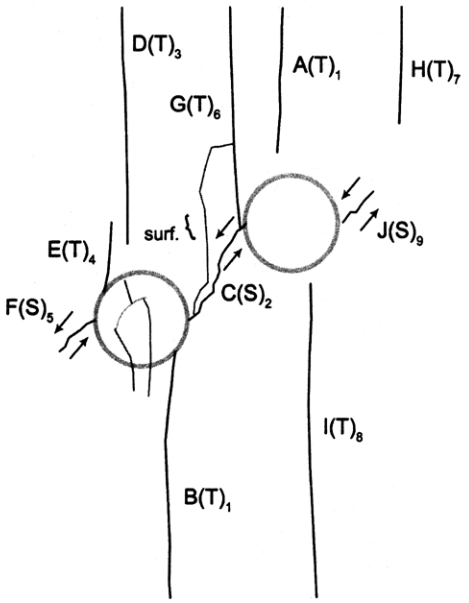

(22.47 MPa)
Time: 5 minutes & 0.366 seconds
HS Image # - 3598

Shear crack (J) initiates at the boundary of the right-hand inclusion and propagates upwards towards the right specimen boundary.

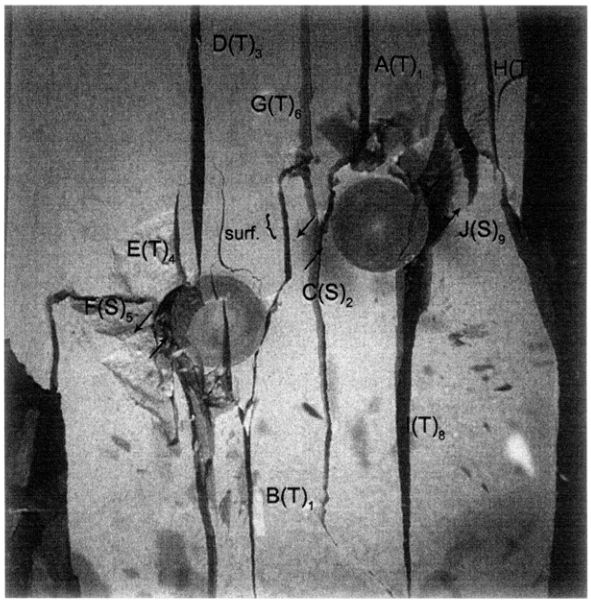

(Recorded by High Speed Video System)

(0 MPa) – Final Picture

Time: 5 minutes & 0.571 seconds

HS Image # - 2577

SUMMARY

Specimen Number: CR(UI)-30-0B (20080926)

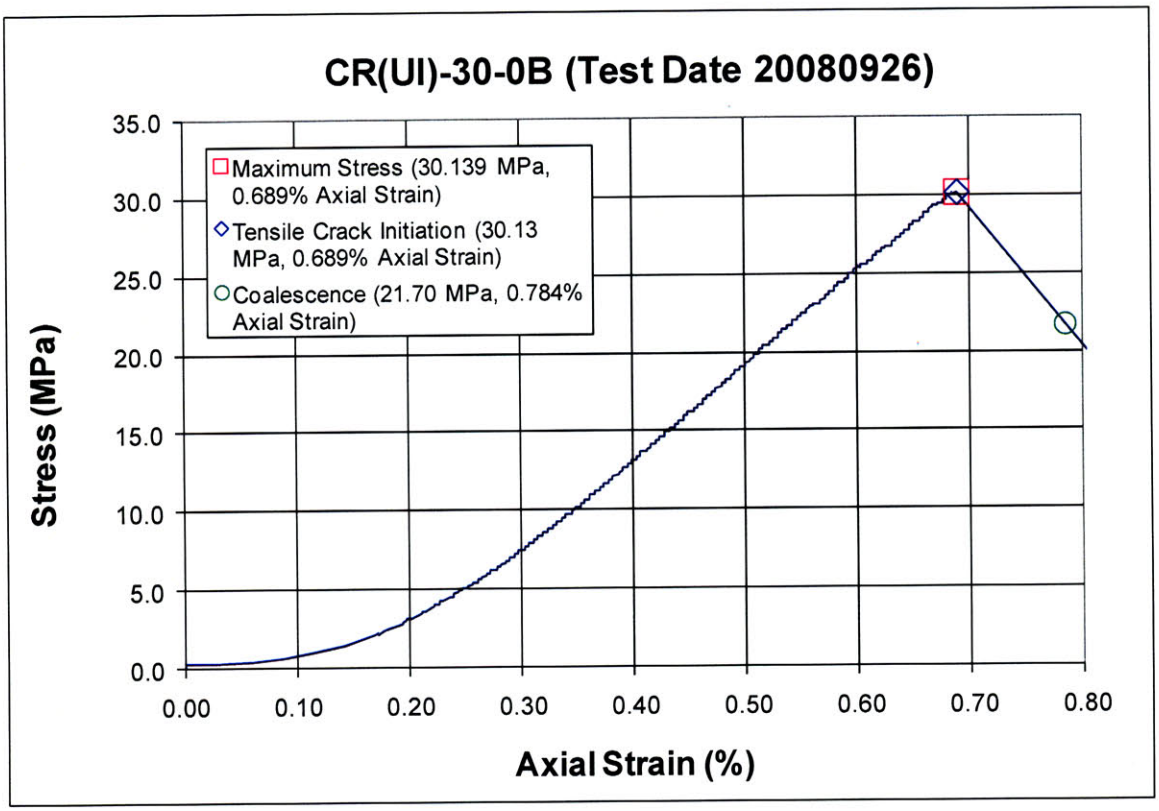

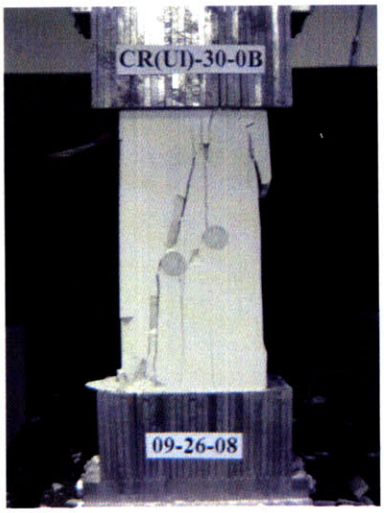

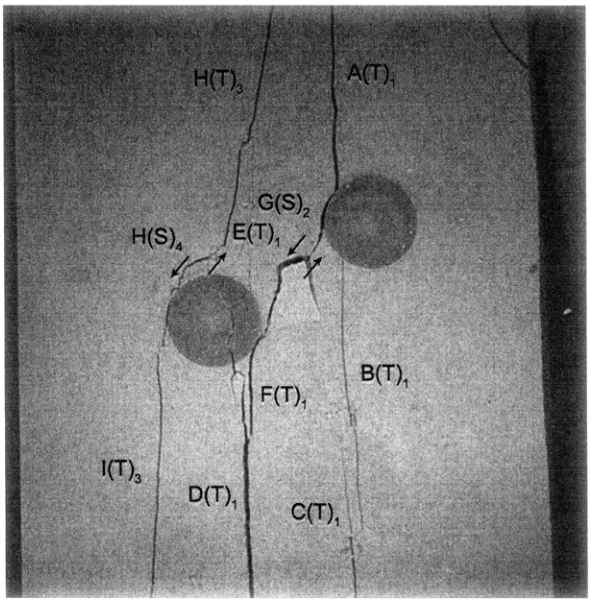

(Recorded by High Speed Video System)

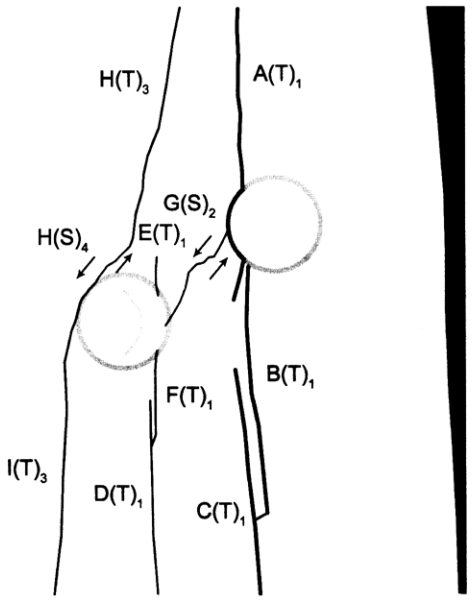

(19.69 MPa)
Time: 6 minutes & 17.280 seconds
HS Image # - 5251

Tensile crack (I) continues to propagate until its coalescence with the boundary of the left-hand inclusion boundary. Shear crack (H) initiates at the tip of tensile crack (H) and propagates until its coalescence with tensile crack (I).

SUMMARY

Specimen Number: CR(UI)-30-0C (20080926)

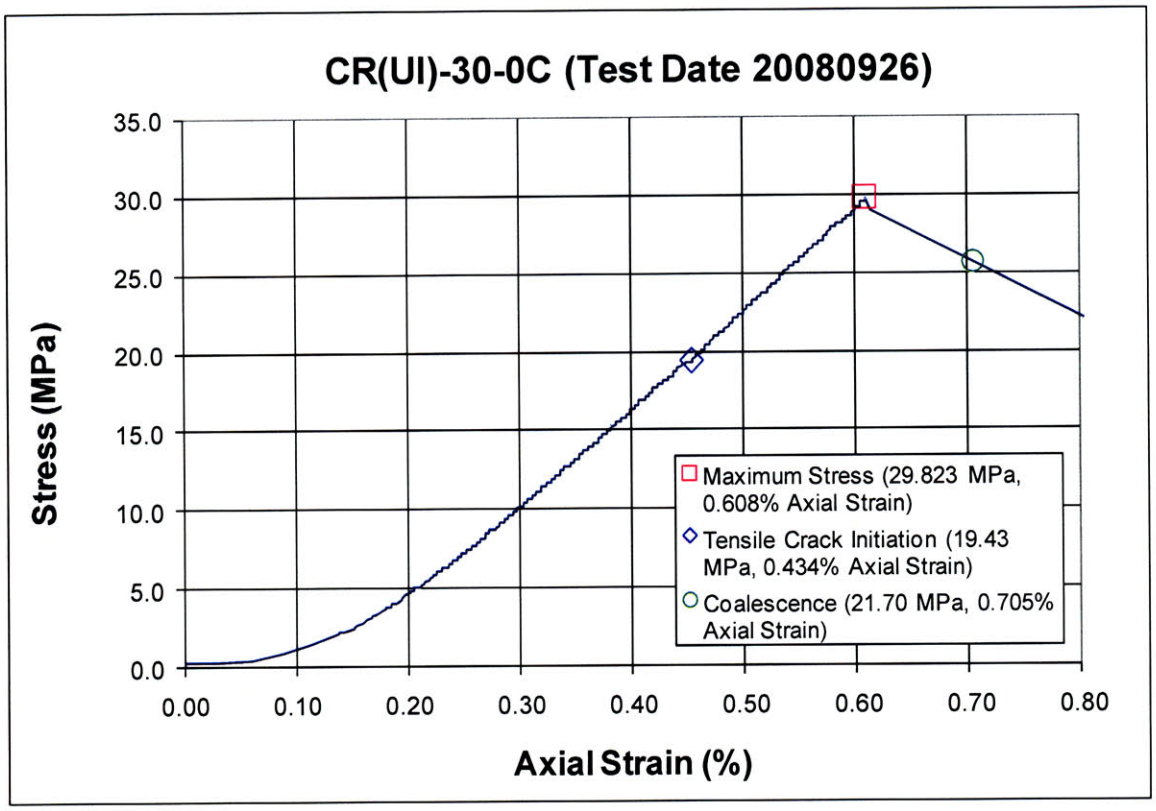

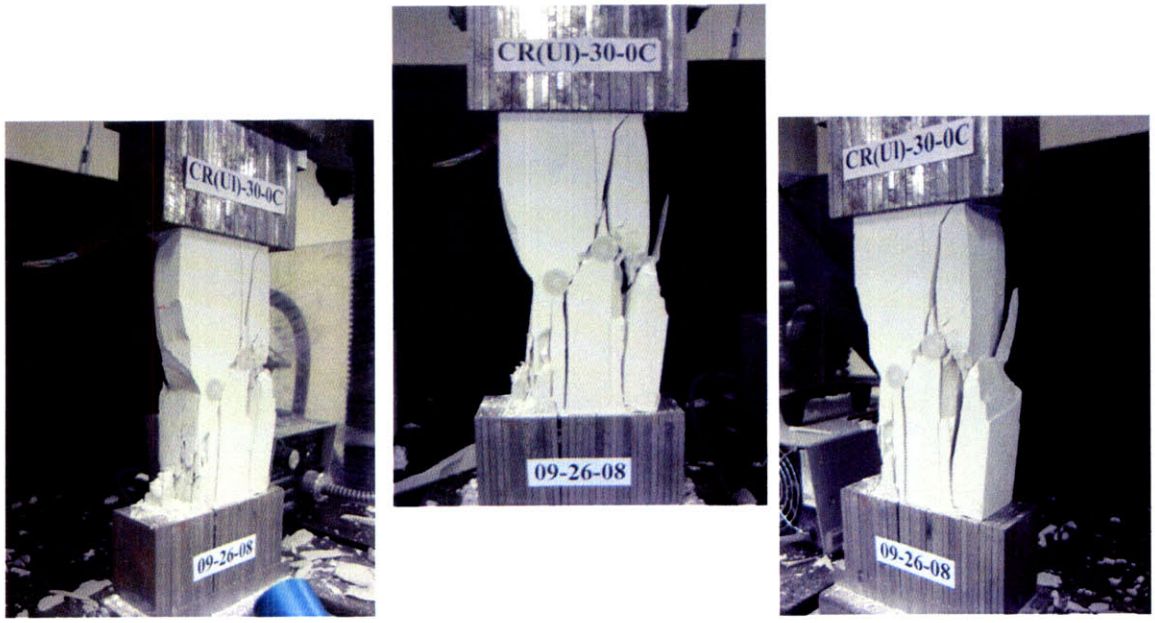

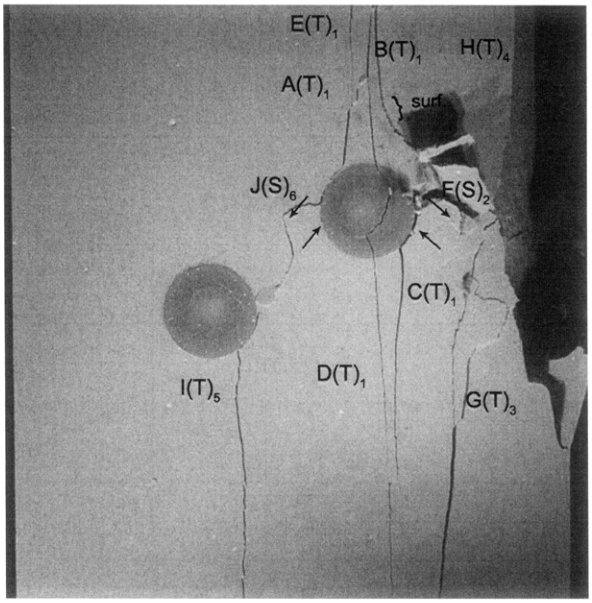

(Recorded by High Speed Video System)

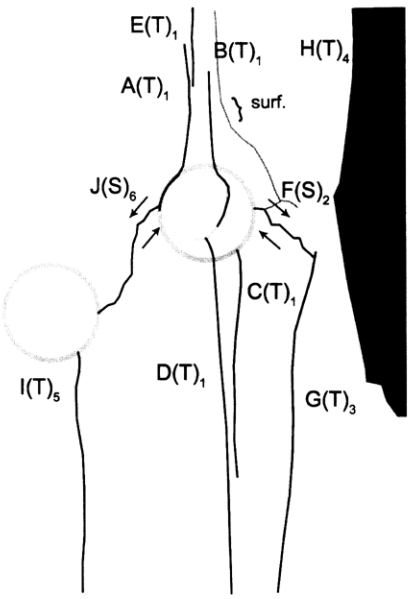

(25.64 MPa) – Ultimate Failure
Time: 6 minutes & 14.202 seconds
HS Image # - 2989

Shear crack (J) continues to propagate until its coalescence with the boundary of the left-hand inclusion.

SUMMARY

Specimen Number: CR(PI)-60-0A (20081027)

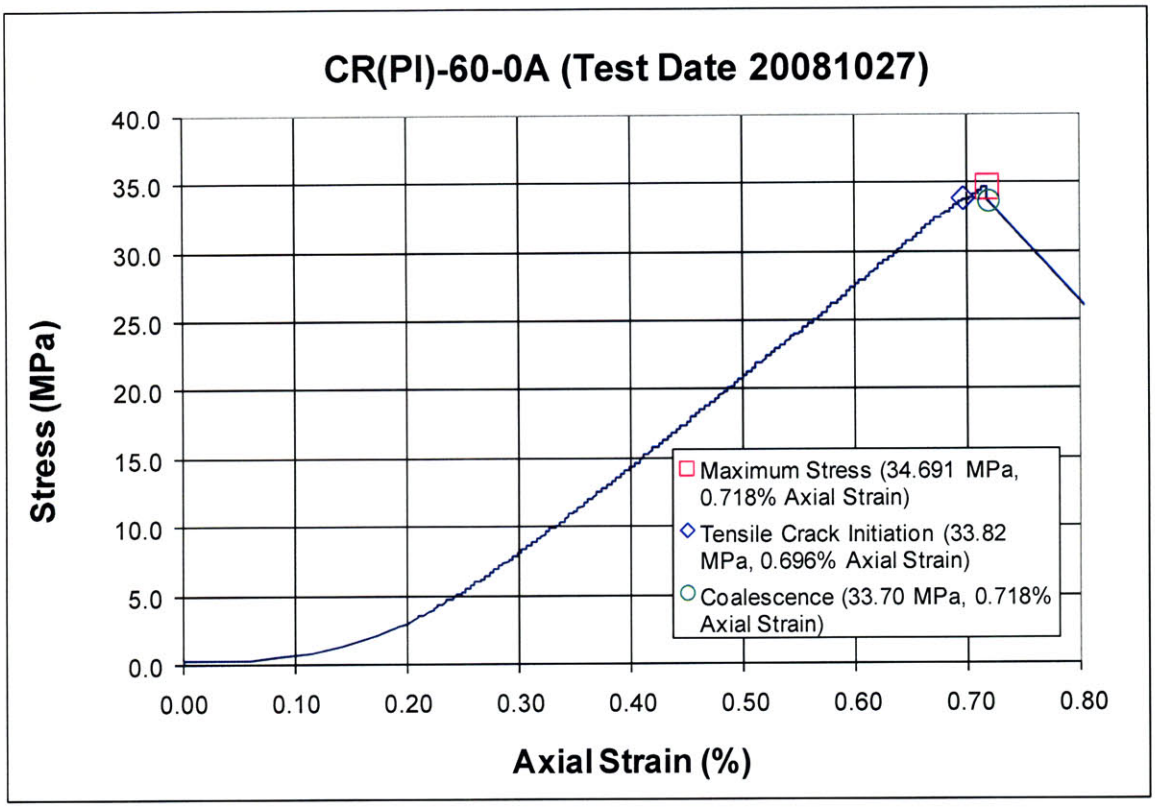

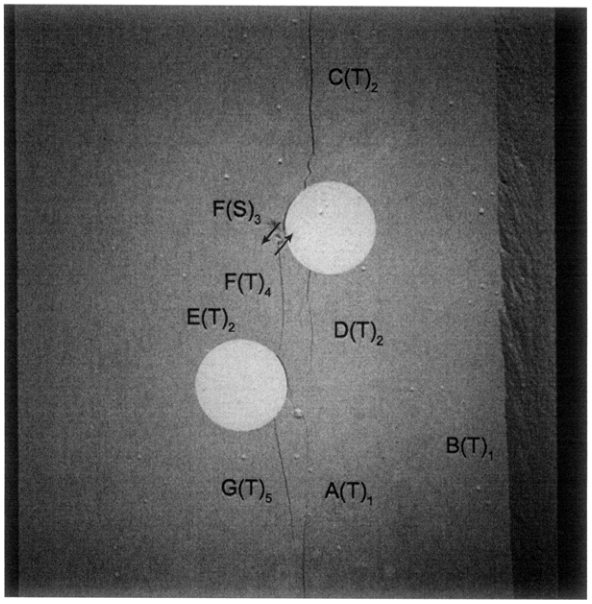

(Recorded by High Speed Video System)

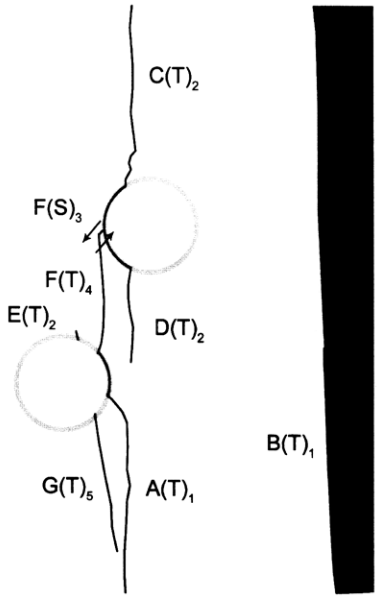

(33.52 MPa)
Time: 7 minutes & 27.286 seconds
HS Image # - 3057

Tensile crack (G) initiates at the boundary of the left-hand inclusion and propagates downwards towards tensile crack (A).

Spalling occurs adjacent to shear crack (F).

Specimen Number: CR(PI)-60-0B (20081027)

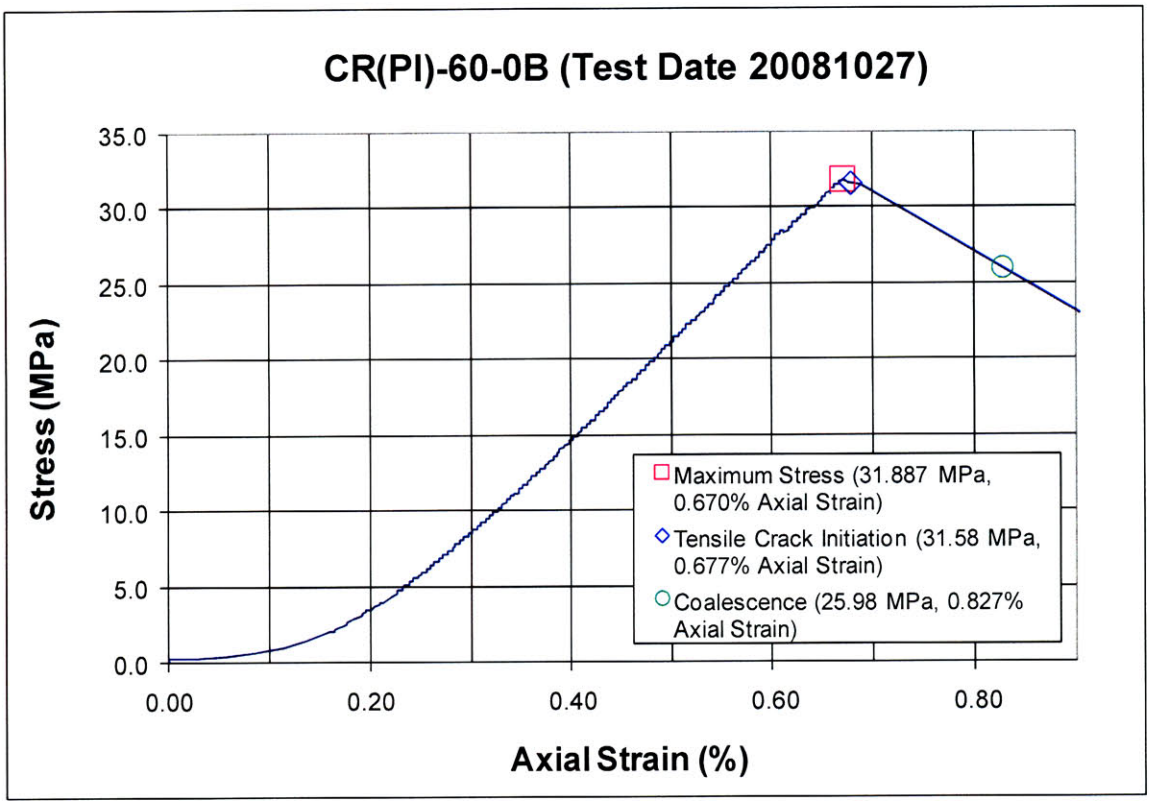

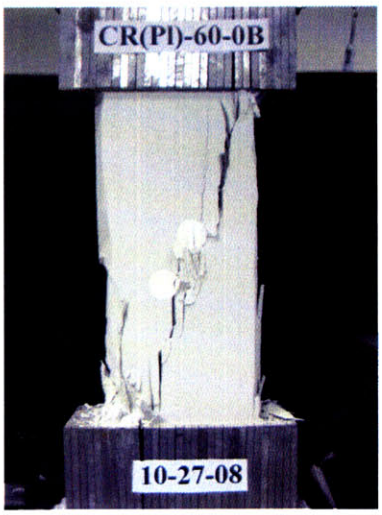

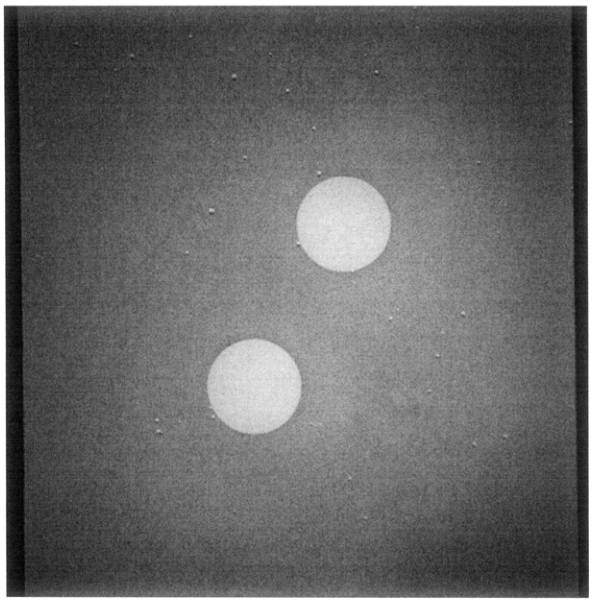

(Recorded by High Speed Video System)

Initial Inclusion Geometries:
CIRCLES – Plaster Material

Inclusions **less** stiff than matrix.

High Speed Camera Frame Rate:
5000 pps

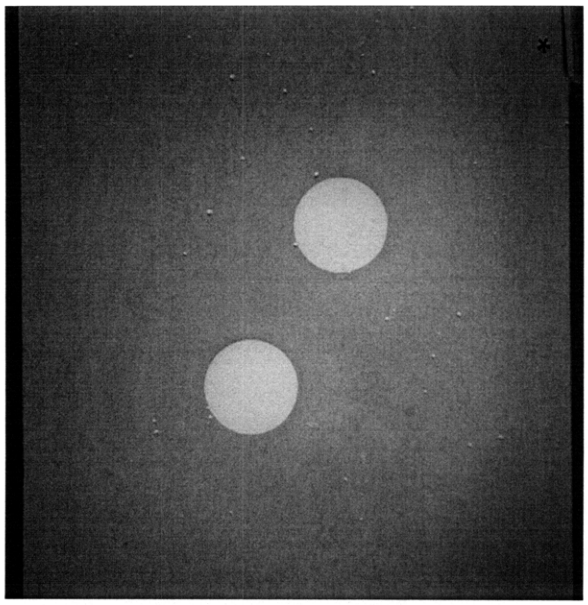

(Recorded by High Speed Video System)

(31.887 MPa) [Max. Stress]
Time: 6 minutes & 48.23 seconds

Prior to tensile crack initiation, a small piece of specimen detaches (*) from the upper right specimen boundary.

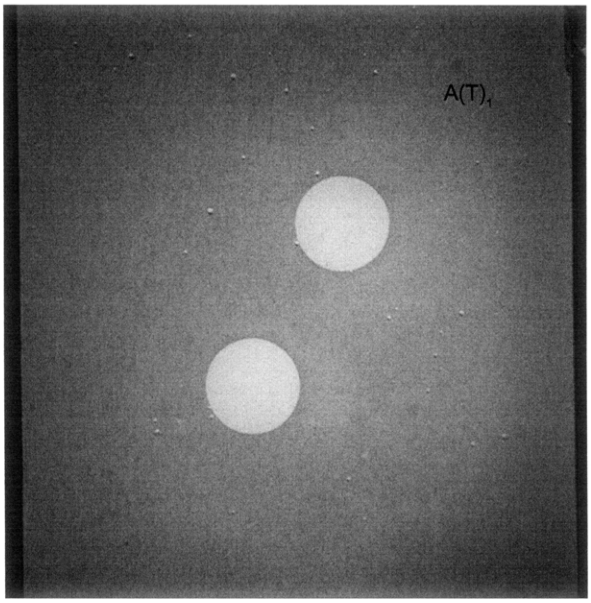

(Recorded by High Speed Video System)

A(T)1

(31.58 MPa)

- Tensile Crack Initiation

Time: 6 minutes & 48.471 seconds

HS Image # - 3773

Tensile crack (A) initiates at the upper specimen boundary and propagates downwards towards the right-hand inclusion.

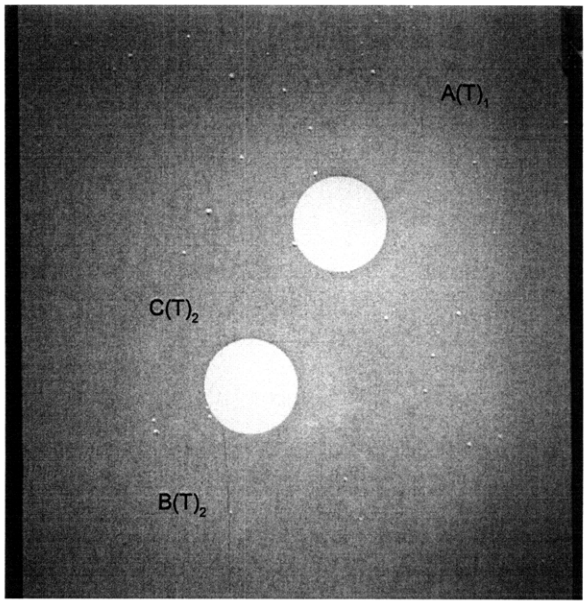

(Recorded by High Speed Video System)

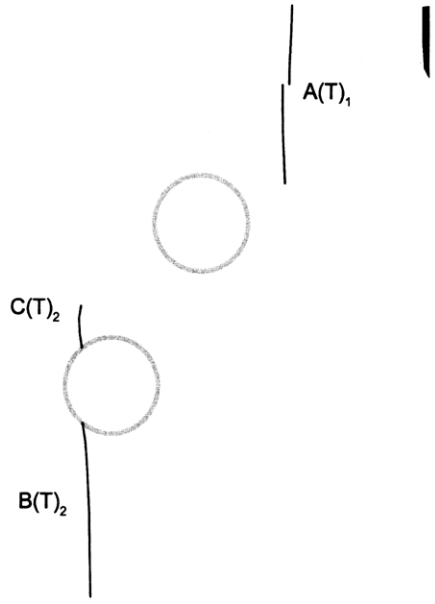

(31.58 MPa)
Time: 6 minutes & 48.472 seconds
HS Image # - 3769

Tensile cracks (B&C) initiate at the boundary of the left-hand inclusion and propagate downwards and upwards, respectively.

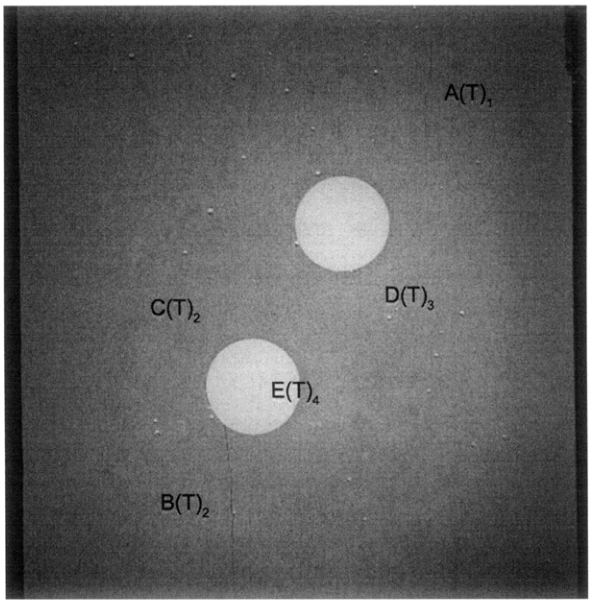

(Recorded by High Speed Video System)

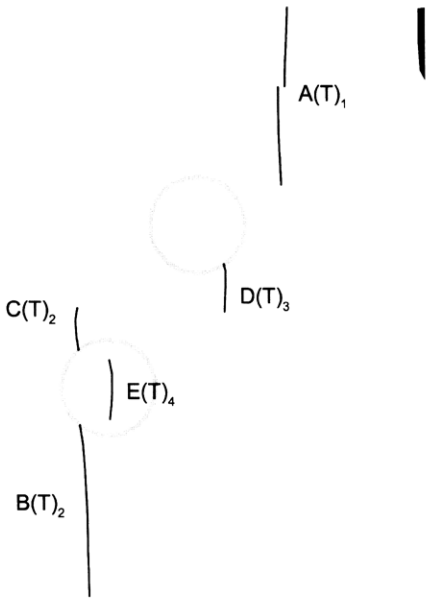

(31.57 MPa)
Time: 6 minutes & 48.482 seconds
HS Image # - 3718

Tensile crack (D) initiates at the boundary of the right-hand inclusion and propagates downwards.

Tensile crack (E) then initiates within the center of the left-hand inclusion.

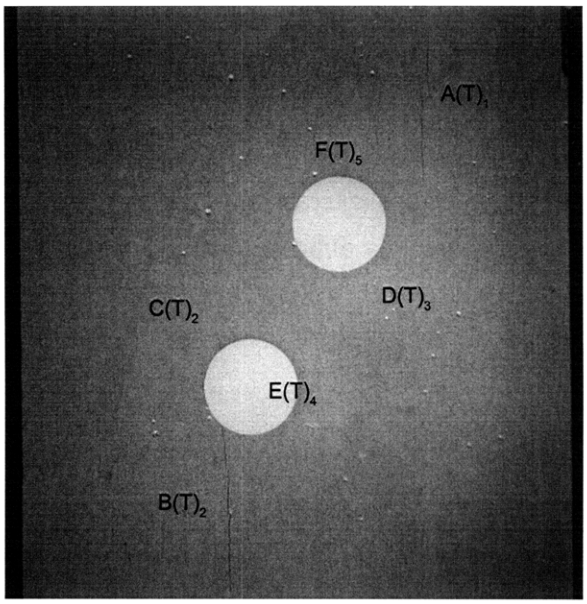

(Recorded by High Speed Video System)

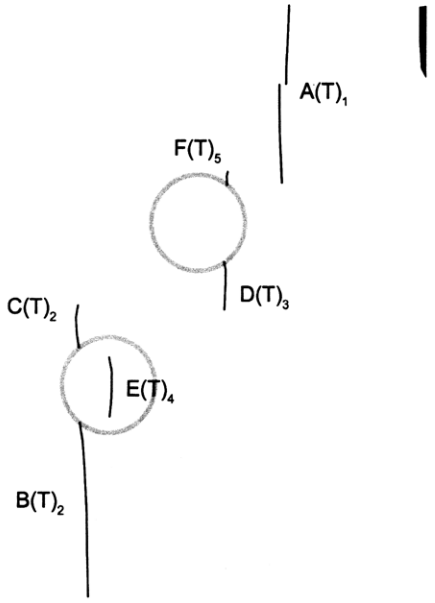

(31.53 MPa)
Time: 6 minutes & 48.585 seconds
HS Image # - 3207

Tensile crack (F) initiates at the boundary of the right-hand inclusion and propagates upwards.

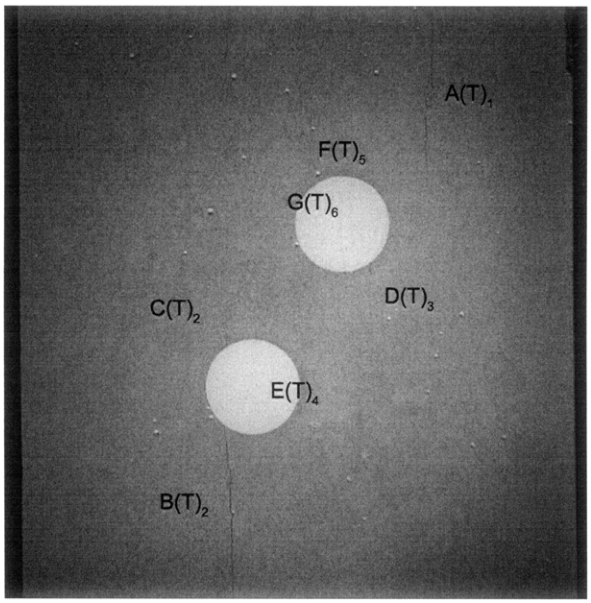

(Recorded by High Speed Video System)

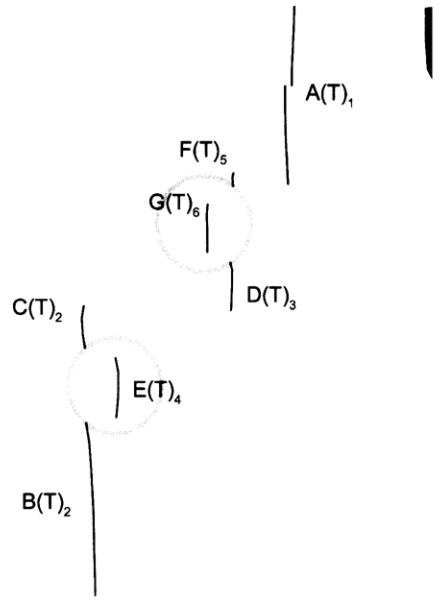

(31.52 MPa)
Time: 6 minutes & 48.604 seconds
HS Image # - 3112

Tensile crack (G) initiates within the center of the right-hand inclusion.

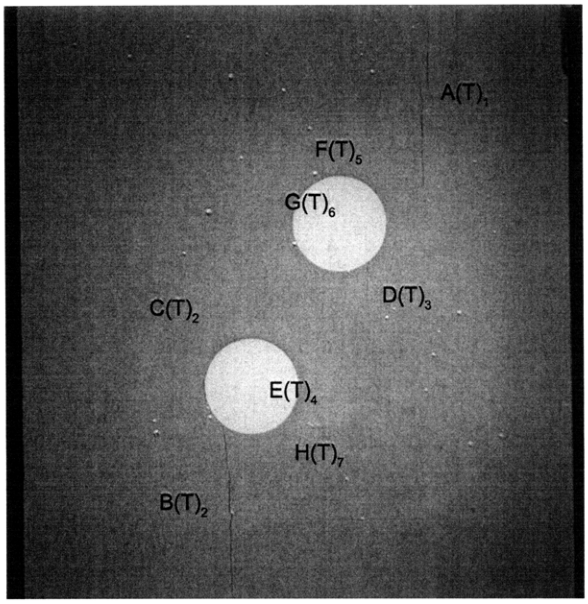

(Recorded by High Speed Video System)

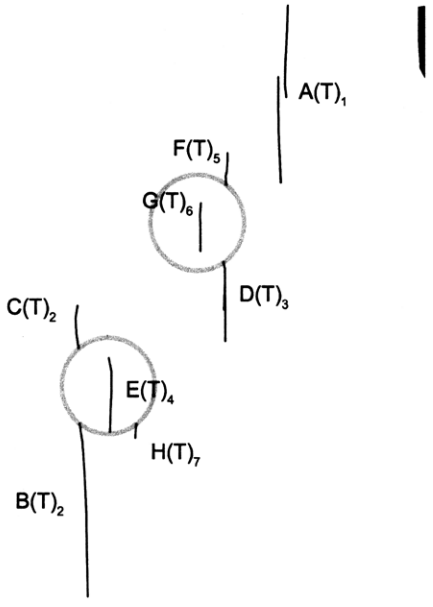

(31.51 MPa)
Time: 6 minutes & 48.634 seconds
HS Image # - 2962

Tensile crack (H) initiates at the boundary of the left-hand inclusion and propagates downwards.

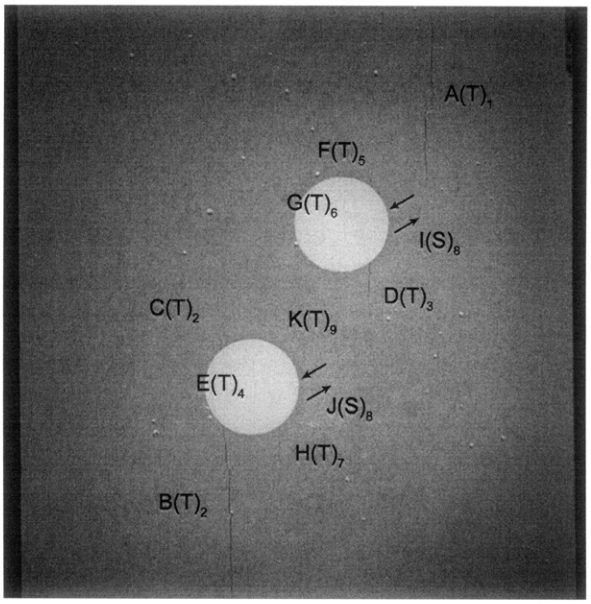

(Recorded by High Speed Video System)

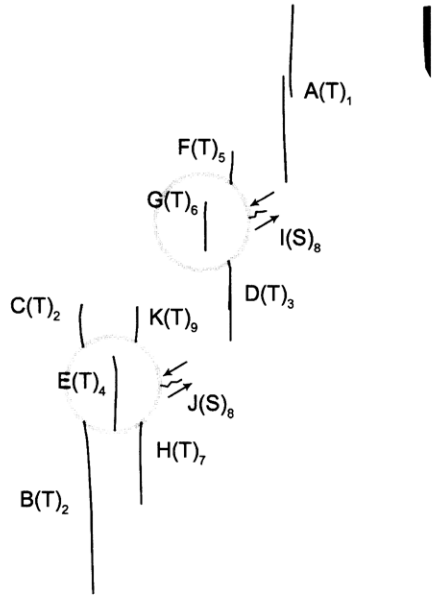

(27.89 MPa)
Time: 6 minutes & 48.675 seconds
HS Image # - 2757

Shear cracks (I&J) initiate at the boundary of the right-hand and left-hand inclusions, respectively, and propagate upwards and to the right.

Tensile crack (K) then initiates at the boundary of the left-hand inclusion and propagates upwards.

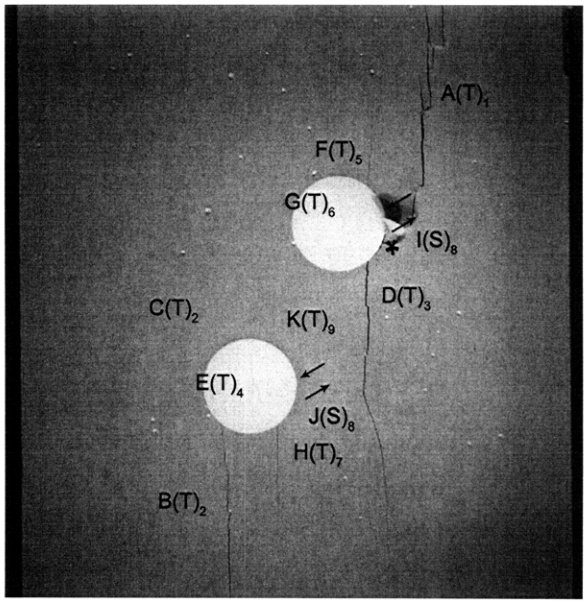

(Recorded by High Speed Video System)

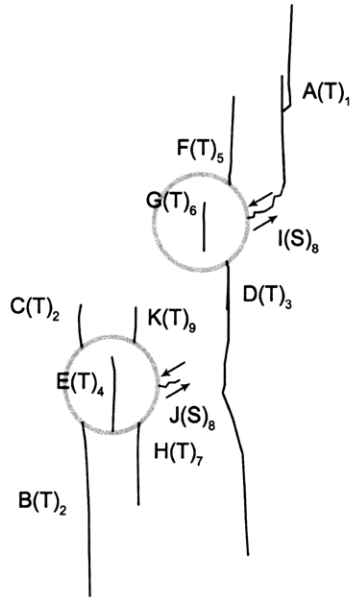

(26.73 MPa)
Time: 6 minutes & 48.688 seconds
HS Image # - 2692

Shear crack (I) continues to propagate until its coalescence with tensile crack (A). As a result, spalling (*) occurs adjacent to shear crack (I).

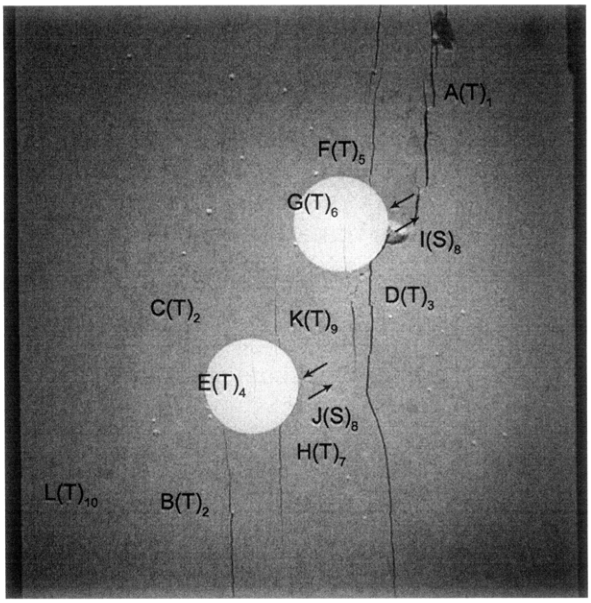

(Recorded by High Speed Video System)

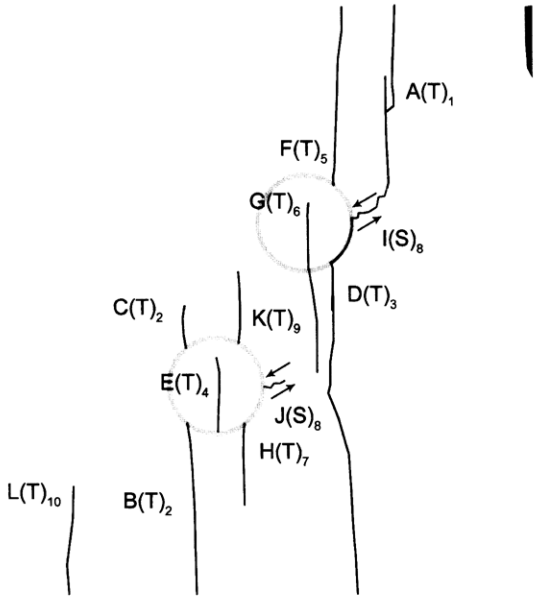

(26.29 MPa)
Time: 6 minutes & 48.693 seconds
HS Image # - 2667

Tensile crack (G) continues to propagate downwards into the hydrocal matrix.

Tensile crack (L) then initiates at the lower specimen boundary and propagates upwards.

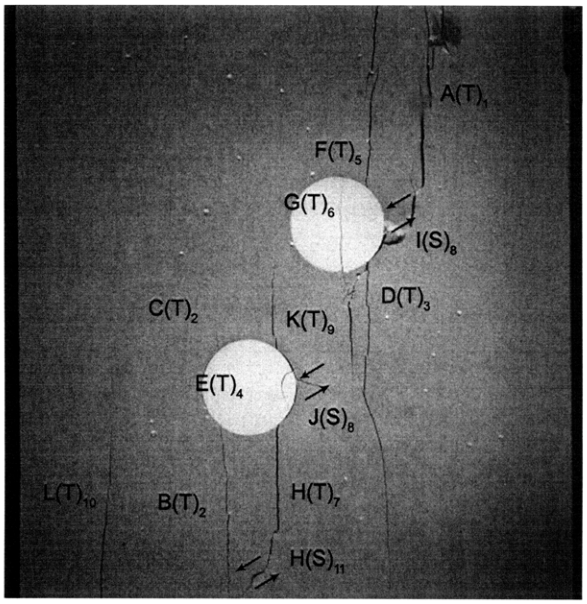

(Recorded by High Speed Video System)

(26.00 MPa)
Time: 6 minutes & 48.696 seconds
HS Image # - 2651

Shear crack (H) initiates at the tip of tensile crack (H) and propagates downwards until its coalescence with tensile crack (B).

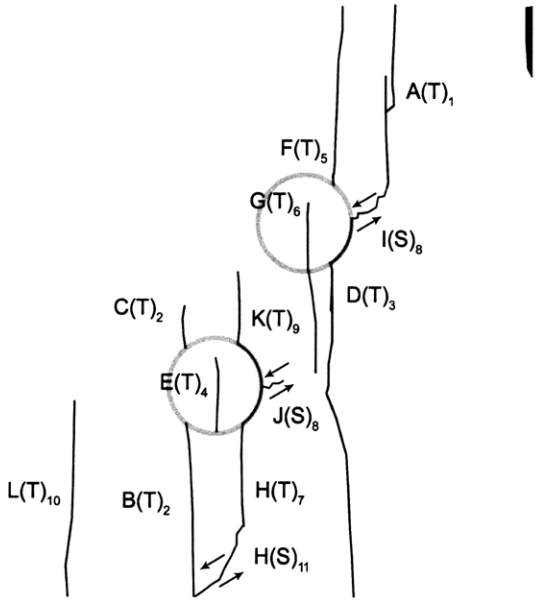

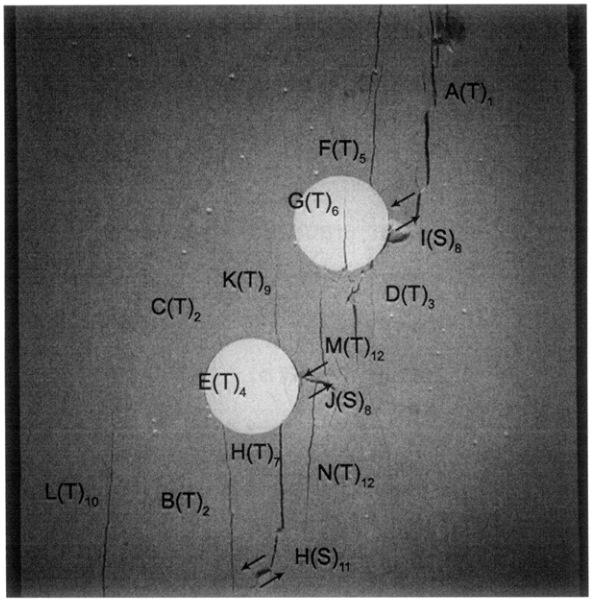

(Recorded by High Speed Video System)

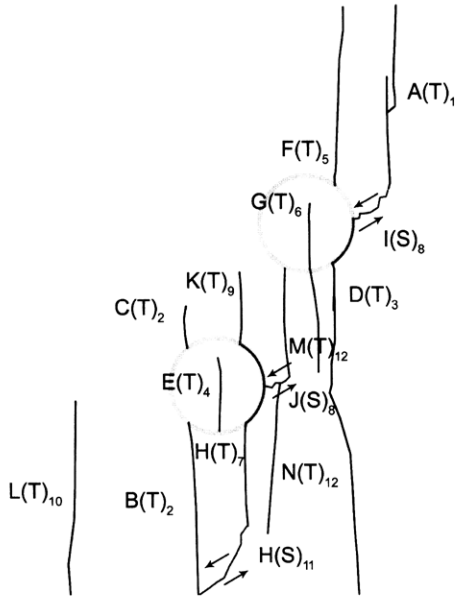

(25.98 MPa) - Coalescence
Time: 6 minutes & 48.696 seconds
HS Image # - 2650

Tensile cracks (M&N) initiate at shear crack (J) and propagate upwards and downwards, respectively. Tensile crack (M) continues to propagate until its coalescence with the boundary of the right-hand inclusion.

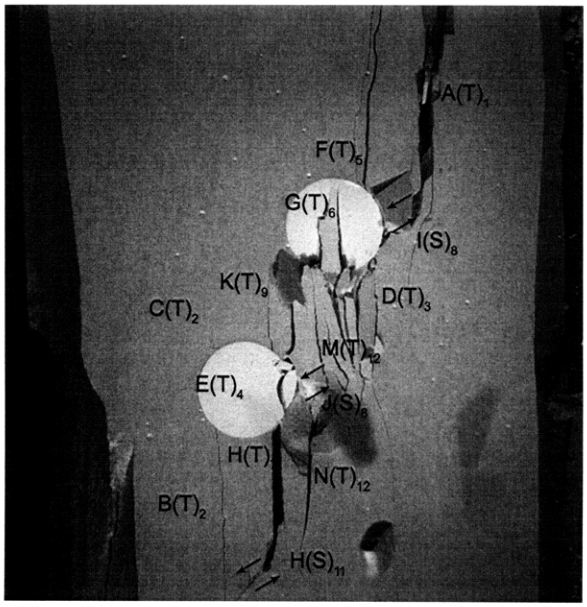

(Recorded by High Speed Video System)

(0 MPa) – Final Picture

Time: 6 minutes & 49.226 seconds

HS Image # - 1

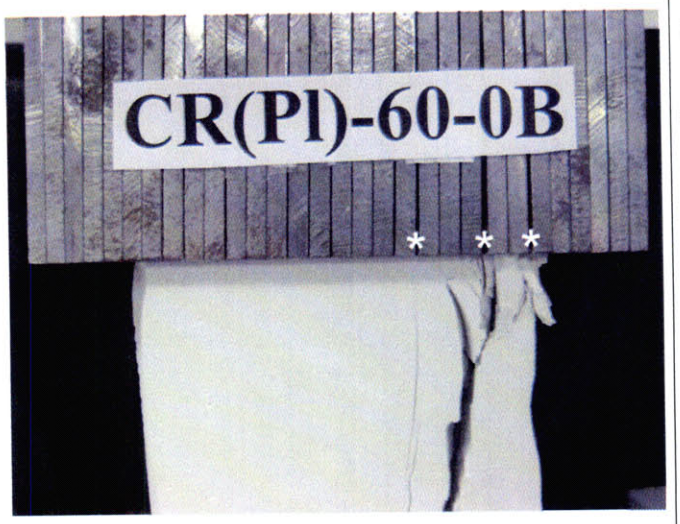	Upper edge of the specimen. The cracks marked with a (*) coincide with the openings between the teeth of the brush platen.
	Lower edge of the specimen. The cracks marked with a (*) coincide with the openings between the teeth of the brush platen.

SUMMARY

Specimen Number: CR(PI)-60-0C (20081027)

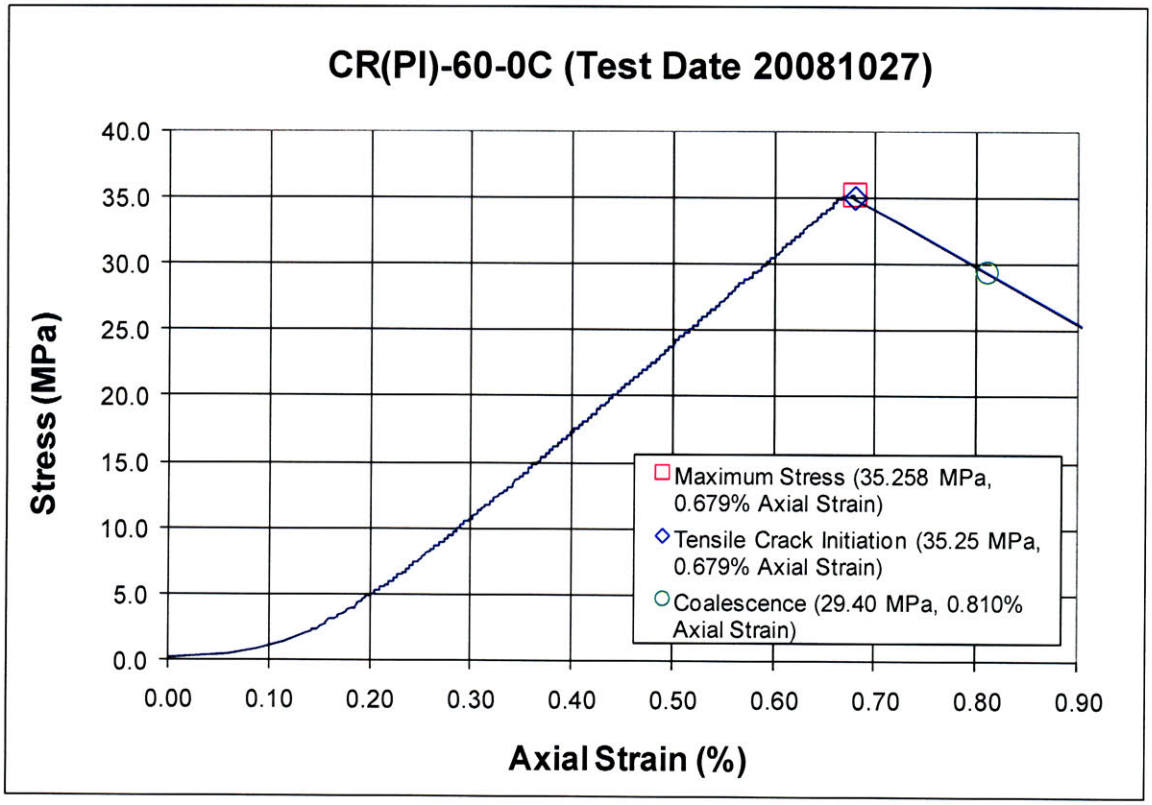

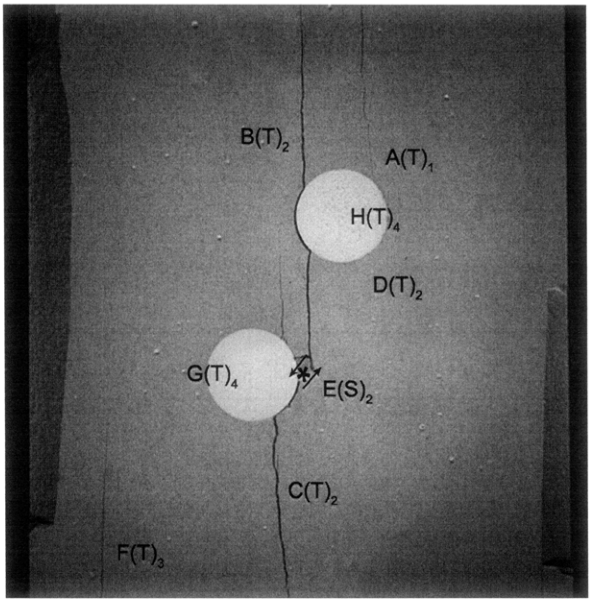

(Recorded by High Speed Video System)

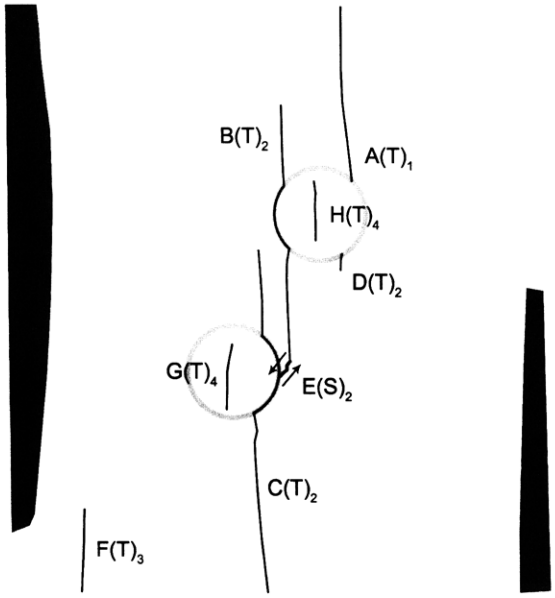

(29.38 MPa) – Coalescence
Time: 7 minutes & 27.601 seconds
HS Image # - 2775

Tensile crack (F) initiates at the lower specimen boundary and propagates upwards.

Tensile cracks (G&H) then initiate simultaneously within the centers of their respectively inclusions.

Spalling (*) occurs adjacent to shear crack (E).

SUMMARY

Specimen Number: CR(UI)-60-0A (20081027)

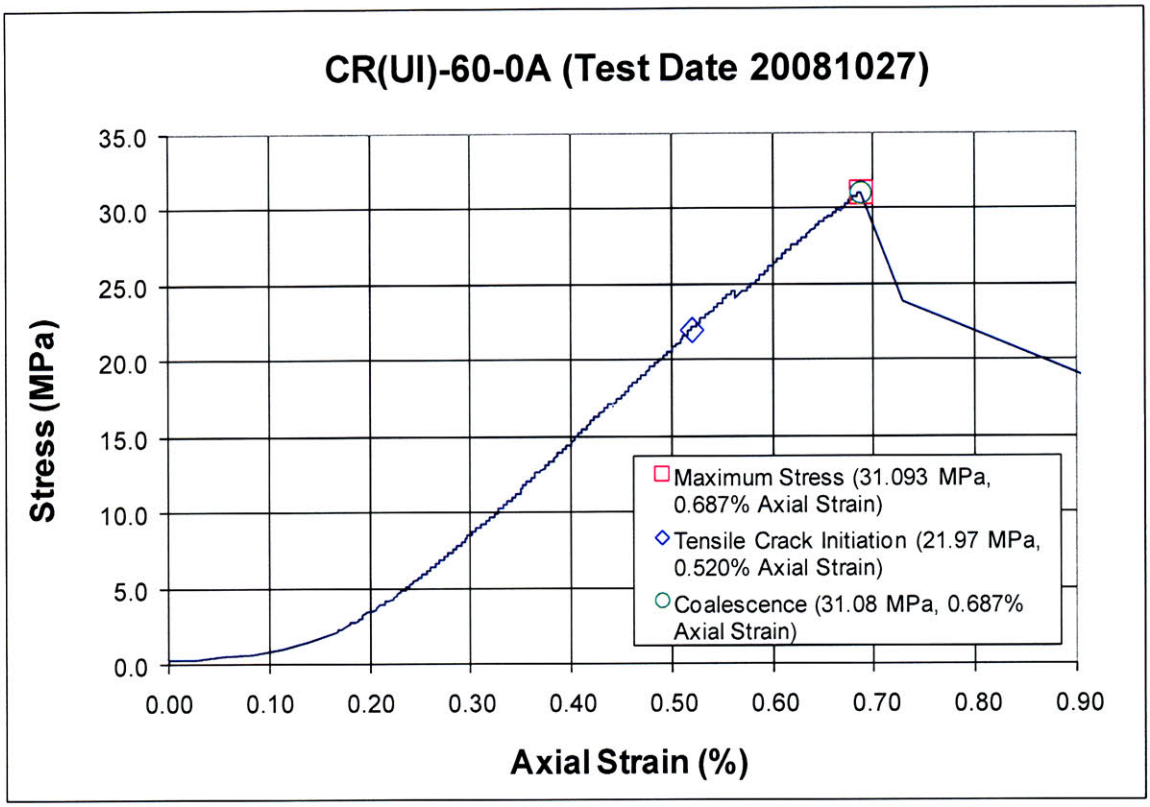

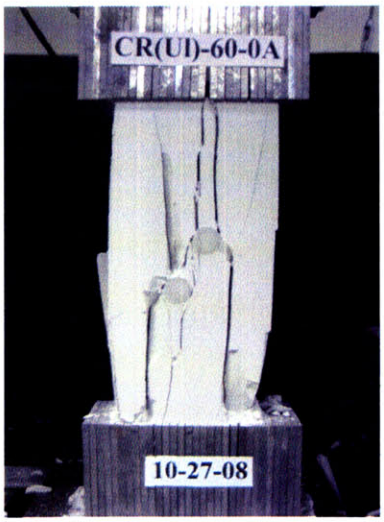

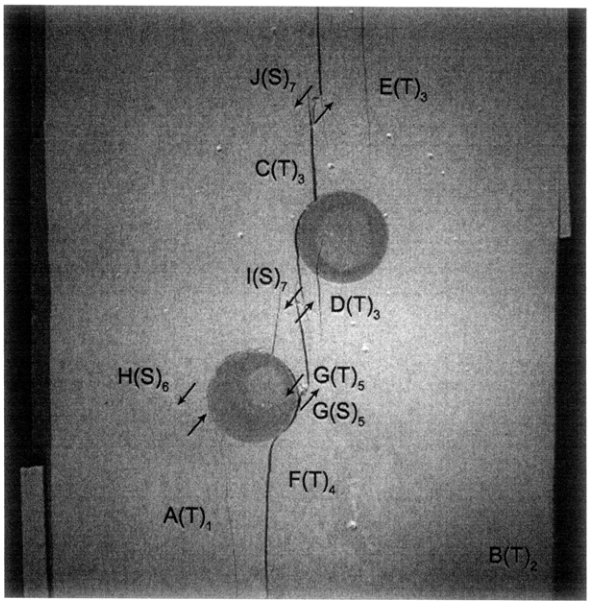

(Recorded by High Speed Video System)

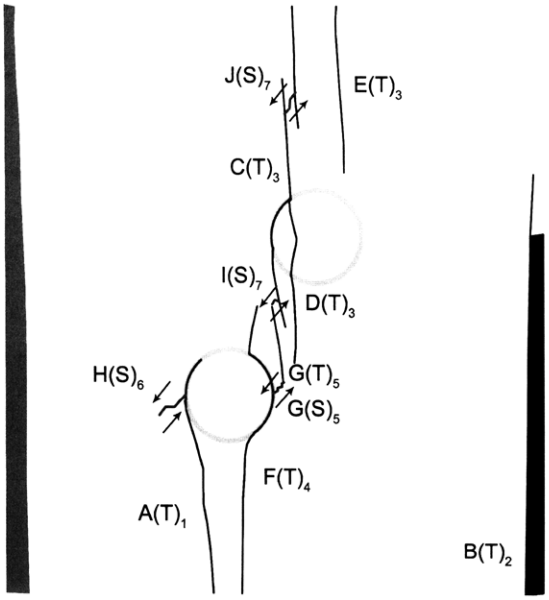

(31.08 MPa) - Coalescence
Time: 6 minutes & 30.128 seconds
HS Image # - 3679

Shear crack (I) initiates and coalesces tensile cracks (C&G).

Shear crack (J) initiates and coalesces the upper two portions of tensile crack (C).

SUMMARY

Specimen Number: CR(UI)-60-0B (20081027)

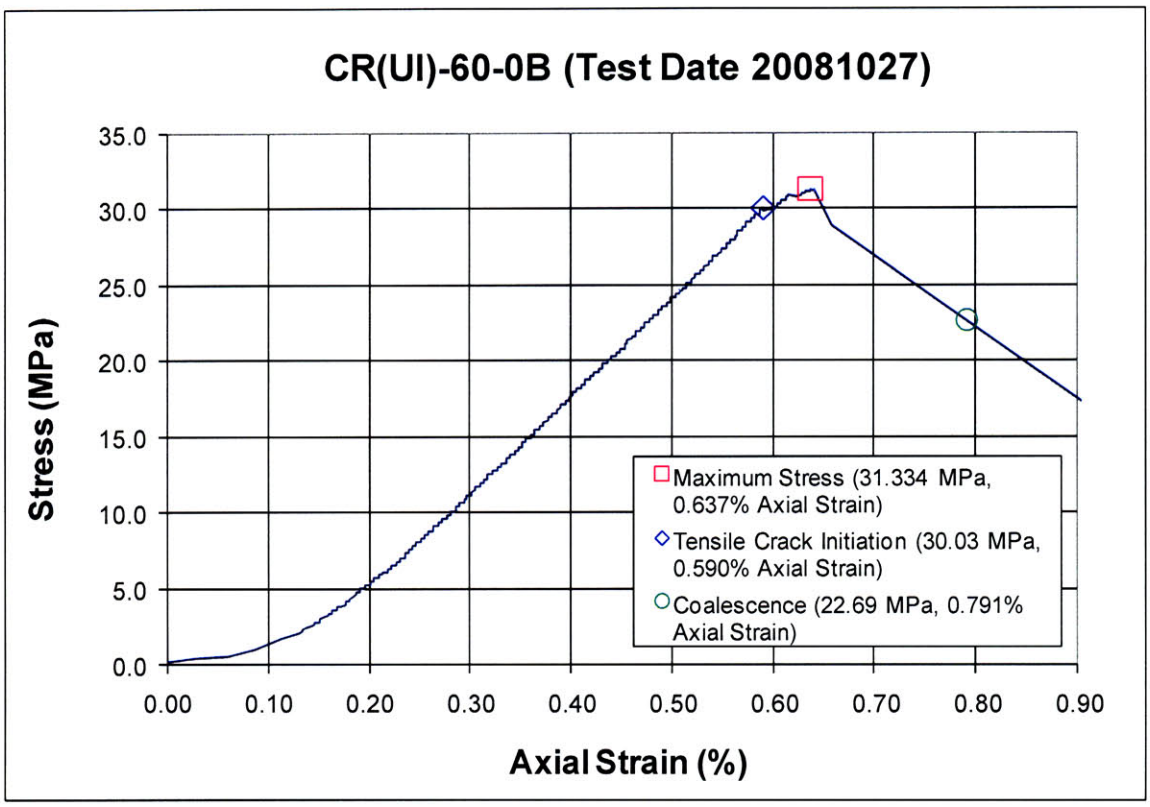

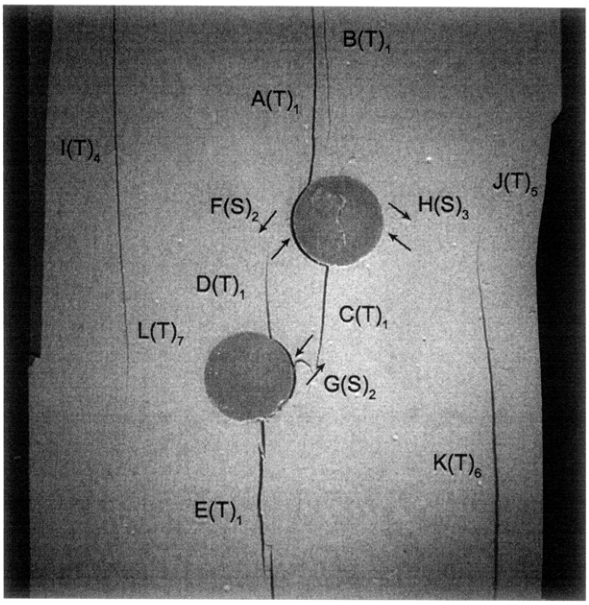

(Recorded by High Speed Video System)

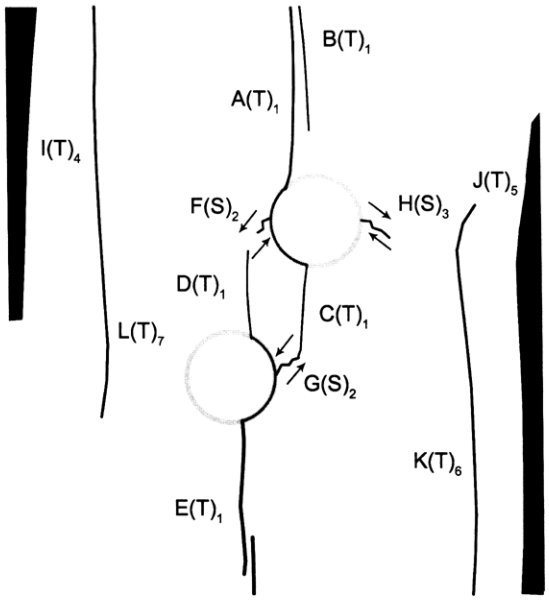

(22.69 MPa) - Coalescence
Time: 6 minutes & 32.883 seconds
HS Image # - 2509

Tensile crack (K) initiates at the lower specimen boundary and propagates upwards.

Tensile crack (L) then initiates at the upper specimen boundary and propagates downwards.

Shear crack (G) continues to propagate until its coalescence with tensile crack (C).

Note the curved nature of tensile cracks (K&L) when they propagate adjacent to the two inclusions.

Specimen Number: CR(UI)-60-0C (20081027)

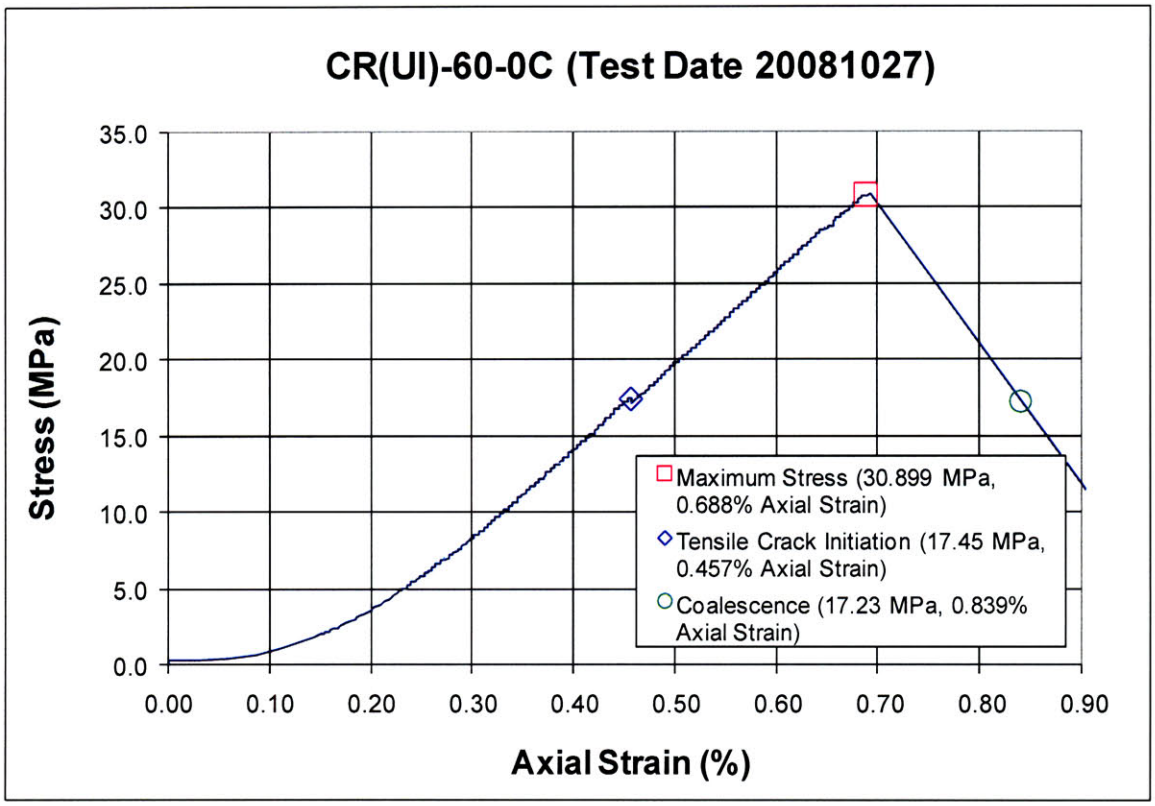

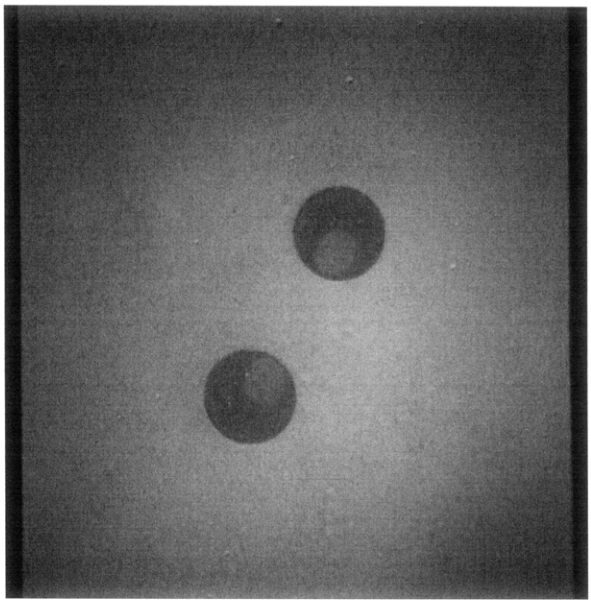

(Recorded by High Speed Video System)

Initial Inclusion Geometries:
CIRCLES – Ultracal Material

Inclusions **more** stiff than matrix.

High Speed Camera Frame Rate:
5000 pps

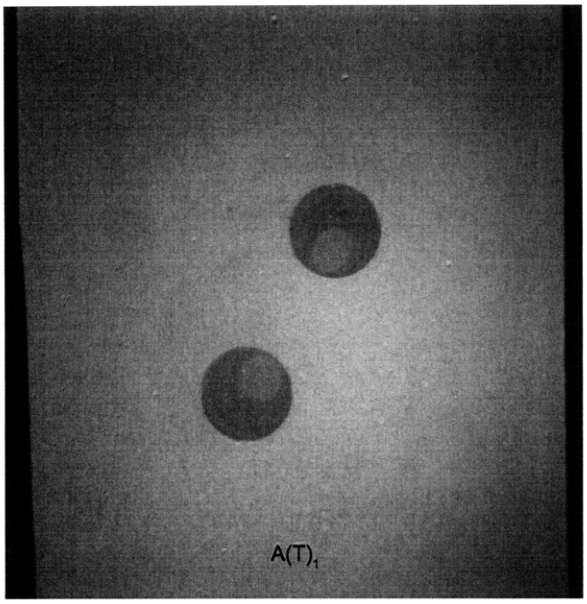

(Recorded by High Speed Video System)

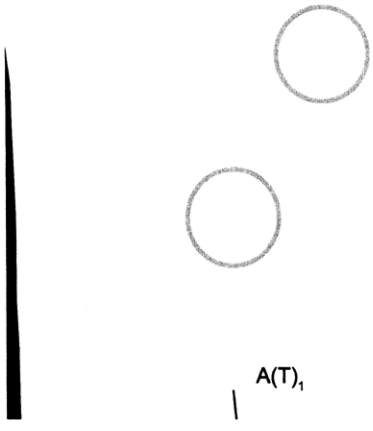

(17.45 MPa)

- Tensile Crack Initiation

Time: 3 minutes & 21.89 seconds

Prior to tensile crack initiation at the inclusion boundaries, a piece of specimen detaches from the left boundary.

Tensile crack (A) also initiates at the lower specimen boundary and propagates upwards towards the left-hand inclusion.

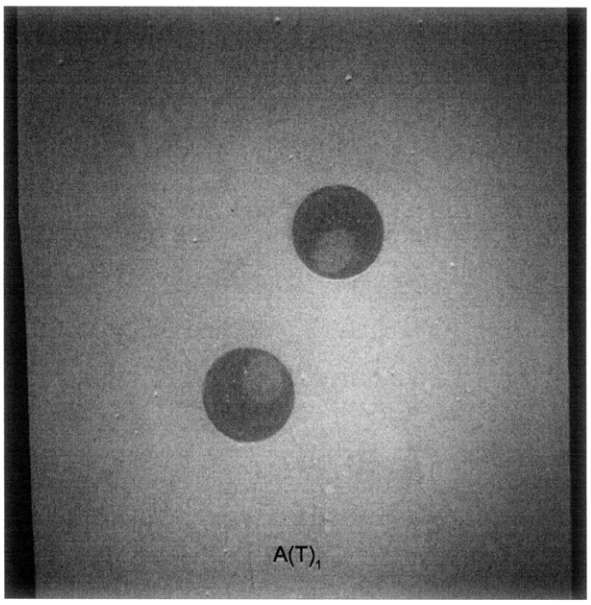

(Recorded by High Speed Video System)

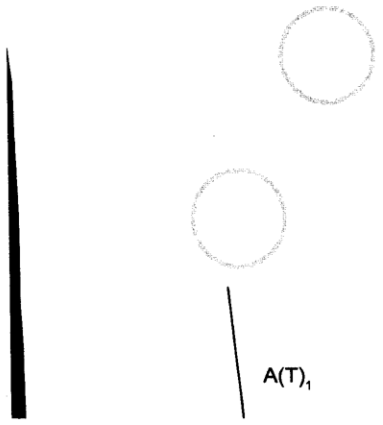

(30.90 MPa) [Max. Stress]
Time: 6 minutes & 32.674 seconds

Tensile crack (A) continues to propagate towards the left-hand inclusion.

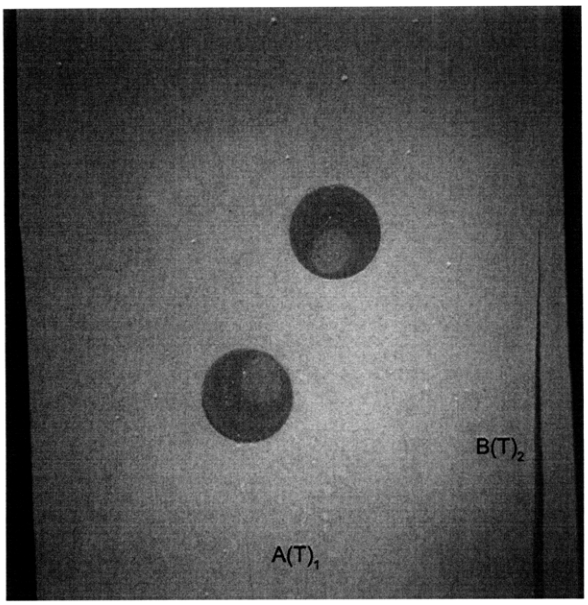

(Recorded by High Speed Video System)

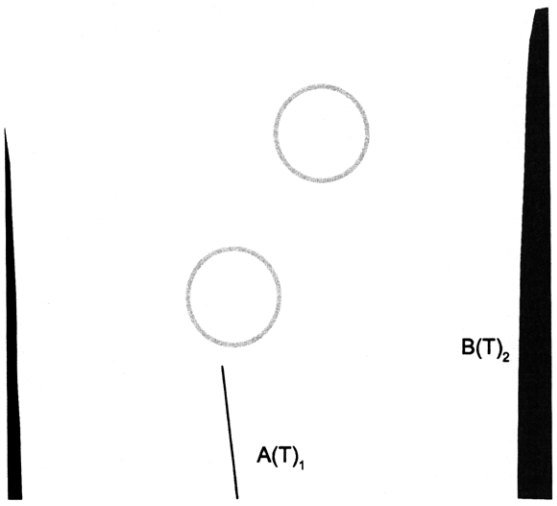

(30.86 MPa)
Time: 6 minutes & 32.798 seconds
HS Image # - 5147

Tensile crack (B) initiates at the lower specimen boundary and propagates upwards, which results in the detachment of a surficial piece of specimen from the right boundary.

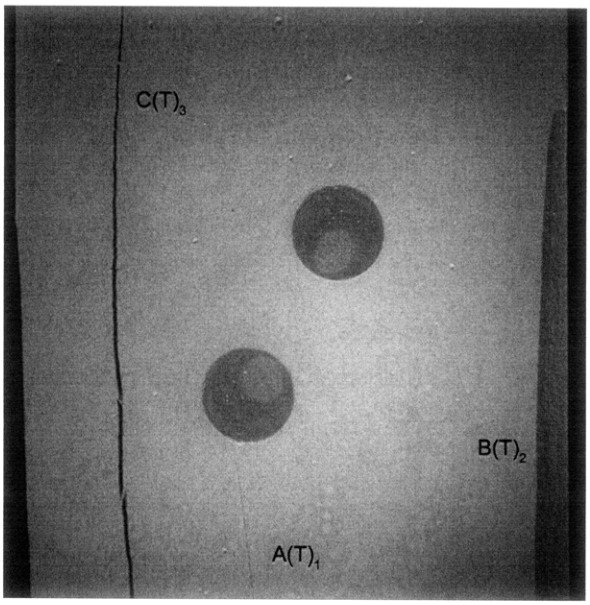

(Recorded by High Speed Video System)

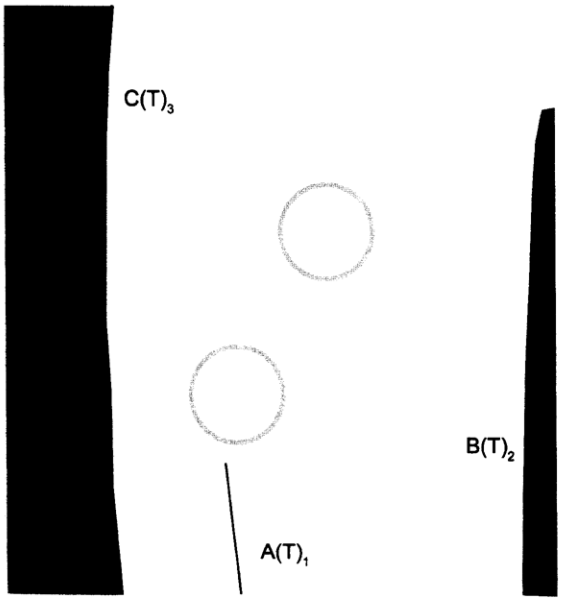

(30.88 MPa)
Time: 6 minutes & 33.076 seconds
HS Image # - 3786

Tensile crack (C) initiates at the upper specimen boundary and propagates downwards until it intersects with the lower specimen boundary. This results in the detachment of a very large specimen piece from the intact specimen.

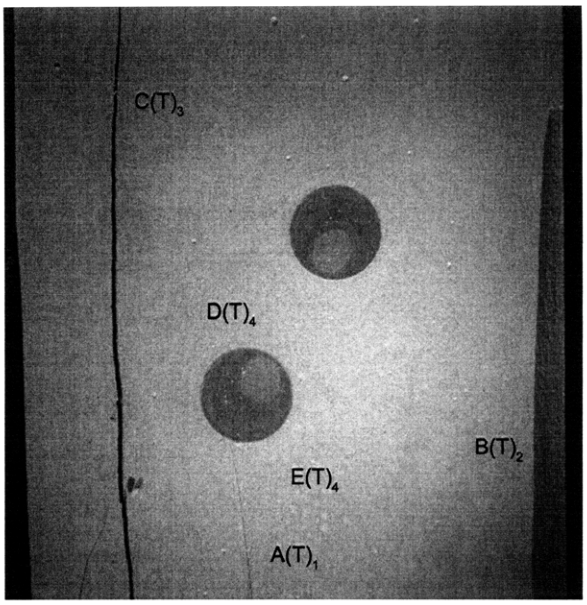

(Recorded by High Speed Video System)

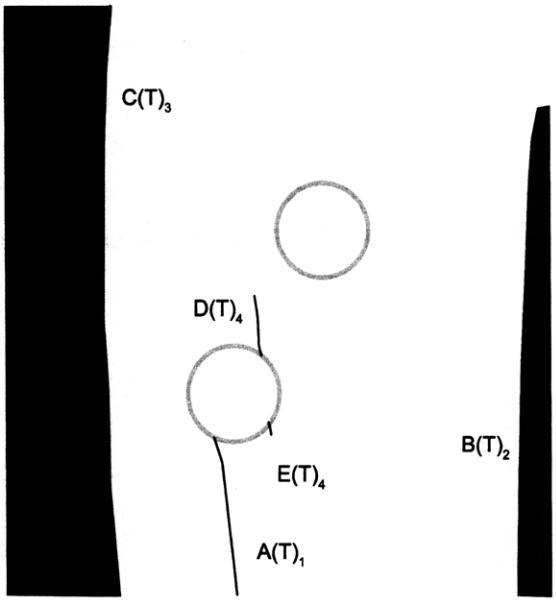

(29.07 MPa)
Time: 6 minutes & 33.093 seconds
HS Image # - 3702

Tensile cracks (D&E) initiate at the boundary of the left-hand inclusion and propagate upwards and downwards, respectively.

Tensile crack (A) continues to propagate upwards until its coalescence with the left-hand inclusion boundary.

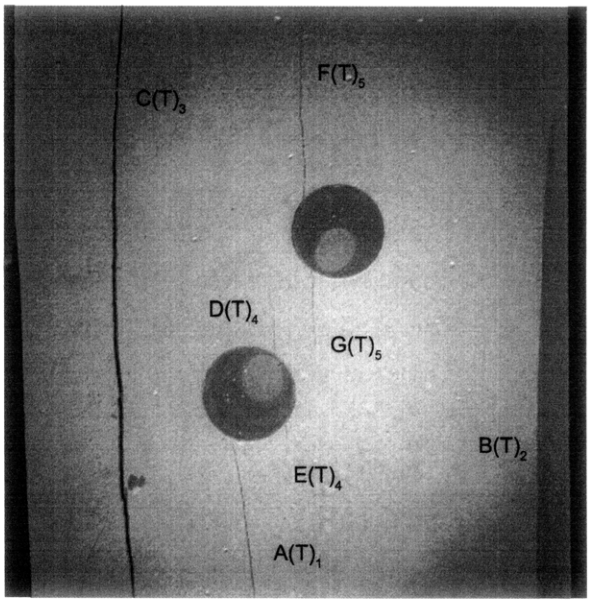

(Recorded by High Speed Video System)

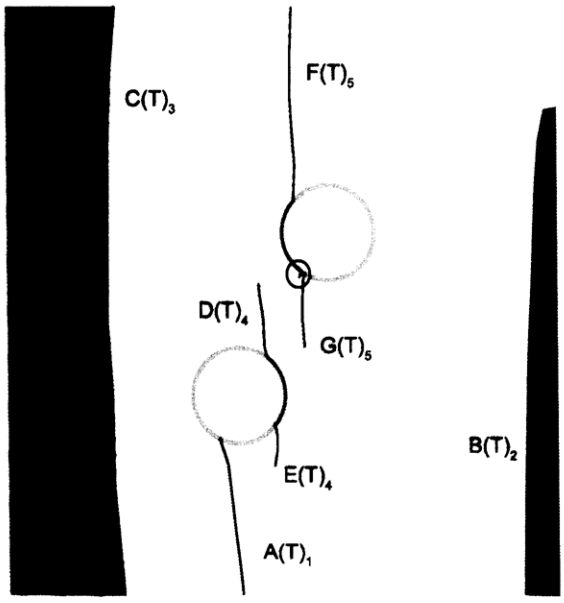

(29.00 MPa)
Time: 6 minutes & 33.093 seconds
HS Image # - 3699

Tensile cracks (D&E) propagate along the left-hand inclusion boundary until coalescence. The exact propagation sequence could not be determined from the high speed camera footage.

Tensile cracks (F&G) initiate at the boundary of the right-hand inclusion and propagate upwards and downwards, respectively. It is then assumed that only tensile crack (F) propagates along the inclusion boundary and into the surrounding hydrocal matrix. This assumption is based on the observation that no inclusion debonding has occurred between tensile cracks (G) and the encircled tensile crack, which is assumed to be an extension of tensile crack (F). Refer to the circled portion of the sketch.

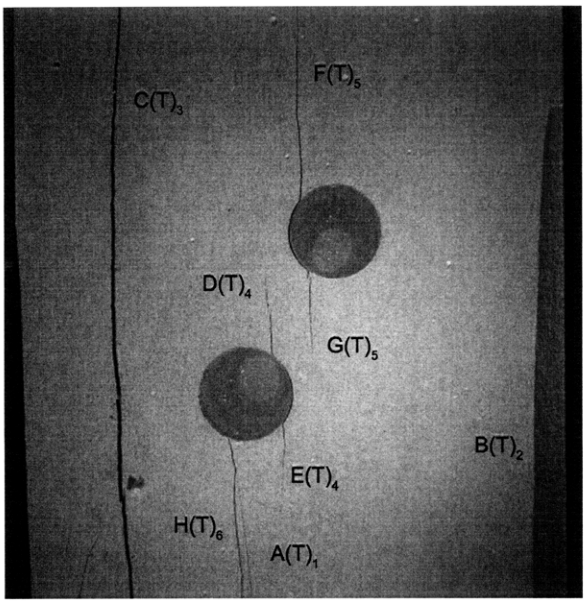

(Recorded by High Speed Video System)

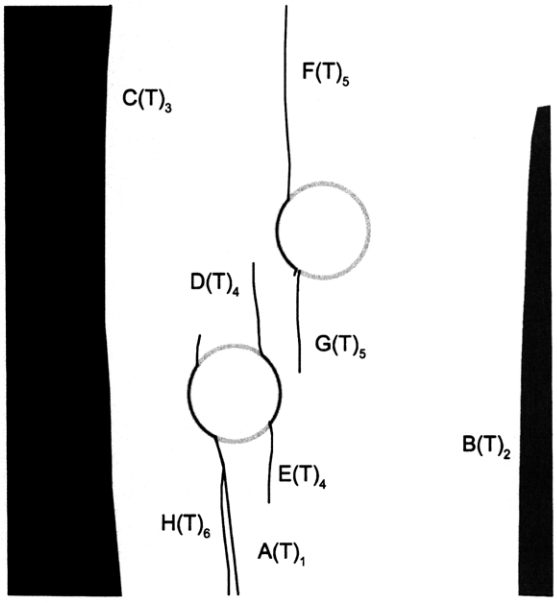

(28.98 MPa)
Time: 6 minutes & 33.094 seconds
HS Image # - 3698

It is assumed that tensile crack (H) initiates below the left-hand inclusion and propagates upwards and coalesces with tensile crack (A). Tensile crack (H) then propagates along a portion of tensile crack (A), the boundary of the left-hand inclusion, and then into the surrounding hydrocal matrix above the left-hand inclusion.

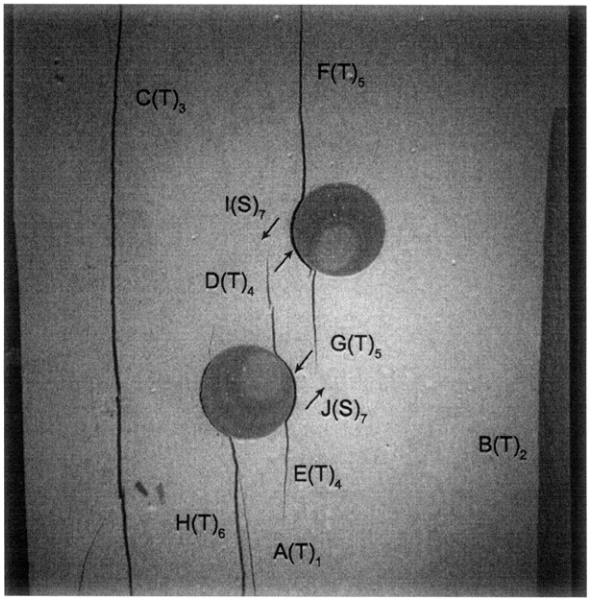

(Recorded by High Speed Video System)

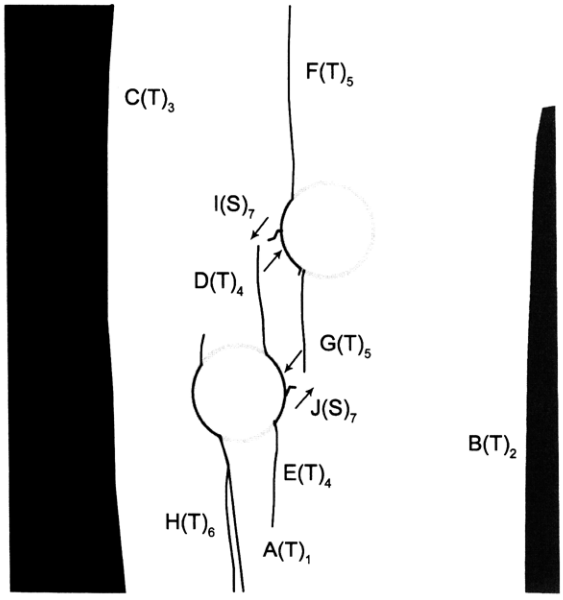

(26.84 MPa)
Time: 6 minutes & 33.113 seconds
HS Image # - 3599

Shear cracks (I&J) initiate at the boundary of the right-hand and left-hand inclusion, respectively. Shear crack (I) propagates downwards towards tensile crack (D), while shear crack (J) propagates upwards towards tensile crack (G).

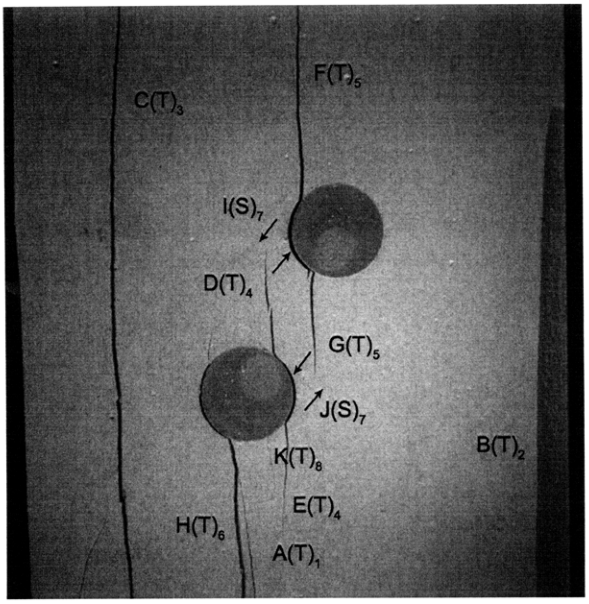

(Recorded by High Speed Video System)

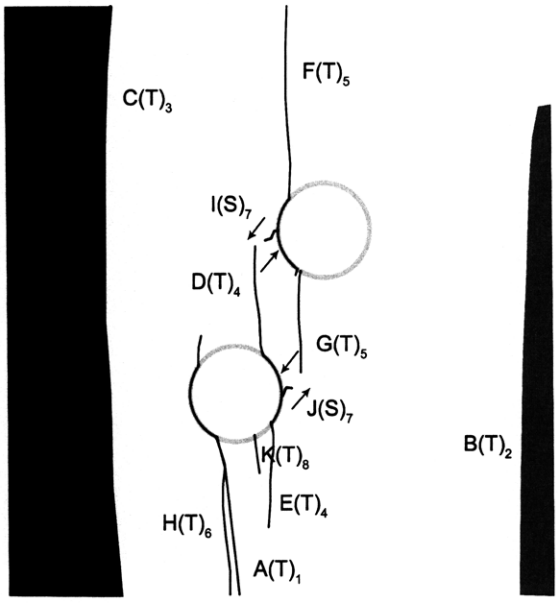

(21.29 MPa)
Time: 6 minutes & 33.165 seconds
HS Image # - 3342

Tensile crack (K) initiates at the boundary of the left-hand inclusion and propagates downwards.

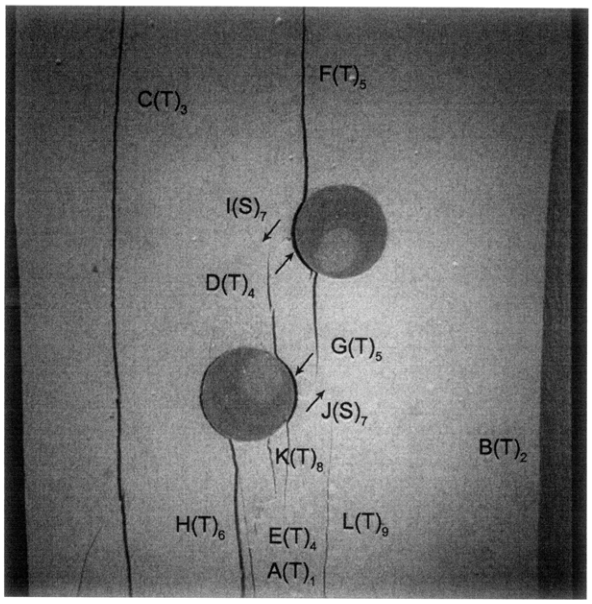

(Recorded by High Speed Video System)

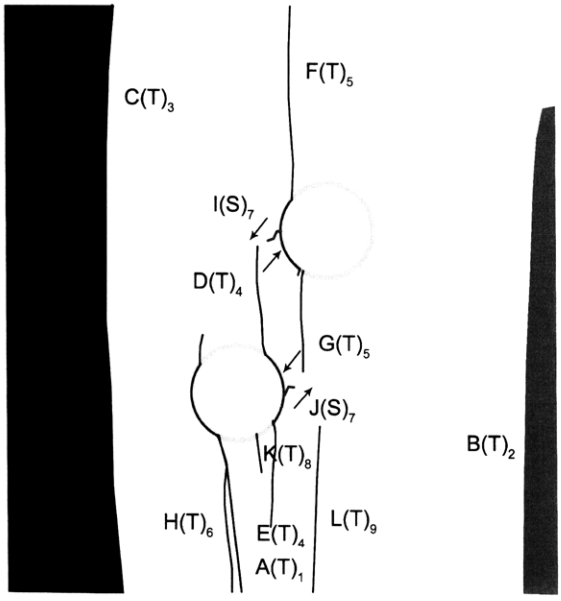

(20.32 MPa)
Time: 6 minutes & 33.174 seconds
HS Image # - 3297

Tensile crack (L) initiates at the lower specimen boundary and propagates upwards.

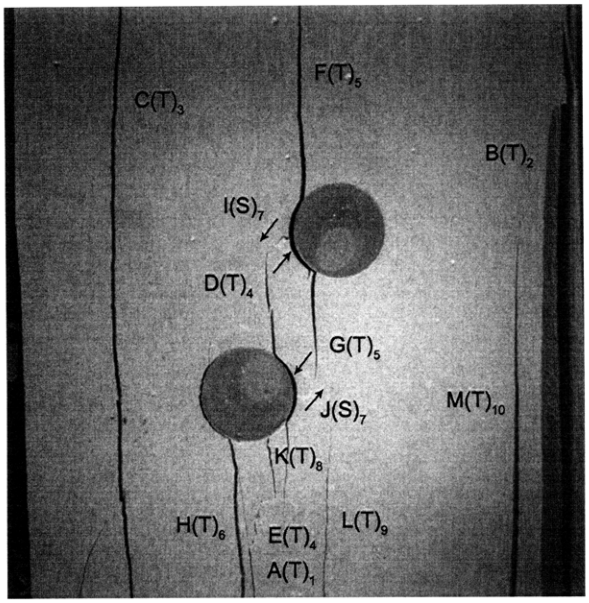

(Recorded by High Speed Video System)

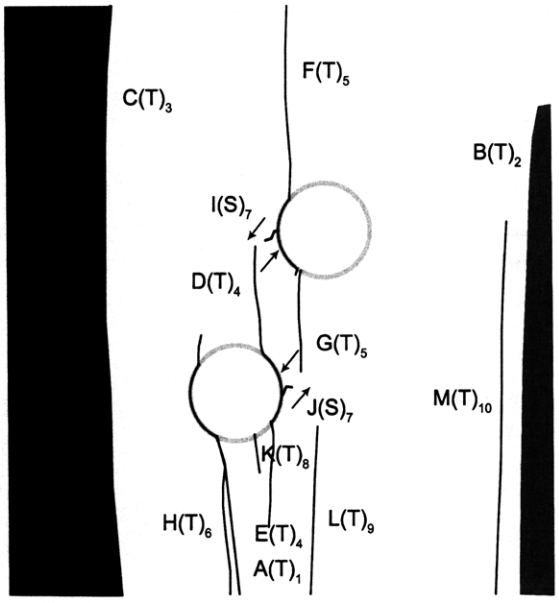

(17.28 MPa)
Time: 6 minutes & 33.202 seconds
HS Image # - 3156

Tensile crack (M) initiates at the lower specimen boundary and propagates upwards.

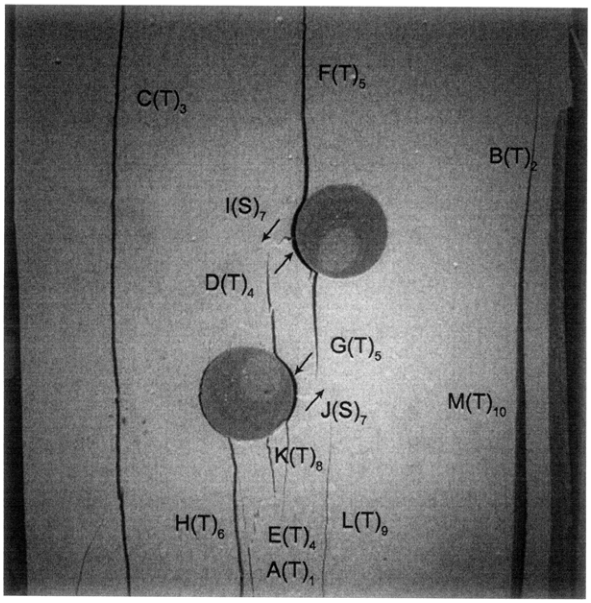

(Recorded by High Speed Video System)

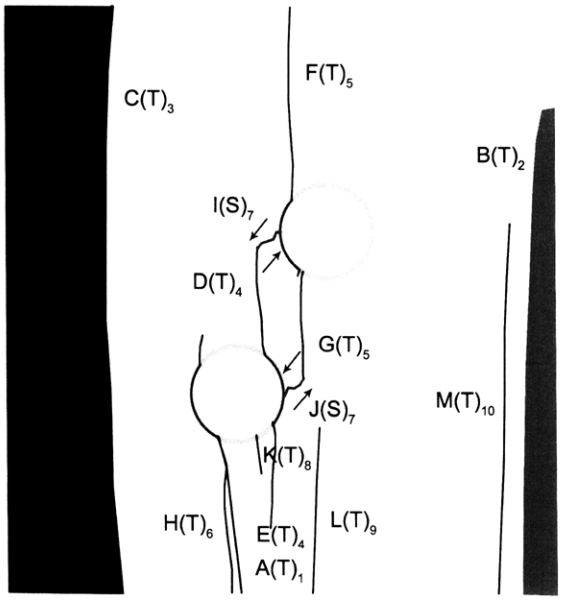

(17.23 MPa)
Time: 6 minutes & 33.202 seconds
HS Image # - 3154

Shear crack (J) continues to propagate until its coalescence with tensile crack (G). Shear crack (I) then coalesces with tensile crack (D), shortly afterwards.

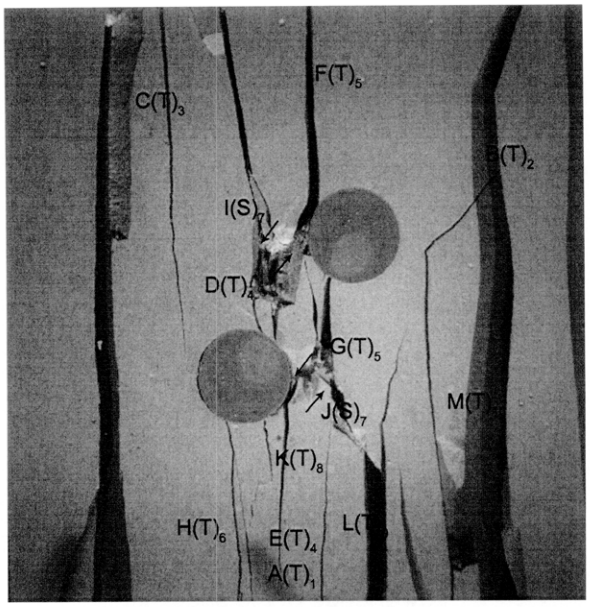

(Recorded by High Speed Video System)

(0 MPa) – Final Picture

Time: 6 minutes & 33.833 seconds

HS Image # - 1

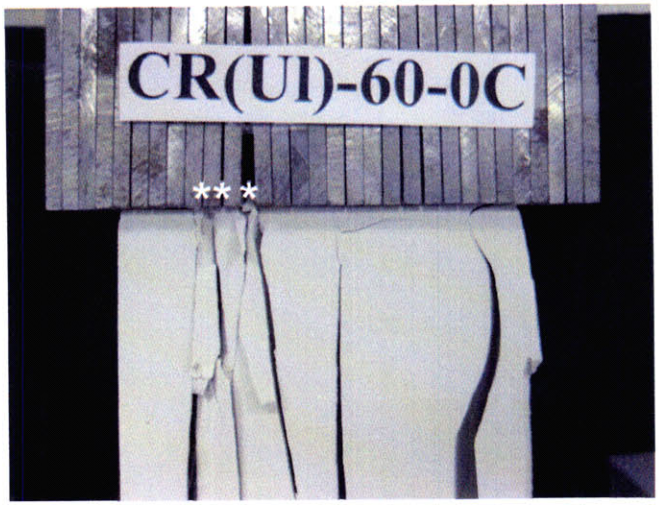	Upper edge of the specimen. The cracks marked with a (*) coincide with the openings between the teeth of the brush platen.
	Lower edge of the specimen. The cracks marked with a (*) coincide with the openings between the teeth of the brush platen.

APPENDIX E – Square, Half-inch Inclusion Pairs

This appendix contains the detailed analyses for specimens with square, half-inch inclusion pairs. These specimens contained either an Ultracal, or plaster, inclusion pair. One complete analysis for every geometric series is presented, while only summaries of the other specimens are presented. For a complete summary of results, refer to Chapter 5. A list of tested specimens is summarized below.

		$\beta = -45°$	$\beta = 30°$	$\beta = 60°$	$\beta = 75°$
Square Inclusions	Plaster	SQ(Pl)-45-0A SQ(Pl)-45-0B* SQ(Pl)-45-0C	SQ(Pl)-30-0A SQ(Pl)-30-0B SQ(Pl)-30-0C*	SQ(Pl)-60-0A SQ(Pl)-60-0B SQ(Pl)-60-0C*	SQ(Pl)-75-0A SQ(Pl)-75-0B* SQ(Pl)-75-0C
	Ultracal	SQ(Ul)-45-0A SQ(Ul)-45-0B* SQ(Ul)-45-0C	SQ(Ul)-30-0A* SQ(Ul)-30-0B SQ(Ul)-30-0C	SQ(Ul)-60-0A* SQ(Ul)-60-0B SQ(Ul)-60-0C	SQ(Ul)-75-0A* SQ(Ul)-75-0B SQ(Ul)-75-0C

* A complete analysis for this specimen is presented in the Appendix.

SUMMARY

Specimen Number: SQ(PI)-45-0A (20080829)

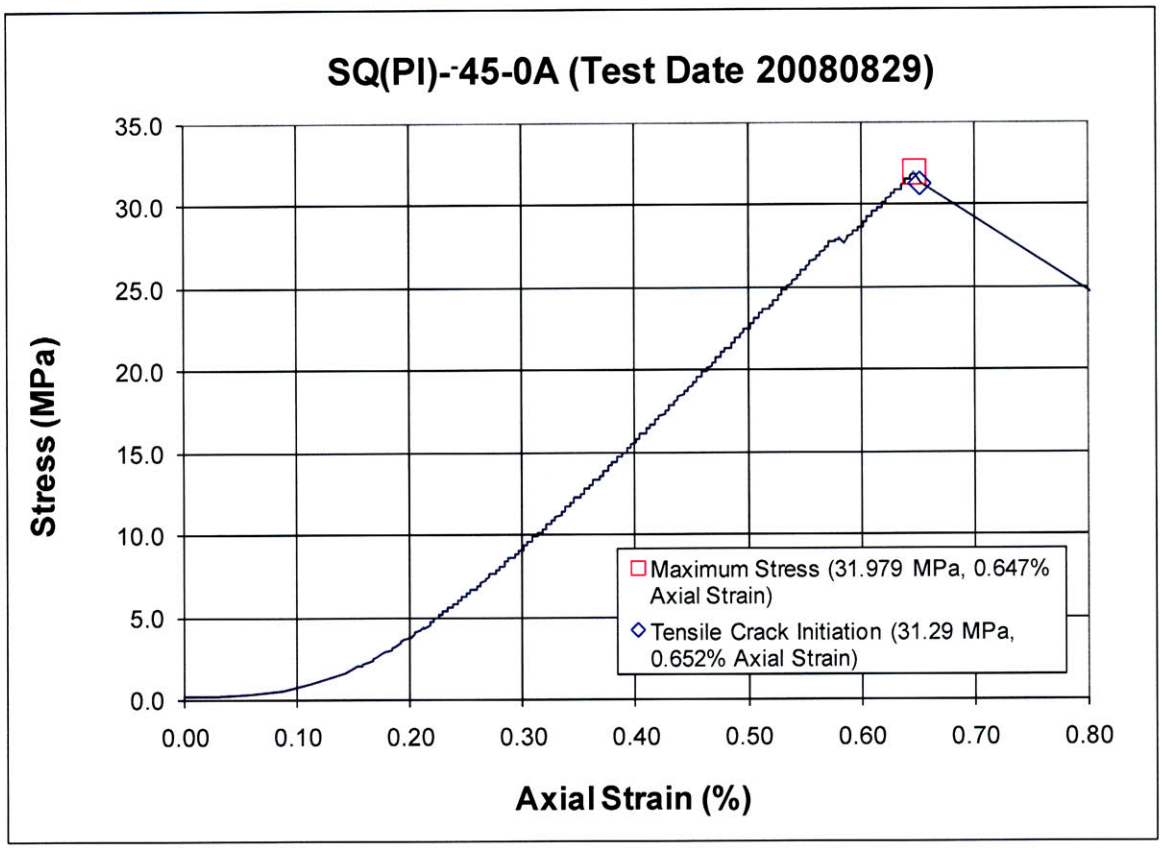

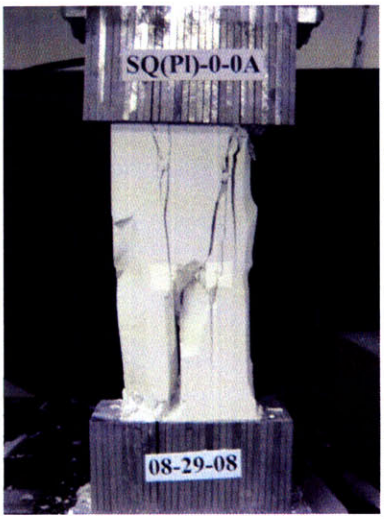

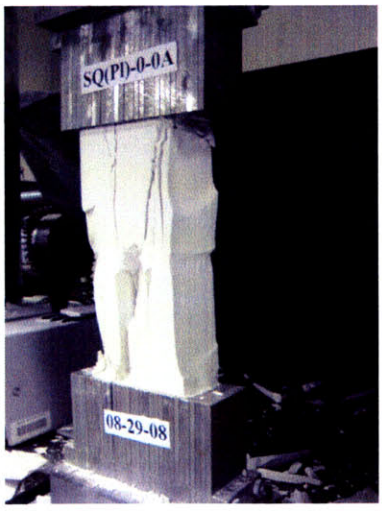

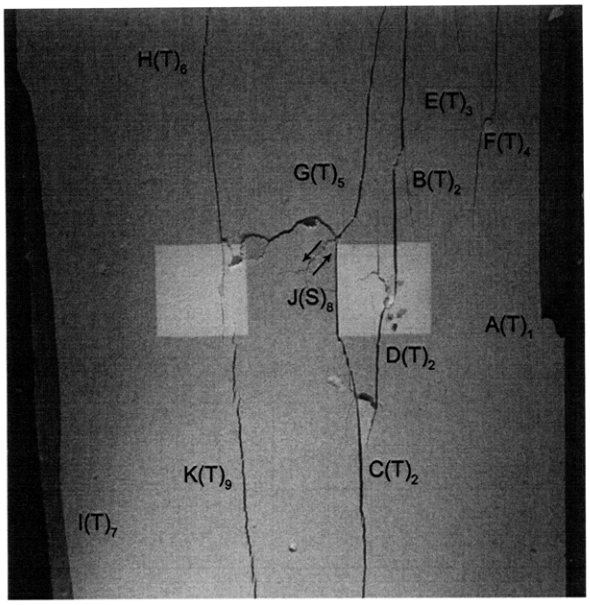

(Recorded by High Speed Video System)

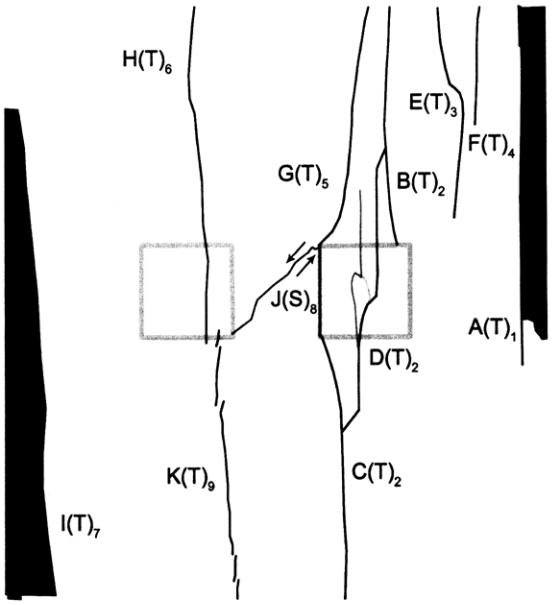

(24.91 MPa) – Ultimate Failure
Time: 6 minutes & 48.437 seconds
HS Image # - 3746

Tensile crack (C) continues to propagate along the inclusion boundary until its coalescence with tensile crack (G).

Shear crack (J) then continues to propagate until its intersection with the lower boundary of the left-hand inclusion, which results in the coalescence of the two inclusions. En echelon tensile crack (K) initiates at the lower specimen boundary and propagates upwards simultaneously with the coalescence of the inclusions.

Specimen Number: SQ(PI)-45-0B (20080829)

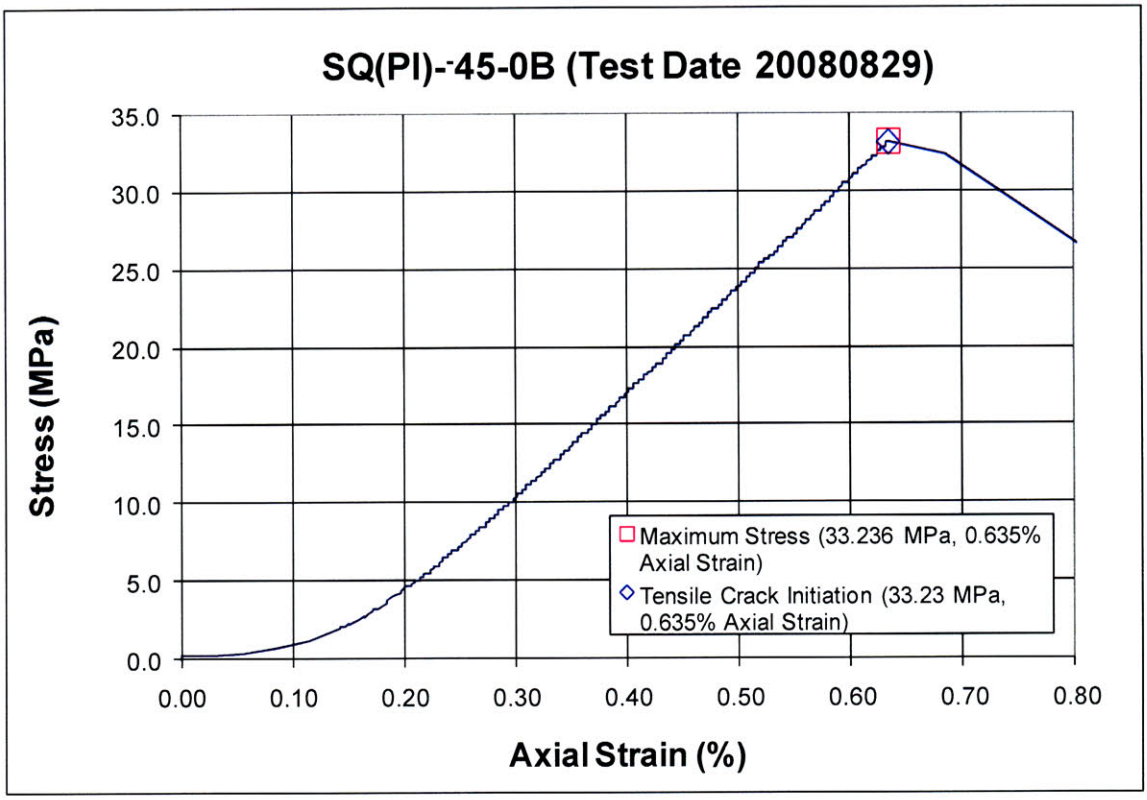

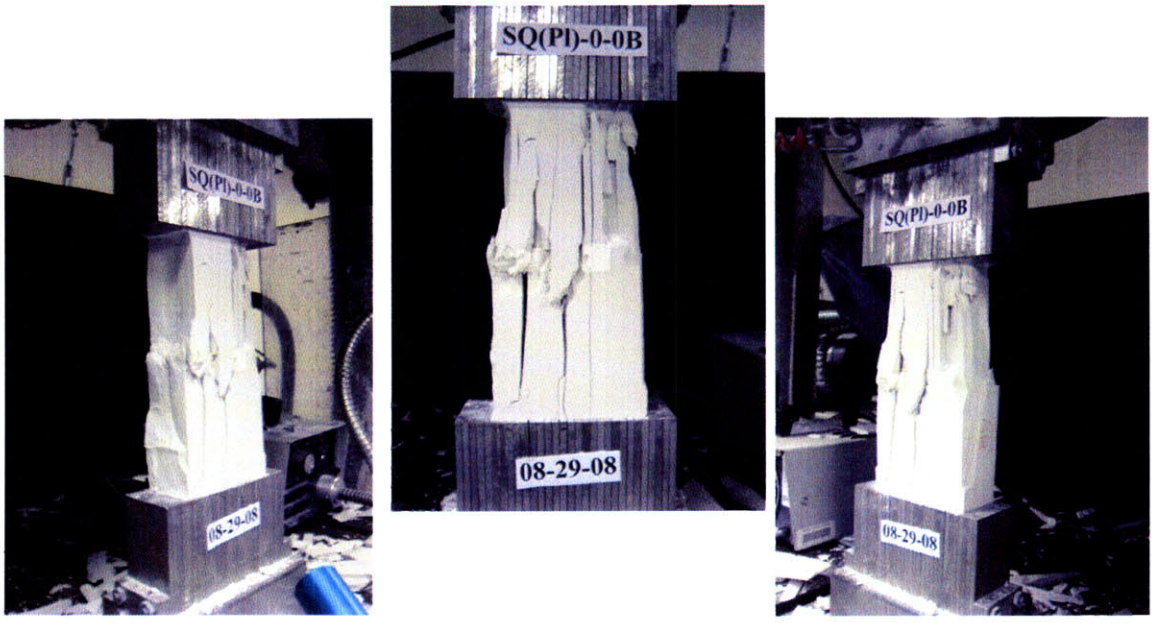

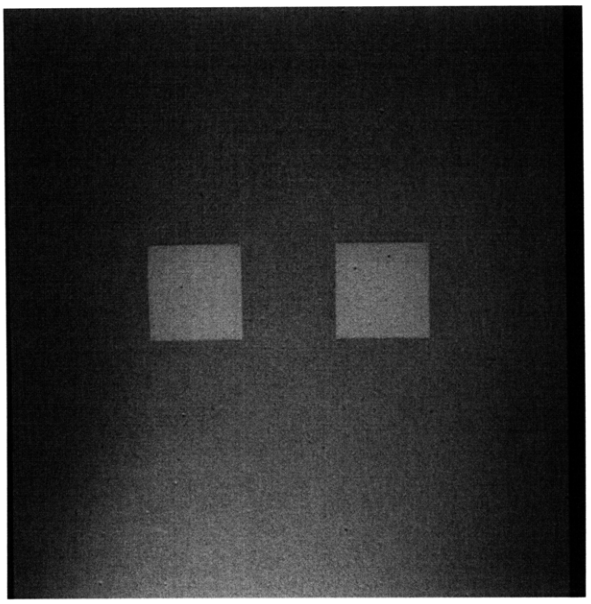

(Recorded by High Speed Video System)

Initial Inclusion Geometries:
SQUARES – Plaster Material

Inclusion **less** stiff than matrix.

High Speed Camera Frame Rate:
5000 pps

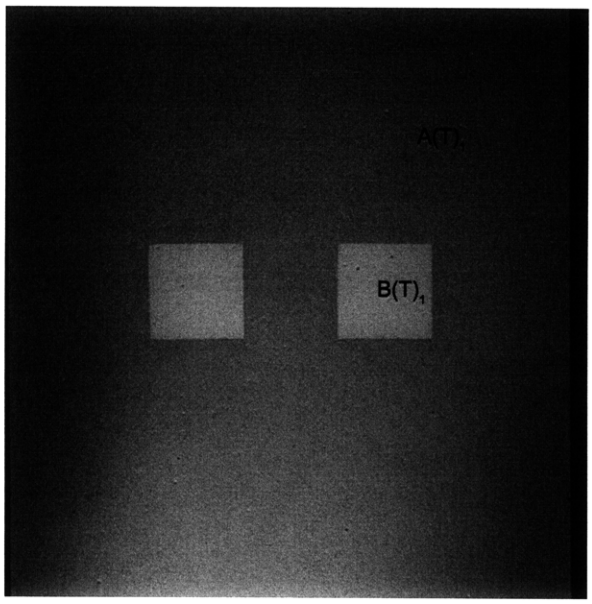

(Recorded by High Speed Video System)

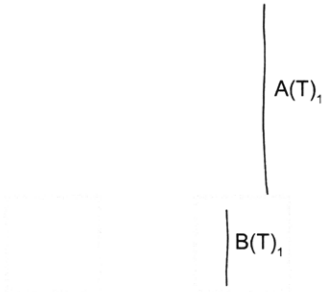

(33.235 MPa) [Max. Stress]

- Tensile Crack Initiation

Time: 7 minutes & 9.154 seconds

HS Image # - 3515

Tensile crack (A) initiates at the upper boundary of the right-hand inclusion and propagates upwards.

Tensile crack (B) initiates "simultaneously" within the right-hand inclusion.

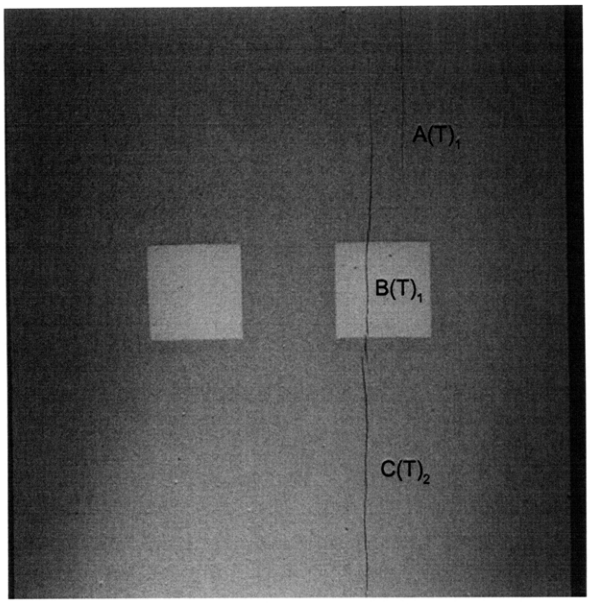

(Recorded by High Speed Video System)

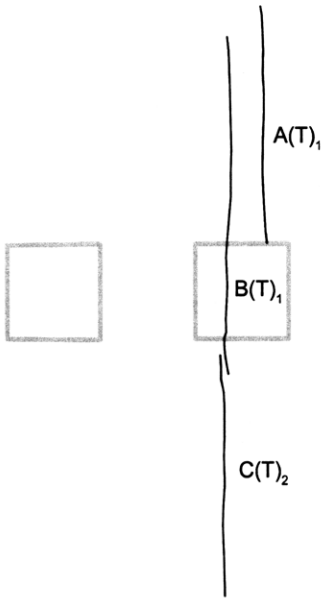

(33.23 MPa)
Time: 7 minutes & 9.154 seconds
HS Image # - 3514

As tensile cracks (A&B) propagate, tensile crack (C) initiates below the right-hand inclusion.

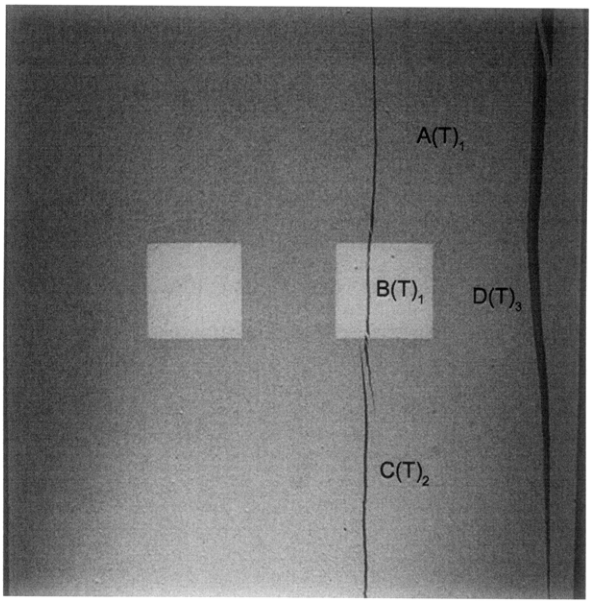

(Recorded by High Speed Video System)

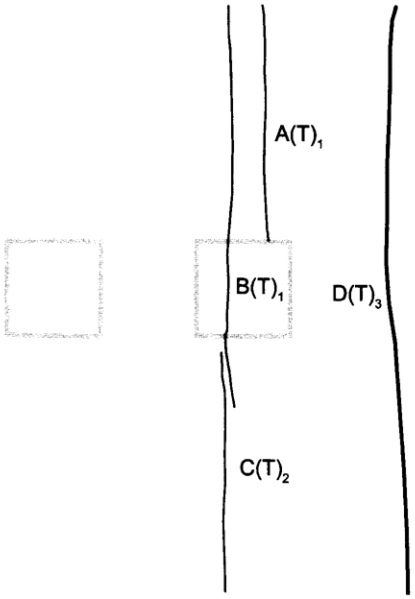

(33.23 MPa)
Time: 7 minutes & 9.155 seconds
HS Image # - 3510

Tensile crack (D) initiates at the upper specimen boundary and propagates downwards, which results in the detachment of a specimen piece from the right-hand specimen boundary.

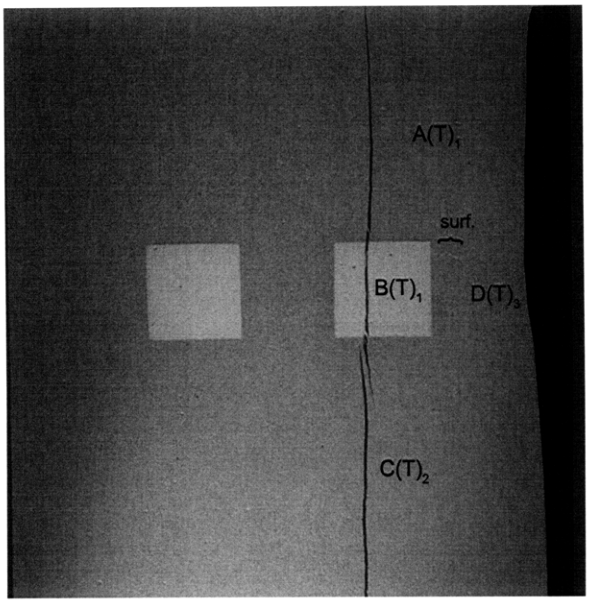

(Recorded by High Speed Video System)

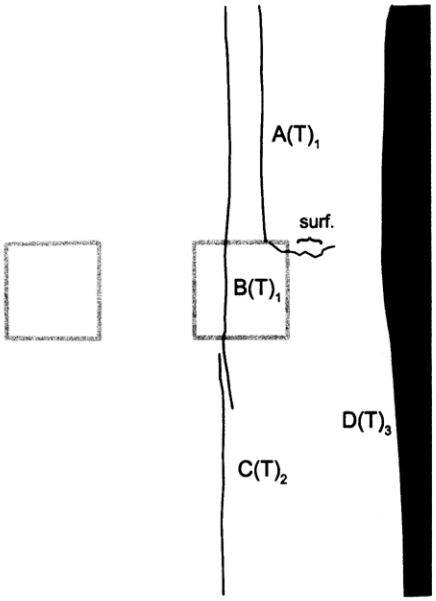

(32.96 MPa)
Time: 7 minutes & 9.236 seconds
HS Image # - 3107

Surface crack (surf.) initiates at the upper corner of the right-hand inclusion and propagates towards the specimen boundary.

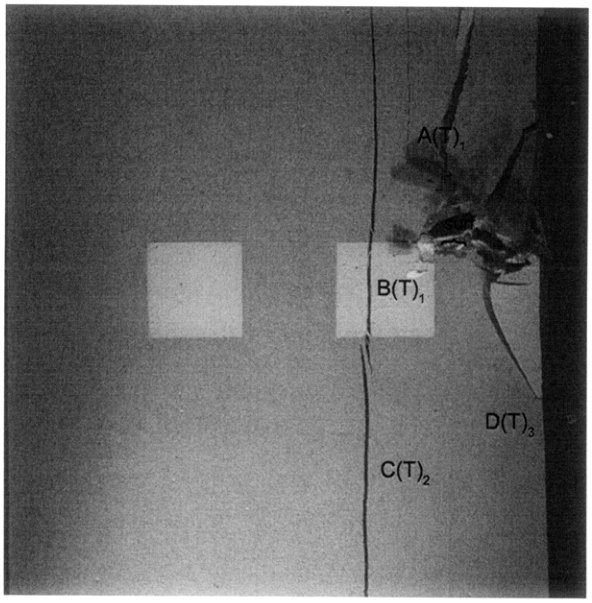

(Recorded by High Speed Video System)

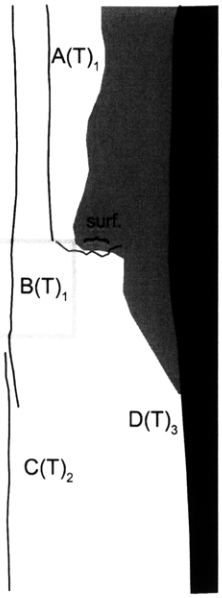

(32.80 MPa)
Time: 7 minutes & 9.281 seconds
HS Image # - 2881

The propagation of surface crack (surf.) results in the detachment of a surficial piece of specimen.

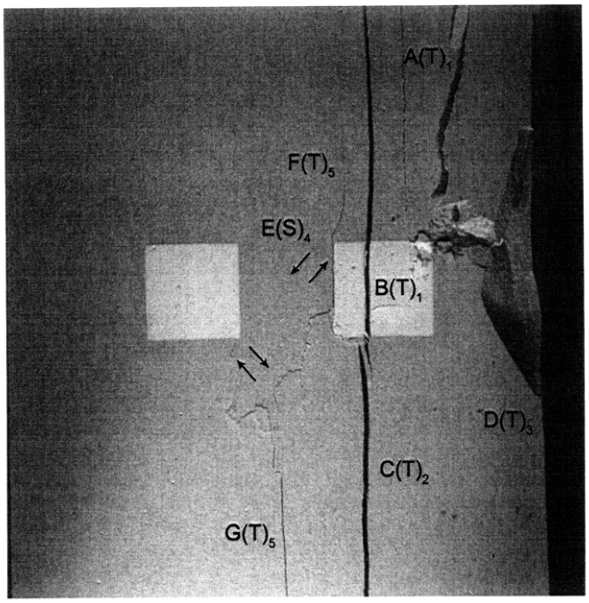

(Recorded by High Speed Video System)

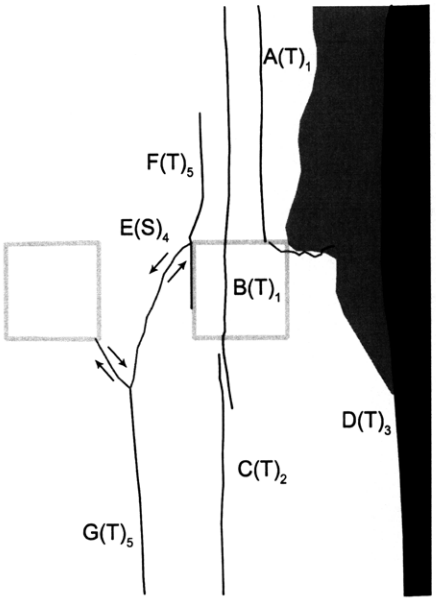

(26.34 MPa) – Ultimate Failure
Time: 7 minutes & 9.459 seconds
HS Image # - 1990

Shear crack (E) initiates at the upper left-hand corner of the right-hand inclusion and propagates downwards.

Tensile cracks (F&G) initiate "simultaneously" after the initiation of shear crack (E). Tensile crack (G) coalesces with shear crack (E), which causes shear crack (E) to change direction and propagate upwards towards the left-hand inclusion.

Tensile crack (F) initiates at the boundary of the right-hand inclusion; however, the exact location was not able to be determined.

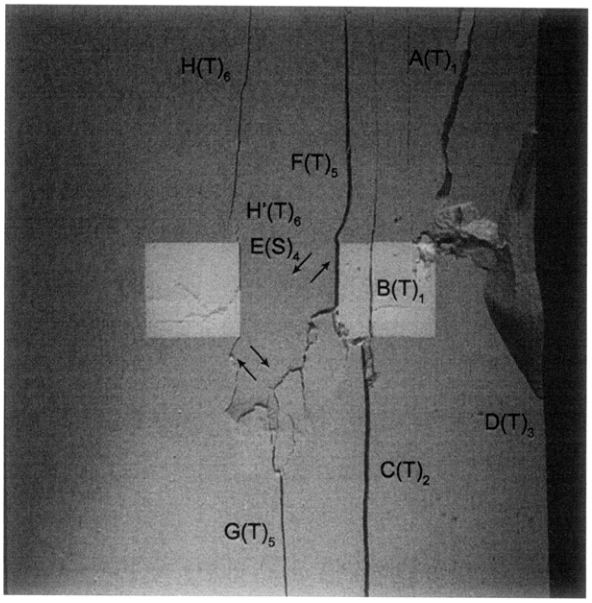

(Recorded by High Speed Video System)

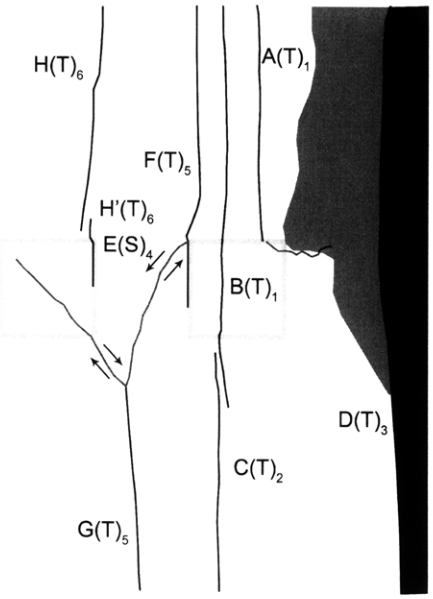

(26.32 MPa)
Time: 7 minutes & 9.459 seconds
HS Image # - 1989

Shear crack (E) propagates through the left-hand inclusion.

Tensile cracks (H&H') initiate "simultaneously". Tensile crack (H) initiates above the left-hand inclusion, while tensile crack (H') initiates at the inclusion boundary.

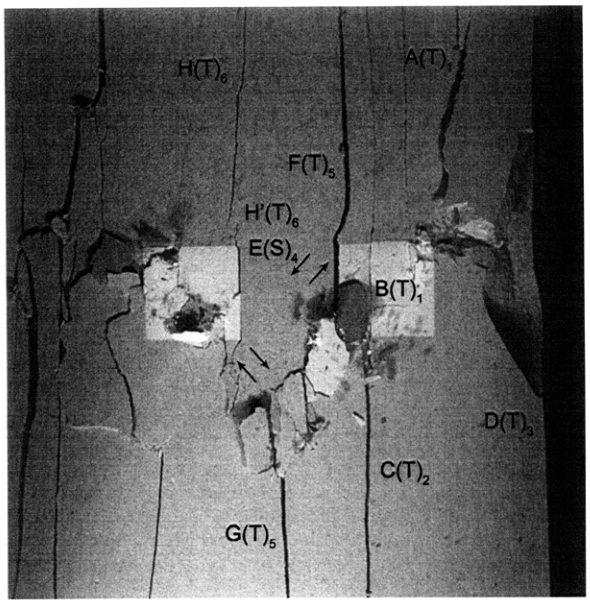

(Recorded by High Speed Video System)

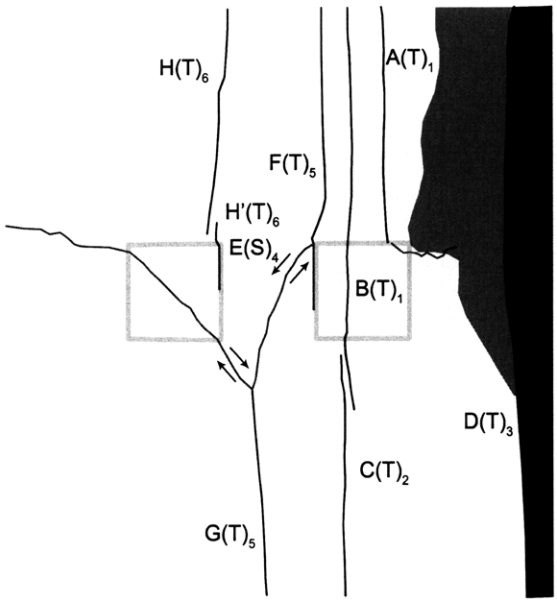

(26.02 MPa)
Time: 7 minutes & 9.462 seconds
HS Image # - 1974

Shear crack (E) continues to propagate until its intersection with the left-hand specimen boundary.

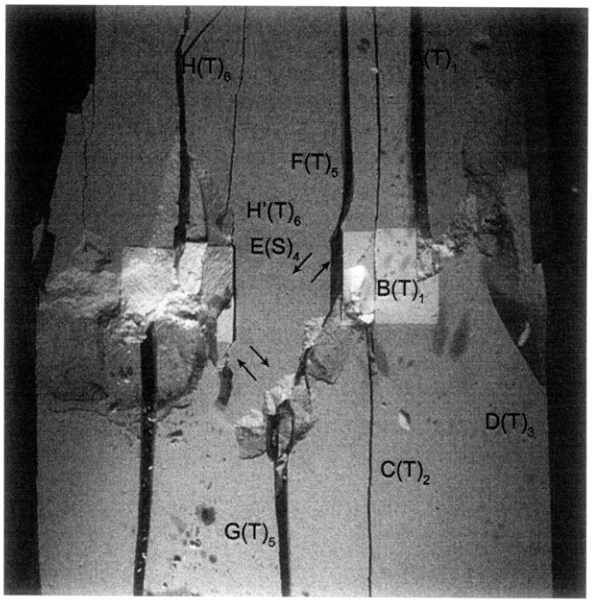

(Recorded by High Speed Video System)

(0 MPa) – Final Picture

Time: 7 minutes & 9.857 seconds

HS Image # - 1

	Upper edge of the specimen. The cracks marked with a (*) coincide with the openings between the teeth of the brush platen.
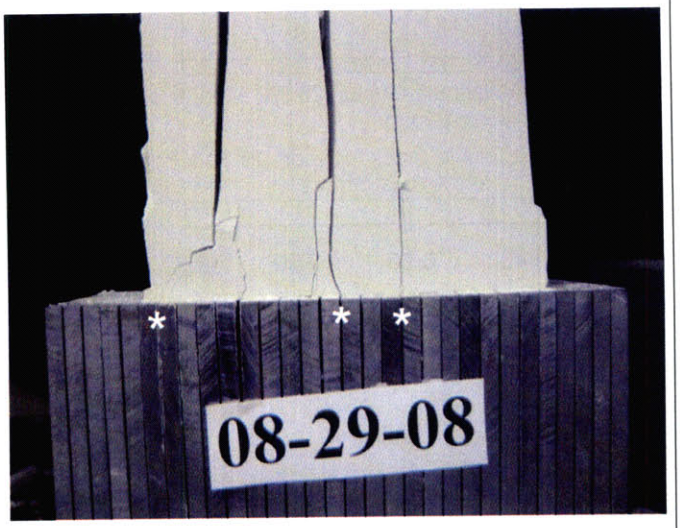	Lower edge of the specimen. The cracks marked with a (*) coincide with the openings between the teeth of the brush platen.

SUMMARY

Specimen Number: SQ(PI)-45-0C (20080829)

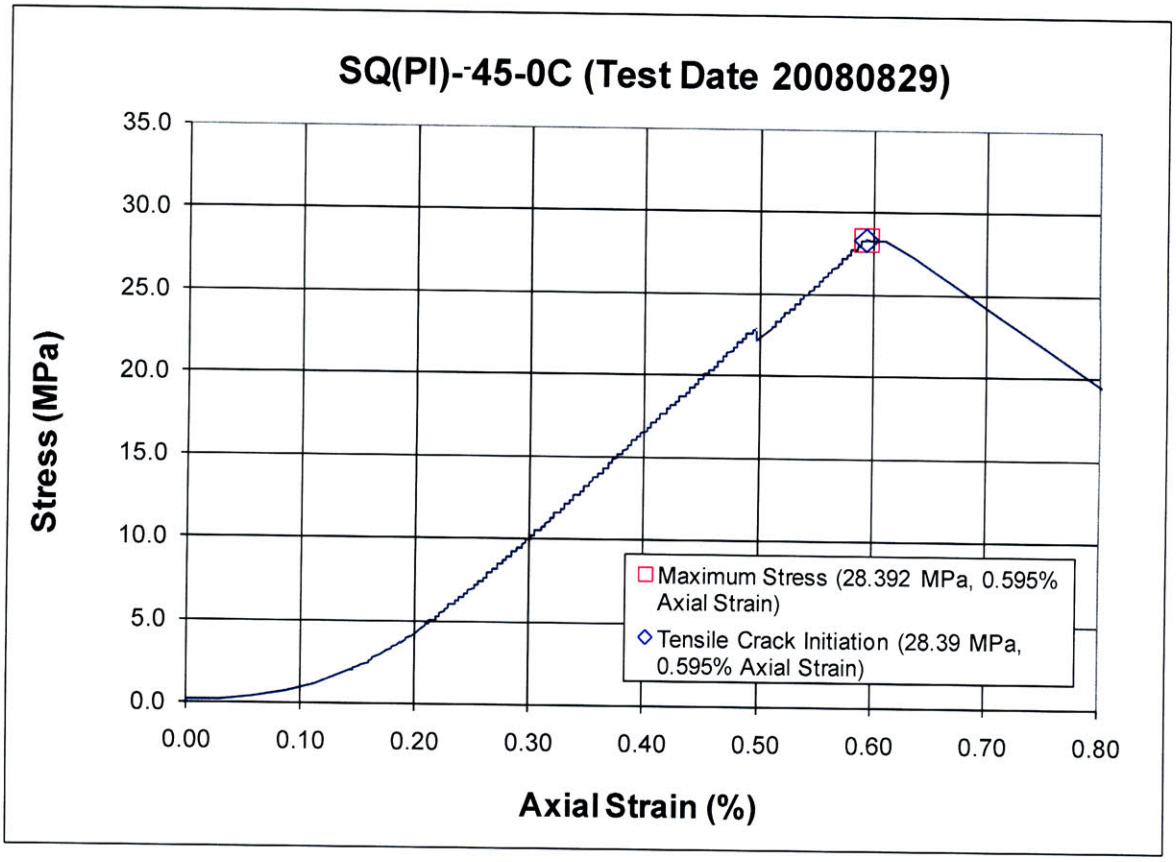

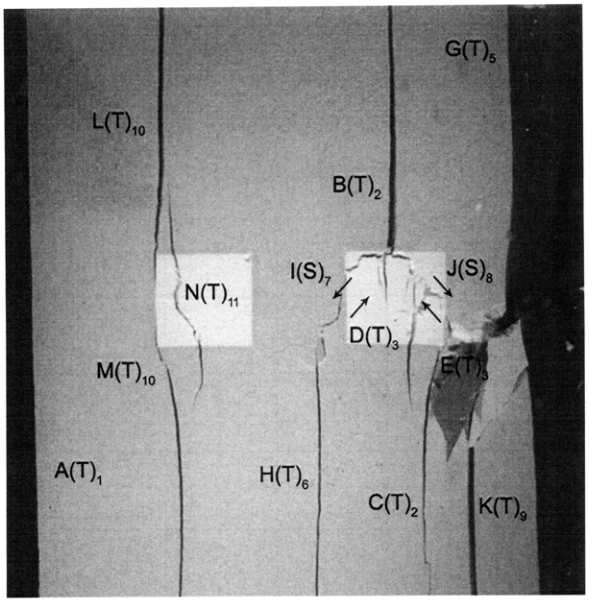

(Recorded by High Speed Video System)

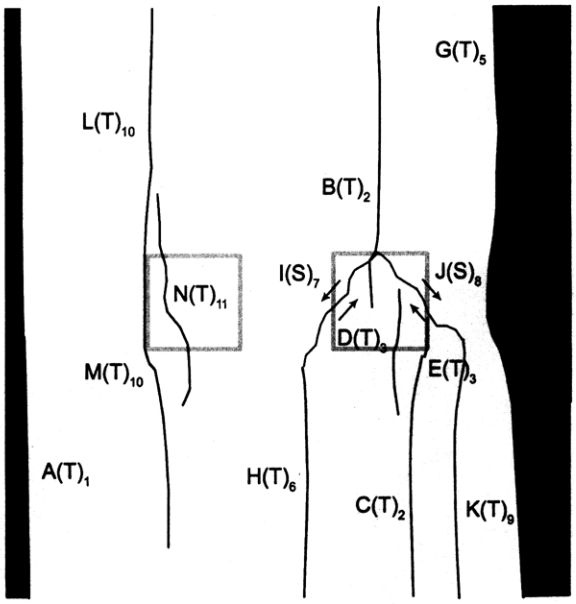

(28.15 MPa)
Time: 5 minutes & 59.644 seconds
HS Image # - 2486

Tensile cracks (L&M) simultaneously propagate around the boundary of the left-hand inclusion and coalesce. Tensile crack (N) then initiates at the left-hand inclusion.

SUMMARY

Specimen Number: SQ(UI)-45-0A (20080828)

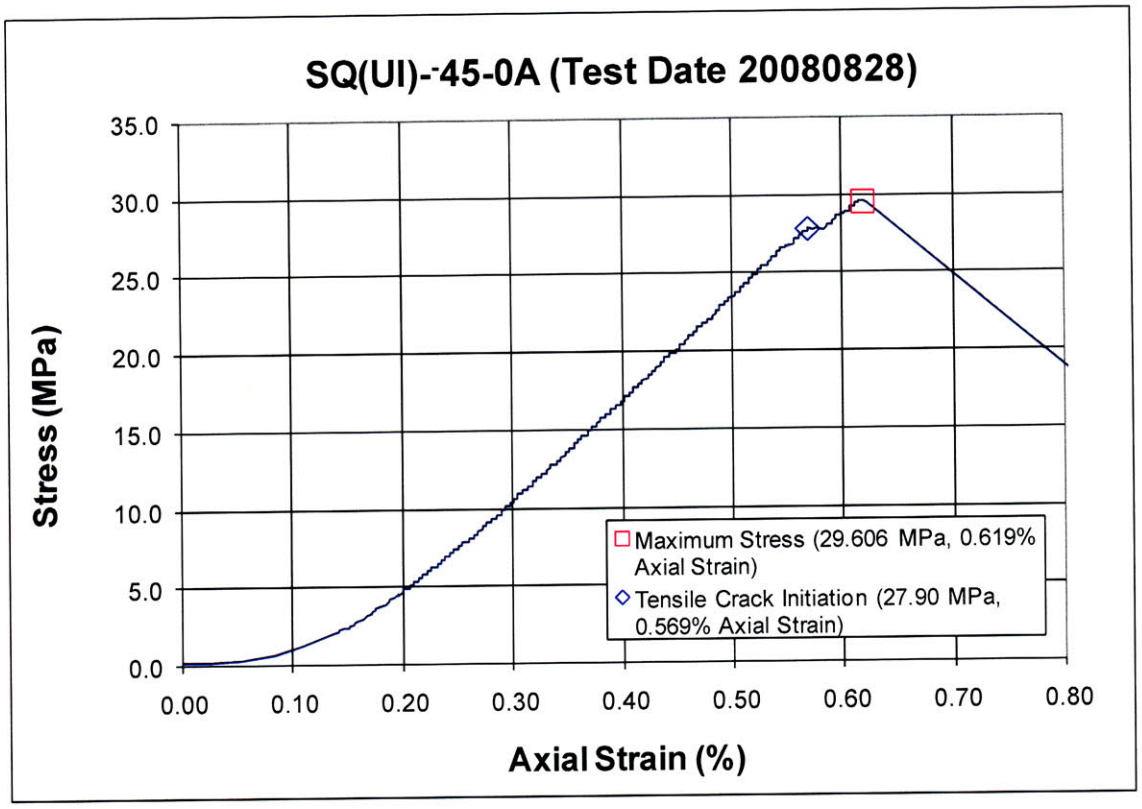

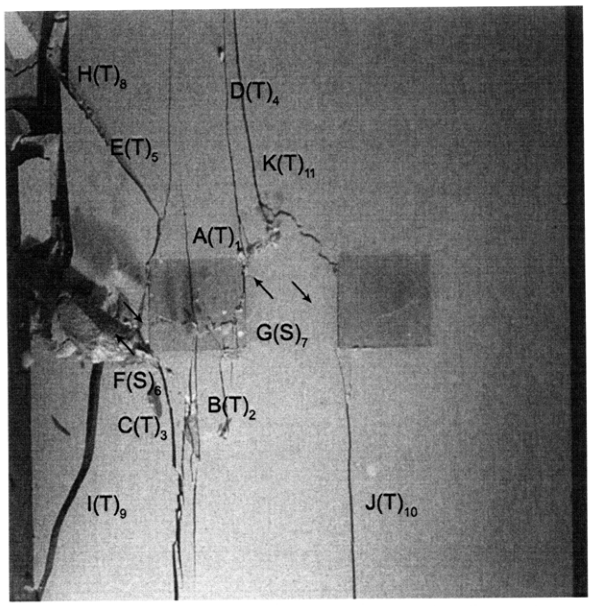

(Recorded by High Speed Video System)

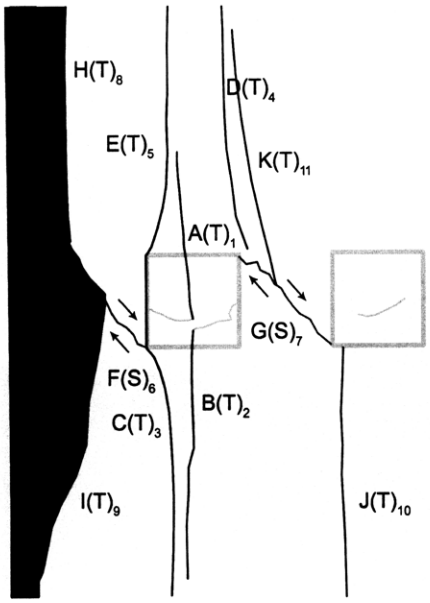

(28.88 MPa)
Time: 6 minutes & 13.198 seconds
HS Image # - 2617

Shear crack (G) propagates until its coalescence with the right-hand inclusion boundary.

Specimen Number: SQ(UI)-45-0B (20080828)

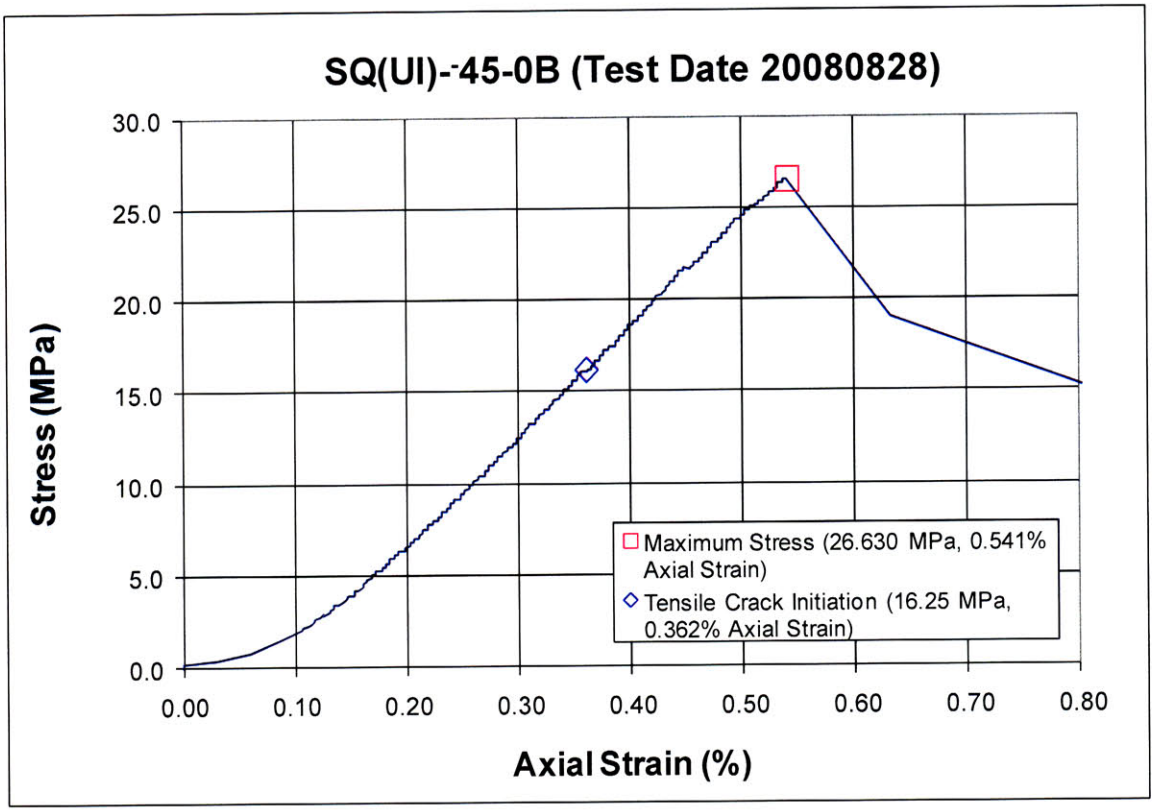

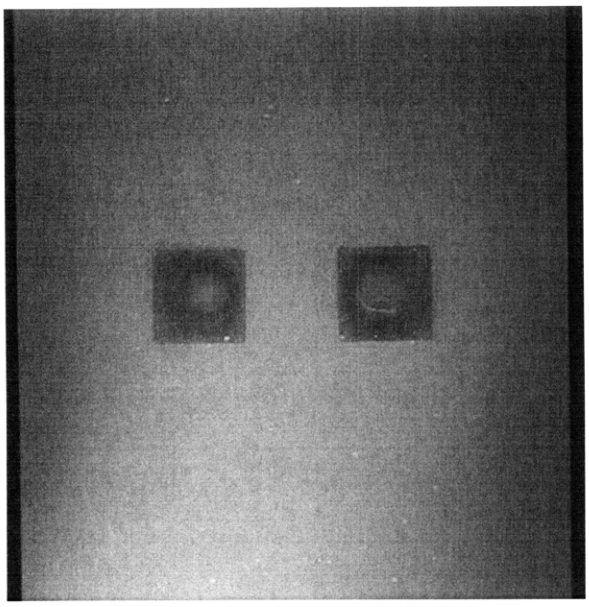

(Recorded by High Speed Video System)

Initial Inclusion Geometries:
SQUARES – Ultracal Material

Inclusion **more** stiff than matrix.

High Speed Camera Frame Rate:
5000 pps

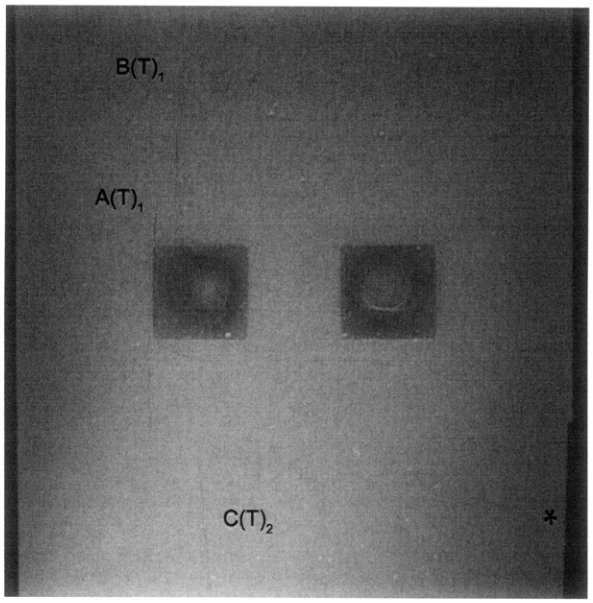

(Recorded by High Speed Video System)

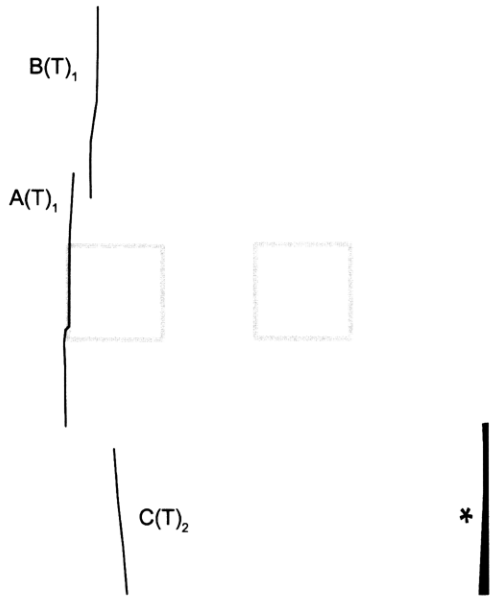

(16.25 MPa)

- Tensile Crack Initiation

Time: 3 minutes & 1.326 seconds

Tensile crack (A) initiates at the upper boundary of the left-hand inclusion and propagates upwards. Tensile crack (B) initiates above the left-hand inclusion and propagates upwards as well.

Tensile crack (A) then begins to propagate along the boundary of the left-hand inclusion and into the matrix. Tensile crack (C) initiates below the left-hand inclusion boundary and propagates downwards.

A small piece of specimen then detaches (*) from the lower right-hand specimen boundary.

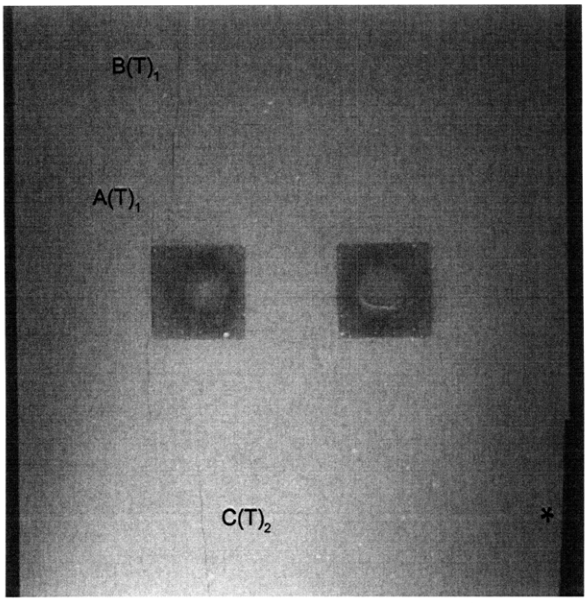

(Recorded by High Speed Video System)

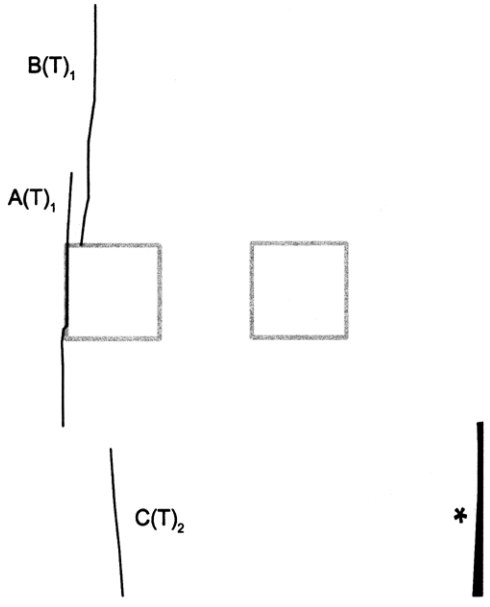

(17.61 MPa)
Time: 3 minutes & 21.08 seconds

Tensile crack (B) propagates downwards until its coalescence with the upper boundary of the left-hand inclusion.

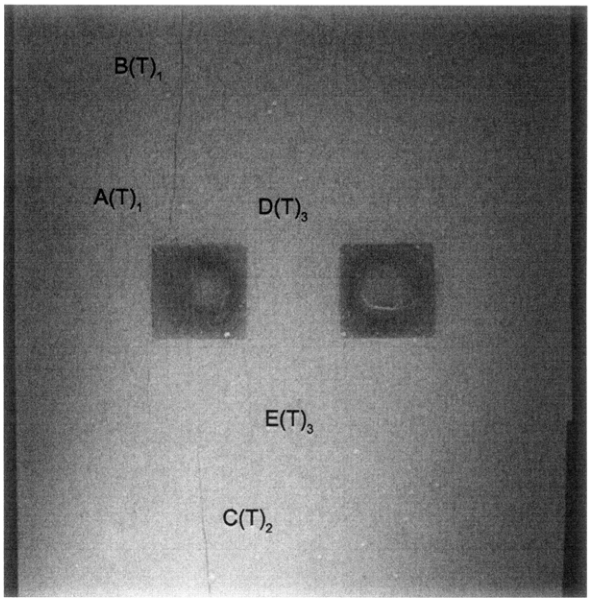

(Recorded by High Speed Video System)

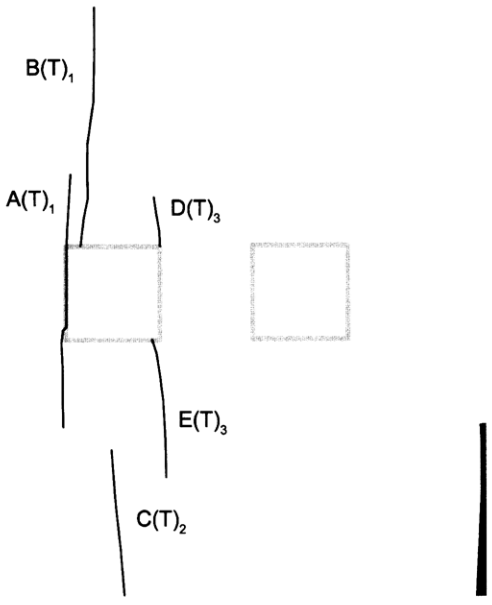

(21.04 MPa)
Time: 4 minutes & 9.83 seconds

Tensile cracks (D&E) initiate at the boundary of the left-hand inclusion and propagate upwards and downwards, respectively.

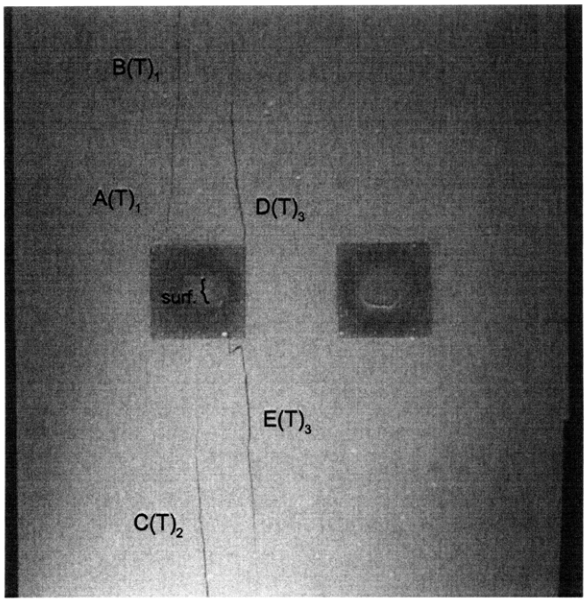

(Recorded by High Speed Video System)

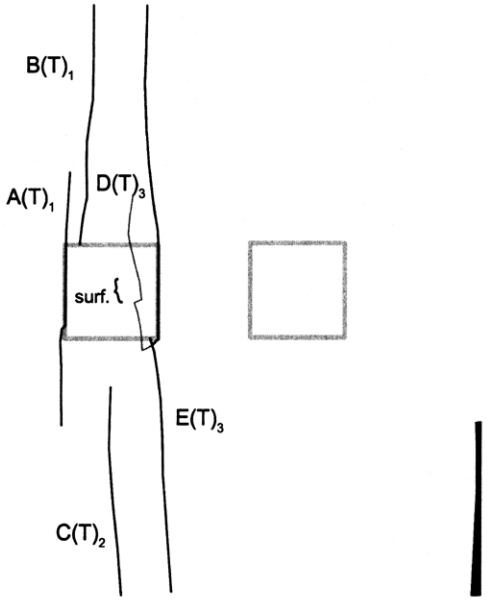

(25.22 MPa)
Time: 5 minutes & 9.58 seconds

Surface crack (surf.) initiates within the left-hand inclusion and propagates away from the inclusion.

Tensile crack (D) then begins to propagate along the boundary of the left-hand inclusion until its coalescence with tensile crack (E).

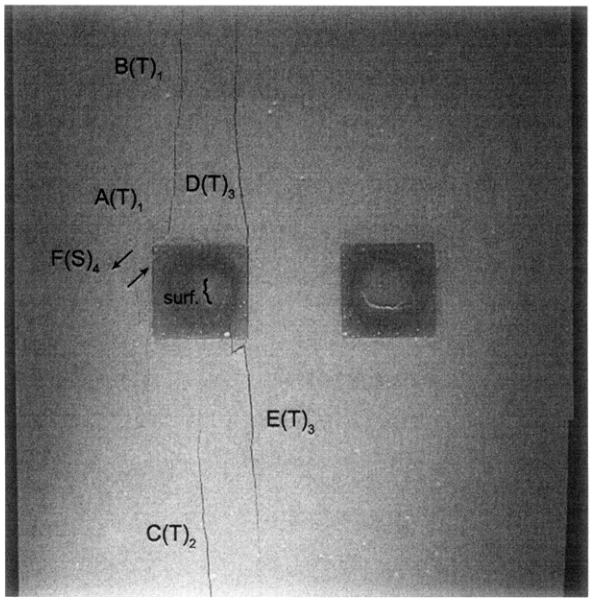

(Recorded by High Speed Video System)

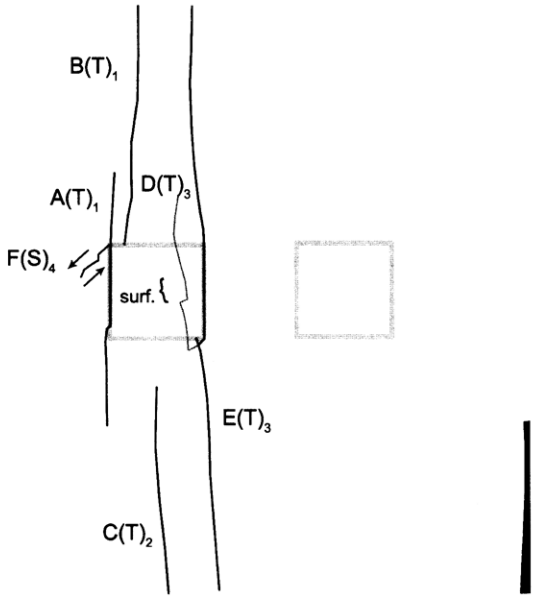

(26.630 MPa) [Max. Stress]
Time: 5 minutes & 29.076 seconds
HS Image # - 4500

Shear crack (F) initiates at the upper boundary of the left-hand inclusion and propagates downwards towards the specimen boundary.

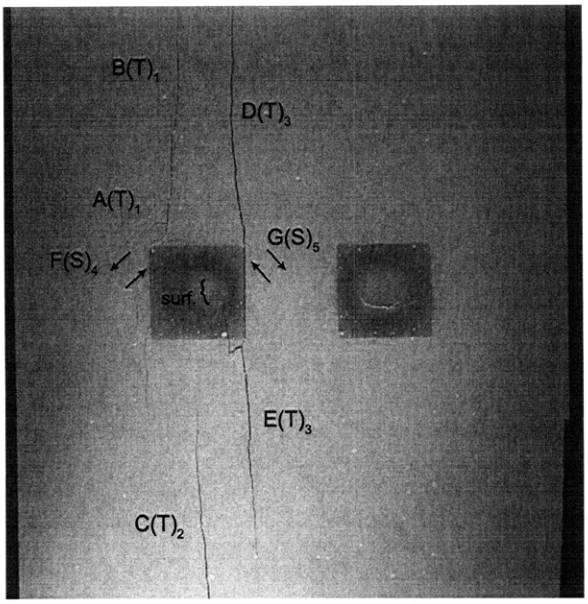

(Recorded by High Speed Video System)

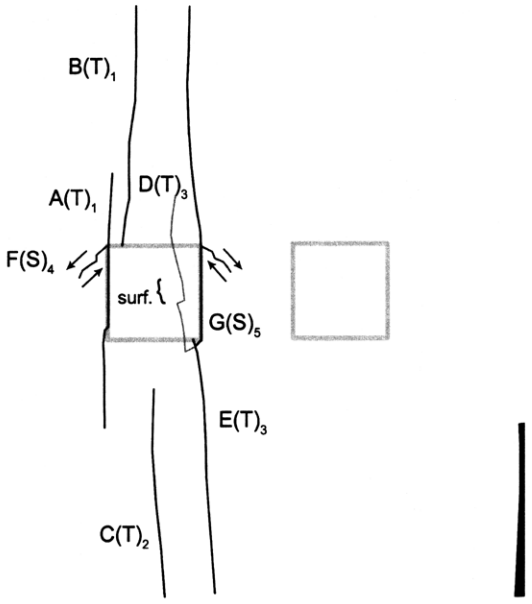

(17.78 MPa)
Time: 5 minutes & 29.351 seconds
HS Image # - 3126

Shear crack (G) initiates at the upper boundary of the left-hand inclusion and propagates downwards towards the right-hand inclusion.

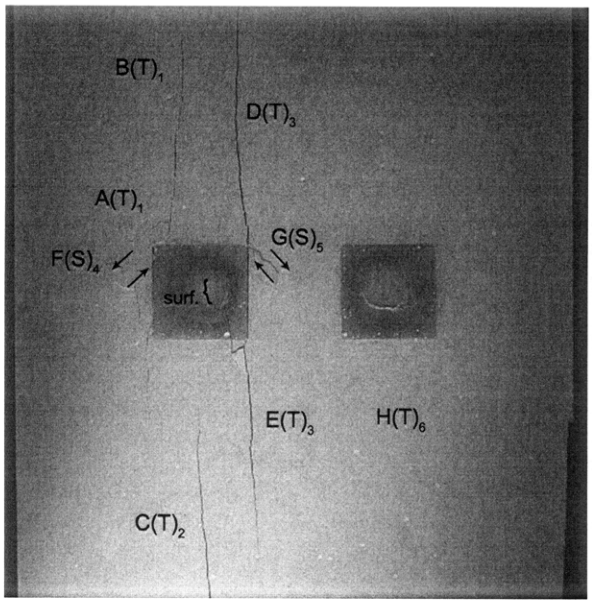

(Recorded by High Speed Video System)

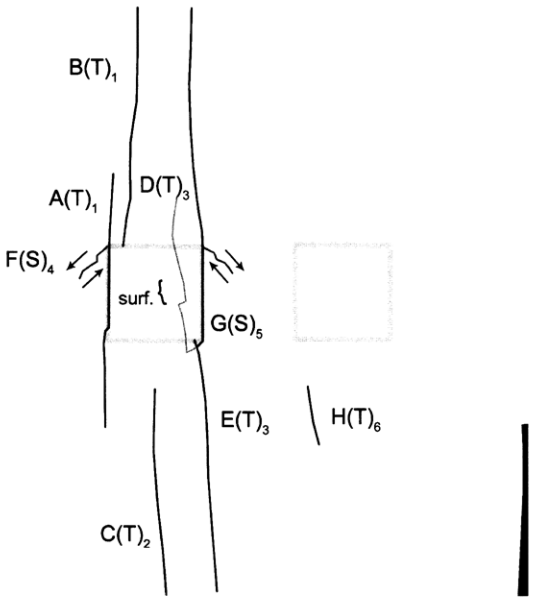

(16.43 MPa)
Time: 5 minutes & 29.374 seconds
HS Image # - 3010

Tensile crack (H) initiates below the right-hand inclusion and propagates downwards.

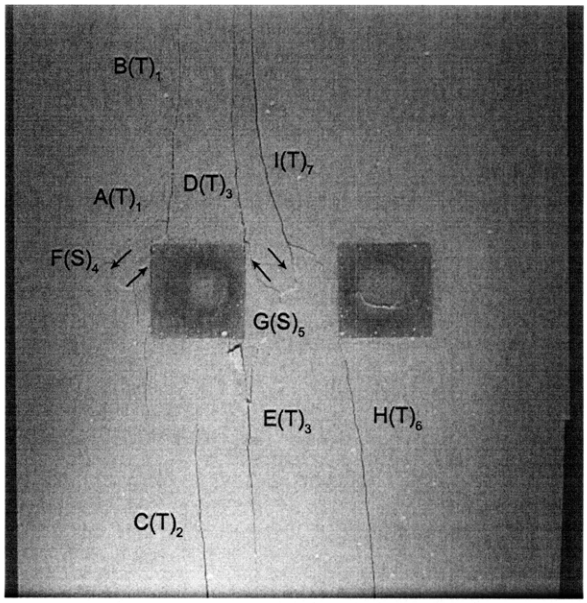

(Recorded by High Speed Video System)

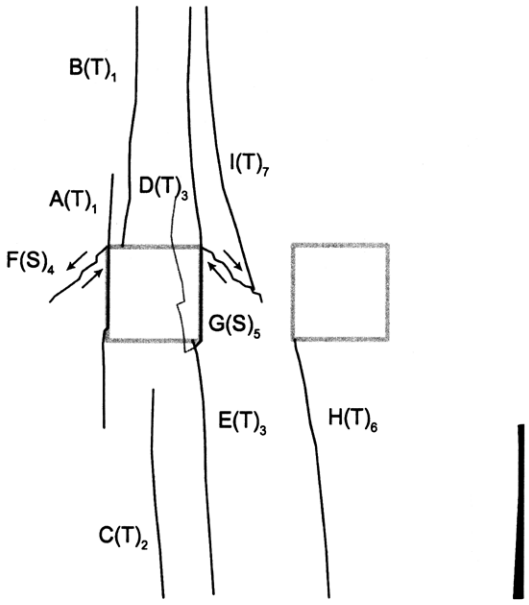

(16.09 MPa)
Time: 5 minutes & 29.380 seconds
HS Image # - 2981

Tensile crack (H) propagates until its coalescence with the boundary of the right-hand inclusion.

Tensile crack (I) then initiates at shear crack (G) and propagates towards the upper specimen boundary.

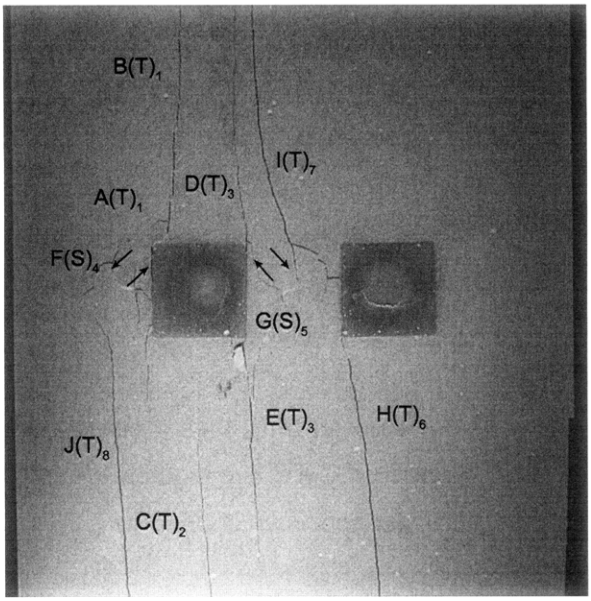

(Recorded by High Speed Video System)

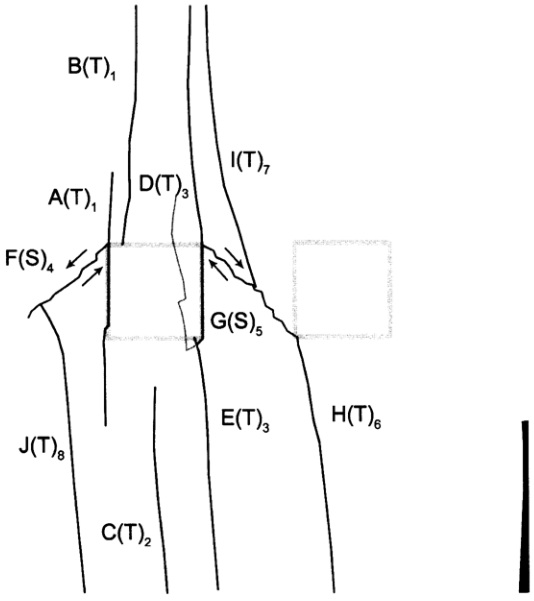

(14.26 MPa)
Time: 5 minutes & 29.411 seconds
HS Image # - 2823

Tensile crack (J) initiates at the lower specimen boundary and propagates upwards until its coalescence with shear crack (F).

Shear crack (G) then coalesces with the boundary of the right-hand inclusion.

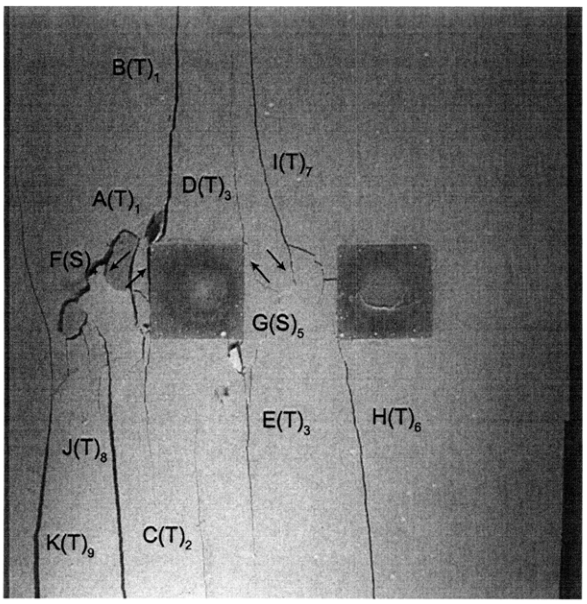

(Recorded by High Speed Video System)

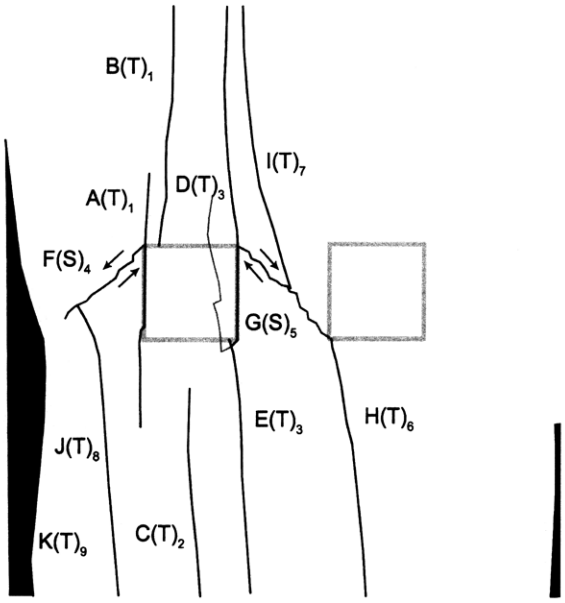

(14.17 MPa) – Ultimate Failure
Time: 5 minutes & 29.413 seconds
HS Image # - 2815

Tensile crack (K) initiates at the lower specimen boundary and propagates until its coalescence with the left-hand specimen boundary, which results in the detachment of a specimen piece.

Note the curved shaped of tensile crack (K) as it propagates adjacent to shear crack (F).

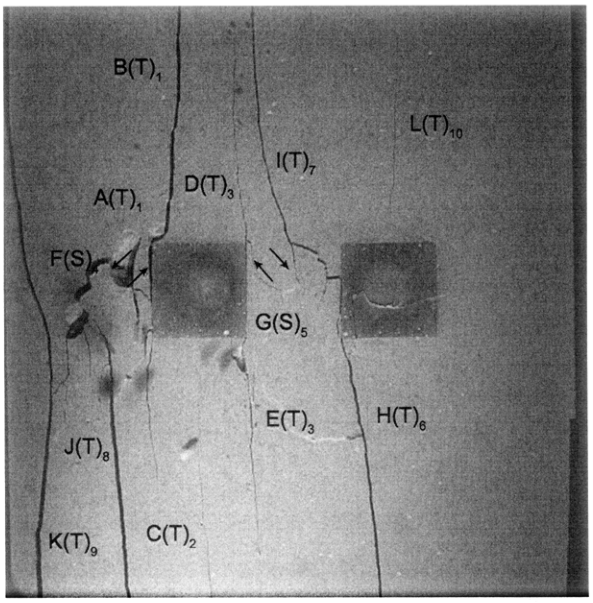

(Recorded by High Speed Video System)

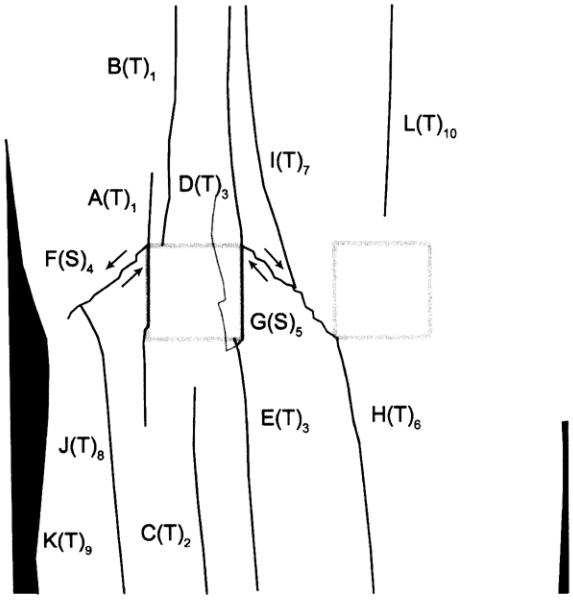

(10.70 MPa)
Time: 5 minutes & 29.473 seconds
HS Image # - 2516

Tensile crack (L) initiates above the right-hand inclusion and propagates upwards.

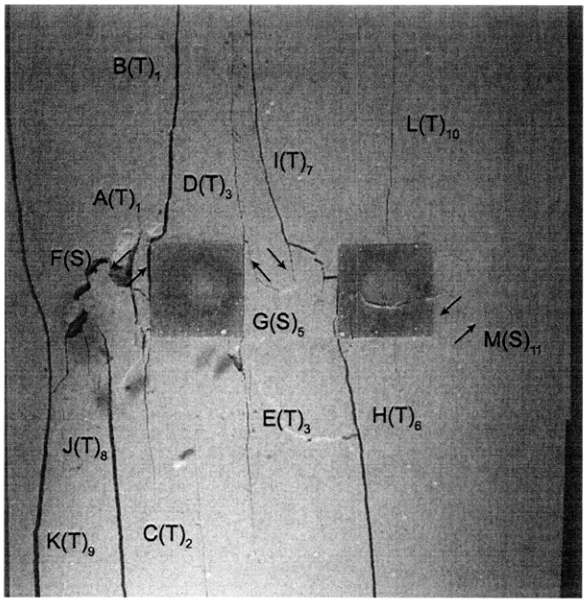

(Recorded by High Speed Video System)

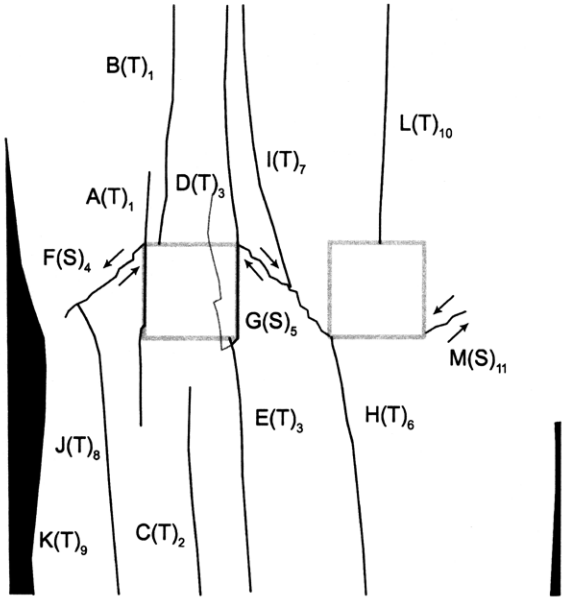

(10.54 MPa)
Time: 5 minutes & 29.476 seconds
HS Image # - 2502

Tensile crack (L) propagates until its coalescence with the boundary of the right-hand inclusion.

Shear crack (M) initiates at the boundary of the right-hand inclusion and propagates upwards towards the specimen boundary.

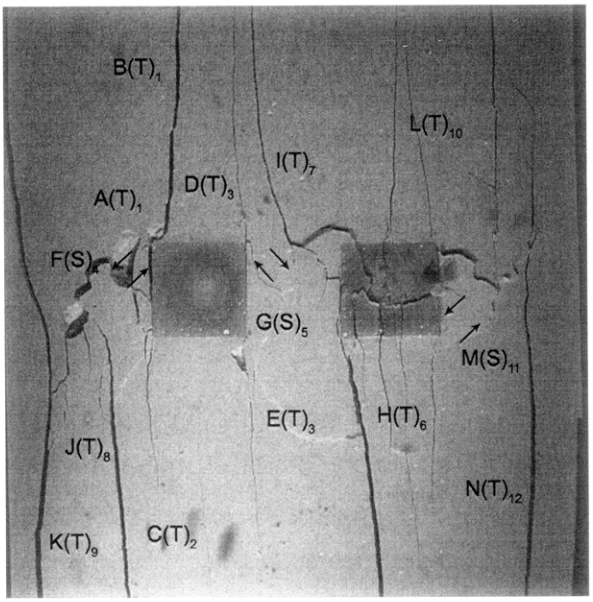

(Recorded by High Speed Video System)

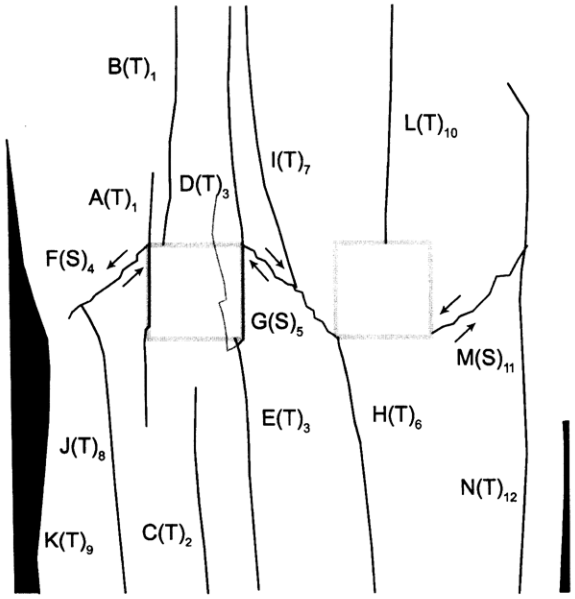

(8.27 MPa)
Time: 5 minutes & 29.515 seconds
HS Image # - 2307

Tensile crack (N) initiates at the lower specimen boundary and propagates upwards, which results in the detachment of a specimen piece.

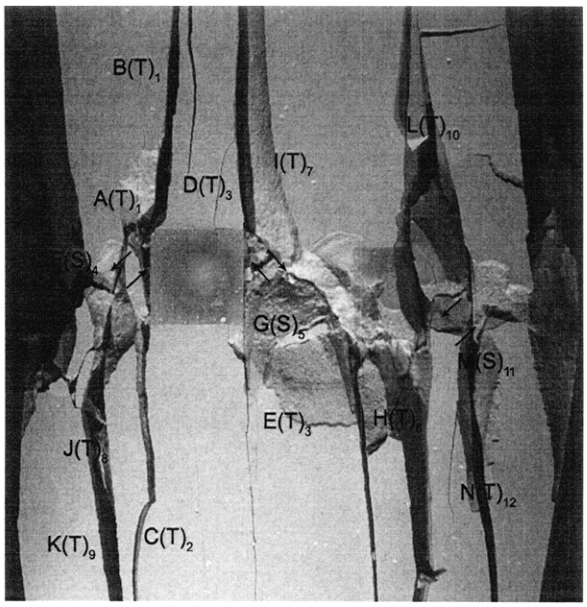

(Recorded by High Speed Video System)

(0 MPa) – Final Picture

A good view of shear crack (G) can be seen in this picture.

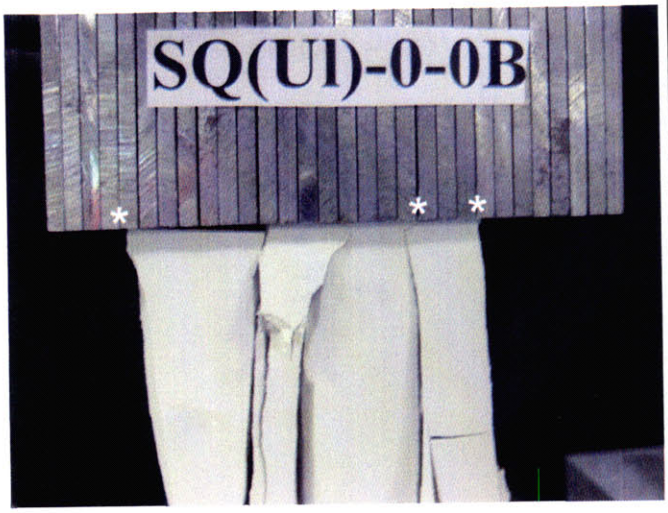	Upper edge of the specimen. The cracks marked with a (*) coincide with the openings between the teeth of the brush platen.
	Lower edge of the specimen. The cracks marked with a (*) coincide with the openings between the teeth of the brush platen.

SUMMARY

Specimen Number: SQ(UI)-45-0C (20080828)

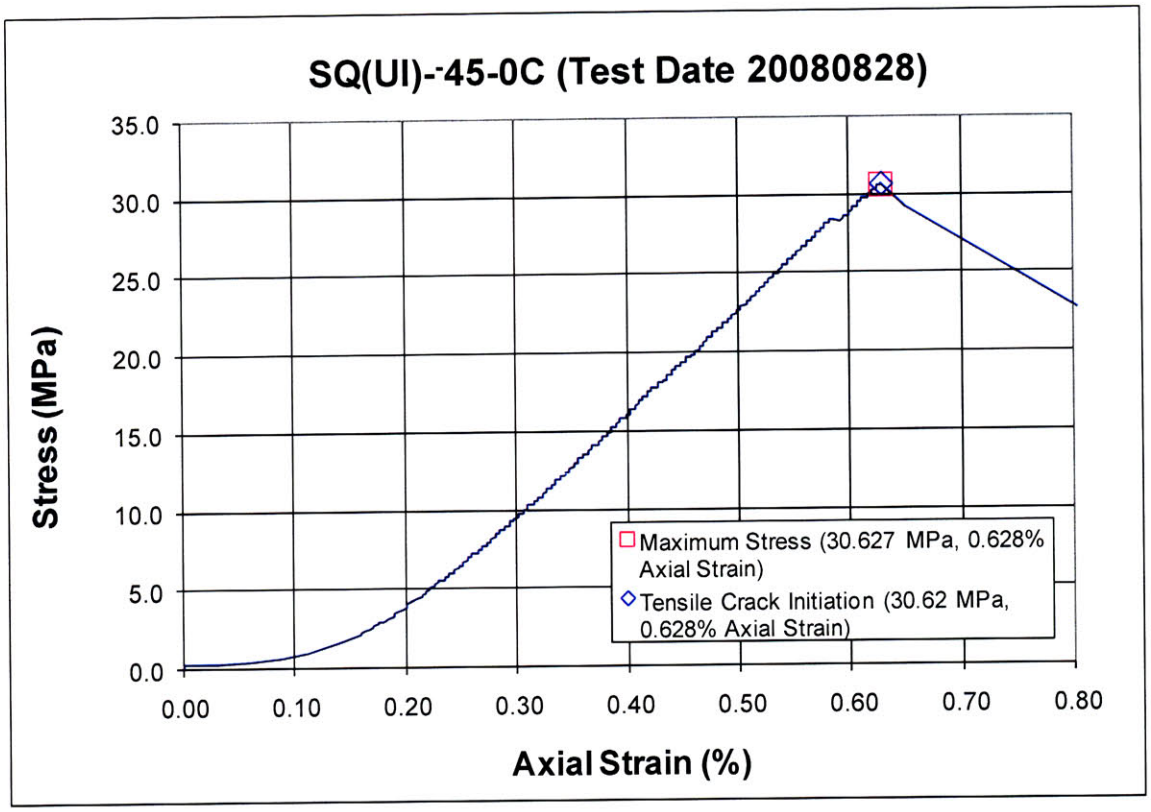

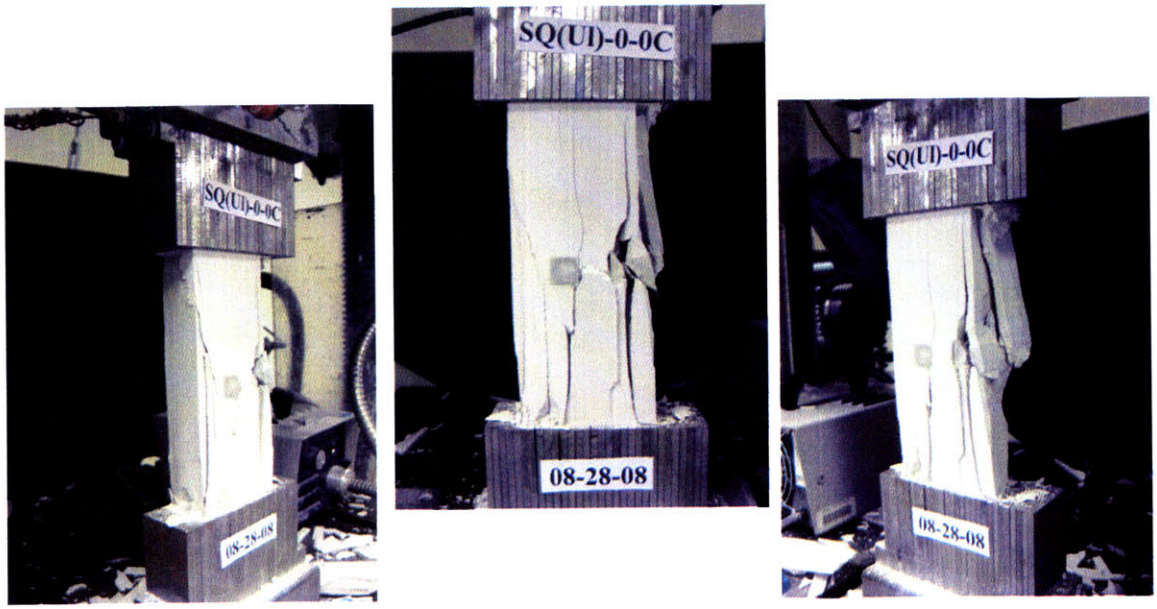

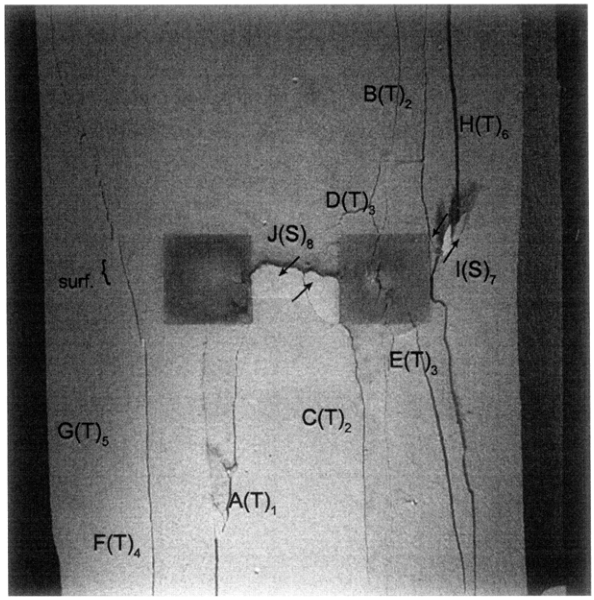

(Recorded by High Speed Video System)

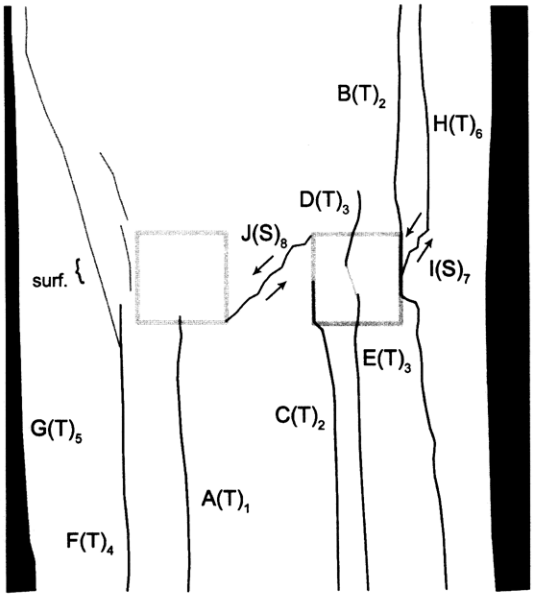

(29.62 MPa) – Ultimate Failure
Time: 6 minutes & 26.584 seconds
HS Image # - 2340

Surface crack (surf.) initiates at tensile crack (F) and propagates upwards.

Shear crack (J) initiates at the upper boundary of the right-hand inclusion and propagates downwards until its coalescence with the boundary of the left-hand inclusion.

SUMMARY

Specimen Number: SQ(PI)-30-0A (20081027)

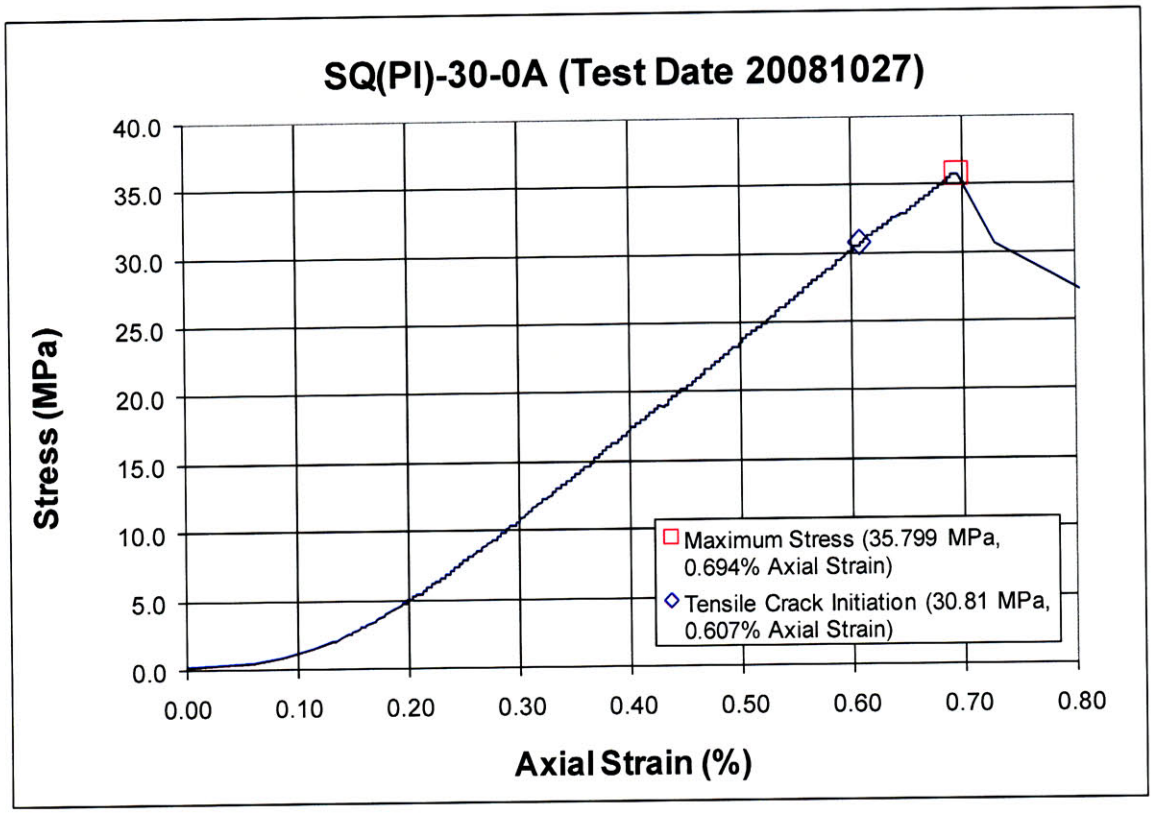

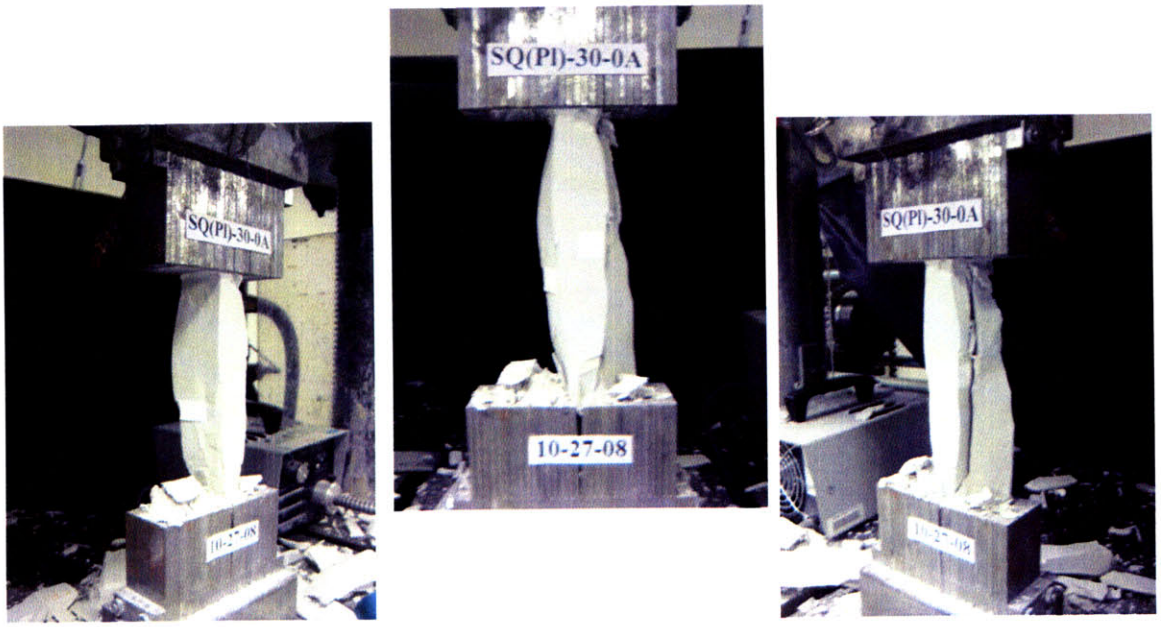

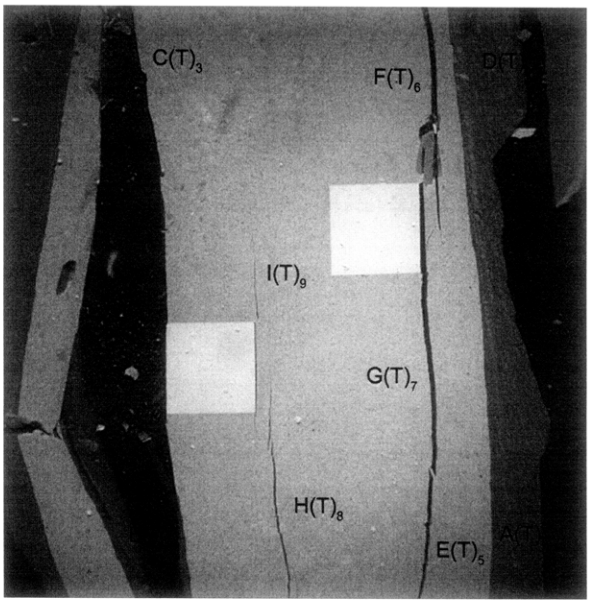

(Recorded by High Speed Video System)

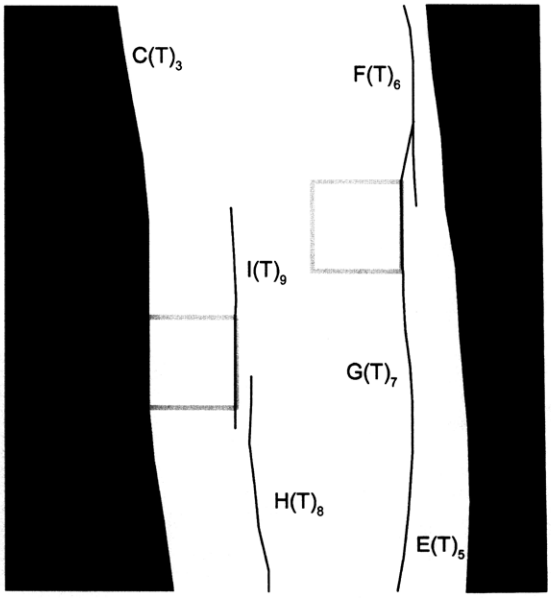

(23.77 MPa)
Time: 7 minutes & 40.728 seconds
HS Image # - 3415

Tensile crack (G) continues to propagate until its coalescence with tensile crack (F).

Tensile crack (H) then initiates at the lower specimen boundary and propagates upwards, adjacent to the left-hand inclusion.

Tensile crack (I) initiates at the boundary of the left-hand inclusion and propagates upwards.

SUMMARY

Specimen Number: SQ(PI)-30-0B (20081027)

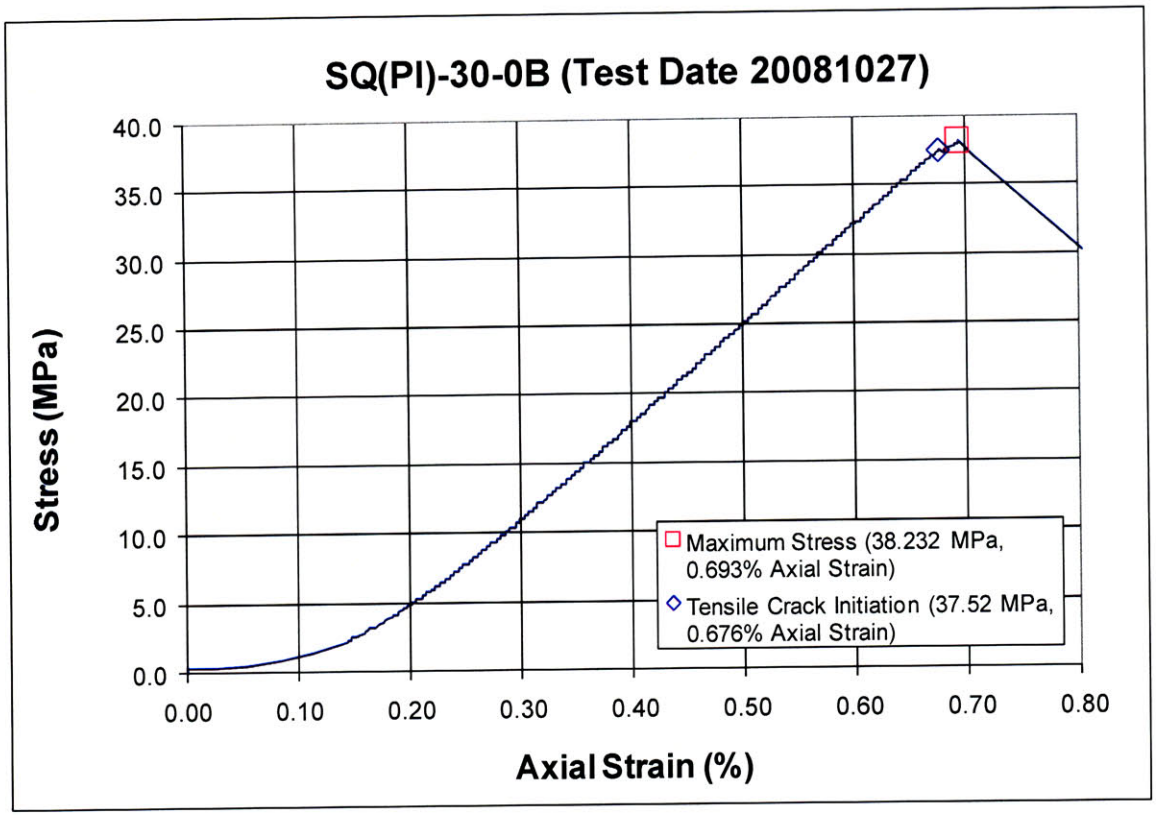

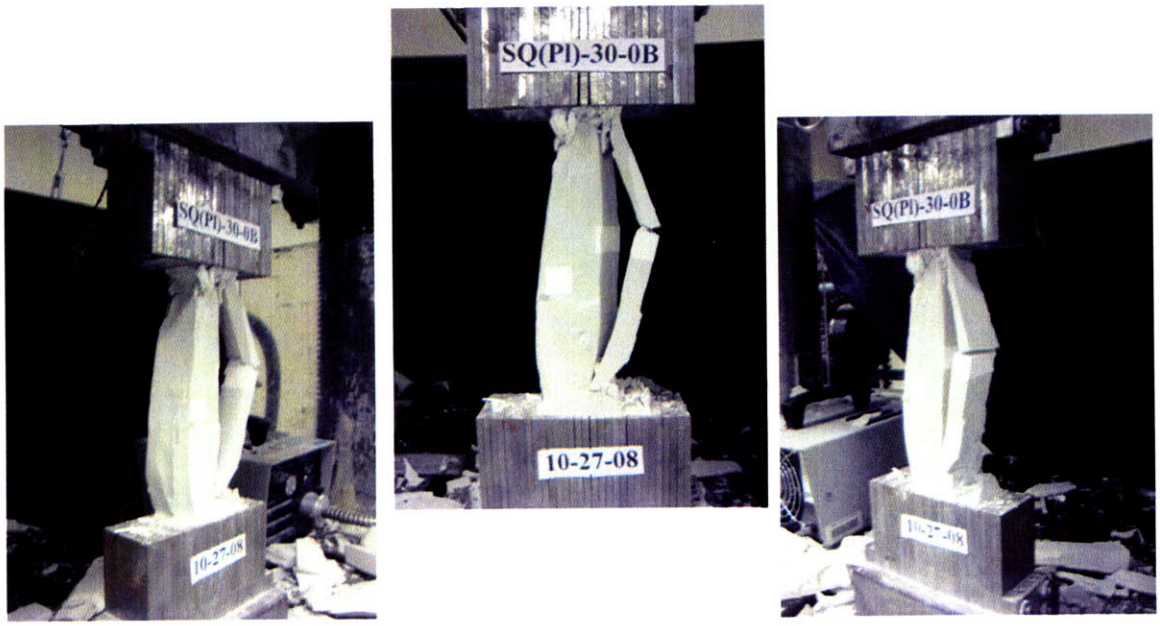

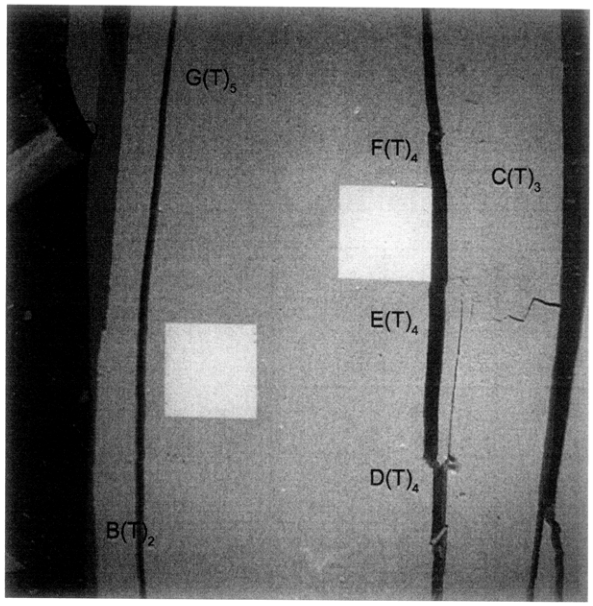

(Recorded by High Speed Video System)

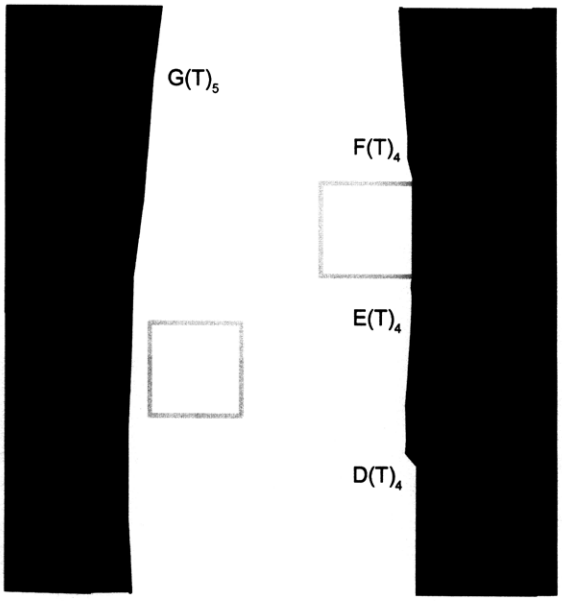

(35.88 MPa)
Time: 8 minutes & 13.108 seconds
HS Image # - 2749

Tensile crack (E) continues to propagate downwards and coalesces with tensile crack (D). This results in the detachment of a large specimen piece at the right boundary.

Tensile crack (G) then initiates at the upper specimen boundary and propagates downwards, which results in the detachment of another piece of specimen at the left boundary.

Specimen Number: SQ(PI)-30-0C (20081027)

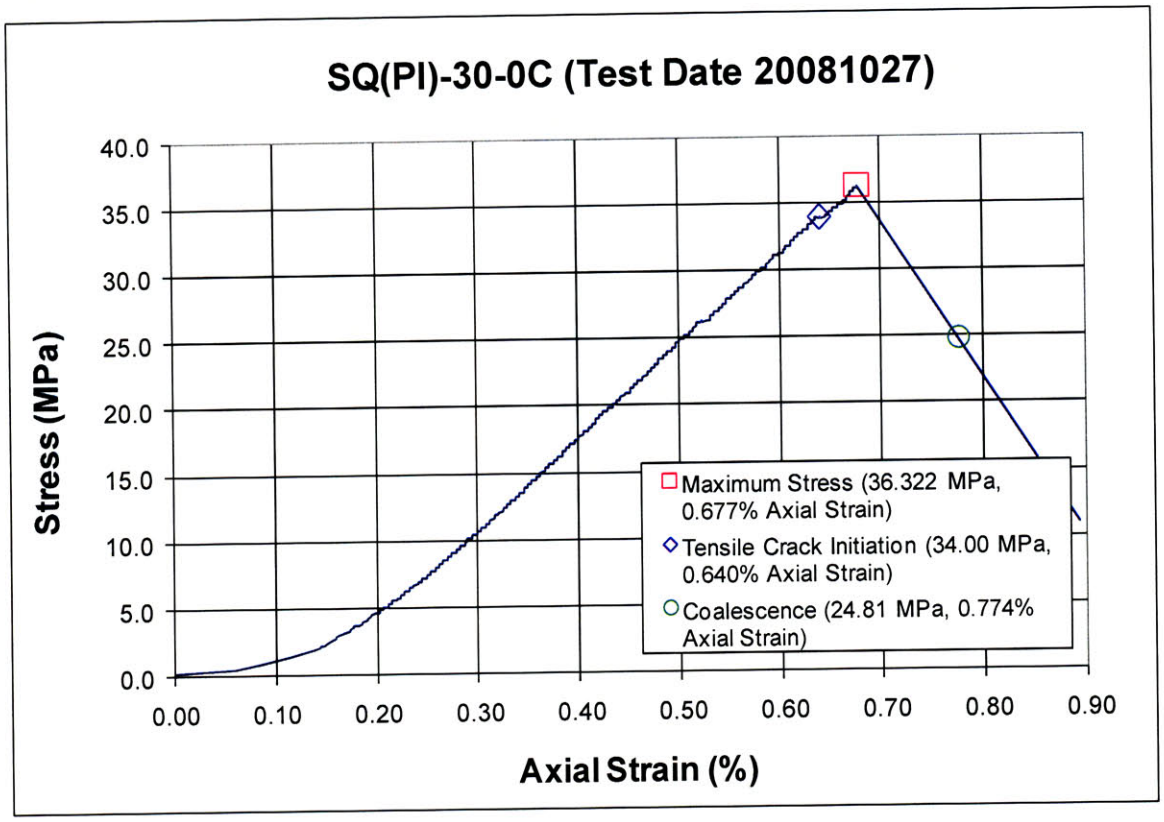

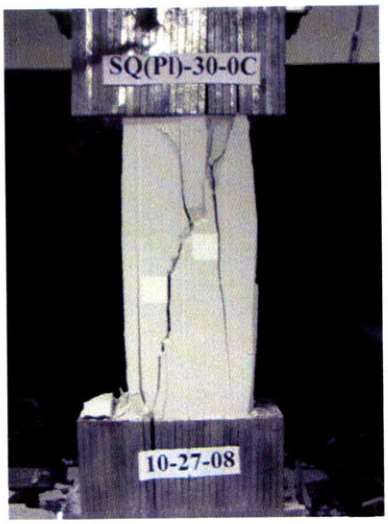

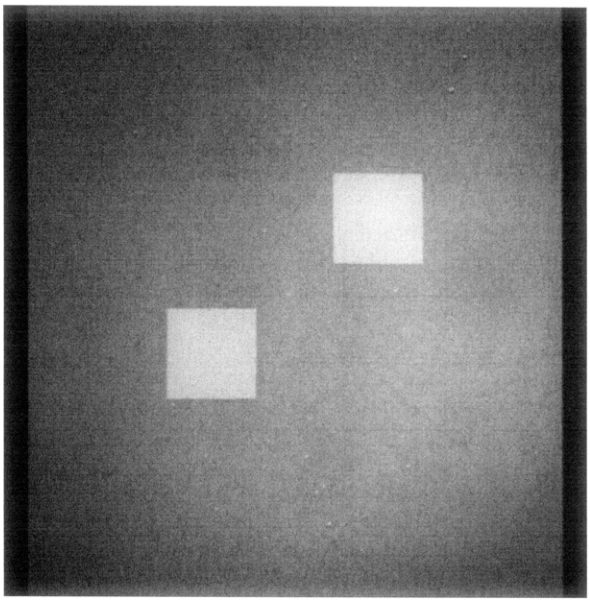

(Recorded by High Speed Video System)

Initial Inclusion Geometries:
SQUARES – Plaster Material

Inclusions **less** stiff than matrix.

High Speed Camera Frame Rate:
5000 pps

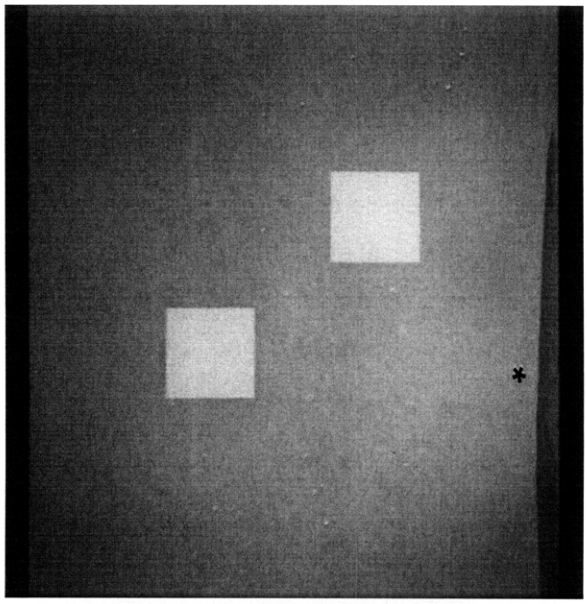

(Recorded by High Speed Video System)

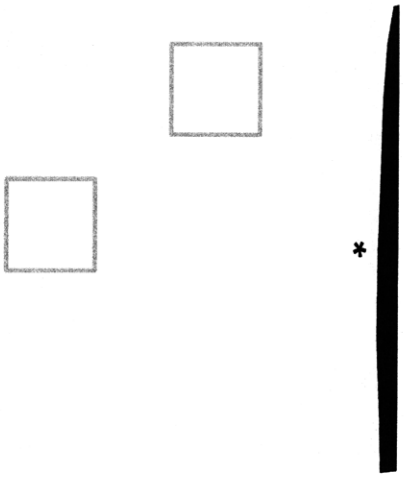

(19.59 MPa)
Time: 3 minutes & 52.126 seconds

Prior to tensile crack initiation at the inclusion boundaries, a surficial piece of specimen detaches (*) at the right specimen boundary.

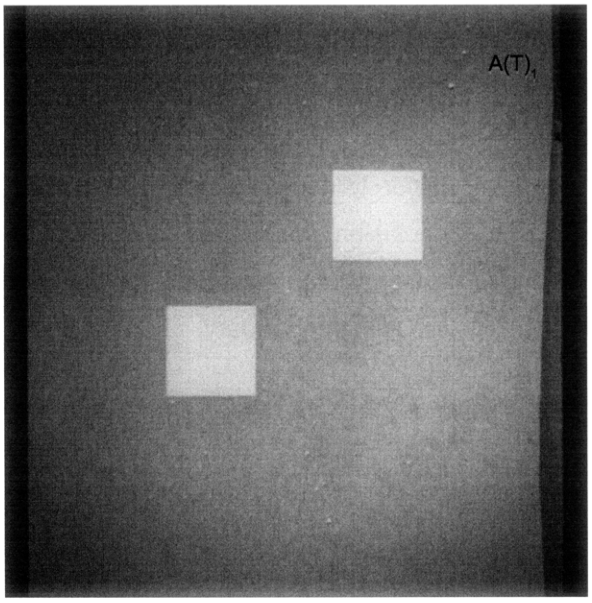

(Recorded by High Speed Video System)

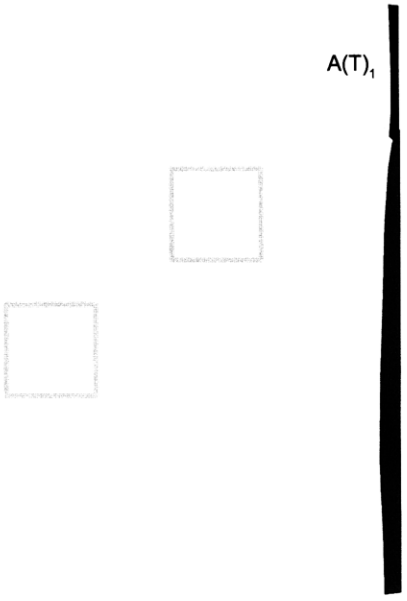

(34.00 MPa)

- Tensile Crack Initiation

Time: 7 minutes & 16.93 seconds

Tensile crack (A) initiates at the upper specimen boundary and propagates downwards. This results in the detachment of another specimen piece at the right boundary.

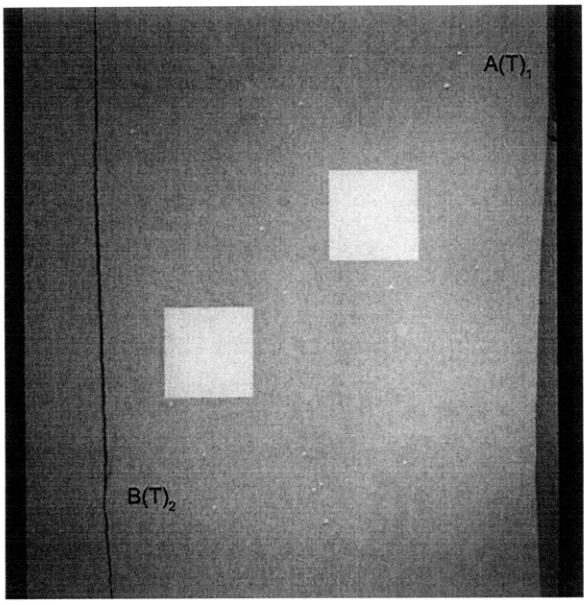

(Recorded by High Speed Video System)

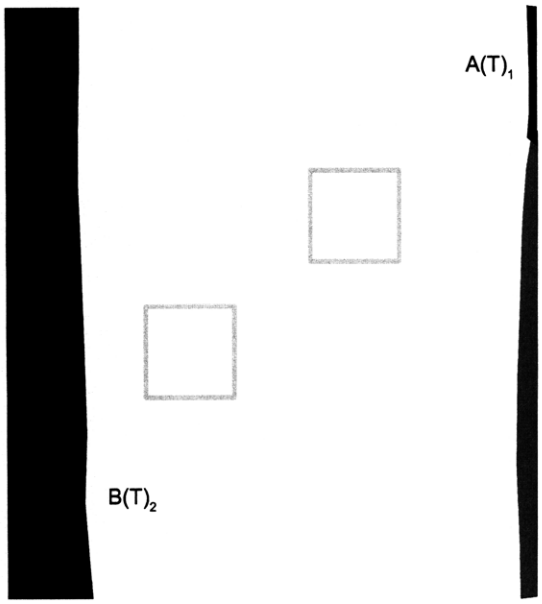

(36.322 MPa) [Max. Stress]
Time: 7 minutes & 49.960 seconds
HS Image # - 3014

Tensile crack (B) initiates at the lower specimen boundary and propagates upwards until its intersection with the upper specimen boundary. This results in the detachment of a specimen piece at the left boundary.

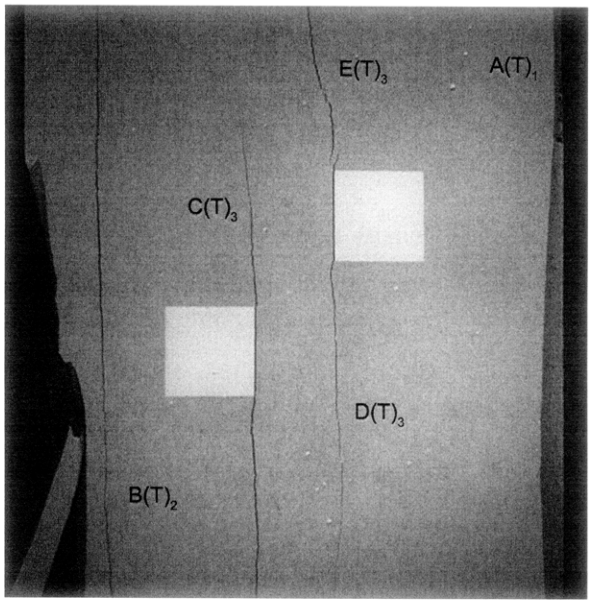

(Recorded by High Speed Video System)

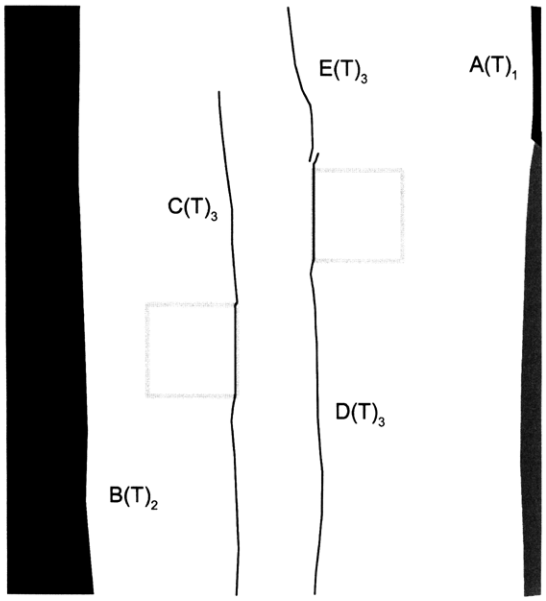

(24.86 MPa)
Time: 7 minutes & 50.049 seconds
HS Image # - 2568

Tensile crack (C) initiates at the lower specimen boundary and propagates upwards, and then along the left-hand inclusion boundary. Tensile crack (C) then continues to propagate upwards into the surrounding hydrocal matrix again.

Tensile crack (D) initiates at the boundary of the right-hand inclusion and propagates downwards.

It is assumed that tensile crack (E) initiates at the upper specimen boundary and propagates downwards towards the right-hand inclusion, though the high speed footage was inconclusive.

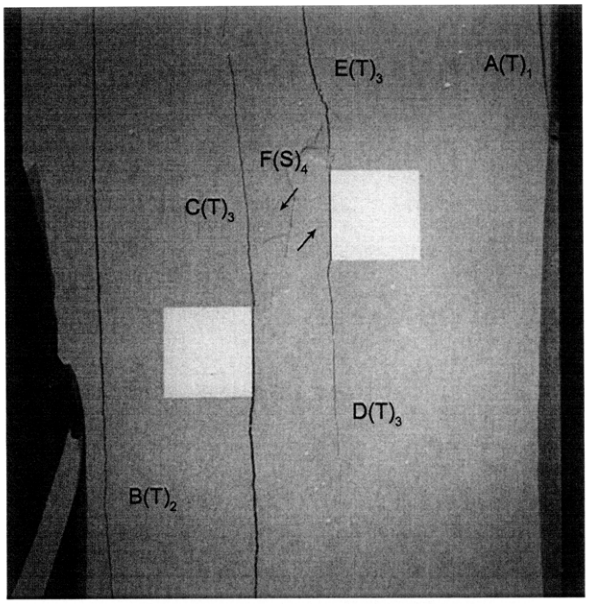

(Recorded by High Speed Video System)

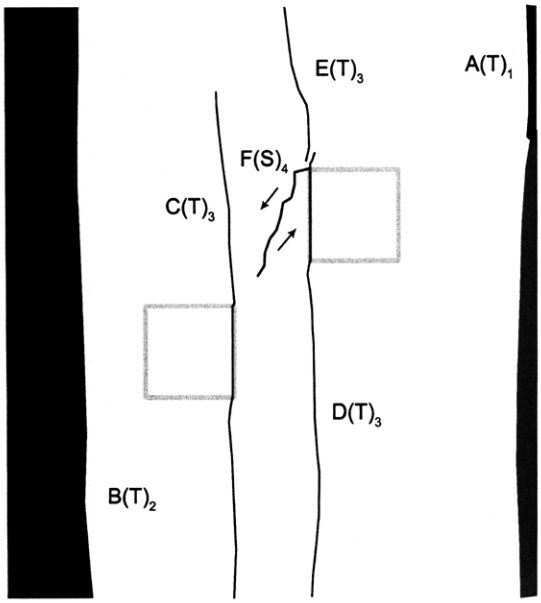

(24.83 MPa)
Time: 7 minutes & 50.050 seconds
HS Image # - 2567

Shear crack (F) initiates at the boundary of the right-hand inclusion and propagates downwards towards the left-hand inclusion.

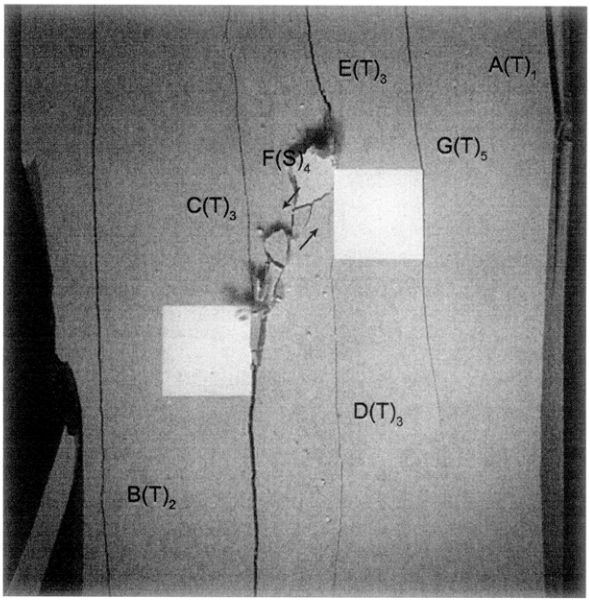

(Recorded by High Speed Video System)

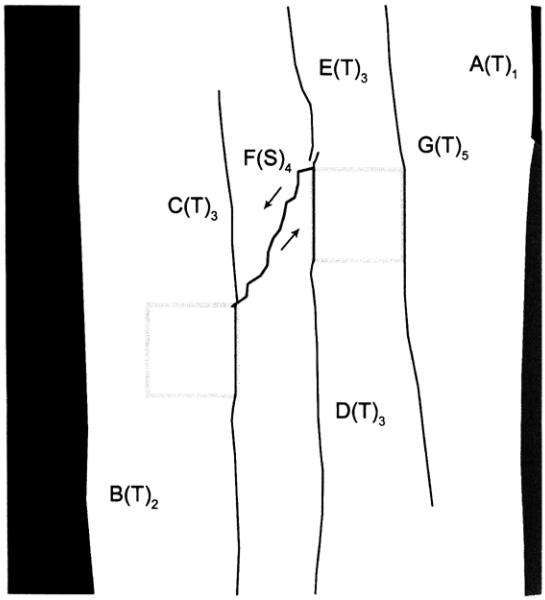

(24.81 MPa) - Coalescence
Time: 7 minutes & 50.050 seconds
HS Image # - 2566

Shear crack (F) continues to propagate until its coalescence with the boundary of the left-hand inclusion.

Tensile crack (G) initiates at the upper specimen boundary and propagates downwards, and then along the right-hand inclusion boundary. Tensile crack (G) then continues to propagate downwards into the surrounding hydrocal matrix, towards the lower specimen boundary.

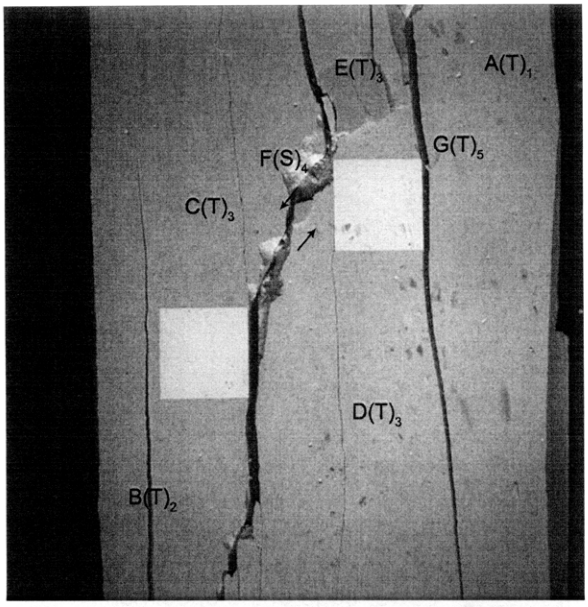

(Recorded by High Speed Video System)

(0 MPa) – Final Picture

Time: 7 minutes & 50.412 seconds

HS Image # - 753

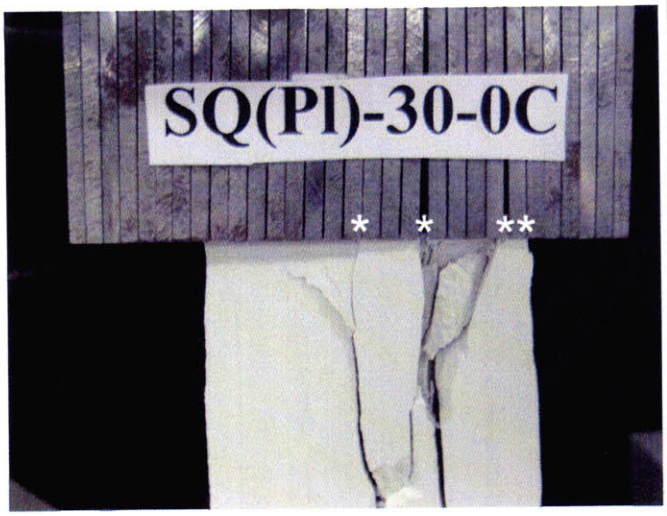	Upper edge of the specimen. The cracks marked with a (*) coincide with the openings between the teeth of the brush platen.
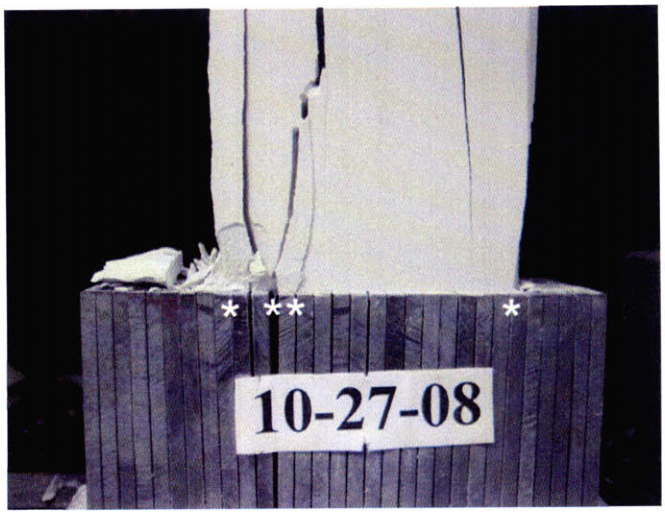	Lower edge of the specimen. The cracks marked with a (*) coincide with the openings between the teeth of the brush platen.

Specimen Number: SQ(UI)-30-0A (20081108)

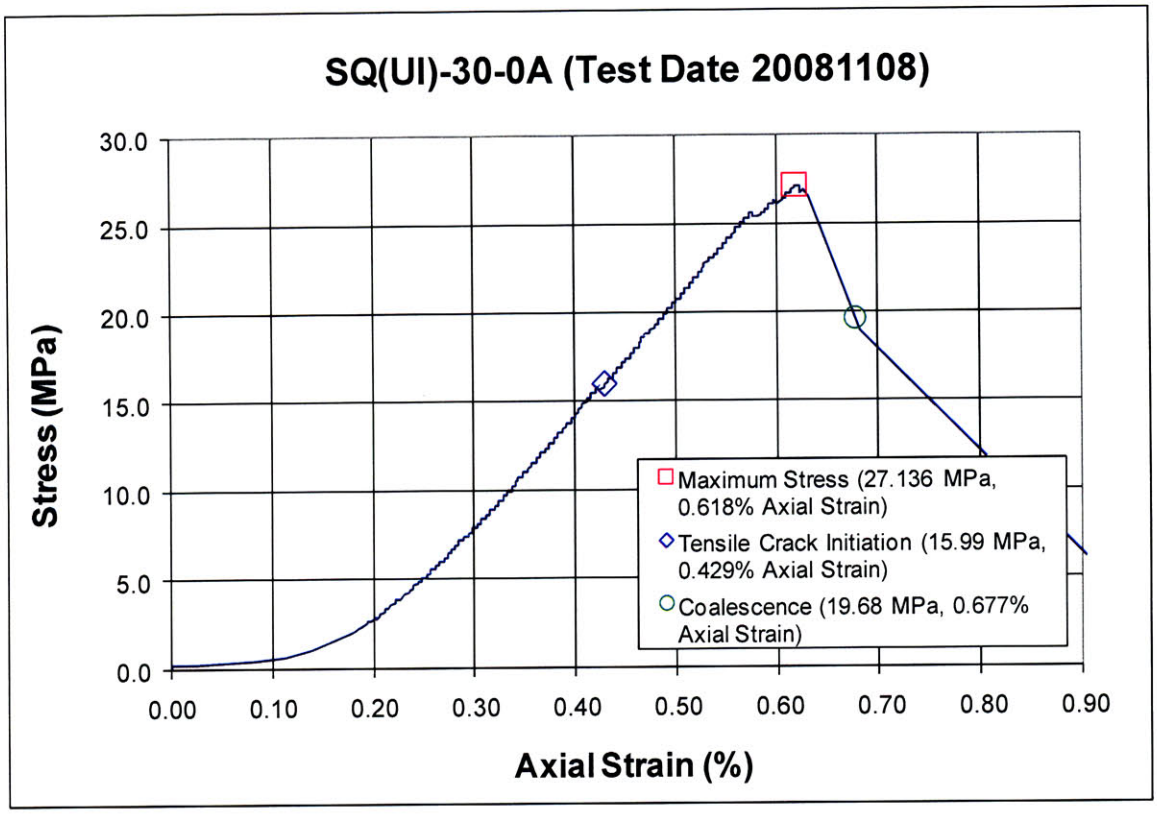

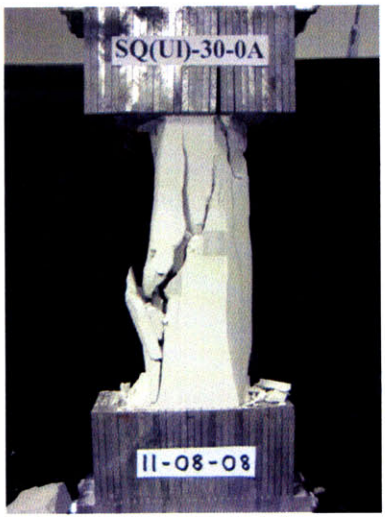

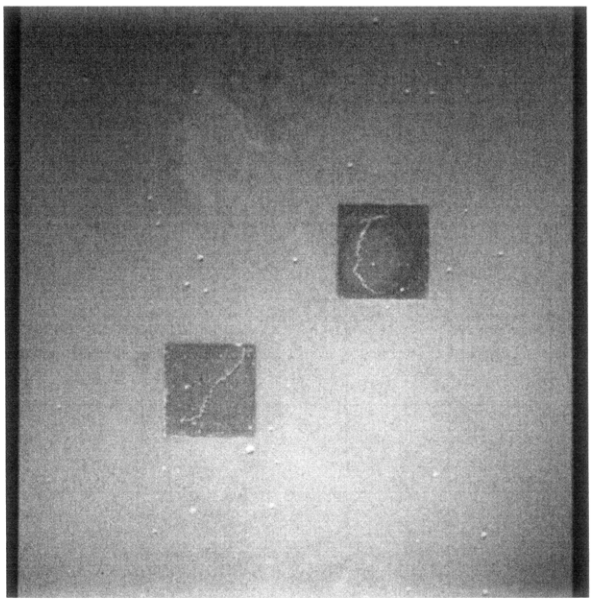

(Recorded by High Speed Video System)

Initial Inclusion Geometries:
SQUARES – Ultracal Material

Inclusions **more** stiff than matrix.

Initial surface cracks present prior to testing.

High Speed Camera Frame Rate:
5000 pps

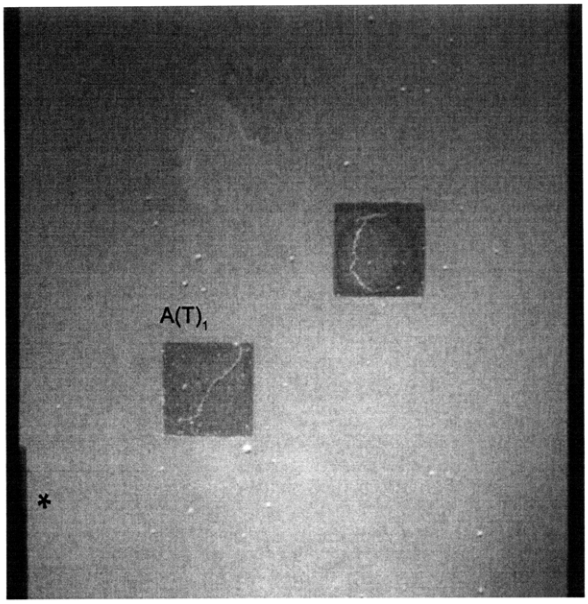

(Recorded by High Speed Video System)

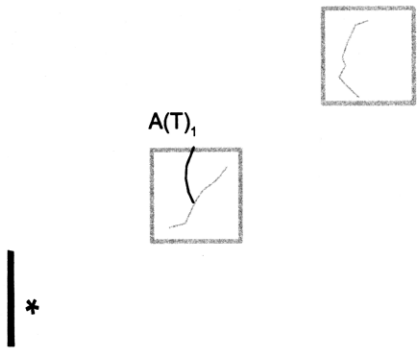

(15.99 MPa)

- Tensile Crack Initiation

Time: 2 minutes & 57.66 seconds

A tensile crack initiates at the lower specimen boundary and propagates upwards; this results in the detachment (*) of a piece at the left specimen boundary.

Tensile crack (A) initiates at a pre-test surface crack within the left-hand inclusion and propagates upwards.

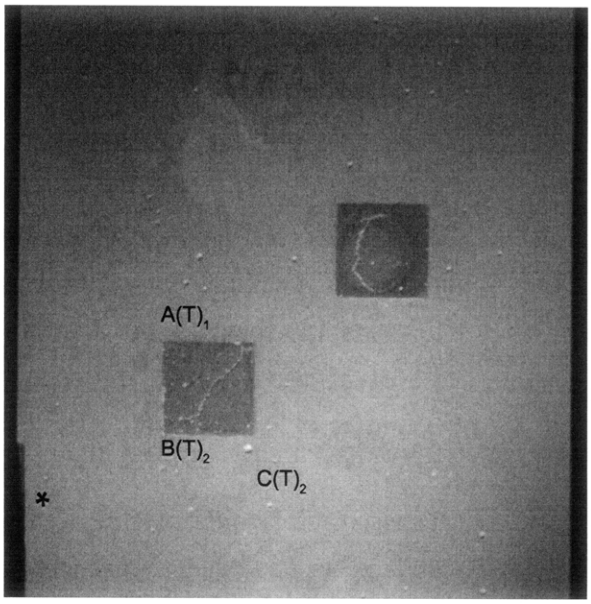

(Recorded by High Speed Video System)

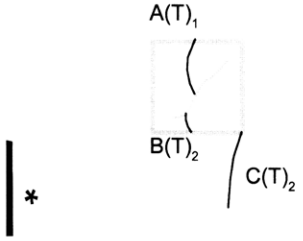

(20.29 MPa)
Time: 3 minutes & 58.23 seconds

Tensile crack (B) initiates at the pre-test surface crack located within the left-hand inclusion and propagates downwards.

Tensile crack (C) initiates at the boundary of the left-hand inclusion and propagates downwards towards the lower specimen boundary.

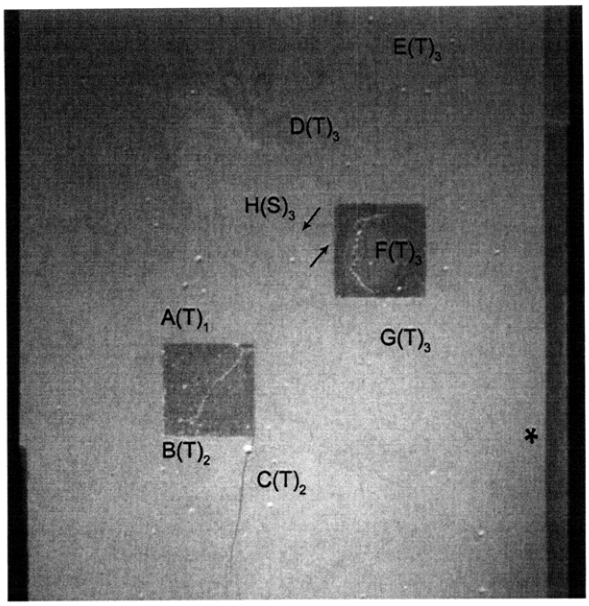

(Recorded by High Speed Video System)

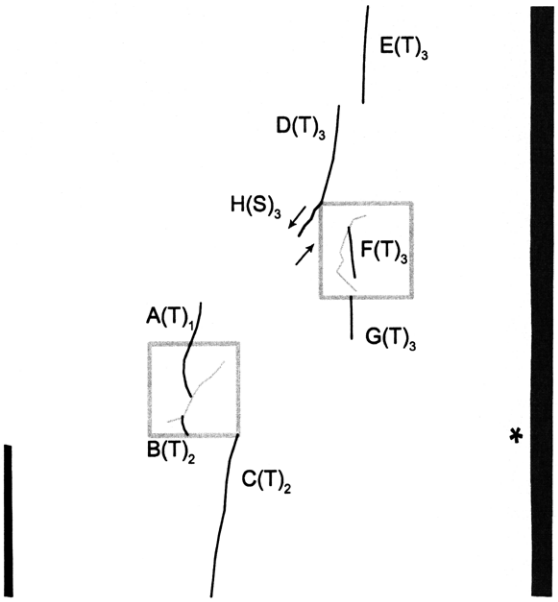

(25.66 MPa)
Time: 5 minutes & 13.63 seconds

A piece of surficial specimen (*) detaches at the right specimen boundary.

Tensile cracks (D,E,F&G) initiate "simultaneously" with shear crack (H).

Tensile crack (D) initiates at the boundary of the right-hand inclusion and propagates upwards.

It is assumed that tensile crack (E) initiates at the upper specimen boundary and propagates downwards, towards the right-hand inclusion.

Tensile crack (F) initiates within the right-hand inclusion.

Tensile crack (G) initiates at the boundary of the right-hand inclusion and propagates downwards.

Shear crack (H) initiates at the boundary of the right-hand inclusion and propagates downwards, towards the left-hand inclusion.

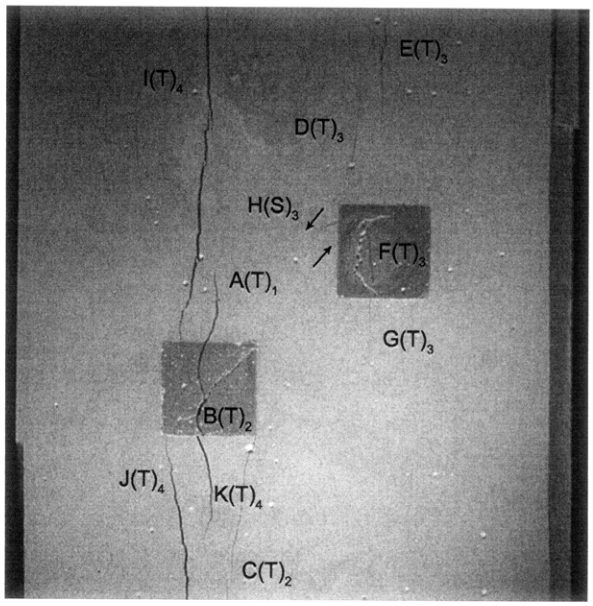

(Recorded by High Speed Video System)

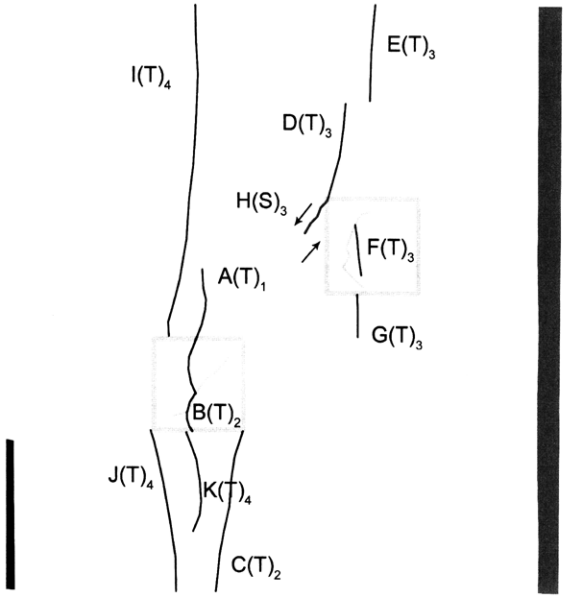

(27.136 MPa) [Max. Stress]
Time: 5 minutes & 34.15 seconds

Tensile crack (B) propagates along the pre-test surface crack within the left-hand inclusion, and coalesces with tensile crack (A).

Tensile cracks (I,J&K) initiate "simultaneously" at the boundary of the left-hand inclusion. Tensile crack (I) propagates upwards towards the upper specimen boundary, while tensile cracks (J&K) propagate downwards.

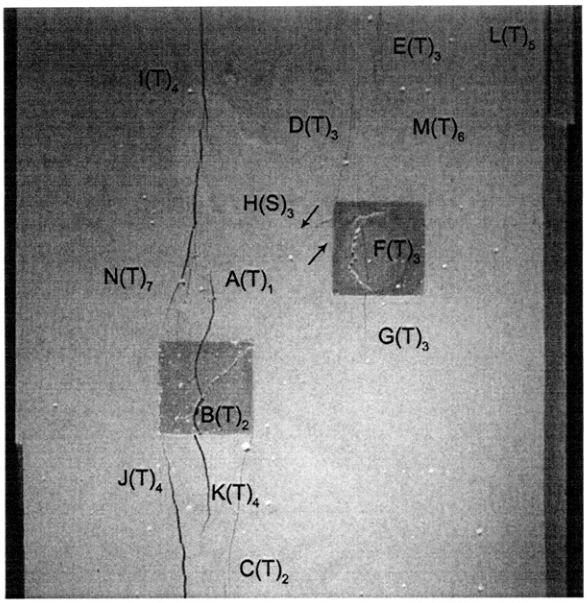

(Recorded by High Speed Video System)

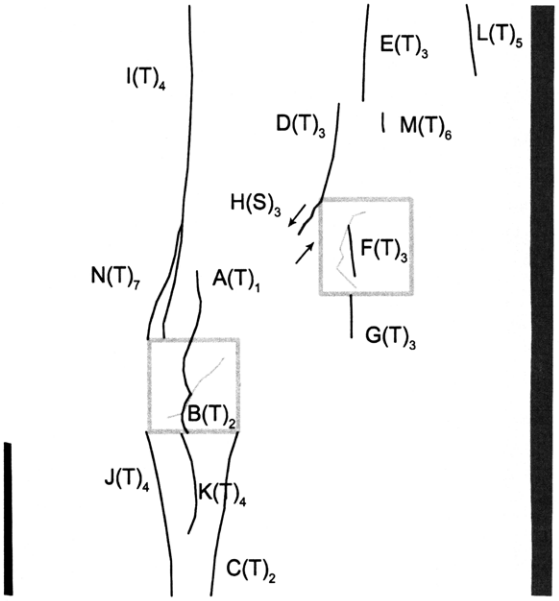

(26.84 MPa)
Time: 5 minutes & 34.425 seconds
HS Image # - 4027

Tensile crack (L) initiates at the upper specimen boundary and propagates downwards.

Tensile crack (M) initiates above the right-hand inclusion and propagates vertically in both directions.

Tensile crack (N) then initiates at the left-hand inclusion boundary and propagates upwards, until its coalescence with tensile crack (I).

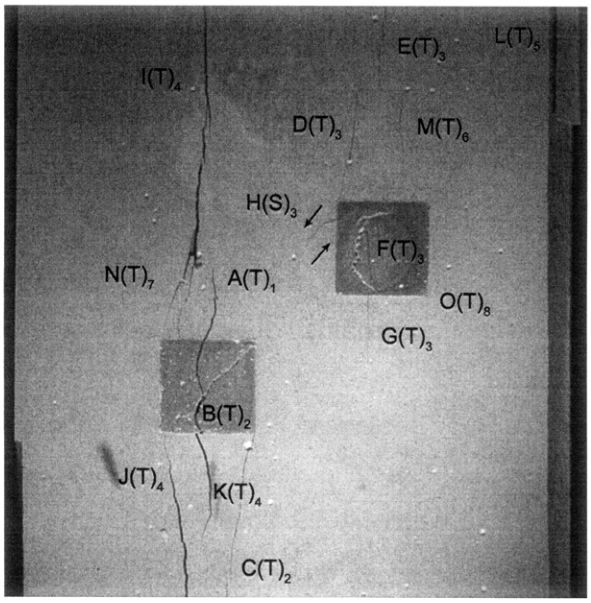

(Recorded by High Speed Video System)

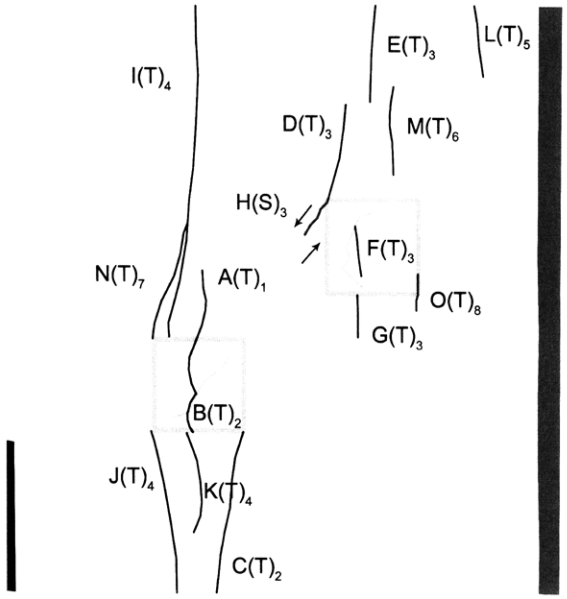

(26.64 MPa)
Time: 5 minutes & 34.520 seconds
HS Image # - 3556

Tensile crack (O) initiates at the boundary of the right-hand inclusion.

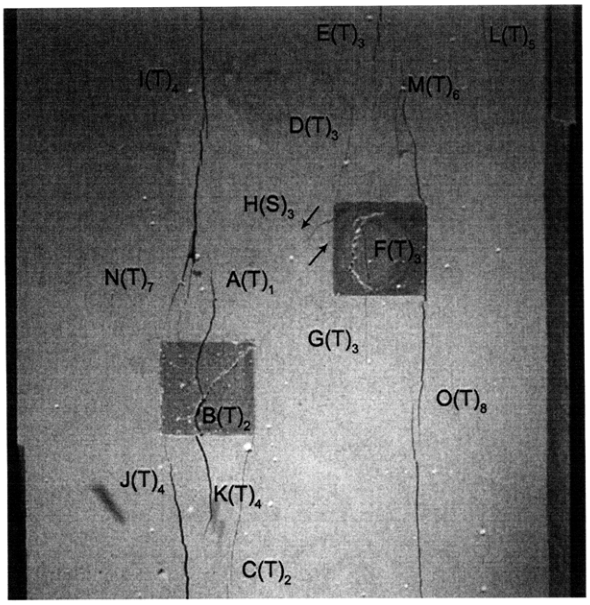

(Recorded by High Speed Video System)

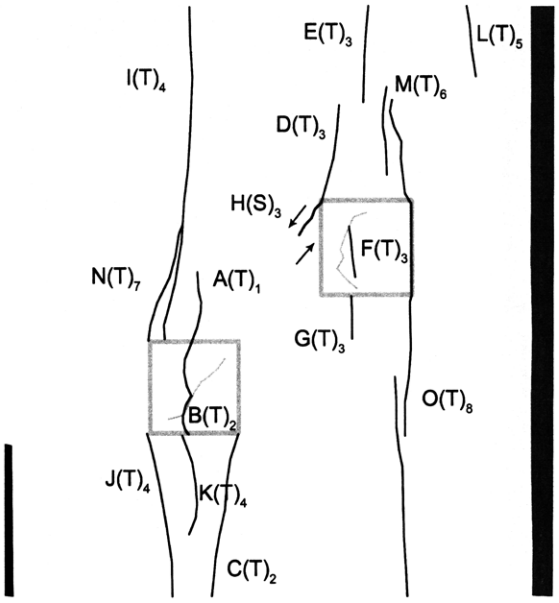

(26.63 MPa)
Time: 5 minutes & 34.525 seconds
HS Image # - 3530

Tensile crack (O) propagates upwards towards tensile crack (M) and also downwards towards the lower specimen boundary.

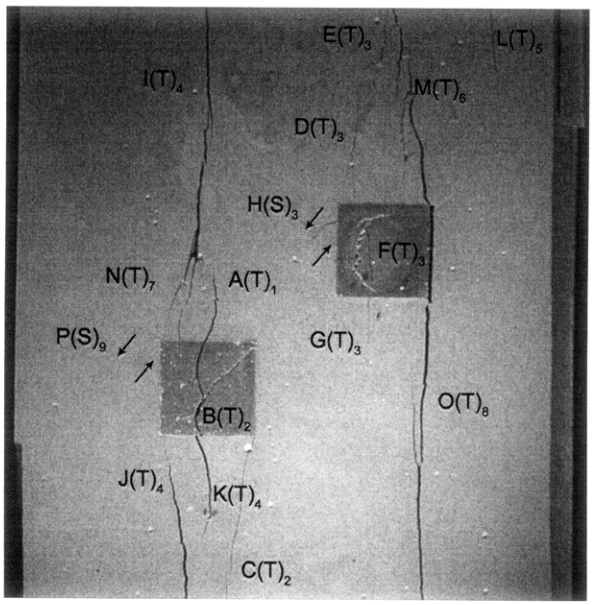

(Recorded by High Speed Video System)

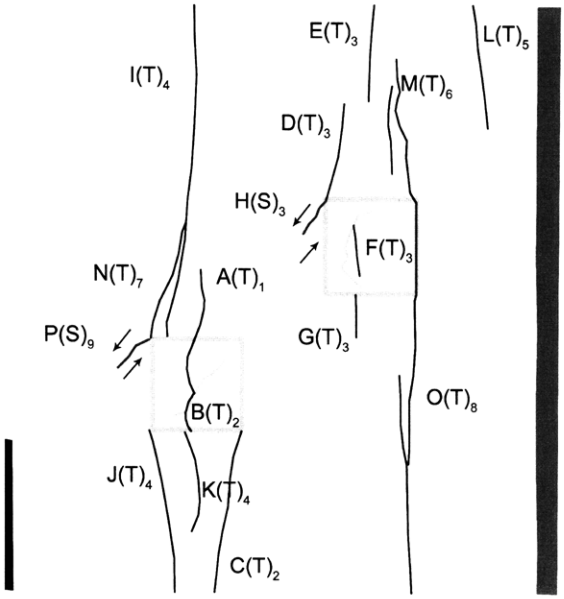

(23.17 MPa)
Time: 5 minutes & 34.591 seconds
HS Image # - 3197

Shear crack (P) initiates at the boundary of the left-hand inclusion and propagates downwards towards the left specimen boundary.

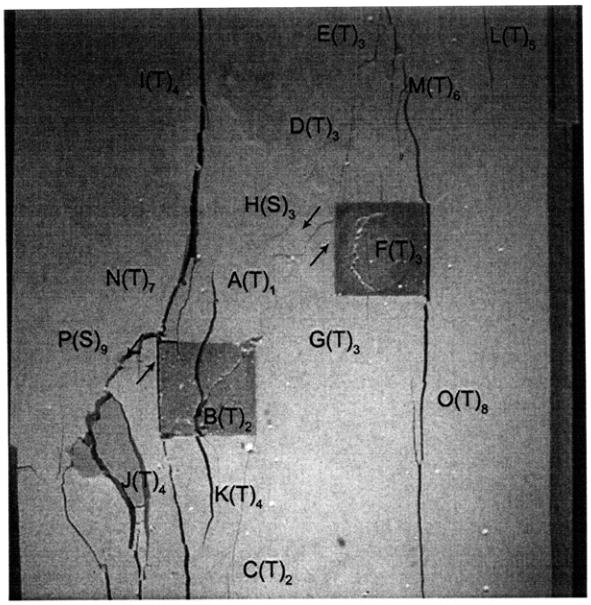

(Recorded by High Speed Video System)

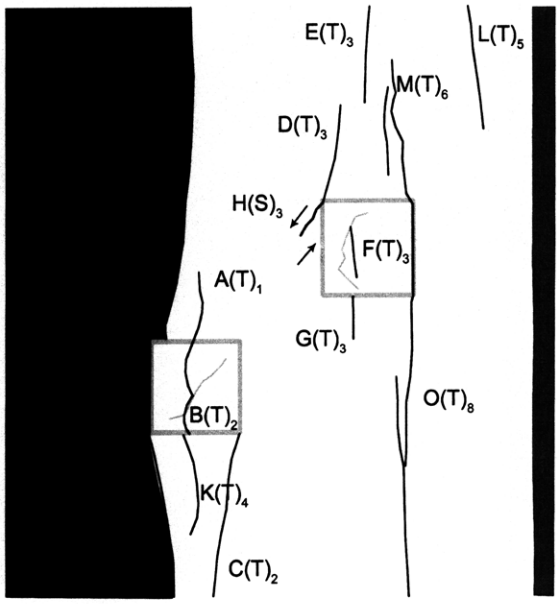

(19.77 MPa)
Time: 5 minutes & 34.637 seconds
HS Image # - 2968

The propagation of shear crack (P) results in the detachment of a large specimen piece at the left specimen boundary.

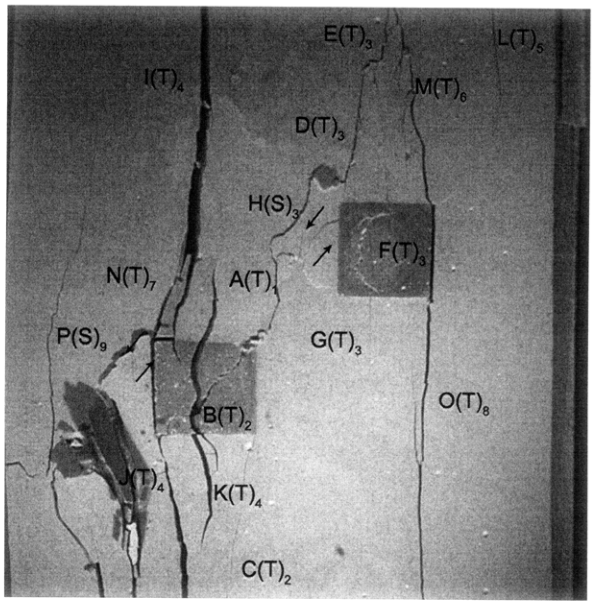

(Recorded by High Speed Video System)

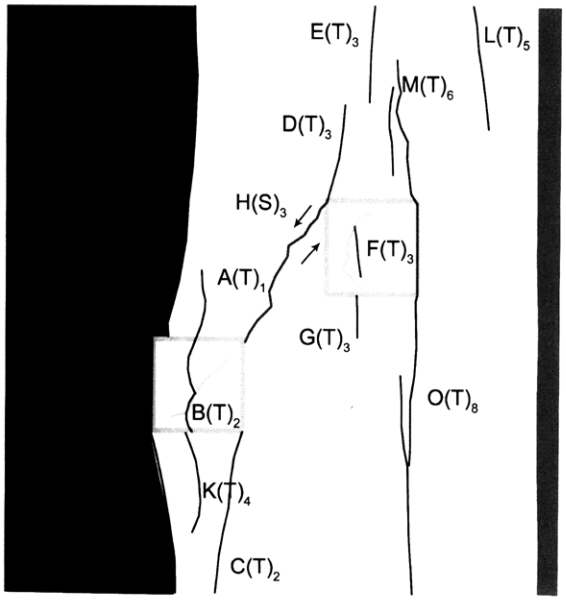

(19.68 MPa) - Coalescence
Time: 5 minutes & 34.638 seconds
HS Image # - 2962

Shear crack (H) propagates until its coalescence with the boundary of the left-hand inclusion.

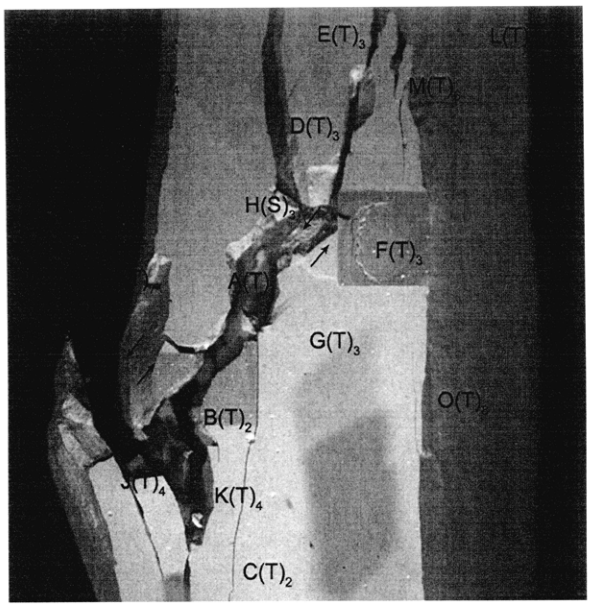

(Recorded by High Speed Video System)

(0 MPa) – Final Picture

Time: 5 minutes & 34.638 seconds

HS Image # - 1

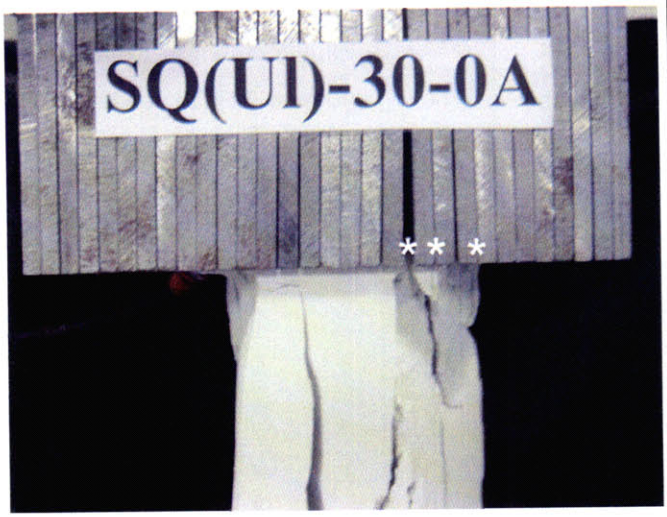	Upper edge of the specimen. The cracks marked with a (*) coincide with the openings between the teeth of the brush platen.
	Lower edge of the specimen. The cracks marked with a (*) coincide with the openings between the teeth of the brush platen.

SUMMARY

Specimen Number: SQ(UI)-30-0B (20081108)

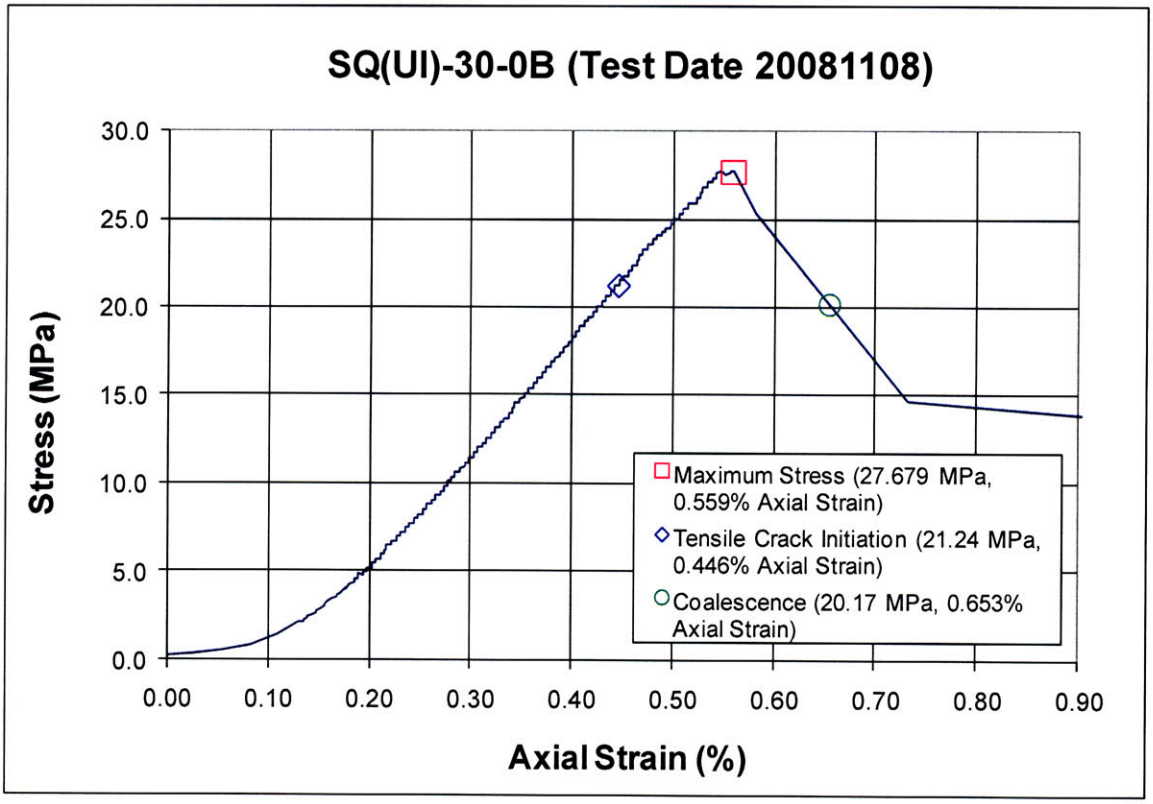

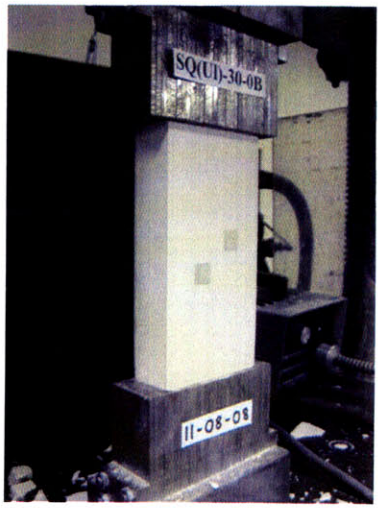

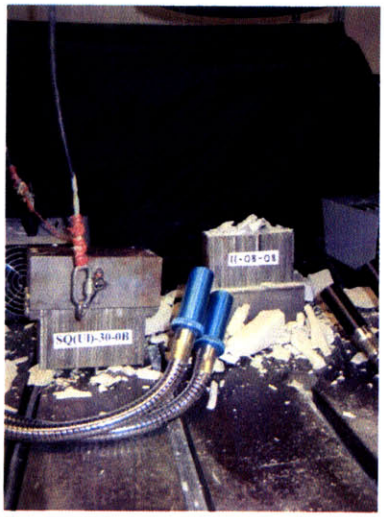

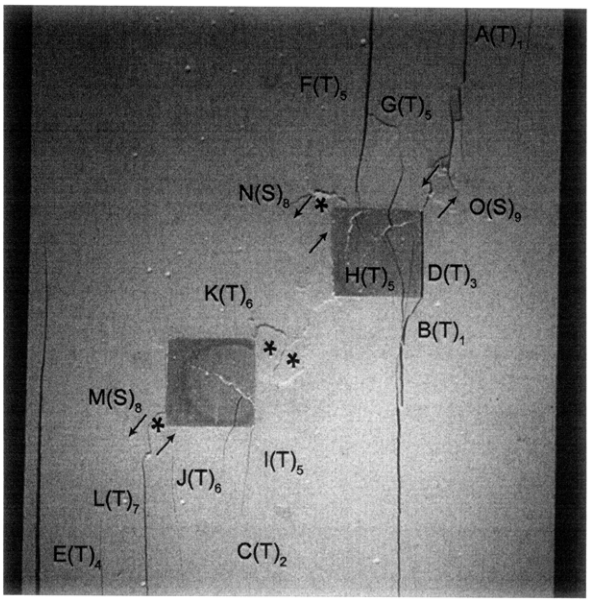

(Recorded by High Speed Video System)

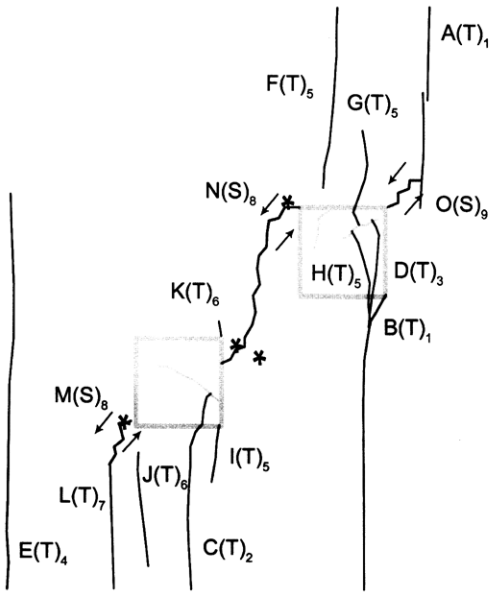

(20.17 MPa) - Coalescence
Time: 5 minutes & 38.945 seconds
HS Image # - 4649

Shear crack (N) continues to propagate, until its coalescence with the boundary of the left-hand inclusion.

Spalling (*) occurs adjacent to shear cracks (M&N).

SUMMARY

Specimen Number: SQ(UI)-30-0C (20081108)

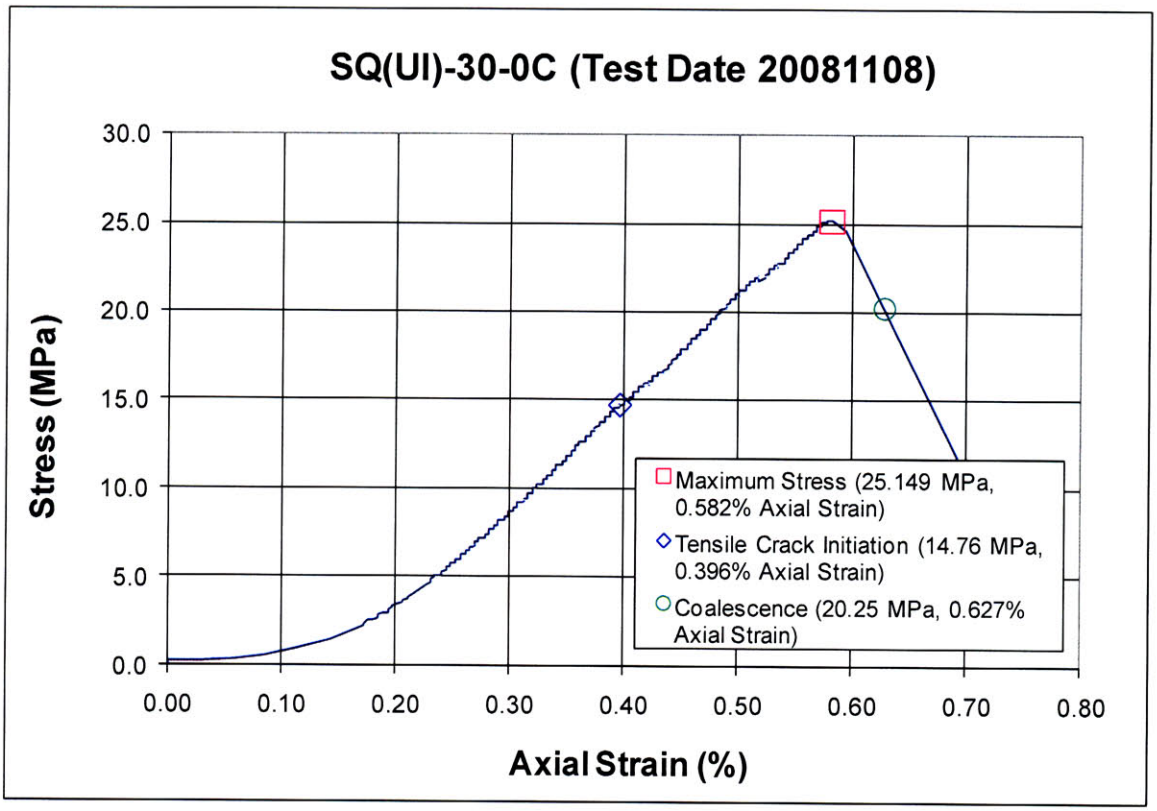

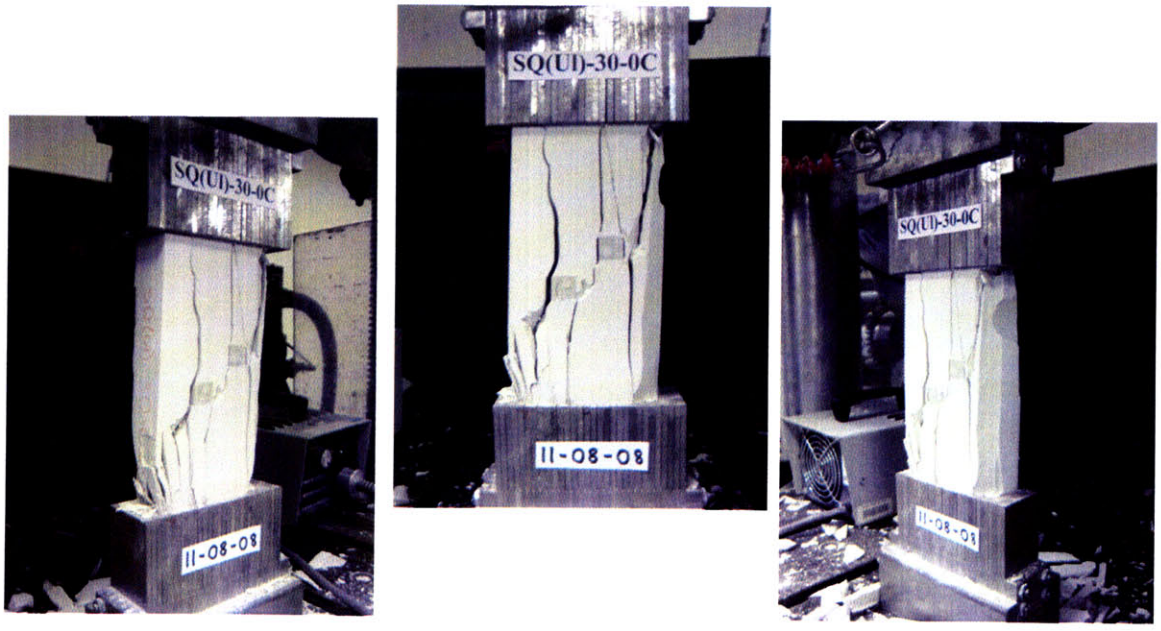

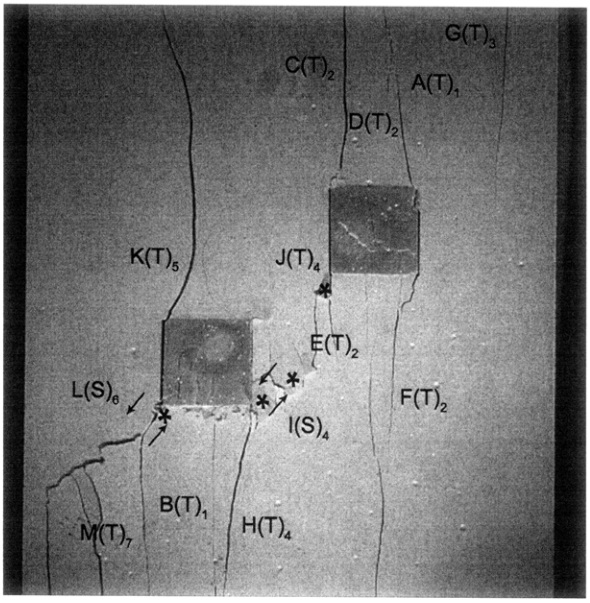

(Recorded by High Speed Video System)

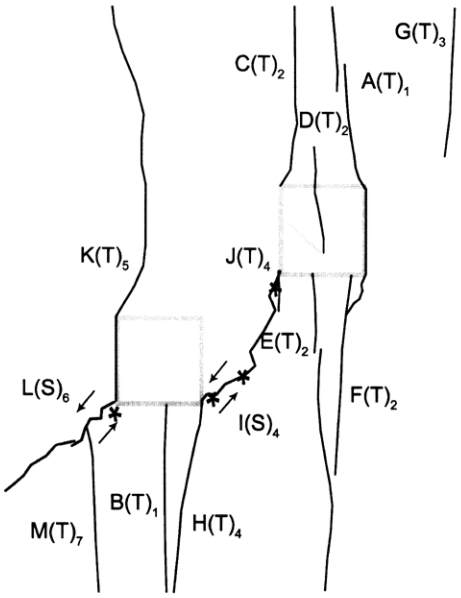

(20.25 MPa) - Coalescence
Time: 4 minutes & 58.966 seconds
HS Image # - 2379

Shear crack (I) continues to propagate, until its coalescence with the boundary of the right-hand inclusion.

Spalling (*) occurs adjacent to shear cracks (I&J).

SUMMARY

Specimen Number: SQ(PI)-60-0A (20081108)

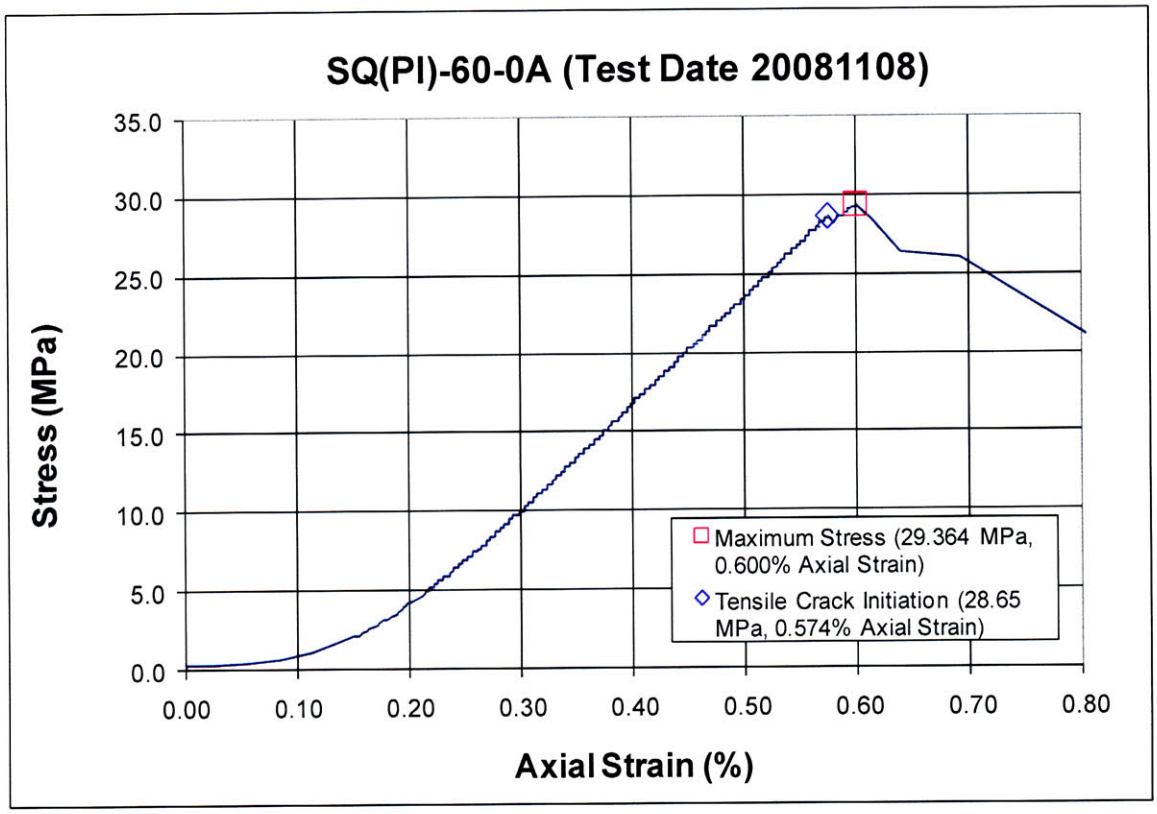

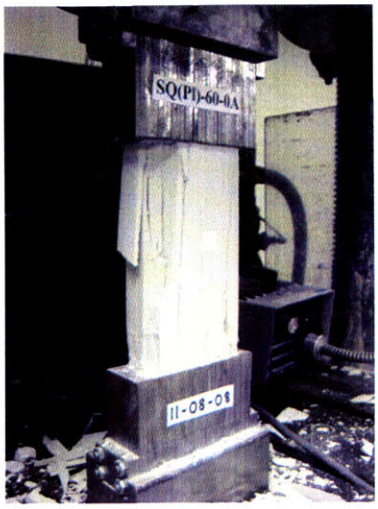

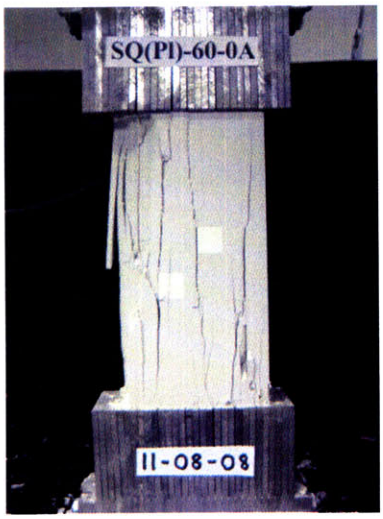

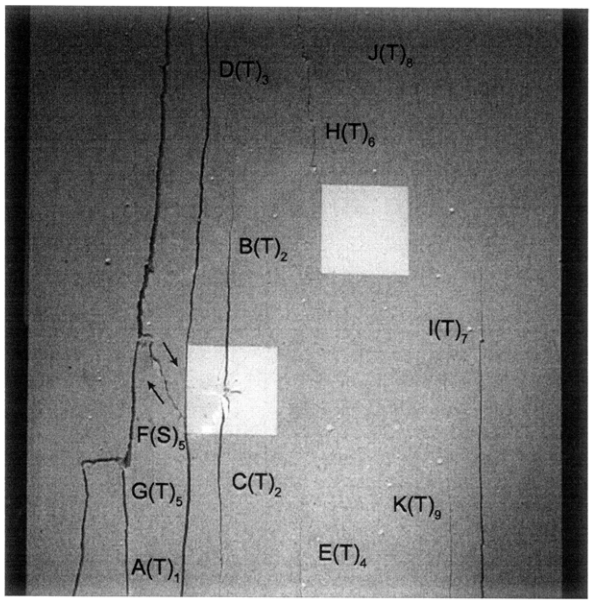

(Recorded by High Speed Video System)

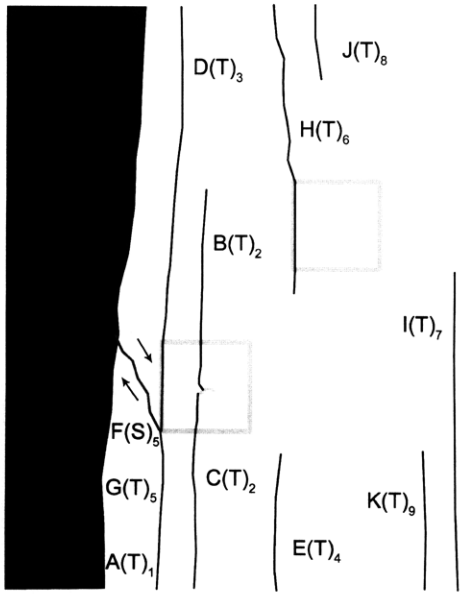

(22.13 MPa)
Time: 6 minutes & 3.779 seconds
HS Image # - 2266

Tensile crack (H) propagates downwards, along the right-hand inclusion boundary.

Tensile crack (J) initiates at the upper specimen boundary and propagates downwards, towards the right-hand inclusion.

Tensile crack (K) initiates at the lower specimen boundary and propagates upwards.

SUMMARY

Specimen Number: SQ(PI)-60-0B (20081108)

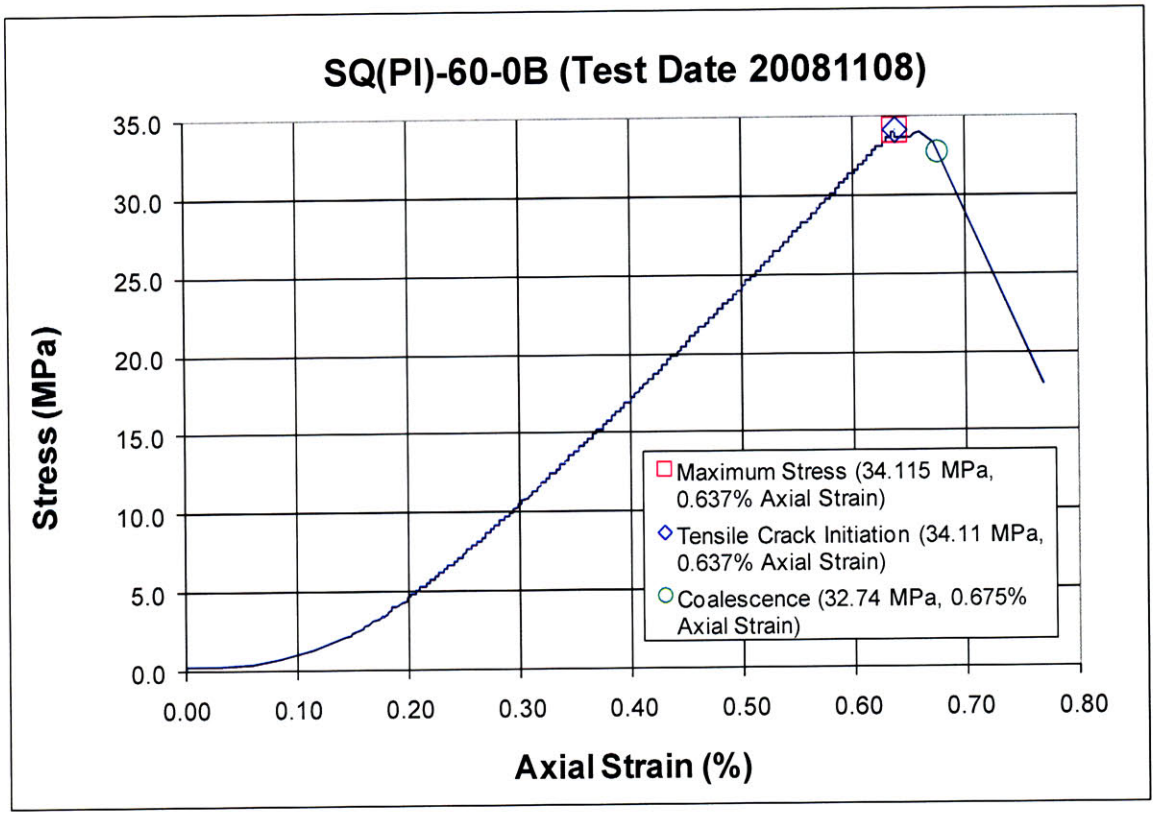

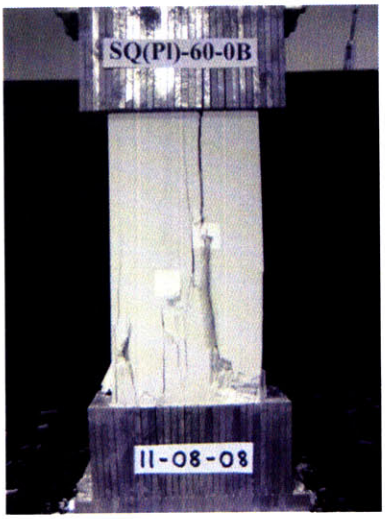

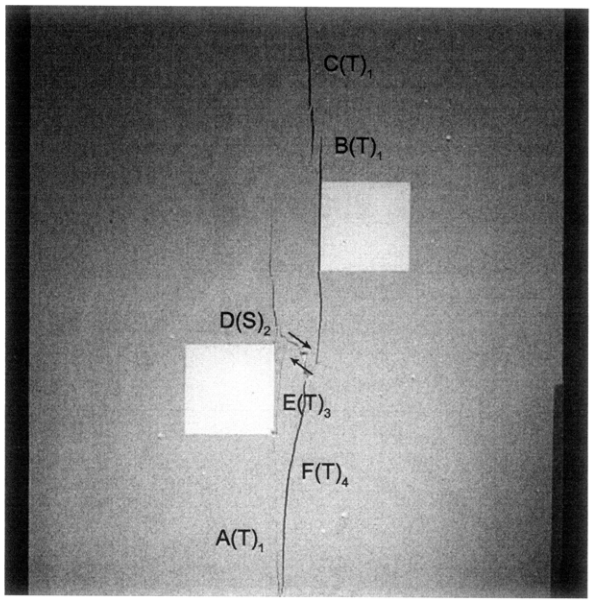

(Recorded by High Speed Video System)

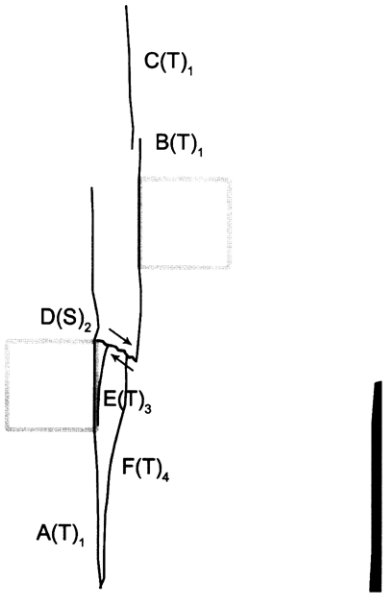

(32.74 MPa) – Coalescence
Time: 7 minutes & 16.114 seconds
HS Image # - 3403

Tensile crack (F) continues to propagate, until its coalescence with tensile crack (A).

Shear crack (D) also continues to propagate, until its coalescence with tensile crack (B).

The two inclusions coalesce in an indirect manner.

Specimen Number: SQ(PI)-60-0C (20081108)

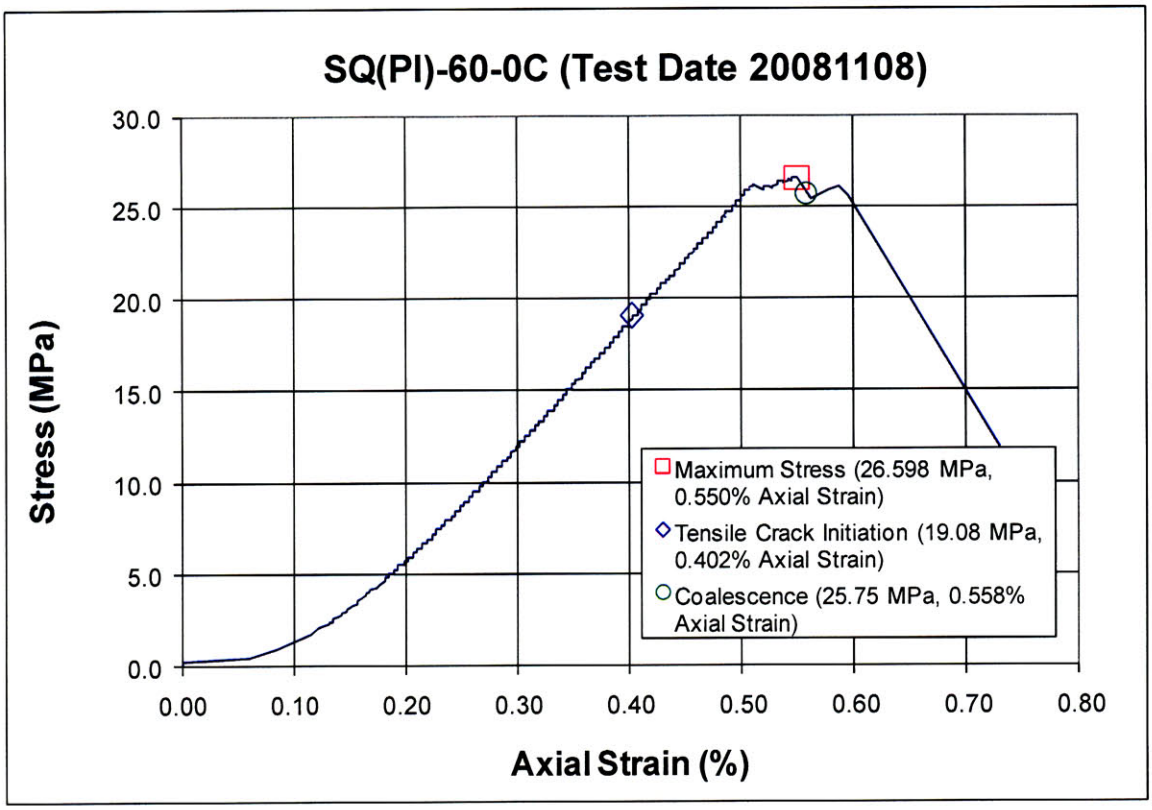

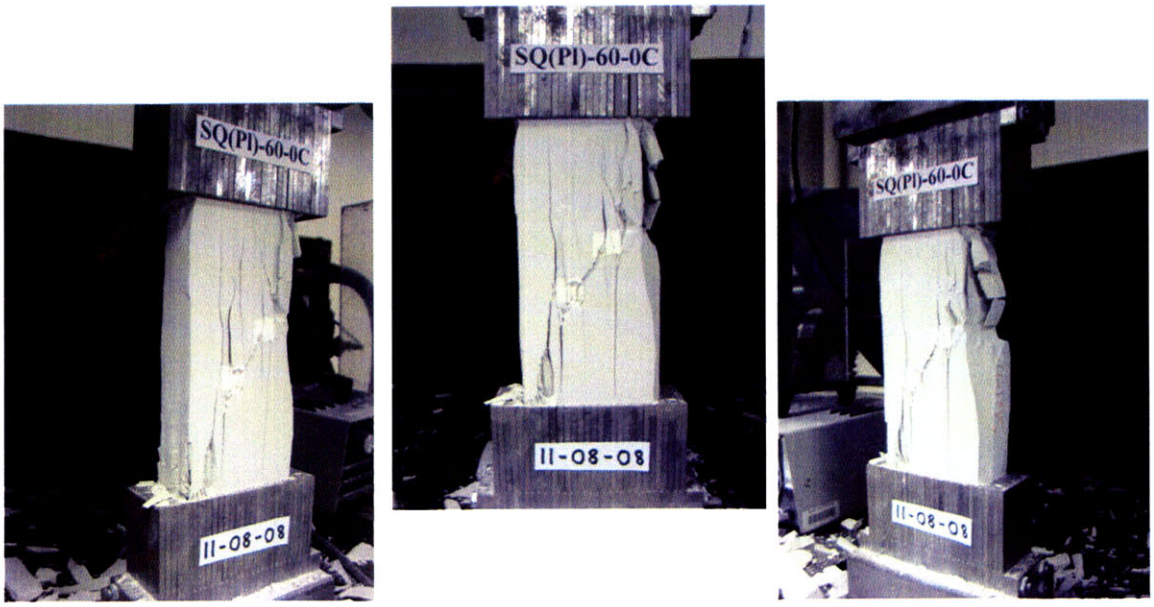

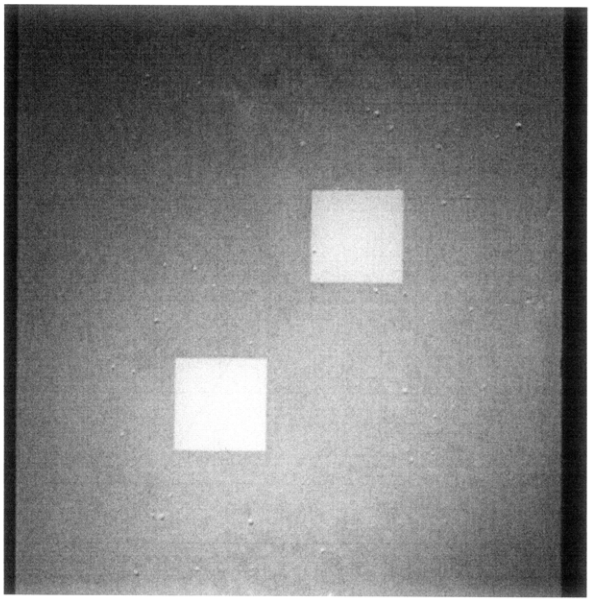

(Recorded by High Speed Video System)

Initial Inclusion Geometries:
SQUARES – Plaster Material

Inclusions **less** stiff than matrix.

High Speed Camera Frame Rate:
5000 pps

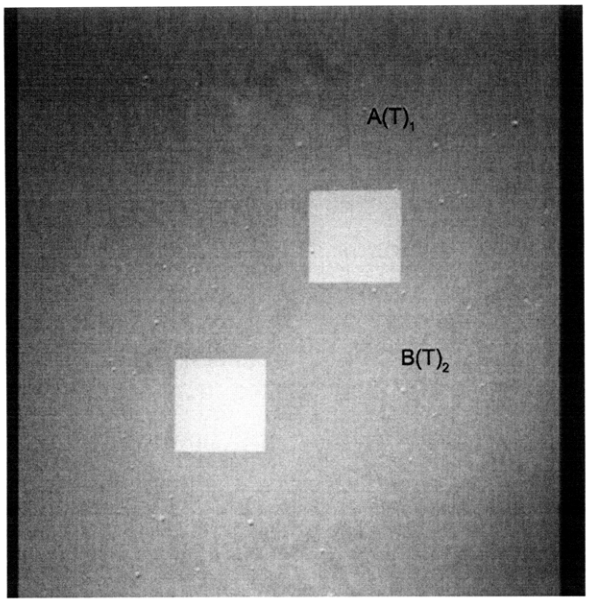

(Recorded by High Speed Video System)

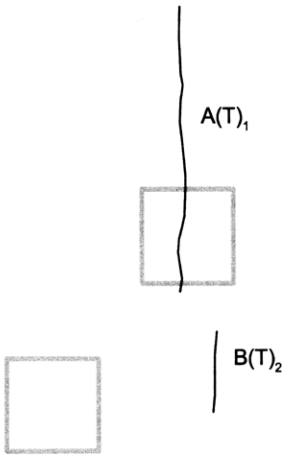

(19.08 MPa)

- Tensile Crack Initiation

Time: 3 minutes & 38.05 seconds

Tensile crack (A) initiates at the upper boundary of the right-hand inclusion and propagates vertically in both directions.

Tensile crack (B) then initiates below the right-hand inclusion and propagates downwards.

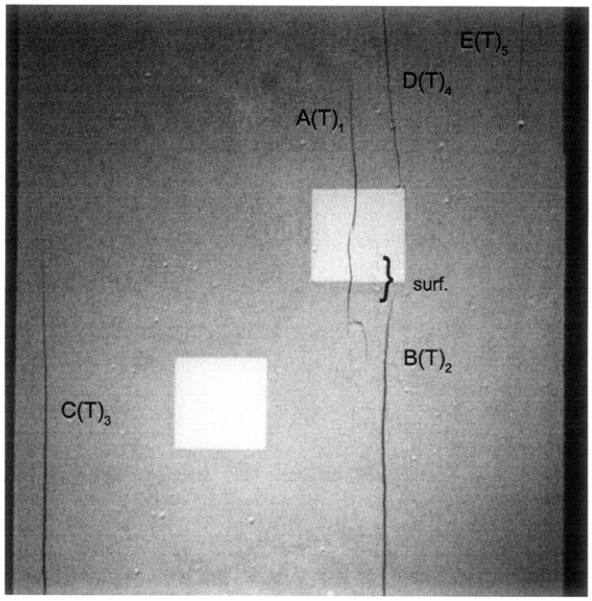

(Recorded by High Speed Video System)

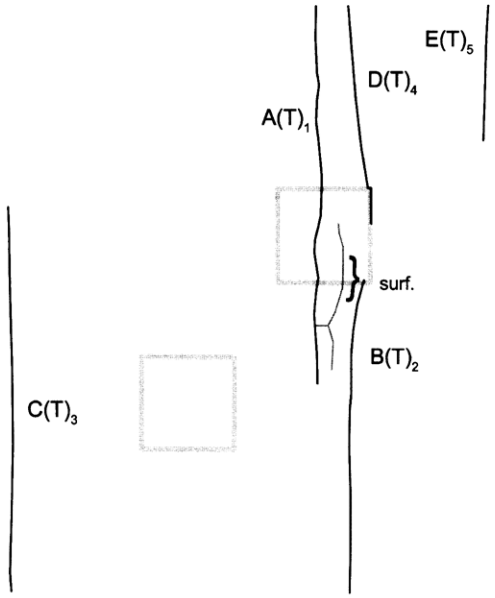

(22.54 MPa)
Time: 4 minutes & 26.66 seconds

Tensile crack (C) initiates at the lower specimen boundary and propagates upwards.

Tensile crack (D) initiates at the boundary of the right-hand inclusion and propagates upwards, and also begins to propagate along the inclusion boundary.

Tensile crack (E) initiates at the upper specimen boundary and propagates downwards.

Surface cracking (surf.) initiates adjacent to tensile crack (A) with an increase in loading.

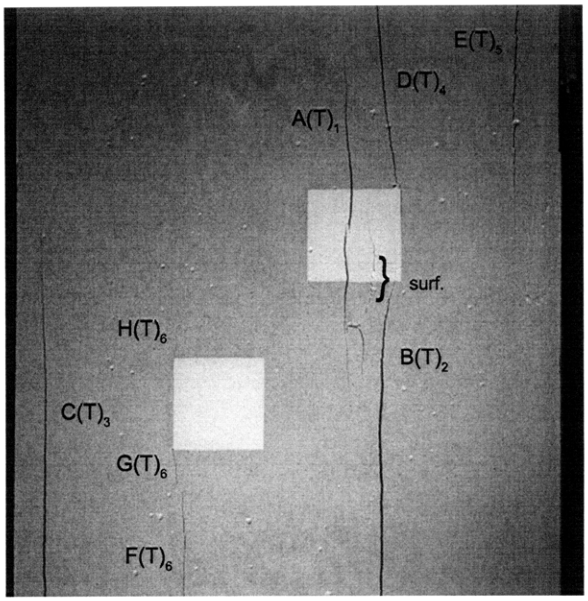

(Recorded by High Speed Video System)

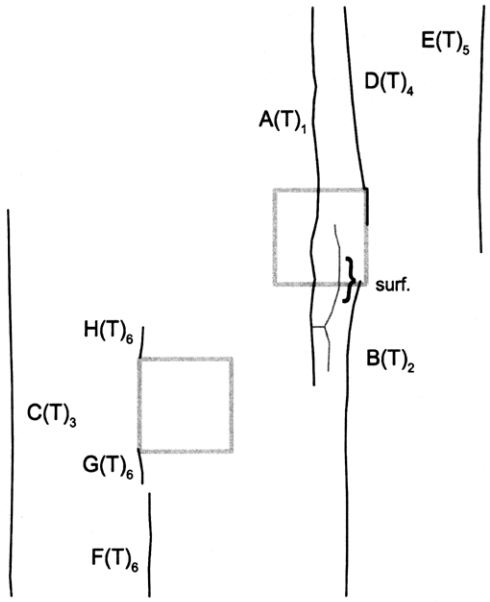

(26.54 MPa)
Time: 5 minutes & 23.042 seconds

Tensile crack (F) initiates at the lower specimen boundary and propagates upwards, towards the left-hand inclusion.

Tensile cracks (G&H) initiate at the boundary of the left-hand inclusion and propagate downwards and upwards, respectively.

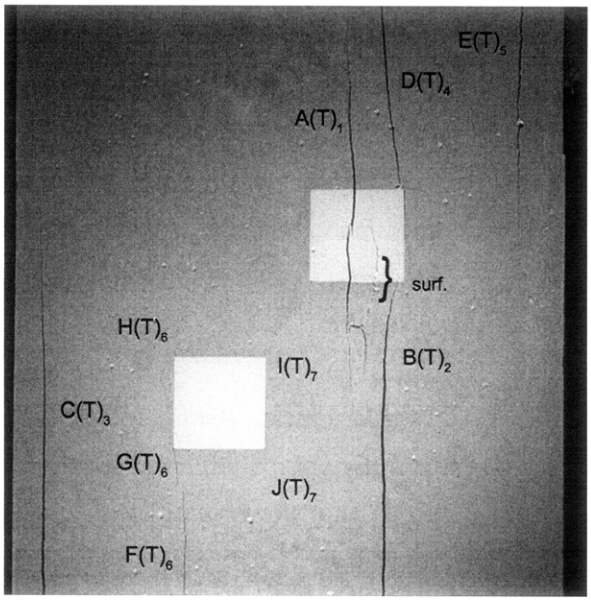

(Recorded by High Speed Video System)

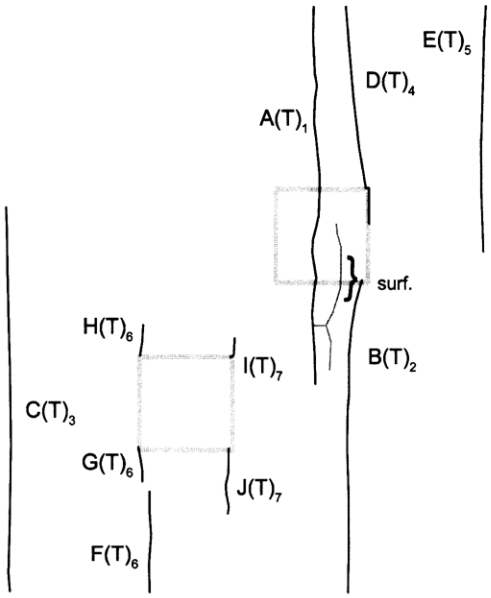

(26.598 MPa) [Max. Stress]
Time: 5 minutes & 23.834 seconds

Tensile cracks (I&J) initiate at the boundary of the left-hand inclusion and propagate upwards and downwards, respectively.

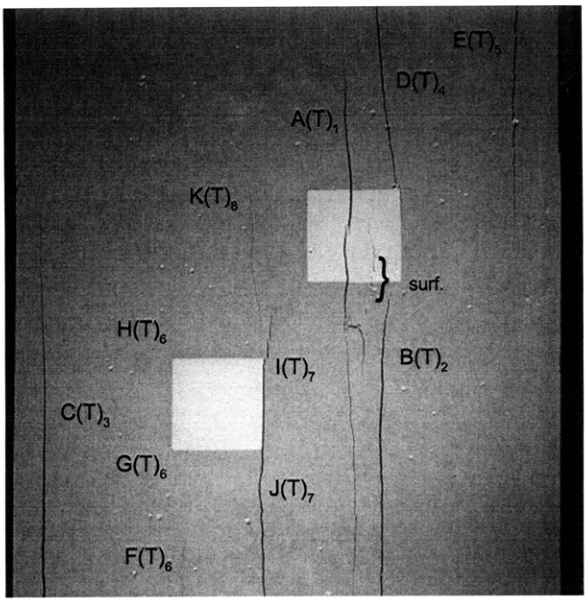

(Recorded by High Speed Video System)

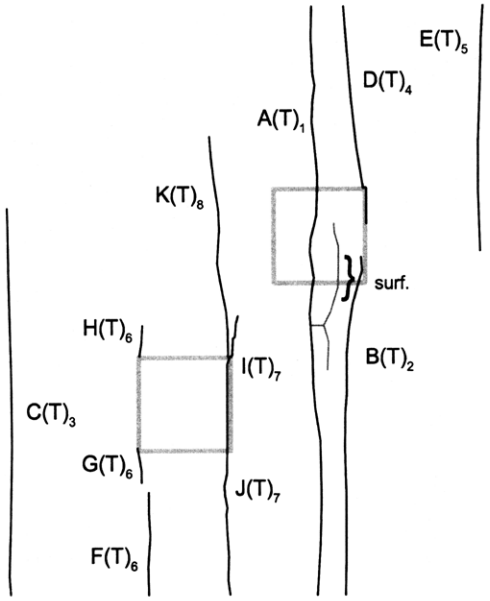

(25.78 MPa)
Time: 5 minutes & 23.908 seconds
HS Image # - 3706

Tensile crack (J) propagates upwards along the left-hand inclusion boundary, until its coalescence with tensile crack (I).

Tensile crack (K) then initiates at the upper boundary of the left-hand inclusion and propagates upwards.

Tensile crack (A) continues to propagate downwards towards the lower specimen boundary.

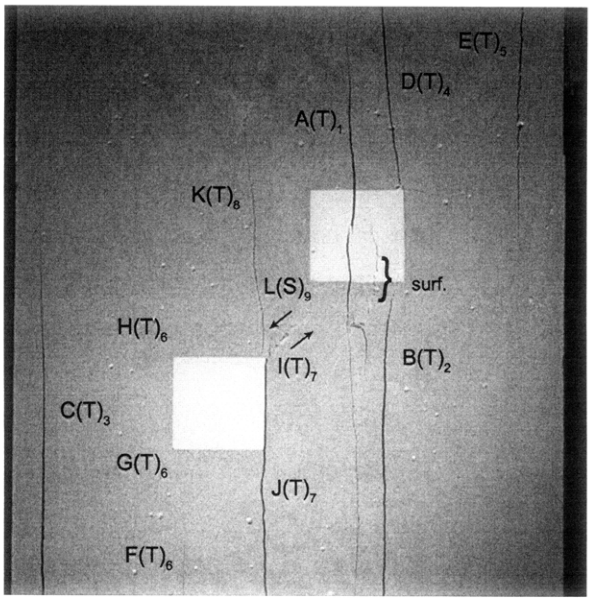

(Recorded by High Speed Video System)

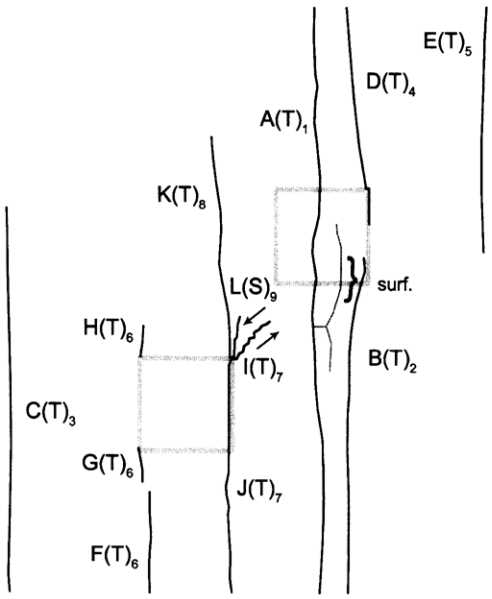

(25.76 MPa)
Time: 5 minutes & 23.910 seconds
HS Image # - 3696

Shear crack (L) initiates at the boundary of the left-hand inclusion and propagates upwards towards the right-hand inclusion.

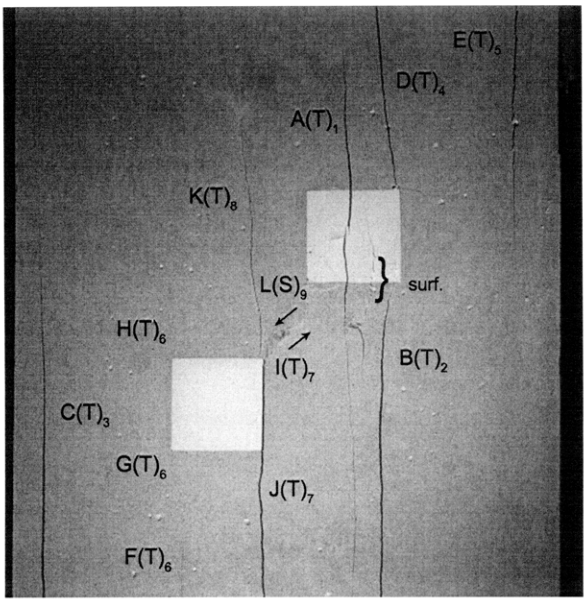

(Recorded by High Speed Video System)

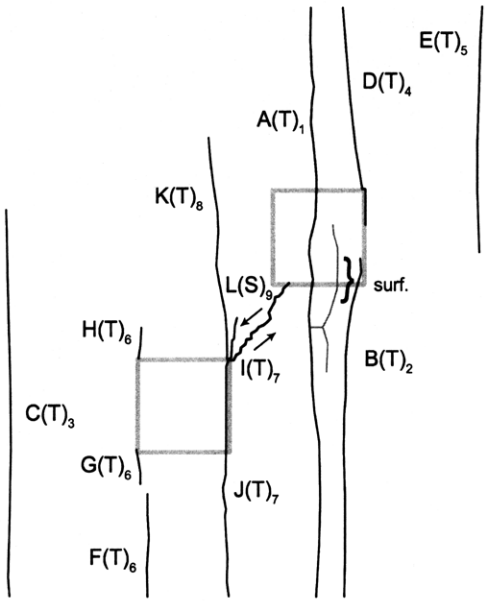

(25.75 MPa) - Coalescence
Time: 5 minutes & 23.910 seconds
HS Image # - 3695

Shear crack (L) continues to propagate, until its coalescence with the right-hand inclusion.

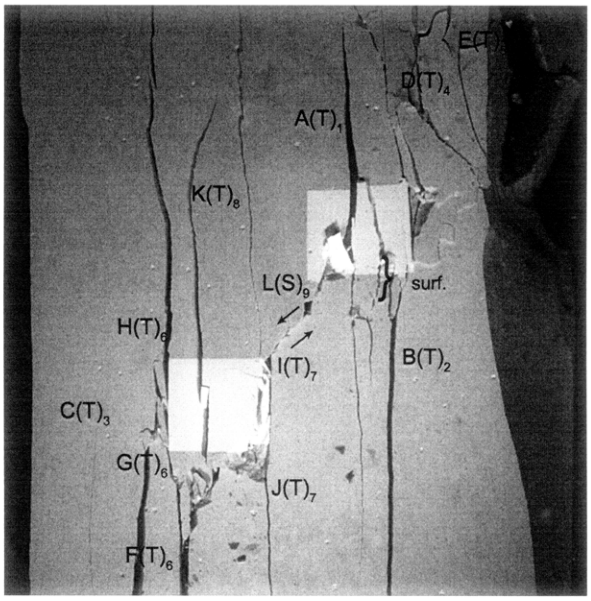

(Recorded by High Speed Video System)

(0 MPa) – Final Picture

Time: 5 minutes & 24.649 seconds

HS Image # - 1

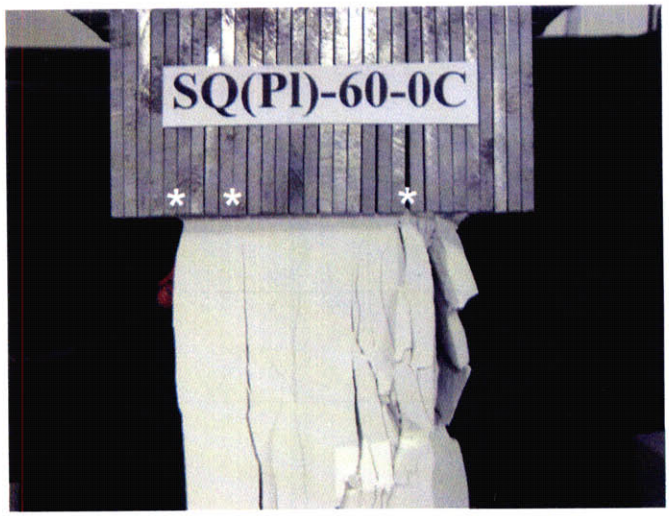	Upper edge of the specimen. The cracks marked with a (*) coincide with the openings between the teeth of the brush platen.
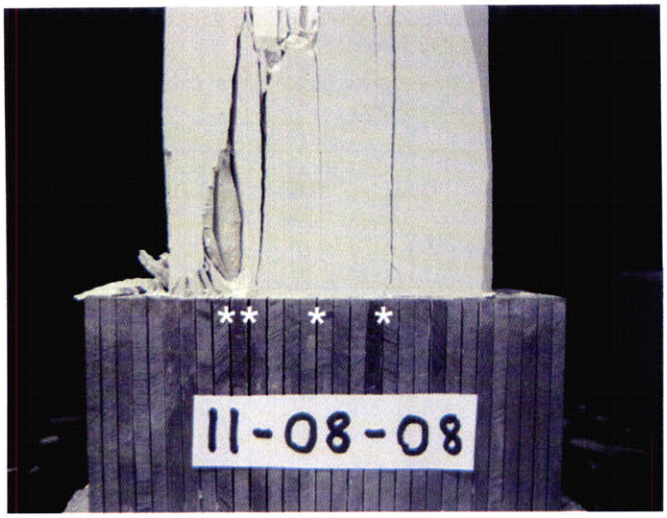	Lower edge of the specimen. The cracks marked with a (*) coincide with the openings between the teeth of the brush platen.

Specimen Number: SQ(UI)-60-0A (20081108)

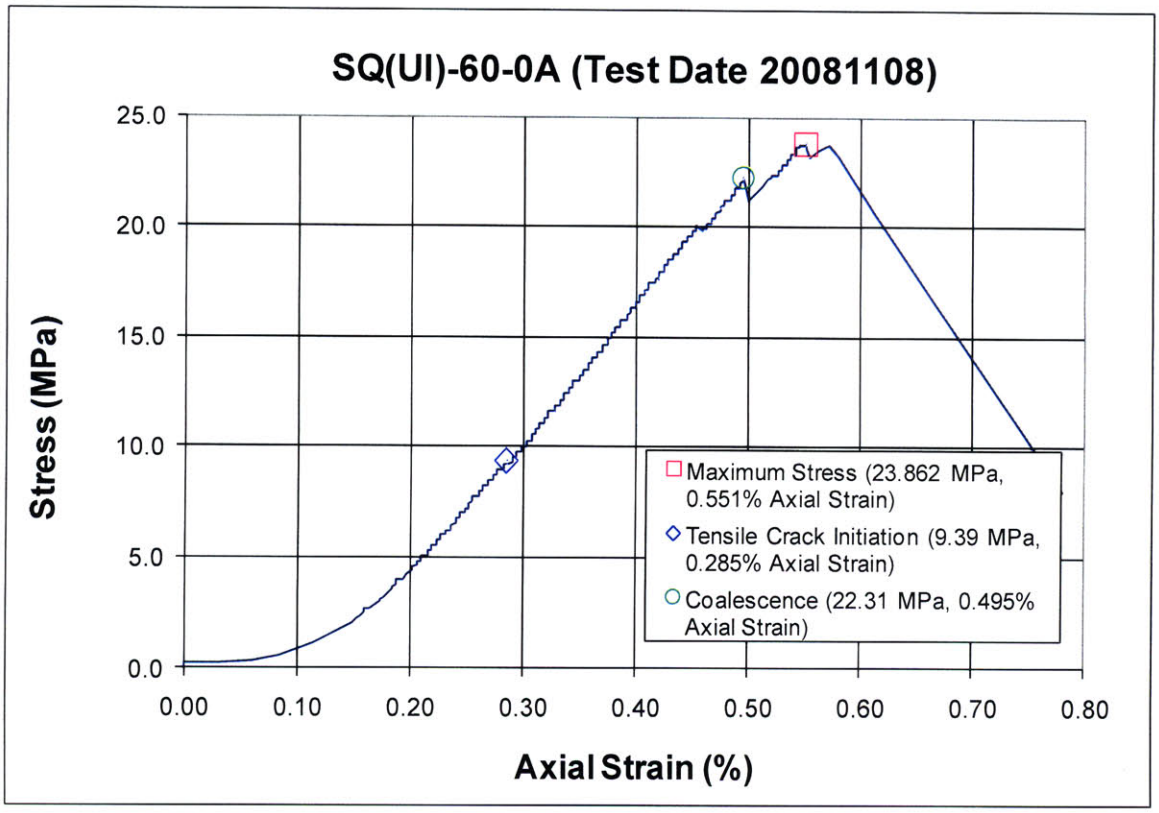

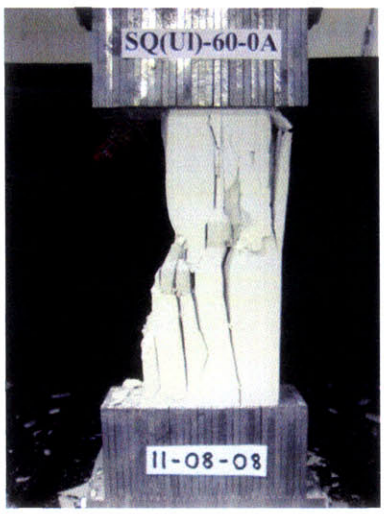

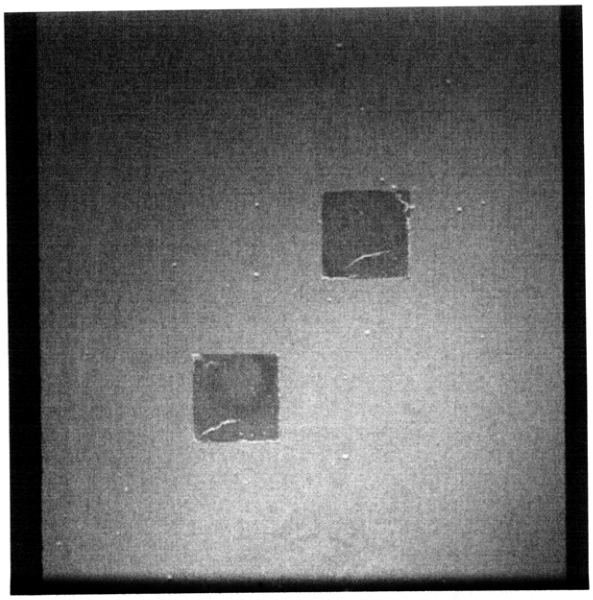

(Recorded by High Speed Video System)

Initial Inclusion Geometries:
SQUARES – Ultracal Material

Inclusions **more** stiff than matrix.

Initial surface cracks present prior to testing.

High Speed Camera Frame Rate:
5000 pps

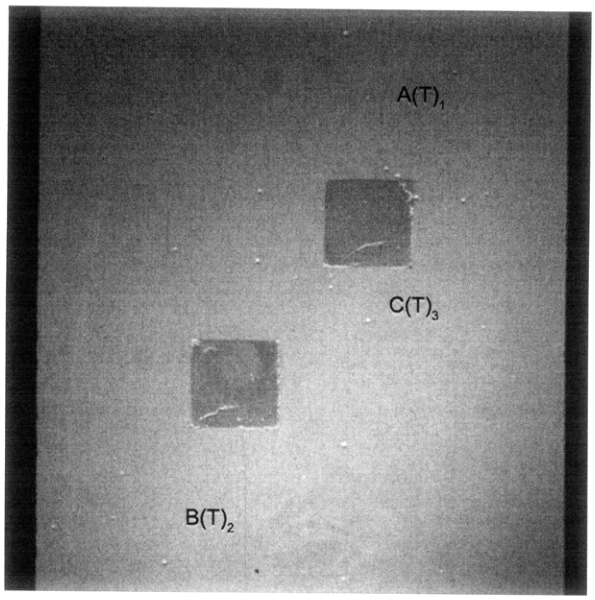

(Recorded by High Speed Video System)

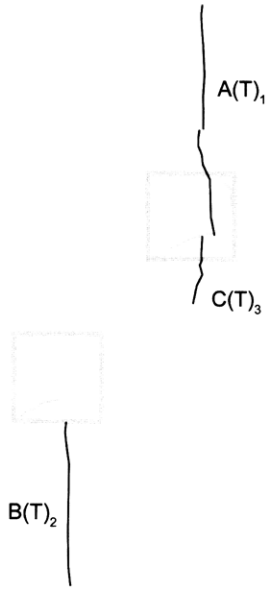

(9.39 MPa)

- Tensile Crack Initiation

Time: 1 minute & 24.87 seconds

Tensile crack (A) initiates at a pre-test surface crack located within the right-hand inclusion and propagates upwards.

Tensile crack (B) initiates at the boundary of the left-hand inclusion and propagates downwards.

Tensile crack (C) initiates at the same pre-test surface crack as tensile crack (A) and propagates downwards.

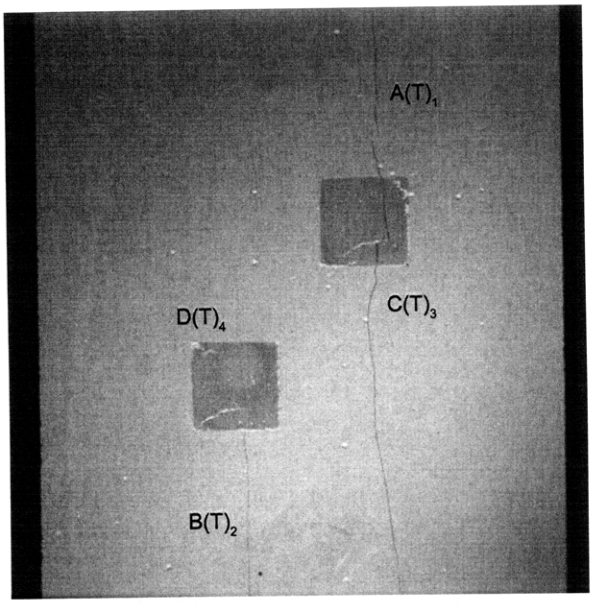

(Recorded by High Speed Video System)

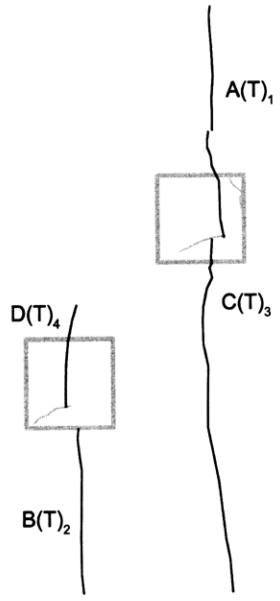

(16.94 MPa)
Time: 3 minutes & 12.25 seconds

As tensile cracks (A&C) continue to propagate, tensile crack (D) initiates at the pre-test surface crack located within the left-hand inclusion and propagates upwards.

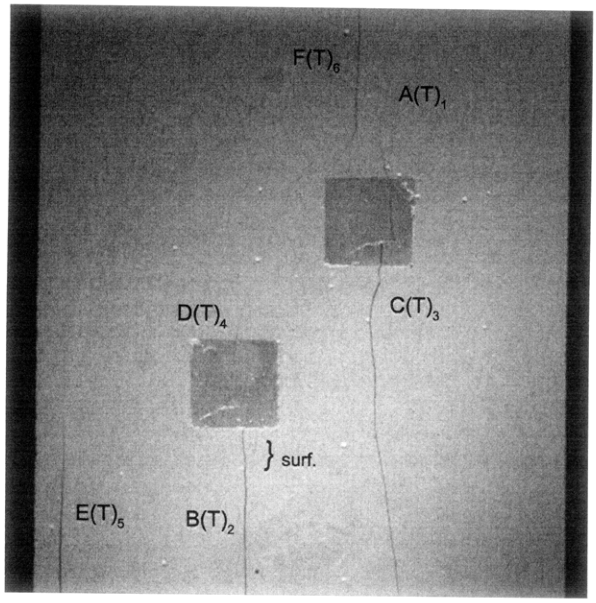

(Recorded by High Speed Video System)

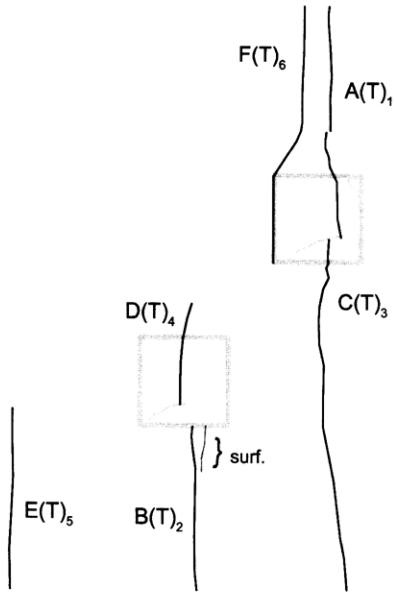

(20.13 MPa)
Time: 3 minutes & 57.57 seconds

Tensile crack (E) initiates at the lower specimen boundary and propagates upwards.

Tensile crack (F) then initiates above the right inclusion and propagates upwards and downwards. Tensile crack (F) then intersects and propagates along the boundary of the right-hand inclusion.

Surface crack (surf.) initiates at the boundary of the left-hand inclusion and propagates downwards, adjacent to tensile crack (B).

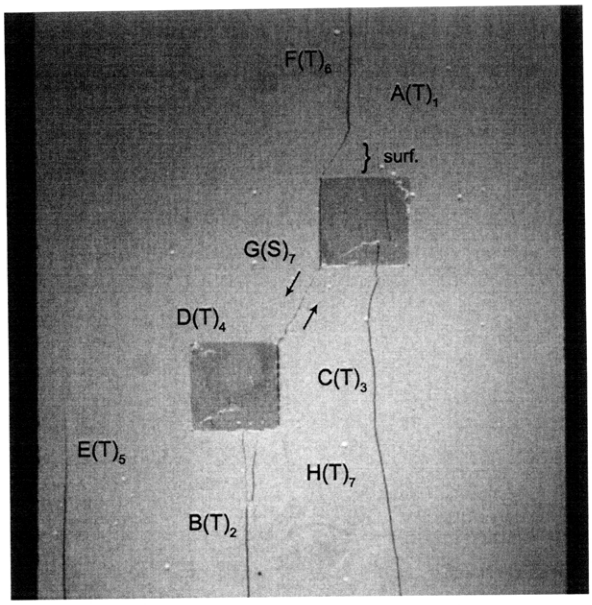

(Recorded by High Speed Video System)

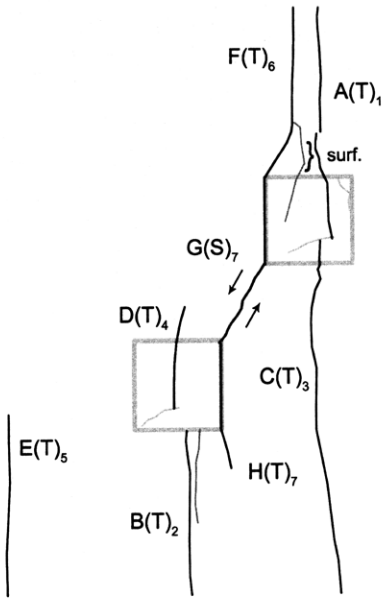

(22.31 MPa) - Coalescence
Time: 4 minutes & 28.95 seconds

A new surface crack (surf.) initiates adjacent to tensile crack (F).

Shear crack (G) then initiates at the right-hand inclusion boundary and propagates downwards, until its coalescence with the left-hand inclusion.

Tensile crack (H) initiates at the left-hand inclusion boundary, where the coalescence of shear crack (G) occurred, and propagates downwards along the boundary.

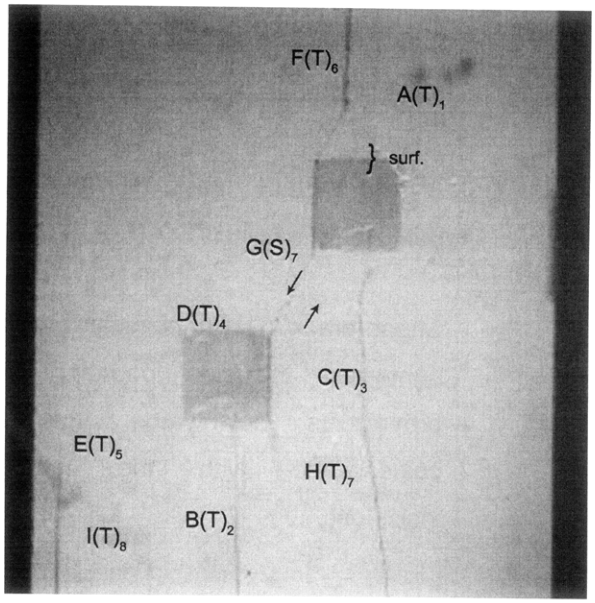

(Recorded by Camcorder)

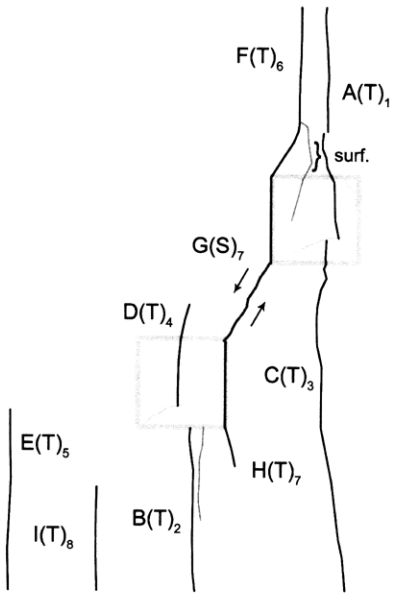

(23.862 MPa) [Max. Stress]
Time: 4 minutes & 50.46 seconds

Tensile crack (I) initiates at the lower specimen boundary and propagates upwards.

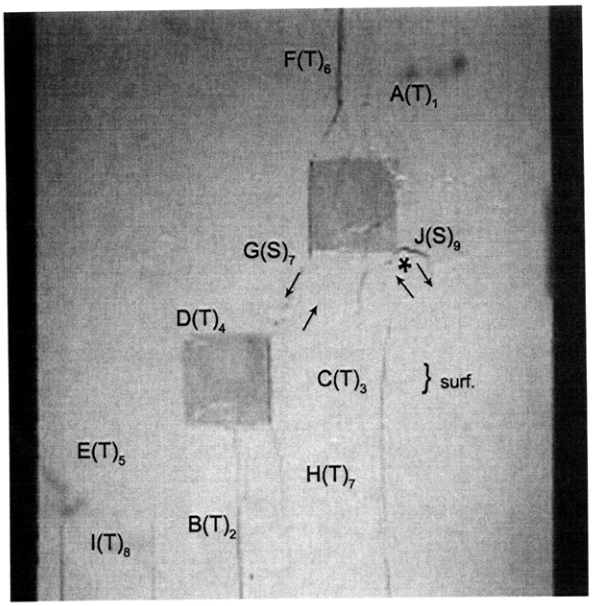

(Recorded by Camcorder)

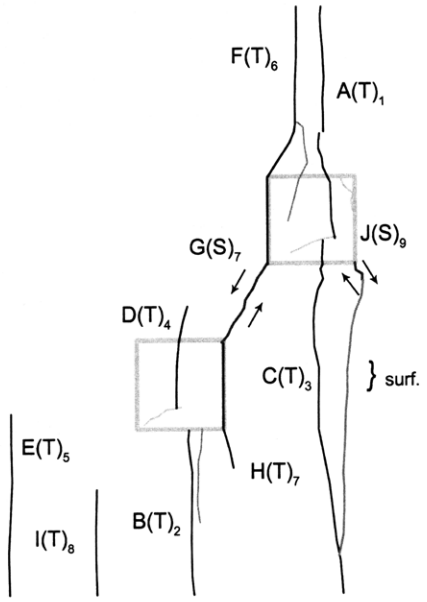

(23.78 MPa) – Ultimate Failure
Time: 4 minutes & 51.06 seconds

Shear crack (J) initiates at the boundary of the right-hand inclusion and propagates downwards. Spalling (*) initiates adjacent to shear crack (J).

A surface crack (surf.) then initiates at shear crack (J) and propagates downwards, until its coalescence with tensile crack (C).

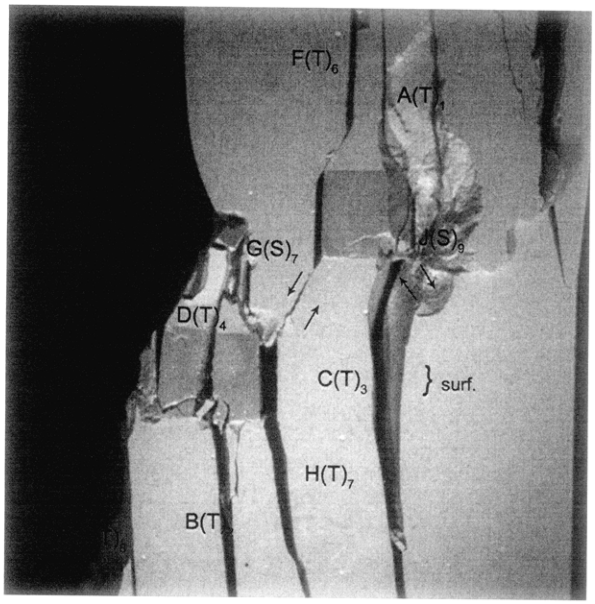

(Recorded by High Speed Video System)

(0 MPa) – Final Picture

HS Image # - 2945

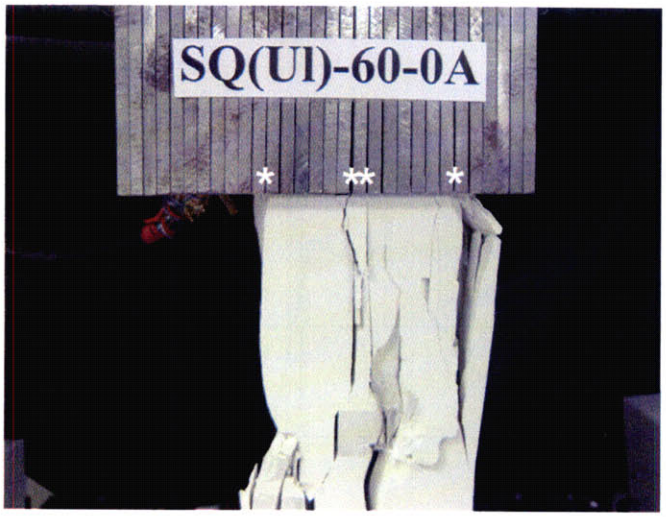	Upper edge of the specimen. The cracks marked with a (*) coincide with the openings between the teeth of the brush platen.
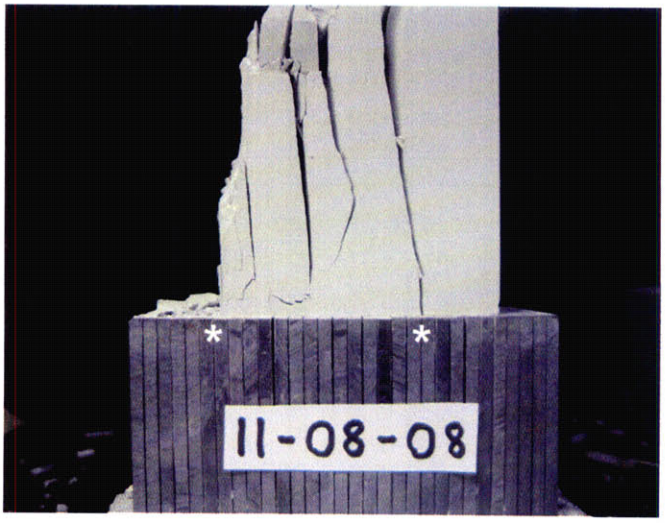	Lower edge of the specimen. The cracks marked with a (*) coincide with the openings between the teeth of the brush platen.

SUMMARY

Specimen Number: SQ(UI)-60-0B (20081108)

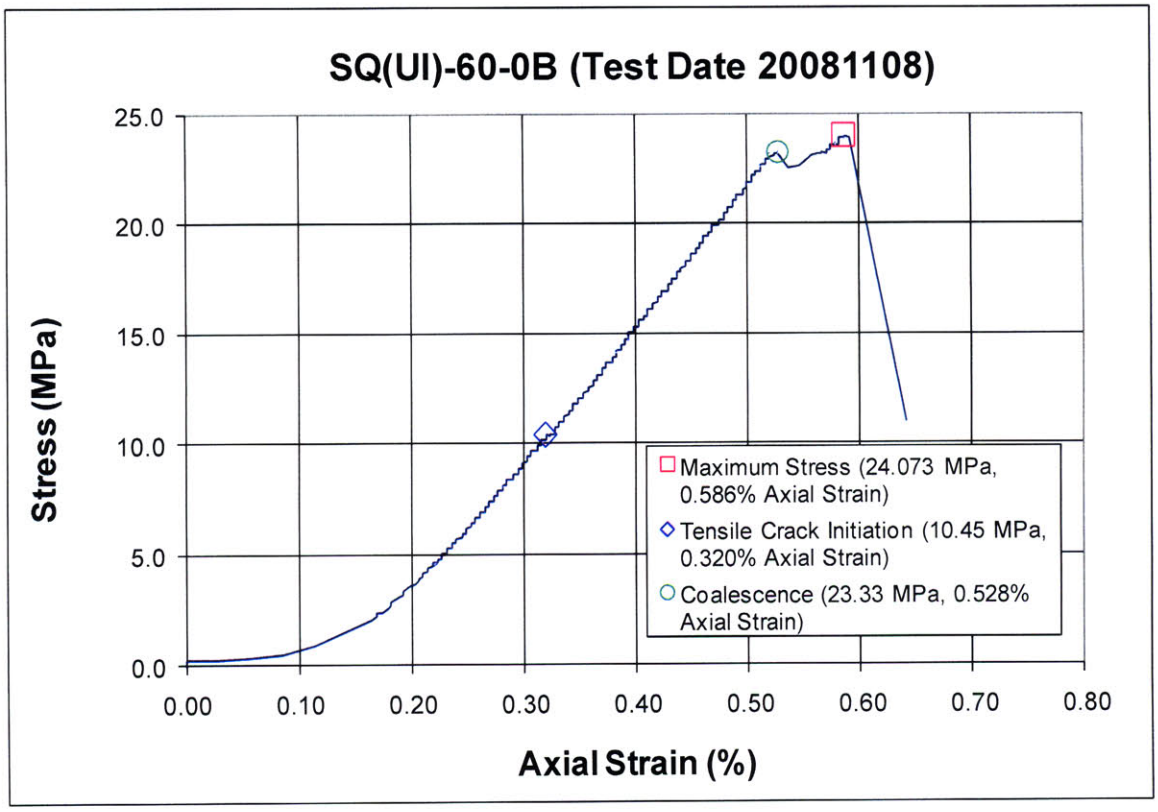

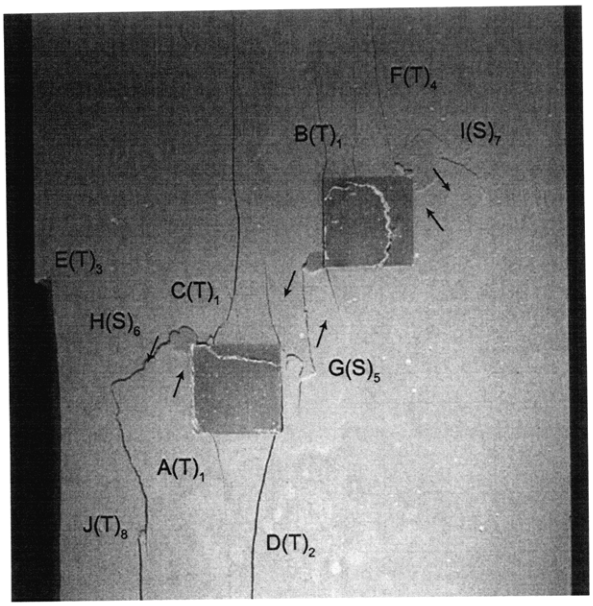

(Recorded by High Speed Video System)

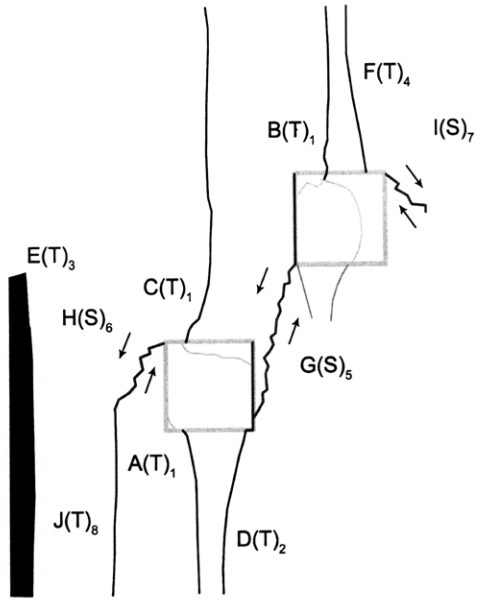

(24.073 MPa) [Max. Stress]
Time: 4 minutes & 54.36 seconds

Tensile crack (J) initiates at the lower specimen boundary and propagates upwards, until its coalescence with shear crack (H).

SUMMARY

Specimen Number: SQ(UI)-60-0C (20081108)

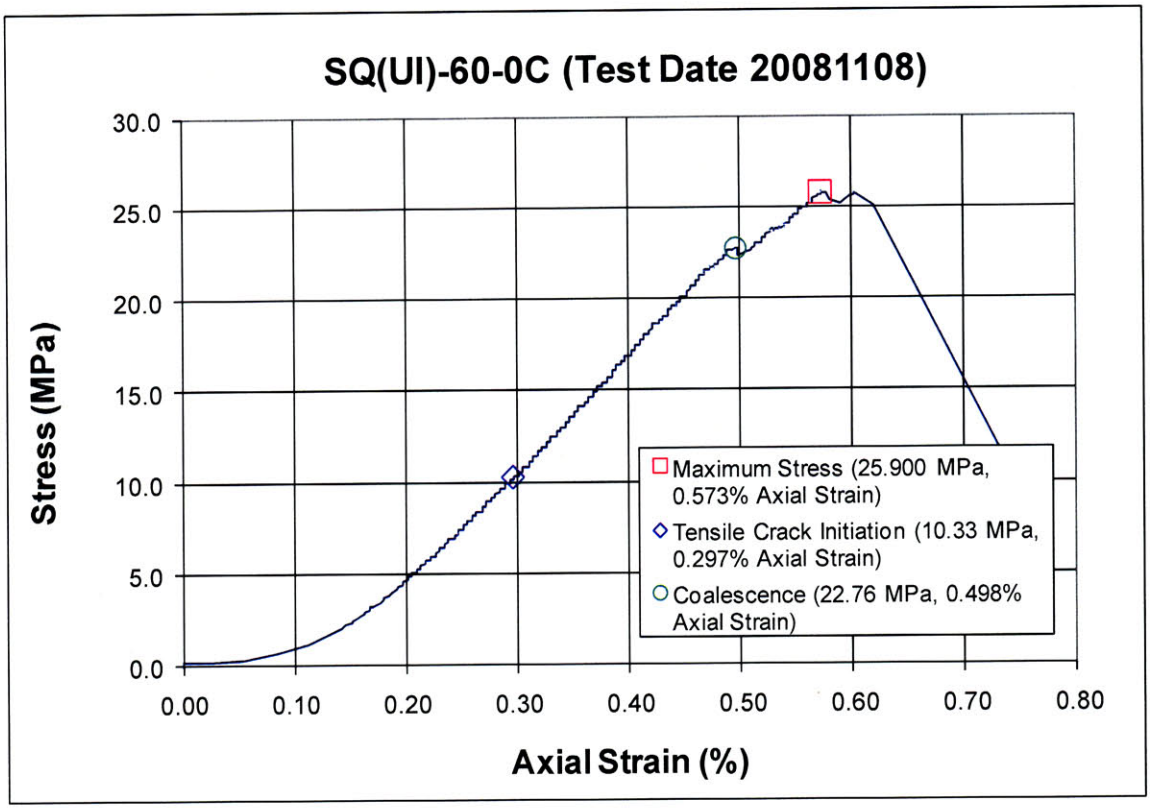

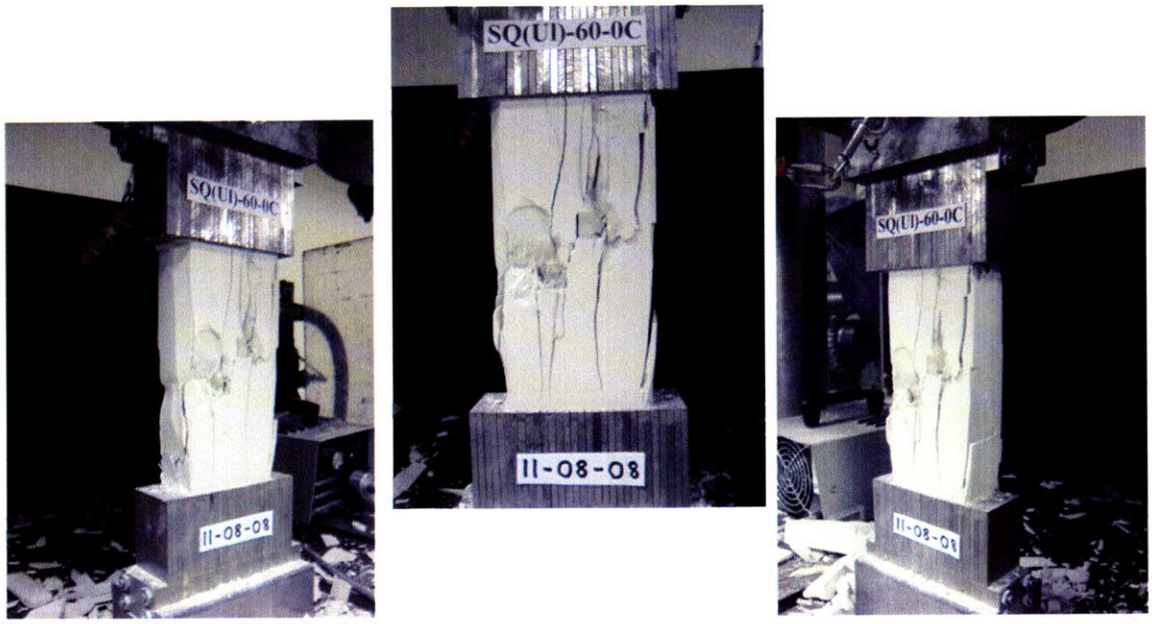

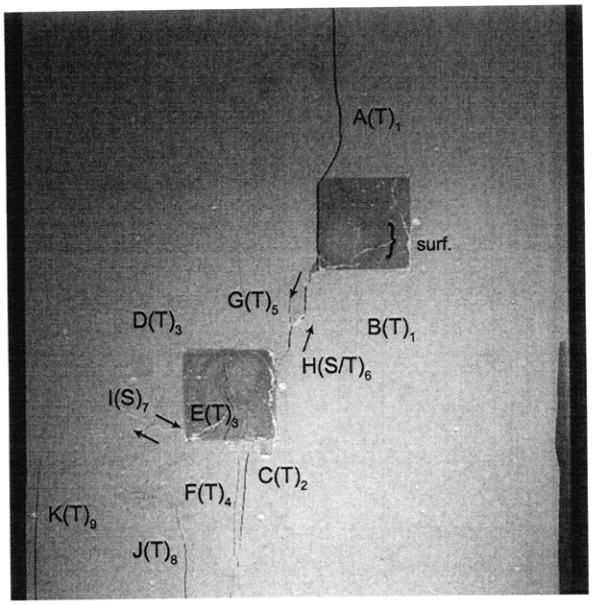

(Recorded by Camcorder)

(25.900 MPa) [Max. Stress]
Time: 5 minutes & 17.13 seconds

Shear crack (I) initiates at the boundary of the left-hand inclusion and propagates upwards.

Tensile crack (J) initiates at the lower specimen boundary and propagates upwards, until its coalescence with shear crack (I).

Tensile crack (K) then initiates at the lower specimen boundary and propagates upwards.

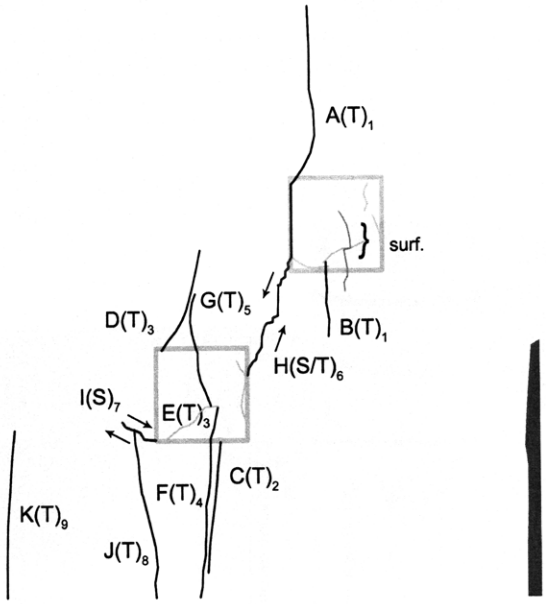

SUMMARY

Specimen Number: SQ(PI)-75-0A (20090213)

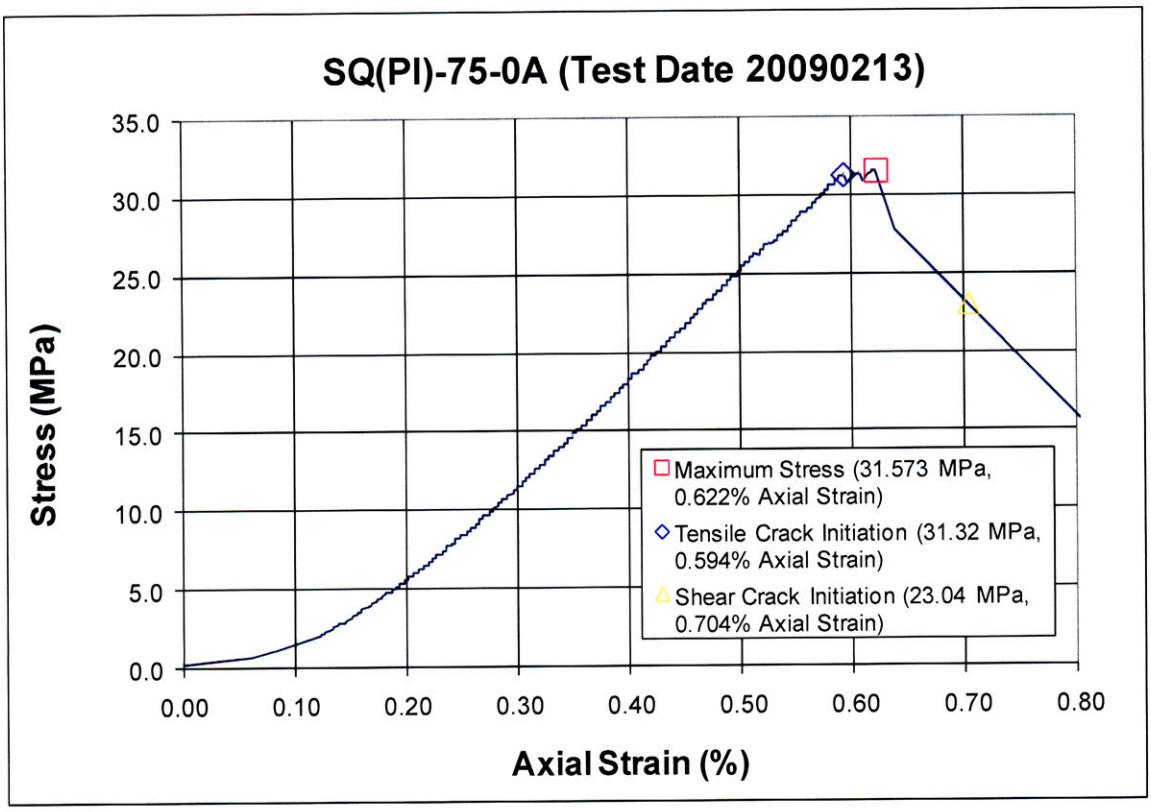

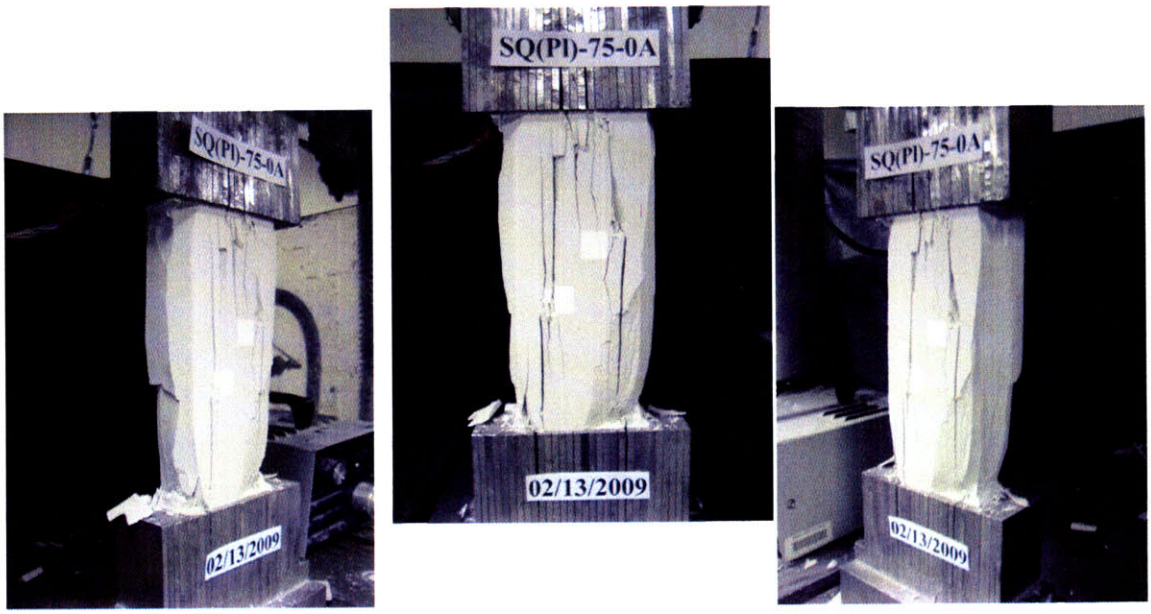

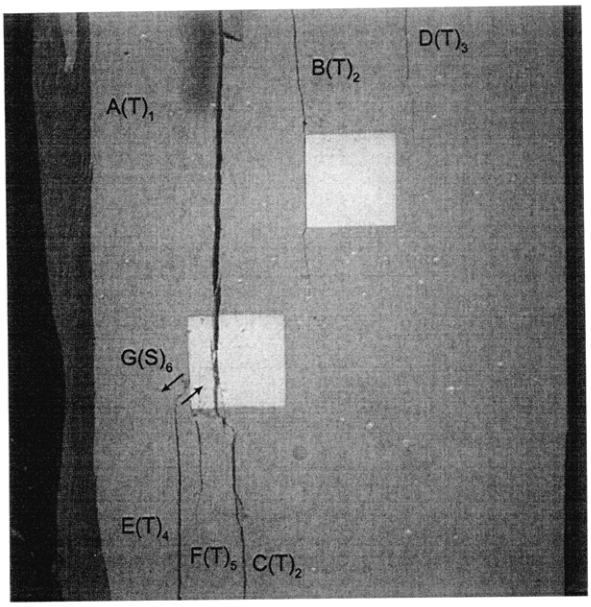

(Recorded by High Speed Video System)

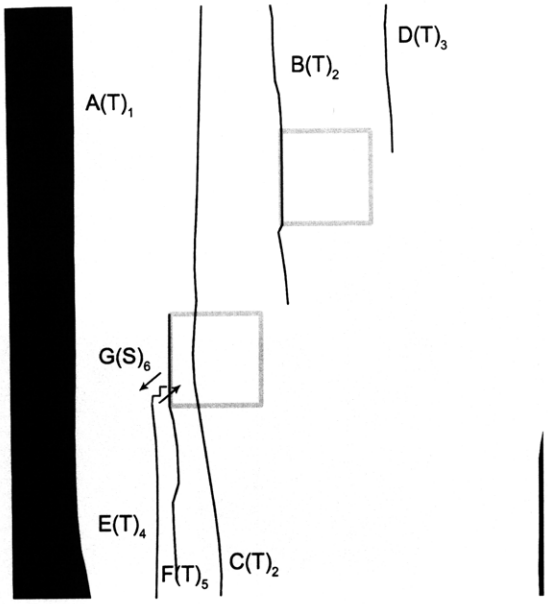

(23.04 MPa)

- Shear Crack Initiation

Time: 6 minutes & 35.656 seconds

HS Image # - 3089

As debonding initiates at the boundary of the left-hand inclusion, tensile crack (F) initiates and propagates downwards.

Shear crack (G) then initiates at the left-hand inclusion boundary and propagates, until its coalescence with tensile crack (E).

Specimen Number: SQ(PI)-75-0B (20090213)

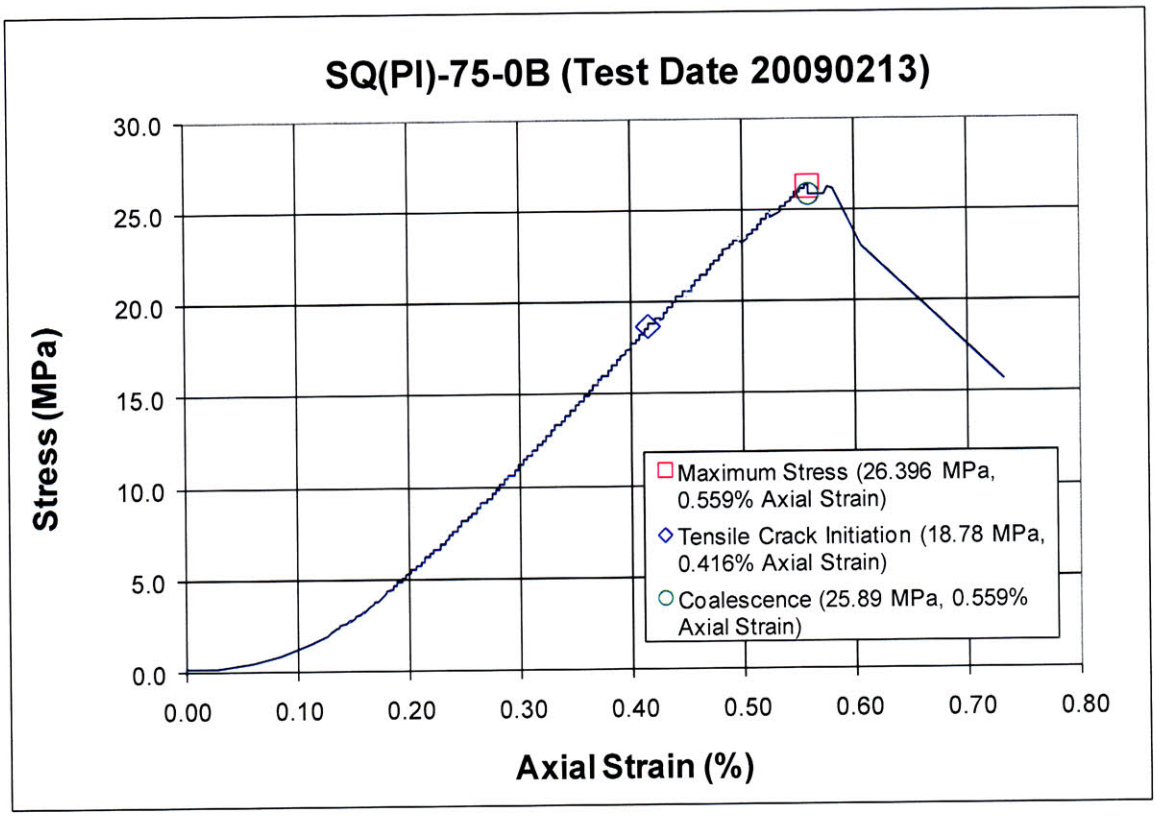

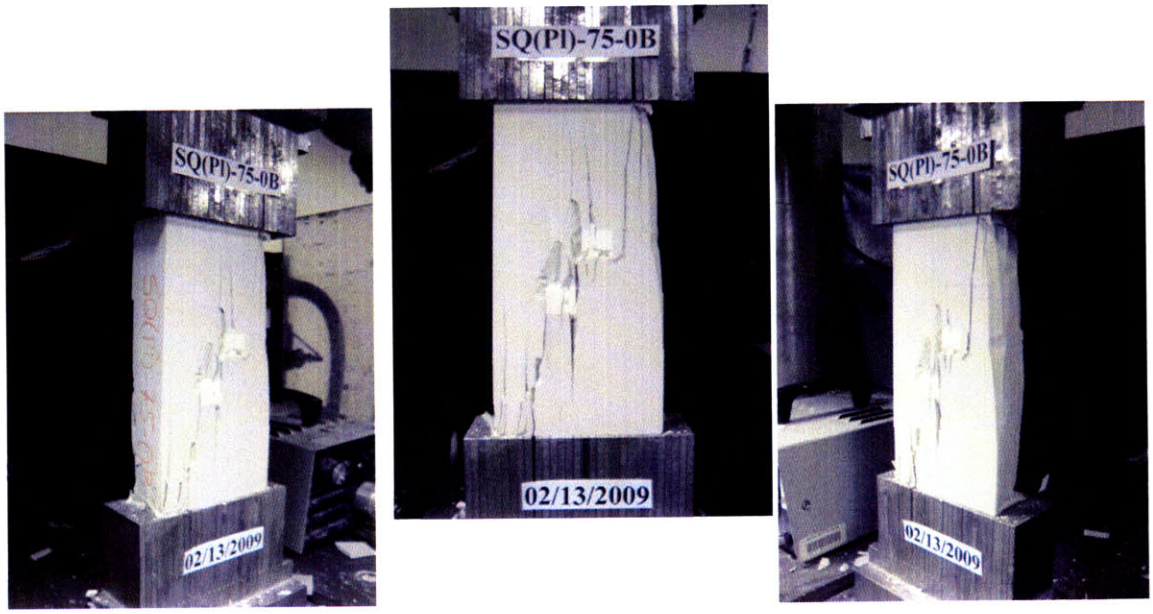

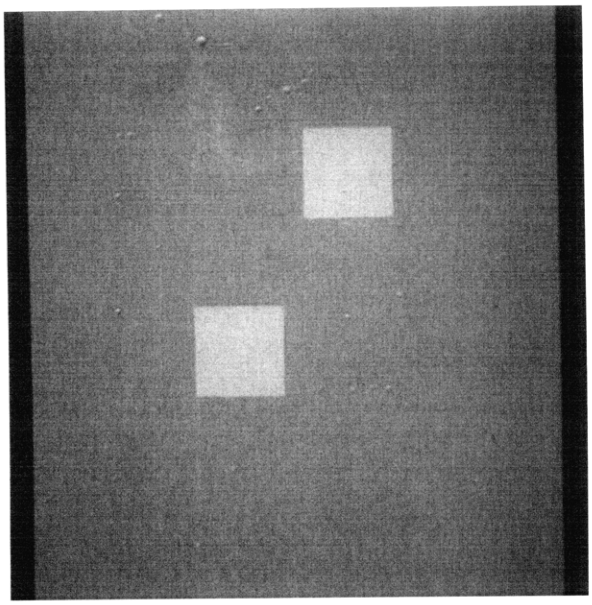

(Recorded by High Speed Video System)

Initial Inclusion Geometries:
SQUARE – Plaster Material

Inclusions **less** stiff than matrix.

High Speed Camera Frame Rate:
5000 pps

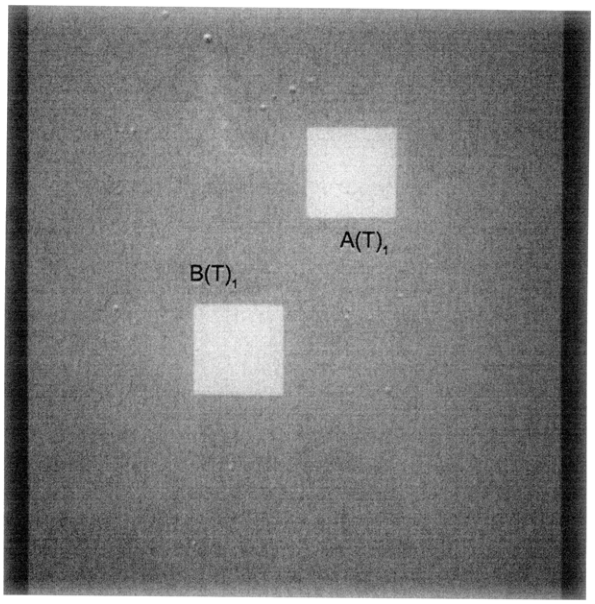

(Recorded by High Speed Video System)

(18.78 MPa)

- Tensile Crack Initiation

Time: 3 minutes & 36.30 seconds

Tensile cracks (A&B) initiate simultaneously at the lower right-hand and upper left-hand inclusion boundary, respectively.

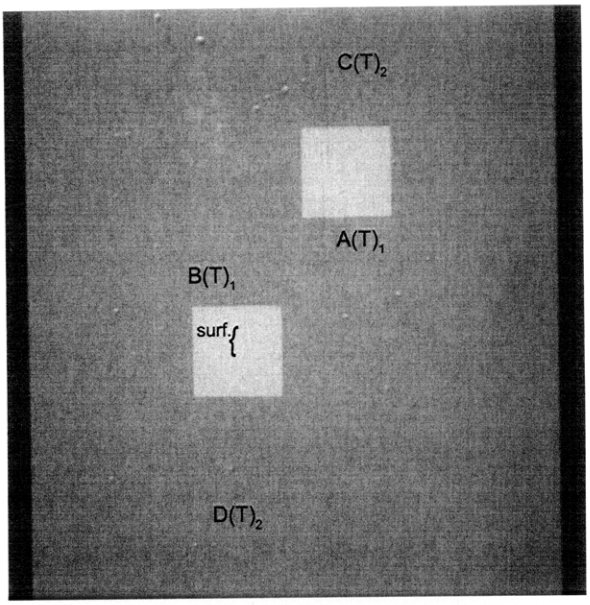

(Recorded by High Speed Video System)

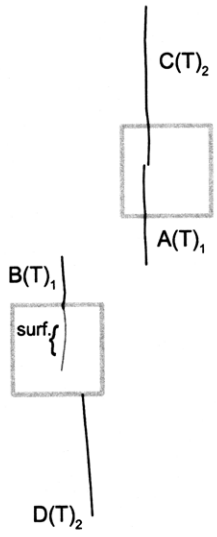

(19.19 MPa)
Time: 3 minutes & 42.27 seconds

The following occurs "simultaneously":

Tensile crack (A) propagates upwards and downwards.

Tensile crack (B) propagates upwards, as surface crack (surf.) propagates downwards, into the inclusion, from the same initiation point as tensile crack (B).

Tensile crack (C) initiates at the upper right-hand inclusion boundary, and propagates upwards and downwards.

Tensile crack (D) initiates at the lower left-hand inclusion boundary and propagates downwards.

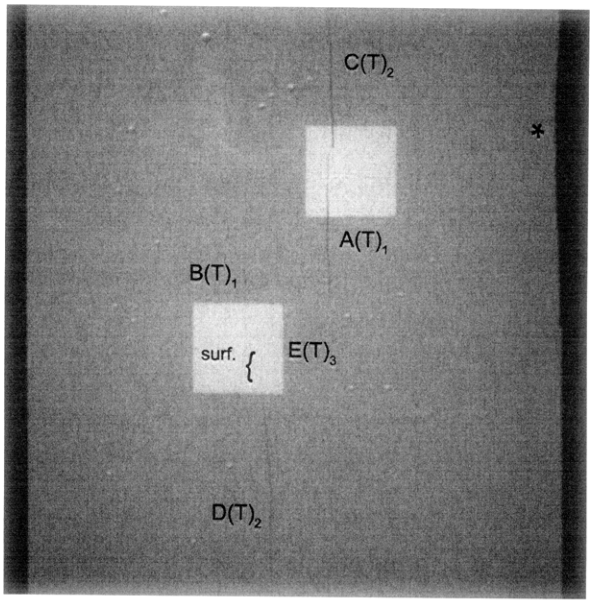

(Recorded by High Speed Video System)

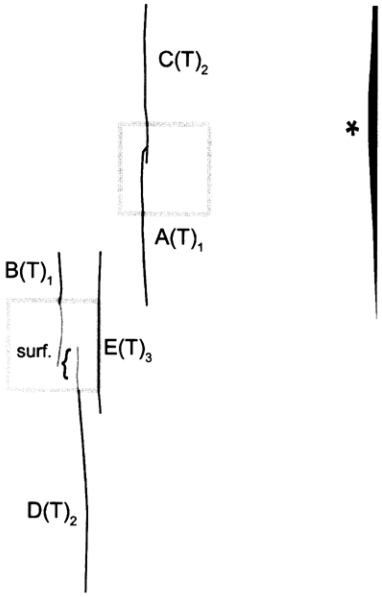

(24.96 MPa)
Time: 5 minutes & 3.25 seconds

A piece of specimen (*) detaches from the upper right specimen boundary. Tensile crack (A) continues to propagate until its coalescence with tensile crack (C).

Debonding then initiates at the boundary of the left-hand inclusion. This results in the initiation of tensile crack (E), which propagates upwards and downwards.

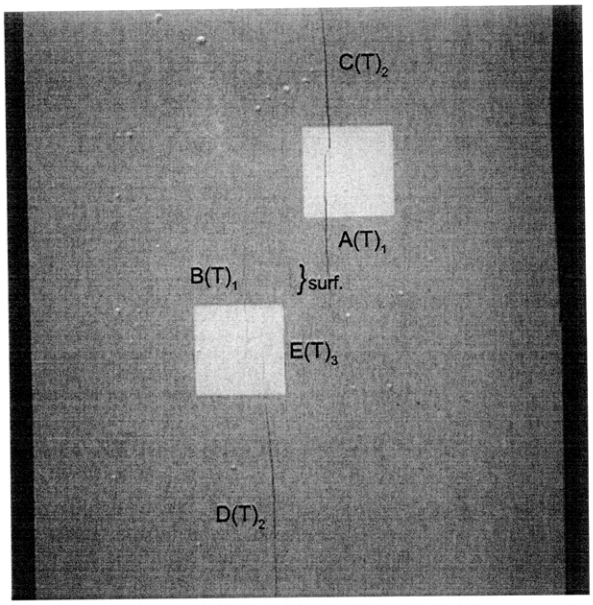

(Recorded by High Speed Video System)

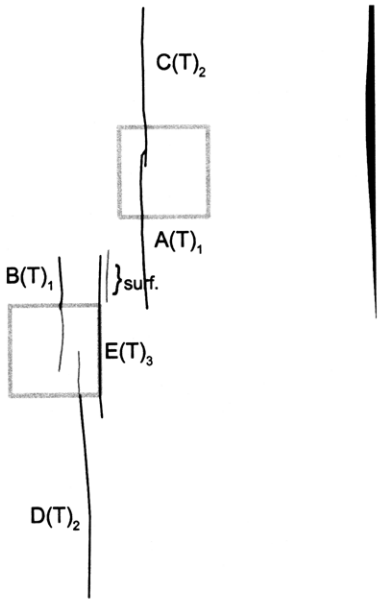

(26.396 MPa) [Max. Stress]
Time: 5 minutes & 23.576 seconds

Surface crack (surf.) initiates adjacent to tensile crack (E).

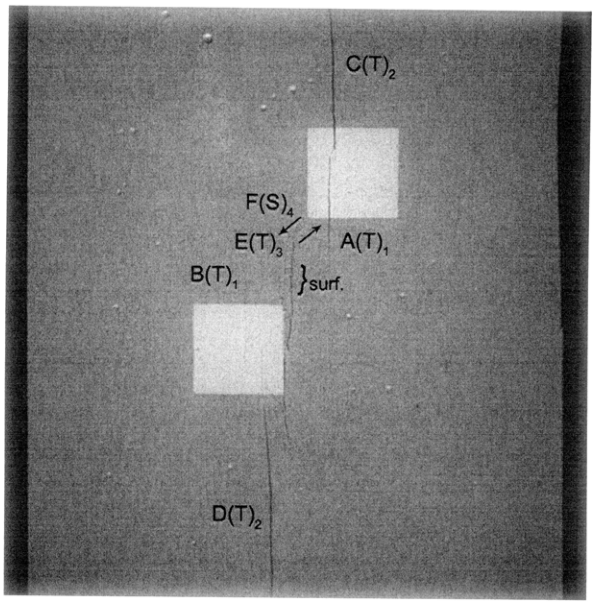

(Recorded by High Speed Video System)

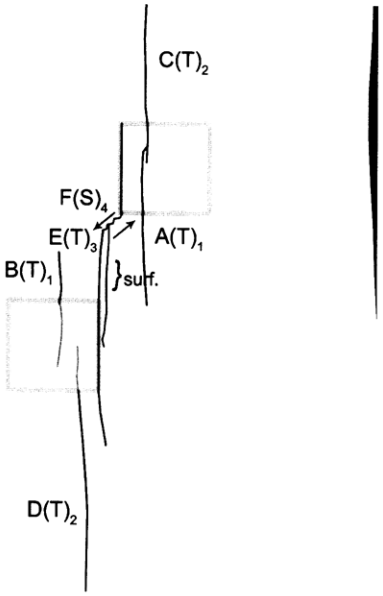

(25.89 MPa) – Coalescence
Time: 5 minutes & 23.678 seconds
HS Image # - 5318

Shear crack (F) initiates at the right-hand inclusion boundary and propagates downwards, until its coalescence with tensile crack (E). This results in debonding at the left boundary of the right-hand inclusion.

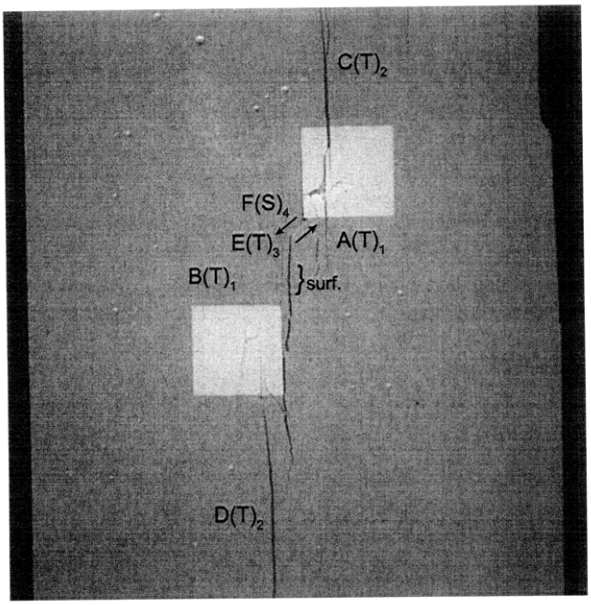

(Recorded by High Speed Video System)

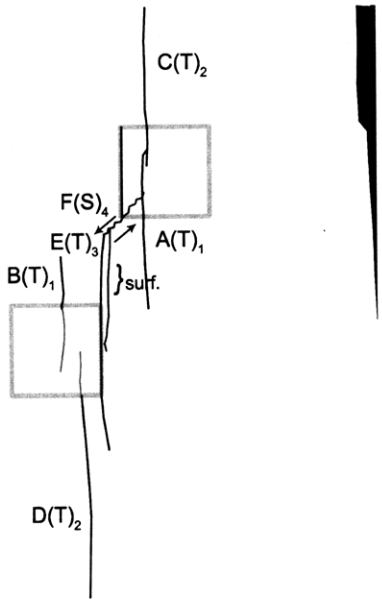

(24.45 MPa)
Time: 5 minutes & 24.032 seconds
HS Image # - 3550

Shear crack (F) continues to propagate upwards, until its coalescence with tensile crack (A).

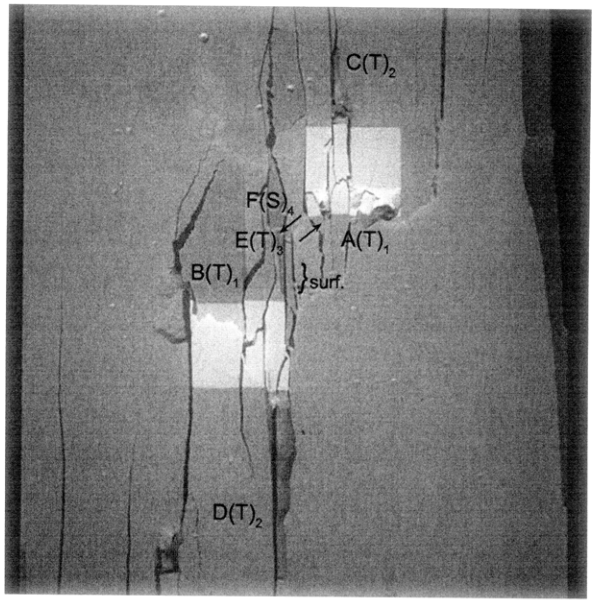

(Recorded by High Speed Video System)

(0 MPa) – Final Picture

Time: 5 minutes & 24.706 seconds

HS Image # - 179

	Upper edge of the specimen. The cracks marked with a (*) coincide with the openings between the teeth of the brush platen.
	Lower edge of the specimen. The cracks marked with a (*) coincide with the openings between the teeth of the brush platen.

SUMMARY

Specimen Number: SQ(PI)-75-0C (20090213)

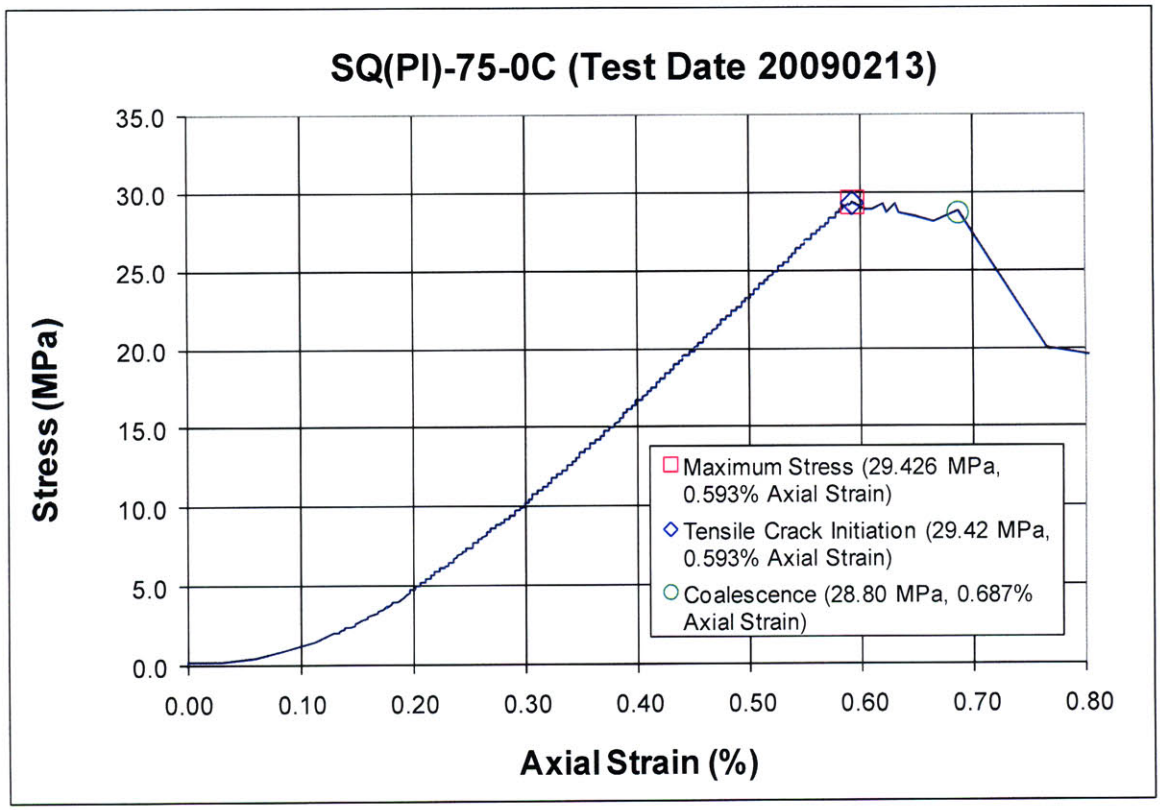

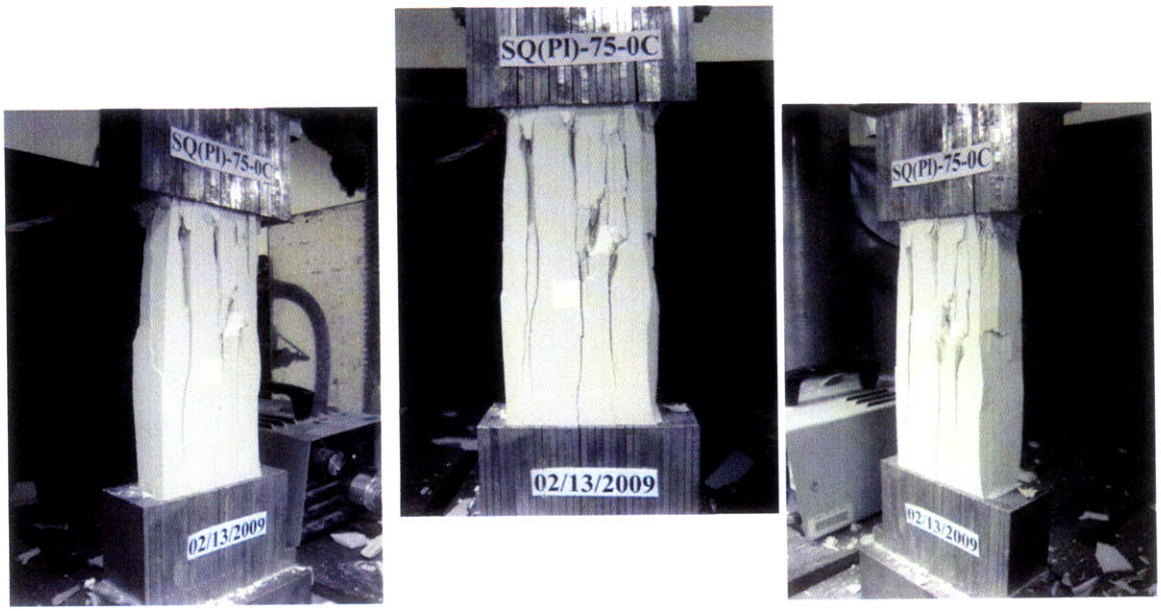

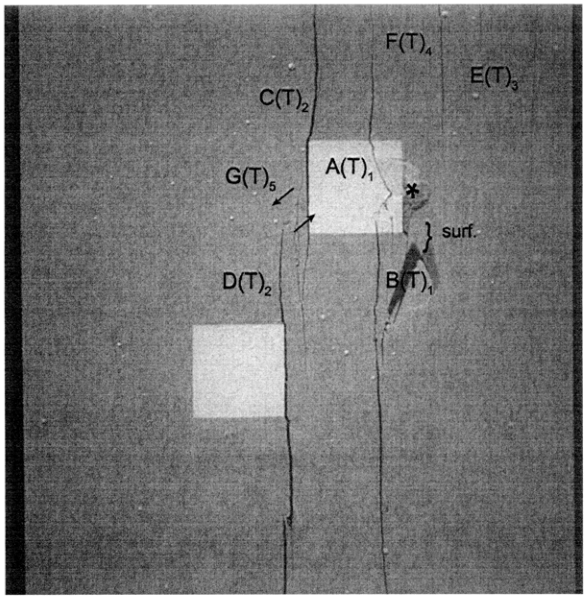

(Recorded by High Speed Video System)

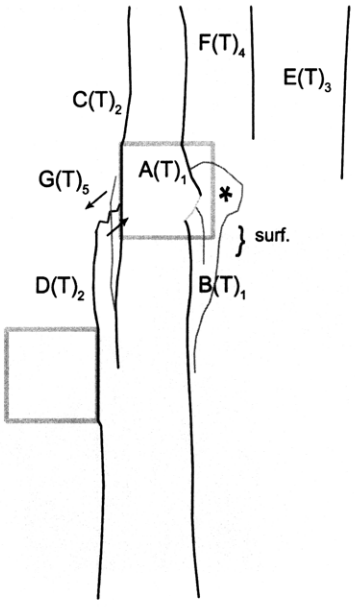

(28.80 MPa) – Coalescence
Time: 6 minutes & 9.290 seconds
HS Image # - 3037

The propagation of surface crack (surf.) results in the detachment (*) of a surficial piece of specimen.

Shear crack (G) then initiates at the tip of tensile crack (D) and propagates upwards, until its coalescence with the right-hand inclusion boundary.

Specimen Number: SQ(UI)-75-0A (20090213)

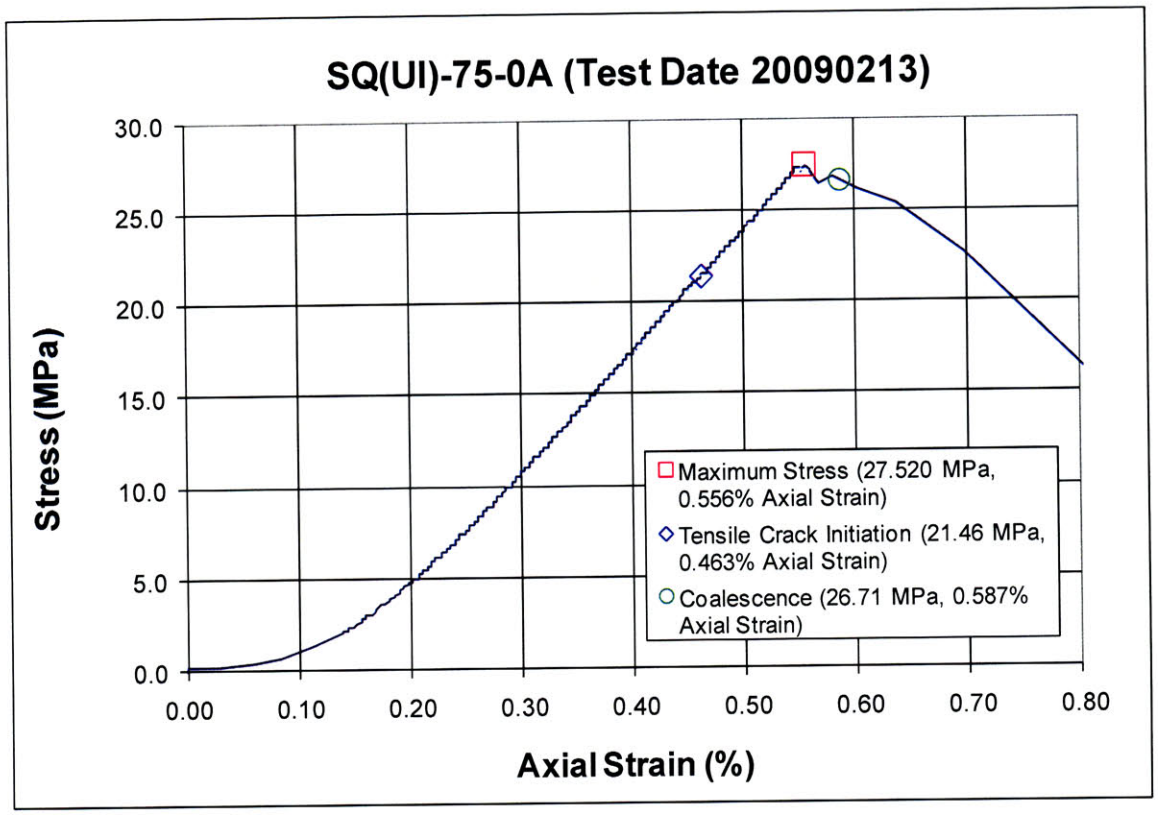

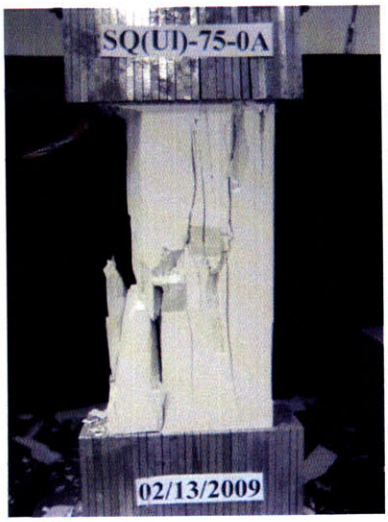

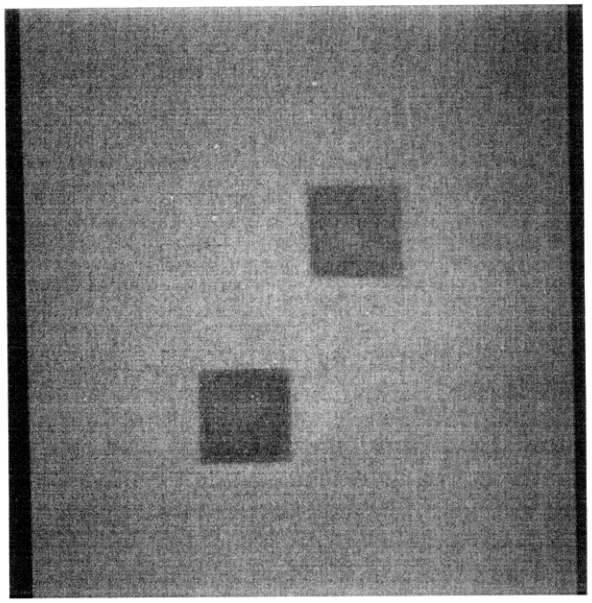

(Recorded by High Speed Video System)

Initial Inclusion Geometries:
SQUARE – Ultracal Material

Inclusions **more** stiff than matrix.

Pre-test surface crack located within right-hand inclusion.

High Speed Camera Frame Rate:
5000 pps

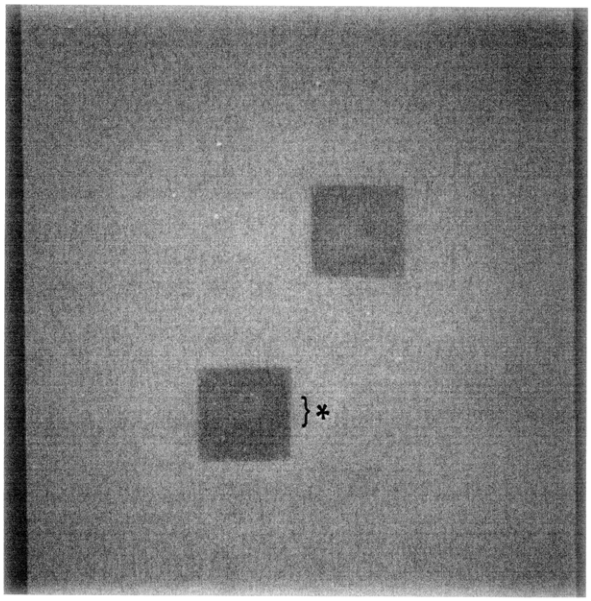

(Recorded by High Speed Video System)

(18.85 MPa)
Time: 3 minutes & 37.31 seconds

Debonding (*) initiates at the left-hand inclusion boundary.

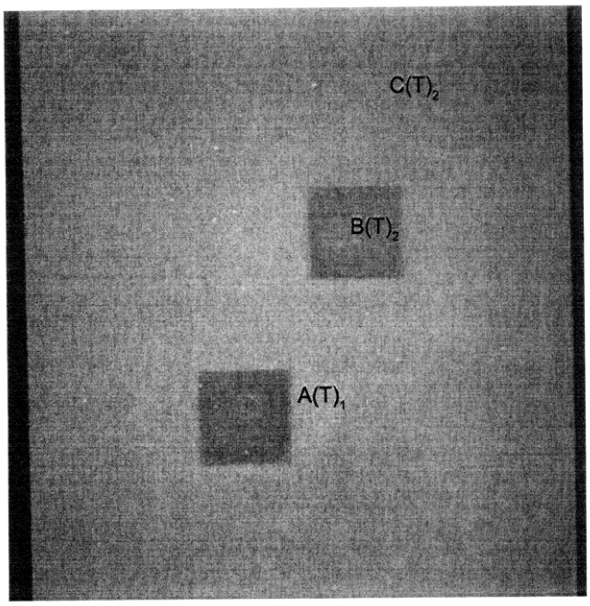

(Recorded by High Speed Video System)

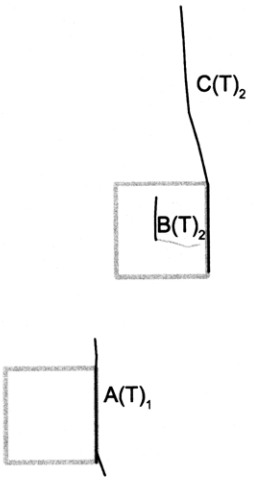

(21.46 MPa)

- Tensile Crack Initiation

Time: 4 minutes & 13.66 seconds

Tensile crack (A) initiates at the left-hand inclusion boundary and propagates upwards and downwards.

Tensile crack (B&C) then initiate. Tensile crack (B) initiates at the pre-test surface crack located within the right-hand inclusion. Tensile crack (C) initiates at the right-hand inclusion boundary, where debonding occurred, and propagates upwards.

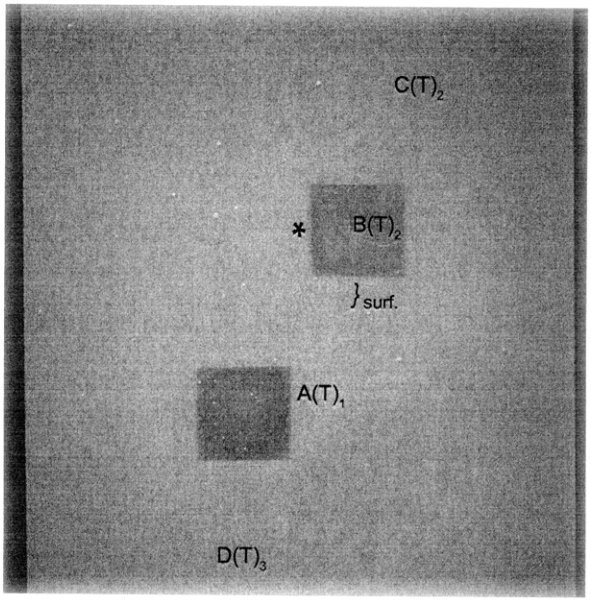

(Recorded by High Speed Video System)

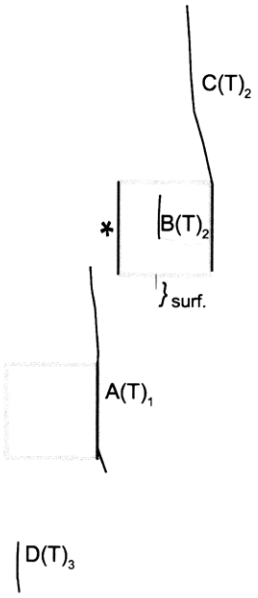

(23.12 MPa)
Time: 4 minutes & 37.27 seconds

Tensile crack (D) initiates at the lower specimen boundary and propagates upwards.

Surface crack (surf.) then initiates at the lower boundary of the right-hand inclusion and propagates downwards, while debonding (*) initiates at the right-hand inclusion.

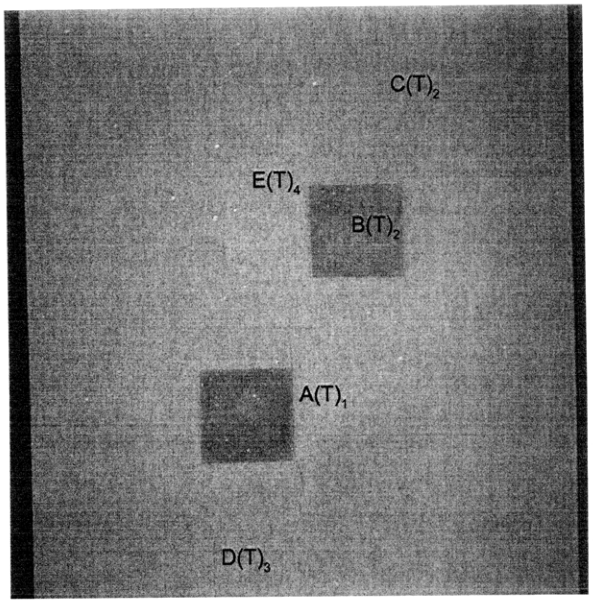

(Recorded by High Speed Video System)

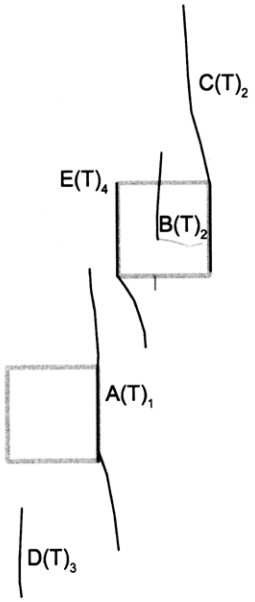

(23.71 MPa)
Time: 4 minutes & 45.44 seconds

Tensile crack (E) initiates at the right-hand inclusion boundary and propagates downwards.

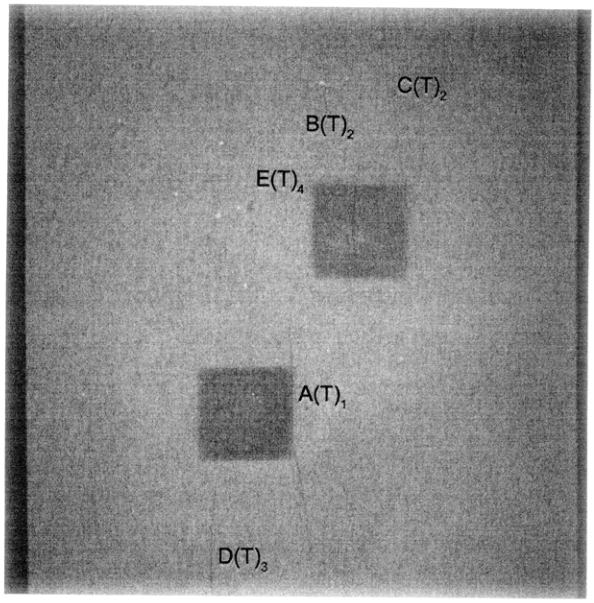

(Recorded by High Speed Video System)

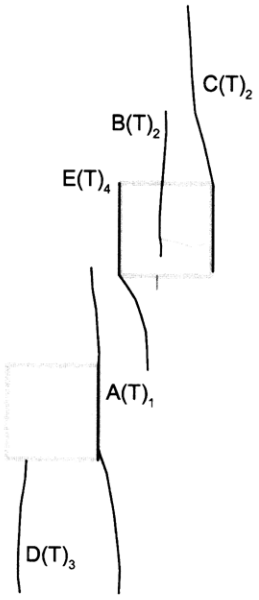

(27.31 MPa)
Time: 5 minutes & 35.84 seconds

Tensile crack (D) continues to propagate and coalesces with the lower left-hand inclusion boundary.

Tensile crack (B) also begins to propagate downwards from its initiation point at the pre-test surface crack.

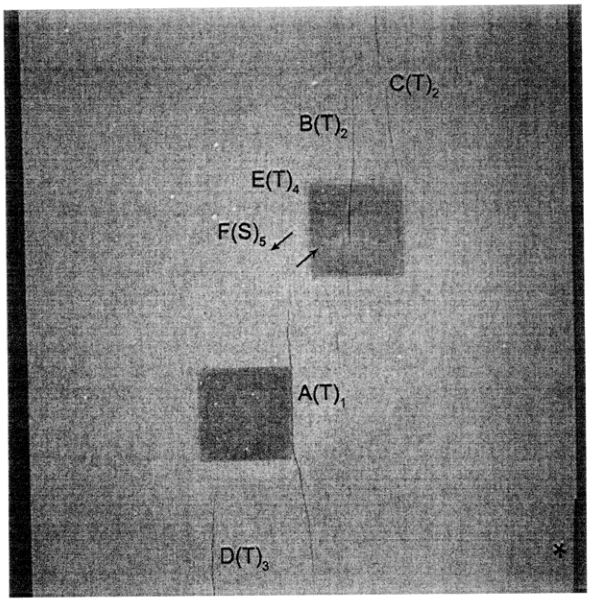

(Recorded by High Speed Video System)

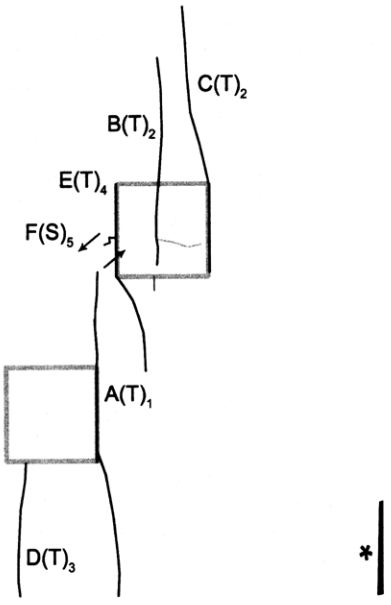

(27.520 MPa) [Max. Stress]
Time: 5 minutes & 38.83 seconds

Shear crack (F) initiates at the right-hand inclusion boundary and propagates downwards towards tensile crack (A).

A small piece of specimen then detaches (*) from the lower right specimen boundary.

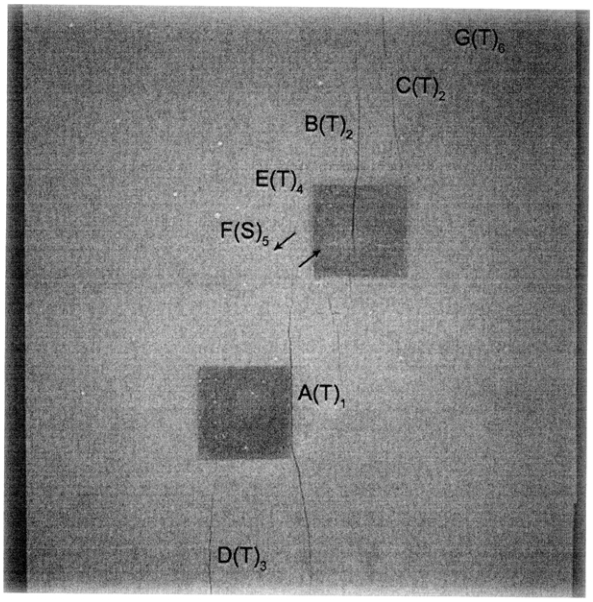

(Recorded by High Speed Video System)

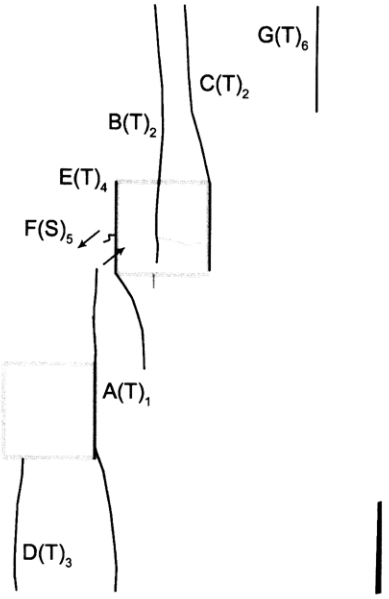

(26.68 MPa)
Time: 5 minutes & 39.162 seconds
HS Image # - 4957

Tensile crack (G) initiates at the upper specimen boundary and propagates downwards.

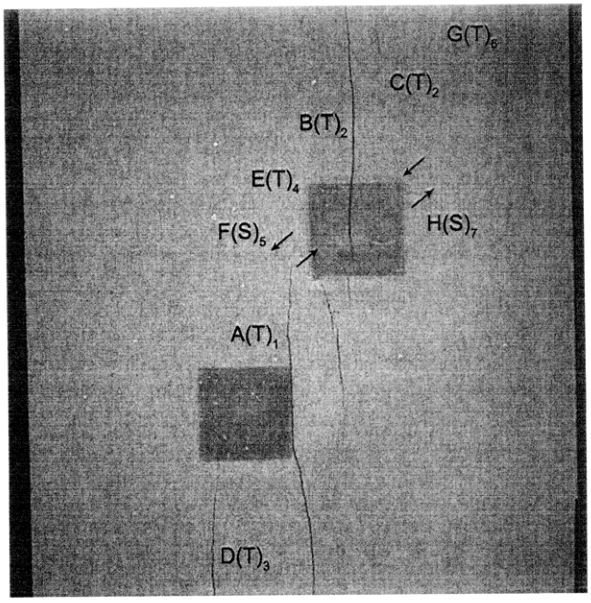

(Recorded by High Speed Video System)

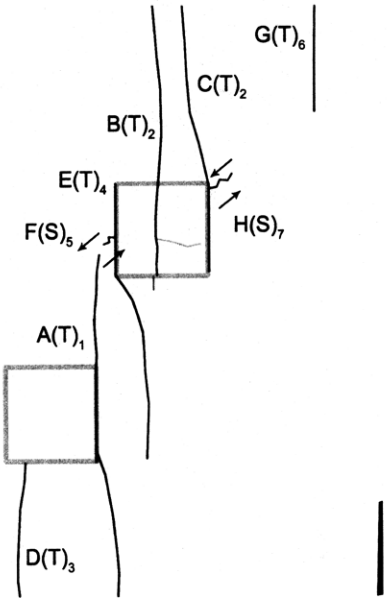

(26.84 MPa)
Time: 5 minutes & 39.235 seconds
HS Image # - 4593

Shear crack (H) initiates at the right-hand inclusion boundary and propagates upwards.

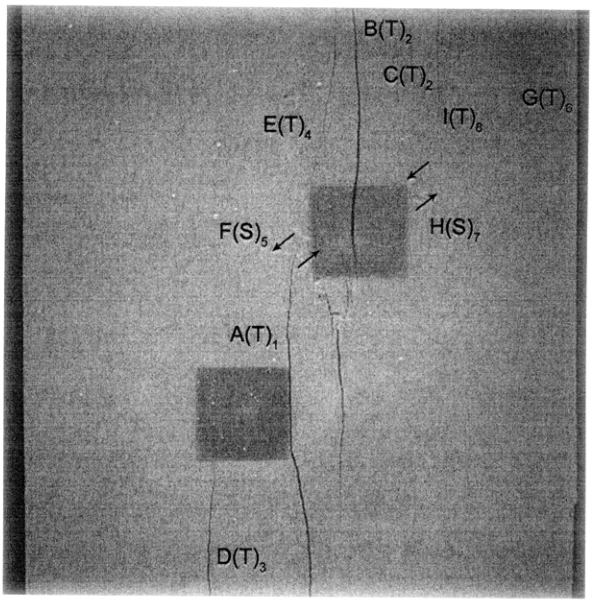

(Recorded by High Speed Video System)

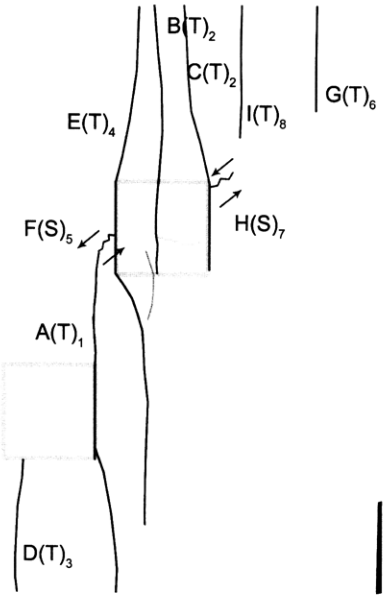

(26.71 MPa) – Coalescence
Time: 5 minutes & 39.254 seconds
HS Image # - 4496

Tensile crack (I) initiates at the upper specimen boundary and propagates downwards.

Shear crack (F) continues to propagate until its coalescence with tensile crack (A). This results in the upwards propagation of tensile crack (E), as well as, the increase in aperture of tensile cracks (A&B).

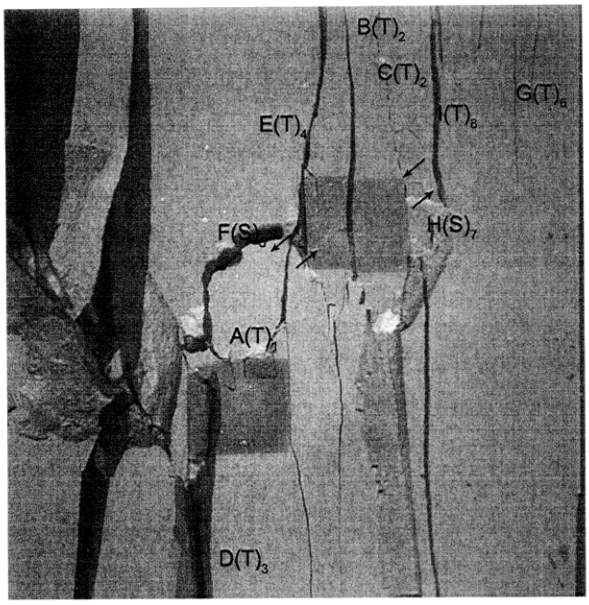

(Recorded by High Speed Video System)

(0 MPa) – Final Picture

Time: 5 minutes & 40.153 seconds

HS Image # - 1

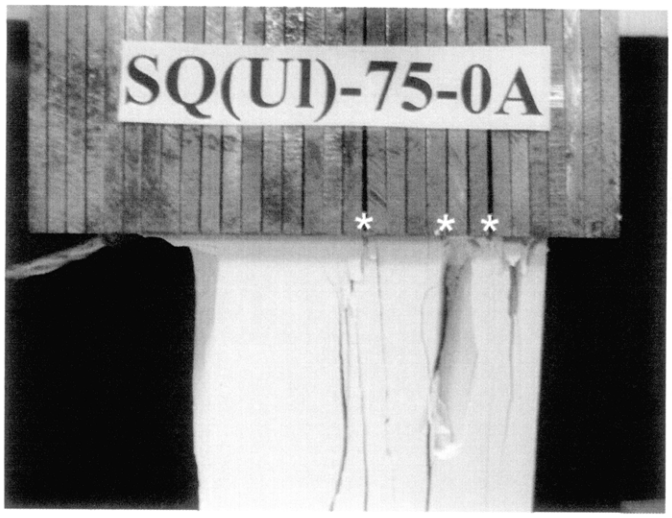	Upper edge of the specimen. The cracks marked with a (*) coincide with the openings between the teeth of the brush platen.
	Lower edge of the specimen. The cracks marked with a (*) coincide with the openings between the teeth of the brush platen.

SUMMARY

Specimen Number: SQ(UI)-75-0B (20090213)

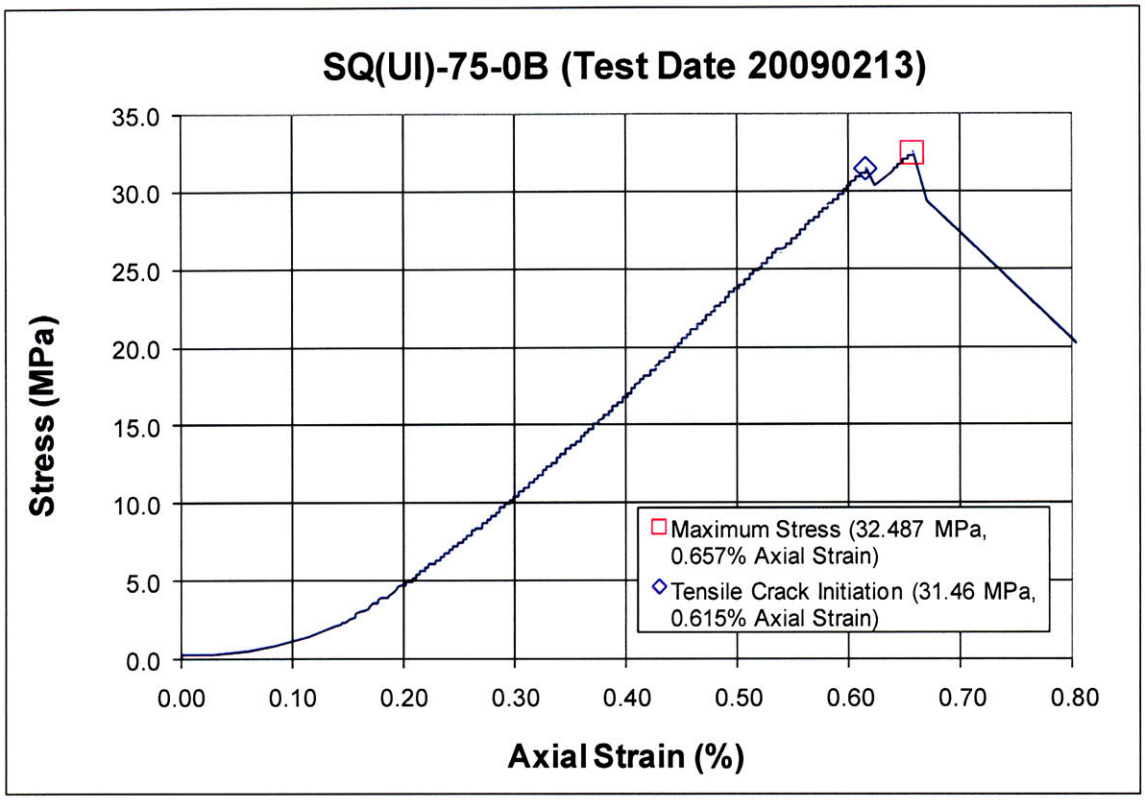

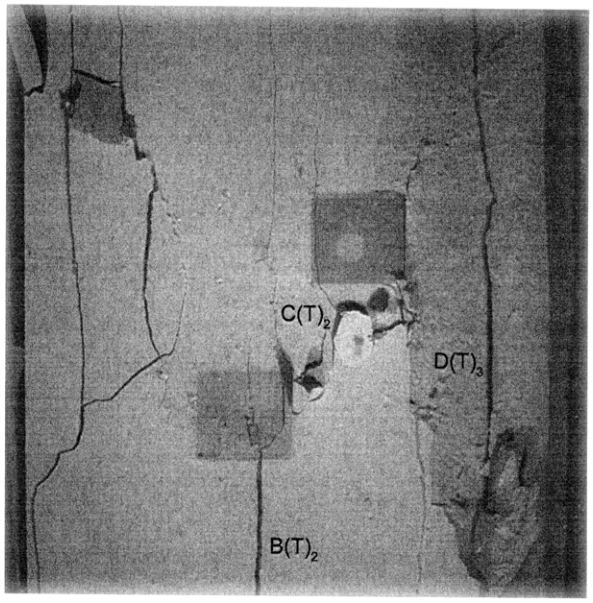

(Recorded by High Speed Video System)

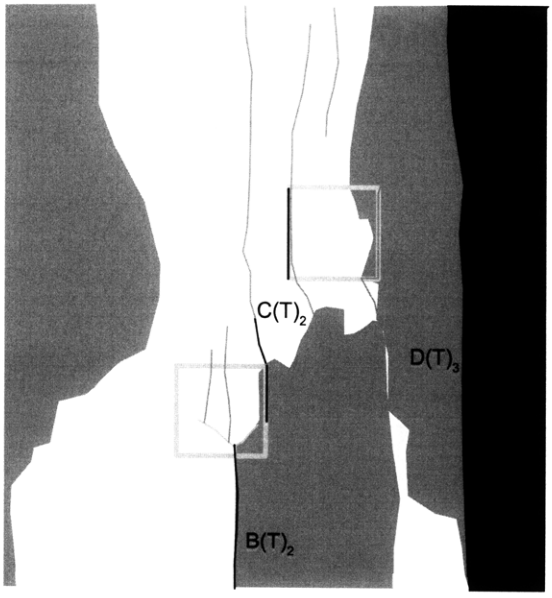

(22.29 MPa)
Time: 6 minutes & 53.847 seconds
HS Image # - 3157

An extensive amount of surficial detachment occurs throughout the specimen.

SUMMARY

Specimen Number: SQ(UI)-75-0C (20090213)

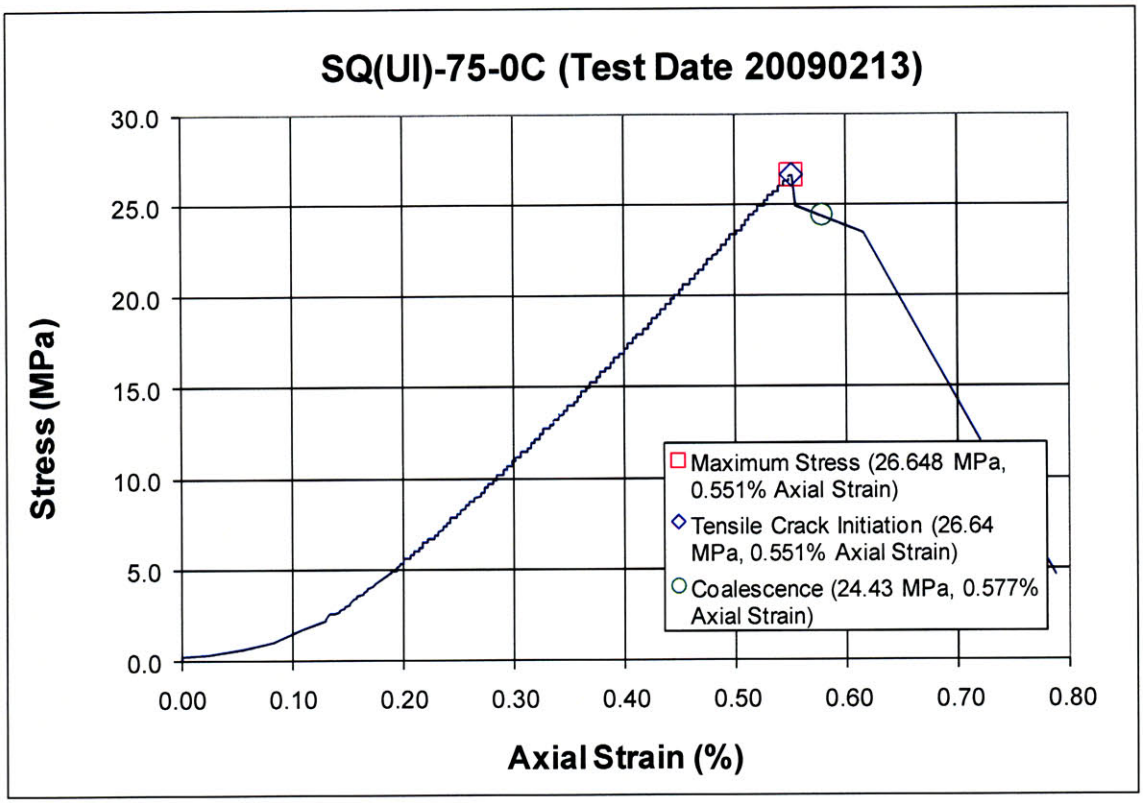

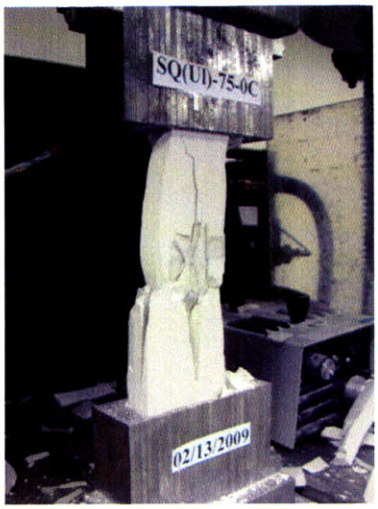

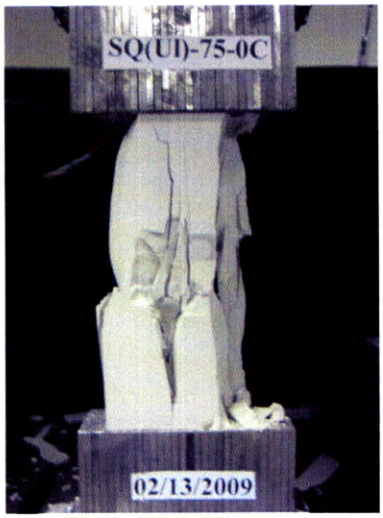

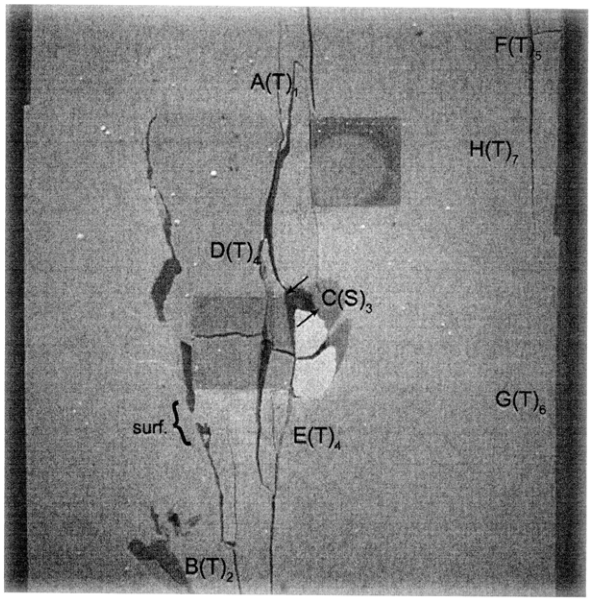

(Recorded by High Speed Video System)

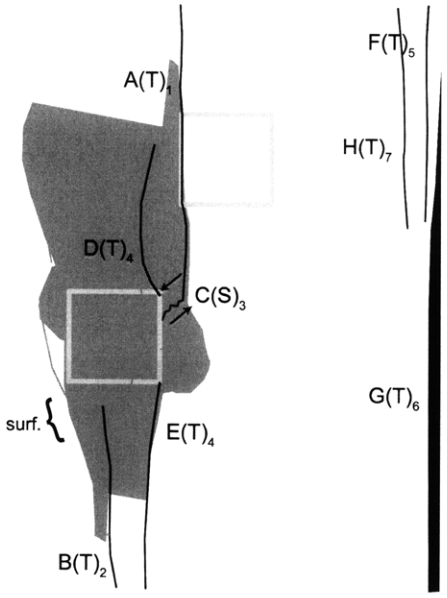

(23.95 MPa)
Time: 5 minutes & 27.469 seconds
HS Image # - 2524

An extensive amount of surficial detachment occurs at the region of the left-hand inclusion.